НАЦІОНАЛЬНА АКАДЕМІЯ НАУК УКРАЇНИ
ІНСТИТУТ ФІЗІОЛОГІЇ ім. О.О. БОГОМОЛЬЦЯ

Кваліфікаційна наукова
праця на правах рукопису

ШКРИЛЬ В'ЯЧЕСЛАВ МИХАЙЛОВИЧ

УДК 577.352:546.41

ДИСЕРТАЦІЯ

РІАНОДИН РЕЦЕПТОР ОПОСЕРЕДКОВАНА КАЛЬЦІЄВА СИГНАЛІЗАЦІЯ В М'ЯЗОВИХ І НЕРВОВИХ КЛІТИНАХ

03.00.02 – Біофізика

Подається на здобуття наукового ступеня доктора біологічних наук

Дисертація містить результати власних досліджень. Використання ідей, результатів і текстів інших авторів мають посилання на відповідне джерело

В.М. Шкриль

Науковий консультант: Лук'янець Олена Олександрівна

доктор біологічних наук, професор

Київ – 2024

АНОТАЦІЯ

Шкриль В.М. Ріанодин рецептор опосередкована кальцієва сигналізація в м’язових і нервових клітинах. - Кваліфікаційна наукова праця на правах рукопису за сукупністю наукових статей.

Дисертація на здобуття наукового ступеня доктора біологічних наук за спеціальністю 03.00.02 – біофізика – Інститут фізіології ім. О.О. Богомольця НАН України, Київ, 2024.

У роботі представлені результати комплексного дослідження клітинних та молекулярних механізмів, які беруть участь у регуляції внутрішньоклітинної кальцієвої сигналізації у м’язових і нервових клітинах шляхом вивчення ролі ріанодинових рецепторів (RyRs). Ці рецептори відповідають за вивільнення кальцію з сарко/ендоплазматичного ретикулуму в цитозоль. Процес вивільнення кальцію з депо має велике значення для функціонування м'язів і нервової системи.

На локальному рівні активність RyRs реєструється як кальцієві спалахи, які розглядалися як локальні зміни концентрації кальцію під час його вивільнення з саркоплазматичного ретикулуму (СР) внаслідок одночасного відкриття декількох RyRs. Розуміння динаміки Ca^{2+} спалахів є важливою для кальцієвої сигналізації. Численні експериментальні, комп’ютерні та біофізичні дослідження були спрямовані на вивчення механізмів ініціації, припинення та регуляції кальцієвих спалахів. Розуміння ролі як спалахів, так і роботи залучених RyRs на рівні регуляції та динаміки кальцієвого сигналу у нормі та патології слугує основою для з’ясування функціональних змін Ca^{2+} сигналу на клітинному або субклітинному рівнях.

Актуальність досліджень ріанодинових рецепторів в кальцієвій сигналізації полягає в тому, що вони є потенційними мішенями для розвитку нових ліків від різних захворювань, пов'язаних з порушенням кальцієвої концентрації в клітинах. Наприклад, деякі хвороби м'язів, такі як дистрофія скелетних м’язових волокон, аритмії серця, а також нейродегенеративні захворювання, можуть бути пов'язані зі зміною функціональності RyRs.

Для детального дослідження ріанодин рецептор опосередкованої кальцієвої сигналізації було застосовано наступні біофізичні методики: епіфлуоресценція та конфокальна мікроскопія з використанням кальцій-чутливих флуоресцентних барвників для визначення динаміки концентрації кальцію; метод петч-клемп для реєстрації трансмембранних Ca^{2+} струмів; локальне вивільнення зв'язаного кальцію під час фотолізного спалаху з кальцієвого буфера; комп'ютерне моделювання та обробка кальцієвих сигналів для розрахунку кальцієвих потоків; статистична обробка отриманих результатів.

У даному дослідженні властивості кальцієвих спалахів у кардіоміоцитах передсердь були вперше досліджені за допомогою чотиривимірної конфокальної мікроскопії. Були запропоновані алгоритми для виявлення спалахів Ca^{2+} у місці вивільнення. Попередньо під час конфокального сканування ліній або площини клітини спонтанні Ca^{2+} спалахи реєструвалися розфокусованими, оскільки місце їхнього виникнення невідомо. В даній роботі зареєстровані спалахи, які знаходилися в місці вивільнення, мали вищу амплітуду порівняно з іншими розфокусованими спалахами. Було показано, що амплітуда Ca^{2+} спалахів зареєстрованих у місці вивільнення мали модальний розподіл. Струм вивільнення Ca^{2+}, що лежить в основі такого спалаху, становив приблизно 11 пА, що свідчить про активність між 20 та 30 відкритими RyRs. Ця методика дозволяє досліджувати RyRs, визначати потік вивільнення з великою достовірністю, що дає можливості використати її для фармакологічних досліджень ріанодинових рецепторів.

Для детального вивчення динаміки кальцію в кардіоміоцитах із високою часовою роздільною здатністю була застосована методика надшвидкісної конфокальної візуалізації. Це дозволило виявити ступінчасту кінетику зростаючої фази спалахів Ca^{2+}, та підтвердити участь групи каналів RyRs. Двовимірна реєстрація транзієнтів Ca^{2+} в міоцитах шлуночка демонструє асинхронну активацію сайтів вивільнення, при відкритті RyRs. З латентністю в 2.5 мс після подачі електричного стимулу спостерігався вхід Ca^{2+}, який супроводжувався вивільненням Ca^{2+} з СР з додатковою затримкою в 3 мс. Пік вивільнення Ca^{2+} спостерігався через 4 мс після його початку. Показано, що динаміку збільшення Ca^{2+}, який входить у кардіоміоцит та кальцій-індукованого вивільнення кальцію можливо достовірно розділити на рівні окремих центрів вивільнення кальцію як у клітинах передсердя, так і у шлуночків міокарда, як у часі, так і просторі.

Було отримано перші прямі докази того, що в міоцитах передсердь зміна кінетики реституції вивільнення Ca^{2+} з саркоплазматичного ретикулуму від стимулу до стимулу є ключовим причинним механізмом виникнення Ca^{2+}-альтернацій, як важливий механізм утворення серцевої аритмії. Показано, що просторово обмежене фотовивільнення Ca^{2+} та інозитол-3-фосфату дозволяє регулювати активність RyRs через механізм кальцій-індукованого вивільнення кальцію (CICR). Це додатково може допомогти вивчити альтернації серця, та надає можливості розробки нових стратегій лікування аритмій серця.

В даній роботі було ідентифіковано мікродомени в скелетних м'язах, де кальцій, що вивільняється з СР, має прямий доступ до мітохондрій. Була виявлена кореляція між активністю RyRs та окислювально-відновним потенціалом мітохондрій у клітинах скелетних м'язів, як фактор появи спонтанних кальцієвих спалахів. Встановлено, що активні форми кисню можуть регулювати RyRs та вивільнення Ca^{2+} із СР. Надмірне утворення ROS та аномальні сигнали Ca^{2+} в дистрофічних скелетних м'язах є взаємопов'язаними явищами, утворюючи порочне коло шкідливих подій, які сприяють аномальній чутливості при осмотичному стресі. Було виявлено значно збільшену експресію NAD(P)H-оксидази у скелетних м'язах миші лінії mdx, що сприяло підвищеному утворенню ROS. При осмотичному шоці, додатково відбувається збільшення мітохондріального кальцію та посилення утворення мітохондріального ROS в mdx скелетних м’язових волокнах порівняно з нормальними.

Кальцій-індуковане вивільнення кальцію, яке відбувається через активацію RyRs кальцієм, було досліджено за допомогою методу штучного локалізованого підвищення концентрації кальцію (SLICs) на м'язових волокнах амфібій та ссавців. В скелетних м'язових клітинах жаби SLICs індукували CICR-відповіді з пороговим значенням [Ca^{2+}] для ініціації реакції на рівні 0.5 мкМ, підтверджуючи роль CICR за фізіологічних умов у скелетних м'язах амфібій. Проте у скелетних м'язових волокнах миші було зафіксовано, що RyRs не активуються при концентрації кальцію аж до 8 мкМ. Це, разом з високим пороговим значенням активації RyRs, може пояснювати слабку реакцію вивільнення кальцію, навіть за умов, що агенти, які активують RyRs, були присутні в великих концентраціях. Це суперечить гіпотезі про фізіологічну роль CICR у механізмі збудження-скорочення у скелетних м’язах ссавців.

Дослідження ролі ріанодинових рецепторів у регуляції внутрішньоклітинного кальцієвого сигналу в пірамідних нейронах гіпокампу показало, що відповіді на електричну стимуляцію включають в себе кальцієві сигнали, подібні до тих, що спостерігаються в міоцитах передсердь. Аналіз показав асинхронний та затриманий ріст концентрації вільного кальцію в окремих ділянках нейрона. Було зафіксовано затримку у зростанні концентрації вільного Ca^{2+} в центральній ділянці порівняно з примембранними ділянками та дендритного дерева. Активація ріанодинових рецепторів за допомогою кофеїну призводила до швидкого збільшення $[Ca^{2+}]$ у примембранній зоні, дендритному дереві та центральній ділянці. Більш коротка електрична стимуляція не викликала збільшення сигналу Ca^{2+} через кальцій-індуковане вивільнення кальцію. Для вивільнення кальцію з ендоплазматичного ретикулуму через RyRs була необхідна тривала електрична стимуляція.

Порушення регуляції функції RyRs пов'язане з різними захворюваннями, і розуміння механізмів, які регулюють активність RyRs, має вирішальне значення для розробки терапевтичних стратегій. Результати цього дослідження не тільки поглиблять наше розуміння фундаментальних принципів внутрішньоклітинної Ca^{2+} сигналізації, але надають уявлення про молекулярну основу різних захворювань, пов'язаних з дисфункцією RyRs.

Був запропонований новий метод просторової, складної, дифракційно-обмеженої фотоактивації та фотовивільнення в живих клітинах. Така методика дозволяє локально активувати окремі сайти вивільнення кальцію або групу RyRs каналів у живих клітинах, що може бути використано для вивчення їхніх структурних і функціональних деталей з високою точністю.

Також була адаптована та модифікована формула Грінкевича для визначення вмісту вільного кальцію в клітині при двох хвильовому методі збудження

флуоресцентного барвника, при використанні для реєстрації сигналів ПЗЗ камерою. Адаптація включає в себе корекцію фотознебарвнення та виправлення помилки віднімання фону. Також був розроблений підхід, який розширює чутливість кількісної концентраційної візуалізації до приблизно 1000-кратного діапазону концентрацій і з необхідними рівняннями для інтерпретації флуоресцентних зображень, отриманих за допомогою пари флуоресцентних барвників з однаковим флуорофором, але різною константою дисоціації для кальцію.

Отримані дані щодо змін внутрішньоклітинної концентрації кальцію в м’язових і нервових клітинах, вказують на складний процес регуляції кальцієвого сигналу. Мітохондрія, залежно від її функціональної близькості до СР, бере активну участь у регуляції внутрішньоклітинної концентрації кальцію і може модулювати активність RyRs через механізми, що включають АТФ і ROS. Регуляція кальцієвого сигналу відбувається завдяки змінам активності ріанодинових рецепторів, які модифікують своє функціонування через зміну окислювально-відновного потенціалу мітохондрій, впливу активних форм кисню, NAD(P)H-оксидази, а також в залежно від їхнього функціонального розташування на периферії або в центрі клітини, і модуляцію самим кальцієм.

Ключові слова: *кальцій, мембранний транспорт, ріанодинові рецептори, кальцієві канали L-типу, мітохондрії, АТФ,* Ca^{2+} *та* Mg^{2+}*-ATPase, активні форми кисню, окиснювальний стрес, м'язи, кардіоміоцити, нейрони, петч-клемп, мікроскопія.*

SUMMARY

Shkryl V.M. Ryanodine receptor-mediated calcium signaling in muscle and nerve cells. – Collection of scientific manuscripts.

The thesis focuses on conducting a comprehensive investigation into the cellular and molecular mechanisms involved in the regulation of intracellular calcium signaling in muscle and nerve cells by examining the role of ryanodine receptors (RyRs). These receptors are responsible for the release of calcium from the sarco/endoplasmic reticulum into the cytosol. The process of releasing calcium from the store is essential for the functioning of muscles and the nervous system.

At the local level, RyRs activity visible as calcium sparks, which are regarded as localized fluctuations in calcium concentration resulting from its release from the sarcoplasmic reticulum (SR) due to the simultaneous opening of multiple RyRs. Understanding the dynamics of Ca^{2+} sparks is crucial for comprehending calcium signaling. Numerous experimental, computational, and biophysical studies have been conducted to investigate the mechanisms underlying the initiation, termination, and regulation of calcium sparks. Understanding the role of both sparks and the involving of RyRs in regulating the dynamics of calcium signaling in both normal and pathological conditions provides a foundation for elucidating functional changes in Ca^{2+} signaling at the cellular or subcellular levels.

The relevance of research on ryanodine receptors (RyRs) in calcium signaling lies in their potential as targets for the development of novel drugs aimed at treating various diseases linked to disrupted calcium concentration within cells. For instance, conditions such as muscle fiber dystrophy, cardiac arrhythmias, and neurodegenerative diseases may be associated with alterations in RyRs functionality.

To address these research objectives, a range of biophysical techniques were employed. These methods include epifluorescence and confocal microscopy, employing calcium-sensitive fluorescent dyes to monitor changes in calcium concentration. Additionally, the patch clamp method was utilized for recording transmembrane Ca^{2+} currents. Localized calcium release from calcium buffers was induced through flash photolysis. The research also involved computer modeling and calcium signal processing to calculate calcium fluxes; the numerical results underwent statistical analysis and processing.

In the present study, the properties of calcium sparks in atrial cardiomyocytes were first investigated using four-dimensional confocal microscopy. Algorithms have been proposed to detect Ca^{2+} sparks at the site of release. Previously, during confocal scanning of lines or planes, Ca^{2+} sparks obtained almost unfocused because their origin was unknown. In the present study, the recorded sparks located at the site of release of calcium had a higher amplitude compared to other unfocused spikes. It was shown that the amplitude of Ca^{2+} sparks recorded in focus had a modal distribution. The underlying Ca^{2+} release current was approximately 11 pA, indicating activity between 20 and 30 open RyRs. This technique enables the precise study of RyRs and the determination of release flux with high accuracy, thereby facilitating its application in pharmacological investigations of ryanodine receptors.

For a detailed investigation of calcium dynamics in cardiomyocytes with high temporal resolution, we employed the technique of ultrafast confocal imaging. This method enabled us to uncover the stepwise kinetics of the rising phase of Ca^{2+} sparks, confirming the involvement of RyRs channel groups. Two-dimensional recording of Ca^{2+} transients in ventricular myocytes demonstrates asynchronous activation of release sites upon opening of RyRs. Ca^{2+} entry occurred with a latency of 2.5 ms after the electrical stimulus, followed by Ca^{2+} release from the SR with an additional delay of 3 ms. The peak of Ca^{2+} release was noted 4 ms after its initiation. It has been shown that the dynamics of Ca^{2+} influx into the cardiomyocyte and calcium-induced calcium release (CICR) can be reliably separated at the level of individual calcium release sites in both atrial and ventricular myocardial cells, both in time and space.

Furthermore, we obtained the first direct evidence that the state of ryanodine receptors in atrial cardiomyocytes influences calcium alternans. Our findings demonstrated that beat-to-beat alternation of the time-dependent restitution properties and refractory kinetics of the SR Ca^{2+} release mechanism represents a key mechanism underlying cardiac alternans. The spatially limited photorelease of Ca^{2+} and inositol 3-phosphate allows the regulation of RyRs activity through the CICR mechanism. Additionally, it can help to study cardiac alternatives and provides opportunities to develop new strategies for the treatment of cardiac arrhythmias.

In this study, we have identified microdomains within skeletal muscle where calcium has direct access to mitochondria upon release from the SR. We found a correlation between the activity of RyRs, as evidenced by the occurrence of spontaneous calcium sparks, and the mitochondrial redox potential in skeletal muscle cells. Our investigations revealed that the appearance of calcium sparks in permeabilized muscle fibers is contingent upon the balance between mitochondrial production of reactive oxygen species (ROS) and the cellular scavenging mechanisms for these species.

Further studies have demonstrated that ROS can induce aberrant RyRs activity in intact skeletal cells, leading to the emergence of calcium sparks at the cell's periphery under osmotic stress. Excessive production of ROS and abnormal Ca^{2+} signaling in dystrophic skeletal muscle are interconnected, forming a vicious cycle of harmful events that contribute to abnormal sensitivity during osmotic stress. A significantly increased expression of NAD(P)H oxidase was found in the skeletal muscles of mdx mice, contributing to elevated ROS production. Under osmotic shock, there is an additional increase in mitochondrial calcium and heightened mitochondrial ROS production in mdx skeletal muscle fibers compared to normal ones, which amplifies abnormal Ca^{2+} signaling.

We investigated CICR, which occurs when RyRs are activated by calcium, using the synthetic localized increase in calcium concentration (SLICs) method in both amphibian and mammalian skeletal muscle fibers. In frog muscle cells, SLICs induced CICR responses with a threshold $[Ca^{2+}]$ value of 0.5 μM, confirming the role of CICR under physiological conditions in amphibian skeletal muscle. However, in mouse muscle fibers, we observed that RyRs were not activated even at a concentration of up to 8 μM. This high threshold value for the activation of RyRs by Ca^{2+} suggests a limited calcium release response unless agents capable of activating RyRs are present in substantial concentrations. These findings raise questions about the hypothesis concerning the physiological role of CICR in the excitation-contraction mechanism in mammalian skeletal muscle. In summary, calcium-induced calcium release appears to contribute to the physiological release of calcium ions in frog but not in mouse skeletal muscles.

In hippocampal pyramidal neurons, Ca^{2+} responses to electrical stimulation were found to be similar to those observed in atrial myocytes. Our analysis revealed an asynchronous and delayed increase in free calcium concentration in specific areas of the neuron. The central area exhibited a delay in the rise of free Ca^{2+} concentration compared to the membrane areas and dendritic tree. Activation of ryanodine receptors by caffeine resulted in a rapid increase in $[Ca^{2+}]$ in the membrane zone, dendritic tree and central region. Additionally, we identified conditions that promote the release of calcium from the endoplasmic reticulum through the CICR mechanism. It was observed that short-term electrical stimulation did not enhance the Ca^{2+} signal through calcium-induced calcium release, while longer stimulation was sufficient to trigger calcium release from the endoplasmic reticulum via RyRs.

Dysregulation of RyRs function is implicated in various diseases, emphasizing the importance of comprehending the mechanisms governing RyRs activity for the development of therapeutic interventions. The findings of this study will not only enhance our understanding of the fundamental principles of intracellular Ca^{2+} signaling but also shed light on the molecular underpinnings of diverse diseases linked to RyRs dysfunction.

A novel method for spatially complex, diffraction-limited photoactivation and photorelease in living cells has been introduced. This innovative technique enables the localized activation of individual calcium release sites or a cluster of RyRs channels within living cells, facilitating the study of their structural and functional intricacies with exceptional precision.

The Grynkiewicz formula for determining the free calcium concentration within a cell through the two-wave method of fluorescent dye excitation has been adapted and refined to image by a CCD camera. This adaptation incorporates corrections for photobleaching and addresses errors in background subtraction. Furthermore, an approach has been devised to extend the sensitivity of quantitative concentration imaging across an approximately 1000-fold concentration range. Equations necessary for interpreting fluorescence images acquired using a pair of fluorescent dyes with identical fluorophores but differing dissociation constants for calcium have also been provided.

The data obtained regarding changes in intracellular calcium concentration in muscle and nerve cells indicate a complex process of calcium signal regulation. Mitochondria, depending on their functional proximity to the SR, actively participate in the regulation of intracellular calcium concentration and modulate ryanodine receptor activity via mechanisms involving ATP and ROS. Regulation of calcium signaling is attributed to variations in the activity of ryanodine receptors, which adapt their functionality in response to alterations in mitochondrial redox potential, the influence of reactive oxygen species, NAD(P)H oxidase, and their specific subcellular localization—whether in the periphery or at the center of the cell. Furthermore, calcium itself plays a modulatory role in their function.

Keywords: *calcium, membrane transport, ryanodine receptors, L-type of* Ca^{2+} *channels, mitochondria, ATP,* Ca^{2+} *and* Mg^{2+}*-ATPase, reactive oxygen species, oxidative stress, muscle, cardiomyocytes, neurons, patch-clamp, microscopy.*

ПЕРЕЛІК НАУКОВИХ РОБІТ, ОПУБЛІКОВАНИХ ЗА ТЕМОЮ ДИСЕРТАЦІЇ

Основні наукові результати дисертації, опубліковані у фахових виданнях, віднесених до першого і другого квартилів (Q1 і Q2) відповідно до класифікацій SCImago Journal and Country Rank або Journal Citation Reports:

1. **SHKRYL, V. M.** 2022. The spatio-temporal properties of calcium transients in hippocampal pyramidal neurons in vitro. Front Cell Neurosci, 16, 1054950.
2. **SHKRYL, V. M.** 2020. Error correction due to background subtraction in ratiometric calcium measurements with CCD camera. Heliyon, 6, e04180.
3. FIGUEROA, L., **SHKRYL, V. M.**, BLATTER, L. A. & RÍOS, E. 2013. Using two dyes with the same fluorophore to monitor cellular calcium concentration in an extended range. PLoS One, 8, e55778. (Особисто дисертантом проведено експериментальні дослідження, статистичний аналіз, формулювання висновків та оформлення статті).
4. **SHKRYL, V. M.** & BLATTER, L. A. 2013. Ca(2+) release events in cardiac myocytes up close: insights from fast confocal imaging. PLoS One, 8, e61525. (Особисто дисертантом проведено експериментальні дослідження, їх аналіз та інтерпретування результатів, оформлення ілюстрацій та написання статті).
5. **SHKRYL, V. M.**, BLATTER, L. A. & RÍOS, E. 2012. Properties of Ca2+ sparks revealed by four-dimensional confocal imaging of cardiac muscle. J Gen Physiol, 139, 189-207. (Особисто дисертантом проведено експериментальні дослідження, їх аналіз та інтерпретування результатів та оформлення статті).
6. **SHKRYL, V. M.**, MAXWELL, J. T., DOMEIER, T. L. & BLATTER, L. A. 2012. Refractoriness of sarcoplasmic reticulum Ca2+ release determines Ca2+ alternans in atrial myocytes. Am J Physiol Heart Circ Physiol, 302, H2310-20. (Особисто дисертантом проведено частину експериментальна досліджень, статистичний аналіз, формулювання висновків та написання статті).
7. **SHKRYL, V. M.**, MAXWELL, J. T. & BLATTER, L. A. 2012. A novel method for spatially complex diffraction-limited photoactivation and photobleaching in living cells. J Physiol, 590, 1093-100. (Особисто дисертантом проведено

експериментальні дослідження, їх аналіз та інтерпретування результатів, оформлення ілюстрацій та оформлення статті).

8. FIGUEROA, L., **SHKRYL, V. M.**, ZHOU, J., MANNO, C., MOMOTAKE, A., BRUM, G., BLATTER, L. A., ELLIS-DAVIES, G. C. & RÍOS, E. 2012. Synthetic localized calcium transients directly probe signalling mechanisms in skeletal muscle. J Physiol, 590, 1389-411. (Особисто дисертантом брав участь у складанні експериментальної установки, проводив частину експериментальна досліджень, статистичний аналіз, а також брав участь у оформлення статті).
9. **SHKRYL, V. M.**, MARTINS, A. S., ULLRICH, N. D., NOWYCKY, M. C., NIGGLI, E. & SHIROKOVA, N. 2009. Reciprocal amplification of ROS and Ca(2+) signals in stressed mdx dystrophic skeletal muscle fibers. Pflugers Arch, 458, 915-28. (Особисто дисертантом проведено конфокальні дослідження, їх аналіз та статистичний аналіз результатів, написання статті).
10. MARTINS, A. S. *, **SHKRYL, V. M.** *, NOWYCKY, M. C. & SHIROKOVA, N. 2008. Reactive oxygen species contribute to Ca2+ signals produced by osmotic stress in mouse skeletal muscle fibres. *J Physiol,* 586**,** 197-210. (Особисто дисертантом проведено конфокальні дослідження, їх аналіз та інтерпретування результатів, написання статті). (* перший автор)
11. **SHKRYL, V. M.** & SHIROKOVA, N. 2006. Transfer and tunneling of Ca2+ from sarcoplasmic reticulum to mitochondria in skeletal muscle. *J Biol Chem,* 281**,** 1547-54. (Особисто дисертантом проведено епіфлуоресценті та конфокальні дослідження, їх аналіз та інтерпретування результатів, оформлення ілюстрацій та написання статті).
12. ISAEVA, E. V.*, **SHKRYL, V. M.*** & SHIROKOVA, N. 2005. Mitochondrial redox state and Ca2+ sparks in permeabilized mammalian skeletal muscle. *J Physiol,* 565**,** 855-72. (Особисто дисертантом проведено конфокальні дослідження, їх аналіз та інтерпретування результатів, написання статті). (* перший автор)

Додатково наукові результати дисертації:

1. SHKRYL, V. M. 2017. Intracellular Calcium Fluxes in Excitable Cells. Neurophysiology, 49, 384-392.
2. SHKRYL, V.M. 2017. Основні принципи конфокальної мікроскопії кальцієвих сигналів. Біофізичний вісник, 2(38), 20-34. doi: 10.26565/2075-3810-2017-38-03.
3. ШКРИЛЬ, В.М. 2017. Спосіб визначення вмісту вільного кальцію в клітині при двохвильовому методі збудження флуоресцентного барвника. пат. 117834 Україна. № U 2017 00787. заявл. 30.01.2017 ; опубл. 10.07.2077, Бюл. № 13.
4. SHKRYL V.M., BLATTER L.A. 2020. Ca signaling during excitation-contraction coupling in cardiac myocytes. In: «Neurophysiological Essays of Platon Kostyuk and his Students» (Eds. Krishtal O.A., Lukyanetz E.A.). Akademperiodyka, Kyiv, p. 237-243. (Особисто дисертантом проведено аналіз даних літератури, оформлення ілюстрацій та написання статті).
5. ROZUMNA, N. M., SHKRYL, V. M., GANZHA, V. V. & LUKYANETZ, E. A. 2021. Effects of Modeling of Hypercalcemia and β-Amyloid on Cultured Hippocampal Neurons of Rats. *Neurophysiology (Ukraine),* 52**,** 348-357. (Особисто дисертантом проведено експериментальні дослідження, аналіз та інтерпретування отриманих результатів, оформлення статті).
6. SHKRYL, V. M., GANZHA, V. V. & LUKYANETZ, E. A. 2021. Effect of memantine on calcium signaling in hippocampal neurons cultured with β-amyloid. *Fiziologichnyi Zhurnal,* 67**,** 1-8. (Особисто дисертантом проведено експериментальні дослідження, аналіз та інтерпретування отриманих результатів, оформлення статті).
7. SHKRYL, V. M., TURYTSKA, T. G., YAVORSKY, V. A., LYASHENKO, V. P., LUKASHOV, S. M. & LUKYANETZ, E. A. 2021. Effect of caffeine and coffee diets on calcium signalling in rat hippocampal neurons. *Fiziologichnyi Zhurnal,* 67**,** 37-43. (Особисто дисертантом проведено експериментальні дослідження, аналіз та інтерпретування отриманих результатів, оформлення статті).

Наукові праці, які засвідчують апробацію матеріалів дисертації:

1. Hanzha V.V., Rozumna N.M. Shkryl V. M., Lukyanets O. O. 2023. The influence of dantrolene on hippocampal neurons in conditions of cultivation with amyloid-β. Збірник тез доповідей IX з'їзду Українського біофізичного товариства. С. 209-211.
2. Ганжа ВВ, Розумна НМ, Шкриль ВМ, Лук'янець ОО. 2022. Вплив дантролену на життєздатність нейронів культури гіпокампу щурів в умовах культивації з амілоїдом-β. Фізіол. журн., Т. 68(3S), С. 9.
3. Shkryl V. M., Ganzha V. V., Lukyanetz E. A. 2022. Influence of dantrolene on cytoplasmic calcium in hippocampal pyramidal neurons in vitro treated with amyloid-beta. Fiziologichnyi Zhurnal. T. 68(3S), C. 37.
4. Shkryl V.M. 2022. The spatio-temporal changes in the intracellular calcium level in the pyramidal hippocampal neurons. Fiziologichnyi Zhurnal. T. 68(3S), C. 47.
5. Ганжа ВВ, Шкриль ВМ, Розумна НМ, Лук'янець ОО. 2021. Дослідження впливу кальцію на життєздатність нейронів культури гіпокампу щурів в умовах культивації з Aβ-амілоїдом.// тези доповідей III науково-практичної конференції студентів та молодих вчених з міжнародною участю: «Від експериментальної та клінічної патофізіології до досягнень сучасної медицини і фармації».– Харків, 12 травня, С. 54.
6. Shkryl VM, Rozumna NM, Ganzha VV, Lukyanetz EA. 2021. Effects of hypercalcemia and β-amyloid on intracellular calcium concentration in hippocampal cultured neurons of rats. 42 Наукові читання імені О.О. Богомольця. 24 травня, 2021. – С. 107. DOI: 10.32345/conf.2021/NMU/Kyiv
7. Ганжа ВВ, Шкриль ВМ, Розумна НМ, Лук'янець ОО. 2021. Вплив мемантину на нейрони гіпокампу щурів при їх культивуванні з амілоїдом Aβ-1-42. // Мат. Всеукраїнської науково-практичної конференції перші читання присвячені Д.О.Альперну: «Актуальні питання патологічної фізіології». – Харків, 26 березня, 2021. – С. 41-42.
8. Шкриль ВМ, 2019. Вивільнення іонів кальцію з внутрішнього депо в збудливих клітинах. Фізіол. журн., Т. 65(3), 37-38

9. Lukyanetz EA, Chopovska VV, Kravenska EV, Yavorskaya EN, Shkryl VM. 2014. Effect of β-amyloid on calcium signaling in rat hippocampal neurons. Programme book of 9th FENS Forum of Neuroscience, Milan, Italy, July 5-9 2014, Abstract Number: FENS-2031 p. 320
10. Kysilov BA, Shkryl VM, Lukyanetz EA. 2013. Changes in calcium homeostasis in cultured hippocampal rat neurons under action of beta-amyloid. Kiev Taras Shevchenko symposium for young scientist.
11. Блашкив Т.В., Шкрыль В.М., Широкова Н.В. 2012. Малат-аспартатные митохондриальные переносчики принимают участие в регуляции частоты спарков в пермеабилизированных волокнах скелетной мышцы крыс. Актуальные вопросы биологической физики и химии, Севастополь 2012, С48 -50
12. Figueroa L, Shkryl VM, Zhou J, Manno C, Momotake A, Brum G, Blatter LA Ellis-Davies G and Rios E. 2012. Quantification of the CICR Response to Artificial Ca Sparks in Striated Muscle. Biophysical Journal 102(3) pp. 311a.
13. Shkryl VM, Blatter LA, Ríos E. 2011. 4-D Scanning of Calcium Sparks in Cardiomyocytes Reveals their In-Focus Amplitude. Biophysical Journal 100(3) pp. 558a - 559a.
14. Figueroa L, Shkryl V, Zhou J, Momotake A, Ellis-Davies G, Blatter LA, Brum G, Rios E. 2011. Different Capabilities for CICR of Skeletal Muscle of Amphibians and Mammals, Demonstrated through the Response to Artificial Ca Sparks. Biophysical Journal 100(3) pp. 353a.
15. Shkryl VM, Maxwell JT, Blatter LA. 2011. Spatially Complex Diffraction-Limited Photolysis of Caged Calcium and IP3 Combined with High-Speed Confocal Imaging. Biophysical Journal 100(3) pp. 558a.
16. Figueroa L, Shkryl V, Zhou J, Momotake A, Ellis-Davies G, Blatter LA, Brum G, Rios E. 2011. Different Capabilities for CICR of Skeletal Muscle of Amphibians and Mammals, Demonstrated through the Response to Artificial Ca Sparks. Biophysical Journal 100(3) pp. 353a.

17. Shkryl VM, Littwitz C, Domeier TL, Blatter LA. 2010. Refractoriness of Ryanodine Receptors During Calcium Alternans in Rabbit Atrial Myocytes. Biophysical Journal 98(3, Supplement 1), 103a.
18. Figueroa L, Shkryl V, Zhou J, Momotake A, Ellis-Davies G, Blatter LA, Rios E. 2010. CICR and Calcium-Dependent Inactivation, Quantified Through the Response to Artificial Ca Sparks in Single Muscle Cells. Biophysical Journal 98(3, Supplement 1), 294a.
19. Figueroa L, Zhou J, Shkryl V, Blatter LA, Momotake A, Ellis-Davies G, Rios E. 2010. Flux in Artificial Ca Sparks Generated by 2-Photon Release from a Novel Cage Confocally Imaged at Microsecond Resolution. Biophysical Journal 98(3, Supplement 1), 294a.
20. Shkryl VM & Blatter LA. 2009. New Insight Into Cardiomyocyte Ca Signaling Obtained By Fast Confocal Imaging. Biophysical Journal 96(3), 277a-278a.
21. Shkryl VM & Blatter LA. 2008. Spatial properties of Ca sparks and Ca transients in atrial and ventricular myocytes recorded with high-speed 2-dimensional confocal microscopy. Biophysical Journal, 94(1), 300a.
22. Shkryl VM, Zima AV, Blatter LA. 2007. Mechanisms of mitochondrial Ca extrusion in intact atrial myocytes. Biophysical Journal, 92(1), 137a.
23. Shkryl VM & Shirokova N. 2006. Local mitochondrial Ca^{2+} transients in skeletal muscle in the presence of EGTA and BAPTA. Biophysical Journal, 90(1), 21a.
24. Shkryl VM & Shirokova N. 2006. ROS scavengers inhibit stress-induced Ca^{2+} sparks in skeletal muscle fibers. Biophysical Journal, 90(1), 20a.
25. Shkryl VM & Shirokova N. 2005. Mitochondrial redox state and Ca^{2+} sparks in permeabilized mammalian skeletal muscle. Biophysical Journal 88(1), 86a.
26. Shkryl VM, Isaeva EV & Shirokova N. 2005. Transfer of Ca^{2+} from sarcoplasmic reticulum to mitochondria in permeabilized mammalian skeletal muscle. Biophysical Journal 88(1), 440a.
27. Isaeva EV, Shkryl VM & Shirokova N. 2004. Energized mitochondria delay the onset of Ca2+ sparks in permeabilized mammalian muscle fibers. Biophysical Journal 86 (1), 579A.

ПЕРЕЛІК ОСНОВНИХ УМОВНИХ ПОЗНАЧЕНЬ ТА СКОРОЧЕНЬ

АТФ – аденозинтрифосфорна кислота

AR – коефіцієнт альтернацій

BAPTA – 1,2-bis(o-aminophenoxy)ethane-N,N,N',N'-tetraacetic кислота

Ca^{2+} – іони кальцію

$[Ca^{2+}]$ – внутрішньоклітинна концентрація іонів кальцію

$[Ca^{2+}]m$ – концентрації кальцію в мітохондрії

$[Ca^{2+}]SR$ – концентрації кальцію в саркоплазматичний ретикулум

CICR – кальцій-індуковане вивільнення кальцію

СР – саркоплазматичний ретикулум

CRU – окрема одиниця вивільнення Ca^{2+}

DHPRs – дигідропіриадинові рецептори

DCF – флуоресцентний барвник CM-H2DCFDA

ECC – процес спряження збудження в скорочення

EDL – довгий м'яз-розгинач пальців

ЕР – ендоплазматичний ретикулум

EFS – стимуляція електричним полем

EGTA – ethylene glycol-bis(β-aminoethyl ether)-N,N,N',N'-tetraacetic кислота

F_{340} – флуоресценція або інтенсивність при 340 нм.

F_{380} – флуоресценція або інтенсивність при 380 нм.

FCCP – Carbonyl cyanide-p-trifluoromethoxyphenylhydrazone

FDB – м'яз підошовної частини стопи

FRAP – відновлення флюоресценції після фотознебарвлення

FWHM – повна ширина на половині максимуму

ICa – трансмембранний струм через кальцієві канали

IP_3Rs – інозитол-3-фосфатних рецепторів

j-SR – з’єднані СР розташовані поблизу поверхневої мембрани

Kd – константа дисоціації

Ma^{2+} – іони магнію

МДД – м‘язова дистрофія Дюшена

MnTBAP - manganese(III) tetrakis(4-benzoic acid)porphyrin
Mn-cpx 3 - Mn(III) meso-tetrakis(N-ethylpyridinium-2-yl)porphyrin
NAD(P)H – Нікотинамідаденіндинуклеотидфосфат
NADH – нікотинамідаденіндинуклеотид
NMDA – каналів іонотропних рецепторів глутамату
NCX – натрій-кальцієвий обмінник
NDBF-EGTA – нітродибензофуран-EGTA
NOXs –оксидаза NAD(P)H
NOS – синтаза оксиду азоту
NP-EGTA - нітрофеніл EGTA
nj-SR – нез’єднані СР, що знаходяться в глибших ділянках клітини
ПД – потенціал дії
ПЗЗ – пристрій з зарядовим зв'язком
PICR – вивільнення Ca^{2+}, індуковане фотолізом
$PICR_L$ – вивільнення Ca^{2+}, індуковане фотолізом, після великого транзієнту
$PICR_S$ – вивільнення Ca^{2+}, індуковане фотолізом, після малого транзієнту
ROI – область інтересу
ROS – активні форми кисню
RyRs – ріанодинові рецептори
RyR_1,RyR_2 та RyR_3 – ріанодинові рецептори 1, 2 та 3 типу
SERCA – саркоплазматичний/ендоплазматичний ретикулума Ca^{2+}-АТФаза
SLICs – штучне локалізоване підвищення концентрації [Ca2+]
SOD – супероксиддисмутази
Soleus – камбалоподібний м'яз
Т-трубочка – поперечна трубочка
TIRON – 4,5-Dihydroxy-1,3-benzenedisulfonic кислота
TG – тапсигаргін
TRPV-канали – канали транзієнтного рецепторного потенціалу
VGCC – потенціал-керованих кальцієвих каналів
4-CMC – 4-Chloromethcathinone

ЗМІСТ

ВСТУП

Актуальність даної роботи. Ріанодинові рецептори (RyRs) є важливими компонентами кальцієвої сигналізації в м'язових і нервових клітинах. Вони є одними з основних структур, які контролюють вивільнення кальцію з сарко(ендо)плазматичного ретикулуму в цитоплазму. Ці рецептори унікальні тим, що їх активність може бути регульована як підвищенням, так і зниженням концентрації внутрішньоклітинного кальцію (Woll and Van Petegem, 2022).

Іони кальцію (Ca^{2+}) є поширеним вторинним посередником, регуляція якого в збудливих клітинах контролює багато фізіологічних шляхів, таких як збудження, м’язове скорочення, вивільнення медіаторів, синаптична пластичність, секреція, запліднення, транскрипція генів та апоптозу тощо (Pozzan et al., 1994, Berridge et al., 2000, Eisner et al., 2023). Процес вивільнення кальцію з депо має велике значення для функціонування м'язів і нервової системи.

На локальному рівні активність RyRs реєструється як кальцієві спалахи, які розглядаються як локальні зміни концентрації кальцію під час його вивільнення з саркоплазматичного ретикулуму (СР) внаслідок одночасного відкриття декількох RyRs. Розуміння динаміки Ca^{2+} спалахів є важливою для кальцієвої сигналізації. Численні експериментальні, комп’ютерні та біофізичні дослідження були спрямовані на вивчення механізмів ініціації, припинення та регуляції кальцієвих спалахів (Hoang-Trong et al., 2015). Розуміння ролі як спалахів, так і роботи залучених RyRs на рівні регуляції та динаміки кальцієвого сигналу у нормі та патології слугує основою для з’ясування функціональних змін Ca^{2+} сигналу на клітинному або субклітинному рівнях.

Актуальність досліджень ріанодинових рецепторів в кальцієвій сигналізації полягає в тому, що вони є потенційними мішенями для розвитку нових ліків від різних захворювань, пов'язаних з порушенням кальцієвої концентрації в клітинах. Наприклад, деякі хвороби м'язів, такі як дистрофія м’язових волокон, аритмії серця, а також нейродегенеративні захворювання, можуть бути пов'язані зі зміною функціональності RyRs.

Характеристики кальцієвих сигналів визначаються функціонуванням складного комплексу молекулярних механізмів – іонних каналів, кальцій-зв'язувальних білків, каналів вивільнення кальцію з внутрішньоклітинних депо, а також участь обмінників або помп, які забезпечують виведення кальцію з цитозолю клітини. У збудливих клітинах (нервових, м'язових і секреторних) зумовлений деполяризацією вхід кальцію спричиняє додаткове збільшення концентрації цього іону завдяки вивільненню з кальцієвих депо, що здійснює регуляційний вплив на відповідні клітинні функції (Augustine et al., 2003, Endo, 2009, Dewenter et al., 2017).

У найзагальнішому вигляді кальцій часто розглядають як посередника, що впливає на внутрішньоклітинні процеси шляхом зміни внутрішньоклітинної концентрації іонізованої форми цього елемента ($[Ca^{2+}]$). Цей показник змінюється від 50 нМ у стані спокою до близько 10 мкМ на піках низки фізіологічних сигналів (Berridge et al., 2000). Вхід Ca^{2+} із позаклітинного середовища здійснюється під час активації потенціал-керованих кальцієвих каналів (VGCC), каналів іонотропних рецепторів глутамату (NMDA) та ацетилхолінових рецепторів, а також каналів транзієнтного рецепторного потенціалу (TRPV-каналів) плазматичної мембрани. Основною внутрішньоклітинною структурою, яка сприймає та обробляє кальцієві сигнали, що надходять від кальцієвих каналів плазматичної мембрани, є ендоплазматичний ретикулум (ЕР); відповідна структура в м'язових волокнах визначена як саркоплазматичний ретикулум (СР). Вивільнення кальцію з внутрішньоклітинних депо має вигляд осциляцій і залежить від активності каналів у мембранах кальцій-зв’язуючих клітинних органел (ЕР або СР, мітохондрій, апарату Гольджі, ядра). Додаткове збільшення цитозольної концентрації кальцію за рахунок вивільнення з ЕР/СР відбувається за рахунок відкривання каналів інозитол-3-фосфатних рецепторів (IP_3Rs) та/або ріанодинових рецепторів (RyRs).

У ссавців було ідентифіковано три ізоформи RyRs (RyR1, RyR2 і RyR3), які кодуються трьома різними генами на різних хромосомах. RyR1 і RyR2 знайдені переважно в скелетних і серцевих м'язах відповідно, де вони відіграють центральну роль у зв'язку збудження-скорочення (Fill and Copello, 2002). RyR3 був виявлений у пірамідних нейронах СА1 зони гіпокампу, що призводять до специфічних змін у синаптичній пластичності гіпокампу (Balschun et al., 1999).

Існують високоселективні препарати, які здатні активувати або інгібувати RyRs в збудливих клітинах. Найбільш відомими з них є кофеїн, ріанодин, 4-хлор-м-крезол (4-CMC), дантролен, рутенієвий червоний, тетракаїн і прокаїн (Viero et al., 2012). Кофеїн є агоністом RyRs і використовується як фармакологічний інструмент для вивчення опосередкованого ріанодиновими рецепторами вивільнення Ca^{2+} з внутрішньоклітинних депо (Kong et al., 2008, Porta et al., 2011). Кофеїн сенсибілізує RyRs до Ca^{2+} і сприяє вивільненню Ca^{2+} з ЕР при базальному рівні цитозольного Ca^{2+}. Іншим препаратом - інгібітором RyRs є дантролен (Fruen et al., 1997, Fill and Copello, 2002), який у концентрації 10 мкМ знижує ймовірність відкриття каналів RyRs на ~50% (Diszházi et al., 2019).

Оскільки кальцієві сигнали на периферії та в центрі клітини можуть значно різнитися, то дуже важливо не тільки визначати концентрацію кальцію в тому чи іншому локусі, а і з'ясовувати просторові та часові характеристики відповідних змін цієї величини. При цьому необхідно не тільки розділяти кальцієвий сигнал на потоки кальцію, що йдуть між різними клітинними компартментами, а й визначати характеристики зазначених потоків.

Одним із зручних об'єктів для вивчення зміни внутрішньоклітинної концентрації кальцію, опосередкованої ріанодиновими рецепторами, є кардіоміоцити. У цих клітинах, за фізіологічних умов, реалізовано механізм кальцій-індукованого вивільнення кальцію, коли збільшення концентрації кальцію біля RyR2 спроможне відкрити сам канал (Liang, 2008, Dewenter et al., 2017).

Вивільнення Ca^{2+} з СР складається із дискретних подій вивільнення Ca^{2+}, які мають стереотипний вигляд, та може бути візуалізовано за допомогою конфокальної флуоресцентної мікроскопії та флуоресцентних Ca^{2+}-чутливих барвників і отримали назву Ca^{2+} спалахів (Ca^{2+} sparks; (Cheng et al., 1993, Nelson et al., 1995, Tsugorka et al., 1995)). Це сукупне явище, створене групою RyRs каналів, визначених як кластер каналів вивільнення або одиниці вивільнення Ca^{2+} (CRU; (Franzini-Armstrong and Jorgensen, 1994)).

Вивільнення Ca^{2+} з СР є обов'язковим кроком в процесі спряження збудження-скорочення (ECC) скелетного м'яза. Так під час деполяризації поперечної трубчастої мембрани та активації DHPRs (ще відомі як L-тип кальцієвих каналів) та RyRs відбувається вивільнення Ca^{2+} з СР (Nakai et al., 1996, Ríos et al., 1993, Schneider and Chandler, 1973). Взаємодія DHPR та RyRs в скелетному м'язі алостерична, за допомогою датчику напруги та активації RyRs не вимагає Ca^{2+} завдяки CICR (Rios and Pizarro, 1988, Shirokova et al., 1996). За фізіологічних умов Ca^{2+}-спалахи майже не зафіксовано в інтактних скелетних м'язових волокнах дорослих ссавців (Conklin et al., 1999). Кілька маніпуляцій можуть усунути фізіологічне гальмування CICR у м'язових клітинах ссавців. Такі втручання як пермеабілізація мембрани (Kirsch et al., 2001, Lamb, 2002), порушення функції мітохондрій (Isaeva and Shirokova, 2003) та осмотичний шок викликають появу Ca^{2+} спалахів в інтактних м'язових волокнах (Wang et al., 2005). Такі механізми виявлення CICR (та і Ca^{2+} спалахів) у м'язах ссавців досі невизначені, а розуміння таких складних біофізичних процесів є важливою задачею.

Мітохондрія є однією з основних субклітинних структур у скелетних м'язах ссавців. Ключова роль цих органел полягає у виробництві енергії шляхом генерування АТФ (Gillis, 1997, Madsen et al., 1996, Sembrowich et al., 1985). Також переконливо те що мітохондрія приймає участь у внутрішньоклітинному гомеостазі Ca^{2+}, що грає важливу роль під час циклу скорочення-розслаблення (Bruton et al., 2003).

Вважається, що Kd для мітохондріального поглинання Ca^{2+} є надто низьким, що мітохондрія нездатна опрацювати швидку транзієнту зміну кальцію (Brini, 2003). Рандольф та ін. показали, що мітохондрія здатна швидко змінювати вміст кальцію під час не тільки тетанічних, а і поодиноких скорочень м'язів (Rudolf et al., 2004). Між мітохондрією і СР має бути тісний зв'язок, щоб забезпечити швидке поглинання кальцію під час зв'язку збудження зі скороченням, що потрібно перевірити в наших експериментах.

Мітохондрії виконують не лише функцію по виробництву АТФ, але також грають ключову роль у інших клітинних процесах. Збільшення концентрації кальцію в мітохондрії ($[Ca^{2+}]_m$) посилює виробництво нікотинамідаденіндинуклеотиду (NADH), транспорт електронів, змінює вміст протонів, та сприяє виробництву активних форм кисню (ROS; (Duchen, 2000, Hajnóczky et al., 1999, Rizzuto et al., 2004)). Тому важливо з'ясувати вплив перерахованих вище процесів на зміну концентрації кальцію та їх взаємозв'язок з вивільненням з СР.

ROS беруть участь у регуляції різних сигнальних подій у скелетних м'язах, таких як гомеостаз Ca^{2+} та скорочення м'язів (Andrade et al., 1998, Pattwell and Jackson, 2004, Posterino et al., 2003). Вважається, що ROS впливають на внутрішньоклітинну Ca^{2+} сигналізацію через редокс модуляцію кількох основних Ca^{2+} сигнальних білків, включаючи RyRs (Feng et al., 2000, Trimm et al., 1986). Було показано, що окислення, або нітрозативна модифікація RyRs через окислення внутрішньоклітинного середовища може, принаймні частково відповідальна за появу Ca^{2+} спалахів (або CICR) при стресі м'язів. Важливо перевірити, чи ROS-залежні механізми відповідальні за розвиток Ca^{2+} спалахів у скелетних м'язах.

М‘язова дистрофія Дюшена (МДД) є одним з найтяжких спадкових захворювань м‘язів. Вважається, що нестача дистрофіну робить сарколему скелетних м‘язових волокон більш вразливою до механічних навантажень під час скорочень або ексцентричного розтягування (Ervasti and Campbell, 1993, Hoffman et al., 1987). Існують ознаки того, що окислювальний стрес (окремо або поєднані з механічним навантаженням) може сприяти розвитку дистрофінопатії (Tidball and Wehling-Henricks, 2007). Як у м‘язових волокнах пацієнтів з МДД, так і у миші лінії mdx рівень більшості антиоксидантних ферментів та антиоксидантів значно збільшені (Austin et al., 1992, Dudley et al., 2006). Базальна або фонова генерація ROS, як правило, також підвищена (Whitehead et al., 2008). Потрібно з'ясувати чи ROS сприяє вивільненню Ca^{2+} з СР через RyRs, які можуть підпадати окислювальним/ нітрозитивним модифікаціям (Marks et al., 2009, Stamler and Meissner, 2001), та підсилюватися окислювальним стресом окремо або в поєднанні з механічним навантаженням.

Як зазначалося вище, досі залишається суперечливим, що RyRs за рахунок CICR сприяє фізіологічному вивільненню Ca^{2+} у скелетних м'язах ссавців. Як переконливо сформував Ендо (Endo, 2009), два основні спостереження суперечать цьому: одне з них полягає в тому, що імовірно Ca^{2+} потоки за фізіологічних умов, виміряні в інтактних клітинах або клітинах при фіксації потенціалу (Royer et al., 2008) набагато перевищує значення CICR, виміряні в волокнах із знятою мембраною (Murayama et al., 2000). Інше спостереження стосується того, що CICR має бути здійснено тільки завдяки кальцію, без одночасного залучення інших процесів. Так, наприклад, Ca^{2+} спалахи, які в серцевому м’язі вважається ознакою CICR (Cheng et al., 1993), в скелетних м’язах не можуть бути чистим проявом CICR, оскільки вони ініціюються датчиком напруги DHPR, а також можуть припинятися реполярізацією (Lacampagne et al., 2000). Сигналом для скорочення скелетних м'язів є швидке збільшення цитозольної концентрації Ca^{2+}, що вимагає координованого відкриття каналів ріанодинових рецепторів у саркоплазматичному ретикулумі. Відкриття каналів контролюється дигідропіридиновими рецепторами, які є чутливими до потенціалу плазматичної мембрани та Т-трубочок. Чи посилюється такий сигнал за рахунок Ca^{2+}-індукованого вивільнення Ca^{2+}, залишається дискусійним.

В кардіоміоцитах поява Ca^{2+} спалахів відбувається за рахунок CICR не тільки для ініціації, але і для поширення в кластері (Cheng et al., 1993, Endo et al., 1970, Fabiato and Fabiato, 1978). Ca^{2+} спалахи виникають у міоцитах шлуночків міокарду (Niggli and Shirokova, 2007), а також у міоцитах передсердь (Blatter et al., 1997, Kockskamper et al., 2001, Sheehan et al., 2006). У міоцитах шлуночків добре розвинута тривимірна мережа поперечних (Т) трубочок (Soeller and Cannell, 1999) яка забезпечує швидке розповсюдження потенціалу дії по всьому об’єму клітини (Cheng et al., 1994). Навпаки, у міоцитах передсердь мережа Т-трубочок слабо розвинута або зовсім відсутня (Huser et al., 1996, Mackenzie et al., 2001), а близьке розташування DHPRs та RyRs існує лише на периферії клітини. При цьому СР поширений по всій клітині та містить RyRs, здатні вивільнювати Ca^{2+} і генерувати Ca^{2+} спалахи (Sheehan et al., 2006). Така різноманітна будова міоцитів робить дуже зручним об’єктом досліджень змін Ca^{2+} сигналів у функціонуванні клітин.

Кількість залучених каналів RyRs, часові властивості поодинокої події, тривалість відкриття окремих каналів у кластері, механізми, що лежать в основі закриття RyRs, ступень локально внутрішнього виснаження СР, величини струму та часу до піку спалаху Ca^{2+}, залишаються невизначеними або тільки починають з'ясовуватися. Спонтанність спалахів Ca^{2+} та невизначеність місця вивільнення ускладнюють точне визначення параметрів спалахів Ca^{2+} та потребують поліпшення методів визначення цих явищ. Додатково, сучасні можливості швидкої конфокальної мікроскопії надають змогу детальніше досліджувати зміни внутрішньоклітинної концентрації кальцію у міоцитах міокарду як на локальному, так і на рівні цілої клітини.

Порушення механізму вивільнення Ca^{2+} з СР або зміни відновлення RyRs можуть викликати зміни концентрації кальцію збудливої клітини та її функціонування. З біофізичної точки зору, дослідження цих явищ є дуже цікавим. Альтернації серця – порушення скоротливої функції серця, що проявляється в регулярному чергуванні відносно сильних скорочень зі слабкими. Альтернація серця є визнаним фактором ризику серцевої аритмії та раптової серцевої смерті (Ter Keurs and Boyden, 2007, Walker and Rosenbaum, 2005). На клітинному рівні альтернації проявляється у вигляді варіацій цитозольних Ca^{2+}-транзієнтів змінної амплітуди з регулярною частотою симуляцій кардіоміоцита.

На підставі теорії циклу змін концентрації Ca^{2+} у кардіоміоциті, комп'ютерних досліджень та експериментальних даних (Weiss et al., 2006, Weiss et al., 2011), було виявлено два параметри які критичні при стимул-стимул регуляції $[Ca^{2+}]$ та появи альтернацій, це: фракційне вивільнення Ca^{2+} та ефективність цитозольного секвестрування кальцію. В свою чергу, вони можуть залежати від властивостей реституції та рефракторної кінетики механізму вивільнення Ca^{2+} з СР, що потрібно дослідити.

Інша картина Ca^{2+} сигналізації спостерігається у нейронах головного мозку. Так, RyRs у периферичних і центральних нейронах можуть підсилювати і подовжувати вхідні Ca^{2+} сигнали за рахунок CICR (Holliday et al., 1991, Kano et al., 1995, Llano et al., 1994). Деякі дослідження показали, що виснаження або блокування ріанодинчутливих Ca^{2+} депо суттєво не змінює амплітуду і форму Ca^{2+} транзієнту індукованого деполяризацію та не вносять суттєвого внеску у Ca^{2+} транзієнти, викликаних низькочастотною активністю (Garaschuk et al., 1997). Однак, було встановлено, що у сомі пірамідальних нейронів є ретикулярна мережа ЕР, яка поширюється на дендрити та на всю довжину аксона, включаючи пресинаптичні бутони (de Juan-Sanz et al., 2017). Крім того, повідомлялося, що повторна тетанічна синаптична стимуляція пірамідальних клітин CA1 зони на зрізах гіпокампу індукують вивільнення Ca^{2+} з дендритних або пресинаптичних ріанодинчутливих Ca^{2+} депо (Alford et al., 1993, Tran and Stricker, 2021). Таким чином, роль ріанодинових рецепторів у регуляції внутрішньоклітинної концентрації кальцію в нейронах потребує подальших досліджень. Особливо актуальним є встановлення впливу рівня електричного стимулювання нервових клітин на процес вивільнення кальцію.

Отже, актуальність цієї роботи визначається потребою в теоретичному узагальненні та експериментальному вирішенні наукової проблеми ролі ріанодинових рецепторів у кальцієвій сигналізації в м’язових і нервових клітинах, а також у ряді клітинних механізмів (активації RyRs; мітохондрія як фабрика АТФ та ROS; зміна потоку кальцію; збудження або інгібування активності клітини) за допомогою біофізичних методів. Метою наших досліджень було визначення процесу розповсюдження кальцієвого сигналу на рівні Ca^{2+} спалахів, а також динаміки концентрації цього іону на рівні цілої клітини та її органел у відповідь на нормальні або зміни функціонального стану клітини (альтернації Ca^{2+}) та патологічних умов (аритмії серця або м’язовій дистрофії Дюшена). Біофізичні властивості, що обумовлюють тонку регуляцію внутрішньоклітинного кальцію через зміни активності RyRs та враховують фактори мітохондріальної регуляції, дії вільних радикалів кисню, активність NAD(P)H оксидази та вплив самого кальцію, є вкрай важливими для розуміння клітинного гомеостазу та функціональної активності клітини.

Зв’язок роботи з науковими програмами, планами, темами. Дисертаційна робота виконана згідно плану науково-дослідної тематики відділу біофізики іонних каналів Інституту фізіології ім. О.О. Богомольця НАН України та інших програм, що виконуються відділом (номер державної реєстрації 0118U007344, 0116U004470 та 0120U001281). Частина роботи була виконана в рамках програм міжнародного співробітництва “Клітинні системи в нормі на патології” в Університеті Медицини та

Стоматології Нью-Джерсі, США та Медичному Центрі Університету Раш, Чикаго, США.

Мета дослідження: полягала у з’ясуванні ролі ріанодинових рецепторів у формуванні та модуляції концентрації іонів кальцію у м’язових і нервових клітинах на рівні клітини, чи окремої її ділянки.

Завдання дослідження. Згідно з цією метою були поставленні наступні завдання:

1. Дослідити просторово-часові властивості змін концентрації іонів кальцію на рівні елементарних та глобальних кальцієвих сигналів за участі ріанодинових рецепторів в міоцитах передсердь та шлуночків.
2. Дослідити активність ріанодинових рецепторів як поодиноких подій вивільнення Ca^{2+} з саркоплазматичного ретикулуму — спалахи Ca^{2+} за допомогою багатомірної конфокальної мікроскопії.
3. В міоцитах передсердь дослідити альтернації кальцію при постійній частоті стимуляції міоцита. З’ясувати роль потенціал-керованих Ca^{2+} каналів плазматичної мембрани та кінцевого, діастолічного рівня Ca^{2+} в СР під час Ca^{2+} альтернацій в міоцитах передсердь. Проаналізувати вплив рефрактерності до вивільнення Ca^{2+} із СР, за рахунок RyRs, як можливого чинника виникнення Ca^{2+} альтернацій.
4. Дослідити можливість мітохондрій секвеструвати кальцій який вивільнюються з СР за рахунок RyRs в скелетних м’язових волокнах. Вивчити функціональне розташування мітохондрій та СР.
5. Встановити вплив мітохондріального окислювально-відновлювального стану на регуляцію вивільнення Ca^{2+} із СР за участі RyRs та появу Ca^{2+} спалахів у пермеабілізованих скелетних м'язових волокнах ссавців.
6. Виявити взаємозв'язок між балансом активних форм кисню та аномальним сплеском Ca^{2+} спалахів у скелетних м'язових волокнах лінії миші mdx після механічного стресу у вигляді осмотичного шоку та порівняти з нормальними тваринами. Встановити, чи можуть поглиначі ROS інгібувати стрес-індуковані Ca^{2+} спалахи. Визначити задіяні джерела ROS у скелетних м'язових волокнах mdx, при осмотичному стресі.

7. Визначити, чи призводить штучне локалізоване підвищення концентрації Ca^{2+} в скелетних м'язових волокнах миші та жаби до вивільнення цього іона з СР при активації RyRs. Чи відповідають отримані реакції характеристикам "класичного" кальцій-індукованого вивільнення кальцію? З'ясувати відмінності у величині потоку вивільнення кальцію з СР та поріг активації RyRs кальцієм між м'язовими волокнами жаби та миші.
8. Дослідити просторово-часові властивості кальцієвого сигналу в пірамідальних нейронах гіпокампу щурів. Виявити роль RyRs в модуляції Ca^{2+} сигналу під час короткочасної або тривалої стимуляції в різних частинах нейрона.

Об'єкт дослідження: регуляція концентрації іонів кальцію ріанодиновими рецепторами у м'язових і нервових клітинах.

Предмет дослідження: зміни та формування внутрішньоклітинної концентрації іонів кальцію в кардіоміоцитах, скелетних м'язових волокнах та пірамідних нейронах гіпокампу за рахунок зміни активності ріанодинових рецепторів.

Методи досліджень: включають біофізичні підходи, такі як епіфлюоресцентна та конфокальна мікроскопія, з використанням кальцій-чутливих флуоресцентних барвників, для визначення змін концентрації кальцію; метод петч-клемп реєстрації трансмембранних Ca^{2+} струмів; локальне вивільнення зв'язаного кальцію за допомогою флешфотолізу; комп'ютерне моделювання та обробка кальцієвого сигналу для розрахунків потоків кальцію; статистична обробка числових результатів.

Наукова новизна одержаних результатів

Використання надшвидкісної конфокальної візуалізації динаміки Ca^{2+} в серцевих міоцитах дозволило виявити ступінчасту кінетику зростаючої фази Ca^{2+} спалаху. Показано, що динаміку збільшення Ca^{2+}, який входить у клітину та кальцій-індукованого вивільнення кальцію можливо достовірно розділити на рівні окремих центрів вивільнення кальцію як у клітинах передсердя, так і у шлуночків міокарда, як у часі, так і просторі.

Вперше було вивчено властивості Ca^{2+} спалахів, що зареєстровані у місці вивільнення кальцію від групи каналів RyRs. Вони мали більшу амплітуду та модальний розподіл амплітуди з одною модою. Струм вивільнення Ca^{2+}, який лежав в основі таких спалахів, становив 11 пА. Для досягнення цього струму потрібно активувати від 20 до 30 відкритих каналів RyRs.

Прямо показано, що в міоцитах передсердь зміна кінетики реституції вивільнення Ca^{2+} з саркоплазматичного ретикулуму від стимулу до стимулу є ключовим причинним механізмом виникнення Ca^{2+}-альтернацій, як важливий механізм утворення серцевої аритмії.

Було ідентифіковано субклітинні мікродомени, в яких Ca^{2+} має переважний доступ до мітохондрій у функціональній та структурній близькості до СР у скелетних м'язах. Було виявлено наявність двох груп мітохондрій, одна з них розміщена безпосередньо біля СР, де Ca^{2+} поглинається мітохондріями завдяки відкриттю каналів RyRs.

Розкриті нові аспекти регуляції мітохондріального окислювального-відновлювального стану щодо регуляції вивільнення Ca^{2+} із саркоплазматичного кальцієвого депо на прикладі активності групи RyRs в скелетних м’язах. ROS спричиняють аномальну активність RyRs в інтактних скелетних волокнах (появу кальцієвих спалахів) при осмотичному стресі. В дистрофічних волокнах скелетних м'язів під впливом осмотичного стресу, розбалансованість в ROS сигналах призводить до того, що Ca^{2+} спалахи з’являлися не тільки на периферії клітини, а також поширювалися в центр клітини, а інгібітори NAD(P)H-оксидази ефективно пригнічували стрес-індуковану активність ріанодинових рецепторів. Збільшення мітохондріального кальцію та посилення утворення мітохондріального ROS в mdx волокнах підсилює аномальні Ca^{2+} сигнали.

Показано суперечливу роль Ca^{2+}-індукованого вивільнення Ca^{2+} з СР за рахунок відкриття каналів RyRs в скелетних м’язах. За фізіологічних умовах у скелетних м'язових клітинах жаби були зареєстровані CICR-відповіді. Проте, у скелетних м'язових волокнах миші, RyRs не реагують на стимул кальцію до 8 мкМ, та мають значно нижчий потік вивільнення, що разом із значно вищим порогом активації рецепторів пояснює незначну відповідь при відсутності препаратів, що відкривають канали, та вказує на відсутність CICR у процесі збудження-скорочення у скелетних м’язах ссавців в нормі.

Отримані нові дані про роль RyRs у кальцієвій сигналізації в пірамідальних нейронах гіпокампу щурів. Зростання концентрації вільного Ca^{2+} є асинхронним і затримується в центральній ділянці порівняно з примембранними ділянками або ділянками дендритного дерева, де спостерігається швидший розвиток Ca^{2+} сигналу. Короткочасна електрична стимуляція недостатня для того, щоб викликати вивільнення Ca^{2+} з ендоплазматичного ретикулуму через кальцій-індуковане вивільнення кальцію. Натомість, для активації RyRs та вивільнення Ca^{2+} необхідна тривала стимуляція.

Результати дослідження є внеском у комплексне розуміння ріанодин рецептор-опосередкованої кальцієвої сигналізації в м'язових і нервових клітинах у нормі та патології.

Теоретичне та практичне значення роботи.

Представлена робота є важливою в галузі біофізики, оскільки розширює сучасні уявлення щодо функції ріанодинових рецепторів у модуляції клітинної концентрації кальцію в збудливих клітинах, як з теоретичної, так і з практичної точки зору. У роботі детально розглянуті біофізичні властивості кальцієвої сигналізації м'язової і нервової клітин, як на рівні окремих органел: саркоплазматичного ретикулуму та мітохондрії, так і мікроклітинних доменів та центрів вивільнення кальцію, шляхом регуляції окислювально-відновлювального стану клітини, мітохондріального NADH сигналу або за участі трансмембранних Ca^{2+} каналів L-типу та активності ріанодинових рецепторів за рахунок кальцій-індукованого вивільнення кальцію.

Результати цього дослідження є значним кроком вперед у нашому розумінні механізмів, що лежать в основі альтернуючого серцебиття, та надає можливостей розробки нових стратегій лікування аритмій.

Порушення регуляції функції RyRs призводить до різних захворювань. Тому розуміння процесів, які регулюють активність RyRs, має вирішальне значення для розробки терапевтичних стратегій. Результати цього дослідження не тільки поглиблять наше розуміння фундаментальних принципів внутрішньоклітинної Ca^{2+} сигналізації, але надають уявлення про молекулярну основу різних захворювань, пов'язаних з дисфункцією RyRs.

Вперше запропоновано методичні підходи дослідження Ca^{2+} спалахів у місці вивільнення з СР, ґрунтовані на тривимірному конфокальному скануванні флуоресценції, що має бути використаним для дослідження RyRs, визначати потік вивільнення кальцію, та надає можливість використати її для фармакологічних досліджень ріанодинових рецепторів.

Запропоновано методичні підходи для вивчення біофізичних процесів збудливих клітин, базуючись на швидкісній конфокальній візуалізації для дослідження Ca^{2+} сигналів з часовою роздільною здатністю, подібною до методу петч-клемп, але у менш інвазивний метод, з можливістю розділення по всій клітині.

Був запропонований новий метод просторової, складної, дифракційно-обмеженої фотоактивації та фотознебарвлення в живих клітинах. Така методика дозволяє локально активувати окремі сайти вивільнення кальцію або групу RyRs каналів у живих клітинах, що може бути використано для вивчення їхніх структурних і функціональних деталей з високою точністю.

Також була адаптована та модифікована формула Грінкевича для визначення вмісту вільного кальцію в клітині при двох хвильовому методі збудження флуоресцентного барвника при використані ПЗЗ камери. Адаптація включає в себе корекцію фотознебарвлення та виправлення помилки віднімання фону. Ця модифікація необхідна для визначення концентрації кальцію двох хвильовому методі збудження флуоресцентного барвника и повинна використовуватися в подальших дослідження.

Представлені результати мають загальне біологічне значення і поглиблюють наше розуміння кальцієвої сигналізації в м’язових і нервових клітинах. З практичної точки зору, отримані дані є основою для подальшого вивчення молекулярних механізмів процесу перетворення збудження в скорочення як у кардіоміоцитах, так і в скелетних м’язових волокнах, а також розкривають розуміння ролі кальцій-залежних функцій у нервових клітинах.

Особистий внесок здобувача. Дисертаційна робота є особистою працею здобувача. Мету, завдання роботи, методи досліджень, аналіз літературних та отриманих матеріалів роботи проведено, опубліковано та викладено в представленій дисертаційній роботі особисто. Автором проведено науковий пошук та критичний аналіз наявних даних літератури щодо обґрунтування регуляції внутрішньоклітинного кальцію за рахунок ріанодинових рецепторів. При проведенні досліджень автором особисто виконано основну частину експериментальної роботи, аналіз отриманих результатів, їх наукову інтерпретацію та узагальнення, формулювання висновків та написання статей. Деякі експерименти були проведені зі співавторами опублікованих робіт. Дослідження участі мітохондрії в регуляції кальцієвого гомеостазу при його вивільненні з СР депо за участі RyRs в м’язових волокнах та вплив мітохондріального окислювального-відновлювального стану на вивільнення Ca^{2+} із СР депо за участі RyRs, та виявлення регуляції окислювального-відновлювального стану в дистрофічних м’язових волокнах миші лінії mdx було проведено на базі Школи Медицини Нью-Джерсі Університету медицини та стоматології Нью-Джерсі (Ньюарк, США; проф. Н. Широкова). Експерименти з вивчення просторо-часових властивостей змін концентрації іонів кальцію на рівні елементарних; глобального кальцієвого сигналу за участю ріанодинових рецепторів в процесі передачі збудження та скорочення клітин передсердя та шлуночків міокарду; вивчення Ca^{2+} альтернацій в міоцитах передсердь та шлуночків як дія на рефрактерність вивільнення Ca^{2+} з саркоплазматичного ретикулуму; можливості нового методу просторово складної дифракційно-обмеженої фотоактивації та фотовідновлення в живих клітинах були проведені на базі кафедри фізіології та біофізики, Медичного центру Університету РАШ (Чикаго, США; проф. Блатер Л.). Досліди по визначенню розподілу амплітуди елементарних подій вивільнення Ca^{2+} за участі декількох RyRs при використанні багатомірної конфокальної мікроскопії; визначення якім чином відбувається регуляція RyRs кальцієм на зовні рецептору; ефект кальцій-індукованого активації даних рецепторів та вивільнення Ca^{2+} із СР депо в скелетному м’язі на локальне збільшення концентрації кальцію були проведені на базі кафедри фізіології та біофізики, Медичного центру Університету РАШ (Чикаго, США; проф. Ріос Е.). Автор щиро вдячний проф. Н. Широкова Школи Медицини Нью-Джерсі Університету медицини та стоматології Нью-Джерсі (Ньюарк, США), проф. Л. Блатеру та проф. Е. Ріусу Медичного центру Університету РАШ (Чикаго, США) за плідну співпрацю. Частина експериментів була проведена у співпраці з д.б.н. Оленою Ісаєвою, PhD Figueroa L., PhD Maxwell J.T., PhD Domeier T.L., PhD Martins A.S., к.б.н. Наталією Розумною та к.б.н. Вітою Ганжою. Вони є співавторами відповідних статей. Автор щиро висловлює подяку науковому консультанту, професору О. О. Лук'янець, за невимовну підтримку та цінні поради під час написання дисертаційної роботи, та висловлює щирі подяки співробітникам відділу біофізики іонних каналів Інституту фізіології ім. О.О. Богомольця за підтримку у написанні дисертаційної роботи.

Апробація результатів дисертації. Основні положення матеріалів дисертації докладалися на семінарах Інституту ім. О. О. Богомольця НАН України, а також на наступних міжнародних симпозіумах і з'їздах: Американського Біофізичного Товариства (Лонг Біч, 2005, Солт Лейк Сіті, 2006, Балтімор 2007, Лонг Біч 2008, Бостон, 2009, Сан Франциско, 2010, Балтімор 2011, Сан Дієго, 2012); Всеукраїнської конференції Товариства Нейронаук (Київ, 2017, 2022 Україна); Українського Фізіологічного Товариства (Київ, 2019, 2021, Україна) та XI з'їзд Українського біофізичного товариства (Київ, 2023 Україна).

Публікації. Результати дисертації викладено у 12 статтях (опублікованих у виданнях, віднесених до першого і другого квартилів; Q1 і Q2) та 5 статтях віднесених до третього і четвертого квартилів (Q3 і Q4) відповідно до класифікації SCImago Journal and Country Rank або Journal Citation Reports, одним розділом у нейрофізіологічному нарисі, патентом на корисну модель та 27 тезах міжнародних конференцій та з'їздів.

РОЗДІЛ 1. ЗМІНИ ВНУТРІШНЬОКЛІТИННОЇ КОНЦЕНТРАЦІЇ КАЛЬЦІЮ У КАРДІОМІОЦИТАХ

1.1 Роль іонів кальцію у спряженні збудження і скорочення у кардіоміоцитах

УДК 612.17:546.41:577.352

Роль іонів кальцію у спряженні збудження і скорочення у кардіоміоцитах

В.М. Шкриль

Інститут фізіології ім. О. О. Богомольця НАН України, Київ; e-mail: slava@biph.kiev.ua

Кальцій є важливим сигнальним елементом та універсальним внутрішньоклітинним посередником, а також визначальним іоном у спряженні збудження і скорочення. Цей огляд присвячено опису кальцієвих рецепторів у цьому процесі у міоцитах міокарда. Основними джерелами підвищення внутрішньоклітинної концентрації іонів кальцію є його надходження з позаклітинного середовища за рахунок дигідропіридинових рецепторів і вивільнення з внутрішніх депо саркоплазматичного ретикулума через активацію ріанодинових рецепторів. Відсутність системи поперечних трубочок у міоцитах передсердя робить процес вивільнення Ca^{2+} специфічним порівняно з міоцитами шлуночків міокарда. У міоцитах передсердь, але не шлуночків, експресуються також інозитолтрифосфатні рецептори, які доповнюють регуляцію Ca^{2+}-сигналу. Описані в цьому огляді останні дані щодо внутрішньоклітинних кальцієвих рецепторів розкривають більш детально спряження збудження і скорочення та деталізують Ca^{2+} - залежну регуляцію кардіоміоцитів.

Ключові слова: Ca^{2+}; ріанодиновий рецептор; кардіоміоцит; кальційіндуковане вивільнення кальцію; дигідропіридиновий рецептор.

У кардіоміоциті спряження збудження і скорочення супроводжується низкою безперервних, послідовних і пов’язаних між собою процесів: від електричного збудження міоцита і кальцієвої мобілізації до розвитку скорочення в міокарді [1]. Потенціал дії (ПД), що з’являється при збудженні серцевої клітини, деполяризує сарколему. Це спричиняє до відкривання потенціалкерованих кальцієвих каналів L-типу (дигідропіридинових рецепторів, DHPR) і різкого підвищення локальної концентрації іонів кальцію поблизу плазмалеми та біля саркоплазматичного ретикулума (СР). Ca^{2+}, що ввійшов до клітини, активує канали вивільнення кальцію (ріанодинові рецептори; RyRs) у СР, що призводить до додаткового виходу Ca^{2+} з депо і різкого збільшення його концентрації в цитозолі [1]. У цьому процесі іон кальцію є вторинним посередником, запускаючи вивільнення кальцію із СР, що насамкінець і зумовлює до скорочення. Детально опишемо ці процеси.

Спряження збудження і скорочення

Міокард складається з різних типів клітин, які можна поділити на серцеві волокна – кардіоміоцити і клітини сполучної тканини – фібробласти. Останні, на відміну від кардіоміоцитів, є електрично незбудливими клітинами, що можуть утворювати щілинні контакти з міоцитами. Кардіоміоцити відрізняються за своїми структурами і функціями. Їх можна поділити на клітини шлуночків і передсердь, котрі виконують скоротливу функцію міокарда, на клітини синоатріального та атріовентрикулярного вузлів серцевого ритму, пучок Гіса, а також на волокна провідної системи шлуночків, які також називають волокнами Пуркіньє. Вони забезпечують поширення збудження по міокарду шлуночків. Розмір клітин міокарда може становити від декількох мікрометрів у діаметрі і сотень мікрометрів у довжину. Клітини передсердя мають меншу ширину порівняно з міоцитами шлуночків. Основними внутрішньоклітинними компонентами кардіоміоцита є міофібрили (скоротливий апарат), мітохондрії та СР [1]. Клітини вузлів серцевого ритму генерують запускаючий імпульс, який спричинює швидке відкривання натрієвих каналів (2 мс), і іони натрію, що входять у клітину, деполяризують сарколему міоцита, що призводить до початку скорочення кардіоміоцитів. У період між скороченнями (діастола, розслаблений стан) сарколема добре проникна для калію, але непроникна для натрію [2].

При деполяризації кардіоміоцита у сарколемі відкриваються потенціалкеровані кальцієві канали L-типу, що зумовлює збільшенню локальної концентрації кальцію у щілинному просторі біля устя відкритих каналів, між сарколемою та СР [3]. Кальцій, що входить у щілинний простір, дифундує до саркоплазматичної мембрани ретикулума, активуючи RyRs за допомогою кальційіндукованого вивільнення кальцію (CICR; [4]), що призводить до глобального вивільнення кальцію з депо і дифузії його до скоротливого апарата. Частка кальцію, що входить у клітину через DHPR-канали, набагато менша від тієї, яка вивільняється з депо (СР) [5]. Коли кальцієві канали L-типу відкриті, у щілинному просторі локальна концентрація Ca^{2+} різко збільшується до 10 – 20 мкмоль/л. Цієї концентрації достатньо, щоб активувати ріанодиновий рецептор (RyR) і вивільнити значну частину кальцію з СР [6]. При вивільненні Ca^{2+} з депо його концентрація у щілинному просторі збільшується до 100 мкмоль/л [7]. Іони кальцію дифундують з щілини, активуючи скоротливу систему, тим самим сприяючи скороченню клітини, що забезпечує необхідну силу скорочення серця для перекачування крові по організму.

Скорочення міоцита відбувається циклічно. Спочатку канали RyRs знаходяться переважно у закритому стані. При деполяризації і значному вході кальцію у щілинний простір, кальцій зв'язується з цитозольним місцем активації RyR, що призводить до

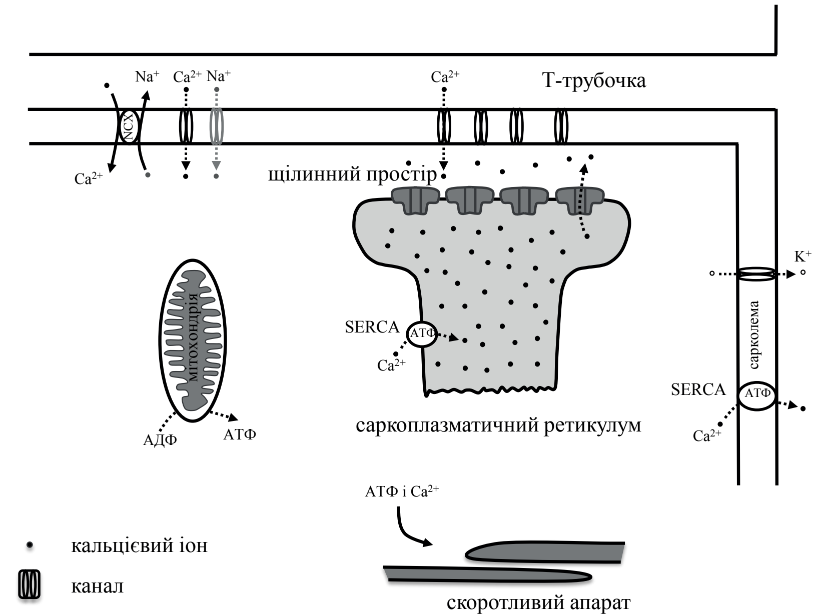

Схематичне зображення спряження збудження і скорочення (з модифікацією з [1]) відкривання каналу і викиду кальцію із СР. При цьому кальцій також починає зв’язується з місцем RyR, відповідальним за інактивацію каналу, переводячи його з відкритого стану до інактивованого. Після того як концентрація кальцію зменшується RyR-канал переходить з інактивованого у закритий стан та готовий до повторного відкривання [1, 8].

Сумарна кількість кальцію, що увійшов через DHPR та вивільнився при відкриванні RyRs у СР, становить значення, необхідне для активації скорочувального апарату [9]. Іони кальцію надходять до актин-міозинового комплексу, зв’язуються з тропоніном-С і за наявності АТФ запускають скорочення (весь процес схематично показано на рисунку). По завершенні скорочення іони кальцію зворотно перерозподіляються у клітині за рахунок активності сарко/ендоплазматичної АТФази (SERCA) і кальцієвого уніпортера мітохондрій та виводяться з клітини за допомогою Na^+/Ca^{2+}-обмінника і АТФази сарколеми. Процес закінчується тим, що K^+ пасивно виходять з клітини, реполяризуючи її мембрану [1].

Для забезпечення транзієнтної зміни кальцієвого сигналу, в секундному часовому інтервалі і амплітуді, достатньої для скорочення, в міоцитах міокарда має існувати висока і водночас гнучка система буферизації Ca^{2+}. У цитоплазмі він зазвичай знаходиться у зв’язаному стані у співвідношенні 100: 1 до вільного. Під час скорочення воно відразу змінюється приблизно до 10: 1 [10]. Буферизація кальцію забезпечує оптимальне видалення вільного Ca^{2+} з цитозолю, щоб забезпечити потрібну кількість, доступну для скорочення в наступному ритмі [11].

Процес активації RyRs по всій клітині відрізняється між міоцитами передсердь і шлуночків серця. Це зумовлено відмінностями структури клітин, оскільки у міоцитах передсердь відсутні системи поперечних трубочок (Transverse tubule; Т-трубочок). Система Т-трубочок забезпечує близькість розташування Ca^{2+}-каналів L-типу до кластерів RyRs по всьому об’ємі клітини.

Система поперечних трубочок

Система Т-трубочок складається з вузьких трубочок, що пронизують клітину вглиб. Їх внутрішня частина сполучається із зовнішнім простором клітини. Вміст таких трубочок подібний до позаклітинного розчину і має високу концентрацію натрію і низький вміст калію. Як і сарколема, система Т-трубочок бере участь у передачі потенціалу дії. ПД розповсюджується по Т-трубочці, що забезпечує швидке поширення процесу скорочення по всьому об’єму клітини. При цьому ПД поширюється набагато швидше, ніж дифузійні процеси з ділянок з високою концентрацією кальцію [12].

Саркоплазматичний ретикулум (СР)

Система органел малого розміру, що містять Ca^{2+}, розташованих практично по всій клітині, називається СР. У стані спокою вільна концентрація кальцію у ньому становить 1 ммоль/л [13, 14], де його частина зв’язана буфером з високою ємністю і з низькою афінністю до Ca^{2+} [13]. СР можна поділити на два підтипи: цистерни, що прилягають до сарколеми, і саркотрубочна мережа, що оточує скоротливі білки. Цистерни ретикулума контактують як з сарколемою, так і з системою поперечних трубочок, при цьому СР дещо сплюснутий таким чином, що його мембрана та система Т-трубочок є паралельними один до одного. Така спільна структура з мембран СР і Т-трубочок отримала назву діади. У скелетному м’язі організація мембрани дещо складніша: дві цистерни СР прилягають до однієї Т-трубочки з двох боків і утворюють структуру, що отримала назву тріади.

Особливості ультраструктури ріанодинових і дигідропіридинових рецепторів

RyRs групуються у кластери у мембрані СР та утворюють окремі місця викиду Ca^{2+} або кластери [15]. Відстань між окремими рецепторами у кластері становить до 30 нм. Оскільки розмір самого кластера близько 250 нм, це дає змогу розташувати у ньому до 100 RyRs. Кластери RyRs знаходяться у безпосередній близькості до сарколеми або Т-трубочки, з щілиною у 10 – 12 нм. RyRs і Ca^{2+}-канали L-типу часто розташовуються поряд, утворюючи функціональний елемент системи збудження та скорочення, який отримав назву елемент вивільнення кальцію ($ЕВСа^{2+}$, Ca^{2+} release unit; [16]). Ca^{2+}-канали L-типу і RyRs мають велику ймовірність колокалізації в $ЕВСа^{2+}$ і утворюють функціональний елемент [17]. Куплоном називаються узгоджені дії Ca^{2+}-каналів L-типу і RyRs у функціональному елементі [16, 18]. Іншими словами, куплон є функціональною групою синхронно працюючих каналів і сполучних білків СР. Активація одного або декількох RyRs в $ЕВСа^{2+}$ призводить до швидкого підключення інших рецепторів, активуючи їх протягом кількох мілісекунд, що можна бачити в експерименті за допомогою реєстрації мініатюрних кальцієвих сигналів, які отримали назву Ca^{2+}-спалахів (див. нижче).

Ультраструктурні дослідження показали, що, залежно від виду тварин, розміри кластера можуть варіювати від декількох десятків до 200 каналів RyRs [16, 19]. Так, за допомогою імунофлуоресцентної мікроскопії було виявлено, що кардіоміоцити щура містять 40 – 60 RyRs у ділянці $ЕВСа^{2+}$ при більш щільній упаковці або ж 30 – 40 при менш щільній [20]. Пропорція Ca^{2+}-каналів L-типу у серцевому м'язі варіює від 10 до 100 % від загального числа RyRs [21]. Близько 90 % усіх DHPR кардіоміоцита знаходяться біля сполучної щілини у місцях викиду Ca^{2+} [22]. Нещодавно було показано, що маленький розмір кластерів RyRs (10 – 50 од.) дає змогу забезпечити повнорозмірну величину події вивільнення Ca^{2+} з СР (за допомогою активації DHPRs), але не здатний забезпечити спонтанний Ca^{2+}-спалах або хвилю під час діастоли. Збільшення розміру кластера (> 75) поступово підвищує ймовірність спостережень спонтанних Ca^{2+}-спалахів, збільшуючи можливість появи аритміподібної Ca^{2+}-активності [23]. Таким чином, величина кластера RyRs відіграє важливу роль у функціонуванні $ЕВСа^{2+}$.

Ріанодиновий рецептор

RyR є каналом вивільнення кальцію з СР . Свою назву він отримав від алкалоїда ріанодину, який є специфічним і селективним лігандом цього рецептора. Ріанодин у низьких концентраціях (1 – 1000 нмоль/л) прискорює втрати кальцію везикулами СР, але у високих концентраціях (> 100 мкмоль/л) блокує вивільнення кальцію, тобто блокує канал RyR [24]. Сам канал є тетрамером розміром в 560 кДа та складається з 4 однакових субодиниць [25]. У клітинах ссавців існує три ізоформи RyRs: RyR1, RyR2, RyR3 [26]. RyR1 експресується переважно у скелетних м'язах, RyR2 – у кардіоміоцитах і гладеньких м'язах, RyR3 – у нейронах головного мозку і дорсальних гангліїв.

Кальційзалежні місця активації RyR розміщені з цитозольного, так і з люмінального боку рецептора. Ці сайти синергічно доповнюють механізм його відкривання за допомогою активації каналу люмінальним і цитоплазматичним Ca^{2+}. RyRs також мають два місця інгібування в своїх цитоплазматичних доменах з афінністю до Ca^{2+} близько 1 мкмоль/л і 1 ммоль/л. Магній конкурує з Ca^{2+} на цих місцях інгібування RyR, що відіграє важливу роль в модуляції Ca^{2+} - залежної активності в міоцитах [27].

Активація RyR2 і RyR3 є кальційзалежним процесом і запускається у кардіоміоцитах підвищенням цитоплазматичної концентрації Ca^{2+}. Однак регуляція RyR1 має особливості у скелетних м'язах, оскільки цей підтип рецепторів безпосередньо пов'язаний з DHPR через молекули білка напруги CaV1.1, що при деполяризації призводить до зміни його сенсора напруги в мембрані Т-трубочки [28]. При цьому відкривання RyR регулюється безпосередньо деполяризацією плазмалеми, і електричний сигнал передається від L-типу Ca^{2+} каналу безпосередньо на RyR-канал за допомогою сенсорного білка напруги [29].

Такий тип активації RyR отримав назву деполяризація індукованого вивільнення кальцію із СР. Він є прямим і не вимагає входу Ca^{2+} через DHPR-канал. Описаний механізм працює у скелетному волокні, де RyRs відкриваються навіть за відсутності зовнішнього кальцію. У кардіоміоциті такого не відбувається, і зовнішньоклітинний кальцій є необхідним для активації RyRs.

Клітини передсердь і шлуночків серця: морфологія і тип саркоплазматичного ретикулума

Кардіоміоцити, які виконують скоротливу функцію, можна поділити на два типи: клітини передсердь і шлуночків. У міоцитах шлуночків добре розвинена тривимірна мережа Т-трубочок [30]. СР розташовується у безпосередній близькості до них на відстані 10 – 20 нм, утворюючи так звані діади [31], як зазначалося вище. СР, розташований у безпосередній близькості до Т-трубочки, називається сполучним (с-СР). У міоцитах передсердь система Т-трубочок погано розвинена або навіть відсутня [32, 33]. У таких клітинах можна виділити два типи СР: сарколемно-сполучний СР (сс-СР), який знаходиться на периферії клітини, де СР тісно пов’язаний з поверхневою мембраною міоцита [34], і несполучний СР (нс-СР), локалізований у глибині клітини. Таким чином, у міоцитах передсердя сс-СР тісно стикається з L-типом кальцієвих каналів, водночас нс-СР не пов’язаний з DHPRs. Як сс-СР, так і нс-СР беруть активну участь у вивільненні кальцію за допомогою відкривання RyRs [33-35]. Асоціація RyRs з Ca^{2+}-каналами L-типу отримала назву «з’єднання на периферії». На периферії клітини $EBCa^{2+}$ функціонально організовані як класичний куплон [36, 37], що спостерігається у волокнах скелетного м’яза або кардіоміоцитах шлуночків.

Процес вивільнення Ca^{2+} в кардіоміоцитах

Велику частину інформації про процес спряження збудження і скорочення отримано на кардіоміоцитах шлуночків. У цих клітинах при появі ПД активуються Ca^{2+}-канали L-типу як у сарколемі, так і в системі Т-трубочок майже синхронно по всій клітині. Просторова і часова сумація вивільнення Ca^{2+} з окремих $EBCa^{2+}$ призводить до появи глобального клітинного Ca^{2+}-сигналу, який просторово досить однорідний по всьому об’єму.

У клітинах передсердь цей процес відрізняється, що зумовлено відсутністю або слабким розвитком системи Т-трубочок [32, 33]. У результаті вивільнення кальцію з СР не є однорідним і синхронним процесом [2, 9, 32, 38]. ПД і відкривання L-типу Ca^{2+}-каналів забезпечує вхід потрібного кальцію у клітину для активації RyRs за допомогою CICR спочатку лише на периферії клітини (у сс-СР) [2, 34]. Поступово, з затримкою у 2 мс, Ca^{2+}-сигнал поширюється всередину клітини і починається вивільнення Ca^{2+} з нс-СР [2].

Вивільнення кальцію на периферії клітини забезпечує досить високий Ca^{2+}-градієнт, щоб подолати ємність ендогенного буфера [39], і поступово активує RyRs, розташовані всередині клітини за допомогою CICR при дифузії іонів кальцію з периферії до центру. При цьому відбувається послідовне вивільнення і поширення Ca^{2+}-сигналу всередину клітини за допомогою механізму вивільнення-дифузія-вивільнення (ВДВ) [2, 40].

Залишається відкритим питання про те, яким чином першочергово активуються RyRs у мембранах нс-СР. Добре відомо, що RyR2 має низьку чутливість до Ca^{2+} [41-43], що виключає можливість їх активування за допомогою CICR у фізіологічних умовах. На периферії клітини концентрація цитозольного Ca^{2+}, який входить через DHPRs, ледь перевищує 1 мкмоль/л, що не достатньо для відкривання RyRs нс-СР. Але в експерименті при регулярній частоті стимуляції міоцитів передсердя більшість цих рецепторів активуються не лише на периферії, а й у центрі [39]. Тобто сам механізм активації RyR специфічний.

Для більш детального розуміння вивільнення кальцію у міоцитах передсердя опишемо хід поширення кальцієвої хвилі у клітинах шлуночка. Вона поширюється по всій поверхні клітини і спостерігається при перезавантаженні СР іонами кальцію. При цьому збільшення концентрації вільного кальцію ($[Ca^{2+}]_i$) на передньому фронті хвилі викликає локальне, зворотне захоплення Ca^{2+} у СР за допомогою SERCA-помпи. Таке збільшення концентрації кальцію всередині СР підвищує чутливість RyRs до Ca^{2+}, забезпечуючи CICR [44, 45]. Таким чином у кардіоміоцитах шлуночків зменшує поріг активації RyRs Ca^{2+} і дає змогу поширюватися від периферії до центру клітини, активуючи більшу частину рецепторів клітини. Цей механізм був запропонований на підставі непрямих даних [46], теоретичних міркувань [47, 48] і експериментально підтверджений прямими вимірюваннями як цитозольного, так і люмінального Ca^{2+} [49] .

Було запропоновано механізм, що пояснює вивільнення кальцію у кардіоміоцитах передсердь для нс-СР [50]. Як було описано вище, у цих клітинах ПД викликає деполяризацію сарколеми і активує L-тип Ca^{2+}-каналів. За допомогою CICR вивільняється кальцій з сс-СР на периферії клітини, спричиняє початковий градієнт Ca^{2+} у цитоплазмі. Вивільнений кальцій захоплюється SERCA-помпою у прилеглі органели нс-СР, що сенсибілізує RyRs за допомогою збільшення вмісту Ca^{2+} у цих органелах. Це, у свою чергу, знижує поріг активації цитозольного сайту регуляції RyRs і, вже при підвищеній концентрації Ca^{2+} у цитозолі він вивільняється з органел нс-СР. Також підвищується його вмісту у СР, що в свою чергу подовжує час відкритого стану RyRs [51] і збільшує Ca^{2+}-потік через рецептори, як позитивний зворотний зв’язок цього процесу. Поступове поширення сигналу в цитоплазмі підвищує концентрацію кальцію у сусідніх органелах СР, забезпечуючи поступове його вивільнення по всій клітині та призводить до поширення сигналу як всередині мережі СР органел, так і в цитоплазмі. Такий механізм отримав назву вивільнення-поширення-захоплення-вивільнення (ВПЗВ; [50]), який описує процес активації і вивільнення Ca^{2+} всередині міоцитів передсердь. Цей процес подібний до вищеописаного механізму поширення кальцієвої хвилі в міоцитах шлуночка при перезавантаженні СР кальцієм.

Припинення вивільнення Ca^{2+} із саркоплазматичного ретикулума

Оскільки скорочення і розслаблення міокарда є циклічним, регуляція вивільнення Ca^{2+} з депо вимагає наявності механізму припинення його вивільнення. При розслабленні міоцита під час діастоли концентрація іонів кальцію у цитозолі починає знижуватися, що дає змогу йому від’єднатися від тропоніну. $[Ca^{2+}]_i$ відновлюється до низького значення через повернення Ca^{2+} до СР за допомогою SERCA-помпи, виведення іонів з клітини за рахунок Na^+/Ca^{2+}-обмінника і Ca^{2+}-АТФази у сарколемі та його захоплення мітохондріями за допомогою Ca^{2+}-уніпортера.

Існує декілька принципово відмінних механізмів припинення вивільнення Ca^{2+} з СР. Вони регулюється люмінальними механізмами, що ґрунтуються на регуляції відкривання-закривання RyRs власне кальцієм всередині СР [51], люмінальним сенсором стану [44, 52] або за допомогою калсеквістрину (кальційзв’язуючого білка всередині СР; calsequestrin, або CASQ) [53, 54]. Також термінація вивільнення Ca^{2+} може відбуватися за допомогою негативного алостеричного зв’язку між RyRs (закривання одного RyR сприяє закриванню інших каналів [55, 56]), стохастичного виснаження (stochastic attrition), та існує велика ймовірність одночасного переходу каналів до закритого стану [55], або механізму виснаження, при якому зменшується потік Ca^{2+} нижче від порога для підтримки CICR [57, 58]. Процес локального виснаження СР є важливим для регуляції припинення вивільнення іонів кальцію як за нормальних, так і патологічних умов [59].

Припинення вивільнення у міокарді передсердь відрізняється у сс-СР та нс-СР. У центрі цих клітин CASQ має меншу колокалізацію з RyRs і більш слабке їх інгібування, хоча збудливість центральних RyRs є більшою [59, 60]. Знижена експресія білка CASQ призводить до зменшення буферної ємності, і, у свою чергу, – до зниження концентрації загального кальцію всередині СР [50]. У міоцитах передсердя менше виснаження СР на периферії і велика амплітуда Ca^{2+}-сигналу в цитоплазмі цієї ділянки свідчить про більшу ефективність CICR для RyRs сс-СР. Також реактивація RyRs-каналів у нс-СР повільніша, ніж у сс-СР, що пов'язано з відмінностями механізмів вивільнення на периферії і всередині клітини [2]. Специфіка механізму припинення вивільнення Ca^{2+} у нс-СР дає змогу при меншій амплітуді Ca^{2+}-сигналу викликати більше виснаження СР при CICR і сприяє поширенню Ca^{2+} всередину клітини. На периферії клітини він вивільняється з СР у малому об'ємі та з великою ймовірністю активує всі RyRs в $EBCa^{2+}$. При цьому канали практично одночасно інактивуються за допомогою кальційзалежної інактивації. В ділянці нс-СР завдяки більш повільній активації не всі RyRs-канали відразу відкриваються і співвідношення відкритих-закритих поступово змінюється. Через це Ca^{2+}-сигнал у центрі помітно подовжується порівняно з периферією. Така більш тривала робота $EBCa^{2+}$ для нс-СР призводить до більшого виснаження кальцію із СР. Це було підтверджено експериментально за допомогою реєстрації мініатюрних Ca^{2+}-сигналів (спалахів), коли їх амплітуди сильно відрізнялися в центі та на периферії [2].

Кальцієві спалахи

Методи клітинної електрофізіології та конфокальної мікроскопії дали змогу з'ясувати механізми електричної і скоротливої активності міокарда, а також дослідити його фармакологічну регуляцію як на рівні окремої клітини, так і цілого серця. У кардіоміоцитах передсердь і шлуночків міокарда були зареєстровані елементарні, стереотипні, локальні процеси вивільнення кальцію з СР за допомогою відкривання RyRs, які отримали назву кальцієвих спалахів (Ca^{2+} spark) [61]. Такі швидкі викиди кальцію можна візуалізувати за допомогою скануючої, конфокальної мікроскопії з використанням флуоресцентного барвника. Ca^{2+}-спалахи у кардіоміоциті можуть спостерігатися у стані спокою (або при дуже низькій частоті стимуляції), а також з'являються стохастичним чином навіть за відсутності входу Ca^{2+}. Кальцієві спалахи у міоцитах шлуночків спостерігаються по всій клітині у місцях наближення Т-трубочки з СР [31, 61]. У цих клітинах $EBCa^{2+}$ (де і з'являються Ca^{2+}-спалахи) позиціонуються один від одного на відстані 1 мкм радіально або 2 мкм поздовжньо [6], а в міоцитах передсердя $EBCa^{2+}$ розташовані на відстані 2 мкм один від одного [34]. У цих клітинах Ca^{2+}-спалахи спостерігаються як на периферії, так і в центральних ділянках клітини [32, 35, 62], однак перші виникають частіше [35]. Спалахи у міоцитах шлуночків просторово асиметричні; вони на 18% більш в поздовжньому напрямку [35] (хоча Banyasz та співавт. [63] спостерігали просторово симетричні події). Симетричні спалахи були зареєстровані також у скелетних м'язах жаби, але вони подовжувалися у поперечному напрямку при попередній активації RyRs за допомогою кофеїну [64].

Аналіз Ca^{2+}-спалахів має важливе значення для розуміння ролі дифузії іонів кальцію в місцях викиду з СР у спряженні збудження і скорочення. Так, при більш вираженій дифузії Ca^{2+} в одному напрямку, спалах імовірно теж повинен збільшуватися у цьому ж напрямку. Асиметричний спалах може бути пояснено також особливостями спряження збудження і скорочення або умовами реєстрацій. Gonzalez і співавт. [65] пояснювали це явище участю декількох RyRs, задіяних в утворення спалаху. Обмеженість дифузії у будь-якому напрямку може обумовлюватися наявністю певних механічних бар'єрів, що гальмують поширення іонів [66]. Так, якщо Ca^{2+} починає дифундувати однорідно від симетричного кластера RyRs, але потім сягає перешкоди, то починає поширюватися анізотропно. У такому разі і кальцієвий флуоресцентний сигнал буде вкорочений у цьому напрямку. Така асиметрія Ca^{2+}-спалахів може зумовлюватися анізотропністю розташування клітинних органел або міофіламентів у кардіоміоциті. Перешкодою до дифузії Ca^{2+} є також мітохондрії [67], що відіграють активну роль у поглинанні кальцію, як це було запропоновано для клітин серця [68] та інших органів [69, 70].

Кожен Ca^{2+}-спалах являє собою вивільнення кальцію з кластера RyRs при синхронній активності від 6 до 20 каналів [5]. У міоцитах шлуночків глобальний кальцієвий сигнал, що викликається ПД, утворюється просторовим сумуванням окремих спалахів [3, 71]. А у клітинах передсердь він являє собою спочатку сумування Ca^{2+}-спалахів у зоні сарколеми (периферійне підвищення), а потім відображає подальшу їх появу і поступове поширення сигналу вглиб клітини [32, 34].

Інозитолтрифосфатні рецептори

Допоміжним механізмом регуляції скорочення міоцитів передсердь є процес модуляції вивільнення кальцію із СР за допомогою інозитолтрифосфатних рецепторів (IP_3Rs). Вони тісно пов'язані з родиною RyR, розділяючи з ними високу структурну гомологію [72]. IP_3Rs експресуються у міоцитах передсердя з високою щільністю [11]. У клітинах шлуночків вони відсутні [73]. IP_3Rs зазвичай активуються судиноактивним агоністом ангіотензином-II, ендотеліном та іншими під час гуморальної регуляції, що підсилює можливості модуляції процесів скорочення. IP_3 - опосередковане вивільнення кальцію може модулювати процес вивільнення кальцію в міоцитах передсердя [74]. Вплив IP_3Rs більш виражений на периферії клітини і практично відсутній у її центрі. Таким чином, вивільнення кальцію на периферії міоцита має додаткову IP_3Rs, зумовлену регуляцію скорочення клітини.

Стисло узагальнимо цей огляд. Процес вивільнення іонів кальцію у кардіоміоцитах відрізняється у клітинах передсердь і шлуночків. Він ініціюється входом зовнішнього кальцію за допомогою DHPRs. У клітинах шлуночків з розвиненою системою Т-трубочок, деполяризація сарколеми і відкривання L-типу Ca^{2+}-каналів забезпечує концентрацію іонів кальцію, потрібну для активації RyRs за допомогою CICR по всьому об'єму клітини. У міоцитах передсердь, де відсутня система Т-трубочок, деполяризація сарколеми призводить до відкривання L-типу Ca^{2+}-каналів і активує RyRs спочатку лише на периферії клітини. Через декілька мілісекунд Ca^{2+} починає дифундувати всередину клітини і активувати RyRs за допомогою механізмів ВДВ у цитоплазмі та цитозольно-люмінального ВПЗВ. У міоцитах передсердь, але не шлуночків, експресуються також IP_3Rs, які доповнюють регуляцію Ca^{2+}-сигналу, як позитивний IP_3Rs-опосередкований ефект, і гуморальна регуляція процесу скорочення серця. Така специфічна регуляція процесу вивільнення Ca^{2+} в кардіоміоцитах забезпечує вибірковість і унікальність підвищення його внутрішньоклітинного вмісту, дає потрібну концентрацію для скорочення клітин як передсердь, так і шлуночків. Вивільнення кальцію у цих клітинах охарактеризовано як на глобальному рівні Ca^{2+}-транзієнтів, так і на локальному – Ca^{2+}-спалахів. Описані механізми Ca^{2+}-сигналізації дають змогу узагальнити процеси спряження збудження і скорочення у кардіоміоцитах.

За допомогою описаних механізмів вивільнення Ca^{2+} в процесі спряження збудження і скорочення доповнює наше розуміння фізіології скорочення кардіоміоцита. Картина активації і термінації вивільнення Ca^{2+} в цілому з'ясована. Хоч залишаються деякі моменти стосовно: активації і припинення вивільнення Ca^{2+} з СР; точної кількості RyRs, що беруть участь у Ca^{2+}-спалаху; рівня виснаження кальцію в СР; морфологічних особливостей; точної локалізації RyRs з іншими рецепторами і каналами. Дослідження, як на рівні окремих каналів, так і всього процесу в цілому, важливі для розуміння не тільки фундаментальних основ фізіології скорочення серця, але і патологічних станів, наприклад серцевої недостатності. Поява нових флуоресцентних систем реєстрації зі збільшеною часовою і просторовою здатністю, і нових Ca^{2+}-чутливих зондів та комп'ютерного моделювання, дасть змогу деталізувати приховані механізми вивільнення кальцію в кардіоміоцитах.

The author of this study confirm that the research and publication of the results were not associated with any conflicts regarding commercial or financial relations, relations with organizations and/or individuals who may have been related to the study, and interrelations of co-authors of the article.

В.М. Шкрыль

РОЛЬ ИОНОВ КАЛЬЦИЯ В СОПРЯЖЕНИИ ВОЗБУЖДЕНИЯ И СОКРАЩЕНИЯ В КАРДИОМИОЦИТАХ

Кальций является важным сигнальным элементом и универсальным внутриклеточным посредником, и определяющим ионом в процессе сопряжения возбуждения и сокращения. Данный обзор посвящен описанию кальциевых рецепторов в этом процессе в миоцитах миокарда. Основными источниками повышения внутриклеточной концентрации кальция являются его поступление из внеклеточной среды за счет дигидропиридиновых рецепторов и высвобождение из внутренних депо саркоплазматического ретикулума (СР) путем активации рианодиновых рецепторов (RyR). Отсутствие системы поперечных трубочек в миоцитах предсердия делает высвобождение Ca^{2+} специфическим в сравнении с желудочками миокарда. В миоцитах предсердий, но не желудочков, экспрессируются также инозитолтрифосфатные рецепторы, которые дополняют регуляцию Ca^{2+}-сигнала. Описанные в данном обзоре последние данные относительно внутриклеточных кальциевых рецепторов раскрывают более детально сопряжение возбуждения и сокращения и детализируют Ca^{2+} - зависимую регуляцию кардиомиоцита.

Ключевые слова: Ca^{2+}; рианодиновый рецептор; кардиомиоцит; кальцийиндуцированное высвобождение кальция; дигидропиридиновый рецептор.

V.M. Shkryl

ROLE OF CALCIUM IONS IN EXCITATION-CONTRACTION COUPLING IN CARDIOMYOCYTES

Calcium is an important signaling element and universal intracellular messenger and the determining ion of Excitation-Contraction Coupling. This review describes calcium receptors at this process in cardiomyocytes. The main sources of increase of intracellular calcium level is entry from extracellular medium by dihydropyridine receptors and release from internal stores, in particular, from the sarcoplasmic reticulum (SR) via activation of ryanodine receptors. The absence of a transverse tubular network in the atria myocytes makes the Ca^{2+} release process specific to the ventricular cells of the myocardium. Atrial myocytes, but not ventricular, also express inositol triphosphate receptors that complement the regulation of Ca^{2+} signal. Described in this review the latest data on intracellular calcium receptors disclosed in more detail of Excitation-Contraction Coupling and details Ca^{2+}-dependent regulation of cardiomyocyte.

Key words: Ca^{2+}; ryanodine receptor; cardiomyocyte; calcium induced calcium release; dihydropyridine receptor.

Bogomoletz Institute of Physiology National Academy of Sciences of Ukraine; Kyiv, e-mail: slava@biph.kiev.ua

REFERENCES

1. Bers DM. Cardiac excitation-contraction coupling. Nature. 2002;415(6868):198-205.
2. Shkryl VM, Blatter LA. Ca(2+) release events in cardiac myocytes up close: insights from fast confocal imaging. PLoS One. 2013;8(4):e61525.
3. Cannell MB, Cheng H, Lederer WJ. Spatial non-uniformities in $[Ca^{2+}]_i$ during excitation-contraction coupling in cardiac myocytes. Biophys J. 1994;67(5):1942-56.
4. Fabiato A. Calcium-induced release of calcium from the cardiac sarcoplasmic reticulum. Am J Physiol. 1983;245(1):C1-14.
5. Shkryl VM, Blatter LA, Rios E. Properties of Ca^{2+} sparks revealed by four-dimensional confocal imaging of cardiac muscle. J Gen Physiol. 2012;139(3):189-207.
6. Bers DM. Calcium cycling and signaling in cardiac myocytes. Annu Rev Physiol. 2008;70:23-49.
7. Langer GA, Peskoff A. Calcium concentration and movement in the diadic cleft space of the cardiac ventricular cell. Biophys J. 1996;70(3):1169-82.
8. Jones PP, Guo W, Chen SRW. Control of cardiac ryanodine receptor by sarcoplasmic reticulum luminal Ca^{2+}. J Gen Physiol. 2017;149(9):867-75.
9. Blatter LA, Kockskamper J, Sheehan KA, Zima AV, Huser J, Lipsius SL. Local calcium gradients during excitation-contraction coupling and alternans in atrial myocytes. J Physiol. 2003;546(Pt 1):19-31.
10. MacGowan GA, Kirk JA, Evans C, Shroff SG. Pressure-

calcium relationships in perfused mouse hearts. Am J Physiol Heart Circ Physiol. 2006;290(6):H2614-24.
11. Gambardella J, Trimarco B, Iaccarino G, Santulli G. New Insights in Cardiac Calcium Handling and Excitation-Contraction Coupling. Adv Exp Med Biol. 2018;1067:373-85.
12. Cleemann L, Wang W, Morad M. Two-dimensional confocal images of organization, density, and gating of focal Ca^{2+} release sites in rat cardiac myocytes. Proc Natl Acad Sci U S A. 1998;95(18):10984-9.
13. Rios E. Perspectives on "Control of Ca release from within the cardiac sarcoplasmic reticulum". J Gen Physiol. 2017;149(9):833-6.
14. Shannon TR, Guo T, Bers DM. Ca^{2+} scraps: local depletions of free $[Ca^{2+}]$ in cardiac sarcoplasmic reticulum during contractions leave substantial Ca^{2+} reserve. Circ Res. 2003;93(1):40-5.
15. Franzini-Armstrong C, Jorgensen AO. Structure and development of E-C coupling units in skeletal muscle. Annu Rev Physiol. 1994;56:509-34.
16. Franzini-Armstrong C, Protasi F, Ramesh V. Comparative ultrastructure of Ca^{2+} release units in skeletal and cardiac muscle. Ann N Y Acad Sci. 1998;853:20-30.
17. Carl SL, Felix K, Caswell AH, Brandt NR, Ball WJ, Jr., Vaghy PL, et al. Immunolocalization of sarcolemmal dihydropyridine receptor and sarcoplasmic reticular triadin and ryanodine receptor in rabbit ventricle and atrium. J Cell Biol. 1995;129(3):673-82.
18. Stern MD, Pizarro G, Rios E. Local control model of excitation-contraction coupling in skeletal muscle. J Gen Physiol. 1997;110(4):415-40.
19. Soeller C, Crossman D, Gilbert R, Cannell MB. Analysis of ryanodine receptor clusters in rat and human cardiac myocytes. Proc Natl Acad Sci U S A. 2007;104(38):14958-63.
20. Hou Y, Jayasinghe I, Crossman DJ, Baddeley D, Soeller C. Nanoscale analysis of ryanodine receptor clusters in dyadic couplings of rat cardiac myocytes. J Mol Cell Cardiol. 2015;80:45-55.
21. Wibo M, Bravo G, Godfraind T. Postnatal maturation of excitation-contraction coupling in rat ventricle in relation to the subcellular localization and surface density of 1,4-dihydropyridine and ryanodine receptors. Circ Res. 1991;68(3):662-73.
22. Franzini-Armstrong C, Protasi F, Ramesh V. Shape, size, and distribution of Ca(2+) release units and couplons in skeletal and cardiac muscles. Biophys J. 1999;77(3):1528-39.
23. Galice S, Xie Y, Yang Y, Sato D, Bers DM. Size Matters: Ryanodine Receptor Cluster Size Affects Arrhythmogenic Sarcoplasmic Reticulum Calcium Release. J Am Heart Assoc. 2018;7(13):1-13.
24. Fabiato A. Effects of ryanodine in skinned cardiac cells. Fed Proc. 1985;44(15):2970-6.
25. Takeshima H, Nishimura S, Matsumoto T, Ishida H, Kangawa K, Minamino N, et al. Primary structure and expression from complementary DNA of skeletal muscle ryanodine receptor. Nature. 1989;339(6224):439-45.
26. McPherson PS, Campbell KP. Characterization of the major brain form of the ryanodine receptor/Ca^{2+} release channel. J Biol Chem. 1993;268(26):19785-90.
27. Laver DR. Regulation of the RyR channel gating by Ca(2+) and Mg(2+). Biophys Rev. 2018;10(4):1087-95.
28. Hernandez-Ochoa EO, Schneider MF. Voltage sensing mechanism in skeletal muscle excitation-contraction coupling: coming of age or midlife crisis? Skelet Muscle. 2018;8(1):22.
29. Rios E, Brum G. Involvement of dihydropyridine receptors in excitation-contraction coupling in skeletal muscle. Nature. 1987;325(6106):717-20.
30. Soeller C, Cannell MB. Examination of the transverse tubular system in living cardiac rat myocytes by 2-photon microscopy and digital image-processing techniques. Circ Res. 1999;84(3):266-75.
31. Shacklock PS, Wier WG, Balke CW. Local Ca^{2+} transients (Ca^{2+} sparks) originate at transverse tubules in rat heart cells. J Physiol. 1995;487 (Pt 3):601-8.
32. Huser J, Lipsius SL, Blatter LA. Calcium gradients during excitation-contraction coupling in cat atrial myocytes. J Physiol. 1996;494 (Pt 3):641-51.
33. Mackenzie L, Bootman MD, Berridge MJ, Lipp P. Predetermined recruitment of calcium release sites underlies excitation-contraction coupling in rat atrial myocytes. J Physiol. 2001;530(Pt 3):417-29.
34. Kockskamper J, Sheehan KA, Bare DJ, Lipsius SL, Mignery GA, Blatter LA. Activation and propagation of Ca(2+) release during excitation-contraction coupling in atrial myocytes. Biophys J. 2001;81(5):2590-605.
35. Sheehan KA, Zima AV, Blatter LA. Regional differences in spontaneous Ca^{2+} spark activity and regulation in cat atrial myocytes. J Physiol. 2006;572(Pt 3):799-809.
36. Scriven DR, Asghari P, Moore ED. Microarchitecture of the dyad. Cardiovasc Res. 2013;98(2):169-76.
37. Stern MD, Song LS, Cheng H, Sham JS, Yang HT, Boheler KR, et al. Local control models of cardiac excitation-contraction coupling. A possible role for allosteric interactions between ryanodine receptors. J Gen Physiol. 1999;113(3):469-89.
38. Berlin JR. Spatiotemporal changes of Ca^{2+} during electrically evoked contractions in atrial and ventricular cells. Am J Physiol. 1995;269(3 Pt 2):H1165-70.
39. Sheehan KA, Blatter LA. Regulation of junctional and non-junctional sarcoplasmic reticulum calcium release in excitation-contraction coupling in cat atrial myocytes. J Physiol. 2003;546(Pt 1):119-35.
40. Keizer J, Smith GD, Ponce-Dawson S, Pearson JE. Saltatory propagation of Ca2+ waves by Ca2+ sparks. Biophys J. 1998;75(2):595-600.
41. Meissner G, Henderson JS. Rapid calcium release from cardiac sarcoplasmic reticulum vesicles is dependent on Ca^{2+} and is modulated by Mg^{2+}, adenine nucleotide, and calmodulin. J Biol Chem. 1987;262(7):3065-73.
42. Cannell MB, Soeller C. Numerical analysis of ryanodine receptor activation by L-type channel activity in the cardiac muscle diad. Biophys J. 1997;73(1):112-22.
43. Qin J, Valle G, Nani A, Chen H, Ramos-Franco J, Nori A, et al. Ryanodine receptor luminal Ca^{2+} regulation:

swapping calsequestrin and channel isoforms. Biophys J. 2009;97(7):1961-70.

44. Gyorke I, Gyorke S. Regulation of the cardiac ryanodine receptor channel by luminal Ca^{2+} involves luminal Ca^{2+} sensing sites. Biophys J. 1998;75(6):2801-10.
45. Gyorke S, Belevych AE, Liu B, Kubasov IV, Carnes CA, Radwanski PB. The role of luminal Ca regulation in Ca signaling refractoriness and cardiac arrhythmogenesis. J Gen Physiol. 2017;149(9):877-88.
46. Keller M, Kao JP, Egger M, Niggli E. Calcium waves driven by "sensitization" wave-fronts. Cardiovasc Res. 2007;74(1):39-45.
47. Ramay HR, Jafri MS, Lederer WJ, Sobie EA. Predicting local SR Ca(2+) dynamics during Ca(2+) wave propagation in ventricular myocytes. Biophys J. 2010;98(11):2515-23.
48. Sobie EA, Williams GSB, Lederer WJ. Ambiguous interactions between diastolic and SR Ca^{2+} in the regulation of cardiac Ca^{2+} release. J Gen Physiol. 2017;149(9):847-55.
49. Maxwell JT, Blatter LA. Facilitation of cytosolic calcium wave propagation by local calcium uptake into the sarcoplasmic reticulum in cardiac myocytes. J Physiol. 2012;590(23):6037-45.
50. Maxwell JT, Blatter LA. A novel mechanism of tandem activation of ryanodine receptors by cytosolic and SR luminal Ca^{2+} during excitation-contraction coupling in atrial myocytes. J Physiol. 2017;595(12):3835-45.
51. Chen H, Valle G, Furlan S, Nani A, Gyorke S, Fill M, et al. Mechanism of calsequestrin regulation of single cardiac ryanodine receptor in normal and pathological conditions. J Gen Physiol. 2013;142(2):127-36.
52. Ching LL, Williams AJ, Sitsapesan R. Evidence for Ca(2+) activation and inactivation sites on the luminal side of the cardiac ryanodine receptor complex. Circ Res. 2000;87(3):201-6.
53. Terentyev D, Viatchenko-Karpinski S, Gyorke I, Volpe P, Williams SC, Gyorke S. Calsequestrin determines the functional size and stability of cardiac intracellular calcium stores: Mechanism for hereditary arrhythmia. Proc Natl Acad Sci U S A. 2003;100(20):11759-64.
54. Gyorke S, Stevens SC, Terentyev D. Cardiac calsequestrin: quest inside the SR. J Physiol. 2009;587(Pt 13):3091-4.
55. Stern MD. Theory of excitation-contraction coupling in cardiac muscle. Biophys J. 1992;63(2):497-517.
56. Marx SO, Gaburjakova J, Gaburjakova M, Henrikson C, Ondrias K, Marks AR. Coupled gating between cardiac calcium release channels (ryanodine receptors). Circ Res. 2001;88(11):1151-8.
57. Laver DR, Kong CH, Imtiaz MS, Cannell MB. Termination of calcium-induced calcium release by induction decay: an emergent property of stochastic channel gating and molecular scale architecture. J Mol Cell Cardiol. 2013;54:98-100.
58. Gillespie D, Fill M. Pernicious attrition and inter-RyR2 CICR current control in cardiac muscle. J Mol Cell Cardiol. 2013;58:53-8.
59. Blatter LA. The intricacies of atrial calcium cycling during excitation-contraction coupling. J Gen Physiol. 2017;149(9):857-65.
60. Schulson MN, Scriven DR, Fletcher P, Moore ED. Couplons in rat atria form distinct subgroups defined by their molecular partners. J Cell Sci. 2011;124(Pt 7):1167-74.
61. Cheng H, Lederer WJ, Cannell MB. Calcium sparks: elementary events underlying excitation-contraction coupling in heart muscle. Science. 1993;262(5134):740-4.
62. Blatter LA, Huser J, Rios E. Sarcoplasmic reticulum Ca^{2+} release flux underlying Ca^{2+} sparks in cardiac muscle. Proc Natl Acad Sci U S A. 1997;94(8):4176-81.
63. Banyasz T, Chen-Izu Y, Balke CW, Izu LT. A new approach to the detection and statistical classification of Ca^{2+} sparks. Biophys J. 2007;92(12):4458-65.
64. Brum G, Gonzalez A, Rengifo J, Shirokova N, Rios E. Fast imaging in two dimensions resolves extensive sources of Ca^{2+} sparks in frog skeletal muscle. J Physiol. 2000;528(Pt 3):419-33.
65. Gonzalez A, Kirsch WG, Shirokova N, Pizarro G, Brum G, Pessah IN, et al. Involvement of multiple intracellular release channels in calcium sparks of skeletal muscle. Proc Natl Acad Sci U S A. 2000;97(8):4380-5.
66. Cheng H, Lederer MR, Xiao RP, Gomez AM, Zhou YY, Ziman B, et al. Excitation-contraction coupling in heart: new insights from Ca^{2+} sparks. Cell Calcium. 1996;20(2):129-40.
67. Budko AY, Strutynska NA, Okhay IY, Semenykhina OM, Sagach VF. [Ca(2+) accumulation in isolated rat heart mitochondria under maintenance of mitochondrial potential]. Fiziol Zh. 2015;61(6):17-25. [Ukrainian].
68. Bassani RA, Bassani JW, Bers DM. Relaxation in ferret ventricular myocytes: unusual interplay among calcium transport systems. J Physiol. 1994;476(2):295-308.
69. Jouaville LS, Ichas F, Holmuhamedov EL, Camacho P, Lechleiter JD. Synchronization of calcium waves by mitochondrial substrates in Xenopus laevis oocytes. Nature. 1995;377(6548):438-41.
70. Shkryl VM, Shirokova N. Transfer and tunneling of Ca^{2+} from sarcoplasmic reticulum to mitochondria in skeletal muscle. J Biol Chem. 2006;281(3):1547-54.
71. Niggli E. Localized intracellular calcium signaling in muscle: calcium sparks and calcium quarks. Annu Rev Physiol. 1999;61:311-35.
72. Santulli G, Nakashima R, Yuan Q, Marks AR. Intracellular calcium release channels: an update. J Physiol. 2017; 595(10):3041-51.
73. Domeier TL, Zima AV, Maxwell JT, Huke S, Mignery GA, Blatter LA. IP_3 receptor-dependent Ca^{2+} release modulates excitation-contraction coupling in rabbit ventricular myocytes. Am J Physiol Heart Circ Physiol. 2008;294(2):H596-604.
74. Kockskamper J, Zima AV, Roderick HL, Pieske B, Blatter LA, Bootman MD. Emerging roles of inositol 1,4,5-trisphosphate signaling in cardiac myocytes. J Mol Cell Cardiol. 2008;45(2):128-47.

Матеріал надійшов до редакції 20.04.2018

1.2 Реєстрація процесів вивільнення Ca^{2+} в кардіоміоцитах за допомогою високошвидкісної конфокальної мікроскопії

Кардіоміоцити є зручним об’єктом для вивчення змін внутрішньоклітинної концентрації кальцію за рахунок змін активності ріанодинових рецепторів. В кардіоміоцитах за фізіологічних умов реалізовано механізм кальцій-індукованого вивільнення кальцію, коли збільшення концентрації кальцію біля ріанодинового рецептору спроможне відкрити сам канал.

Просторова і часова сумація Ca^{2+} подій з окремих одиниць вивільнення Ca^{2+} (CRU), які реєструються як спалахи кальцію, призводить до виникнення загальноклітинного Ca^{2+}-транзієнту (Cheng et al., 1994). У міоцитах шлуночків вивільнення Ca^{2+}, індуковане ПД, є високосинхронізованим і просторово відносно однорідним. На противагу цьому, в клітинах передсердь Т-трубочкова система є або погано розвинена, або повністю відсутня (Huser et al., 1996, Smyrnias et al., 2010). В клітинах передсердь виділяють два типи СР, виходячи з їх розташування: з’єднані СР (j-SR) розташовані поблизу поверхневої мембрани передсердь, тоді як нез’єднані СР (nj-SR) знаходяться в глибших ділянках клітини і не асоціюються з поверхневою мембраною. Обидва типи СР містять RyRs (Smyrnias et al., 2010, Kockskamper et al., 2001, Woo et al., 2003), які організовані у 3D масив RyRs-кластерів і здатні активно вивільняти Ca^{2+}. Завдяки такій ультраструктурній організації, ПД-індуковане вивільнення Ca^{2+} у клітинах передсердь є просторово неоднорідним (Huser et al., 1996, Blatter et al., 2003). ПД-індукована деполяризація активує вхід Ca^{2+} через L тип кальцієвих каналів та CICR через RyRs j-SR. Зростання периферійного $[Ca^{2+}]$ викликає Ca^{2+}-хвилю в доцентровому напрямку через механізм "вивільнення-дифузія-вивільнення" (Blatter, 2017)." У міоцитах шлуночків мережа Т-трубочок забезпечує швидке розповсюдження потенціалу дії по всьому об’єму клітини (Cheng et al., 1994) та майже одночасне вивільнення кальцію по всій клітині (Bers, 2002).

Ми використали швидку конфокальну мікроскопію для дослідження індукованих ПД транзієнтів Ca^{2+} в міоцитах передсердь і шлуночків, з метою отримати глибше розуміння змін внутрішньоклітинної концентрації кальцію за рахунок входу Ca^{2+}, локального вивільнення Ca^{2+} з СР та його клітинного розповсюдження під час ЕСС. Додатково ми досліджували Ca^{2+} спалахи з високою часовою роздільною здатністю для виявлення особливостей процесів вивільнення Ca^{2+} і кількісні характеристики каналів, що беруть участь у цих подіях.

У першій серії експериментів, ми зосередилися на дослідженні просторово-часової регуляції Ca^{2+}-транзієнтів під час нормального ЕСС у міоцитах передсердь. Для цього, ПД-залежні Ca^{2+} транзієнти було викликано за допомогою стимуляції електричним полем при частоті 0.7 Гц.

На рис. 1.1A та D представлена послідовність двовимірних зображень $[Ca^{2+}]$ ранньої фази електрично викликаного Ca^{2+} транзієнту. Записи були зроблені при частоті 1719 Гц у центрально-аксіальному розрізі, а саме на рівній відстані від верхньої та нижньої меж клітини в аксіальному (z) вимірі в клітинах передсердь і шлуночків, відповідно. Так, в міоцитах передсердь вивільнення Ca^{2+} було просторово неоднорідним та ініціювалося у дискретних ділянках периферії, де знаходиться j-SR. Крім того, вивільнення Ca^{2+} виявилося асинхронним між периферійними місцями вивільнення j-SR і займало 3.0±0.1 мс (n = 7) для активації усіх детектованих периферійних сайтів вивільнення (див. рис. 1.1C). Як можна побачити на рис. 1.1B, концентрація $[Ca^{2+}]$ в центральній (CT) субклітинній ділянці, яка віддалена від клітинної мембрани, починала зростати із певною затримкою. У цьому місці, яке відповідає nj-SR, рівень $[Ca^{2+}]$ збільшувався набагато повільніше і досягав піку, який був менший за максимальний рівень $[Ca^{2+}]$, зафіксований на периферії клітини.

Щоб глибше зрозуміти процес, який ініціює Ca^{2+} транзієнт у клітинах передсердь, ми вивчали спонтанні Ca^{2+} спалахи. Данні події, на периферії клітини, що виникають від j-SR CRU у передсердях, мають виражену анізотропію, переважно поширюючись у поздовжньому напрямку. У поздовжньому (x-вісь) напрямку середнє значення FWHM складає 2.50±0.07 мкм (n = 30 проаналізованих спалахів), тоді як у поперечному напрямку це значення становить 1.51±0.05 мкм.

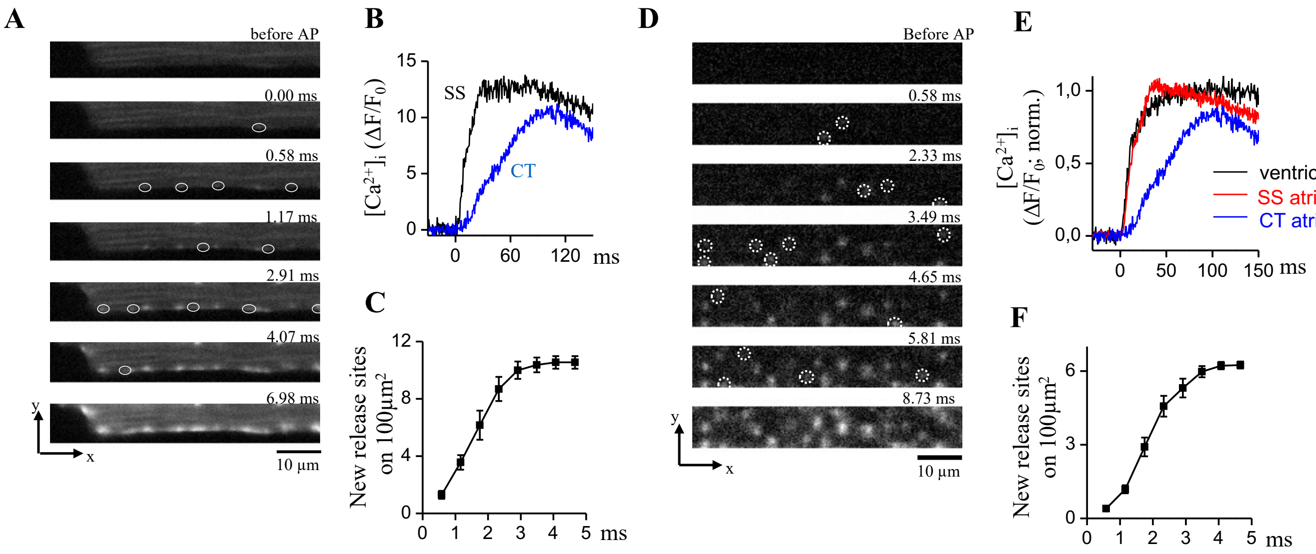

Рисунок 1.1. ПД-індуковані Ca^{2+}-транзієнти в інтактних міоцитах передсердь та шлуночків. (A) Серія конфокальних x-y зображень ранньої фази Ca^{2+} транзієнту в міоциті передсердь, викликаного стимуляцією електричним полем. (B) Порівняння транзієнтів Ca^{2+} в субсарколеммальній області (SS, асоційованій з j-SR) та в центральній області (CT, асоційованій з nj-SR). (C) Кумулятивне залучення окремих областей вивільнення Ca^{2+} j-SR CRU. Ці області виявлені в субсарколеммальній зоні розміром 75 мкм на 2 мкм і нормалізовані до кількості CRU/100 мкм^2. (D) Серія конфокальних двовимірних зображень ранньої фази Ca^{2+} транзієнту в міоциті шлуночка. Білі овали та кружечки позначають місця першого виявлення Ca^{2+} вивільнення з CRU. t = 0 відповідає часу першого виявлення подій CRU. (E) Нормалізовані транзієнти Ca^{2+}, зареєстровані з різних областей: j-SR шлуночка, nj-SR передсердя, і j-SR передсердя. (F) Кумулятивне залучення окремих областей вивільнення Ca^{2+} j-SR CRU. Ці області були виявлені в ділянці інтересу розміром 60 мкм на 7,5 мкм та нормалізовані до кількості CRU/100 мкм^2.

У міоцитах шлуночків спостерігається декілька характерних особливостей Ca^{2+}-транзієнту: локалізовані сигнали вивільнення Ca^{2+} з окремих CRU з'являються випадковим чином по всій клітині без чіткої субклітинної локалізації; рекрутування CRU не є повністю синхронізованим. Як зображено на рис. 1.1F, кількість активованих CRU зростала постійно протягом приблизно 4 мс. У середньому активація всіх виявлених ділянок вивільнення досягалася за 3.9±0.1 мс (n = 9). Локальні збільшення [Ca^{2+}] з периферичних і центральних CRU, які рекрутувалися одночасно, були майже ідентичними.

За відсутності системи Т-трубочок в міоцитах передсердь Ca^{2+} входить тільки біля сарколеми, активує вивільнення Ca^{2+} з примембранних СР та поступово розповсюджується до центру за рахунок механізму кальцій-індукованого вивільнення кальцію.

На рис. 1.1E представлено нормалізовані локальні транзієнти Ca^{2+}, отримані з окремих ділянок вивільнення передсердного j-SR (SS), шлуночкового j-SR та передсердного nj-SR (CT). Часова динаміка фази швидкого зростання сигналів кальцію з шлуночкових та передсердних SS-ділянок була майже ідентична, у той час як динаміка зростання $[Ca^{2+}]$ в області передсердного CT була значно повільнішою. Таким чином, з точки зору динаміки локального вивільнення Ca^{2+}, ділянки шлуночкового та передсердного j-SR демонстрували дуже схожі характеристики, тоді як вивільнення з передсердних nj-SR CRUs мало виразно відмінний просторово-часовий профіль.

Глобальний транзієнт Ca^{2+} виникає внаслідок потоку Ca^{2+} через клітинну мембрану, а також істотного потоку Ca^{2+} через RyRs під час вивільнення Ca^{2+} з СР. В наступних експериментах намагалися розділити ці два компоненти потоку з використанням високошвидкісної реєстрації Ca^{2+}. На рис. 1.2A зображено ранню фазу росту загальноклітинного глобального транзієнту Ca^{2+} ($\Delta F/F_0$), який ініційований ПД у міоциті шлуночка, усереднений по області спостереження розміром приблизно 550 $мкм^2$ (200×31 пікселя) для отримання сигналу із зменшеним рівнем шуму. Мітка "1" вказує на момент прикладання електричного стимулу. Для розділення на потоки було отримано першу похідну від цього сигналу, що зображено на рис. 1.2B, як перша похідна сигналу $[Ca^{2+}]$ ($d(\Delta F/F_0)/dt$). Перша фаза, яку можна визначити за часом прикладання електричного стимулу (маркер "1") і моментом початку зростання сигналу $d(\Delta F/F_0)/dt$ (маркер "2"), вказує на латентний період між електричним стимулом та активацією потоку Ca^{2+}. Латентний період складав 2.5±0.3 мс (n = 9 міоцитів шлуночків). Протягом другої фази (між маркерами "2" і "3") $d(\Delta F/F_0)/dt$ утримувався на постійному рівні, збільшуючись повільно. Цей період, ймовірно, відображає вхід Ca^{2+} в клітину. На час t = 5.5±0.2 мс (маркер "3"), швидкість потоку стрімко зросла, досягнувши піку (маркер "4") приблизно в $d(\Delta F/F_0)/dt = 748\pm71$ с-1, через 9.9±0.7 мс після початку стимулу. Ця фаза зміни Ca^{2+} потоку відображає вивільнення кальцію з СР за рахунок відкриття RyRs каналів.

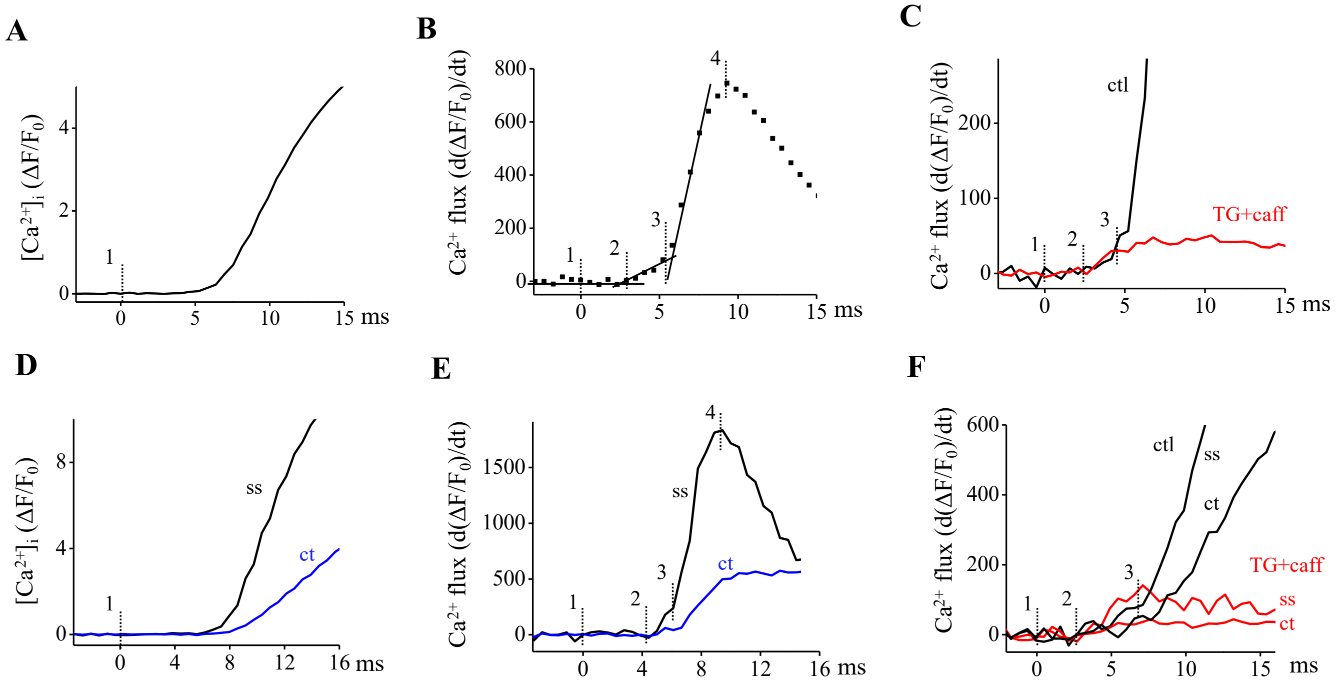

Рисунок 1.2. Субклітинні потоки Ca^{2+} під час ECC, ідентифіковані за допомогою швидкої реєстрації Ca^{2+}. (A) Глобальний Ca^{2+}-транзієнт ($\Delta F/F_0$), ініційований стимуляцією міоцита шлуночка електричним полем. Маркер "1" відзначає момент застосування електричного стимулу. Маркери "2" і "3" розташовані відповідно до аналізу на панелі B. (B) Перша похідна $\Delta F/F_0$ (с-1) сигналу з панелі A, яка відображає потік Ca^{2+}. Маркери "2" і "3" демонструють різкі зміни швидкості потоку Ca^{2+}, тоді як маркер "4" позначає максимальний потік Ca^{2+}. (C) Просторово усереднений потік Ca^{2+} у контрольних умовах (Ctl) та під час інгібування функції СР за допомогою тапсигаргіну (TG; 1 мМ) і кофеїну (caff; 10 мМ). (D) Субклітинні транзієнти Ca^{2+} ($\Delta F/F_0$), спричинені стимуляцією електричним полем, зареєстровані в субсарколемальній (SS) j-SR та центральній (CT) nj-SR областях міоцита передсердя. (E) Перша похідна від сигналів SS і CT Ca^{2+}, представляє рівень субклітинного потоку Ca^{2+}. Маркери від "1" до "4" такі ж, як на панелі B. (F) Швидкість субклітинного потоку Ca^{2+} (SS, CT) у контрольних умовах та під дією комбінації тапсигаргіну та кофеїну. Двовимірні зображення отримані з часовою роздільною здатністю в 1719 Гц.

На рисунку 1.2C представлено потоки Ca^{2+} у контрольних міоцитах шлуночків та в міоцитах з пригніченою активністю СР. Функція вивільнення кальцію з СР була пригнічена шляхом її повного виснаження кофеїном (10 мМ) та блокуванням зворотного завантаження завдяки дії блокатора SERCA - тапсигаргіну (TG; 1 мМ).

Усунення вивільнення Ca^{2+} з СР зупиняло значне зростання потоку Ca^{2+}, яке зазвичай спостерігається після маркера "3". Однак латентний період (2.1±0.1 мс; n = 11 міоцитів) та подальше повільне зростання сигналу $d(\Delta F/F_0)/dt$ залишилися незмінними. Пікове значення сигналу $d(\Delta F/F_0)/dt$ досягало 50±5 с-1 через 7.7±0.7 мс після електричного стимулу. Отже, ці дані підтверджують гіпотезу, що фаза "1-2" (латентність) відображає час, потрібний для поширення деполяризації та активації іонних каналів поверхневої мембрани. Фаза "2-3" характеризує вхідний потік Ca^{2+} і була ідентична як для контрольних міоцитів, так і для клітин з пригніченою активністю СР. Фаза "3-4" визначена як потік, відповідальний за вивільнення Ca^{2+} з СР, оскільки вона відсутня при блокуванні функцій СР.

Аналогічний аналіз було проведено для міоцитів передсердь. У цих клітинах потоки Ca^{2+} для SS (j-SR) та CT (nj-SR) регіонів аналізувалися окремо. На рис. 1.2D представлено зростання $[Ca^{2+}]$ ($\Delta F/F_0$), індукованого стимуляцією за допомогою електричного поля, яке було прикладено у точці "1". Цей графік демонструє затримку та повільне зростання $[Ca^{2+}]$ в ділянці CT. На рис. 1.2E відображено першу похідну від $\Delta F/F_0$, яка характеризує основні потоки Ca^{2+}. У ділянці SS, аналогічно до клітин шлуночків, латентний період (3.6±0.7 мс; n = 6 міоцитів передсердь) супроводжується поступовим зростанням, яке починається з маркера "2", яке змінювалося швидким зростанням після 6.4±0.3 мс від моменту застосування електричного стимулу (маркер "3"), досягаючи піку на рівні 1183±180 с-1 через 11.8±0.6 мс. Натомість для сигналу CT $d(\Delta F/F_0)/dt$ немає вираженої фази повільного зростання, і він починає зростати лише через 2.2±0.3 мс після першої зміни SS-сигналу (маркер "2"). Максимальний потік в області CT був у 3,5±0,3 рази менший в порівнянні з периферією і досягав свого піку через 5.3±1.7 мс. На рис. 1.2F представлені потоки Ca^{2+} для областей SS і CT в міоцитах передсердя під контрольними умовами та при неактивному СР (TG+Caff). В області SS $d(\Delta F/F_0)/dt$ він зростає через 2.1±0.1 мс (n = 6) після застосування електричного стимулу і досягає свого максимуму (164±30 с-1) через 6.5±0.5 мс. За цей час у контрольних клітинах розпочинається потік вивільнення Ca^{2+} з СР. Потік вивільнення Ca^{2+} в області CT у 4.0±0.7 рази менший, ніж в області SS.

У міоцитах шлуночків зміна потоків Ca^{2+} в примембранному регіоні міоцита передсердь була подібною як у контролі, так і пригніченою функцією вивільнення кальцію з СР. Проте в центральній ділянці міоцита передсердь зміна потоку кальцію починала з'являтися тільки після маркера 3, що стає більш явним при блокуванні функції вивільнення СР, тобто тільки після початку вивільнення кальцію в примебранній, сарколемній ділянці клітини. За відсутності системи Т-трубочок в міоцитах передсердь при деполяризації клітини Ca^{2+} входить тільки біля сарколеми та активує вивільнення Ca^{2+} в цих СР та поступово дифундуючи і активуючи віддалені ділянки міоцита з поступовим вивільненням кальцію та його дифузію до центру завдяки CICR.

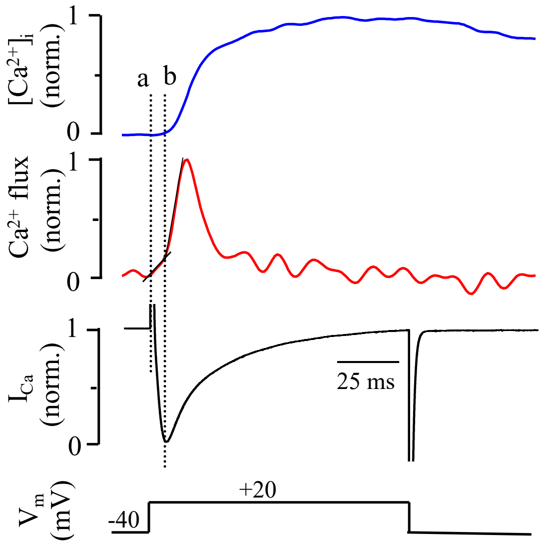

Рисунок 1.3. Вимірювання $[Ca^{2+}]$ і I_{Ca}. Представлено одночасні вимірювання $[Ca^{2+}]$ та I_{Ca} у міоциті шлуночка під час фіксації потенціалу в конфігурації "ціла клітина" методу петч-клемп. По порядку зверху вниз зображено: $[Ca^{2+}]$ ($\Delta F/F_0$), потік Ca^{2+} ($d(\Delta F/F_0)/dt$), I_{Ca} та керуюча напруга. Подані криві відображають середні значення 15 послідовних деполяризаційних імпульсів, прикладених до однієї й тієї ж клітини, нормалізованих до відповідної максимальної амплітуди. У даних експериментах флуоресценцію Fluo-4 зафіксовано за допомогою фотоелектронного помножувача. Маркер "a" позначає початок деполяризаційного імпульсу; маркер "b" вказує на зміну в швидкості потоку, яка, ймовірно, корелює з активацією CICR зі сторони СР.

Таким чином, використання швидкої двовимірної візуалізації Ca^{2+} дозволило нам визначити потоки Ca^{2+}, асоційовані з входом Ca^{2+} та вивільненням Ca^{2+} з СР. Далі ми намагалися підтвердити оптично виміряні сигнали входу та вивільнення Ca^{2+}, проводячи одночасне вимірювання $[Ca^{2+}]$ та мембранних Ca^{2+}-струмів (I_{Ca}) методом петч-клемп. Просторово усереднені дані $[Ca^{2+}]$ та I_{Ca} були отримані з окремих міоцитів шлуночків (див. рис. 1.3). Міоцит був підтриманий на потенціалі -40 мВ і періодично деполяризовувався до +20 мВ протягом 100 мс для активації максимального струму через L-типу Ca^{2+} каналів. Сигнал потоку Ca^{2+} показував поступове зростання майже одразу після початку деполяризаційного імпульсу (маркер "a"), яке різко переходило в швидке підвищення (маркер "b"). Ця виражена зміна швидкості потоку (маркер "b") мала місце через 5.7 мс після старту деполяризаційного імпульсу і корелювала з моментом вивільнення Ca^{2+} з СР, виявленого оптичними методами (маркер "3" на рис. 1.2А).

Дані, представлені на рисунках 1.2 та 1.3, підтверджують, що швидка двовимірна конфокальна кальцієва мікроскопія із частотою дискретизації 1-2 кГц може надавати відомості про потоки Ca^{2+}, які є основою для ЕСС. Її часова роздільна здатність наближена до такої ж здатності методу петч-клемп. Водночас, цей метод має перевагу в тому, що він менше порушує внутрішньоклітинне середовище, оскільки клітинна мембрана залишається неушкодженою.

Через 2.5 мс після подачі електричного стимулу відбувається вхід Ca^{2+} у клітину. Після додаткової затримки в 3 мс відбувається вивільненням Ca^{2+} з СР. Максимальне вивільнення Ca^{2+} з депо спостерігається ще через 4 мс. Такий детальний розділ потоків кальцію є важливим для розуміння змін внутрішньоклітинної концентрації кальцію в міоцитах міокарду.

Загально прийнято, що спалахи Ca^{2+} виникають через координоване відкриття обмеженої кількості RyRs каналів, які відповідають за вивільнення Ca^{2+}, які організовані у кластери на мембрані СР. Однак, питання про те, скільки окремих каналів вивільнення бере участь у формуванні сигналу спалаху, досі залишається предметом активних дискусій.

Зазвичай, при лінійному скануванні спалахів Ca^{2+} використовується швидкість конфокального сканування в діапазоні 0.5-1 кГц. Така часова роздільна здатність може ставити певні обмеження на точність реєстрації швидких компонентів спалаху Ca^{2+}, наприклад, його фази зростання. Це може ускладнювати інтерпретацію таких сигналів, особливо з огляду на механізми роботи воріт каналу та кількість задіяних у процесі каналів. Користуючись перевагами високої часової роздільної здатності LSM

5 LIVE, ми реєстрували спалахи Ca^{2+}, в міоциті передсердь, у режимі лінійного сканування у часі (x-t) з частотою 40 кГц (25 мкс на лінію), як це представлено на рис. 1.4A. Профіль флуоресценції шириною в один піксель (0.3 мкм) ($\Delta F/F_0$), отриманий з центру спалаху, наведено на рис. 1.4B (вгорі). Відзначений спалах має час зростання (до піку) близько 6 мс.

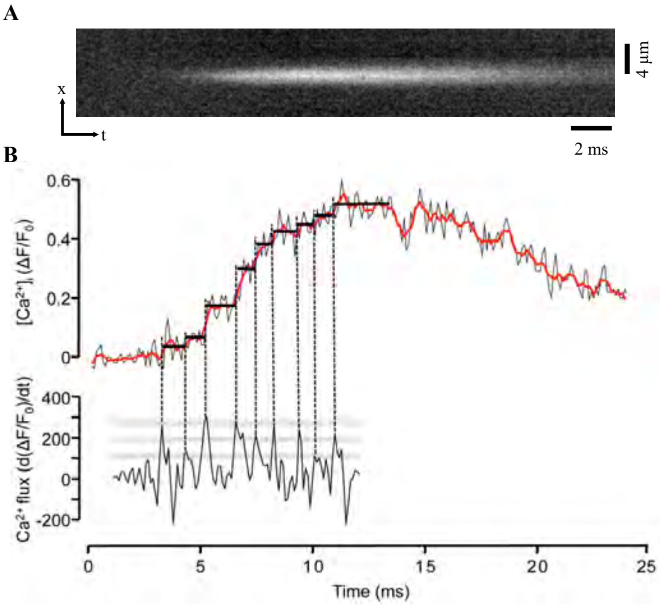

Рисунок 1.4. Ультрашвидкий запис Ca^{2+} спалаху. (A) Зображення лінійного сканування x-t, зроблене із швидкістю 40 000 ліній/с. (B) Вгорі: профіль $\Delta F/F_0$ шириною в один піксель (0,3 мкм) з центру спалаху. Для покращення якості сигналу його було усереднено до 10 000 ліній/с. Червона лінія відображає 5-точкове рухоме середнє. Внизу представлена перша похідна від сигналу $\Delta F/F_0$ фази зростання спалаху, позначена як $d(\Delta F/F_0)/dt$ (c-1). Вертикальними пунктирними лініями виділені максимуми $d(\Delta F/F_0)/dt$, які вказують на пікові значення потоку вивільнення Ca^{2+}. Для ідентифікації дискретних зростань в сигналі $\Delta F/F_0$ були використані пікові значення $d(\Delta F/F_0)/dt$, позначені горизонтальними суцільними лініями. Сірі області вказують на дискретні рівні $d(\Delta F/F_0)/dt$. Визначення дискретного рівня $d(\Delta F/F_0)/dt$ використовувалося, коли ми спостерігали не менше двох пікових значень $d(\Delta F/F_0)/dt$ з однаковою амплітудою.

Детальний аналіз фази зростання показав ступінчасте збільшення [Ca^{2+}], що вказано горизонтальними лініями на рис. 1.4B. Для виявлення таких ступінчастих змін фази зростання було розраховано першу похідну сигналу $\Delta F/F_0$ ($d(\Delta F/F_0)/dt$), яка представлена на рис. 1.4B (внизу). Ця похідна відображає основні потоки Ca^{2+} (Sheehan and Blatter, 2003). Під час фази зростання були виявлені декілька дискретних піків в $d(\Delta F/F_0)/dt$, вказуючи на максимуми потоку вивільнення Ca^{2+}. Ці піки, позначені вертикальними пунктирними лініями, були використані для визначення дискретних кроків у сигналі [Ca^{2+}], що показано на рис. 1.4B суцільними чорними лініями. У поданому прикладі (подібні спостереження проводилися на 7 міоцитах) за допомогою цього методу було виявлено 9 дискретних рівнів сигналу $\Delta F/F_0$, що свідчить про участь групи RyRs каналів при вивільню кальцію при спалаху.

Двовимірна реєстрація транзієнтів Ca^{2+} демонструє асинхронну активацію сайтів вивільнення. Це дозволило послідовно фіксувати вхід Ca^{2+} через потенціал-керовані Ca^{2+}-канали поверхневої мембрани, а також подальшу активацію Ca^{2+}-індукованого вивільнення Ca^{2+}. З латентністю в 2,5 мс після подачі електричного стимулу спостерігався вхід Ca^{2+}, який супроводжувався вивільненням Ca^{2+} з СР з додатковою затримкою в 3 мс. Пік вивільнення Ca^{2+} спостерігався через 4 мс після його початку. Час входу та вивільнення Ca^{2+} підтверджено одночасним вимірюванням [Ca^{2+}] та мембранного струму за допомогою методу петч-клемп у конфігурації "ціла клітина". У клітинах передсердя активація окремих ділянок вивільнення Ca^{2+} з j-SR викликала просторово локалізовані події вивільнення Ca^{2+}, які формували периферійне кільце з підвищеним рівнем [Ca^{2+}], що поступово поширювалися як хвиля до центру клітини. У міоцитах шлуночків асинхронні сигнали вивільнення Ca^{2+} з окремих ділянок, без домінуючого субклітинного розташування, передували загальноклітинному Ca^{2+} транзієнту. Користуючись високошвидкісною конфокальною мікроскопією та флуоресцентними індикаторами з високим квантовим виходом, ми дослідили динаміку Ca^{2+} та деталі функціонування окремих одиниць вивільнення Ca^{2+} з СР за рахунок RyRs. Цей метод дозволив нам надійно відокремити динаміку входу Ca^{2+} та CICR на рівні окремих CRU в інтактних клітинах. Ми також показали, що: Ca^{2+} спалахи у міоцитах передсердь мають характеристики, які сприяють доцентровому поширенню активації. Зростаюча фаза Ca^{2+} спалаху проявляє ступінчасту кінетику, що свідчить про участь групи RyRs каналів при вивільненні кальцію при спалаху, надаючи потенційно цінну інформації про механізми відкриття каналів всередині CRU.

OPEN ACCESS Freely available online PLOS | ONE

Ca^{2+} Release Events in Cardiac Myocytes Up Close: Insights from Fast Confocal Imaging

Vyacheslav M. Shkryl[1], **Lothar A. Blatter**[2]*

1 Deptartment of General Physiology of the Nervous System, A. A. Bogomoletz Institute of Physiology, Kiev, Ukraine, 2 Department of Molecular Biophysics and Physiology, Rush University Medical Center, Chicago, Illinois, United States of America

Abstract

The spatio-temporal properties of Ca^{2+} transients during excitation-contraction coupling and elementary Ca^{2+} release events (Ca^{2+} sparks) were studied in atrial and ventricular myocytes with ultra-fast confocal microscopy using a Zeiss LSM 5 LIVE system that allows sampling rates of up to 60 kHz. Ca^{2+} sparks which originated from subsarcolemmal junctional sarcoplasmic reticulum (j-SR) release sites in atrial myocytes were anisotropic and elongated in the longitudinal direction of the cell. Ca^{2+} sparks in atrial cells originating from non-junctional SR and in ventricular myocytes were symmetrical. Ca^{2+} spark recording in line scan mode at 40,000 lines/s uncovered step-like increases of $[Ca^{2+}]_i$. 2-D imaging of Ca^{2+} transients revealed an asynchronous activation of release sites and allowed the sequential recording of Ca^{2+} entry through surface membrane Ca^{2+} channels and subsequent activation of Ca^{2+}-induced Ca^{2+} release. With a latency of 2.5 ms after application of an electrical stimulus, Ca^{2+} entry could be detected that was followed by SR Ca^{2+} release after an additional 3 ms delay. Maximum Ca^{2+} release was observed 4 ms after the beginning of release. The timing of Ca^{2+} entry and release was confirmed by simultaneous $[Ca^{2+}]_i$ and membrane current measurements using the whole cell voltage-clamp technique. In atrial cells activation of discrete individual release sites of the j-SR led to spatially restricted Ca^{2+} release events that fused into a peripheral ring of elevated $[Ca^{2+}]_i$ that subsequently propagated in a wave-like fashion towards the center of the cell. In ventricular myocytes asynchronous Ca^{2+} release signals from discrete sites with no preferential subcellular location preceded the whole-cell Ca^{2+} transient. In summary, ultra-fast confocal imaging allows investigation of Ca^{2+} signals with a time resolution similar to patch clamp technique, however in a less invasive fashion.

Citation: Shkryl VM, Blatter LA (2013) Ca^{2+} Release Events in Cardiac Myocytes Up Close: Insights from Fast Confocal Imaging. PLoS ONE 8(4): e61525. doi:10.1371/journal.pone.0061525

Editor: Bradley Steven Launikonis, University of Queensland, Australia

Received December 6, 2012; **Accepted** March 11, 2013; **Published** April 18, 2013

Funding: This work was supported by the National Institutes of Health Grants HL62231, HL80101 and HL101235, and the Leducq Foundation (to LAB). The funders had no role in study design, data collection and analysis, decision to publish, or preparation of the manuscript.

Competing Interests: The authors have declared that no competing interests exist.

* E-mail: Lothar_Blatter@rush.edu

Introduction

Excitation-contraction coupling (ECC) refers to the process that links cell membrane depolarization to Ca^{2+} mobilization and development of contractile force in the heart [1]. Action potential (AP) depolarization activates voltage-gated L-type Ca^{2+} channels (LCC; also referred to as dihydropyridine receptors) in the surface membrane, resulting in localized (sub-membrane) increases in cytosolic Ca^{2+} ($[Ca^{2+}]_i$). Calcium that enters the cell activates sarcoplasmic reticulum (SR) Ca^{2+} release channels (ryanodine receptors, RyRs) through a process known as calcium-induced calcium release (CICR; [2]). RyRs and LCCs face each other in the diadic cleft formed by the close approximation of surface and SR membranes. RyRs assemble as clusters of channels in the SR membrane and form individual Ca^{2+} release units (CRU; [3]). Together with the diadic cleft and sarcolemmal Ca^{2+} channels CRUs are organized in discrete signaling domains or couplons [4]. In response to an AP hundreds of CRUs are activated essentially simultaneously. The spatial and temporal summation of Ca^{2+} release from individual CRUs gives rise to the whole-cell Ca^{2+} transient [5,6,7]. Because of the extensive transverse (t) tubular network - a 3-dimensional network of surface membrane invaginations that assure physical proximity of surface membrane Ca^{2+} channels and CRUs throughout the entire cell volume [8] - AP-induced Ca^{2+} release in ventricular myocytes is highly synchronized and spatially rather homogeneous.

In contrast, in atrial cells the t-tubular system is poorly developed or even entirely lacking [7,9,10,11,12]. In atrial cells two types of SR can be defined, based on their location relative to the surface membrane. Junctional SR (j-SR) is found in the cell periphery where it is organized in peripheral couplings, i.e. the SR membrane is found in close spatial association with the surface membrane, similar to the diadic cleft in ventricular myocytes [13,14]. In contrast, non-junctional SR (nj-SR) is found in deeper regions of the cell and does not associate with the surface membrane. Both j-SR and nj-SR possess RyRs [10,11,12,13,15,16,17] which are organized in a 3-dimensional array of RyR clusters, and are capable of active SR Ca^{2+} release. As a consequence of these ultrastructural arrangements AP-induced Ca^{2+} release is spatially inhomogeneous (for review see e.g. [7,18,19]): AP-induced membrane depolarization activates Ca^{2+} entry through LCCs and CICR through RyRs of the j-SR. Elevation of peripheral $[Ca^{2+}]_i$ propagates via CICR in a Ca^{2+} wave-like fashion in centripetal direction by a diffusion-reaction process or a 'fire-diffuse-fire' mechanism [20].

Elementary Ca^{2+} release events, arising from the activation of individual CRUs, have been termed Ca^{2+} sparks ([21]; for a recent comprehensive review see [22]), although Ca^{2+} release events of smaller magnitude, possibly arising from single RyRs, have been postulated [23,24,25]. To date Ca^{2+} sparks have been detected in a wide range of mammalian species (for review see [22]). In atrial cells Ca^{2+} sparks originate from j-SR and nj-SR, however with a high prevalence for the cell periphery [7,16,26,27,28].

While sparks have been demonstrated in cardiac myocytes already two decades ago [21], it has remained a matter of debate, how many RyRs within a CRU contribute to a spark. Available data on how many RyRs a CRU of a cardiac myocyte contains vary widely and range from less than ten to several hundred RyRs [29,30,31,32,33,34,35,36]. However, it is still not established whether a fraction or all RyRs of a cluster are activated in a spark. Indeed, published reports on how many channels contribute to a cardiac spark vary widely and range from a single or only a few channels to the whole CRU, thus possibly involving several hundred channels [21,32,37,38,39,40,41,42].

The fact that such critical questions have remained inconclusive is, at least in part, linked to methodological and technical limitations hampering the recording of locally restricted and rapidly changing subcellular Ca^{2+} signals. The last two decades have seen significant improvements in Ca^{2+} indicator dyes that have allowed the field to move forward at considerable pace [43]. Nonetheless, the vast majority of studies on local Ca^{2+} signaling have used line scan confocal microscopy in conjunction with fluorescent Ca^{2+} indicator dyes. While line scan imaging provides a reasonable temporal resolution (typical sampling rates used are in the 0.5–1 kHz range) it is severely limited by the fact that a cellular event such as a Ca^{2+} spark, a Ca^{2+} wave or the whole-cell Ca^{2+} transient occurs in a 3-dimensional space, however its optical recording by line scan imaging is reduced to one spatial dimension. Therefore, line scan data notoriously suffer from out-of-focus problems (the event of interest originates from a different optical plane than the recording plane) and how reliably complex 3-dimensional spatial properties can be captured with this approach. Recently, novel technical imaging tools, consisting of a fast 2-D (or x-y) confocal scanning mechanism (LSM 5 LIVE slit scanner) in conjunction with the ability to move the plane of focus vertically in rapid and reproducible manner, have enabled us to achieve x-y-z-t (or 4-D) imaging of sparks with a reasonable time resolution und to gain novel insight into the properties of cardiac Ca^{2+} sparks [41]. With this technique we were able to determine the true in-focus amplitude of Ca^{2+} sparks and make the observation that sparks had a modal amplitude distribution. Here, we extended fast confocal imaging to the study of AP-induced Ca^{2+} transients in atrial and ventricular myocytes with the goal to gain new insight into Ca^{2+} entry, local Ca^{2+} release and cellular spread of activation during ECC, and to explore Ca^{2+} sparks at high temporal resolution to reveal the characteristics of the underlying Ca^{2+} release and gating properties of the channels involved.

Materials and Methods

Myocyte Isolation

Single myocytes were isolated from cat [26,44,45,46] and rabbit [47] hearts as described previously. The investigation conforms with the Guide for the Care and Use of Laboratory Animals of the National Institutes of Health. All procedures and protocols for animal handling and cell isolation were fully approved by the Institutional Animal Care and Use Committee of Loyola University Chicago (Permit number 05-016) and the Institutional Animal Care and Use Committee of Rush University Medical Center Chicago (Permit number 09-055). All efforts were made to minimize suffering. Briefly, animals were anesthetized with thiopental sodium (50 mg kg^{-1}, I.P.). After thoracotomy, hearts were excised, mounted on a Langendorff apparatus, and retrogradely perfused via the aorta with oxygenated collagenase (cats) or Liberase Blendzyme TH (rabbits) containing solution (37°C). Myocytes were used for experimentation within 1–6 hours after isolation.

Chemicals, Solutions and Experimental Conditions

Chemicals were obtained from Sigma-Aldrich (St. Louis, MO) unless otherwise noted. During experiments myocytes were superfused continuously with normal Tyrode solution (composition in mM: NaCl 135: KCl 4; $CaCl_2$ 2; $MgCl_2$ 1; D-glucose 10; HEPES 10; pH 7.4 adjusted with NaOH). All experiments were performed at room temperature (22–25°C). APs were elicited by electrical field stimulation by applying 1 ms voltage pulses of suprathreshold amplitude through a pair of platinum electrodes.

$[Ca^{2+}]_i$ Measurements and Confocal Microscopy

Changes of $[Ca^{2+}]_i$ were measured using fluorescence laser scanning confocal microscopy. Intact atrial and ventricular myocytes were loaded with the fluorescent Ca^{2+} indicator Fluo-4 by 20 min incubation in Tyrode solution containing 10 μM of the membrane permeant acetoxymethyl ester form of the indicator (Fluo-4/AM; Molecular Molecular Probes/Life Technologies, Grand Island, NY) at room temperature. 15–20 min were allowed for de-esterification of the dye. Fluo-4 was excited with the 488 nm line of an argon ion laser and emitted fluorescence was measured at wavelengths >515 nm. Confocal imaging at high temporal resolution was performed with a slit scanning confocal microscope (LSM 5 LIVE; Carl Zeiss, Oberkochen, Germany) equipped with a 63×, 1.20 n.a. water-immersion objective (C-Apochromat; Carl Zeiss). High-speed data acquisition was achieved by bi-directional scanning. 2-dimensional (2-D) imaging (also referred to as x-y imaging) yielded images of 512×53 or 512×31 pixels (pixel distance of 0.3 μm) recorded at 1038 and 1719 Hz, respectively. The x-dimension is defined as the longitudinal axis of the cell. The y-dimension refers to the transverse cell axis and the z-dimension defines the axial (or vertical) cell dimension. The point-spread function of the system had full-width at half maximum (FWHM) values of 0.52, 0.46, and 1.25 μm, respectively, in the x, y, and z directions [41]. Changes of $[Ca^{2+}]_i$ are presented as background-subtracted normalized fluorescence ($\Delta F/F_0$) where F is the fluorescence intensity, F_0 is resting fluorescence recorded under steady-state conditions at the beginning of an experiment, and $\Delta F = F - F_0$. Average data are presented as mean ± SEM.

Electrophysiology

Experiments for simultaneous $[Ca^{2+}]_i$ and membrane Ca^{2+} current measurements were performed in rabbit ventricular myocytes using the voltage-clamp technique in the whole-cell ruptured patch configuration, using an Axopatch 200A amplifier, the Axon Digidata 1440A interface and pCLAMP 10.2 software (Molecular Devices, Sunnyvale, CA). The patch pipette solution contained (in mM): 120 L-aspartate; 120 CsOH; 20 TEA-Cl; 20 HEPES; 1 L-gluthathione (reduced); 1 DM-nitrophen (EMD Chemicals, Philadelphia, PA); 4 ATP-Na, 0.25 $CaCl_2$ and 0.1 Fluo-4 pentapotassium salt (Molecular Probes); pH 7.2 adjusted with CsOH). Currents were recorded at 100 kHz and low-pass filtered at 5 kHz.

Results

Spatio-temporal Characteristics of Ca^{2+} Transients and Ca^{2+} Sparks in Atrial Myocytes

In a first set of experiments we investigated the spatio-temporal organization of Ca^{2+} transients during normal ECC in atrial myocytes. AP-dependent Ca^{2+} transients were elicited by electrical field stimulation (0.7 Hz). As shown previously cat atrial myocytes are devoid of a t-tubular network [7], however RyR Ca^{2+} release channels are present throughout the cell with the exception of the nuclear region [13]. Fig. 1A shows a sequence of 2-D [Ca^{2+}]$_i$ images of the early phase of an electrically evoked Ca^{2+} transient in an atrial cell, recorded at 1719 Hz from a central axial plan, i.e. at equal distance from the top and bottom cell borders in the axial (z) dimension. Ca^{2+} release appeared spatially inhomogeneous and initiated at discrete sites in the periphery where the j-SR is located. Ca^{2+} release was also found to be asynchronous among peripheral j-SR release sites and required 3.0±0.1 ms (n = 7 atrial myocytes) for all detectable peripheral release sites to be activated (Fig. 1B). This is likely an underestimation of the time required to recruit all j-SR release sites because the appearance of new sites at later times becomes increasingly obscured by the overall increase of [Ca^{2+}]$_i$. Fig. 1C shows a single peripheral release site at higher magnification. The series of 2-D images reveals that from the point source of Ca^{2+} of the release site, Ca^{2+} diffuses laterally (x-dimension), and also centripetally (y-dimension). Fig. 1D shows the time course of the increase of [Ca^{2+}]$_i$ at an individual j-SR release site and a peripheral subsarcolemmal (SS) non-release site at a lateral distance of ~1 μm, revealing a time delay that was characteristic for subsarcolemmal Ca^{2+} diffusion. Traces representing the SS j-SR region were recorded within <1 μm from the edge of the cell. Ca^{2+} release from peripheral j-SR sites eventually gave rise to a rather homogeneous elevation of [Ca^{2+}]$_i$ in the cell periphery, obscuring individual release sites. On average this homogeneous 'ring' of increased [Ca^{2+}]$_i$ was complete 10.1±1.5 ms after application of the electrical stimulus. As shown in Fig. 1E [Ca^{2+}]$_i$ started to rise with a delay at a central (CT) subcellular location distant from the cell membrane. At this location, which corresponds to the nj-SR, [Ca^{2+}]$_i$ rose much more slowly and peaked at a level that was below peak [Ca^{2+}]$_i$ in the cell periphery. As previously established [13,26] activation of Ca^{2+} release from release units of the nj-SR in atrial cells occurs by propagating CICR or a 'diffuse-fire-diffuse' mechanism where Ca^{2+} released from a peripheral release site diffuses over a short distance (1–2 μm) to a neighboring more centrally located release site where it activates CICR. Through this sequence of events activation of Ca^{2+} release in atrial cells becomes spatially inhomogeneous and propagates from the periphery to the center of the myocyte in a Ca^{2+} wave-like fashion.

It is generally agreed that the AP-induced whole-cell Ca^{2+} transient is the result of spatial and temporal summation of elementary Ca^{2+} release events from individual CRU, termed Ca^{2+} sparks [21,22]. To gain additional insight into the process that initiates the Ca^{2+} transient in atrial cells we investigated spontaneous Ca^{2+} sparks from peripheral j-SR CRUs. Fig. 2A shows a series of 2-D images of a spontaneous peripheral Ca^{2+} spark. Images were recorded at a sampling rate of 1038 Hz. Sparks in the cell periphery arising from atrial j-SR CRUs are highly anisotropic with a preferential spread in the longitudinal direction. FWHM in longitudinal (x-dimension) direction was 2.50±0.07 μm (n = 30 sparks analyzed), whereas the average FWHM in transverse direction was 1.51±0.05 μm. Below the panel of 2-D images, two line scan images (x-t- and y-t-images) are shown that were constructed from the stack of 2-D images. For the x-t image a single line of pixels in the x-dimension was extracted at a fixed value of y from each consecutive 2-D image and the lines were stacked from left to right along the time axis. Analogously, a single line of pixels in the y-dimension was extracted at a fixed value for x. While the x-t-image shows a symmetrical spread of [Ca^{2+}]$_i$ from the site of initiation, the y-t-image clearly shows an anisotropic spread. The degree of anisotropy was quantified as eccentricity (e). Eccentricity was defined as the ratio of FWHM of Ca^{2+} sparks measured along two perpendicular axis within the focal plane and by convention the larger value was divided by the smaller measurement, or $e = \mathrm{FWHM}_{\mathrm{wide}}/\mathrm{FWHM}_{\mathrm{narrow}}$. For peripheral j-SR Ca^{2+} sparks in atrial myocytes the average eccentricity was e = 1.71±0.05, i.e. peripheral sparks were approximately 70% wider along the longitudinal cell axis with all sparks analyzed extending more in the longitudinal dimension.

In contrast, sparks recorded from central (nj-SR) regions revealed a different geometry (Fig. 2B). Sparks were essentially symmetrical in x and y, with an average eccentricity of e = 1.12±0.03, i.e. on average FWHM measured along two perpendicular axes differed by 12% only with no preferential direction.

The structural arrangements of surface cell and SR membranes in the peripheral couplings of the j-SR can explain the preferential spread of Ca^{2+} when imaged in a single confocal plane cutting across such a coupling. As discussed above, during ECC Ca^{2+} release propagates by CICR from the cell periphery to the center of the cell. We therefore explored the spatio-temporal properties of peripheral Ca^{2+} sparks for patterns that indicate transverse or centripetal spread of Ca^{2+}. For this purpose we determined frame-by-frame the x-y-coordinates of maximal fluorescence which identifies a point source of Ca^{2+} release. As shown in Fig. 2C the location of maximal fluorescence was stable in the longitudinal (x) direction, arguing for a symmetrical lateral dissipation of Ca^{2+} out of the diadic cleft of the peripheral couplings. In contrast, in transverse (y) direction the location of maximal fluorescence shifted by ~0.5 μm from the cell membrane towards cell center over the time course of 20 ms, thus facilitating the spread of excitation in centripetal direction. This spatial pattern cannot be explained by simple Ca^{2+} diffusion away from a fixed point source of Ca^{2+} and may suggest a preferential direction of Ca^{2+} release propagation possibly within a peripheral CRU.

Spatio-temporal Characteristics of AP-induced Ca^{2+} Transients in Ventricular Myocytes

Ventricular myocytes are equipped with an extensive t-tubular membrane system that is organized in a sarcomeric pattern and functionally allows conduction of the AP into deeper regions of the myocyte. Transverse tubules provide the structural basis that CRUs are all in close contact with the cell membrane that hosts voltage-gated Ca^{2+} channels. Through this arrangement membrane depolarization by an AP allows the synchronous delivery of a triggering amount of Ca^{2+} into the diadic cleft (formed by t-tubular and SR membranes) to induce CICR. Because the t-tubular system guarantees synchronicity for CICR activation, the onset of Ca^{2+} release appears spatially and temporally rather homogeneous, although upon closer examination inhomogeneities have been observed [7,26,48,49,50].

Fig. 3A shows high-resolution 2-D images of the early phase of an AP-induced Ca^{2+} transient from a ventricular myocytes. The images were recorded from a central focal plane equidistant from the bottom and the top of the cell at a sampling rate of 1719 Hz. Several characteristic features of a ventricular Ca^{2+} transient become evident: (1) localized Ca^{2+} release signals from individual CRUs appeared randomly throughout the cell with no obvious

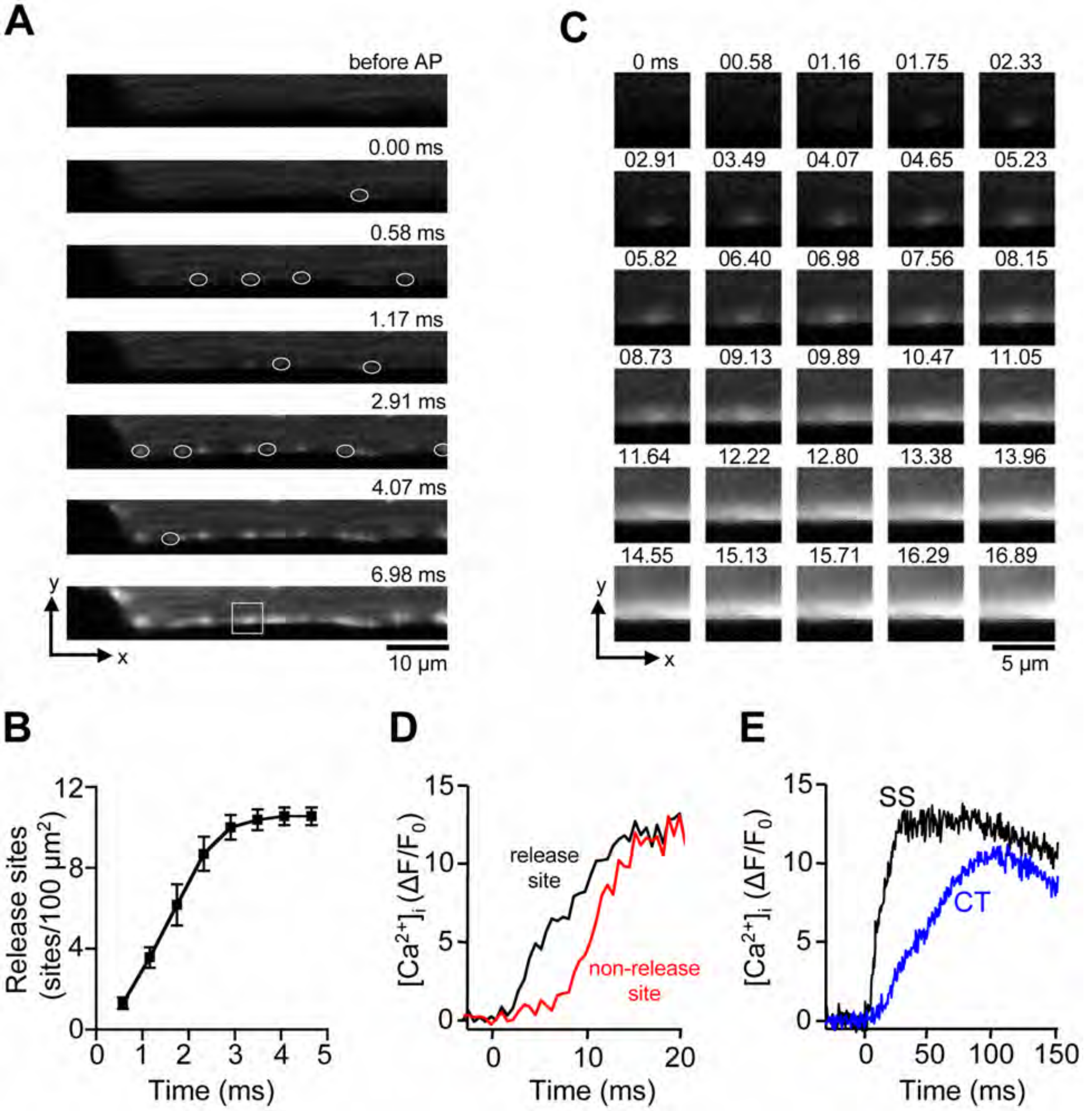

Figure 1. AP-induced Ca^{2+} transients in atrial myocytes. A, series of confocal 2-D images of the early phase of a Ca^{2+} transient evoked by electrical field stimulation. White ovals mark the first appearance of individual Ca^{2+} release sites of the j-SR in the SS region. t = 0 indicates the image frame where the first activated CRU was detected. **B**, cumulative recruitment of individual j-SR CRUs. CRUs were detected in a SS region of 75 µm×2 µm and normalized to number of CRUs/100 µm^2. **C**, Sequential 2-D images of an individual SS j-SR release site, marked by the white box in panel A, recorded at 0.58 ms time intervals. **D**, Evolution of [Ca^{2+}]$_i$ at an individual SS CRU and an adjacent non-release site at a distance of ~1 µm. The traces were recorded from a 1 pixel sized regions (0.09 µm^2). **E**, comparison of SS (j-SR) and CT (nj-SR; recorded at a distance of ~4 µm from the cell membrane) Ca^{2+} transients.

doi:10.1371/journal.pone.0061525.g001

preferential subcellular location; (2) recruitment of CRUs is not entirely synchronized. As shown in Fig. 3B the number of activated CRUs steadily increased over the course of ~4 ms. On average, activation of all detectable release sites was reached after 3.9±0.1 ms (n = 9 ventricular myocytes). (3) Local increases of [Ca^{2+}]$_i$ from peripheral and central CRUs that were recruited at the same time, were essentially indistinguishable (Fig. 3C).

In atrial myocytes, the arrangement of surface membrane and j-SR membranes of the peripheral couplings have a certain resemblance with ventricular myocytes. The common features are that the peripheral couplings form diadic clefts were both

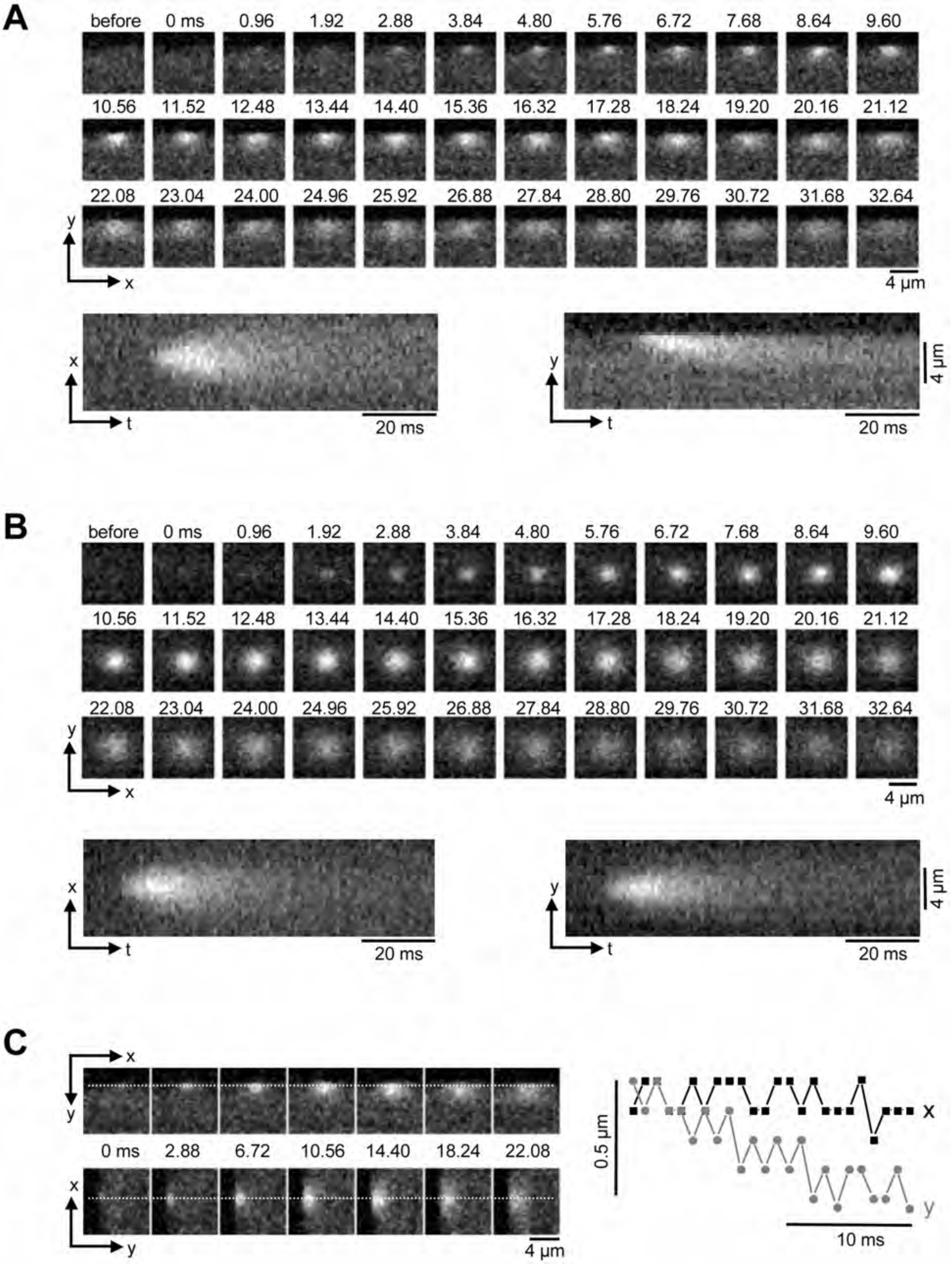
A
before
0 ms
0.96
1.92
2.88
3.84
4.80
5.76
6.72
7.68
8.64
9.60
10.56
11.52
12.48
13.44
14.40
15.36
16.32
17.28
18.24
19.20
20.16
21.12
22.08
23.04
24.00
24.96
25.92
26.88
27.84
28.80
29.76
30.72
31.68
32.64
y
x
4 µm
x
t
20 ms
y
t
20 ms
4 µm
B
before
0 ms
0.96
1.92
2.88
3.84
4.80
5.76
6.72
7.68
8.64
9.60
10.56
11.52
12.48
13.44
14.40
15.36
16.32
17.28
18.24
19.20
20.16
21.12
22.08
23.04
24.00
24.96
25.92
26.88
27.84
28.80
29.76
30.72
31.68
32.64
y
x
4 µm
x
t
20 ms
y
t
20 ms
4 µm
C
x
y
0 ms
2.88
6.72
10.56
14.40
18.24
22.08
x
y
4 µm
0.5 µm
x
y
10 ms

Figure 2. Ca^{2+} sparks in atrial myocytes. A, Series of confocal 2-D images of a spontaneous Ca^{2+} spark originating from the SS j-SR, recorded at 0.96 ms intervals (top). Bottom: reconstructed line scan images (x-t and y-t) from the 2-D series. **B**, analogous to panel A: spontaneous Ca^{2+} spark recorded from a CT nj-SR Ca^{2+} release unit. **C**, movement of the x-y -coordinates of maximal fluorescence during a SS Ca^{2+} spark. Left: the spatial coordinates of peak fluorescence intensity were recorded along the dashed lines in x- and y-dimension. Right: x-t and y-t plots of the location of maximal fluorescence, indicating a preferential movement of the point source of Ca generating the spark in centripetal direction.
doi:10.1371/journal.pone.0061525.g002

membranes associate closely and voltage-gated Ca^{2+} channels face clusters of RyRs [13]. Peripheral couplings are found spaced approximately 2 µm apart. Therefore, we reasoned that the spatio-temporal pattern of CRU activation by an AP would be

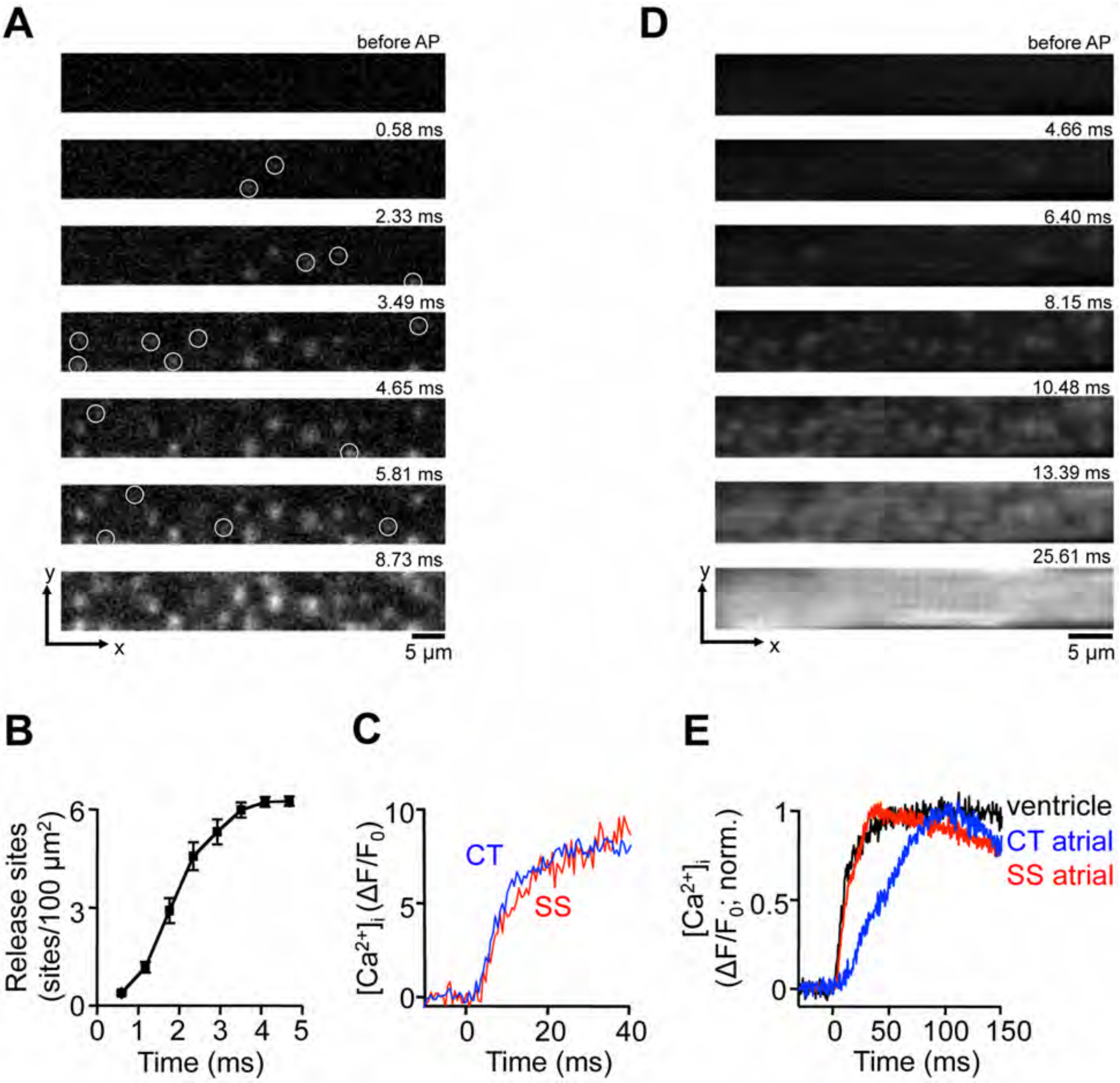

Figure 3. Ca^{2+} release signals in ventricular myocytes. A, series of confocal 2-D images of the early phase of a Ca^{2+} transient evoked by electrical field stimulation in a ventricular myocytes. White circles mark the first appearance of individual j-SR Ca^{2+} release sites. t = 0 indicates the image frame where the first activated CRU was detected. **B**, cumulative recruitment of individual j-SR CRUs. CRUs were detected in a region of interest encompassing the j-SR and measuring 60 µm×7.5 µm. Detected CRUs were normalized to number of CRUs/100 µm^2. **C**, evolution of [Ca^{2+}]$_i$ at individual SS and CT j-SR release sites. The traces were recorded from a 1 pixel sized regions (0.09 µm^2). **D**, series of confocal 2-D images of the early phase of a Ca^{2+} transient evoked by electrical field stimulation in an atrial myocyte and recorded from a focal plane positioned in the SS j-SR space at the bottom of the cell. **E**, normalized Ca^{2+} transients recorded from ventricular j-SR (black), CT nj-SR atrial (blue) and SS j-SR atrial (red) release sites.
doi:10.1371/journal.pone.0061525.g003

distinctly different from the one shown in Fig. 1A if we would be able to capture exclusively CRUs from the peripheral j-SR. For this purpose we positioned the focal plane at the bottom of the cell just above the bottom surface membrane. Fig. 3D shows a sequence of 2-D images of the recruitment of j-SR release sites induced by AP depolarization. Similar to ventricular myocytes, no preferential subcellular locations where activation started could be identified, recruitment of j-SR CRUs was temporally asynchronous and it required ~10 ms for activation of all CRUs. Fig. 3E shows normalized local Ca^{2+} transients recorded from individual release sites of the atrial j-SR (SS), ventricular j-SR and atrial nj-SR (CT). The time course of the rapid rising phase of the ventricular and the atrial SS signals were virtually identical, whereas the rise of $[Ca^{2+}]_i$ at the atrial CT site was significantly slower. Thus, in respect to the dynamics of local Ca^{2+} release ventricular and atrial j-SR sites behaved remarkably similar, whereas release from atrial nj-SR CRUs revealed a distinctly different spatio-temporal pattern.

Ultra-fast Line Scan Imaging of Ca^{2+} Sparks

It is generally agreed that Ca^{2+} sparks result from the concerted opening of a finite number of RyR Ca^{2+} release channels organized in clusters in the SR membrane. It is, however still a matter of debate how many individual release channels contribute to a spark signal, and the reported numbers vary widely, ranging from small numbers of less than a dozen to over a hundred such channels (see Introduction and Discussion).

Conventional confocal line scan imaging of Ca^{2+} sparks typically employs scanning speeds in the 0.5–1 kHz range. Such time resolution can impose severe limitations for the fidelity of recording of fast components of a Ca^{2+} spark such as its rising phase, and may hamper the interpretation of such signals in terms of the underlying channel gating and number of channels involved. Taking advantage of the high temporal resolution capabilities of the LSM 5 LIVE, we recorded Ca^{2+} sparks in line scan (x-t) mode with an acquisition rate of 40 kHz (25 μs/line) as shown in Fig. 4A. Fig. 4B (top) shows a single pixel-wide (0.3 μm) fluorescence profile ($\Delta F/F_0$) obtained from the center of the spark. The spark shown had a rise time (time-to-peak) of ~6 ms. Detailed analysis of the rising phase of the Ca^{2+} spark revealed step-like increases of $[Ca^{2+}]_i$ (marked by horizontal lines in Fig. 4B). To identify step-like changes of the rising phase of the spark the first derivative of the $\Delta F/F_0$ signal was calculated ($d(\Delta F/F_0)/dt$; Fig. 4B bottom). The first derivative of the $\Delta F/F_0$ signal represents an approximation of the underlying Ca^{2+} fluxes [26,51]. During the rising phase of the spark the $d(\Delta F/F_0)/dt$ revealed several discrete peaks identifying maxima of Ca^{2+} release flux. The timing of these peaks (vertical dashed lines) was used to identify discrete steps in the $[Ca^{2+}]_i$ signal marked by solid black lines in Fig. 4B. In the example shown (similar observation were made in 7 myocytes) 9 distinct levels of the $\Delta F/F_0$ signal could be identified with this approach. The improved temporal resolution of Ca^{2+} spark recording may open new avenues to investigate RyR gating within a CRU in-situ by a non-invasive approach as will be discussed below.

Ca^{2+} Fluxes During ECC Identified with High-speed Imaging

During ECC AP depolarization enables Ca^{2+} entry through voltage-gated Ca^{2+} channels that is followed by CICR from the SR. Thus, the global Ca^{2+} transient is the result of Ca^{2+} flux across the cell membrane and a much larger Ca^{2+} flux through RyR SR Ca^{2+} release channels. In the next set of experiments we set out to identify these two flux components with high speed Ca^{2+} imaging. Fig. 5Aa shows a whole cell global Ca^{2+} transient ($\Delta F/F_0$) induced by an AP in a ventricular cell and averaged over a region of interest of ~550 μm^2 (200×31 pixels) to obtain a low noise signal. Marker '1' identifies the time when the electrical stimulus was applied to trigger an AP. Fig. 5Ab shows the first derivative of the $[Ca^{2+}]_i$ signal ($d(\Delta F/F_0)/dt$) representing the underlying Ca^{2+} flux. The first derivative signal revealed three distinct phases. The first phase, defined by the time of application of the electrical stimulus (marker '1') and the begin of the rise of the $d(\Delta F/F_0)/dt$ signal (marker '2') was defined as the latency period between electrical stimulus and activation of Ca^{2+} flux, presumably resulting from Ca^{2+} entry. The latency period was 2.5±0.3 ms (n = 9 ventricular myocytes). During the following phase (between markers '2' and '3') $d(\Delta F/F_0)/dt$ increased steadily at a slow rate. At t = 5.5±0.2 ms (marker '3') the flux rate rather abruptly increased and peaked (marker '4') on average at $d(\Delta F/F_0)/dt = 748 \pm 71\ s^{-1}$, 9.9±0.7 ms after application of the electrical stimulus. Fig. 5Ac compares the Ca^{2+} fluxes in control ventricular cells and myocytes with a disabled SR. The SR was disabled by complete depletion with caffeine (10 mM) and prevention of refilling by treatment with the SERCA blocker thapsigargin (1 μM). Elimination of SR Ca^{2+} release abolished the large increase of Ca^{2+} flux normally observed after marker '3', however the latency period (2.1±0.1 ms; n = 11 myocytes) and the subsequent slow rise of the $d(\Delta F/F_0)/dt$ signal were preserved. The $d(\Delta F/F_0)/dt$ signal peaked at $50 \pm 5\ s^{-1}$, 7.7±0.7 ms after the electrical stimulus. In conclusion, these observations are consistent with the hypothesis that phase '1–2' (latency) marks the time interval that is required for the spread of depolarization and activation of surface membrane ion channels. Phase '2–3' represents Ca^{2+} entry flux, and was identical in control myocytes and cells with disabled SR function. Phase '3–4' is identified as Ca^{2+} release flux from the SR, since it was completely abolished when the SR was eliminated.

Fig. 5B shows an analogous analysis of data obtained in atrial myocytes. In atrial cells Ca^{2+} fluxes were further analyzed separately for SS (j-SR) and CT (nj-SR) regions. Fig. 5Ba shows the time course of the increase of $[Ca^{2+}]_i$ ($\Delta F/F_0$) induced by electrical field stimulation applied at marker '1', revealing the delayed and slower rise of $[Ca^{2+}]_i$ in the CT region. Fig. 5Bb shows the first derivative of the $\Delta F/F_0$ representing the underlying Ca^{2+} fluxes. In the SS region, similar to ventricular cells, a latency period (3.6±0.7 ms; n = 6 atrial myocytes), was followed by a slow increase (starting at marker '2') that changed to a fast increase of $d(\Delta F/F_0)/dt$ at 6.4±0.3 ms after application of the electrical stimulus (marker '3') and peaked at $1183 \pm 180\ s^{-1}$ after 11.8±0.6 ms. In contrast the CT $d(\Delta F/F_0)/dt$ signal did not reveal an obvious slow rising phase and did not start to rise until 2.2±0.3 ms after the first change of the SS signal (marker '2') was observed. Maximal flux in the CT region was 3.5±0.3 times less than in the periphery and peaked 5.3±1.7 ms later. Fig. 5Bc shows regional (SS, CT) atrial Ca^{2+} fluxes in control and myocytes with disabled SR (TG+Caff). In the SS region $d(\Delta F/F_0)/dt$ started to increase 2.1±0.1 ms (n = 6 atrial myocytes) after the electrical stimulus was applied and flux reached a maximum ($164 \pm 30\ s^{-1}$) after 6.5±0.5 ms, approximately at the time when in control cells SR Ca^{2+} release flux started. Ca^{2+} release flux in the CT region was 4.0±0.7 times smaller compared to the SS region.

In summary, fast 2-D Ca^{2+} imaging enabled us to identify Ca^{2+} fluxes associated with Ca^{2+} entry and Ca^{2+} release from the SR. Next, we attempted to validate the optically measured Ca^{2+} entry and release signals (Fig. 5) with simultaneous measurements of $[Ca^{2+}]_i$ and membrane Ca^{2+} currents (I_{Ca}) recorded with the patch clamp technique. Spatially averaged $[Ca^{2+}]_i$ and I_{Ca} measurements were obtained from single

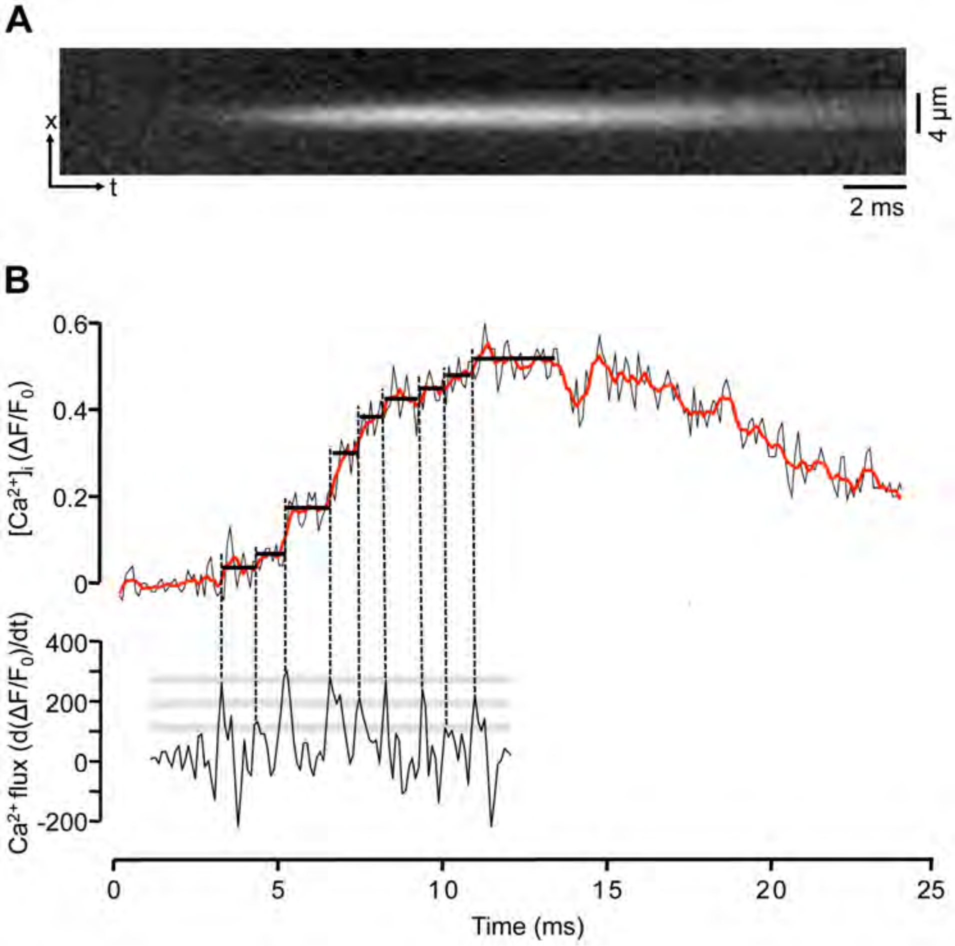

Figure 4. Ultra-fast Ca^{2+} spark recordings. A, x-t line scan image recorded at 40,000 lines/s. **B**, Top: one pixel-wide (0.3 µm) ΔF/F$_0$ profile recorded from the center of the spark. For noise reduction data were averaged to 10,000 lines/s. The red trace represents a 5-point moving average. Bottom: d(ΔF/F$_0$)/dt (s^{-1}), first derivative of the ΔF/F$_0$ signal of the rising phase of the spark. Vertical dashed lines mark maxima of the d(ΔF/F$_0$)/dt signal identifying maxima of Ca^{2+} release flux. The discrete peaks of the d(ΔF/F$_0$)/dt signal were used to identify step-like increases of the ΔF/F$_0$ signal (marked by horizontal solid black lines). Grey bars indicate discrete d(ΔF/F$_0$)/dt levels. A discrete d(ΔF/F$_0$)/dt level was defined when at least two d(ΔF/F$_0$)/dt peaks of the same amplitude were observed.
doi:10.1371/journal.pone.0061525.g004

ventricular myocytes (Fig. 6). Cells where held at −40 mV and repetitively depolarized to +20 mV for 100 ms to elicit maximal LCCs. Fig. 6 shows from top to bottom, [Ca^{2+}]$_i$ (ΔF/F$_0$), Ca^{2+} flux (d(ΔF/F$_0$)/dt), I$_{Ca}$ and the command voltage. The Ca^{2+} flux signal showed a slow steady increase shortly after the begin of the depolarization pulse (marker 'a'). The slow increase of Ca^{2+} flux abruptly increased at marker 'b', giving way to a rapid rise of the Ca^{2+} flux rate. The distinct change in flux rate (marker 'b') occurred 5.7 ms after the begin of the depolarization pulse and correlated well with the begin of SR Ca^{2+} release determined by optical methods (marker '3' in Fig. 5A).

In conclusion, the data presented in Figures 5 and 6 provide evidence that fast 2-D confocal Ca^{2+} imaging with sampling rates in the 1–2 kHz range can generate information on Ca^{2+} fluxes underlying ECC with a time resolution that is approaching the time resolution of the patch clamp technique, however has the advantage of lesser perturbation of the intracellular environment since the surface membrane of the cell remains intact.

Discussion

In this study, we investigated the behavior and interactions of CRUs during electrically evoked Ca^{2+} transients and individual elementary Ca^{2+} release events (Ca^{2+} sparks) in atrial and ventricular myocytes with 2-D and line scan confocal imaging at high recording speeds. The key findings of our investigation were as follows:

First, the recruitment of individual CRUs by AP depolarization was spatially inhomogeneous and temporally asynchronous. Spatial inhomogeneity was particularly pronounced in atrial myocytes that lack a t-tubular membrane system. Second, high-speed confocal Ca^{2+} imaging allowed to resolve a distinct sequency of events during a Ca^{2+} transient, consisting of a latency period, Ca^{2+} entry and SR Ca^{2+} release, by an optophysiological approach [22], that has a time resolution comparable to electrophysiological recording (patch clamp) methods, however, is considerably less invasive since the integrity of cell membrane and cytosolic environment remains intact. Third, ultra-fast line scan recordings revealed step-like changes of [Ca^{2+}]$_i$ during the

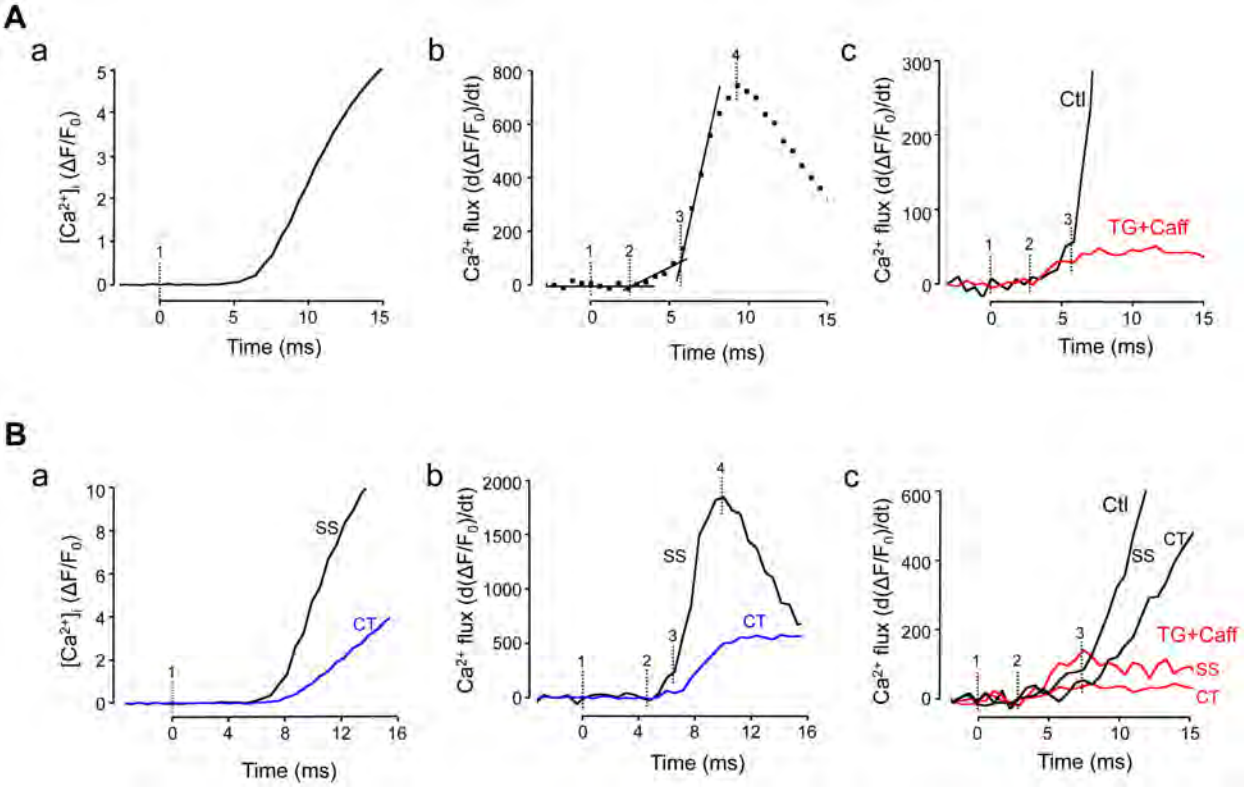

Figure 5. Subcellular Ca^{2+} fluxes during ECC identified by fast Ca^{2+} imaging. A, global Ca^{2+} transient ($\Delta F/F_0$) elicited by electrical field stimulation of a ventricular myocyte (panel **a**). Marker '1' indicates the application of the electrical stimulus. Markers '2' and '3' were positioned according to the analysis in panel b. Panel **b**: first derivative of $\Delta F/F_0$ (s^{-1}) from panel a, representing Ca^{2+} flux. Markers '2' and '3' indicate abrupt changes in Ca^{2+} flux rate, and marker '4' indicates maximal Ca^{2+} flux. Panel **c**: spatially averaged Ca^{2+} flux under control conditions (Ctl) and during inhibition of SR function with thapsigargin (TG; 1 μM) and caffeine (Caff; 10 mM). **B**, subcellular Ca^{2+} transients ($\Delta F/F_0$) elicited by electrical field stimulation and recorded from subsarcolemmal (SS) j-SR and central (CT) nj-SR regions of an atrial myocyte (panel **a**). Panel **b**: first derivative of SS and CT Ca^{2+} signals representing subcellular Ca^{2+} flux rates. Markers '1' to '4' as in panel A. Panel **c**: subcellular (SS, CT) Ca^{2+} flux rates in control and in the presence of thapsigargin+caffeine. 2-D images were recorded 1719 Hz time resolution.
doi:10.1371/journal.pone.0061525.g005

rising phase of Ca^{2+} sparks that may provide novel insights into RyR gating properties within individual CRUs.

Activation of SR Ca^{2+} release in atrial myocytes was asynchronous at two different levels. As has been described before [7,10,13,26,52,53], due the lack (or poor development) of the t-tubular system, subsarcolemmal Ca^{2+} release originating at the peripheral couplings of the j-SR preceded Ca^{2+} release from the nj-SR in central regions of the cell, and peak CT [Ca^{2+}]$_i$ lagged behind by tens of milliseconds during AP-triggered Ca^{2+} transients (Fig. 1E). However, the initial activation of j-SR Ca^{2+} release in the cell periphery was also asynchronous and spatially inhomogeneous (Fig. 1B). Recruitment of detectable peripheral CRUs extended over at least 3 ms. A similar asynchronous activation pattern was found in ventricular myocyes where recruitment of all discernable CRUs required ~4 ms. These numbers are low-end estimates. At later times the progressing global increase of [Ca^{2+}]$_i$ and Ca^{2+} diffusion away from activated release sites starts to obscure the recruitment of new sites and hampers their detectability at later times. Using line scan imaging numerous studies have found evidence for spatial inhomogeneities (e.g. [26,48,49]) that can be exacerbated in pathological conditions [50]. However, it is difficult to discern whether in line scan data apparent inhomogeneities arise from asynchronous activation of CRUs, silent or missing CRUs, or are the result of the inherent shortcoming of this recording mode that the scanned line potentially is missing CRUs (for example, when randomly placed between 2 neighboring Z-disks that are typically spaced ~2 μm apart [13]). In 2-D imaging the problem is alleviated since the radial distance (i.e. the distance within the plane of a Z-disk) between CRUs is in the sub-micrometer range [29,30,32,33], i.e. within the range of the spatial resolution of the microscope. In other words, upon AP stimulation all events recorded in 2-D mode originating from CRUs at the intersection of the focal plane and the plane of the Z-disk or from CRUs located on the Z-disk at distances that are within the point-spread function of the microscope (see Methods) will be detected. Consequently, every CRU that becomes activated during an AP within the resolved volume surrounding the focal plane will be captured. Thus, delays and asynchrony between activation of individual CRUs can more reliably be recorded.

Fast 2-D Ca^{2+} imaging allowed also to separate Ca^{2+} entry from SR Ca^{2+} release during an AP-induced Ca^{2+} transient by optical methods (Figures 5 and 6). By analyzing the first derivative of the Ca^{2+} transient three distinct phases could be discerned during the first ten milliseconds of the Ca^{2+} transient. First, a latency period of ~2.5 ms between stimulus application and the first indication of an increase of [Ca^{2+}]$_i$ was observed. The second phase, characterized by a slow increase of [Ca^{2+}]$_i$ and lasting until 5.5

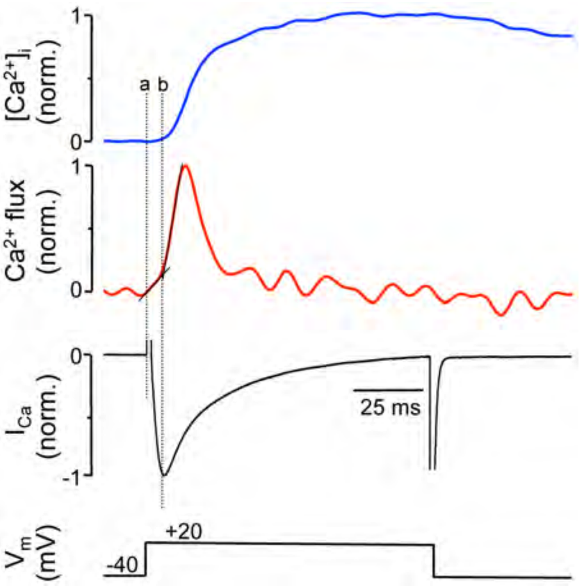

Figure 6. Simultaneous $[Ca^{2+}]$ and I_{Ca} measurements. Simultaneous measurements of $[Ca^{2+}]_i$ and I_{Ca} from a voltage-clamped (ruptured patch configuration) ventricular myocyte. Shown from top: $[Ca^{2+}]_i$ ($\Delta F/F_0$), Ca^{2+} flux ($d(\Delta F/F_0)/dt$), I_{Ca} and the command voltage. Traces represent averages of 15 successive depolarization pulses applied to the same cell and were normalized to their respective maximal amplitude. In these experiments whole-cell Fluo-4 fluorescence was recorded using a photomultiplier tube. Marker 'a': begin of depolarization pulse; marker 'b': change in flux rate, presumably identifying activation of CICR from the SR.
doi:10.1371/journal.pone.0061525.g006

(ventricular) and 6.4 ms (atrial myocytes) after the begin of the pulse, represents Ca^{2+} entry across the surface membrane which was confirmed with simultaneous patch clamp and $[Ca^{2+}]_i$ measurements (Fig. 6). This conclusion was supported by the fact, that the rise of $[Ca^{2+}]_i$ was still observed when SR Ca^{2+} release was disabled, and the change in $[Ca^{2+}]_i$ coincided well with the current recordings. The third phase, characterized by an abrupt increase of release flux by approximately an order of magnitude, peaked 10–12 ms after the pulse. Phase 3 was completely abolished when the SR was disabled. The data indicate that 2-D Ca^{2+} imaging with 1–2 kHz time resolution is capable of distinguishing between trigger and released Ca^{2+} in intact myocytes by an optophysiological approach, with the advantage that cell membrane and cytosolic environment are kept undisturbed.

Despite substantial progress made towards the understanding of Ca^{2+} release and ECC in atrial tissue, several key questions have remained unanswered. For example, with the lack of t-tubules the CRUs of the nj-SR (which account for a large majority of atrial CRUs) do not have the characteristics of a typical couplon. Specifically, the RyRs are not facing into a narrow diadic cleft where upon activation of LCCs $[Ca^{2+}]_i$ rapidly increases to concentrations that are several orders magnitude higher than resting $[Ca^{2+}]_i$. With the inherent low Ca^{2+}-sensitivity of the RyR [54,55] it is difficult to reconcile how $[Ca^{2+}]_i$ can rise sufficiently high in the vicinity of RyRs of the nj-SR to lead to channel opening and Ca^{2+} release. Furthermore, it has even been suggested that Ca^{2+} sequestering mitochondria in the subsarcolemmal space of atrial myocytes constitute a Ca^{2+} barrier [15], making the propagation of CICR from peripheral j-SR to nj-SR even more problematic. As shown previously [41], atrial sparks have a relatively large Ca^{2+} flux (~11 pA) and large numbers of channels involved (20–30 RyRs) with an enhanced propensity to open and a diminished influence of negative feedback mechanisms as well as an extended spatial spread (see also [40]). All these features tend to facilitate propagation of release from nj-SR. Interestingly, in contrast to Ca^{2+} sparks recorded from nj-SR and sparks in ventricular cells, the location of maximal fluorescence identifying a point source of Ca^{2+} release of peripheral atrial sparks is not spatially fixed, but moves in centripetal direction during the evolution of the spark (Fig. 2C). Thus, peripheral atrial sparks reveal some inherent feature for directional propagation that facilitates the saltatory advancement of activation from j-SR to the nj-SR, although it remains to be determined what constitutes the structural or functional basis of this special feature.

The question how many RyRs are found in an individual CRUs has remained rather elusive. Earlier reports suggested the number to be in the range of 50–250 RyRs [23,29,30,31,32,33,35]. However, novel advanced technologies, including super-resolution imaging techniques [56] that go beyond diffraction-limited resolution, and 3-dimensional electron microscopy tomography [57], have revealed new aspects of the make up of the cardiac CRU [36,58,59]: CRUs are variable in size, of irregular geometry, lack the regular arrays of RyRs typical of skeletal muscle, and show a smaller density of RyRs than previously assumed. Furthermore, individual CRUs can assemble in groups to form 'super-clusters' resulting in variable degrees of coordination of Ca^{2+} release from sub-clusters. These recent studies that generated evidence of incomplete packaging of CRUs with RyRs and the existence of sub-domains of smaller sizes have corrected the number of RyRs per CRU towards lower values in the range of a few tens to less than ten RyRs [29,34,36]. While recent technological advances for studying CRUs have generated valuable novel insights, it is still far from being established how many RyRs actively contribute to Ca^{2+} release of a spark. The estimates, just for cardiac myocytes alone, range from possibly only one or only a very small fraction of the cluster (<10 RyRs), to whole-cluster activation with possibly contribution from several hundred channels [21,32,37,38,39,40,41,42]. The ionic current or ionic flux underlying a spark is estimated to be in the range of 3–5 pA [38,40,60,61,62,63], although it tends to be higher in atrial myocytes (11 pA; [41]). Ca^{2+} currents through single cardiac RyR channels reconstituted in lipid bilayer and recorded under physiological ionic conditions gave unitary current values of 0.3–0.7 pA [64]. Based on these estimates only ~5–35 RyRs passing current simultaneously would participate in a single spark. This leads to the paradox that the estimated number of participating channels is nearly an order of magnitude smaller than the higher estimates for the number of RyRs per CRU. Recent results indicate that the current underlying a spark is quantal in nature. By using 'sparklets' - local Ca^{2+} signals of known magnitude arising from LCCs [39] - to calibrate Ca^{2+} sparks, it could be demonstrated that Ca^{2+} sparks have a quantal substructure and that Ca^{2+} spark release flux is made up of quanta of 1.2 pA. Furthermore, the number of quanta in a spark varies dynamically from one to ≤8 [62]. Whether single quanta reflect the opening of a single RyR or a group of tightly coupled channels is unclear. Cooperativity of activation and inactivation among release channels or 'coupled gating' [65,66,67] could enable entire groups of channel to generate a single quantum. In support of multichannel quanta is also the observation that the measured quantum size (1.2 pA) is larger than the estimates for RyR unitary currents (~0.5 pA, lasting ~10 ms) under physiological ionic conditions. Thus, quantal release with a low number of individual quanta does not necessarily rule out the involvement of a larger number of RyRs. In addition, the observation of RyR super-clusters raises the possibility that quantal release reflects the concerted activation of sub-clusters [56]. Since sub-clusters vary in size and number of RyRs this model could explain quantal release with quanta of variable sizes, however this would require a looser definition of the term 'quantal' to avoid violation of a stricter definition of 'quanta' which suggests entities of identical magnitude. Our data shown in Fig. 4 may point towards coordinated gating of an entire RyR cluster with a high degree of cooperativity. The $d(\Delta F/F_0)/dt$ signal shown in Fig. 4B, at first glance, is reminiscent of single-channel gating with the peaks indicating channel openings. On the other hand, we have shown previously that in the same species atrial Ca^{2+} sparks involve release from 20–30 RyRs [41]. Coupled gating with a high degree of cooperativity within a CRU, where the entire RyR cluster behaves essentially as a single channel, could reconcile this apparent paradox. Upon closer examination, in the $d(\Delta F/F_0)/dt$ signal in Fig. 4B at least three distinct amplitude levels can be identified (grey bars). Thus, the data could be consistent with coupled gating of the entire cluster or a small number of subclusters, but do not exclude a quantal nature of Ca^{2+} release since quantal release consisting of a small number of quanta (even 1 or 2 quanta only) has been demonstrated [62].

While entirely speculative at this point, the progressive activation of RyR sub-clusters within a CRU may also explain the centripetal propagation of Ca^{2+} release found in subsarcolemmal atrial CRUs (Fig. 2C). Furthermore, to reconcile the paradox of a presumably small fraction of active channels and a large number channels present in a CRU, several possibilities need to be considered. For one, the unitary RyR current could be much smaller (possibly in the femto-ampere range) during a spark than measured in the bilayer because the rapid rise of Ca^{2+} in the diadic cleft together with local SR depletion could significantly decrease the driving force for Ca^{2+} flux. Conceivably, powerful, however yet to be identified inhibitory mechanisms, negative cooperativity among RyRs (opening of a RyR reduces the open probability of its neighbors), strong Ca^{2+}-dependent RyR inactivation or the recently proposed 'pernicious attrition' Ca^{2+} release termination mechanism [68] could prevent the activation of an entire CRU by intra-cluster CICR. As recently suggested, Mg^{2+} binding to the RyR could be responsible for such a strong inhibitory mechanism [69].

In summary, we demonstrate here that high-speed confocal imaging with sampling rates in the 1–40 kHz range in conjunction with high quantum yield fluorescent indicators allows to study Ca^{2+} dynamics and intricacies of single SR Ca^{2+} release units. With this technique we showed that dynamics of Ca^{2+} entry and CICR can reliably be distinguished at the level of individual CRUs in intact cells, that Ca^{2+} sparks of atrial myocytes have inherent properties that facilitate centripetal propagation of activation, and that the rising phase of Ca^{2+} sparks reveals step-like kinetics which bears potentially valuable information about intra-CRU channel gating. These findings have important ramifications for the understanding of the structural and functional organization of CRUs, CICR and ECC.

Author Contributions

Conceived and designed the experiments: VMS LAB. Performed the experiments: VMS. Analyzed the data: VMS LAB. Contributed reagents/materials/analysis tools: LAB. Wrote the paper: VMS LAB.

References

1. Bers DM (2002) Cardiac excitation-contraction coupling. Nature 415: 198–205.
2. Fabiato A (1983) Calcium-induced release of calcium from the cardiac sarcoplasmic reticulum. Am J Physiol 245: C1–14.
3. Franzini-Armstrong C, Jorgensen AO (1994) Structure and development of E-C coupling units in skeletal muscle. Annu Rev Physiol 56: 509–534.
4. Stern MD, Song LS, Cheng H, Sham JS, Yang HT, et al. (1999) Local control models of cardiac excitation-contraction coupling. A possible role for allosteric interactions between ryanodine receptors. J Gen Physiol 113: 469–489.
5. Cheng H, Cannell MB, Lederer WJ (1994) Propagation of excitation-contraction coupling into ventricular myocytes. Pflugers Arch 428: 415–417.
6. Cheng H, Lederer MR, Xiao RP, Gomez AM, Zhou YY, et al. (1996) Excitation-contraction coupling in heart: new insights from Ca2+ sparks. Cell Calcium 20: 129–140.
7. Huser J, Lipsius SL, Blatter LA (1996) Calcium gradients during excitation-contraction coupling in cat atrial myocytes. J Physiol 494 (Pt 3): 641–651.
8. Soeller C, Cannell MB (1999) Examination of the transverse tubular system in living cardiac rat myocytes by 2-photon microscopy and digital image-processing techniques. Circ Res 84: 266–275.
9. Cordeiro JM, Spitzer KW, Giles WR, Ershler PE, Cannell MB, et al. (2001) Location of the initiation site of calcium transients and sparks in rabbit heart Purkinje cells. J Physiol 531: 301–314.
10. Mackenzie L, Bootman MD, Berridge MJ, Lipp P (2001) Predetermined recruitment of calcium release sites underlies excitation-contraction coupling in rat atrial myocytes. J Physiol 530: 417–429.
11. Smyrnias I, Mair W, Harzheim D, Walker SA, Roderick HL, et al. (2010) Comparison of the T-tubule system in adult rat ventricular and atrial myocytes, and its role in excitation-contraction coupling and inotropic stimulation. Cell calcium 47: 210–223.
12. Bootman MD, Higazi DR, Coombes S, Roderick HL (2006) Calcium signalling during excitation-contraction coupling in mammalian atrial myocytes. Journal of cell science 119: 3915–3925.
13. Kockskamper J, Sheehan KA, Bare DJ, Lipsius SL, Mignery GA, et al. (2001) Activation and propagation of Ca(2+) release during excitation-contraction coupling in atrial myocytes. Biophys J 81: 2590–2605.
14. McNutt NS, Fawcett DW (1969) The ultrastructure of the cat myocardium. II. Atrial muscle. J Cell Biol 42: 46–67.
15. Mackenzie L, Roderick HL, Berridge MJ, Conway SJ, Bootman MD (2004) The spatial pattern of atrial cardiomyocyte calcium signalling modulates contraction. J Cell Sci 117: 6327–6337.
16. Woo SH, Cleemann L, Morad M (2003) Spatiotemporal characteristics of junctional and nonjunctional focal Ca2+ release in rat atrial myocytes. Circ Res 92: e1–11.
17. Carl SL, Felix K, Caswell AH, Brandt NR, Ball WJ, Jr., et al. (1995) Immunolocalization of sarcolemmal dihydropyridine receptor and sarcoplasmic reticular triadin and ryanodine receptor in rabbit ventricle and atrium. J Cell Biol 129: 672–682.
18. Bootman MD, Smyrnias I, Thul R, Coombes S, Roderick HL (2011) Atrial cardiomyocyte calcium signalling. Biochimica et biophysica acta 1813: 922–934.
19. Blatter LA, Kockskamper J, Sheehan KA, Zima AV, Huser J, et al. (2003) Local calcium gradients during excitation-contraction coupling and alternans in atrial myocytes. J Physiol 546: 19–31.
20. Keizer J, Smith GD, Ponce-Dawson S, Pearson JE (1998) Saltatory propagation of Ca2+ waves by Ca2+ sparks. Biophysical journal 75: 595–600.
21. Cheng H, Lederer WJ, Cannell MB (1993) Calcium sparks: elementary events underlying excitation-contraction coupling in heart muscle. Science 262: 740–744.
22. Cheng H, Lederer WJ (2008) Calcium sparks. Physiological reviews 88: 1491–1545.
23. Brochet DX, Xie W, Yang D, Cheng H, Lederer WJ (2010) Quarky Calcium Release in the Heart. Circ Res.
24. Lipp P, Niggli E (1996) Submicroscopic calcium signals as fundamental events of excitation–contraction coupling in guinea-pig cardiac myocytes. J Physiol 492 (Pt 1): 31–38.
25. Lipp P, Niggli E (1998) Fundamental calcium release events revealed by two-photon excitation photolysis of caged calcium in Guinea-pig cardiac myocytes. J Physiol 508 (Pt 3): 801–809.
26. Sheehan KA, Blatter LA (2003) Regulation of junctional and non-junctional sarcoplasmic reticulum calcium release in excitation-contraction coupling in cat atrial myocytes. J Physiol 546: 119–135.
27. Woo SH, Cleemann L, Morad M (2005) Diversity of atrial local Ca2+ signalling: evidence from 2-D confocal imaging in Ca2+-buffered rat atrial myocytes. J Physiol 567: 905–921.
28. Sheehan KA, Zima AV, Blatter LA (2006) Regional differences in spontaneous Ca2+ spark activity and regulation in cat atrial myocytes. J Physiol 572: 799–809.
29. Hayashi T, Martone ME, Yu Z, Thor A, Doi M, et al. (2009) Three-dimensional electron microscopy reveals new details of membrane systems for Ca2+ signaling in the heart. J Cell Sci 122: 1005–1013.

30. Franzini-Armstrong C, Protasi F, Ramesh V (1999) Shape, size, and distribution of Ca(2+) release units and couplons in skeletal and cardiac muscles. Biophysical journal 77: 1528–1539.
31. Soeller C, Crossman D, Gilbert R, Cannell MB (2007) Analysis of ryanodine receptor clusters in rat and human cardiac myocytes. Proceedings of the National Academy of Sciences of the United States of America 104: 14958–14963.
32. Scriven DR, Asghari P, Schulson MN, Moore ED (2010) Analysis of Cav1.2 and ryanodine receptor clusters in rat ventricular myocytes. Biophysical journal 99: 3923–3929.
33. Chen-Izu Y, McCulle SL, Ward CW, Soeller C, Allen BM, et al. (2006) Three-dimensional distribution of ryanodine receptor clusters in cardiac myocytes. Biophys J 91: 1–13.
34. Jayasinghe ID, Baddeley D, Kong CH, Wehrens XH, Cannell MB, et al. (2012) Nanoscale organization of junctophilin-2 and ryanodine receptors within peripheral couplings of rat ventricular cardiomyocytes. Biophysical journal 102: L19–21.
35. Brochet DX, Yang D, Di Maio A, Lederer WJ, Franzini-Armstrong C, et al. (2005) Ca2+ blinks: rapid nanoscopic store calcium signaling. Proc Natl Acad Sci U S A 102: 3099–3104.
36. Baddeley D, Jayasinghe ID, Lam L, Rossberger S, Cannell MB, et al. (2009) Optical single-channel resolution imaging of the ryanodine receptor distribution in rat cardiac myocytes. Proceedings of the National Academy of Sciences of the United States of America 106: 22275–22280.
37. Sobie EA, Dilly KW, dos Santos Cruz J, Lederer WJ, Jafri MS (2002) Termination of cardiac Ca(2+) sparks: an investigative mathematical model of calcium-induced calcium release. Biophys J 83: 59–78.
38. Izu LT, Mauban JR, Balke CW, Wier WG (2001) Large currents generate cardiac Ca2+ sparks. Biophys J 80: 88–102.
39. Wang SQ, Song LS, Lakatta EG, Cheng H (2001) Ca2+ signalling between single L-type Ca2+ channels and ryanodine receptors in heart cells. Nature 410: 592–596.
40. Blatter LA, Huser J, Rios E (1997) Sarcoplasmic reticulum Ca2+ release flux underlying Ca2+ sparks in cardiac muscle. Proc Natl Acad Sci U S A 94: 4176–4181.
41. Shkryl VM, Blatter LA, Rios E (2012) Properties of Ca2+ sparks revealed by four-dimensional confocal imaging of cardiac muscle. J Gen Physiol 139: 189–207.
42. Bridge JH, Ershler PR, Cannell MB (1999) Properties of Ca2+ sparks evoked by action potentials in mouse ventricular myocytes. J Physiol 518 (Pt 2): 469–478.
43. Bruton JD, Cheng AJ, Westerblad H (2012) Methods to detect Ca(2+) in living cells. Advances in experimental medicine and biology 740: 27–43.
44. Wu JY, Vereecke J, Carmeliet E, Lipsius SL (1991) Ionic currents activated during hyperpolarization of single right atrial myocytes from cat heart. Circ Res 68: 1059–1069.
45. Rubenstein DS, Lipsius SL (1995) Premature beats elicit a phase reversal of mechanoelectrical alternans in cat ventricular myocytes. A possible mechanism for reentrant arrhythmias. Circulation 91: 201–214.
46. Kockskamper J, Blatter LA (2002) Subcellular Ca2+ alternans represents a novel mechanism for the generation of arrhythmogenic Ca2+ waves in cat atrial myocytes. J Physiol 545: 65–79.
47. Domeier TL, Blatter LA, Zima AV (2009) Alteration of sarcoplasmic reticulum Ca2+ release termination by ryanodine receptor sensitization and in heart failure. J Physiol 587: 5197–5209.
48. Cheng H, Cannell MB, Lederer WJ (1995) Partial inhibition of Ca2+ current by methoxyverapamil (D600) reveals spatial nonuniformities in [Ca2+]i during excitation-contraction coupling in cardiac myocytes. Circ Res 76: 236–241.
49. Heinzel FR, Bito V, Volders PG, Antoons G, Mubagwa K, et al. (2002) Spatial and temporal inhomogeneities during Ca2+ release from the sarcoplasmic reticulum in pig ventricular myocytes. Circulation research 91: 1023–1030.
50. Heinzel FR, Bito V, Biesmans L, Wu M, Detre E, et al. (2008) Remodeling of T-tubules and reduced synchrony of Ca2+ release in myocytes from chronically ischemic myocardium. Circulation research 102: 338–346.
51. Sipido KR, Wier WG (1991) Flux of Ca2+ across the sarcoplasmic reticulum of guinea-pig cardiac cells during excitation-contraction coupling. J Physiol 435: 605–630.
52. Berlin JR (1995) Spatiotemporal changes of Ca2+ during electrically evoked contractions in atrial and ventricular cells. Am J Physiol 269: H1165–1170.
53. Woo SH, Cleemann L, Morad M (2002) Ca2+ current-gated focal and local Ca2+ release in rat atrial myocytes: evidence from rapid 2-D confocal imaging. J Physiol 543: 439–453.
54. Cannell MB, Soeller C (1997) Numerical analysis of ryanodine receptor activation by L-type channel activity in the cardiac muscle diad. Biophys J 73: 112–122.
55. Meissner G, Henderson JS (1987) Rapid calcium release from cardiac sarcoplasmic reticulum vesicles is dependent on Ca2+ and is modulated by Mg2+, adenine nucleotide, and calmodulin. The Journal of biological chemistry 262: 3065–3073.
56. Soeller C, Baddeley D (2012) Super-resolution imaging of EC coupling protein distribution in the heart. Journal of molecular and cellular cardiology.
57. Das T, Hoshijima M (2012) Adding a new dimension to cardiac nano-architecture using electron microscopy: Coupling membrane excitation to calcium signaling. Journal of molecular and cellular cardiology.
58. Hayashi H, Shiferaw Y, Sato D, Nihei M, Lin SF, et al. (2007) Dynamic origin of spatially discordant alternans in cardiac tissue. Biophys J 92: 448–460.
59. Asghari P, Scriven DR, Hoskins J, Fameli N, van Breemen C, et al. (2012) The structure and functioning of the couplon in the mammalian cardiomyocyte. Protoplasma 249 Suppl 1: S31–38.
60. Cheng H, Wang SQ (2002) Calcium signaling between sarcolemmal calcium channels and ryanodine receptors in heart cells. Front Biosci 7: d1867–1878.
61. Soeller C, Cannell MB (2002) Estimation of the sarcoplasmic reticulum Ca2+ release flux underlying Ca2+ sparks. Biophys J 82: 2396–2414.
62. Wang SQ, Stern MD, Rios E, Cheng H (2004) The quantal nature of Ca2+ sparks and in situ operation of the ryanodine receptor array in cardiac cells. Proc Natl Acad Sci U S A 101: 3979–3984.
63. Santiago DJ, Curran JW, Bers DM, Lederer WJ, Stern MD, et al. (2010) Ca Sparks Do Not Explain all Ryanodine Receptor-Mediated SR Ca Leak in Mouse Ventricular Myocytes. Biophys J 98: 2111–2120.
64. Kettlun C, Gonzalez A, Rios E, Fill M (2003) Unitary Ca2+ current through mammalian cardiac and amphibian skeletal muscle ryanodine receptor Channels under near-physiological ionic conditions. The Journal of general physiology 122: 407–417.
65. Marx SO, Gaburjakova J, Gaburjakova M, Henrikson C, Ondrias K, et al. (2001) Coupled gating between cardiac calcium release channels (ryanodine receptors). Circulation research 88: 1151–1158.
66. Marx SO, Ondrias K, Marks AR (1998) Coupled gating between individual skeletal muscle Ca2+ release channels (ryanodine receptors). Science 281: 818–821.
67. Porta M, Diaz-Sylvester PL, Neumann JT, Escobar AL, Fleischer S, et al. (2012) Coupled gating of skeletal muscle ryanodine receptors is modulated by Ca2+, Mg2+, and ATP. American journal of physiology Cell physiology 303: C682–697.
68. Gillespie D, Fill M (2013) Pernicious attrition and inter-RyR2 CICR current control in cardiac muscle. Journal of molecular and cellular cardiology.
69. Zahradnikova A, Valent I, Zahradnik I (2010) Frequency and release flux of calcium sparks in rat cardiac myocytes: a relation to RYR gating. The Journal of general physiology 136: 101–116.

1.3 Активність ріанодинових рецепторів як поодиноких подій вивільнення Ca^{2+} з саркоплазматичного ретикулуму — спалахи Ca^{2+}, виявлених за допомогою чотиривимірної конфокальної мікроскопії

Точне виявлення вивільнення Ca^{2+} з СР через відкриття групи RyRs, які реєструються у вигляді кальцієвих спалахів, ускладнено через спонтанну природу таких явищ. Використання конфокального сканування лінії або площі в часі призводить до неточності виявлення місць вивільнення кальцію. Отримані дані таких подій характеризуються визначеними параметрами із певними похибками (Rios et al., 1999).

У даному дослідженні використовуються можливості двох інноваційних інструментів: швидкого сканування в площині x-y за допомогою щілинного конфокального сканера (LSM 5 LIVE; Carl Zeiss) та техніки швидкого переміщення фокусу в площині z для отримання зображень в трьох просторових вимірах та у часі (x-y-z-t) для реєстрації спалахів. Таке сканування ефективно усуває помилки розфокусування, та дозволяє ідентифікацію Ca^{2+} спалахів у фокальній площині. Внаслідок цього ми маємо можливість характеризувати морфометричні характеристики великої групи спалахів, зосереджених у фокусі. Ці вимірювання, вперше так чітко визначені, були використано для детального вивчення механізмів контролю вивільнення Ca^{2+}.

Ca^{2+} спалах, який зареєстрований у місці вивільнення представлено на рис. 1.5. Час сканування одного зображення був 1.16 мс (з часом сканування лінії 15.7 мкс), а час отримання всіх трьох зображень, по зміні z1, z2, z3 — 5.6 мс (див. рис. 1.5A). На рис. 1.5B зображено профілі інтенсивності флуоресценції (шириною 2 пікселі), які проведено через центри спалахів, і всі вони відповідають одному й тому ж місцю на послідовних зображеннях (рис. 1.5A). Зауважується, що на декількох трійках зображень піки флуоресценції у площині z_2 є більшими (виділено зірочками) порівняно з площами z_1 та z_3. Цей кальцієвий спалах відповідає критерію фокусування, коли у середній площі спалах має максимальну амплітуду.

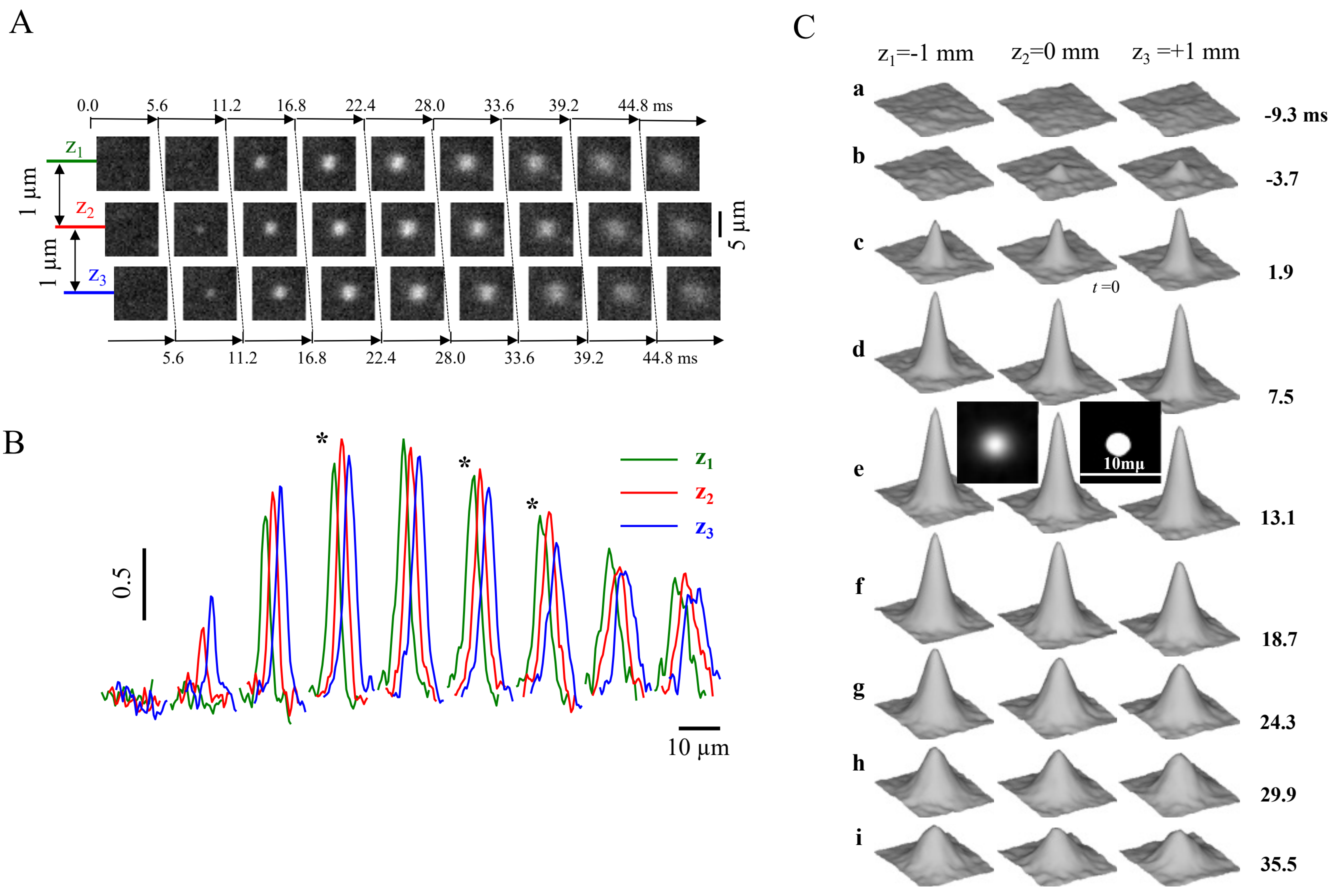

Рисунок 1.5. Сканування у трьох вимірах простору та часу. (A) Квадратні фрагменти послідовних x-y зображень флуоресценції кардіоміоцита передсердя. Як показано, вертикальні положення відповідають розташуванню трьох площинах сканування (z_1 = -1 мкм, z_2 = 0 мкм і z_3 = +1 мкм). Час збору даних для тріо x-y сканувань, як показано горизонтальними стрілками, становив 5,6 мс. (B) Профілі $\Delta F(x)/F_0(x)$ у центральній частині зображень з підпункту A, кольорово кодовані відповідно до значень z. Зірочками позначено трійки профілів, де амплітуда виявилася найвищою при z_2. (C) Приклад спалаху у фокусі. Усереднені зображення 150 спалахів у фокусі з часом наростання спалаху T = 11.2 мс, отримані в різний час і при різних розташуваннях z. Початок відліку часу (t = 0) відповідає часу першого виявлення, яке відбувається значно пізніше початку події. Ліва квадратна панель у рядку *e* зображує усереднений спалах в момент пікової амплітуди у точці z_2 у відтінках сірого. Права квадратна панель відображає область x-y білим кольором, де середнє значення F/F_0 перевищує половину максимального значення.

На рис. 1.5C представлено усереднене значення 150 спалахів, виявлених у фокусі, які мають спільний параметр T = 11.2 мс, як час наростання спалаху. Час першого виявлення (t = 0) настає значно пізніше початку події. Дані про ці спалахи також використовувались для розрахунку потоку вивільнення Ca^{2+}.

Алгоритм автоматичного детектування, розроблений для x-y зображень (Brum et al., 2000), був застосований до 34 000 x-y-z сканувань (тобто тріо x-y зображень для трьох значень z), отриманих з 34 клітин (по 1000 x-y-z або 3000 x-y сканувань на кожну клітину). З них 6906 спалахів було виявлено, і 767 з них визнано зосередженими у фокусі.

Гістограми амплітуд (визначені як a = пікове значення $\Delta F/F_0$) для двох груп представлені на рис. 1.6A. Гістограма для всіх виявлених спалахів (рис. 1.6A, пунктирна чорна лінія), монотонно зменшується, за винятком діапазону при низьких значеннях ($a<0.4$), де виявлення не відбувається. Натомість гістограма амплітуд спалахів у фокусі (рис. 1.6A, суцільна зелена лінія) має моду з піком біля $a = 0.7$.

На рис. 1.6B, аналогічно рис. 1.6A, ми порівнювали просторову ширину при половинній амплітуді (FWHM) виявлених спалахів. У даному випадку розбіжності між показниками для спалахів у фокусі та для всіх виявлених спалахів виявилися менш вираженими. Обидва розподіли були асиметричні, зосереджуючись навколо значення близько 2.6 мкм, проте розподіл для спалахів у фокусі був трохи вужчим. Видно, що вимірювання просторової ширини менше піддається впливу розфокусування, ніж вимірювання амплітуди спалаху.

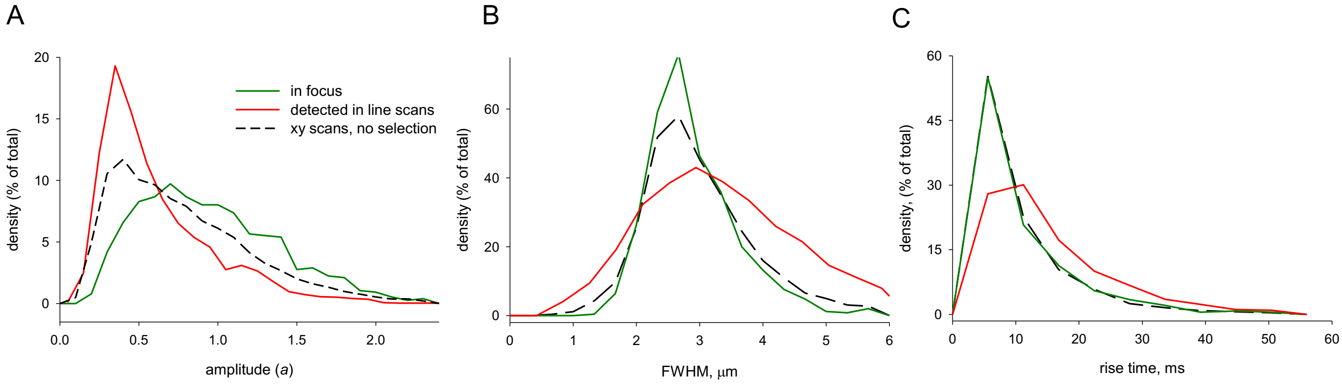

Рисунок 1.6. Властивості спалахів у фокусі. Гістограми розподілу амплітуд (A), повна ширина при половинній амплітуді (FWHM; B) та часу наростання (C) для всіх спалахів, виявлених на x-y сканування (чорний, пунктир), спалахів у фокусі (зелений) та спалахів, виявлених на реконструйованих лінійних скануваннях (червоний).

На рис. 1.6C представлено гістограми часу наростання спалаху T (від моменту першого виявлення до досягнення пікової амплітуди). T завжди вимірювався на центральній площині (z_2), з 5.6 мс для кожного зображення і, відповідно, до дискретного розподілу. Часу наростання спалаху *T* був практично однаковий для сфокусованих та всіх виявлених спалахів. Для згенерованих Ca^{2+} спалахів, що реєструються при скануванні лініями ці параметри істотно відрізнялись (червоні криві на рис.1.6). Розподіл амплітуд, отриманий на реконструйованих лінійних скануваннях, схильний до низьких значень. У той час, розподіли ширини та часу наростання виявляються більш дисперсними в порівнянні з відповідними показниками на x-y скануваннях.

Основна перевага визначення того, що спалах знаходиться у фокусі, полягає в тому, що потік вивільнення Ca^{2+} може бути визначений з більшою достовірністю. Ми розрахували потік вивільнення, застосувавши "зворотний" метод (Rios et al., 1999) до середніх значень спалахів у фокусі з однаковим часом наростання (як показано на рис. 1.5C, T = 11.2 мс). Розрахунок, як описано у роботі Ríos та ін. (Rios et al., 1999), припускає радіальну симетрію події. Це припущення добре виконується і в нашому випадку. Графічне підтвердження цього надано для середнього значення при T = 11.2 мс чорними вставками в рядку *e* на рис. 1.5C, де показано середнє значення на піку спалаху в градаціях сірого (ліворуч) та його маску (праворуч), що створена контуром середнього значення в області, де його флуоресценція перевищує половину амплітуди. Цей контур майже круглий, що свідчить про симетричність усередненого значення, хоча не виключає можливої асиметрії в окремих випадках.

Метод розрахунку потоку вивільнення вимагає встановлення значень концентраціям і кінетичним параметрам відповідних Ca^{2+}-буферних молекул і систем виведення, згідно з роботою (Santiago et al., 2010).

Результати розрахунку проілюстровано на рис. 1.7. На рис. 1.7A,a представлена флуоресценція, усереднена по куту φ (як схематично зображено на рис. 1.7A,b), побудована як функція радіальної відстані r і часу з моменту першого виявлення. На рис. 1.7A,c зображено ту саму флуоресценцію в псевдокольорі. Флуоресценція усереднена спочатку за 150 подіями, а потім за полярним кутом, що пояснює майже повну відсутність шуму в результатах.

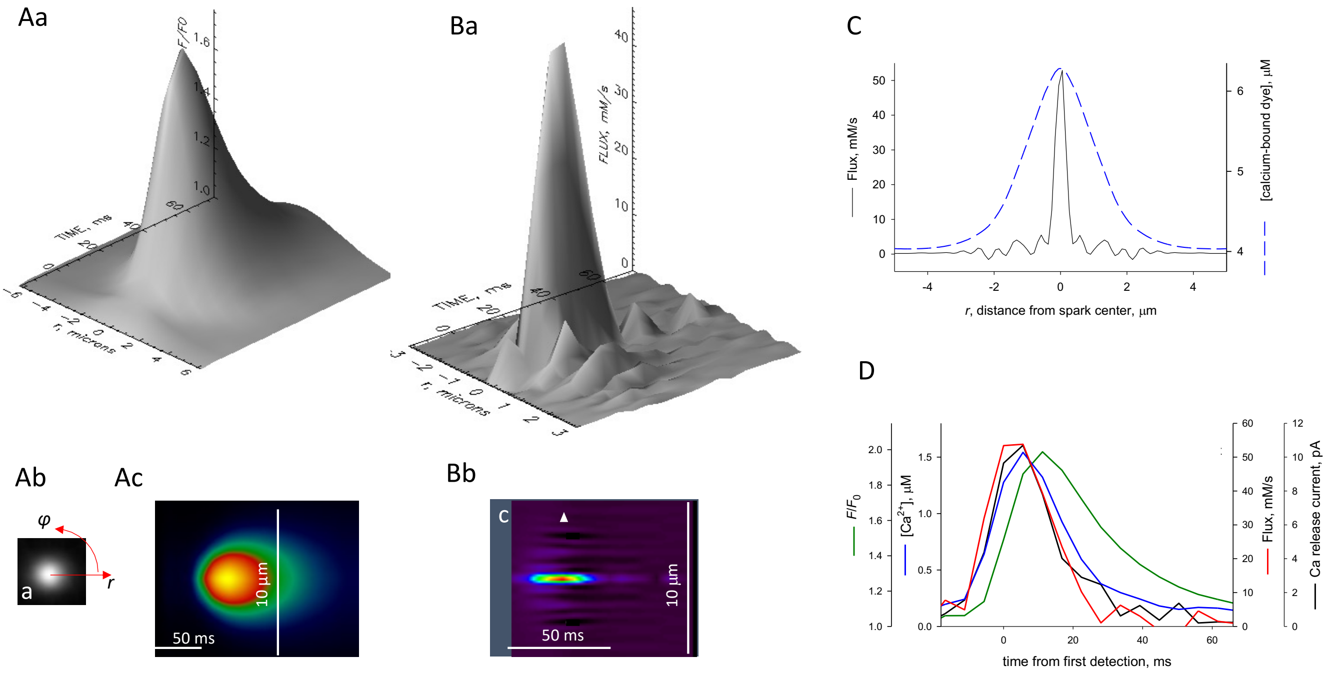

Рисунок 1.7. Потік вивільнення Ca^{2+} спалаху з $T = 11.2$ мс. (Aa) Нормована флуоресценція $F/F_0(r, t)$, отримана шляхом усереднення за полярним кутом φ (як показано на рис. A,b) спалаху з $T = 11.2$ мс (проілюстровано на рис. 1.5C). $F/F_0(r, t)$ представлено в псевдокольорі на рисунку A,c. (B,a) Потік вивільнення, розрахований з $F/F_0(r, t)$, представлений у вигляді поверхні або в псевдокольорі (рис. B,b). (C) Радіальна залежність флуоресценції (і пропорційна їй величина, концентрація Ca^{2+}-зв'язаного Fluo-4; штриховий профіль) в момент піку в порівнянні з розрахованим потоком вивільнення для спалаху з $T = 11.2$ мс. (D) Часовий профіль просторового максимуму флуоресценції (зелений), розрахованого вільного $[Ca^{2+}]$ (синій), потоку вивільнення (червоний) і струму вивільнення (чорний), виміряних для наступних усереднених зображеннях спалахів з $T = 11.2$ мс.

Розрахований потік вивільнення кальцію проілюстровано на рис. 1.7B,a. Просторовий розмір джерела, оцінений на рис. 1.7B,b, є значно меншим порівняно з розмірами флуоресцентної події. Кількісні характеристики потоку наведено на рис. 1.7C та D. На панелі 1.7C представлені радіальні профілі спалаху та розрахованого потоку. Основний потік зосереджено у ділянці діаметром близько 0.5 мкм, що приблизно відповідає просторовій роздільній здатності мікроскопа, що свідчить про менші розміри джерело має розміри менші за цю границю. На панелі 1.7D наведені часові залежності флуоресценції (F/F_0), розрахованої концентрації вільного Ca^{2+} (мкМ) і потоку вивільнення Ca^{2+} (мМ/с) для зазначеного середнього значення спалаху. Піковий потік вивільнення Ca^{2+} було розраховано на рівні 53 мМ/с. Хоча при цій роздільній здатності часові властивості описуються не ідеально, помітно, що пік потоку передує піку вільного [Ca^{2+}] та обидва вони — піку флуоресценції. На графіку представлено струм вивільнення Ca^{2+}, розрахований шляхом інтегрування потоку за об'ємом джерела. Час виникнення струму приблизно співпадає з часом потоку, і його пік досягає приблизно 11 пА. Цей показник пікового струму відповідає верхнім межам діапазону, визначеного для клітин серця (Blatter et al., 1997, Santiago et al., 2010, Izu et al., 2001, Cheng and Wang, 2002, Wang et al., 2004). Такий рівень струму вимагає активності від 20 до 30 каналів, що водночас генерують струми розміром від 0.3 до 0.5 пА (Kettlun et al., 2003). Зазначена тут кількість каналів значно перевищує ту, яка визначалася на основі спостережень квантовоного потоку в спалахах від периферійних куплонів, де $N < 6$; (Wang et al., 2004). Згідно з дослідженням Каннелла і Конга (Cannell and Kong, 2011), складне багатокуплонне джерело могло б пояснити спостереження квантованих спалахів у відповідності з більш високими оцінками числа каналів, зробленими в інших дослідженнях та підтвердженими у даній роботі.

Вперше було запропоновано методику дослідження Ca^{2+} спалахів у місці вивільнення, ґрунтовану на тривимірному конфокальному скануванні флуоресценції. Спалахи, зареєстровані в зоні фокусу, характеризувалися більшими амплітудами порівняно зі загально виявленими спалахами і мали модальний розподіл з піком приблизно ~0.7 нормованої амплітуди. Під час цих спалахів піковий потік вивільнення Ca^{2+} становив 53 мМ/с, а супутній струм був 11 пА, що вимагає залучення каналів із 20-30 ріанодинових рецепторів.

The Journal of General Physiology

Properties of Ca^{2+} sparks revealed by four-dimensional confocal imaging of cardiac muscle

Vyacheslav M. Shkryl, Lothar A. Blatter, and Eduardo Ríos

Department of Molecular Biophysics and Physiology, Section of Cellular Signaling, Rush University, Chicago, IL 60612

Parameters (amplitude, width, kinetics) of Ca^{2+} sparks imaged confocally are affected by errors when the spark source is not in focus. To identify sparks that were in focus, we used fast scanning (LSM 5 LIVE; Carl Zeiss) combined with fast piezoelectric focusing to acquire *x–y* images in three planes at 1-µm separation (*x-y-z-t* mode). In 3,000 *x–y* scans in each of 34 membrane-permeabilized cat atrial cardiomyocytes, 6,906 sparks were detected. 767 sparks were in focus. They had greater amplitude, but their spatial width and rise time were similar compared with all sparks recorded. Their distribution of amplitudes had a mode at $\Delta F/F_0 = 0.7$. The Ca^{2+} release current underlying in-focus sparks was 11 pA, requiring 20 to 30 open channels, a number at the high end of earlier estimates. Spark frequency was greater than in earlier imaging studies of permeabilized ventricular cells, suggesting a greater susceptibility to excitation, which could have functional relevance for atrial cells. Ca^{2+} release flux peaked earlier than the time of peak fluorescence and then decayed, consistent with significant sarcoplasmic reticulum (SR) depletion. The evolution of fluorescence and release flux were strikingly similar for in-focus sparks of different rise time (T). Spark termination involves both depletion of Ca^{2+} in the SR and channel closure, which may be synchronized by depletion. The observation of similar flux in sparks of different T requires either that channel closure and other termination processes be independent of the determinants of flux (including $[Ca^{2+}]_{SR}$) or that different channel clusters respond to $[Ca^{2+}]_{SR}$ with different sensitivity.

INTRODUCTION

In striated muscles, action potentials cause intracellular Ca^{2+} channels to open, and the ensuing Ca^{2+} release initiates contraction. In cardiac muscle and in skeletal muscle of some taxonomic classes, Ca^{2+} release is composed of discrete events from SR Ca^{2+} channels (RyRs) of fairly stereotypical appearance, which have been visualized with confocal fluorescence microscopy and fluorescent Ca^{2+}-sensitive dyes, and termed "Ca^{2+} sparks" (Cheng et al., 1993; Nelson et al., 1995; Tsugorka et al., 1995). Ca^{2+} sparks are a collective phenomenon produced by a group of mutually interacting RyR channels within a couplon (Stern et al., 1997, 1999), defined as the release channels in a cluster or Ca^{2+} release unit (Franzini-Armstrong and Jorgensen, 1994) together with its associated L-type Ca^{2+} channels and/or voltage sensors. Ca^{2+} sparks occur in ventricular (Niggli and Shirokova, 2007) as well as in atrial myocytes (e.g., Blatter et al., 1997; Kockskämper et al., 2001; Sheehan et al., 2006). In ventricular myocytes, the well-developed 3-D network of transverse (t) tubules (Soeller and Cannell, 1999) ensures that in response to an action potential, all couplons are activated synchronously, which results in a highly uniform Ca^{2+} release throughout the entire cell volume (Cheng et al., 1994). In contrast, in atrial myocytes, the t-tubular network is poorly developed or entirely absent (Hüser et al., 1996; Cordeiro et al., 2001; Mackenzie et al., 2001), and close apposition of surface membrane Ca^{2+} channels and RyRs only exists in the cell periphery. The SR, however, extends throughout the entire cell and contains RyRs capable of Ca^{2+} release and generation of Ca^{2+} sparks (Sheehan et al., 2006). Although sparks appear to require the phenomenon of CICR (Endo et al., 1970; Fabiato and Fabiato, 1978; Cheng et al., 1993; Klein et al., 1996) for both initiation and propagation within the channel cluster, many other mechanistic details of these events remain unknown or poorly understood. Thus, numbers of channels involved, time course of their unitary current, duration of opening of the individual channels within a couplon, the mechanisms underlying their closure, the degree of local intra-SR depletion, and even the behavior of channels and currents at the time when the spark peaks have remained uncertain or are just starting to be elucidated.

Many of these unknowns could be eliminated by an accurate quantification of sparks, in terms of their so-called morphometric parameters. These include peak amplitude, spatial width (or full width at half maximum

---

Correspondence to Eduardo Ríos: erios@rush.edu

V.M. Shkryl's present address is Dept. of General Physiology of the Nervous System, A.A. Bogomoletz Institute of Physiology, 01024 Kiev, Ukraine.

Abbreviations used in this paper: DHPR, dihydropyridine receptor; ecc, excitation–contraction coupling; FWHM, full width at half maximum; nj-SR, nonjunctional SR.

The Rockefeller University Press $30.00
J. Gen. Physiol. Vol. 139 No. 3 189–207
www.jgp.org/cgi/doi/10.1085/jgp.201110709

[FWHM]), rise time, decay time constant and other measures of duration, and integral evaluations of intensity or signal mass (ZhuGe et al., 2000; Chandler et al., 2003). For instance, the local amplitude of the change in [Ca^{2+}] together with knowledge of the unitary channel current will provide an indication of the number of channels open. Similar insights will be derived from the accurate knowledge of spatial width. In this regard, a combination of modeling and experimental testing have shown that spatial width of sparks grows with the time that the release channels remain open (Zhou et al., 2003), but widths that reach values beyond certain limits at early times, for example in "protoplatykurtic" sparks (Zhou et al., 2005), reflect spatially large sources rather than small groups of channels. Finally, detailed knowledge of spatial aspects of sparks and their evolution in time can be used to reconstruct the underlying release current by different methods that yield mutually consistent results (see Ríos et al., 1999, and Soeller and Cannell, 2002, for alternative methods, named "backward" and "forward" to distinguish whether the effect [the change in [Ca^{2+}]] or the cause [the release current] is the starting point of the calculation). An accurate morphometry of sparks is therefore essential for the elucidation of their control mechanisms.

Crucial determinants of control of Ca^{2+} sparks are believed to depend on cytosolic Ca^{2+} itself, including complementary mechanisms of activation (CICR) and inactivation (Ca^{2+}-dependent inactivation; Sham et al., 1998, for cardiac; Baylor et al., 1983, and Melzer et al., 1984, for skeletal). These result in channels that do not open or close independently but gate concertedly. Whether or not channels gate independently changes another morphometric property, the distribution of spark amplitudes, which will be a sum of decaying exponential functions of amplitude if arising from openings of individual channels that are mutually independent (and are "Markovian" or memoryless, e.g., Colquhoun and Hawkes, 1983; see also http://en.wikipedia.org/wiki/Markov_process for a brief definition), but will typically have a mode or preferred amplitude if channels gate concertedly (Bridge et al., 1999; Cannell and Soeller, 1999; Ríos et al., 2001; Wang et al., 2002). For instance, it has been argued that the rise time characteristics are incompatible with the idea that a spark arises from a single RyR channel with a reversible Markovian gating scheme (Shirokova et al., 1999; Ríos et al., 2001; Wang et al., 2002). On the other hand the spark amplitude experimentally recorded in line-scan mode always obeys a monotonically decaying distribution, regardless of the true spark amplitude (Cheng et al., 1999; Ríos et al., 2001).

A major obstacle to reaching the desired accuracy in measures of spark parameters is that measurements are done on confocal images, including line scans (x–t, herein called 2-D) and x–y scans (referred to as 3-D imaging). In either case, sparks are imaged without knowledge of the location of its originating couplon relative to the line or plane of scanning. Starting with the work of Pratusevich and Balke (1996), it has become increasingly clear that all morphometric spark parameters are affected by the out-of-focus error. Out-of-focus errors include reduced amplitude, increased spatial spreading, and slower kinetics. Among the parameters, amplitude is most affected, decaying sharply with distance from source to scanning line or plane, whereas rise time and FWHM are less distorted (Pratusevich and Balke, 1996; Smith et al., 1998). It is because of this susceptibility to focus error that the distribution of amplitudes of sparks detected in line scans must be monotonously decreasing.

Theoretical approaches have been developed to recover the true spark amplitude, allowing quantitative corrections of spark amplitudes as if all sparks would have been in focus (Shirokova and Ríos, 1997; Izu et al., 1998; Ríos et al., 2001). Specifically Ríos et al. (2001) provide an equation to derive the distribution of true amplitudes from the distribution histogram of measured amplitudes.

Although these procedures have value, as they demonstrated, for example, a mode in the distribution of true amplitudes, consistent with expectations for groups of nonindependent channels, the correction formula has not been verified. Moreover, it requires knowledge of other parameters, which are also affected by the out-of-focus error and therefore are not knowable with certainty.

Here, we take advantage of two novel tools, the fast x–y scanning provided by a slit confocal scanner (LSM 5 LIVE; Carl Zeiss) and the ability to move the plane of focus vertically in rapid and reproducible manner to achieve x-y-z-t (or 4-D) imaging of sparks. 4-D scanning eliminates the out-of-focus error because it allows identification of sparks that are imaged in focus. In this way, we characterize morphometrically a large group of sparks in focus. We use these, for the first time well-determined measures, to both clarify aspects of control of Ca^{2+} release and produce a strict test of the theory of scanning in lower dimensions.

Part of this work has been presented in abstract form (Shkryl, V.M., and L.A. Blatter. 2008. Biophysical Society 52nd Annual Meeting. Abstr. 495; Shkryl, V.M., and L.A. Blatter. 2009. Biophysical Society 53rd Annual Meeting. Abstr. 1415; Shkryl et al. 2011. Biophysical Society 55th Annual Meeting. Abstr. 3032).

MATERIALS AND METHODS

Cell isolation and solutions

Single myocytes were isolated from cat atria as described previously (Wu et al., 1991; Kockskämper and Blatter, 2002; Sheehan and Blatter, 2003). The procedure for cell isolation was fully approved by the Institutional Animal Care and Use Committee. In brief, adult mongrel cats of either sex were anesthetized with sodium pentobarbital (50 mg kg^{-1}). After thoracotomy, hearts were quickly excised, mounted on a Langendorff apparatus, and retrogradely perfused with oxygenated collagenase–containing solution at 37°C. Myocytes were used 1–6 h after isolation. Freshly isolated myocytes were plated on glass coverslips in normal Tyrode's solution (composition in mM: 135 NaCl, 4 KCl, 2 $CaCl_2$, 1 $MgCl_2$, 10 D-glucose, and 10 HEPES, with pH adjusted to 7.4 with NaOH).

Imaging of Ca^{2+} sparks was performed in cells permeabilized with saponin (0.005%) for 40 s (Zima et al., 2003) in an internal solution composed of (in mM): 120 potassium aspartate, 15 KCl, 5 KH_2PO_4, 5 MgATP, 0.35 EGTA, 0.14 $CaCl_2$, 0.75 $MgCl_2$, 10 phosphocreatine sodium salt, 4% dextran, and 10 HEPES, with pH adjusted to 7.2 with KOH. Subsequently, the bath solution was exchanged to a saponin-free internal solution containing 40 µM fluo-4 pentapotassium salt (Invitrogen). The free [Ca^{2+}] and [Mg^{2+}] of this solution were 100 nM and 1 mM, respectively. All experiments were performed at room temperature (22–24°C). Chemicals were purchased from Sigma-Aldrich.

Fluo-4 was excited at 488 nm, and emission was collected at >520 nm. The cell was positioned with its long axis parallel to the *x* scanning direction (which in slit scanners is acquired simultaneously at all points of a 512-pixel line).

4-D confocal image acquisition and multidimensional analysis of sparks

Fluorescence image acquisition was performed on a slit scanning confocal microscope (LSM 5 LIVE; Carl Zeiss) equipped with a 63×, 1.20 n.a. water-immersion objective (C-Apochromat; Carl Zeiss) and a piezoelectric focusing attachment, which by moving the objective allowed us to collect three *x–y* images (512 × 31 pixels; pixel distance of 0.42 µm) in succession, separated by 1 µm in the vertical (*z*) direction. The point-spread function of the system with the focusing attachment had FWHM values of 0.52, 0.46, and 1.25 µm, respectively, in the *x*, *y*, and *z* directions. The scan time for an individual image was 1.16 ms (line dwell time of 15.7 µs), and the acquisition time for one trio of images was 5.6 ms (Fig. 1 A; note that the acquisition time for a trio is longer than the sum of scan times for three images because of the time required for scanner fly back and movement of the piezoelectric focusing attachment). A total of 1,000 trios, or 3,000 *x–y* images, were acquired for each cell at the same location. To refer to such series of images we will use interchangeably the terms "*x-y-z-t* series" and "4-D series." We will refer to series at a single *z* position as "*x-y-t*" or "3-D series." Similarly, "*x–t* series" will be also called "2-D" or line scans.

Images in 4-D and 3-D series were normalized to resting fluorescence by a procedure in which individual images $F(x,y)$ are divided pixel by pixel by a normalizing image $F_0(x,y)$ constructed by averaging every image with spark regions blanked. The set of blanked images was also used to compute a bleaching correction function (see Brum et al., 2000, for details).

Sparks were detected automatically in normalized, bleach-corrected *x-y-t* series using the algorithm developed by Brum et al. (2000), which is an adaptation to 3-D scans of the procedure introduced for line scans (Cheng et al., 1999). The procedure identifies the location coordinates of the center of mass of each spark, a maximum of $\Delta F/F_0$ (where $\Delta F = F - F_0$) in each image, a subseries of consecutive images recognized as corresponding to the same spark and a peak of the maximum of $\Delta F/F_0$ within the subseries, which we refer to as peak amplitude or just amplitude (*a*). The analysis also produced for each spark a time of first detection, an interval between first detection and the attainment of peak amplitude (rise time, *T*), plus several measures of the spatial properties, including width in *x* and *y*, and eccentricity.

For this study, we specifically developed a definition and automatic determination of FWHM. We defined FWHM as the diameter of a circle having the same area as the 2-D intercept of the spark at the time of peak amplitude and the plane located at half this amplitude (i.e., the *x–y* region where $\Delta F/F_0$ was less than half-amplitude). At every point in time during its evolution, the spark fluorescence is a function of *x* and *y* that resembles a bivariate Gaussian (examples in Fig. 1 A). An alternative set of parameters was derived by fitting to every spark in every image a bivariate Gaussian function. Parameters of fit included two coordinates of the center, an amplitude, and elliptic semi-axes (a and b). In this description, the FWHM is equal to the geometric mean ($(2a \times 2b)^{1/2}$) of the two elliptic axes. Both definitions of parameters yielded essentially identical results.

Other numerical routines were used to produce subsets of the 4-D database, including 3-D (*x-y-t*) series at constant *z* and 2-D (*x–t*) series at constant *z* and *y*. In turn, these simpler subsets were analyzed for event detection and flux calculation by programs

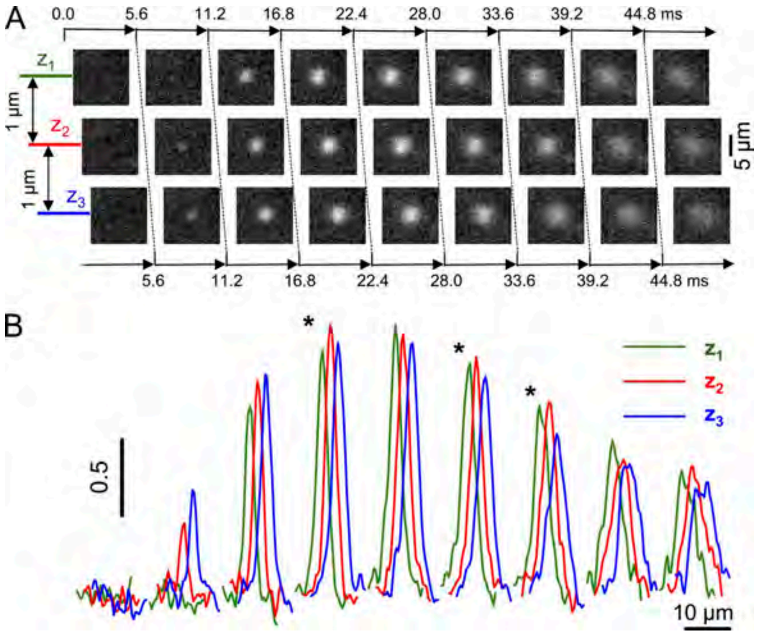

Figure 1. Scanning in three dimensions of space and time. (A) Square sections of successive *x–y* scan images of fluorescence of an atrial cardiomyocyte. As illustrated in the diagram, the vertical positions correspond to the *z* positions of three scanned planes ($z_1 = -1$ µm, $z_2 = 0$ µm, and $z_3 = +1$ µm). As indicated by the horizontal arrows, the acquisition time for a trio of *x–y* scans was 5.6 ms. (B) Profiles ($\Delta F(x)/F_0(x)$) at the central y value of the images in A, color-coded to *z* value. Asterisks mark image trios where the amplitude was largest in z_2. The example spark appears to be in focus.

developed earlier (Cheng et al., 1999; Brum et al., 2000). All of the numerics were implemented in the IDL programming environment (ITT Visual Information Solutions).

Methods to decide whether a spark is in focus

A spark that appears to be in focus is illustrated in Fig. 1. In Fig. 1 B, fluorescence intensity profiles (2 pixels wide) of intensity traced through the centers of the sparks, of which all correspond to the same location in successive images (Fig. 1 A), are shown. It can be seen that in several trios of images, the peaks of fluorescence in the z_2 plane are greater (asterisks) than in the z_1 and z_3 planes. This spark therefore satisfies the simplest criterion for being in focus, namely, that its amplitude be greatest in the central plane, z_2. This simple criterion, however, failed for several reasons. It is strongly biased toward acceptance of sparks of narrow width and is susceptible to limitations in scanning speed, limitations that will become clearer when describing Fig. 5. After testing several other procedures, we opted for a "three-point criterion," so named because it uses asymmetrically all three measures of amplitude, from all three focal planes (z_1, z_2, and z_3). The criterion, which is described in the Appendix, allows defining the 2-D vertical thickness of the slice where the sparks must originate to be considered in focus. All sparks deemed to be in focus in this study were identified by this criterion, with $2D = 0.2$ µm.

Reconstruction of line-scan images from 3-D scans

One of the aims of this work is to compare the properties of sparks imaged in focus with those inferred from images obtained in line-scan mode, which include sparks that may or may not be in focus. For this purpose, we derived from the database of 4-D series a set of images equivalent to line scans. The extraction of such reconstructed line scans is illustrated with Fig. 4 A.

For each image at a single value of z ($z_2 = 0$ µm), a line was extracted, namely the group of 512 values $F(x_j, y_n, z_2)$ at a set value of y ($y_n = 6$ µm, the approximate center of the range of y values), with j varying from 1 to 512. The lines extracted at the same y and z values in 1,000 successive images constitute together a 2-D series $F(x_j, t_k)$, the reconstructed line-scan image (with k varying from 1 to 1,000). One such line scan is represented in Fig. 4 A. The interval between sets of x-y-z scans (or the interval between x–y trios) was 5.6 ms, which is then the temporal increment of the line scan.

RESULTS

Cat atrial myocytes, which are devoid of a t-tubular system (Hüser et al., 1996), are known to generate spontaneous Ca^{2+} sparks from RyR clusters located in the nonjunctional SR (nj-SR) membranes (Sheehan et al., 2006). Thus, atrial Ca^{2+} sparks from nj-SR result entirely from SR Ca^{2+} release and lack any potential component from Ca^{2+} influx. We studied Ca^{2+} spark properties in these cells using a fast slit confocal scanner (cf. Toomre and Pawley, 2006, for brief description) in combination with a fast piezoelectric focusing attachment to acquire confocal x–y images successively in three vertical planes, at 1-µm separation. The imaging process, which we call 4-D scanning, is illustrated in Fig. 1 (see Table 1 for a list of terms and symbol definitions). Fig. 1 A includes a series of images from an atrial cardiomyocyte (with plasma membrane permeabilized and in a solution containing fluo-4). Square regions from the successive images are shown, including a spark that appears to be in focus. The relative position in the figure of each square image in the horizontal direction suggests the time at which it was acquired, whereas the vertical positions in the figure correspond to the three z positions of the scanned planes ($z_1 = -1$ µm, $z_2 = 0$ µm, and $z_3 = +1$ µm). Fig. 1 B plots the central profiles ($\Delta F(x)/F_0(x)$, where x corresponds to the longitudinal axis of the cell) through every frame, color-coded to z position.

The example spark shown in Fig. 1 appears to be in focus because it is somewhat more intense in the central (z_2) plane of scanning (asterisks in B mark image trios where the amplitude was largest in z_2). As stated in Materials and methods, the simple criterion that an in-focus spark would be detected with greater amplitude in the central plane led to biased results. Therefore, the three-point criterion (cf. Appendix), which is also satisfied by this example, was used to identify in-focus sparks. In the following sections, we will explore the properties of sparks in focus and compare them with those of all detected sparks.

Properties of in-focus sparks

An algorithm of automatic detection developed for x–y images (Brum et al., 2000) was applied to 34,000 x-y-z scans (i.e., trios of x–y images at three z values) obtained from 34 cells at 1,000 x-y-z (or 3,000 x–y) scans per cell. In these, 6,906 sparks were detected, of which 767 were found to be in focus by the three-point criterion.

The histograms of amplitudes (defined as a = peak $\Delta F/F_0$) of the two groups are represented in Fig. 2 A. Note that the histogram of all sparks detected (Fig. 2 A,

TABLE 1

List of symbols

Symbol	Description
$x, y, z,$	Spatial coordinates (x, horizontal, axial; y, transverse; z, vertical)
r, φ	Polar spatial coordinates (radial and angle)
$F, F_0, F/F_0, \Delta F/F_0$	Fluorescence, initial, normalized, increase
a, FWHM, T	Spark amplitude, FWHM, rise time
$g(a), l(a), u(a)$	Probability density of the distributions of amplitude (in focus, 3-D, 2-D)
$G(a), L(a), U(a)$	Histograms, sampling of the distributions $g(a)$, $l(a)$, $u(a)$
$h(z,\sigma)$	Gaussian function of vertical coordinate z with standard error σ
ζ	Vertical separation of spark source and focal plane
δ	Normalized difference in fluorescence (defined by Eq. 1)
$C3$	"Three-point criterion" (limit value of δ for sparks in focus)
D	Half depth of slice in focus, µm
ρ	Pearson's linear correlation coefficient
$[Ca^{2+}]$, $[Ca^{2+}]_{cyto}$, $[Ca^{2+}]_{SR}$	Free Ca^{2+} concentration, in cytosol, in SR
N, P_o, i	Number of channels, channel open probability, unitary current

dashed black line), referred to as $L(a)$, is monotonically decreasing, except for a region of the domain at low values of a (<0.4), where detection fails. In contrast, the histogram of in-focus spark amplitudes (Fig. 2 A, $G(a)$, solid green trace) features a mode at about $a = 0.7$. The implications of the distribution of amplitudes of sparks in focus will be fully considered in Discussion.

In Fig. 2 B, we compared in the same way as in Fig. 2 A the spatial width (FWHM) of detected sparks. In this case, the differences between the values reported for in-focus sparks and those of all detected sparks were much smaller; both distributions spread asymmetrically around a mode, close to 2.6 µm, but the distribution of in-focus sparks was slightly narrower. Clearly, the measurement of spatial width is much less compromised by out-of-focus error than that of spark amplitude.

In Fig. 2 C, histograms of rise time T (from the time of first detection to that of peak amplitude) are shown. T was measured always in the central plane (z_2). This resulted in a temporal resolution of 5.6 ms per image and consequently a coarse distribution. It is also necessary to point out that rise time here is defined as starting from the frame of first detection. This definition underestimates the true rise time and will warrant a reinterpretation of measured times (compare below).

These cells produced on average rather wide sparks of moderate amplitude. Averages of these parameters are listed in Table 2 for the 4-D, 3-D, and 2-D datasets.

The newly found method to identify sparks in focus obviously allows for a variety of other studies. Wang et al. (2004) found a quantized distribution of the rates of rise of fluorescence, indicative of quantized levels of flux, in sparks of peripheral couplons located in focus by activation of ventricular myocytes via loose patch clamp. To compare, and even though the present imaging was done at a much coarser temporal and spatial resolution, we computed initial rates of rise of fluorescence (rate of rise in a 5.6-ms interval from first detection) for individual sparks in the in-focus group. The values had a broad distribution between 0.01 and 0.12 ms^{-1}. There was no evidence of quantization.

Morphometric parameters of in-focus sparks are weakly correlated

In addition to the morphometric parameter values, other properties of sparks with interesting mechanistic implications are the correlations among these parameters. The correlations found in published studies have been poor for sparks of both skeletal and cardiac muscle cells. For example, linear correlation coefficients (Pearson's ρ) between rise time and amplitude of 0.09 and 0.12 were found in two studies of frog skeletal muscle (Ríos et al., 1999, 2008). In cardiac myocytes, correlations between amplitude, rise time, and width revealed ρ values between 0.07 and 0.17 (Shen et al., 2004).

A chief factor determining the poor correlations is the contribution to the variance in amplitude by the out-of-focus error (i.e., the absence of knowledge of the separation ζ between scanned line and spark source), which amounts to between 80 and 90% of the total variance (Ríos et al., 2008). The newly found ability to identify sparks in focus should remove the uncertainty of location, therefore reducing the out-of-focus contribution

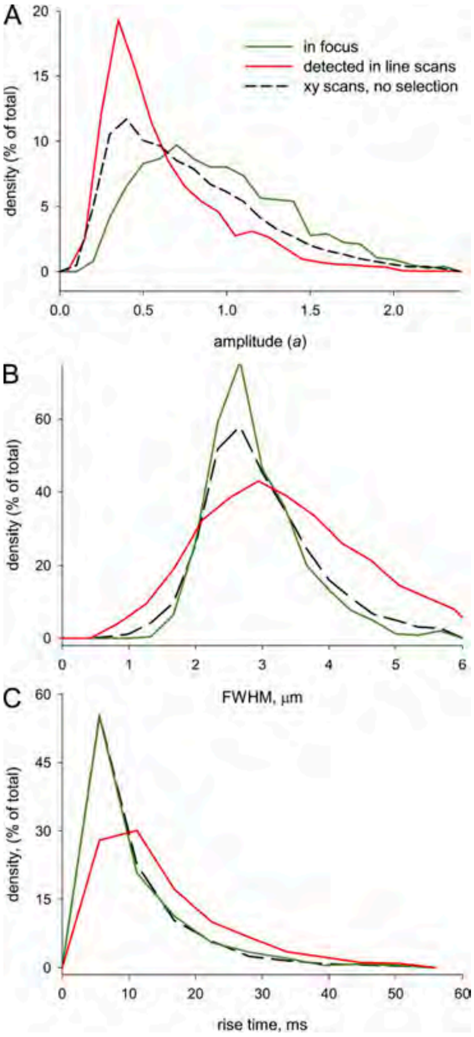

Figure 2. Properties of sparks in focus. Histograms of amplitudes (A), FWHM (B), and rise time (C) for all sparks detected in *x–y* scans (black, dashed), sparks in focus (green), and sparks detected in reconstructed line scans (red). Note that the amplitude histograms differ greatly among the three groups of sparks, but the other distributions diverge less. In-focus sparks have greater amplitudes and a mode in the distribution of this variable. Their modal width is not very different than that of the other groups, and their rise times are nearly identical to those of the entire set of detected sparks. The distribution of amplitudes measured in reconstructed line scans is heavily biased toward low values, whereas those of widths and rise times are more disperse than the corresponding ones in *x–y* scans. Relevant parameters of these distributions are listed in Table 2.

TABLE 2

Average morphometric parameters of sparks in various dimensions

Mode	Amplitude	Rise time	FWHM	N sparks
		ms	*μm*	
4-D	1.05	13.5	3.35	767
In-focus	(0.01)	(0.24)	(0.02)	
3-D	0.82	10.7	3.18	6,906
	(0.005)	(0.10)	(0.01)	
2-D	0.61	17.4	3.85	2,910
	(0.007)	(0.22)	(0.03)	

The SEM is in parentheses. The row with heading "4-D In focus" lists values for sparks detected in *x-y-z-t* series, the 4-D mode, which satisfy the in-focus criterion. *x-y-z-t* series were obtained from 34 cells; each series consists of 1,000 trios of *x–y* images successively at three *z* positions, for a total of 3,000 images per series. The row with heading "3-D" includes all sparks detected in *x-y-t* series at the z_2 position ($z = 0$), whether or not they were in focus. "2-D" refers to sparks detected in line-scan images constructed from the *x-y-t* series at position z_2 as described in Materials and methods. Fig. 4 has an example line-scan image constructed this way. It should be noted that the three modes (4-D, 3-D, and 2-D) are just different ways to analyze the full 4-D database.

to the variance in amplitude, and thus provide a better gauge of existing correlations.

The correlations among the parameters amplitude, rise time, and FWHM are illustrated by joint histograms in Fig. 3. The left-side panels represent the histograms of all sparks (3-D mode), whereas the corresponding histograms of events in focus are on the right side. Positive correlations were found in every case and were usually modest. Amplitude and width had ρ = 0.04 for all sparks and 0.14 for those in focus. For rise time and width, ρ increased from 0.14 to 0.26 in going from all sparks to those in focus, whereas for rise time and amplitude, ρ increased from 0.33 to 0.36. In sum, correlations between all three morphometric parameters were

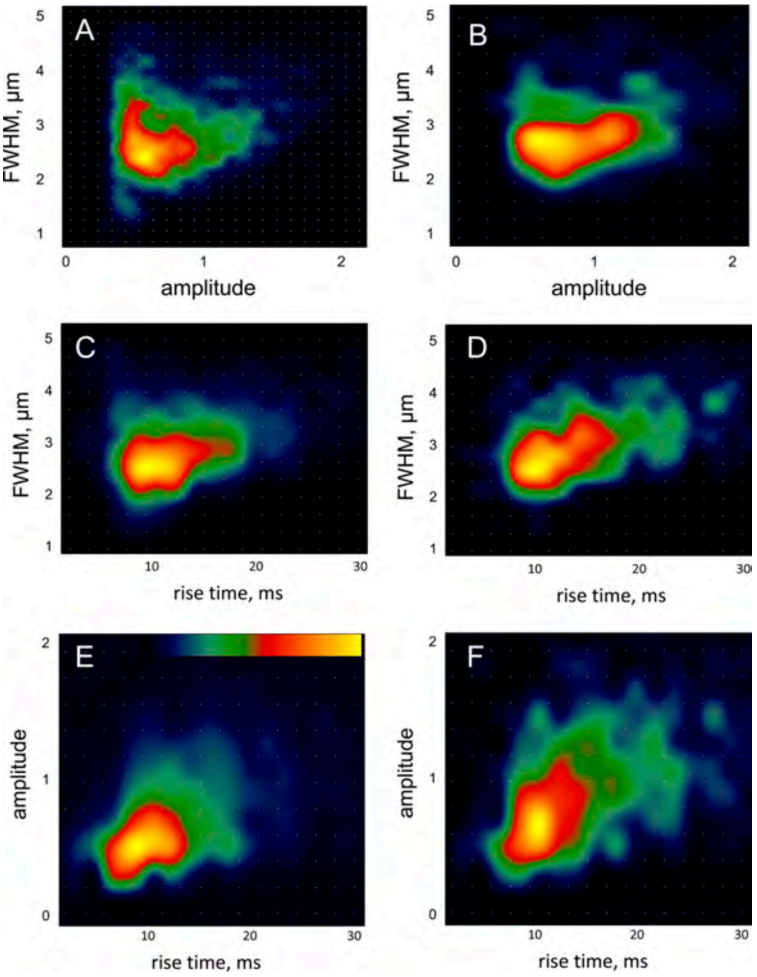

Figure 3. Correlations between spark parameters. Joint histograms of amplitude and width (A and B), rise time and width (C and D), and rise time and amplitude (E and F) for the set of all sparks detected in *x–y* images (A, C, and E) and for in-focus sparks (B, D, and F). The total number of sparks included was 6,906 (all sparks) and 767 (in-focus sparks). The first-order correlation coefficient ρ (a, FWHM) was 0.037 for all sparks and 0.14 for sparks in focus. ρ (T, FWHM) was 0.14 (all) and 0.26 (in focus). ρ (T, a) was 0.33 (all) and 0.36 (in focus). The color table starts at 0 (black) for all panels, whereas the maximum (yellow) corresponds to 143, 35, 201, 85, 149, and 70 events, respectively, for A–F.

positive and modest, and all of them increased for sparks in focus. The strongest positive correlation was found between rise time and amplitude. The issue of correlations will be encountered again when considering properties of averages of sparks.

The most relevant advantage of identifying sparks in focus is that the local Ca^{2+} transient, determined with minimal error, can then be used to derive the underlying flux of Ca^{2+} release. This will be done in the Discussion section.

The morphometric properties of sparks in line-scan images

It seemed interesting to compare the presumably true properties of sparks revealed by the present technique with those found using the line-scan (or 2-D) mode, which is still the standard of spark acquisition. A set of images equivalent to line scans was derived from the database of *x-y-z-t* series as described in Materials and methods and analyzed to derive their morphometric parameters in the standard way. One reconstructed line scan is shown in Fig. 4 A. A total of 2,910 sparks in 2-D were derived from the 4-D database. The number is less than in the *x-y-t* or 3-D case (6,906) because the method used one line per *x–y* image at a fixed *z* value and therefore missed a substantial portion of the images, resulting in fewer identified sparks. From these numbers, and considering that the length of scanning inside cells was on average 117 µm, a frequency of events can be calculated as $f = 2{,}910 \times (117\ \mu m)^{-1} \times (5.6\ s)^{-1} \times (34\ cells)^{-1} \times 100 = 13.1\ events \times s^{-1} \times (100\ \mu m)^{-1}$.

The histograms of amplitude, rise time, and spatial width of this group are represented in red traces in Fig. 2. The histogram of amplitude (referred to as $U(a)$) decays monotonically (except in a region of low amplitude, $a < 0.4$, where density increases as a result of increased detectability) and with positive curvature, in agreement with expectations from the theory of line-scan imaging (Ríos et al., 2001, and Discussion). The histogram of FWHM is broader for the 2-D case (Fig. 2 B, red), but other properties (like mode and skewness) are robustly conserved in all dimensional approaches (i.e., 2-, 3-, and 4-D). A similar broadening occurs with the histogram of rise times (Fig. 2 C).

DISCUSSION

This work evaluates quantitatively the properties of sparks imaged in focus, based on the availability of a fast confocal scanner, which combined with a rapid change-of-focus mechanism allows for actual scanning in three spatial dimensions. This mode of scanning can be repeated at a rate sufficient to characterize the evolution of sparks in space and time.

4-D scanning can be used to define sparks in focus

The identification of in-focus sparks reliably and reproducibly hinges critically on a robust criterion for the identification of the optical plane from where the sparks originate. Several approaches have been proposed. Sparks elicited by sparklets, the highly localized Ca^{2+} signal originating from Ca^{2+} entry through voltage-gated Ca^{2+} channels in the cell membrane near a patch electrode, are considered to be in focus (Wang et al., 2001, 2004), whereas the simultaneous recording of cytosolic sparks and the corresponding intra-SR Ca^{2+} depletion signal (termed Ca^{2+} blinks; Brochet et al., 2005) is an objective

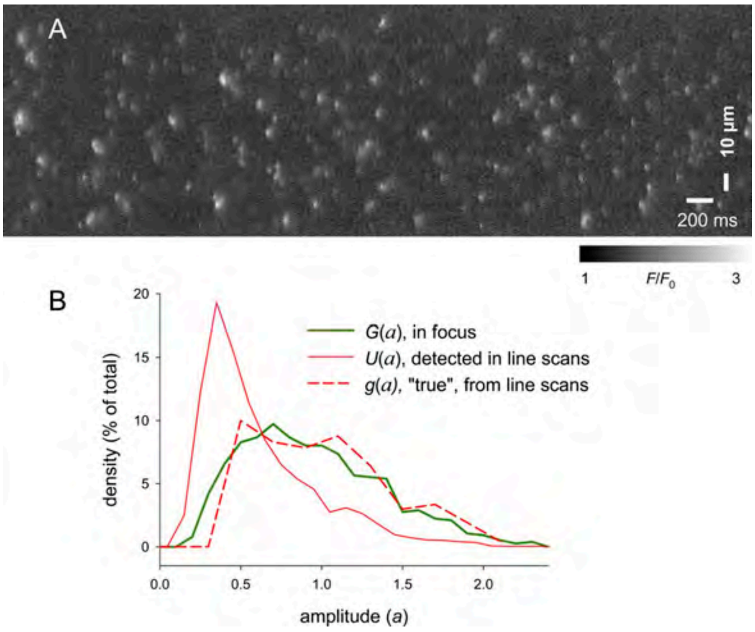

Figure 4. Properties of in-focus sparks derived from line-scan images. (A) Line-scan image reconstructed from 1,000 trios of *x–y* images obtained successively, at 5.6-ms intervals, from the same cell. The image is formed by one line of pixels taken from the central (z_2) image of every trio, at 512 values of *x* and one value of *y* ($y = 6$ µm). Size of image was reduced (from 512 × 1,000 to 298 × 1,000) by eliminating pixels corresponding to *x* values outside the cell boundary. Lines are placed vertically in the figure and stacked from left to right. One reconstructed line scan was derived for each of 34 cells studied. (B) Red solid trace, $U(a)$: histogram of amplitudes of 2,910 sparks detected by the conventional algorithm from all 34 reconstructed line scans. This plot is also in Fig. 2 A. Dashed trace, $g(a)$: distribution of "true" amplitudes derived substituting $U(a)$ for $u(a)$ in Eq. 1. Green trace, $G(a)$: amplitude histogram of sparks in focus, reproduced from Fig. 2 A.

criterion that circumscribes the location to the smaller volume where the blink signal can be detected (Zima et al., 2008a,b, 2010). Here, we demonstrate a novel approach, which relies on the near-simultaneous imaging of Ca^{2+} sparks in multiple planes and a robust criterion to determine where the spark originates.

In principle, a straightforward criterion for deciding whether sparks are in focus would be a fluorescence signal greatest in the central (z_2) plane. This criterion was not useful for several reasons. It was biased toward the detection of narrow sparks, and it did not take into consideration the fact that spark amplitude changes during the time it takes to acquire one x-y-z stack. Another limitation is that the criterion, consisting in simply comparing pairwise the amplitudes at z_2 and the other two planes, does not use all the information available. An alternative approach was based on the realization that separation from the focal plane, in either direction, resulted in asymmetric and predictable changes in the measurements at z_1, z_2, and z_3. In other words, if the center of a spark moves away from the central plane, the measured amplitude at the central plane decreases, but the other two measures, at z_1 and z_3, change in opposite directions. These simple considerations, together with the fact that sparks are extremely well described by Gaussian functions of space, were combined in the three-point criterion (Fig. A1 in Appendix). The criterion had the additional advantage of an adjustable stringency associated with a measure of the depth of the volume where events would be identified as being in focus.

In principle, it is not possible to know whether or not a selection process works correctly. This is simply because there is no known comparable population of in-focus sparks. We used instead two properties expected of a good selection. One is that the quantitative properties of the group of sparks classified as in focus should converge as the criterion is applied with increasing stringency (Appendix, Fig. A2). Additionally, the limiting properties to which sparks converge should be consistent with predictions made by the theory of line scanning (Shirokova and Ríos, 1997; Izu et al., 1998; Cheng et al., 1999; Ríos et al., 2001). Reliance on this theory seems justified, as some of its predictions have been quantitatively confirmed with simulations (Ríos et al., 2008), whereas others are consistent with sparks observed under special conditions, which assure their being in focus (Bridge et al., 1999; Soeller and Cannell, 2002, 2004; Wang et al., 2002, 2004).

As illustrated in Fig. A2, we found convergence of the histogram of amplitudes as stringency increased (within the limitations of the test). Specifically, the distribution of amplitudes lost density at low amplitudes and increased it at higher amplitudes, as predicted by the theory. There were no major changes in rise time and spatial width, other than a slight narrowing of the distribution of spatial widths, again consistent with expectations for sparks in focus. In increasingly stringent applications of the selection procedure, we also found convergence of width and rise time. In the next subsection, we evaluate quantitatively the agreement between observations and predictions by the theory of line scanning.

In-focus sparks have a preferred amplitude

A meaningful characteristic of sparks imaged in focus is a histogram of amplitudes $G(a)$ with a modal value (Fig. 2 A). This is in sharp contrast with the distribution of amplitudes reported by line or 2-D scanning. First, note here the distinction between $U(a)$, the histogram of amplitudes reported by line scanning, and $u(a)$, the distribution that such a histogram samples. $U(a)$ could be found in the present work, for the same group of images, as the histogram of amplitudes of the sparks found by applying our automatic detector to line scans reconstructed from sequences of x–y frames at z_2. The reconstructed line-scan images are illustrated in Fig. 4 A, and the $U(a)$ of such line scans is in Fig. 2 A (red trace). According to the theory of line scanning, $u(a)$ is a monotonically decaying function. $U(a)$ is consistent with the expectation, except for a rise explained by missed events at very low values of a.

Ríos et al. (2001) provide an equation,

$$g(a) = -\frac{1}{2\pi\sigma^2}\frac{d\left(a \cdot u(a)\right)}{da}, \tag{1}$$

to derive the distribution of true spark amplitudes $g(a)$ from $u(a)$. In Fig. 4 B, we reproduce $U(a)$ from Fig. 2 A (red, solid), and plot (red, dashed) the estimate of $g(a)$ obtained substituting $U(a)$ in Eq. 1. This estimated $g(a)$ compares reasonably well with $G(a)$, reproduced from Fig. 2 A (green). The agreement serves both as additional confirmation of the new method to define sparks in focus and as confirmation of significant properties of Ca^{2+} sparks.

Specifically, we confirm earlier conclusions, reached for both skeletal and cardiac ventricular muscle, that sparks have a preferential amplitude. In both tissues, the conclusions applied to special conditions. In the case of skeletal muscle, a modal amplitude was found in $g(a)$ functions derived via Eq. 1 in cells exposed to low concentrations of caffeine (Ríos et al., 2001). In cardiac muscle, a modal $G(a)$ was found in sparks elicited by sparklets near a patch electrode (therefore considered to be in focus; Wang et al., 2001, 2004). A modal amplitude was also found for groups of sparks originating from the same location in a cell, presumably from a single couplon firing repetitively (Bridge et al., 1999; Soeller and Cannell, 2002). Furthermore, the amplitudes of local SR Ca^{2+} depletion signals corresponding to Ca^{2+} sparks (Ca^{2+} blinks) reveal a modal distribution (Zima et al., 2008b).

As stated in earlier work, the main implication of the existence of a preferential amplitude of sparks is that their sources are not single Markovian channels (Bridge et al., 1999; Ríos et al., 2001; Wang et al., 2001, 2004). The existence of a mode in the distribution of amplitudes has been reproduced by models in which sparks are generated by channel clusters, interacting via CICR, calcium-dependent inactivation, or mechanical contact.

Although the simplicity of the procedure to find sparks in focus and its initial tests and results are reassuring, there are also inherent limitations to the method. First, only three vertical (z) positions were scanned, and the spatial resolution was set low in every dimension (as a compromise between the increased volume of data and the finite rate of data acquisition). Second, the vertical scanning reduced the time resolution of the recordings (in our case to 5.6 ms between successive x-y-z scans or image trios), which particularly affects the accuracy of the recording of rapidly changing features of the fluorescence signal, such as the rise time.

The properties of sparks in focus can be determined with precision

Fig. 5 shows averages of 150 sparks that were found to be in focus and had the additional common property of a $T = 11.2$ ms. What this means is that the peak amplitude was reached two frames later than the frame of first detection. This number, 11.2 ms, has precision limited by the large (5.6-ms) interval. In Fig. 5, images are arranged in three columns and nine rows. Each column contains averages at the same z position. Each row represents images (image trio, cf. Materials and methods) obtained in the same 5.6-ms interval. The interval of first detection is labeled c. At this time, the spark became sufficiently different from noise to be accounted for by the detection algorithm. The time of first detection ($t = 0$) occurs substantially later than the start of the event. This is clearly shown in Fig. 5, where the sparks that form the average started to develop in row a, while they were first detected 11.2 ms later in row c. The discrepancy between start of the event and time of detection is the result of the chosen stringency of the spark detection algorithm, and leads to an underestimate of rise time (by ~11.2 ms).

It should be kept in mind that the images were obtained in the order z_1, z_2, z_3. This means that images on the right-most column were obtained later, resulting in a systematic excess in amplitude during the rising phase and a corresponding deficit during the decaying phase. These differences are especially noticeable at times when the spark is changing rapidly (as in rows b, c, f, and g). At these times, the simple expectation that an in-focus spark should be measured with greatest amplitude at z_2 is clearly invalid. This property helps explain why a more elaborate criterion was needed to decide whether a spark is in focus.

The morphometric parameter values of this average are fairly representative of the histograms in Fig. 3. The amplitude is 1.04, and the FWHM is 2.98 µm. The averaged spark data (Fig. 5) were also used for the Ca^{2+} release flux calculation discussed in the next subsection.

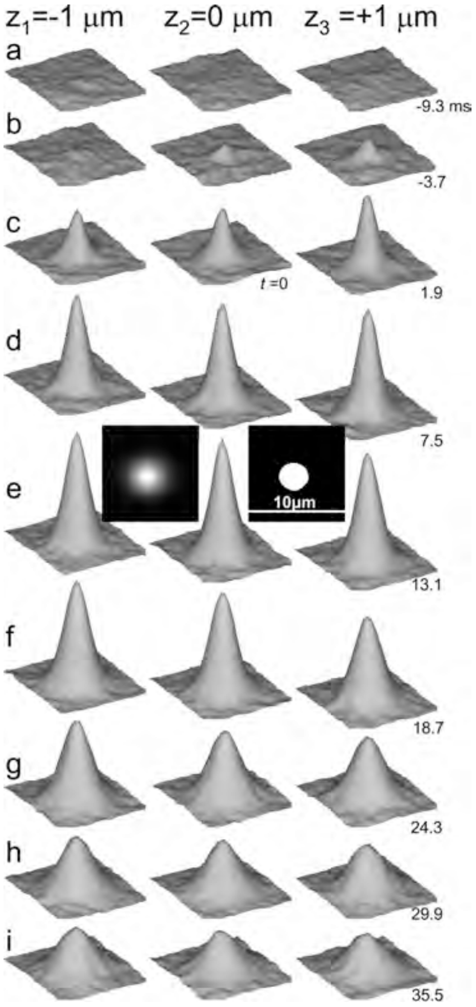

Figure 5. The average spark of $T = 11.2$ ms. Averages of images, at different times and z positions, of 150 in-focus sparks with $T = 11.2$ ms. Each column of nine panels contains successive averages at the vertical (z) position listed at top. Each row has the average images obtained at vertical positions z_1, z_2, and z_3 in the same 5.6-ms interval. The interval of first detection is labeled c. The times of acquisition of the images at level z_3 are listed in the third column. The origin of time ($t = 0$) is that of first detection, which occurs substantially later than the start of the event. Note that the spark average at z_2 has greater fluorescence than those at z_1 and z_3 only for the trio obtained at the time of peak amplitude, row e. During the stage of rapid rise of fluorescence, the averages at z_3 are greatest, whereas during the declining phase, it is position z_1 that records the greatest waveforms. The left-side square panel in row e depicts the average spark at the time of peak amplitude, at z_2, in grayscale. The right-side square panel shows in white the x–y region where average F/F_0 is greater than its half-maximum value.

Flux of Ca^{2+} release can be reliably estimated

A key advantage of knowing that a spark is in focus is that the underlying flux of Ca^{2+} release can then be derived with greater confidence. We calculated release flux applying the "backwards" method (Ríos et al., 1999) to averages of in-focus sparks of the same rise time (in the example of Fig. 5, $T = 11.2$ ms). The calculation, as implemented in Ríos et al. (1999) assumes radial symmetry for the event. The assumption applies well to the present case. This is demonstrated graphically for the average at $T = 11.2$ ms by the black insets in row e of Fig. 5, which show the average at its peak in grayscale (left) and a mask (right) formed by the contour of the average in the region where its fluorescence is greater than half amplitude. This contour is an almost perfect circle, a symmetry that applies to the average but does not preclude asymmetries in the individual sources. Furthermore, as detailed in Materials and methods, two measures of spatial width, in orthogonal directions (x and y dimension), were obtained for every spark, and this was done both by measuring diameters at half-maximal amplitude and by fitting a bivariate Gaussian to the spark. We found no significant difference between the average values of the two orthogonal measures, which is of course expected if the average is symmetric.

The method of release flux calculation requires assigning values to concentrations and kinetic parameters of the relevant Ca^{2+}-buffering molecules and removal systems, which was done as in our earlier work (Santiago et al., 2010). The Ca^{2+} buffers and removal processes included in the calculation are listed, with their parameter values, in Table 3. The use of permeabilized cells is advantageous for flux calculations because the cytosolic composition is precisely known. The calculation did not attempt to correct sparks for the blurring effect of the imaging process; the effects of blurring and the deblurring correction on calculated flux were found to be minor by Ríos et al. (1999), especially in cases where the sparks are spatially much wider than the point-spread function of the imaging system.

The calculation and results are illustrated in Fig. 6. In Fig. 6 A is the fluorescence, averaged over the angle φ (as shown schematically in inset a), plotted as a function of radial distance r and time from first detection. Inset b shows the same fluorescence in pseudocolor. That the fluorescence is averaged first over 150 events and then over the polar angle explains the near absence of noise in the result.

The calculated release flux is in Fig. 6 B. The spatial size of the source, which can be appreciated in inset c, is very small compared with the fluorescence event.

Quantitative aspects of the flux are illustrated in Fig. 7. The radial profiles of spark and calculated flux are compared in Fig. 7 A. It can be seen that the flux largely originates at a region of ~0.5 µm in diameter, which is roughly the spatial resolution of the microscope (a result suggesting that the source has dimensions below the limit of resolution). Fig. 7 B depicts temporal dependence of fluorescence (F/F_0), calculated free Ca^{2+} concentration (µM), and Ca^{2+} release flux (mM/s) for the same spark average. The peak Ca^{2+} release flux was calculated as 53 mM/s. Even though temporal aspects are not well described at this time resolution, it can be seen that the peak of the flux precedes the peak of free $[Ca^{2+}]$, and both precede the peak of fluorescence. The graph includes a plot of Ca^{2+} release current, calculated by integrating flux over the volume of the source. The current is approximately cotemporal with the flux and peaks at ~11 pA. This value of peak current is at the higher end of the range of estimates in cardiac cells (Blatter et al., 1997; Izu et al., 2001; Cheng and Wang, 2002; Soeller and Cannell, 2002; Wang et al., 2004; Santiago et al., 2010). Such level of current would require 20–30 channels simultaneously passing currents of 0.3–0.5 pA (Kettlun et al., 2003). Although large, this number of channels is still consistent with a source that remains below the limit

TABLE 3

Release flux calculation

Binding site	Concentration	k_{ON}	k_{OFF}	Diffusion coefficient	Flux
	µM	*(µM ms)$^{-1}$*	*ms^{-1}*	*µm^2 ms^{-1}*	*mM/s*
ATP	5,000	Ca, 0.15	30	0.14	25.3
		Mg, 2e-3	0.2		
EGTA	350	4e-3	2e-3	0.07	0.6
Fluo-4	40	0.032	0.032	0.05	1.4
SERCA	47	0.5	0.5	N.A.	0.9
Troponin	70	5.7e-3	0.011	N.A.	0.1
Sarcolemma	42	0.1	1.3	N.A.	0.1
Free Ca^{2+}*	variable	N.A.	N.A.	0.35	24.7

Model parameters (concentration, reaction rates, and diffusion coefficients) are given for all Ca^{2+} ligands used in the calculation. The last column lists maximal contributions to the flux total by the binding of Ca^{2+} to the corresponding ligand. The last row lists the free Ca^{2+} term in the flux calculation (namely, the flux required to account for the local rate of change of $[Ca^{2+}]$ and diffusion of the free ion). With minor changes, parameters are as in Santiago et al. (2010) and references therein.

of optical resolution. It is also consistent with estimates of the number of contributing channels obtained by noise analysis of spark amplitudes (Bridge et al., 1999), as well as the number of RyRs per couplon derived from RyR binding (Hayashi et al., 2009) and immunostaining studies (Soeller et al., 2007; Cannell and Kong, 2012). The number of channels estimated here is much greater than that derived from the observation of quantized flux in sparks from peripheral couplons ($n < 6$; Wang et al., 2004). Cannell and Kong (2012) argue that a complex, multi-couplon source could reconcile the observation of quantal sparks with the greater estimates of channel numbers derived in other works and confirmed here.

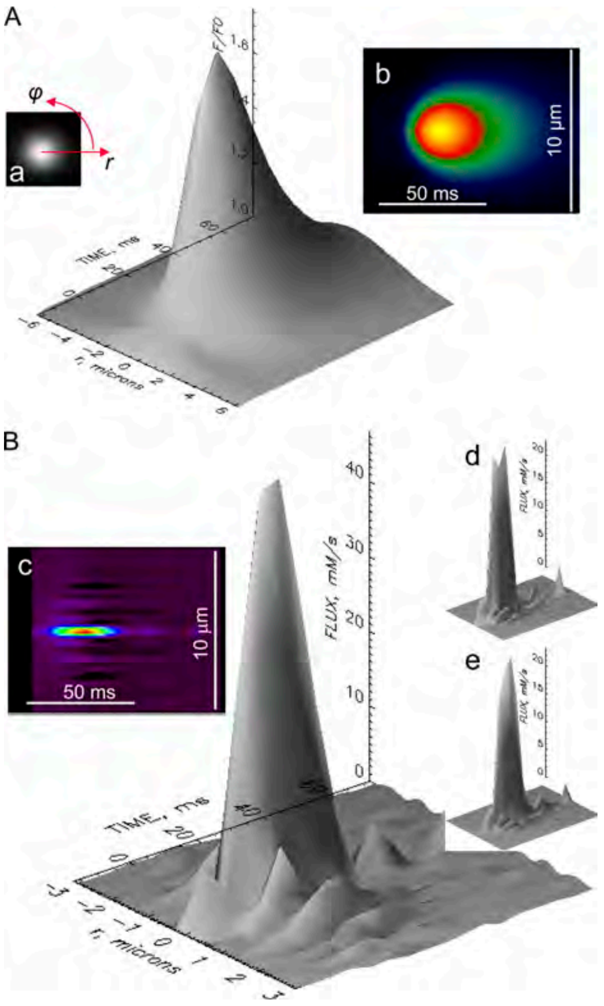

Figure 6. Ca^{2+} release flux of an averaged spark. (A) Normalized fluorescence, $F/F_0(r, t)$, obtained by averaging over the polar angle φ (as shown in inset a) the averaged spark of $T = 11.2$ ms (illustrated in Fig. 5). $F/F_0(r, t)$ is represented in pseudocolor in inset b. (B) Release flux, calculated from $F/F_0(r, t)$, represented as surface plot or in pseudocolor (inset c). The "ATP component" (specifically, flux of Ca^{2+} removal into ATP) and "free Ca^{2+} component" (flux needed to account for local rate of change of free [Ca^{2+}] and diffusion of the free ion) of flux are separately plotted in insets d and e, respectively. Collectively, they constitute >90% of the total at the time of peak release flux (details in Table 3).

The large number of simultaneously active channels in the present study is indicative of a greater than usual tendency of these channels to open. This tendency is manifested in the frequency of sparks detected in the reconstructed line scans (13.1 events; 100 μm^{-1} s^{-1}), which is greater than that reported in studies of intact atrial and ventricular muscle (ranging from ~0.5 to 5 events; 100 μm^{-1} s^{-1}: McCall et al., 1996; Satoh et al., 1997; Li et al., 2005; Sheehan et al., 2006; Copello et al., 2007; Santiago et al., 2010), but is only somewhat higher than frequencies observed in permeabilized ventricular cells (3–11 events; 100 μm^{-1} s^{-1}: Zima et al., 2003, 2004, 2008a,b, 2010; Qin et al., 2009). Part of the increase in frequency may therefore be attributed to an effect of membrane permeabilization, which has been demonstrated directly for the same cell type (cat atrial myocytes; Sheehan et al., 2006), and part to an actual difference between atrial and ventricular cells (cf. discussion below).

The calculation of flux permits an evaluation of the role of different buffer systems in shaping sparks. The calculation of Ca^{2+} release flux produces an estimate of the removal flux associated with every process that is

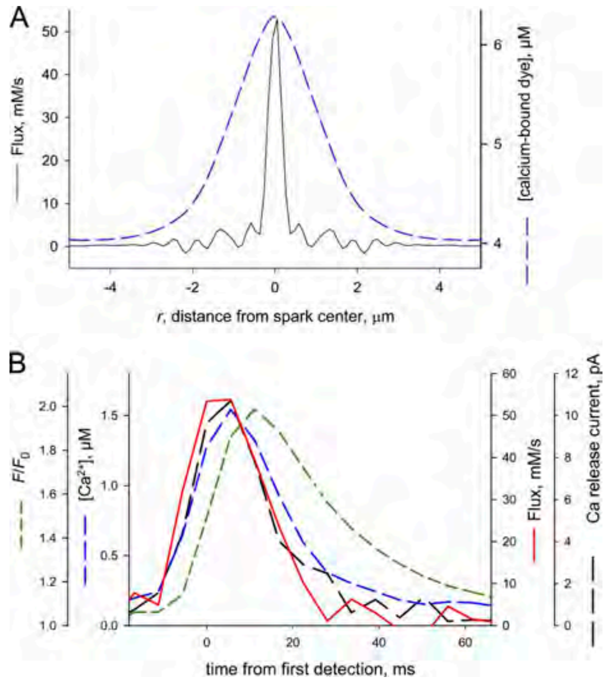

Figure 7. Quantitative properties of release flux. (A) Radial dependence of fluorescence (and its proportional magnitude, concentration of Ca^{2+}-bound fluo-4; dashed trace) at the time of its peak compared with that of calculated release flux for the average of sparks of $T = 11.2$ ms. Although the FWHM of the fluorescence spark was 2.98 μm, that of the flux was 0.45 μm. (B) Time course of spatial maxima of fluorescence (green), calculated free [Ca^{2+}] (blue), release flux (red), and release current (black) measured in successive average images of sparks of $T = 11.2$ ms. Note that flux started to fall before the time of peak fluorescence, an occurrence common for sparks of $T \geq 11.2$ ms.

taken into account. The processes and their maximal calculated removal fluxes for the average spark at $T = 11.2$ ms are listed in Table 3. Of the six processes listed, ATP binding and free Ca^{2+} accumulation and diffusion contribute together >90% of the flux, and their contributions, plotted separately in insets d and e of Fig. 6, have approximately equal maxima.

In addition to stressing the importance of ATP in shaping fast cytosolic Ca^{2+} transients, a notion first introduced by Baylor and Hollingworth (1998), this observation implies that the assumptions regarding specific properties of other ligands are unlikely to affect the results in any significant way. In support of this inference, alternative calculations with threefold changes in either direction in the diffusion coefficients assumed for EGTA and dye caused negligible changes in the resulting flux. Naturally, changes in the assumptions for ATP and Ca^{2+} had a greater effect. The main conclusions, however, were upheld. For example, when the diffusion coefficient D_{ATP} was reduced (increased) by a factor of 2, peak release current decreased by 8% (increased by 12%). When D_{Ca} was reduced (increased) twofold, the peak current was reduced by 4% (increased by 8%). Kinetic milestones, however, including the time to peak flux, and whether or not flux decreased before the peak fluorescence, were not changed in any case.

Conversely, the concentration of free Mg^{2+}, which in turn defines the availability of ATP, becomes an important factor in shaping fast local Ca^{2+} transients.

Release flux and control of channel open time

The determination of spark properties and calculation of flux and current was done for spark averages differing by rise time T. Similar averages as illustrated in Fig. 5 were obtained by binning in-focus sparks according to T, between 5.6 and 28 ms (in increments of 5.6 ms). The five different values of T will be represented by T_j, with j varying from 1 to 5. The properties of averages of sparks of different T are illustrated in Fig. 8. Fig. 8 A plots the amplitudes at different times (with $t = 0$ defined as the time of first detection). A notable aspect is that the early stages of all these averages are fairly similar, with a stage of fast increase, of approximately equal rate for all averages, regardless of the time at which sparks reach peak amplitude. This common rate of rise indicates that the underlying flux of Ca^{2+} release is similar for the five groups (more implications of this observation are discussed below).

The spatial width of these averages is plotted in Fig. 8 B. As discussed above, spatial width, or FWHM, was well defined in the average spark data, independently of the direction in the x–y plane, and there was no significant difference between the average values of FWHM in two orthogonal directions (x and y dimension). This symmetry is inconsistent with the possibility that a spark is originated by an extensive source of size greater than the limit of resolution of the microscope. It is not inconsistent with an asymmetric source, constituted by multiple channels, provided that its size remains below the limit of spatial resolution.

Another intriguing property of these events is revealed by the study of widths. As the plots in Fig. 8 B show, there is no obvious difference in the evolution of width among sparks of different rise time, and the plots show no visible inflection at the times of the peaks. If there is no difference in width among the groups, it follows that release termination has no consequences for spark width. Models of spark production predict some increase in width associated with release termination, superimposed on the increase mandated by simple

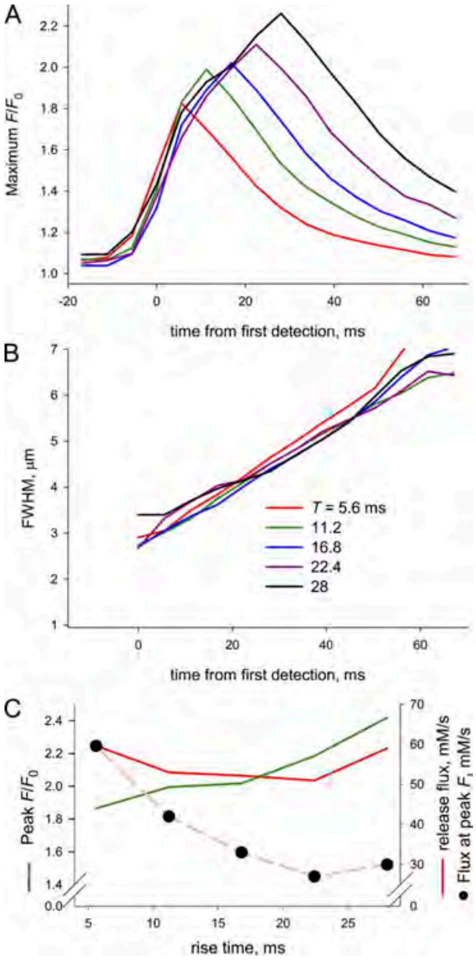

Figure 8. Properties of sparks of different rise times. (A) Amplitudes (i.e., maxima of F/F_0) at successive values of t (time from first detection) for averages of sparks of different T (coded as indicated in B). Note that the early course of fluorescence is similar for all averages (i.e., independent of T). (B) FWHM measured at different times on the same averages. The values are similar and evolve similarly with t for all averages. (C) Dependence of spark parameters with T. Peak fluorescence (green trace) grows with T. Peak flux (red) does not have a clear dependence on T. Flux at time of peak fluorescence (circles) decays monotonically as T increases.

diffusion (a phenomenon named "post-peak expansion" in Zhou et al., 2003). It can also be seen that the increase in width is essentially a linear function of time, in every case. Simple diffusion instead predicts an increase proportional to the square root of time. A possible reason for these discrepancies is that the theory in Zhou et al. (2003) assumes complete termination of Ca^{2+} release at the peak and a constant current during the postulated release time. As discussed below, neither condition is likely to be satisfied by the events observed here.

Peak fluorescence and flux in these averages of sparks of different rise time are summarized in Fig. 8 C. Note first that spark amplitude (i.e., normalized increase in fluorescence at the time of the peak, in green trace) increases with *T*. This property was already presented in Fig. 8 A. In its regard, we noted that the early, rapid rise in fluorescence was similar for all groups of sparks, regardless of their *T*, implying that release flux was similar, and maximal, for all averages at this early time. Peak flux, plotted in red, is indeed similar for all groups, and so is peak current (not depicted).

In Fig. 7 B (illustrating the group of sparks with a common $T = 11.2$ ms), it can be seen that the flux peaked at 5.6 ms, before the time of peak fluorescence. The peak of flux was reached at 5.6 ms in all other cases, implying that flux decayed during the rising phase of the spark. This is demonstrated in Fig. 8 C, where circles plot flux at the time of peak *F* for all five average sparks. That flux at the time of peak *F* is lowest for the sparks of longest rise time suggests that flux decreases monotonically during the rising phase.

These observations regarding the evolution of $[Ca^{2+}]_{cyto}$ and flux have important mechanistic implications. The main observations are as follows: (a) $F(t)$, hence $[Ca^{2+}]_{cyto}(t)$, dF/dt, and $\mathrm{Flux}(t)$ are approximately the same for all groups, up until their respective peak times (T_j). (b) After an early maximum, which occurs at 5.6–11.2 ms, flux decays substantially during the rising phase of the sparks. Observation a suggests that $[Ca^{2+}]_{SR}(t)$ is also very similar for these groups, up until their respective peaks.

These data, plus observations in previous studies, provide constraints for interpreting the underlying channel behavior. Ca^{2+} release current is equal to $N \times Po \times i$, where $N \times Po$ represents the number of open channels in the couplon, and i represents the unitary channel current. Flux and current are proportional; therefore, a decreasing flux or current during the times T_j requires the decay of i, $N \times Po$, or both.

Previous works provide abundant evidence that i decays (because local depletion, inferred from simulations and demonstrated by blinks, implies a decrease in the Ca^{2+} gradient). $N \times Po$ is also expected to decay, as SR depletion has a well-established closing effect on channels (Sobie and Lederer, 2012). A satisfactory quantitative description of sparks and blinks in terms of the above factors, however, does not exist (the article by Sobie and Lederer, 2012, discusses the difficulties that any attempt at such description will find). The present observations, showing that sparks of very different rise times have essentially indistinguishable early stages, set additional constraints and challenges. At least in an approximate and average sense, it can be affirmed that both the number of open channels and the unitary current are evolving similarly (at times before T_j) in the sparks studied here. If that is the case, a justification for the different rise times is not evident. If rise times are associated with the time when most channels are open (as assumed in models of Shen et al., 2004, and Wang et al., 2004), the observation would imply that the open times are not controlled by $[Ca^{2+}]_{SR}$ as is widely believed, or that the control is exerted, but different groups of channels have different sensitivity to it. The latter interpretation is supported by indications that the $[Ca^{2+}]_{SR}$ level at which sparks terminate is variable among couplons, but is highly constant for a given individual release site (Zima et al., 2008a).

Other simulations suggest that the duration of the rising phase of sparks is determined by the interplay of depletion and the varying number of open channels (e.g., Sobie et al., 2002). Certainly, different rates of depletion, associated perhaps with different volumes of SR cisternae or different refilling rates (Picht et al., 2011), could result in fluorescence peaks at different times. The difficulty with such scheme is that it would predict a gradual divergence of *F* between the groups with different rates of depletion, rather than the sharp departure at T_j observed here.

In conclusion, the present observations add to the current picture of control the possibility of other, less deterministic mechanisms. One is closure of groups of channels triggered by depletion at very different $[Ca^{2+}]_{SR}$ levels. A second possibility is that control by $[Ca^{2+}]_{SR}$ is weakened and consequently sparks terminate for reasons other than local SR depletion (a conclusion consistent with the observation of long-lasting sparks of varied durations but constant $[Ca^{2+}]_{SR}$; Zima et al., 2008a). The latter could be a peculiarity of atrial cells, consistent with other indications that the feedback mechanisms that control Ca^{2+} release are weakened in these cells.

In-focus sparks have greater correlations between morphometric variables

As demonstrated by 2-D histograms in Fig. 3, the morphometric parameters *a*, FWHM, and *T* were positively but poorly correlated for sparks detected in 3-D (left-side panels). When the analysis was restricted to sparks in focus, the correlations increased in every case.

A positive correlation between rise time and amplitude is in contrast with previous observations. Indeed, in cardiac myocytes, Wang et al. (2004) noted a quantized distribution of rates of rise of fluorescence, which they attributed to discrete numbers of participating channels (n_q) and a reduction of rise time for sparks of high n_q, which was interpreted as evidence that large currents reduced spark duration by closing channels. In cardiac myocytes, the correlation between amplitude, rise time, and width was weak (albeit positive; Shen et al., 2004). In skeletal muscle of amphibians, an absence of correlation between these variables was noted (Klein et al., 1999; Lacampagne et al., 2000). Ríos et al. (1999, 2008) found a small and not significant negative correlation, which upon a more refined analysis yielded significant correlation in two distinct regions: a region of low T where the correlation was positive, followed by one of significant negative correlation at longer T. Both an absence of correlation and a negative one require some sort of negative feedback that turns off channels when local cytosolic [Ca^{2+}] increases (or [Ca^{2+}] in SR lumen decreases). In the present case, however, a positive correlation was found. That it became more significant when the analysis was restricted to sparks in focus increases confidence in the finding. The positive correlation suggests that the negative feedback mechanisms on channel openness, implied by the aforementioned work, may be less important in atrial cells or under the conditions of the present experiments. The large flux and release current calculated for the observed sparks is also an indication of increased propensity of channels to open, as is the high frequency of these events.

The positive correlation observed between rise time and width is as predicted in spark models (for example, Jiang et al., 1999; Zhou et al., 2003). Finally, the positive correlation between amplitude and width (which follows mathematically when the other two correlations are positive) can be understood as the consequence of both variables increasing with increasing rise time (dependencies that were both found, as documented in Fig. 8). These simple positive correlations are predicted by models in which width and amplitude are determined largely by the duration of the underlying Ca^{2+} release current (which is positively correlated with rise time), rather than those in which longer durations of release are associated with smaller clusters of channels or lower unitary current. The latter associations are consequences of negative feedback mechanisms affecting channel openness. Therefore, these correlations are again indications of weakened negative feedback in the present case.

These cells were subjected to membrane permeabilization, which may have resulted in the increased spark size and frequency, in a way similar to the increase of spark size and frequency observed in cut versus intact skeletal muscle fibers (Baylor et al., 2002; Chandler et al., 2003) and in chemically permeabilized versus intact atrial myocytes (Sheehan et al., 2006), or the appearance of spark-like events in mammalian skeletal muscle cells when they are peeled or saponized (Kirsch et al., 2001).

On the other hand, this weakened negative feedback could be a feature of atrial myocytes, critical for Ca^{2+} release during excitation–contraction coupling (ecc). The lack of t-tubules in atrial myocytes requires a distinctly different mechanism of Ca^{2+} release during ecc. Although in ventricular myoctes all RyR clusters are found in close physical association with a dihydropyridine receptor (DHPR) Ca^{2+} channel in the surface membrane because of the extensive t-tubular system, in atrial myocytes only the RyRs of the junctional SR in the cell periphery are organized in a similar arrangement. Consequently, action potential–induced opening of DHPRs provides the required trigger Ca^{2+} for CICR simultaneously and homogeneously throughout an entire ventricular myocyte, but not in atrial cells. In atrial myocytes, DHPR opening triggers release initially only in the cell periphery, which leads to an elevation of subsarcolemmal cytosolic [Ca^{2+}] that initiates regenerative and propagating CICR from nj-SR. This centripetal propagation of CICR from nj-SR is reminiscent of cardiac Ca^{2+} wave propagation (Berlin, 1995; Hüser et al., 1996; Kockskämper et al., 2001; Mackenzie et al., 2001; Woo et al., 2002; Sheehan and Blatter, 2003). Ultrastructural studies (Kockskämper et al., 2001) showed that nj-SR membranes do not form the narrow diadic clefts that would allow [Ca^{2+}] to rise rapidly on the cytosolic face of the RyR. Thus, to achieve reliable and robust Ca^{2+} release throughout the entire atrial myocyte, other mechanisms need to be postulated. As demonstrated in the present study, the relative large Ca^{2+} flux underlying atrial sparks, the calculated large numbers of channels involved, the enhanced propensity of RyR channels to open, the extended spatial spread (see also Blatter et al., 1997), and a diminished influence of negative feedback mechanisms in this preparation compared with ventricular myocytes all contribute to a situation where lower [Ca^{2+}] levels are required to trigger CICR and propagation of activation during ecc.

Conclusions

We have demonstrated a method to image sparks that are in focus, based on scanning fluorescence in three spatial dimensions. The sparks found to be in focus had substantially greater amplitudes than the population of all detected sparks and, at variance with these, distributed with a broad mode (at $\sim 0.7\ F_0$). Properties of sparks in focus were determined both with accuracy, because the out-of-focus error was removed, and precision, given the large number of events recorded. Among the main morphometric parameters, amplitude was substantially different in the sparks in focus, whereas average width and rise time were not. The Ca^{2+} release flux and current underlying sparks in focus were large, requiring sources of 20–30 channels. The flux peaked early and then decayed during the rising phase of the spark, which is consistent with existing evidence of significant local depletion of the SR, but could also be helped by progressive closure of channels in the cluster. The magnitude and evolution of flux were similar in sparks of different rise time. This feature indicates that the termination of Ca^{2+} release was not robustly controlled by variables associated with flux, including free cytosolic and free SR calcium concentrations, either because different channels responded to these variables in different ways, were controlled by variables other than $[Ca^{2+}]_{cyto}$ and $[Ca^{2+}]_{SR}$, or closed at random. The large sparks, large fluxes, and calculated large numbers of channels involved define a state of enhanced proclivity of channels to open, reflecting a diminished influence of negative feedback mechanisms in this preparation. The lack of association between flux and spark rise time can also be taken as an indication of a general deficit in negative controls, underlying the abundance of local events in these atrial cells. Because atrial myocytes lack a t-tubular system and have to rely on robust cell-wide propagating CICR for the activation of the contractile machinery, this deficit in negative control constitutes an advantage for ecc in these cells. Other properties of local events in focus, including spatial associations, event propagation, and location-specific aspects of Ca^{2+} release, can be studied advantageously with 4-D scanning.

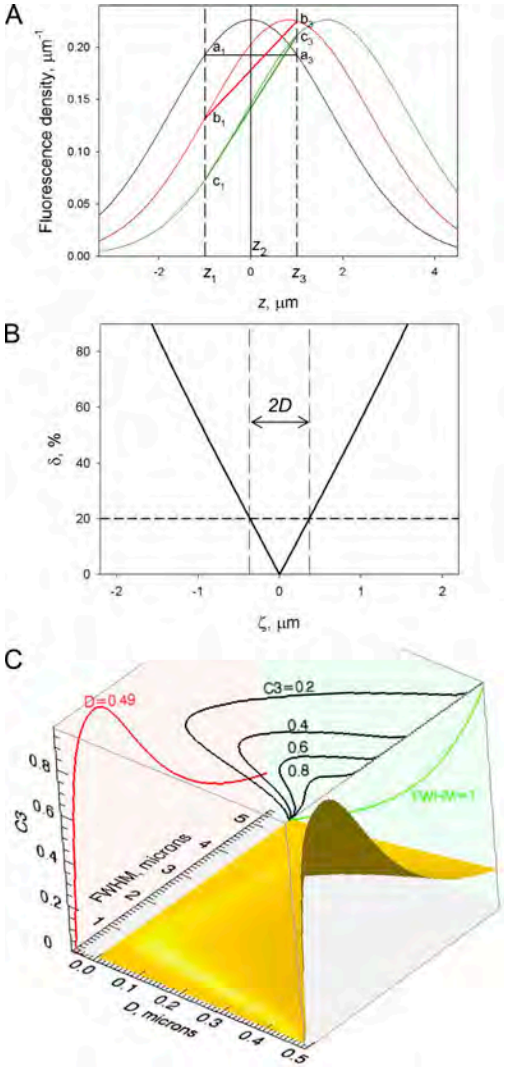

Figure A1. The three-point criterion for sparks in focus. (A) The spatial (*z*) profile of fluorescence of a spark, represented as a Gaussian function,

$$F = \frac{1}{\sigma\sqrt{2\pi}} e^{-\frac{(z-\zeta)^2}{2\sigma^2}},$$

of $\sigma = 1.4$ µm, centered at $\zeta = 0$ (black), 0.825 (red), or 1.65 (green). Segments a_1–a_3, b_1–b_3, and c_1–c_3 join the intersections of these curves with the lines at z_1 (−1 µm) and z_3 (+1 µm). The difference between the ordinates at these intersections increases as the central abscissa ζ moves away from $z = 0$. (B) δ, absolute value of the difference between fluorescence at $z = z_1$ and $z = z_3$, normalized by the value at $z = z_2$ (according to Eq. A1), and plotted versus ζ, the central position (*z* value) of the Gaussian spark. Note that sparks of $\sigma = 1.4$ µm will have $\delta < 0.2$ (or 20%) when their central *z* value satisfies the inequalities, $-0.37 \leq \zeta \leq 0.37$, in other words, when the origin of release is within a spatial slice of height 2 × 0.37 (or *2D*). (C) Generalization of the calculation in B to include σ as a variable. δ, calculated by Eq. A1, is plotted versus ζ and FWHM = $(2 \times \ln 2)^{1/2}\sigma$. This function works as a threshold criterion (hence it is labeled *C3*) as follows: given a set thickness *2D* of the slice of space deemed to be in focus, an experimentally recorded spark will be in focus if its calculated δ is ≤C3 at the set value of *D* and the FWHM measured for the individual spark. In the graph, the line plots are intersections of the *C3* (*D*, FWHM) surface by planes of constant *C3* (black), *D* (red), or FWHM (green).

APPENDIX

A robust procedure for identifying in-focus sparks

The purpose of this appendix is to describe and illustrate a procedure to decide, based on comparison of images at three values of the *z* coordinate, whether a spark is in focus. The procedure and associated criterion are called "three-point" because they use asymmetrically the measures of amplitude at the different *z* positions. In contrast, the simple criterion, whereby a spark is deemed in focus if its amplitude at z_2 is greater than at the other two *z* positions, uses the measures at z_1 and z_3 symmetrically, thus not taking advantage of all the information available.

The procedure is illustrated in Fig. A1. A spark is represented by a Gaussian function of the vertical coordinate *z*. The function has a standard error (σ) of 1.4 µm, which makes it representative of sparks in the present database. We will refer to this function as $h(z,1.4)$. Gaussian sparks with identical σ are depicted centered at two other positions on the *z* axis, separated by 0.825 µm—an arbitrary distance of convenience. Three vertical lines are traced at positions z_1 (−1 µm), z_2 (0 µm), and z_3 (+1 µm), representing the three planes of *x-y-z* scanning. The segments a_1-a_3, b_1-b_3, and c_1-c_3 are the intersections of the functions with the planes z_1 and z_3. Their vertical spans are therefore the differences between the spark intensity measured at the two extreme values of *z*. It can be seen that this difference, as a fraction of the central (z_2 = 0 µm) value, increases steeply as the spark moves away from the central plane.

The absolute value of the difference, as a fraction of the value at z_2, can be calculated as:

$$\delta \equiv \frac{h(-\xi - 1, 1.4) - h(-\zeta + 1, 1.4)}{h(-\zeta, 1.4)}, \qquad \text{(A1)}$$

where ζ is the separation between the focal plane and the center of the displaced spark. δ is represented as a function of ζ in Fig. A1 B. For absolute values of ζ <0.37 µm, δ is <0.2. In other words, when the difference between amplitudes at the two extreme z planes is <20% of the central amplitude, events of σ = 1.4 µm should be restricted to a slice 0.74-µm thick, centered by the focal plane at z = 0 µm.

Inspection of Eq. A1 and Fig. A1 shows that δ decays monotonically as ζ decreases, a property that was used to advantage to generate a scalable criterion for identifying in-focus sparks. Let δ, calculated by Eq. A1 for a set of values of ζ, be less than that calculated for a reference value of ζ, say, D. Because of the monotonic relationship, it follows that all ζ that satisfy the inequality δ (ζ) < δ (D) will be less than D. An equivalent statement is that the origins of sparks at such values of ζ will be contained within the slice of half thickness D. We represent δ (D), the "criterion" threshold, by the symbol *C3*. The criterion can be made applicable to sparks of other spatial widths simply by introducing the corresponding value of σ in place of 1.4 in Eq. A1. *C3* is therefore a function of D and σ (or the proportional quantity $(2 \times \ln 2)^{1/2}\sigma$ = FWHM). *C3* is represented as a function of D and FWHM in Fig. A1 C. (Note that *C3* grows monotonically with D, as shown by the projection in green, but has a modal dependence on FWHM, shown by the projection in red.) Indeed, for very narrow sparks, the δ value calculated by Eq. A1 is small because both terms in the numerator are small. For large values of FWHM, both terms become large but similar, so δ becomes small again.

This criterion proved to be superior for several reasons, which justify their use in the present work. One important advantage is that it satisfied expectations of convergence. Specifically, when this criterion was applied to the same universe of sparks at progressively narrower depths of the in-focus slice (set by the variable D), it produced groups of sparks tending to a limiting set of properties. This is illustrated in Fig. A2 with histograms of amplitudes of the groups of sparks selected by the three-point criterion at progressively lower values of D. As D decreases, the histograms converge to a distribution with greater density at high values of the amplitude. This analysis cannot be taken to a true limit as the spark numbers decrease with D, but the convergence seemed satisfactory as far as it could be explored. Moreover, the loss of density at low values of amplitude and gain at high values was as expected if the selection progressively eliminated out-of-focus sparks. Specifically, the histogram obtained with the criterion applied at a D of 0.1 µm (green trace in Fig. A2) appears to have limit features, while still including a large number of sparks.

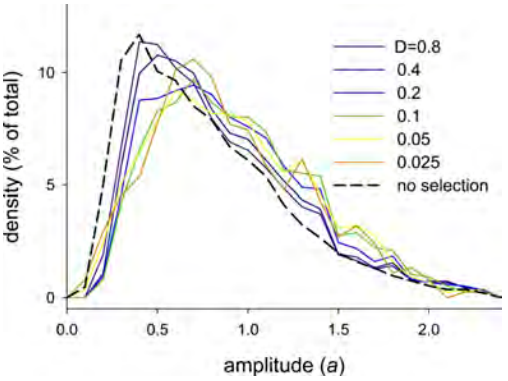

Figure A2. Convergence of the three-point criterion for identification of in-focus sparks. Histograms of amplitudes of sparks selected as in focus by the three-point criterion, at progressively lower values of D (half-depth of in-focus slice). Values of D are indicated on the graph. Note that the features of the histograms vary little at $D \leq 0.1$ µm. In this work, a spark was considered to be in focus if its δ, calculated by Eq. A1, fell below the *C3* value at the measured FWHM on the intercept of the C3 surface (Fig. A1 C) and the plane at D = 0.1 µm.

This work was supported by grants from the National Institutes of Health (AR049184, AR032808, and RR24707 to E. Ríos; HL62231, HL80101, and HL101235 to L.A. Blatter), and the Leducq Foundation (to L.A. Blatter).

Richard L. Moss served as editor.

Submitted: 23 August 2011
Accepted: 26 January 2012

REFERENCES

Baylor, S.M., and S. Hollingworth. 1998. Model of sarcomeric Ca^{2+} movements, including ATP Ca^{2+} binding and diffusion, during activation of frog skeletal muscle. *J. Gen. Physiol.* 112:297–316. http://dx.doi.org/10.1085/jgp.112.3.297

Baylor, S.M., W.K. Chandler, and M.W. Marshall. 1983. Sarcoplasmic reticulum calcium release in frog skeletal muscle fibres estimated from Arsenazo III calcium transients. *J. Physiol.* 344:625–666.

Baylor, S.M., S. Hollingworth, and W.K. Chandler. 2002. Comparison of simulated and measured calcium sparks in intact skeletal muscle fibers of the frog. *J. Gen. Physiol.* 120:349–368. http://dx.doi.org/10.1085/jgp.20028620

Berlin, J.R. 1995. Spatiotemporal changes of Ca^{2+} during electrically evoked contractions in atrial and ventricular cells. *Am. J. Physiol.* 269:H1165–H1170.

Blatter, L.A., J. Hüser, and E. Ríos. 1997. Sarcoplasmic reticulum Ca^{2+} release flux underlying Ca^{2+} sparks in cardiac muscle. *Proc. Natl. Acad. Sci. USA.* 94:4176–4181. http://dx.doi.org/10.1073/pnas.94.8.4176

Bridge, J.H., P.R. Ershler, and M.B. Cannell. 1999. Properties of Ca^{2+} sparks evoked by action potentials in mouse ventricular myocytes. *J. Physiol.* 518:469–478. http://dx.doi.org/10.1111/j.1469-7793.1999.0469p.x

Brochet, D.X., D. Yang, A. Di Maio, W.J. Lederer, C. Franzini-Armstrong, and H. Cheng. 2005. Ca^{2+} blinks: rapid nanoscopic store calcium signaling. *Proc. Natl. Acad. Sci. USA*. 102:3099–3104. http://dx.doi.org/10.1073/pnas.0500059102

Brum, G., A. González, J. Rengifo, N. Shirokova, and E. Ríos. 2000. Fast imaging in two dimensions resolves extensive sources of Ca^{2+} sparks in frog skeletal muscle. *J. Physiol.* 528:419–433. http://dx.doi.org/10.1111/j.1469-7793.2000.00419.x

Cannell, M.B., and C.H. Kong. 2012. Local control in cardiac E-C coupling. *J. Mol. Cell. Cardiol.* 52:298–303. http://dx.doi.org/10.1016/j.yjmcc.2011.04.014

Cannell, M.B., and C. Soeller. 1999. Mechanisms underlying calcium sparks in cardiac muscle. *J. Gen. Physiol.* 113:373–376. http://dx.doi.org/10.1085/jgp.113.3.373

Chandler, W.K., S. Hollingworth, and S.M. Baylor. 2003. Simulation of calcium sparks in cut skeletal muscle fibers of the frog. *J. Gen. Physiol.* 121:311–324. http://dx.doi.org/10.1085/jgp.200308787

Cheng, H., and S.Q. Wang. 2002. Calcium signaling between sarcolemmal calcium channels and ryanodine receptors in heart cells. *Front. Biosci.* 7:d1867–d1878.

Cheng, H., W.J. Lederer, and M.B. Cannell. 1993. Calcium sparks: elementary events underlying excitation-contraction coupling in heart muscle. *Science*. 262:740–744. http://dx.doi.org/10.1126/science.8235594

Cheng, H., M.B. Cannell, and W.J. Lederer. 1994. Propagation of excitation-contraction coupling into ventricular myocytes. *Pflugers Arch.* 428:415–417. http://dx.doi.org/10.1007/BF00724526

Cheng, H., L.S. Song, N. Shirokova, A. González, E.G. Lakatta, E. Ríos, and M.D. Stern. 1999. Amplitude distribution of calcium sparks in confocal images: theory and studies with an automatic detection method. *Biophys. J.* 76:606–617. http://dx.doi.org/10.1016/S0006-3495(99)77229-2

Colquhoun, D., and A.G. Hawkes. 1983. The principles of the stochastic interaction of ion-channel mechanisms. *In* Single-Channel Recording. B. Sakmann and E. Neher, editors. Springer, New York. 135–175.

Copello, J.A., A.V. Zima, P.L. Diaz-Sylvester, M. Fill, and L.A. Blatter. 2007. Ca^{2+} entry-independent effects of L-type Ca^{2+} channel modulators on Ca^{2+} sparks in ventricular myocytes. *Am. J. Physiol. Cell Physiol.* 292:C2129–C2140. http://dx.doi.org/10.1152/ajpcell.00437.2006

Cordeiro, J.M., K.W. Spitzer, W.R. Giles, P.E. Ershler, M.B. Cannell, and J.H. Bridge. 2001. Location of the initiation site of calcium transients and sparks in rabbit heart Purkinje cells. *J. Physiol.* 531:301–314. http://dx.doi.org/10.1111/j.1469-7793.2001.0301i.x

Endo, M., M. Tanaka, and Y. Ogawa. 1970. Calcium induced release of calcium from the sarcoplasmic reticulum of skinned skeletal muscle fibres. *Nature*. 228:34–36. http://dx.doi.org/10.1038/228034a0

Fabiato, A., and F. Fabiato. 1978. Calcium-induced release of calcium from the sarcoplasmic reticulum of skinned cells from adult human, dog, cat, rabbit, rat, and frog hearts and from fetal and new-born rat ventricles. *Ann. NY Acad. Sci.* 307:491–522. http://dx.doi.org/10.1111/j.1749-6632.1978.tb41979.x

Franzini-Armstrong, C., and A.O. Jorgensen. 1994. Structure and development of E-C coupling units in skeletal muscle. *Annu. Rev. Physiol.* 56:509–534. http://dx.doi.org/10.1146/annurev.ph.56.030194.002453

Hayashi, T., M.E. Martone, Z. Yu, A. Thor, M. Doi, M.J. Holst, M.H. Ellisman, and M. Hoshijima. 2009. Three-dimensional electron microscopy reveals new details of membrane systems for Ca^{2+} signaling in the heart. *J. Cell Sci.* 122:1005–1013. http://dx.doi.org/10.1242/jcs.028175

Hüser, J., S.L. Lipsius, and L.A. Blatter. 1996. Calcium gradients during excitation-contraction coupling in cat atrial myocytes. *J. Physiol.* 494:641–651.

Izu, L.T., W.G. Wier, and C.W. Balke. 1998. Theoretical analysis of the Ca^{2+} spark amplitude distribution. *Biophys. J.* 75:1144–1162. http://dx.doi.org/10.1016/S0006-3495(98)74034-2

Izu, L.T., J.R. Mauban, C.W. Balke, and W.G. Wier. 2001. Large currents generate cardiac Ca^{2+} sparks. *Biophys. J.* 80:88–102. http://dx.doi.org/10.1016/S0006-3495(01)75997-8

Jiang, Y.H., M.G. Klein, and M.F. Schneider. 1999. Numerical simulation of Ca^{2+} "sparks" in skeletal muscle. *Biophys. J.* 77:2333–2357. http://dx.doi.org/10.1016/S0006-3495(99)77072-4

Kettlun, C., A. González, E. Ríos, and M. Fill. 2003. Unitary Ca^{2+} current through mammalian cardiac and amphibian skeletal muscle ryanodine receptor channels under near-physiological ionic conditions. *J. Gen. Physiol.* 122:407–417. http://dx.doi.org/10.1085/jgp.200308843

Kirsch, W.G., D. Uttenweiler, and R.H. Fink. 2001. Spark- and ember-like elementary Ca^{2+} release events in skinned fibres of adult mammalian skeletal muscle. *J. Physiol.* 537:379–389. http://dx.doi.org/10.1111/j.1469-7793.2001.00379.x

Klein, M.G., H. Cheng, L.F. Santana, Y.H. Jiang, W.J. Lederer, and M.F. Schneider. 1996. Two mechanisms of quantized calcium release in skeletal muscle. *Nature*. 379:455–458. http://dx.doi.org/10.1038/379455a0

Klein, M.G., A. Lacampagne, and M.F. Schneider. 1999. A repetitive mode of activation of discrete Ca^{2+} release events (Ca^{2+} sparks) in frog skeletal muscle fibres. *J. Physiol.* 515:391–411. http://dx.doi.org/10.1111/j.1469-7793.1999.391ac.x

Kockskämper, J., and L.A. Blatter. 2002. Subcellular Ca^{2+} alternans represents a novel mechanism for the generation of arrhythmogenic Ca^{2+} waves in cat atrial myocytes. *J. Physiol.* 545:65–79. http://dx.doi.org/10.1113/jphysiol.2002.025502

Kockskämper, J., K.A. Sheehan, D.J. Bare, S.L. Lipsius, G.A. Mignery, and L.A. Blatter. 2001. Activation and propagation of Ca(2+) release during excitation-contraction coupling in atrial myocytes. *Biophys. J.* 81:2590–2605. http://dx.doi.org/10.1016/S0006-3495(01)75903-6

Lacampagne, A., M.G. Klein, C.W. Ward, and M.F. Schneider. 2000. Two mechanisms for termination of individual Ca^{2+} sparks in skeletal muscle. *Proc. Natl. Acad. Sci. USA*. 97:7823–7828. http://dx.doi.org/10.1073/pnas.97.14.7823

Li, X., A.V. Zima, F. Sheikh, L.A. Blatter, and J. Chen. 2005. Endothelin-1-induced arrhythmogenic Ca^{2+} signaling is abolished in atrial myocytes of inositol-1,4,5-trisphosphate(IP_3)-receptor type 2-deficient mice. *Circ. Res.* 96:1274–1281. http://dx.doi.org/10.1161/01.RES.0000172556.05576.4c

Mackenzie, L., M.D. Bootman, M.J. Berridge, and P. Lipp. 2001. Predetermined recruitment of calcium release sites underlies excitation-contraction coupling in rat atrial myocytes. *J. Physiol.* 530:417–429. http://dx.doi.org/10.1111/j.1469-7793.2001.0417k.x

McCall, E., L. Li, H. Satoh, T.R. Shannon, L.A. Blatter, and D.M. Bers. 1996. Effects of FK-506 on contraction and Ca^{2+} transients in rat cardiac myocytes. *Circ. Res.* 79:1110–1121.

Melzer, W., E. Ríos, and M.F. Schneider. 1984. Time course of calcium release and removal in skeletal muscle fibers. *Biophys. J.* 45:637–641. http://dx.doi.org/10.1016/S0006-3495(84)84203-4

Nelson, M.T., H. Cheng, M. Rubart, L.F. Santana, A.D. Bonev, H.J. Knot, and W.J. Lederer. 1995. Relaxation of arterial smooth muscle by calcium sparks. *Science*. 270:633–637. http://dx.doi.org/10.1126/science.270.5236.633

Niggli, E., and N. Shirokova. 2007. A guide to sparkology: the taxonomy of elementary cellular Ca^{2+} signaling events. *Cell Calcium*. 42:379–387. http://dx.doi.org/10.1016/j.ceca.2007.02.010

Picht, E., A.V. Zima, T.R. Shannon, A.M. Duncan, L.A. Blatter, and D.M. Bers. 2011. Dynamic calcium movement inside cardiac sarcoplasmic reticulum during release. *Circ. Res.* 108:847–856. http://dx.doi.org/10.1161/CIRCRESAHA.111.240234

Pratusevich, V.R., and C.W. Balke. 1996. Factors shaping the confocal image of the calcium spark in cardiac muscle cells. *Biophys. J.* 71:2942–2957. http://dx.doi.org/10.1016/S0006-3495(96)79525-5

Qin, J., A.V. Zima, M. Porta, L.A. Blatter, and M. Fill. 2009. Trifluoperazine: a rynodine receptor agonist. *Pflugers Arch.* 458:643–651. http://dx.doi.org/10.1007/s00424-009-0658-y

Ríos, E., M.D. Stern, A. González, G. Pizarro, and N. Shirokova. 1999. Calcium release flux underlying Ca^{2+} sparks of frog skeletal muscle. *J. Gen. Physiol.* 114:31–48. http://dx.doi.org/10.1085/jgp.114.1.31

Ríos, E., N. Shirokova, W.G. Kirsch, G. Pizarro, M.D. Stern, H. Cheng, and A. González. 2001. A preferred amplitude of calcium sparks in skeletal muscle. *Biophys. J.* 80:169–183. http://dx.doi.org/10.1016/S0006-3495(01)76005-5

Ríos, E., J. Zhou, G. Brum, B.S. Launikonis, and M.D. Stern. 2008. Calcium-dependent inactivation terminates calcium release in skeletal muscle of amphibians. *J. Gen. Physiol.* 131:335–348. http://dx.doi.org/10.1085/jgp.200709870

Santiago, D.J., J.W. Curran, D.M. Bers, W.J. Lederer, M.D. Stern, E. Ríos, and T.R. Shannon. 2010. Ca sparks do not explain all ryanodine receptor-mediated SR Ca leak in mouse ventricular myocytes. *Biophys. J.* 98:2111–2120. http://dx.doi.org/10.1016/j.bpj.2010.01.042

Satoh, H., L.A. Blatter, and D.M. Bers. 1997. Effects of $[Ca^{2+}]_i$, SR Ca^{2+} load, and rest on Ca^{2+} spark frequency in ventricular myocytes. *Am. J. Physiol.* 272:H657–H668.

Sham, J.S., L.S. Song, Y. Chen, L.H. Deng, M.D. Stern, E.G. Lakatta, and H. Cheng. 1998. Termination of Ca2+ release by a local inactivation of ryanodine receptors in cardiac myocytes. *Proc. Natl. Acad. Sci. USA.* 95:15096–15101. http://dx.doi.org/10.1073/pnas.95.25.15096

Sheehan, K.A., and L.A. Blatter. 2003. Regulation of junctional and non-junctional sarcoplasmic reticulum calcium release in excitation-contraction coupling in cat atrial myocytes. *J. Physiol.* 546:119–135. http://dx.doi.org/10.1113/jphysiol.2002.026963

Sheehan, K.A., A.V. Zima, and L.A. Blatter. 2006. Regional differences in spontaneous Ca^{2+} spark activity and regulation in cat atrial myocytes. *J. Physiol.* 572:799–809.

Shen, J.X., S. Wang, L.S. Song, T. Han, and H. Cheng. 2004. Polymorphism of Ca^{2+} sparks evoked from in-focus Ca^{2+} release units in cardiac myocytes. *Biophys. J.* 86:182–190. http://dx.doi.org/10.1016/S0006-3495(04)74095-3

Shirokova, N., and E. Ríos. 1997. Small event Ca^{2+} release: a probable precursor of Ca^{2+} sparks in frog skeletal muscle. *J. Physiol.* 502:3–11. http://dx.doi.org/10.1111/j.1469-7793.1997.003bl.x

Shirokova, N., A. González, W.G. Kirsch, E. Ríos, G. Pizarro, M.D. Stern, and H. Cheng. 1999. Calcium sparks: release packets of uncertain origin and fundamental role. *J. Gen. Physiol.* 113:377–384. http://dx.doi.org/10.1085/jgp.113.3.377

Smith, G.D., J.E. Keizer, M.D. Stern, W.J. Lederer, and H. Cheng. 1998. A simple numerical model of calcium spark formation and detection in cardiac myocytes. *Biophys. J.* 75:15–32. http://dx.doi.org/10.1016/S0006-3495(98)77491-0

Sobie, E.A., and W.J. Lederer. 2012. Dynamic local changes in sarcoplasmic reticulum calcium: Physiological and pathophysiological roles. *J. Mol. Cell. Cardiol.* 52:304–311. http://dx.doi.org/10.1016/j.yjmcc.2011.06.024

Sobie, E.A., K.W. Dilly, J. dos Santos Cruz, W.J. Lederer, and M.S. Jafri. 2002. Termination of cardiac Ca(2+) sparks: an investigative mathematical model of calcium-induced calcium release. *Biophys. J.* 83:59–78. http://dx.doi.org/10.1016/S0006-3495(02)75149-7

Soeller, C., and M.B. Cannell. 1999. Examination of the transverse tubular system in living cardiac rat myocytes by 2-photon microscopy and digital image-processing techniques. *Circ. Res.* 84:266–275.

Soeller, C., and M.B. Cannell. 2002. Estimation of the sarcoplasmic reticulum Ca^{2+} release flux underlying Ca^{2+} sparks. *Biophys. J.* 82:2396–2414. http://dx.doi.org/10.1016/S0006-3495(02)75584-7

Soeller, C., and M.B. Cannell. 2004. Analysing cardiac excitation-contraction coupling with mathematical models of local control. *Prog. Biophys. Mol. Biol.* 85:141–162. http://dx.doi.org/10.1016/j.pbiomolbio.2003.12.006

Soeller, C., D. Crossman, R. Gilbert, and M.B. Cannell. 2007. Analysis of ryanodine receptor clusters in rat and human cardiac myocytes. *Proc. Natl. Acad. Sci. USA.* 104:14958–14963. http://dx.doi.org/10.1073/pnas.0703016104

Stern, M.D., G. Pizarro, and E. Ríos. 1997. Local control model of excitation–contraction coupling in skeletal muscle. *J. Gen. Physiol.* 110:415–440. http://dx.doi.org/10.1085/jgp.110.4.415

Stern, M.D., L.S. Song, H. Cheng, J.S. Sham, H.T. Yang, K.R. Boheler, and E. Ríos. 1999. Local control models of cardiac excitation–contraction coupling. A possible role for allosteric interactions between ryanodine receptors. *J. Gen. Physiol.* 113:469–489. http://dx.doi.org/10.1085/jgp.113.3.469

Toomre, D., and J.B. Pawley. 2006. Handbook of biological confocal microscopy. *In* Handbook of Biological Confocal Microscopy. J.B. Pawley, editor. Springer, New York. 231.

Tsugorka, A., E. Ríos, and L.A. Blatter. 1995. Imaging elementary events of calcium release in skeletal muscle cells. *Science.* 269:1723–1726. http://dx.doi.org/10.1126/science.7569901

Wang, S.Q., L.S. Song, E.G. Lakatta, and H. Cheng. 2001. Ca^{2+} signalling between single L-type Ca^{2+} channels and ryanodine receptors in heart cells. *Nature.* 410:592–596. http://dx.doi.org/10.1038/35069083

Wang, S.Q., L.S. Song, L. Xu, G. Meissner, E.G. Lakatta, E. Ríos, M.D. Stern, and H. Cheng. 2002. Thermodynamically irreversible gating of ryanodine receptors in situ revealed by stereotyped duration of release in Ca(2+) sparks. *Biophys. J.* 83:242–251. http://dx.doi.org/10.1016/S0006-3495(02)75165-5

Wang, S.Q., M.D. Stern, E. Ríos, and H. Cheng. 2004. The quantal nature of Ca^{2+} sparks and in situ operation of the ryanodine receptor array in cardiac cells. *Proc. Natl. Acad. Sci. USA.* 101:3979–3984. http://dx.doi.org/10.1073/pnas.0306157101

Woo, S.H., L. Cleemann, and M. Morad. 2002. Ca^{2+} current-gated focal and local Ca^{2+} release in rat atrial myocytes: evidence from rapid 2-D confocal imaging. *J. Physiol.* 543:439–453. http://dx.doi.org/10.1113/jphysiol.2002.024190

Wu, J.Y., J. Vereecke, E. Carmeliet, and S.L. Lipsius. 1991. Ionic currents activated during hyperpolarization of single right atrial myocytes from cat heart. *Circ. Res.* 68:1059–1069.

Zhou, J., G. Brum, A. Gonzalez, B.S. Launikonis, M.D. Stern, and E. Ríos. 2003. Ca^{2+} sparks and embers of mammalian muscle. Properties of the sources. *J. Gen. Physiol.* 122:95–114. http://dx.doi.org/10.1085/jgp.200308796

Zhou, J., G. Brum, A. González, B.S. Launikonis, M.D. Stern, and E. Ríos. 2005. Concerted vs. sequential. Two activation patterns of vast arrays of intracellular Ca^{2+} channels in muscle. *J. Gen. Physiol.* 126:301–309. http://dx.doi.org/10.1085/jgp.200509353

ZhuGe, R., K.E. Fogarty, R.A. Tuft, L.M. Lifshitz, K. Sayar, and J.V. Walsh Jr. 2000. Dynamics of signaling between Ca^{2+} sparks and Ca^{2+}-activated K^+ channels studied with a novel image-based method for direct intracellular measurement of ryanodine receptor Ca^{2+} current. *J. Gen. Physiol.* 116:845–864. http://dx.doi.org/10.1085/jgp.116.6.845

Zima, A.V., J. Kockskämper, R. Mejia-Alvarez, and L.A. Blatter. 2003. Pyruvate modulates cardiac sarcoplasmic reticulum Ca^{2+} release in rats via mitochondria-dependent and -independent mechanisms. *J. Physiol.* 550:765–783. http://dx.doi.org/10.1113/jphysiol.2003.040345

1.4 Двофарбні Ca^{2+} зображення стимулу та відповіді в серцевому міоциті

Оптичні сенсори вимірюють зміни концентрації хімічних речовин, але їхні сигнали можуть бути обмежені чутливістю при низьких концентраціях і насиченням сенсора при високих концентраціях, або навпаки. Дослідження клітинної фізіології часто вимагають вимірювань у діапазонах, що виходять за межі можливостей одного флуоресцентного барвника – монітора. Це було очевидно при дослідженні реакції клітин серцевих і скелетних м'язів на штучне, локальне підвищення рівня $[Ca^{2+}]$ - так звані "штучні спалахи Ca^{2+}". Такі зміни можуть широко варіюватися, так само як і очікувані клітинні відповіді, що включали вивільнення Ca^{2+} з саркоплазматичного депо. Для точного моніторингу концентрації Ca^{2+} в межах декількох величин було використано підхід з використанням двох флуоресцентних барвників з різною спорідненістю, але зі спільним флуорофором, що дозволило зберегти інші спектральні області для додаткових вимірювань або застосувань.

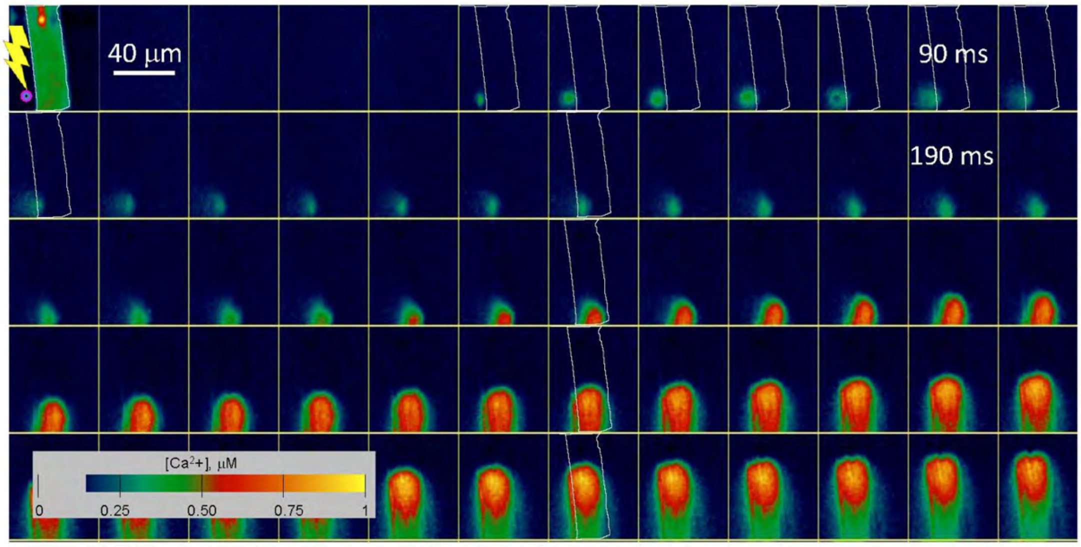

Рисунок 1.8. Вивільнення кальцію в кардіоміоциті передсердя. Зображення $[Ca^{2+}]$, отримані за допомогою рівняння 4 (Figueroa, 2013 #110), з флуоресценції Fluo-4 і Fluo-4FF. Представлені зображення, з яких показано кожен п'ятий кадр, були отримані з інтервалом в 1.8 мс. На першому знімку показана флуоресценція в стані спокою, а також ділянка, де між 5-им і 6-им кадрами було застосовано інфрачервоне світло для вивільнення Ca^{2+} з NP-EGTA та створення штучного спалаху. Ca^{2+}, вивільнений під час спалаху, досягає мембрани і викликає розповсюджену відповідь. "Тригер $[Ca^{2+}]$" вимірюється на клітинній мембрані на кадрі, позначеному як "90 мс". На вибраних кадрах

контур клітини, простежений на першому кадрі, відтворений білим кольором. Незначне зміщення контуру та Ca^{2+}-транзієнта на останніх зображеннях відображає скорочення клітини.

Як показано на рис. 1.8, цитозольний вміст [Ca^{2+}] у кардіоміоциті передсердя кроля було визначено за допомогою флуоресценції Fluo-4 та Fluo-4FF. Клітину, плазмалему якої було пермеабілізовано сапоніном, помістили у внутрішній розчин з відомими концентраціями обох барвників і стимулювали невеликим штучним Ca^{2+}-спалахом. Спалах генерували за рахунок двофотонного розщеплення Ca^{2+}, зв'язаного з NP-EGTA, у концентрації 0.4 мМ. Фотолітичне збудження та отримання зображень здійснювали за допомогою двоконфокального сканера (LSM 5 DUO; Carl Zeiss, Оберкочен, Німеччина).

Клітинна відповідь, яка полягає в вивільненні Ca^{2+} з саркоплазматичного ретикулуму, призводить до поширення хвилі Ca^{2+}. Використання двох барвників надає розширений діапазон, що дозволяє точно, швидко та майже лінійно відстежувати цю хвилю, а також точно візуалізувати штучний спалах. Зокрема, "тригер [Ca^{2+}]" вимірюється у точці, де Ca^{2+} зі штучного спалаху досягає клітинної мембрани, в момент, що передує першому натяку на відповідь (на кадрі з інтервалом 90 мс). Цей тригерний рівень [Ca^{2+}], який в даному прикладі становить 240 нМ, є лише на 50 нМ вищим за рівень [Ca^{2+}] в стані спокою. Систематично змінюючи інтенсивність та тривалість інфрачервоного світла, можна змінити тригерний рівень [Ca^{2+}], щоб визначити мінімальний рівень або "порогове значення [Ca^{2+}]" з точністю до 10 нМ.

Поєднання двох синтетичних флуоресцентних зондів з однаковим флуорофором і різною афінністю до Ca^{2+} дозволило нам розширити діапазон концентрацій, які можна відстежувати з високою точністю. Хоча діапазон концентрацій можна аналогічно розширити, використовуючи барвники різних спектрів, використання двох зондів з одним і тим же флуорофором зберігає інші області спектру для одночасного моніторингу інших параметрів.

OPEN ACCESS Freely available online

PLOS ONE

Using Two Dyes with the Same Fluorophore to Monitor Cellular Calcium Concentration in an Extended Range

Lourdes Figueroa[1], **Vyacheslav M. Shkryl**[2], **Lothar A. Blatter**[1], **Eduardo Ríos**[1]*

1 Section of Cellular Signaling, Department of Molecular Biophysics and Physiology, Rush University, Chicago, Illinois, United States of America, **2** Department of General Physiology of the Nervous System, Laboratory of Biophysics of Ion Channels, A.A. Bogomoletz Institute of Physiology, Kiev, Ukraine

Abstract

We extend the sensitivity of quantitative concentration imaging to an approximately 1000-fold range of concentrations by a method that uses two fluorescent dyes with the same fluorophore, having different affinity for the monitored species. While the formulation and illustration refer to a monitor of calcium concentration, the method is applicable to any species that binds to multiple indicators with the same spectral properties. The use of a common fluorophore has the virtue of leaving vast regions of the electromagnetic spectrum available for other applications. We provide the exact analytic expression relating measured fluorescence to [Ca^{2+}] at equilibrium and an approximate analytic expression that does not require the equilibrium assumption. The sensitivity of the method is calculated numerically for two useful dye pairs. As illustrative application of the enhanced measurement, we use fluo-4 and fluo-4FF to image the calcium wave produced by a cardiac myocyte in response to a small artificial calcium spark.

Citation: Figueroa L, Shkryl VM, Blatter LA, Ríos E (2013) Using Two Dyes with the Same Fluorophore to Monitor Cellular Calcium Concentration in an Extended Range. PLoS ONE 8(2): e55778. doi:10.1371/journal.pone.0055778

Editor: Bradley Steven Launikonis, University of Queensland, Australia

Received November 23, 2012; **Accepted** January 4, 2013; **Published** February 7, 2013

Funding: This work was supported by grants from the National Center for Research Resources, Rush University's Hasterlik Philanthropic Fund and the National Institute of Arthritis and Musculoskeletal and Skin Diseases, NIAMS, (AR049184 and AR032808) to E. Ríos, and the National Heart and Lung Institute (HL62231, HL80101 and HL101235) and the Leducq Foundation to L. Blatter. The funders had no role in study design, data collection and analysis, decision to publish, or preparation of the manuscript.

Competing Interests: The authors have declared that no competing interests exist.

* E-mail: erios@rush.edu

Introduction

Optical sensors of concentration of a chemical species typically yield a signal (a change in fluorescence, absorbance or another measurable property) that grows with the concentration of the indicator bound to the monitored species. Therefore, the signals are limited at low concentrations by the sensitivity and at high concentration by the saturation of the sensor.

Research in cell physiology often calls for dynamic measurement in ranges wider than can be handled by a single monitor. Specifically, we found such need while exploring the response of cardiac and skeletal muscle cells to imposed increases in free [Ca^{2+}]. The procedure was to apply as stimuli synthetic local increases in [Ca^{2+}] (here called "artificial Ca^{2+} sparks") [1], while monitoring the cellular response, expected to consist in release of Ca^{2+} from cellular stores. The applied artificial sparks could be varied in a wide range, from nM to tens of µM, while the cellular responses, the subject of the investigation, were also expected to vary widely. Many other situations can be envisioned that require the ability to monitor precisely the concentration of Ca^{2+} or other species over several orders of magnitude.

To achieve precision within an extended Ca^{2+} concentration range we implemented an approach using two fluorescent dyes with different affinities and a common fluorophore. The advantage of this approach is that it leaves other spectral regions free for additional fluorescence measurements, or other photoconversion applications. In the following we derive the equations necessary to interpret fluorescence images obtained with pairs of dyes and then provide an example use of the technique.

Results and Discussion

Theory

While the method was derived for and will be illustrated with Ca^{2+} sensors, the equations and procedures are independent of the nature of the monitored species. In our laboratory we have used Ca^{2+}-sensitive dyes with the fluorescein fluorophore: fluo-4, with $K_D = 0.45$ µM (determined in our lab), fluo-4FF, with $K_D = 9.7$ µM and fluo-5N, with $K_D = 90$ µM (provided by manufacturers).

For the derivation we assume that the aqueous solution (typically equilibrated with the cytosol) contains a Ca^{2+} sensor D of dissociation constant K_D at total concentration D_T, and a sensor E of dissociation constant K_E at concentration E_T. At steady free concentration [Ca^{2+}] the following equations apply:

$$\frac{[Ca^{2+}](D_T - CaD)}{CaD} = K_D \tag{1}$$

$$\frac{[Ca^{2+}](E_T - CaE)}{CaE} = K_E \tag{2}$$

And the fluorescence F is

$$F = (D_T - CaD)m_D + (E_T - CaE)m_E + CaD\,M_D + CaE\,M_E \tag{3}$$

where CaD and CaE are concentrations, and m_j and M_j represent the molar fluorescence of dye j in its free and Ca^{2+}-bound forms.

F is a single-valued, monotonically increasing function of [Ca^{2+}]. An explicit representation of it can be derived from Eqs. 1–3. This function can be inverted, to derive the free [Ca^{2+}] from *F*, as follows

$$[Ca^{2+}] = \frac{\left[\begin{array}{l}\sqrt{\left[\begin{array}{l}(E_T{}^2 K_D{}^2 M_E{}^2 + (2D_T\, E_T\, K_D K_E\, M_D - 2E_T{}^2 K_D K_E\, m_E + (2D_T\, E_T\, K_D{}^2 - 4D_T\, E_T\, K_D K_E) m_D + 2E_T\, F\, K_D K_E - 2E_T\, F\, K_D{}^2) M_E \\ + D_T{}^2 K_E{}^2\, M_D{}^2 + ((2D_T\, E_T\, K_E{}^2 - 4D_T\, E_T\, K_D K_E) m_E - 2D_T{}^2 K_D K_E m_D - 2D_T\, F\, K_E{}^2 + 2D_T\, F K_D K_E) M_D + E_T{}^2 K_E{}^2 m_E{}^2 + \\ (2D_T\, E_T\, K_D\, K_E\, m_D - 2E_T\, F\, K_E{}^2 + 2E_T\, F\, K_D K_E) m_E + D_T{}^2 K_D{}^2 m_D{}^2 + (2D_T\, F\, K_D K_E - 2D_T\, F\, K_D{}^2) m_D + F^2 K_E{}^2 - 2F^2 K_D K_E + F^2 K_D{}^2\end{array}\right]} \\ - E_T\, K_D M_E - D_T\, K_E M_D - E_T\, K_E m_E - D_T\, K_D m_D + F\, K_E + F\, K_D)\end{array}\right]}{2E_T\, M_E + 2D_T\, M_D - 2F} \tag{4}$$

(Analytical expressions for the concentrations *CaD* and *CaE* can also be derived from equations 1–3 and are available to the reader upon request).

Fig. 1A plots, in red, $\log_{10}$ [Ca^{2+}] vs. *f*, which is *F* normalized to its maximum ($D_T\ M_D$+$E_T\ M_E$), for fluo-4 and fluo-4FF used at equal concentrations. For comparison the same function for fluo-4FF alone is plotted in black. The dependence is in this case

$$[Ca^{2+}] = K_E \frac{F - E_T\, m_E}{E_T\, M_E - F} = K_E \frac{f-1}{R-f} \tag{5}$$

where *R* is the dynamic range, M_E/m_E, of dye E.

The purpose of using two dyes is to extend the range of concentrations that can be measured with high sensitivity. The sensitivity of the dual dye method is compared with that of a single dye in Fig. 1B. The plot in black represents the sensitivity of the single dye, defined as

$$S = \frac{df}{d(\log_{10}[Ca^{2+}])} \tag{6}$$

namely, the slope of the corresponding function in Fig. 1A. The sensitivity, defined logarithmically, peaks at a concentration equal to the dissociation constant of the monitoring reaction. If the change in [Ca^{2+}], rather than its log, is used in the definition, *S* will be maximal at [Ca^{2+}] = 0 and decrease monotonically with increasing dye occupancy. In red is the sensitivity, defined again by function (6), for the two-dye case of fluo-4 and fluo-4FF. Given that the dissociation constants are 0.45 and 9.7 µM, the range of high sensitivity is extended to greater than two orders of magnitude. For an additional comparison we plotted in green trace the sensitivity attained with equal concentrations of fluo-4 and the low affinity dye fluo-5N.

In the representation of Fig. 1B the sensitivity of the two-dye methods is high in an extended range, but it is lower than the maximum attained with the single dye. This is strictly a matter of definition. If sensitivity is defined using the absolute fluorescence change, the two dyes will simply add their contributions.

The derivation above assumed equilibrium between both dyes and calcium. The assumption will not be valid when the goal is to monitor rapid changes with high affinity dyes. The equation that relates [Ca^{2+}] to dye-Ca^{2+} concentrations without assuming equilibrium is

$$\frac{[Ca^{2+}](D_T - CaD)}{CaD + k_{off}{}^{-1}\ d\,CaD/dt} = K_D \tag{7}$$

and there is a corresponding equation for dye E.

We could not integrate analytically the partial differential system constituted by these kinetic equations and equation 3. We could however provide an approximate solution, with the reasonable assumption that the low affinity dye, E, is in

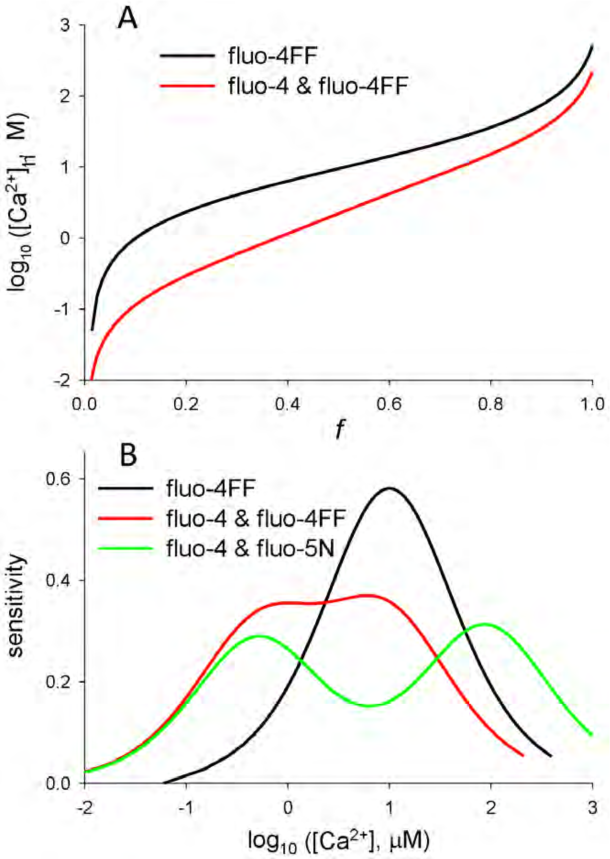

Figure 1. Combining the working ranges of Ca^{2+}-sensitive dyes with the fluorescein fluorophore. *A*, the function relating steady free [Ca^{2+}] to normalized fluorescence, for a single dye (black, equation 5) or two dyes (red, equation 4). *B*, the sensitivity, defined by equation 6, of the single dye (black), or pairs of dyes (red and green).
doi:10.1371/journal.pone.0055778.g001

equilibrium. The approximation therefore provides a kinetic correction for any lag in the reaction of dye D.

A first step is to recognize a relationship between the rates of change of *CaD* and fluorescence *F*.

$$\begin{aligned}\frac{dF}{dt}&=\frac{dCaD}{dt}(M_{\mathrm{D}}-m_{\mathrm{D}})+\frac{dCaE}{dt}(M_{\mathrm{E}}-m_{\mathrm{E}})\\&=\frac{dCaD}{dt}M_{\mathrm{D}}+\frac{dCaE}{dt}M_{\mathrm{E}}\end{aligned}\tag{8}$$

where the simplification is valid for all non ratiometric dyes of high dynamic range, including the fluorescein-based ones in the example below.

An additional simplification should apply whenever the two dyes have very different affinities, namely, when the technique is used as intended. The rate of change of the concentration of the low affinity dye should be negligible in the concentration range detected by the high affinity dye, which is the only range where a kinetic correction is warranted. In this range

$$\frac{dCaD}{dt}=\frac{dF}{dt}\times\frac{1}{M_{\mathrm{D}}}\tag{9}$$

which substituted in equation 7 yields

$$\frac{[Ca^{2+}](D_T-CaD)}{CaD+h}=K_D\tag{10}$$

h represents the known term $M_{\mathrm{D}}{}^{-1}\,k_{\mathrm{off}}{}^{-1}\,\mathrm{d}F/\mathrm{d}t$.

The system of equations 2, 3 and 10 can be solved for [Ca^{2+}], *CaD* and *CaE*. The expression for [Ca^{2+}] is

$$[Ca^{2+}]=\frac{\left[\sqrt{\begin{bmatrix}(E_T{}^2m_{\mathrm{E}}{}^2+(2D_T\,E_T\,M_{\mathrm{D}}-2E_TF)\,m_{\mathrm{E}}+(D_T{}^2M_{\mathrm{D}}{}^2-2D_T\,F\,M_D+F^2)K_E{}^2\\+\begin{pmatrix}((2E_T\,m_D-2E_TM_D)m_E+(-4E_TM_E-2D_TM_D-2F)m_D+4E_TM_{\mathrm{D}}M_{\mathrm{E}}+2D_T\,M_{\mathrm{D}}{}^2\\-2F\,M_D)h+(2D_TE_Tm_D-2E_T{}^2M_E-4D_TE_TM_D+2E_TF)m_E\\+(-4D_T\,E_T\,M_{\mathrm{E}}-2D_T{}^2\,M_{\mathrm{D}}+2D_T\,F)m_{\mathrm{D}}+(2D_TE_TM_D+2E_TF)M_{\mathrm{E}}+2D_T\,F\,M_{\mathrm{D}}-2F^2\end{pmatrix}K_{\mathrm{D}}K_{\mathrm{E}}\\+\begin{pmatrix}+(m_D{}^2-2M_D\,m_{\mathrm{D}}+M_D{}^2)h^2+2D_Dm_D{}^2+(2E_T\,M_{\mathrm{E}}-2D_T\,M_{\mathrm{D}}-2\,F)m_{\mathrm{D}}-2E_T\,M_{\mathrm{D}}M_{\mathrm{E}}+2F\,M_{\mathrm{D}})h\\+D_{\mathrm{T}}{}^2m_D{}^2-2F^2K_{\mathrm{D}}K_{\mathrm{E}}+F^2K_{\mathrm{D}}{}^2+(2D_TE_TM_E-2D_T\,F)m_D+E_T{}^2M_{\mathrm{E}}{}^2-2E_TF\,M_E+F^2\end{pmatrix}K_{\mathrm{D}}{}^2\end{bmatrix}}\\+(-E_T\,m_{\mathrm{E}}-D_T\,M_{\mathrm{D}}+F)\,K_{\mathrm{E}}+((M_D-m_D)h-E_T\,M_{\mathrm{E}}-D_T\,m_{\mathrm{D}}+F)\,K_{\mathrm{D}}\right]}{2E_T\,M_{\mathrm{E}}+2D_T\,M_{\mathrm{D}}-2F}\tag{11}$$

It should be noted that the validity of this equation only extends to the range where equation 9 applies. Equation 11 does not apply when the low affinity dye contributes significantly to the rate of change of fluorescence. Conveniently, an increase in the contribution of the low affinity dye to the signal will in general also reduce the need for a kinetic correction.

Analytical expressions of the concentrations *CaD* and *CaE* with kinetic corrections, are also available to the interested reader.

Experimental example

As an example Fig. 2 shows cytosolic [Ca^{2+}] in a rabbit atrial cardiomyocyte, derived from fluorescence of fluo-4 and fluo-4FF. The cell, whose plasmalemma was permeabilized with saponin, was immersed in an internal solution with known concentrations of both dyes and was stimulated by a small artificial Ca^{2+} spark. The spark was produced by two-photon lysis of the Ca^{2+} cage NP-EGTA, present at a concentration of 0.4 mM. Photolytic irradiation and image acquisition were carried out with a dual confocal scanner (LSM 5 DUO; Carl Zeiss, Oberkochen, Germany).

The resting fluorescence of the cell is represented in the first frame (in a highly expanded color scale). The artificial spark was produced outside the cell by brief irradiation at a diffraction-limited spot 3 µm away from the plasmalemma (target in first frame) with IR light pulsed for two-photon excitation. Images were acquired at one frame every 1.8 ms. The figure shows one every five images of this set (therefore the interval between the frames shown is 9 ms).

The cellular response, consisting in Ca^{2+} release from the sarcoplasmic reticulum, results in a propagating Ca^{2+} wave. The extended range of the two-dye technique allows for accurate, fast, nearly linear monitoring of the wave and precise imaging of the artificial spark. Note in particular the “trigger [Ca^{2+}]” measured at the point where Ca^{2+} in the artificial spark reaches the cell membrane, at a time just before the first hint of a response (the frame at 90 ms). This trigger [Ca^{2+}], 240 nM in the example, was just 50 nM above the resting [Ca^{2+}] level. By systematically varying the intensity and duration of IR light, trigger [Ca^{2+}] could be varied to find a minimum trigger, or “threshold [Ca^{2+}]”, which could be defined with a precision of 10 nM. The ability to measure [Ca^{2+}] in an extended range with a single fluorophore is being used to advantage in current applications, in which we add imaging of [Ca^{2+}]$_{\mathrm{SR}}$ by SEER of fluorescence of mag-indo-1 [2], a ratiometric method that uses excitation and emission lights of lower wavelengths.

Some limitations in the applicability of the technique should be acknowledged. The use of two dyes of different affinity extends the measurable range of concentrations but cannot be construed as providing an extended range where linearity between signal and concentration applies. The linear range is limited to that of the low affinity dye. If the two affinities are very different there may be an additional approximately linear range, at concentrations where the high affinity dye is saturated.

The calculation of [Ca^{2+}] with equation 4 is exact, unless it changes too rapidly compared with the dye reaction rates. The equation requires knowledge of both dye concentrations, which is accurate when cells are permeabilized, as in the example, but may constitute a problem in other cases.

In summary, the combination of two synthetic fluorescent sensors with the same fluorophore and different Ca^{2+} affinity allowed us to extend the range of concentrations that can be monitored with high precision. While the range of concentrations can be similarly extended using dyes of different spectra, the dual application of a single fluorophore preserves other regions of the spectrum for simultaneously monitoring other variables.

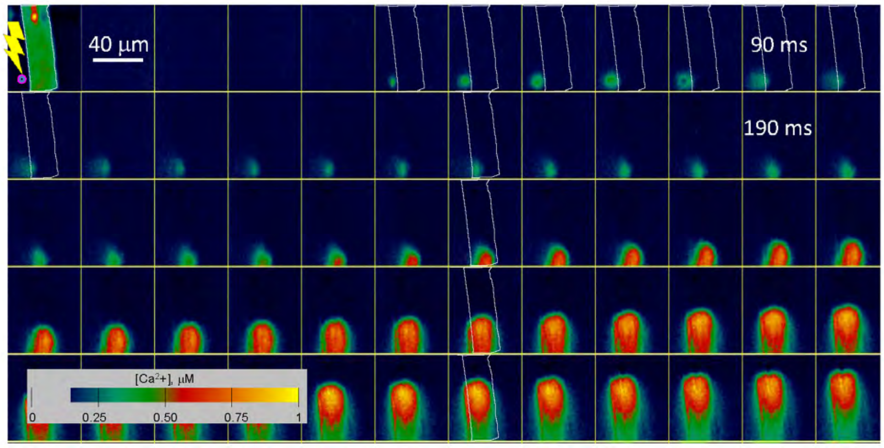

Figure 2. Two-dye images of stimulus and response in a cardiac cell. Images are of [Ca^{2+}] derived by equation 4 from fluorescence of fluo-4 and fluo-4FF. The cell, an atrial cardiomyocyte, was enzymatically dissociated and its plasma membrane permeabilized by saponin. Frames, of which one of every 5 is shown, were acquired at 1.8 ms intervals. The first frame shows resting fluorescence and also the spot where IR light is applied, between the 5th and 6th frames, to un-cage Ca^{2+} from NP-EGTA and produce the artificial spark. Ca^{2+} in the spark reaches the membrane and elicits a propagated response. "Trigger [Ca^{2+}]" is measured at the cell membrane in the frame marked "90 ms". In selected frames, the cell contour traced on the first frame is reproduced in white. A slight offset of contour and Ca^{2+} transient in the last images reflects contractile movement.
doi:10.1371/journal.pone.0055778.g002

Methods

Ethics Statement

The experiment illustrated in Fig. 2 was carried out on single cardiomyocytes isolated from rabbit heart. The investigation conforms to the Guide for the Care and Use of Laboratory Animals of the National Institutes of Health. Procedures and protocols for animal handling and cell isolation were fully approved by the Institutional Animal Care and Use Committee of Rush University Medical Center (Animal Welfare Assurance number A-3120-01; specific protocol permit number 09-055). All efforts were made to minimize suffering.

Preparation of cells and photorelease of caged Ca^{2+}

Briefly, animals were anesthetized with thiopental sodium (50 mg kg−1, I.P.). After thoracotomy, hearts were excised, mounted on a Langendorff apparatus, and retrogradely perfused via the aorta with Liberase Blendzyme TH containing solution (37°C). Myocytes were used for experimentation within 1–6 hours after isolation. Myocytes adhered to the coverslip bottom of a custom chamber on the stage of a microscope, where its plasma membrane was permeabilized by saponin treatment (0.002% for 2 min). Photolytic irradiation and simultaneous image acquisition were carried out with a dual confocal scanner (LSM 5 DUO (Carl Zeiss, Oberkochen, Germany)) combining a slit scanner (LSM 5 *LIVE*) for rapid image acquisition with a conventional pinhole scanner (LSM 510) for irradiation. The spark was produced by two-photon lysis of the Ca^{2+} cage NP-EGTA, which was present in the experimental solution at a concentration of 0.4 mM and equilibrated with a free [Ca^{2+}] of 190 nM. A diffraction-limited spot 3 µm away from the plasmalemma was irradiated for 1 ms with IR light of 710 nm pulsed for two-photon excitation. Images were acquired at one frame every 1.8 ms. [Ca^{2+}] was derived from fluorescence according to equation 4. Parameters D_T and E_T were known in the applied solution. D_T and E_T inside the cell were calculated according to resting fluorescence, assuming that [Ca^{2+}], M_D, m_D, M_E and m_E in cytosol were the same as in the solution, and that both dyes bound equally inside the cell. The molar fluorescence parameters were determined separately in solution for both dyes. Additional details of solution composition, perfusion, irradiation and image acquisition and processing were provided previously [3].

Acknowledgments

We are grateful to Carlo Manno (Rush University) for reading the manuscript. This work was supported by grants from the National Center for Research Resources, Rush University's Hasterlik Philanthropic Fund and the National Institute of Arthritis and Musculoskeletal and Skin Diseases, NIAMS, (AR049184 and AR032808) to E. Ríos, and the National Heart and Lung Institute (HL62231, HL80101 and HL101235) and the Leducq Foundation to Blatter LA.

Author Contributions

Conceived and designed the experiments: ER LB VS LF. Performed the experiments: LF VS ER. Analyzed the data: ER LB. Contributed reagents/materials/analysis tools: ER LB. Wrote the paper: ER.

References

1. Figueroa L, Shkryl VM, Zhou J, Manno C, Momotake A, et al. (2012) Synthetic localized calcium transients directly probe signaling mechanisms in skeletal muscle. J Physiol 590: 1389–1411.
2. Launikonis BS, Zhou J, Royer L, Shannon TR, Brum G, et al. (2005) Confocal imaging of [Ca^{2+}] in cellular organelles by SEER. Shifted Excitation and Emission Ratioing of fluorescence. J Physiol 567:523–543.
3. Shkryl VM, Blatter LA, Ríos E (2012) Properties of Ca^{2+} sparks revealed by four-dimensional confocal imaging of cardiac muscle. J Gen Physiol 139: 189–207.

1.5 Інноваційний підхід до просторово-складної дифракційно обмеженої фотоактивації та фотознебарвлення в живих клітинах

Фотоактивовані зонди представляють великий інтерес як інструменти для детального вивчення внутрішньоклітинних сигнальних шляхів на молекулярному рівні. Система освітлення Mosaic від компанії Andor Technology (Саут-Віндзор, штат Коннектикут, США) базується на високошвидкісному масиві індивідуально керованих мікродзеркал, які можуть нахилятися для направлення безперервного лазерного проміння на зразок з точністю наближеною до дифракційних обмежень. Ця система, інтегрована в конфокальний мікроскоп Nikon A1R, була застосована для вивільнення Ca^{2+} або IP_3 та проведення експериментів з фотознебарвлення в декількох геометрично визначених субклітинних областях, одночасно вимірюючи $[Ca^{2+}]$ за допомогою високошвидкісної конфокальної мікроскопії.

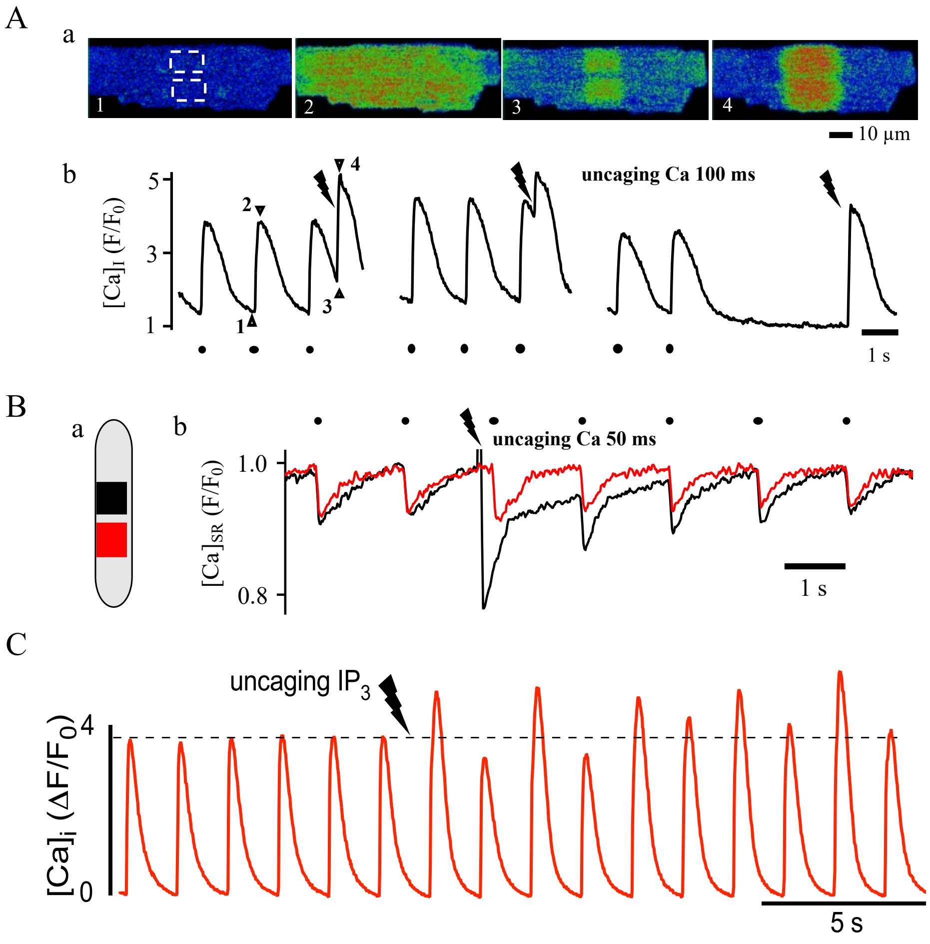

Рисунок 1.9. Вивільнення Ca^{2+} в інтактному кардіоміоциті. (A,a) Fluo-4 флуоресцентні зображення інтактного міоцита шлуночка, завантаженого NP-EGTA. (A,b) Субклітинні транзієнти

Ca^{2+}; вивільнення відбувалося у 2 ROI (405 нм, 100 мс), позначених пунктирними рамками на зображенні no.1 і часово позначених блискавками. Зафарбовані кружечки показують транзієнти Ca^{2+}, ініційовані стимуляцією полем (0.7 Гц). Числа в A,b відповідають зображенням в A,a. (B) Локальні зміни $[Ca^{2+}]_{SR}$ (Fluo-5N) в області ROI вивільнення NP-EGTA (чорна) та контрольній області (червона) в тому ж міоциті. (C) Часовий профіль флуоресценції Fluo-4 в інтактному міоциті, завантаженому речовиною Cag-iso-2-145 (10 мкМ). Вивільнення IP_3 показано блискавкаю.

Вивільнення Ca^{2+} в інтактному кардіоміоциті, який був попередньо завантажений Fluo-4, AM та кейджом NP-EGTA, зображено на рис. 1.9. На A,a зображення 1, пунктиром вказана область вивільнення Ca^{2+} в клітині. Частина A,b демонструє зміни $[Ca^{2+}]$, які були зареєстровані з тих самих ROI. Моменти вивільнення Ca^{2+} під час лазерного збудження (405 нм) відображено у вигляді блискавок у різних точках часу під час циклічних транзієнтів Ca^{2+} під час стимуляції полем з частотою 0.7 Гц або у стані спокою. Амплітуда Ca^{2+}-індукованого вивільнення з СР змінюється в залежності від інтервалу між електрично викликаним транзієнтом і такими, що ініційовані вивільненням з NP-EGTA. Варіації в амплітудах CICR, викликаних вивільненням Ca^{2+} з кейджу, можна пояснити залежним відновленням у часі рефрактерності ріанодинового рецептора. Ці результати свідчать про можливість індукції CICR за допомогою точно спрямованого вивільнення Ca^{2+} з NP-EGTA в інтактних міоцитах, а також про часову залежність цього імпульсу протягом циклу вивільнення Ca^{2+}.

Зміни в концентрації кальцію у люмені СР ($[Ca^{2+}]_{SR}$) після локального вивільнення Ca^{2+} з кейджу в цитоплазмі були досліджені у інтактних міоцитах шлуночків під час їхньої електричної стимуляції (див. рис. 1.9B). У місці локального анкейджінгу в цитоплазмі (чорна лінія) спостерігалося інтенсивне вивільнення Ca^{2+} з СР, після чого потрібно було декілька циклів, щоб вміст Ca^{2+} в СР у цій ділянці повністю відновився. У сусідній області, яка не піддавалася впливу лазерного випромінювання з довжиною хвилі 405 нм, жодних змін у $[Ca^{2+}]_{SR}$ не було зафіксовано. Ці дані демонструють можливість індукції CICR шляхом цільового вивільнення Ca^{2+} з NP-EGTA в строго визначених ділянках інтактних міоцитів шлуночків.

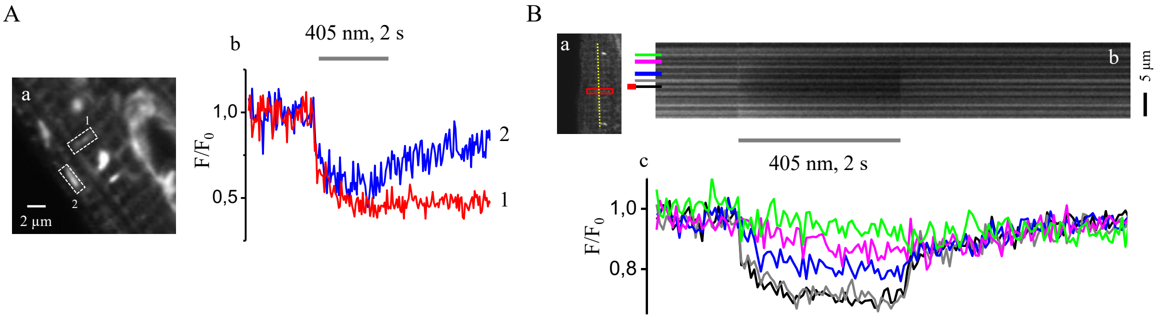

Рисунок 1.10. Експерименти із фотознебарвленням Fluo-5N в СР. (A,b) Динаміка фотознебарвлення Fluo-5N (під дією 405 нм, 2 с) та відновлення його флуоресценції у двох вузьких, перпендикулярно орієнтованих ROI з СР (зображені пунктирними рамками '1' і '2' на панелі A,a). (B,a) Двовимірні зображення флуоресценції Fluo-5N із зони фотознебарвлення та розташування лінійного сканування (позначено жовтою лінією). (B,b) Зображення лінійного сканування, на якому зафіксована флуоресценція Fluo-5N. (B,c) Динаміка фотознебарвлення та відновлення флуоресценції Fluo-5N на окремих ділянках СР у зоні фотознебарвлення (червоний/чорний кольори на панелях b/c) та на зростаючій відстані від зони фотознебарвлення (різні кольори позначають окремі ділянки).

На рис. 1.9C представлено експеримент із інтактним міоцитом передсердя, завантаженим кейджом IP_3. Зв'язаний IP_3 був фотолітично вивільнений з вузької ділянці ROI поблизу сарколеми, де в міоцитах передсердя спостерігається висока концентрація рецепторів IP_3 (Mackenzie et al., 2002). Вивільнення IP_3 може збільшити амплітуду електрично ініційованих транзієнтів Ca^{2+} та викликати Ca^{2+}-альтернації (див. рис. 1.9C). Ці спостереження корелюють з даними про те, що IP_3-залежне вивільнення Ca^{2+} сенсибілізує RyRs до CICR, що сприяє вивільненню Ca^{2+} з СР через RyRs, і призводить до позитивних інотропних та аритмогенних ефектів (Zima and Blatter, 2004).

Система Mosaic була застосована для фотознебарвлення ділянок СР, завантажених Fluo-5N. Рисунок 1.10A,a демонструє типове зображення структур СР та ядерної оболонки, навантажених барвником. Два малих сегмента СР, що включають кілька перпендикулярно орієнтованих з'єднань СР (ROI 1 і 2), були знебарвлені протягом 2 секунд. Рисунок 1.10A,b ілюструє, що кінетика відновлення флуоресценції різнилася в залежності від орієнтації, що свідчить про анізотропні властивості дифузії всередині СР або про характеристики з'єднань у СР (Picht et al., 2011, Zima et al., 2008).

На рис. 1.10B додатково розглядається питання зв'язності всередині мережі СР. Поперекові з'єднань СР був знебарвлений протягом 2 с (червона рамка на рис. 1.10B,a), і були зареєстровані сигнали флуоресценції від окремих з'єднань СР у саркомерних відстанях вздовж пунктирної лінії (див. рис. 1.10B,a). Рисунок 1.10B,b представляє зображення лінійного сканування флуоресценції. На рис. 1.10B,c наведені профілі флуоресценції різних ділянок СР: у місці знебарвлення (червоний/чорний) та на відстані від нього. Поступове зменшення інтенсивності флуоресценції на віддалених ділянках вказує на високу зв'язність перетинів СР, що сприяє дифузії барвника до знебарвлених ділянок. Ці приклади підтверджують, що FRAP-експерименти з використанням системи Mosaic є ефективними для дослідження структурних та функціональних властивостей СР, зі увагою до дифузії та зв’язаності у мережі СР.

Ми представили можливості програмованої цифрової системи освітлення (Mosaic) для фотолізу зв'язаного Ca^{2+} та IP_3 з високою роздільною здатністю. Ця система також була використана для проведення локалізованих FRAP-експериментів у серцевих міоцитах. Дослідження було спрямоване на вивчення внутрішньоклітинної Ca^{2+} сигналізації та структурно-функціональних властивостей вивільнення Ca^{2+} в клітині з безпрецедентною роздільною здатністю.

J Physiol 590.5 (2012) pp 1093–1100

TECHNIQUES FOR PHYSIOLOGY

A novel method for spatially complex diffraction-limited photoactivation and photobleaching in living cells

Vyacheslav M. Shkryl, Joshua T. Maxwell and Lothar A. Blatter

Department of Molecular Biophysics and Physiology, Rush University Medical Center, Chicago, IL 60612, USA

Key points

- For the contraction of a cardiac cell the liberation of calcium ions (Ca^{2+}) from an intracellular Ca^{2+} storing compartment is required.
- This release of Ca^{2+} ions occurs through groups (clusters) of Ca^{2+} release channels that can be activated by cellular signalling molecules such as Ca^{2+} itself or the messenger molecule inositol-1,4,5-trisphosphate (IP_3).
- Here we present a new technique that allows activation of individual release sites or groups of channels in a highly localized manner in living cells and the study of their structural and functional details with high precision.

Abstract Photoactivated probes have gained interest as experimental tools to study intracellular signalling pathways all the way to the molecular level. However technical limitations of the means to activate such compounds have put constraints on their use in spatially highly restricted subcellular areas. The Mosaic digital illumination system uses a high-speed array of individually addressable, tiltable micromirrors to direct continuous-wave laser light onto a specimen with diffraction-limited precision. The system, integrated into a Nikon A1R confocal microscope, was used to uncage Ca^{2+} or IP_3 and conduct photobleaching experiments from multiple geometrically complex subcellular regions while simultaneously measuring $[Ca^{2+}]_i$ with high-speed confocal imaging.

(Received 27 October 2011; accepted after revision 15 December 2011; first published online 19 December 2011)

Corresponding author L. A. Blatter: Department of Molecular Biophysics and Physiology, Rush University Medical Center, 1750 W. Harrison Street, Chicago, IL 60612, USA. Email: lothar_blatter@rush.edu

Abbreviations $[Ca^{2+}]_i$, cytosolic $[Ca^{2+}]$; $[Ca^{2+}]_{SR}$, intra-SR $[Ca^{2+}]$; CICR, Ca^{2+}-induced Ca^{2+} release; DMD, digital micromirror device; FRAP, fluorescence recovery after photobleaching; FWHM, full-width at half-maximum; IP_3, inositol-1,4,5-trisphosphate; LED, light-emitting diode; MEMS, microelectromechanical systems; NE, nuclear envelope; ROI, region of interest; RyR, ryanodine receptor; SR, sarcoplasmic reticulum.

Introduction

Caged compounds are light-sensitive biologically inactive molecules that upon irradiation release the active form of the compound (Adams & Tsien, 1993; Ellis-Davies, 2007). Caged compounds are typically activated by single photon photolysis in the near UV range or by two-photon excitation, and have been used successfully to dissect cellular signalling pathways (Denk, 1994; Lipp & Niggli, 1998; Figueroa *et al.* 2010). While these compounds lend themselves ideally for the study of highly localized subcellular processes with high spatial and temporal

---

V. M. Shkryl and J. T. Maxwell made an equal contribution to this work.

DOI: 10.1113/jphysiol.2011.223446

resolution, such studies have been hampered by technical limitations of simultaneously activating multiple and geometrically complex regions of interest and, at the same time, record the biological response.

Here we demonstrate the use of a programmable digital illumination system (Mosaic; Andor Technology, South Windsor, CT, USA) incorporated into a high-speed high-resolution confocal imaging system (Nikon A1R). The Mosaic incorporates digital mirror device technology that allows projection of a user-defined illumination mask onto the specimen plane and irradiation of the specimen with multiple geometrically complex light patterns of diffraction-limited precision. We demonstrate the capabilities of the Mosaic system for high resolution photolysis of caged Ca^{2+} and IP_3 as well as localized FRAP experiments in cardiac myocytes to investigate intracellular Ca^{2+} signalling and structural and functional properties of intracellular Ca^{2+} release at unprecedented resolution.

Methods

Solutions and chemicals

All chemicals and reagents were purchased from Sigma-Aldrich (St Louis, MO, USA), unless noted otherwise. Intact myocytes were superfused with Tyrode solution containing (in mM): 130 NaCl, 4 KCl, 2 $CaCl_2$, 1 $MgCl_2$, 10 D-glucose, 10 Hepes; pH 7.4 with NaOH.

For permeabilized cell experiments myocytes were exposed to 0.005% saponin for 30 s and bathed in an internal solution containing (in mM): 120 potassium aspartate, 15 KCl, 5 KH_2PO_4, 5 MgATP, 0.35 EGTA, 0.12 $CaCl_2$, 0.75 $MgCl_2$, 10 phosphocreatine, 4% dextran (M_r: 40,000), 10 Hepes; pH 7.2 with KOH. Free $[Ca^{2+}]$ and $[Mg^{2+}]$ of this solution were 150 nM and 1 mM, respectively.

All experiments were conducted at room temperature (22–24°C).

Myocyte isolation

Ventricular and atrial myocytes were isolated from New Zealand White rabbits (2.5 kg; Myrtle's Rabbitry, Thompsons Station, TN, USA) (Wu *et al.* 1991; Kockskamper & Blatter, 2002; Domeier *et al.* 2009). Rabbits were anaesthetized with sodium pentobarbital (50 mg kg^{-1}) and hearts were excised and mounted on a Langendorff apparatus. Hearts were retrogradely perfused with nominally Ca^{2+}-free Tyrode solution for 5 min, followed by minimal essential medium Eagle (MEM) solution containing 20 μM Ca^{2+} and 45 μg ml^{-1} Liberase Blendzyme TH (Roche Applied Science, Indianapolis, IN, USA) for 20 min at 37°C. The left ventricular free wall and both atria were removed from the heart and digested for an additional 5 min in the enzyme solution at 37°C. Digested tissue was then minced, filtered and washed in a MEM solution containing 50 μM Ca^{2+} and 10 mg ml^{-1} bovine serum albumin. Isolated cells were kept in MEM solution with 50 μM Ca^{2+} at room temperature (22–24°C) until indicator dye loading and subsequent experimentation. All protocols were approved by the Institutional Animal Care and Use Committee of Rush University Chicago, and comply with US and UK regulations on animal experimentation (Drummond, 2009).

Ca^{2+} dye and caged compound loading

To directly monitor $[Ca^{2+}]_{SR}$ the SR was loaded with the low-affinity Ca^{2+} indicator fluo-5N (Molecular Probes/Invitrogen, Carlsbad, CA, USA) by incubation of ventricular myocytes with 10 μM of the membrane permeant fluo-5N/AM together with 0.25% Pluronic F-127 in nominally Ca^{2+}-free Tyrode solution for 2.5 h, followed by a 30 min wash, all at 37°C. For measurements of cytosolic $[Ca^{2+}]$ ($[Ca^{2+}]_i$) in intact myocytes, cells were incubated at room temperature with 10 μM fluo-4/AM (Molecular Probes/Invitrogen) for 25 min, followed by a 20 min wash. For uncaging experiments intact cells were loaded with 1 μM of the cell permeant Ca^{2+} chelator NP-EGTA/AM (Molecular Probes/Invitrogen) or 10 μM of the caged IP_3 compound ci-$InsP_3$/PM (Cag-iso-2–145; SiChem GmbH, Bremen, Germany) simultaneously with fluo-4 or after fluo-5N dye loading for 25 min and washed for 20 min. In permeabilzed cell experiments the cell impermeant caged Ca^{2+} compound DM-Nitrophen (17 mM; Calbiochem/EMD Chemicals Inc., NJ, USA) was used in conjunction with 50 μm fluo-4 pentapotassium salt in internal solution. For Ca^{2+} uncaging in droplets the internal solution contained 50 μM fluo-4 pentapotassium salt and 2.1 mM NP-EGTA tetrapotassium salt.

$[Ca^{2+}]$ measurements

Confocal microscopy (Nikon A1R, Nikon Instruments Inc., Melville, NY, USA) was used to image $[Ca^{2+}]_{SR}$ (fluo-5N) and $[Ca^{2+}]_i$ (fluo-4), with both dyes excited at 488 nm and emission collected at >500 nm. Changes in $[Ca^{2+}]_{SR}$ are normalized as $[Ca^{2+}]_{SR} = F/F_0$, where F_0 corresponds to the diastolic fluorescence during pacing. All fluorescence signals were background subtracted. Changes in $[Ca^{2+}]_i$ are expressed as F/F_0 (where F_0 refers to resting baseline fluo-4 fluorescence). Action potentials and global Ca^{2+} transients were elicited by electrical field stimulation using a pair of platinum electrodes (voltage set at ∼50% above the threshold for contraction).

Mosaic illumination system and confocal microscopy

Mosaic is a programmable illumination system (Andor Technology, South Windsor, CT, USA) based on microelectromechanical systems (MEMS) technology. At the heart of the system is a digital micromirror device (DMD). The DMD is a programmable high-speed semiconductor-based light switch consisting of a two-dimensional array of hinge-mounted, individually addressable tiltable micromirrors (rise/fall time $<1\,\mu$s; extinction ratio $>$1000:1). In conjunction with a suitable light source (laser, LED, arc lamp), the Mosaic allows the simultaneous illumination of an arbitrary number of complexly shaped user-defined regions of interest (ROIs) with near diffraction limited precision. The Mosaic illumination system used here was integrated into a Nikon A1R confocal imaging system (Nikon) and controlled by the Nikon NIS Elements interface. The image acquisition software allows mapping of a user-defined illumination mask at the specimen plane. The illumination pattern is defined via graphical user interface and is activated/inactivated via a user defined timing script. The Mosaic module was interfaced with a Nikon Eclipse Ti-E inverted microscope, equipped with a Nikon CFI Apochromat TIRF 60× oil (n.a. 1.49) objective, through the epifluorescence port whereas laser illumination for confocal imaging and the dual-scan head of the A1R were connected to the left side-port of the microscope. Light from a 405 nm (400 W) continuous wave (CW) diode laser (Power Technoloy Inc., Little Rock, AR, USA) was utilized for photoactivation and FRAP experiments.

The spatial resolution of the Mosaic illumination system was determined by evaluating the 3-dimensional bleach pattern in an immobile fluorescent medium that resulted from illuminating the smallest possible region of interest ($0.2 \times 0.2\,\mu$m) at a fixed focal plane. The full-width at half-maximum (FWHM) of the bleached volume was $0.54\,\mu$m in both dimensions within the focal plane (i.e. near-diffraction limited), and $1.8\,\mu$m in the axial dimension.

Results

Fluorescence bleaching and Ca^{2+} uncaging with high spatial precision and resolution

Figure 1*Aa* shows an example of bleaching of a highly localized and spatially complex pattern (‘Ca^{2+}’) in an immobile fluorescent medium with the Mosaic system. Figure 1*Ab* is an example of photorelease of caged Ca^{2+} (NP-EGTA) in a complex pattern (‘Ca’) in a droplet containing the Ca^{2+} indicator fluo-4. Upon computer controlled pattern illumination with 405 nm laser light, Ca^{2+} is released from the caged compound within the pattern and then diffuses in the droplet. These results illustrate the precision and complexity by which excitation light can be delivered to the specimen plane and Ca^{2+} can be liberated from the cage.

Next, *in vivo* Ca^{2+} uncaging in an intact cardiomyocyte pre-loaded with NP-EGTA is shown in Fig. 1*B*. The dashed boxes (Fig. 1*Ba*, image 1) show the area of Ca^{2+} uncaging. Figure 1*Bb* shows changes of $[Ca^{2+}]_i$ recorded from the same ROIs. Time points of Ca^{2+} uncaging by laser illumination (405 nm) are shown as lightning bolts at various time points during Ca^{2+} cycling at 0.7 Hz field stimulation or at rest. The amplitude of Ca^{2+}-induced Ca^{2+} release (CICR) from the sarcoplasmic reticulum (SR) varies with the interval between electrically triggered transient and the transient elicited by uncaging. The differences in amplitudes of CICR triggered by Ca^{2+} uncaging are due to time-dependent recovery from refractoriness of the ryanodine receptor (RyR) Ca^{2+} release channel of the SR. In Fig. 1*C*, Ca^{2+} uncaging generated a Ca^{2+} wave that asymmetrically propagated out of the region of uncaging by means of CICR.

Changes of intraluminal $[Ca^{2+}]$ within the SR ($[Ca^{2+}]_{SR}$) after local Ca^{2+} uncaging in the cytoplasm were also examined in intact electrically stimulated ventricular myocytes (Fig. 1*D*). At the site of local cytoplasmic uncaging (black trace) a massive release of Ca^{2+} from the SR occurred after which it required several beats until SR content recovered completely at that location. A neighbouring second location that was not exposed to 405 nm laser light revealed no effect on $[Ca^{2+}]_{SR}$. These results show the feasibility of inducing CICR by precise localized uncaging of Ca^{2+} from NP-EGTA in highly circumscribed regions in intact ventricular myocytes.

Spatially restricted photorelease of Ca^{2+} and IP_3 alters CICR

Figure 2*A* illustrates the ability of the Mosaic system to photoactivate Ca^{2+} from multiple spatially restricted regions ($0.4\,\mu m^2$). Figure 2*Aa* shows a series of 2D confocal images of changes of $[Ca^{2+}]$ after local uncaging of DM-nitrophen in the cytosol of a permeabilized ventricular myocyte as well as in the extracellular space (dashed line = cell border). The fluo-4 fluorescence profile in Fig. 2*Ab* (top) shows that local uncaging of Ca^{2+} in a small ROI generated a spatially restricted local Ca^{2+} signal outside (ii) the cell. The same signal applied to a cystosolic region triggered CICR from an SR Ca^{2+} release site (i). Reducing the uncaging energy (shorter pulse; Fig. 2*Ab*, bottom) generated identical local Ca^{2+} signals inside and outside the cell, and failed to trigger CICR. These data illustrate that uncaging of Ca^{2+} in a near-diffraction limited volume can be used to probe CICR at individual release sites simultaneously in multiple distinct regions of a cell, with the ability to distinguish between a purely photolytical Ca^{2+} signal and the photolysis+CICR signal.

Figure 2*B* shows a series of 2D images and $[Ca^{2+}]_i$ profiles in an intact atrial myocyte loaded with a caged IP_3 compound. Caged IP_3 was photolytically released from a narrow ROI near the sarcolemma where a higher density of IP_3 receptor Ca^{2+} release channels has been reported in atrial myocytes (Mackenzie *et al.* 2002). Upon uncaging the local increase in IP_3 caused a propagating Ca^{2+} wave initiating from the region of uncaging and spreading throughout the entire cell (Fig. 2*B*a). Uncaging of IP_3 was also able to increase the amplitude of electrically evoked Ca^{2+} transients and induced Ca^{2+} alternans (Fig. 2*B*b). These observations are consistent with our previous findings that IP_3-dependent Ca^{2+} release sensitizes RyRs to CICR and facilitates SR Ca^{2+} release from RyRs, leading to positive inotropic and arrhythmogenic effects (Zima & Blatter, 2004).

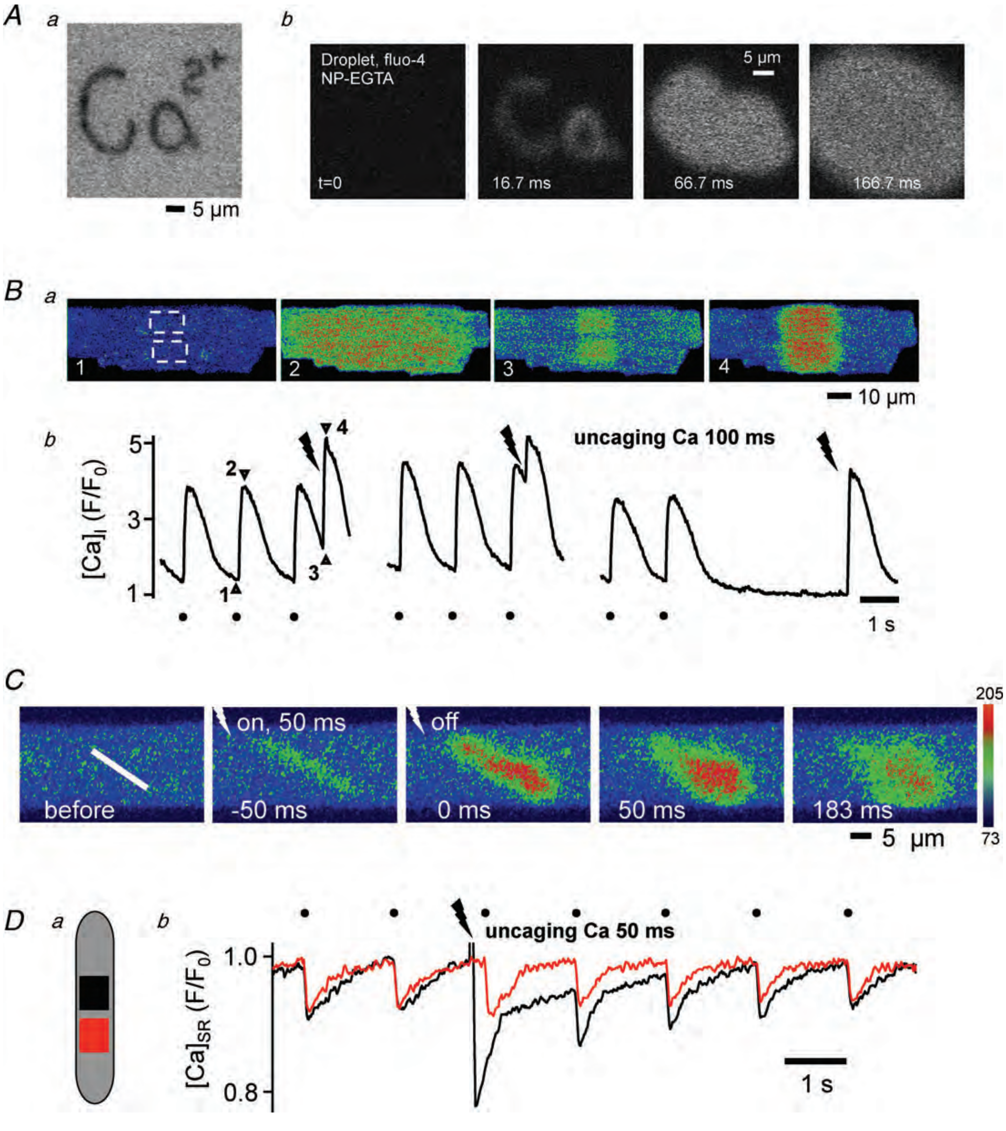

Figure 1. Subcellular uncaging of Ca^{2+}
Aa, complex pattern ('Ca^{2+}') bleaching with Mosaic system in an immobile fluorescent medium. *b*, time series of pattern uncaging ('Ca') of NP-EGTA in a fluo-4 containing solution. *Ba*, Fluo-4 fluorescence images of an intact ventricular myocyte loaded with NP-EGTA. *b*, Subcellular Ca^{2+} transients; uncaging occurred in 2 ROIs (405 nm, 100 ms) marked by the dashed boxes in image no. 1 and at times marked by lightning bolts. Filled circles mark Ca^{2+} transients elicited by field stimulation (0.7 Hz). Numbers in *b* refer to images in *a*. *C*, Ca^{2+} uncaging from a narrow ROI (NP-EGTA; white line, 0.6 μm wide) generated a Ca^{2+} wave which asymmetrically propagated out of the region of uncaging. The colour scale represents arbitrary fluorescence intensity values. *D*, local changes of $[Ca^{2+}]_{SR}$ (Fluo-5N) in a ROI of NP-EGTA uncaging (black) and a control region (red) in the same myocyte.

Spatially restricted photobleaching reveals functional and structural properties of the SR Ca^{2+} store

The Mosaic system was used to photobleach intra-SR regions loaded with fluo-5N. Figure 3*Aa* shows the typical appearance of dye-loaded SR and nuclear envelope (NE) structures. Two small SR segments encompassing a small number of SR junctions of perpendicular orientation (ROI 1 and 2) were bleached for 2s. Figure 3*Ab* shows that the fluorescence recovery kinetics differed depending on orientation, suggesting anisotropic intra-SR diffusion properties and/or connectivity within the SR (Zima *et al.* 2008; Picht *et al.* 2011). Figure 3*B* addresses the question of intra-SR connectivity further. A transverse array of SR junctions was photobleached for 2 s (red box in Fig. 3*Ba*) and fluorescence signals were recorded from individual SR junctions at sarcomeric intervals along the dashed line in Fig. 3*Ba*. Figures 3*Bb* and 3*Bc* show line scan images of recorded fluorescence (F; *b*) and normalized fluorescence (F/F_0; *c*). Figure 3*Bd* shows fluorescence profiles from individual SR junctions at the site of bleaching (red/black) and at increasing distance therefrom. A decremental decrease in fluorescence at distant sites is consistent with high connectivity of SR junctions allowing for dye diffusion into the bleached regions. Note, that in the normalized image (Fig. 3*Bc*) the bright regions, particularly noticeable during the bleaching, represent areas between SR junctions. Figures 3*C* and 3*D* demonstrate that in cardiac myocytes the SR network is not only highly interconnected but is also continuous with the NE. In Fig. 3*C* a transverse row of SR junctions (red) was bleached for 2 s and the changes in fluorescence were recorded from an adjacent SR junction (green) and the nuclear envelope (blue). Dye depletion extended into the nearby NE region. Figure 3*D* demonstrates relatively high dye diffusibility within the NE. Photobleaching of a small segment of the NE caused a rapid decrease of fluorescence that was followed by a slower but nearly as pronounced decline in a distant (>10 μm, blue) NE region. These examples demonstrate that FRAP

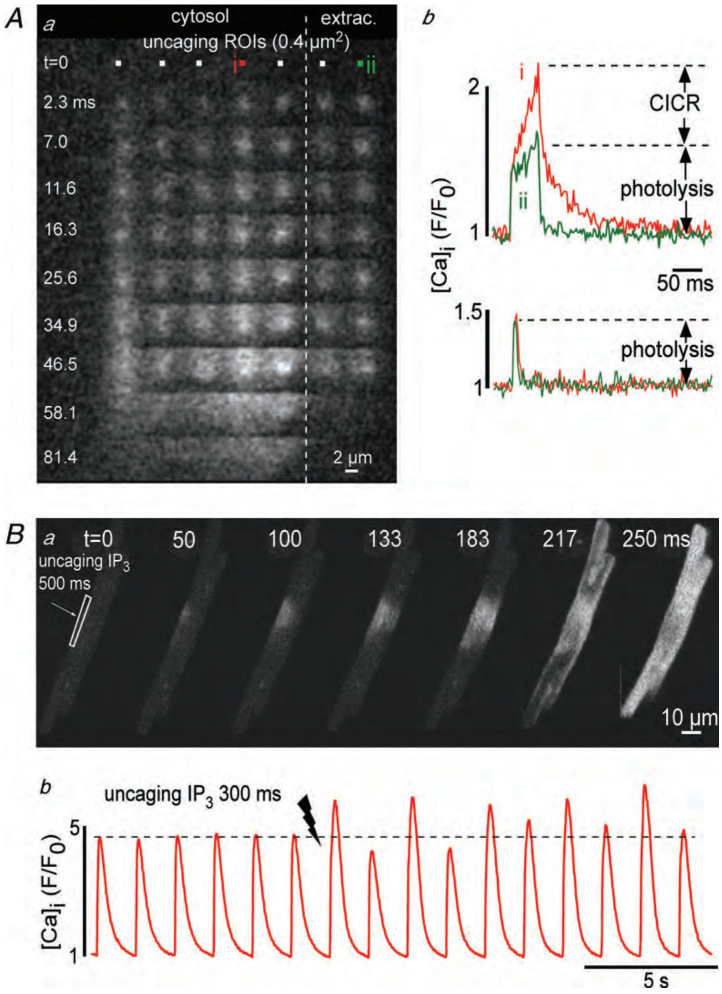

Figure 2. Probing CICR by local uncaging of Ca^{2+} and IP3

Aa, images represent a time series of local changes of [Ca^{2+}] (fluo-4) after simultaneous activation of DM-nitrophen in 7 ROIs (0.4 μm^2) mapped inside and outside (dashed line) of a permeabilized cardiomyocyte. *b*, local Ca^{2+} transients elicited with high (top) and low (bottom) energy 405 nm light pulses inside (i) and outside (ii) of the cell. *B*, IP_3 uncaging in a narrow subsarcolemmal region triggers a propagating Ca^{2+} wave (*a*), enhanced Ca^{2+} transients and elicited Ca^{2+} alternans (*b*).

experiments with the Mosaic system lend themselves for the study of structural and functional SR properties including intra-SR diffusion and connectivity.

Discussion

In this report, we describe how the novel Mosaic digital illumination system integrated into a Nikon A1R confocal microscope can be used to uncage Ca^{2+} or IP_3 from multiple geometrically complex, diffraction-limited subcellular regions and simultaneously measure $[Ca^{2+}]_i$ with high-speed 2D or line scan confocal imaging. We show that with this approach CICR in cardiomyocytes can be studied from multiple individual SR release sites simultaneously. Furthermore highly spatially restricted FRAP experiments allow the study of structural and functional aspects of the SR network.

The system described here also has limitations. The excited region is essentially diffraction limited within the focal plane; however as a wide-field and single-photon illumination system it is not in the axial dimension. While the device provides a rapid control of the photolysis region, photolysis proceeds throughout the specimen as the excitation light passes through. At the focal plane photolysis is largely defined by the pattern written into the micro-mirror device, however this pattern spreads as determined by the numerical aperture of the objective because the exciting beam passes through the entire

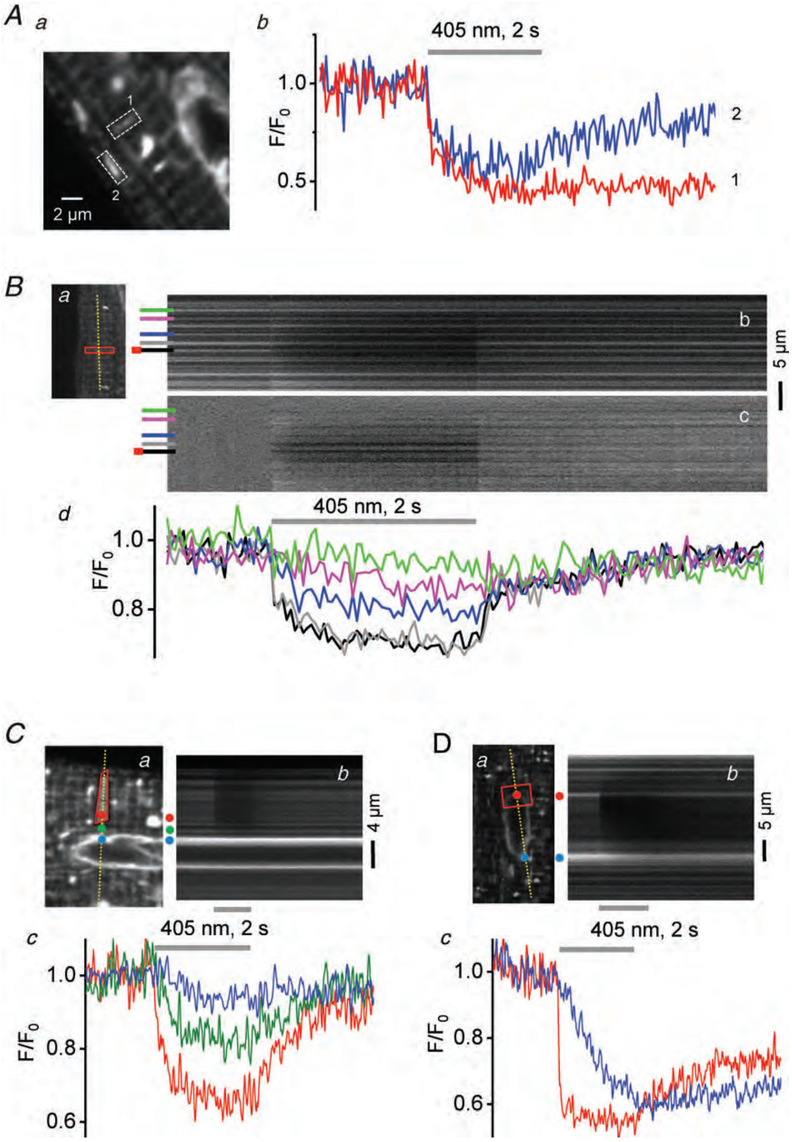

Figure 3. Photobleach experiments of fluo-5N entrapped in the SR
Ab, time course of fluo-5N photobleaching (405 nm, 2 s) and fluorescence recovery in 2 narrow, perpendicularly oriented ROIs of the SR (dashed boxes '1' and '2' in *a*). *Ba*, 2D image of fluo-5N fluorescence with ROI of bleaching and position of line scan. *b* and *c*, line scan images of recorded (*F*; panel *b*) and normalized (F/F_0, panel *c*) fluo-5N fluorescence. *d*, time courses of fluo-5N bleach and recovery at individual SR junctions at the site of bleaching (red/black in panels *b*/*c*) and at increasing distances from bleach (individual junctions marked by different colours). *C* and *D*, Fluo-5N photobleaching and fluorescence recovery in the nuclear envelope and adjacent SR regions. Panels *a*, bleached regions marked by red ROI. Panels *b*, line scan images of fluo-5N fluorescence. Panels *c*, local fluorescence profiles recorded from ROIs marked by coloured dots in panels *a*.

thickness of the cell with the local intensity (which should be proportional to the rate of photolysis) falling with the square of distance from the focal plane. The physiological response will depend on the convolution of the single photon point spread function convolved by both the illumination mask and the dose-response of the system of interest. These limitations set constraints whether indeed single individual Ca^{2+} release sites can be probed with caged compounds or FRAP experiments. Distances between Ca^{2+} release units or couplons in cardiac myocytes have been reported to range between 0.6 and 2 μm (Kockskamper *et al.* 2001; for reference see Hayashi *et al.* 2009), with values for vertical distances of ~0.9–1 μm for rabbit ventricular myocytes (Sachse *et al.* 2009). The dimensions of the excited volume are clearly in the range of an individual release site within the focal plane. However, in the axial dimension the FWHM of the excited volume was 1.8 μm, which exceeds the average distance between neighbouring couplons and is close to twice as large as the axial point-spread function (<1 μm) determined for confocal imaging with a pinhole aperture (~1 airy disk) in place. Nonetheless, the axial dimension of excited volume is smaller than reported for other wide-field systems used for local uncaging (Sobie *et al.* 2007). As shown in Fig. 2*Ab*, to induce local CICR a threshold level of Ca^{2+} is required. Despite the fact that photolysis occurs throughout the entire specimen as the exciting light passes through, the effective volume where concentrations of Ca^{2+} are reached that are sufficient to induce CICR is likely to be considerably smaller. Thus with the appropriate experimental conditions (Ca^{2+} loading of the caged compound, illumination intensity) and with the help of endogenous Ca^{2+} buffers that are particularly efficient in buffering small elevations of $[Ca^{2+}]_i$ it is possible to restrict the functional volume of effective photolysis to encompass only a small number, possibly even a single couplon. When combining uncaging/bleaching with confocal imaging, potential chromatic aberration effects arising from the spectral shifts between different lasers lines used (e.g. 405 nm for photolysis, 488 nm for imaging of the biological response) need to be considered. This effect can be minimized by using highly corrected objective lenses as was done in the present study.

We have demonstrated here only a small number of potential applications for the Mosaic system; however there are numerous possibilities for additional uses. In addition to photobleaching and release of caged compounds, the system can be envisioned to open unprecedented possibilities for highly localized FRET experiments, photoactivation, photoswitching and photoconversion of novel biological compounds, free radical release, spatially constrained drug delivery, and becoming an invaluable tool for the rapidly emerging field of optogenetics (Deisseroth, 2011).

References

Adams SR & Tsien RY (1993). Controlling cell chemistry with caged compounds. *Annu Rev Physiol* **55**, 755–784.

Deisseroth K (2011). Optogenetics. *Nat Methods* **8**, 26–29.

Denk W (1994). Two-photon scanning photochemical microscopy: mapping ligand-gated ion channel distributions. *Proc Natl Acad Sci U S A* **91**, 6629–6633.

Domeier TL, Blatter LA & Zima AV (2009). Alteration of sarcoplasmic reticulum Ca^{2+} release termination by ryanodine receptor sensitization and in heart failure. *J Physiol* **587**, 5197–5209.

Drummond GB (2009). Reporting ethical matters in *The Journal of Physiology*: standards and advice. *J Physiol* **587**, 713–719.

Ellis-Davies GC (2007). Caged compounds: photorelease technology for control of cellular chemistry and physiology. *Nat Methods* **4**, 619–628.

Figueroa L, Shkryl V, Zhou J, Momotake A, Ellis-Davies G, Blatter LA, Rios E & Brum G (2010). CICR and calcium-dependent inactivation, quantified through the response to artificial Ca sparks in single muscle cells. *Biophys J* **98**, 294a.

Hayashi T, Martone ME, Yu Z, Thor A, Doi M, Holst MJ, Ellisman MH & Hoshijima M (2009). Three-dimensional electron microscopy reveals new details of membrane systems for Ca^{2+} signaling in the heart. *J Cell Sci* **122**, 1005–1013.

Kockskamper J & Blatter LA (2002). Subcellular Ca^{2+} alternans represents a novel mechanism for the generation of arrhythmogenic Ca^{2+} waves in cat atrial myocytes. *J Physiol* **545**, 65–79.

Kockskamper J, Sheehan KA, Bare DJ, Lipsius SL, Mignery GA & Blatter LA (2001). Activation and propagation of Ca^{2+} release during excitation-contraction coupling in atrial myocytes. *Biophys J* **81**, 2590–2605.

Lipp P & Niggli E (1998). Fundamental calcium release events revealed by two-photon excitation photolysis of caged calcium in guinea-pig cardiac myocytes. *J Physiol* **508**, 801–809.

Mackenzie L, Bootman MD, Laine M, Berridge MJ, Thuring J, Holmes A, Li WH & Lipp P (2002). The role of inositol 1,4,5-trisphosphate receptors in Ca^{2+} signalling and the generation of arrhythmias in rat atrial myocytes. *J Physiol* **541**, 395–409.

Picht E, Zima AV, Shannon TR, Duncan AM, Blatter LA & Bers DM (2011). Dynamic calcium movement inside cardiac sarcoplasmic reticulum during release. *Circ Res* **108**, 847–856.

Sachse FB, Savio-Galimberti E, Goldhaber JI & Bridge JH (2009). Towards computational modeling of excitation-contraction coupling in cardiac myocytes: reconstruction of structures and proteins from confocal imaging. *Pac Symp Biocomput* 328–339.

Sobie EA, Kao JP & Lederer WJ (2007). Novel approach to real-time flash photolysis and confocal $[Ca^{2+}]$ imaging. *Pflugers Arch* **454**, 663–673.

Wu JY, Vereecke J, Carmeliet E & Lipsius SL (1991). Ionic currents activated during hyperpolarization of single right atrial myocytes from cat heart. *Circ Res* **68**, 1059–1069.

Zima AV & Blatter LA (2004). Inositol-1,4,5-trisphosphate-dependent Ca^{2+} signalling in cat atrial excitation-contraction coupling and arrhythmias. *J Physiol* **555**, 607–615.

Zima AV, Picht E, Bers DM & Blatter LA (2008). Termination of cardiac Ca^{2+} sparks: role of intra-SR [Ca^{2+}], release flux, and intra-SR Ca^{2+} diffusion. *Circ Res* **103**, e105–115.

Author contributions

V.M.S., J.T.M and L.A.B. contributed to the conception and design of the study, analysis and interpretation of data and writing of the manuscript. V.M.S. and J.T.M performed the experimental work. All authors have approved the manuscript.

Acknowledgements

This work was supported by the National Institutes of Health Grants HL62231, HL80101 and HL101235, and the Leducq Foundation.

Author's present address

V. M. Shkryl: Department of General Physiology of Nervous System, A.A. Bogomoletz Institute of Physiology, 4 Bogomoletz Street, Kiev, 01024, Ukraine.

1.6 Рефрактерні властивості вивільнення Ca^{2+} з саркоплазматичного ретикулуму як детермінанта Ca^{2+} альтернацій у міоцитах передсердь

Порушення механізму вивільнення Ca^{2+} з СР або затримка відновлення RyRs може вплинути на періодичні зміни концентрації кальцію збудливої клітини. На клітинному рівні, в кардіоміоцитах були виявлені флуктуації амплітуд цитозольних транзієнтів Ca^{2+} при регулярній частоті стимуляції, які отримала назву альтернації Ca^{2+}.

Альтернації серця розглядаються як визнаний фактор ризику серцевої аритмії та раптової серцевої смерті (Walker and Rosenbaum, 2005). На клітинному рівні, альтернація Ca^{2+} виявляється у вигляді цитозольних транзієнтів Ca^{2+} змінної амплітуди при регулярній частоті стимуляції міоцита. Альтернації серця є результатом взаємодії чисельних факторів, проте вони тісно пов'язані з порушеннями внутрішньоклітинної регуляції рівня Ca^{2+}. У міоцитах передсердь ми вивчали роль потенціалзалежного Ca^{2+}-струму, завантаження Ca^{2+} у СР та реституційних властивостей вивільнення Ca^{2+} з СР у формуванні стимуляція-залежних Ca^{2+}-альтернацій.

Інші фактори, окрім завантаження СР кальцієм, такі як кінетика відновлення вивільнення Ca^{2+} з СР, можуть лежати в основі стимул-стимул серцевих альтернацій. Дійсно, дослідження показали, що відновлення CICR або рефрактерність RyRs-опосередкованого вивільнення Ca^{2+} можуть сприяти нестабільності вивільнення Ca^{2+} у кардіоміоцитах та появі альтернацій (Sobie et al., 2006). Відновлення RyRs-залежного вивільнення Ca^{2+} може відбуватися в часовому масштабі, який співпадає з частотами стимуляції, при якій виникають альтернації. Залежне від часу відновлення вивільнення Ca^{2+} з СР може виявитися критичним фактором для появи Ca^{2+} альтернацій, під час інгібування гліколізу (Hüser et al., 2000).

У першій серії експериментів ми перевірили гіпотезу стосовно можливої флуктуацій кальцієвого струму через L-тип кальцієвого каналу – ICa або діастолічного рівня завантаження СР кальцієм, що може привести до ініціації цитозольних Ca^{2+}-альтернацій у міоцитах передсердь. На рис. 1.11 представлені одночасні записи транзієнтів Ca^{2+} (А) та Ca^{2+} струму (ICa; B) зареєстрованих в міоциті передсердя в умовах фіксації потенціалу. Транзієнти Ca^{2+} ініціювались деполяризацією мембрани до +20 мВ від початкового рівня -40 мВ. У наведеному прикладі стабільні Ca^{2+}-альтернації спостерігалися при частоті стимуляції 1 Гц. Пікове значення ICa (рис. 1.11D) було майже однаковим під час великого (-0.551 нА) і малого (-0.559 нА) транзієнтів Ca^{2+}. Середнє значення відношення амплітуди пікового ICa під час великого транзієнту до малого транзієнту складало 1.008±0.011 (n = 8; рис. 1.11D,b), тобто варіація між стимулами становила менше ніж 1%. При поглибленому аналізі було виявлено, що інактивація ICa дещо швидша під час великого транзієнту Ca^{2+} (синій запис на рис. 1.11D), що відповідає більш вираженій Ca^{2+}-залежній інактивації струму. Крім того, струм, що виникає після реполяризації, був більшим після великоамплітудного транзієнту Ca^{2+}, що вказує на більший вивід Ca^{2+} через поверхневу мембрану за допомогою натрій-кальцієвого обміннику (NCX).

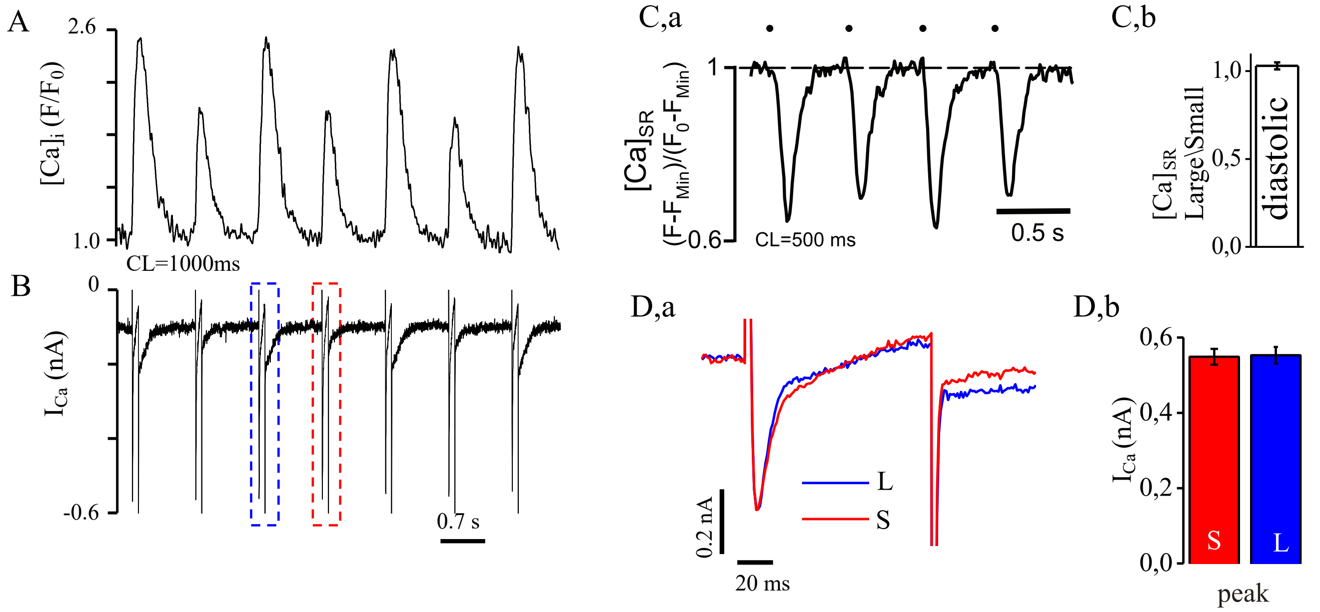

Рисунок 1.11. Аналіз Ca^{2+} струму (ICa) та концентрації Ca^{2+} у СР ($[Ca^{2+}]_{SR}$) під час стимуляції, що індукує Ca^{2+} альтернації. (A) Одночасне вимірювання внутрішньоклітинної концентрації Ca^{2+} ($[Ca^{2+}]$) у міоцитах передсердь кроля. (B) Аналіз ICa за умов фіксації потенціалу. (D,a) Накладення даних ICa, зареєстрованих під час великоамплітудного (L; синій графік) та малоамплітудного (S; червоний графік) транзієнтів Ca^{2+}. Середні амплітуди Ca^{2+}-струмів після малого транзієнту (S) та великого транзієнту (L) зображено на підграфіку (b). (C,a) Вимірювання $[Ca^{2+}]_{SR}$ під час стимуляції, що індукує Ca^{2+} альтернації, з використанням низькоафінного Ca^{2+} індикатора Fluo-5N,

завантаженого в СР. Діастолічний $[Ca^{2+}]_{SR}$ як відношення значень перед малим (S) та великим (L) транзієнтами зображено на підграфіку (b).

У подальших дослідженнях ми вирішили з'ясувати, чи змінюється вміст Ca^{2+} в СР під час Ca^{2+}-альтернацій, використовуючи два різних експериментальних підходи. У першому експерименті ми безпосередньо вимірювали рівень $[Ca^{2+}]_{SR}$ за допомогою низькоафінного індикатора Ca^{2+} Fluo-5N, який був завантажений в СР. Як можна бачити на рис. 1.11C,a кінцевий діастолічний рівень $[Ca^{2+}]_{SR}$ перед значним виснаженням СР при великому транзієнті збігався із рівнем $[Ca^{2+}]_{SR}$, зареєстрованим безпосередньо перед транзієнтом меншої амплітуди. Співвідношення діастолічного $[Ca^{2+}]_{SR}$ перед великим і малим транзієнтами виснаження СР Ca^{2+} дорівнювало 1.03±0.02 (n = 9; рис. 1.11C,b), що свідчить про можливість виникнення Ca^{2+}-альтернацій при стабільному рівні діастолічного $[Ca^{2+}]_{SR}$.

По-друге, ми швидко прикладали 10 мМ кофеїн після великого та малого транзієнта Ca^{2+} під час альтернації, реєструючи цитозольний $[Ca^{2+}]$. Цей підхід дозволив вимірювати вміст СР з субклітинною локалізацією (субсарколемальний j-SR проти центрального nj-SR) за допомогою лазерної скануючої конфокальної мікроскопії. На рис. 1.12A,a представлені усереднені амплітуди транзієнтів Ca^{2+} викликані стимуляцією полем для j-SR. Середнє співвідношення коефіцієнта альтернації (AR) становило 0.54±0.03 для j-SR і 0.61±0.04 для nj-SR (n = 10). Як зазначено на рис. 1.12A,c, відмінності в амплітуді рівня вивільнення Ca^{2+}, індукованого кофеїном (або завантаження СР Ca^{2+}), після великого і малого альтернуючих транзієнтів не спостерігались, так саме як і відмінності між j-SR та nj-SR. Це свідчить про однаковий вміст кальцію в СР перед великим, чи малим Ca^{2+} транзієнтами при альтернаціях кальцію. Наші результати підтвердили попередні вимірювання в міоцитах передсердь (Hüser et al., 2000).

Отже, отримані дані вказують на те, що альтернації цитозольних транзієнтів Ca^{2+} відбуваються за відсутності міжімпульсних змін фізіологічного тригера – кальцієвого струму (ICa) для CICR під час процесу збудження-скорочення. Крім того, для виникнення Ca^{2+} альтернації не потрібні зміни кінцевого діастолічного рівня $[Ca^{2+}]$. Причому, за умов нашого експерименту, можна виключити, що зміни амплітуд

ICa та вміст кальцію в СР є основними детермінантами цитозольних альтернацій Ca^{2+}. Це узгоджується з попередніми результатами досліджень міоцитів передсердь і шлуночків (Hüser et al., 2000, Picht et al., 2006). Тому, в наступних експериментах ми зосередилися на вивченні кінетики рефрактерності вивільнення Ca^{2+} з СР під час Ca^{2+} альтернацій.

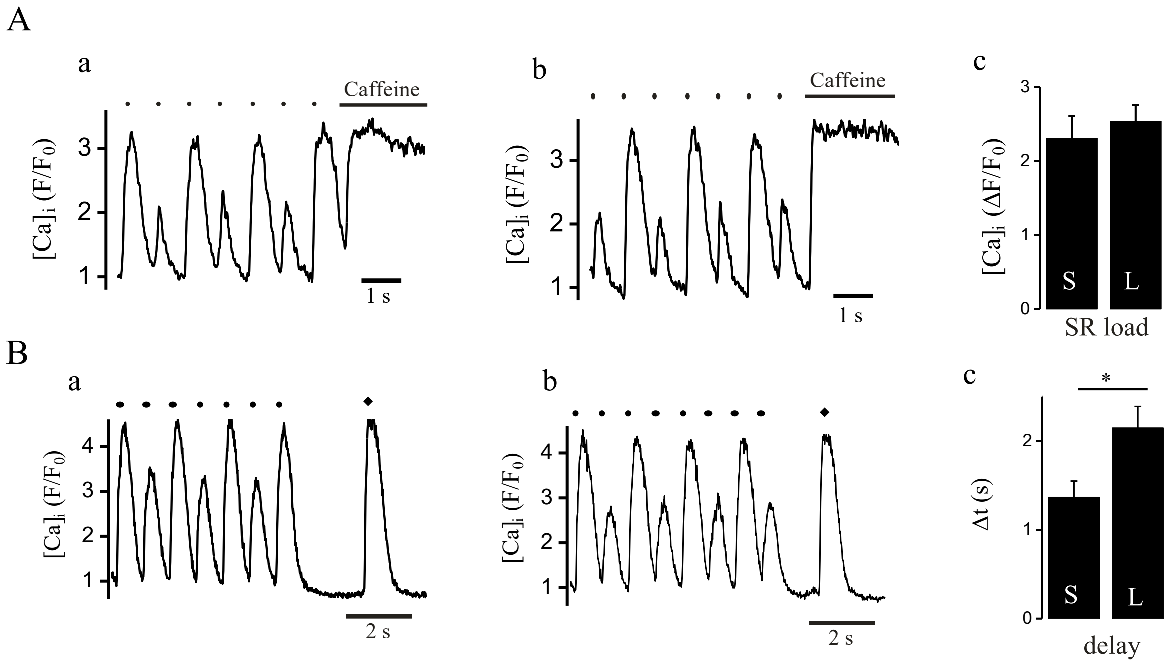

Рисунок 1.12. Глобальні події вивільнення Ca^{2+} при альтернаціях. (A) Субклітинні Ca^{2+}-транзієнти, зафіксовані з субсарколемального СР під час стимуляції, які викликають Ca^{2+}-альтернації. Навантаження СР з Ca^{2+} розраховувалося за амплітудою сигналу [Ca^{2+}], індукованого швидким прикладенням кофеїну (10 мМ) після великого (a) та малого (b) Ca^{2+}-транзієнту під час альтернацій. Середні амплітуди локальних Ca^{2+}-транзієнтів індукованих кофеїном під час альтернації (навантаження SR Ca, n = 14 після малого транзієнту (S) і n = 11 після великого транзієнту (L)) зображено на підграфіку (b). (B) Спонтанне вивільнення Ca^{2+} під час паузи після стимуляції, при Ca^{2+}-альтернаціях. Спонтанні глобальні події вивільнення Ca^{2+} (відзначені суцільними ромбами) зафіксовані протягом 10-секундної паузи після великого (a) та малого (b) альтернуючого Ca^{2+}-транзієнту. Значення [Ca^{2+}] усереднено по ширині клітини. Середній час затримки спонтанного глобального вивільнення Ca^{2+} після малого та великого транзієнту під час альтернацій зображено на підграфіку (частина c; n = 6).

Щоб оцінити доступність або рефрактерність механізму вивільнення Ca^{2+} після Ca^{2+}-транзієнту в умовах альтернації, ми індукували Ca^{2+}-альтернацію шляхом стимуляції і вимірювали час до появи (латентність) спонтанного глобального вивільнення Ca^{2+} (наприклад, у вигляді Ca^{2+}-хвилі або спонтанного ПД) протягом періоду спокою після стимуляції. На рис. 1.12B представлено час появи спонтанного глобального вивільнення Ca^{2+} після великого транзієнту Ca^{2+} (a) та малого транзієнту Ca^{2+} (b). Середня латентність спонтанного глобального вивільнення Ca^{2+} (див. рис. 1.12B,c) була 1.41±0.24 с після малого транзієнту і 2.12±0.42 с після великого транзієнту ($n = 6$, $P < 0.05$). Значно коротша латентність після малого Ca^{2+}-транзієнту порівняно відповідним часом після великого транзієнту свідчить про те, що рефрактерність механізму вивільнення Ca^{2+} з СР значно зменшується після малого транзієнту або збільшується після великого транзієнту.

Відновлення вивільнення Ca^{2+} з СР після його інактивації під час альтернації було додатково вивчено за допомогою методики, де ступінчасте збільшення $[Ca^{2+}]$ під час альтернації викликалося за рахунок фотолітичного вивільнення Ca^{2+} з його зв'язаного стану у кейджу (DM-nitrophen (Kaplan and Ellis-Davies, 1988)). Вивільнення Ca^{2+} з СР за допомогою анкейджінгу з DM-nitrophen отримало назву "вивільнення Ca^{2+}, індуковане фотолізом" (PICR). Міоцити передсердь аналізували методом фіксації потенціалу методом петч-клемп, стимулюючи їх 100-мс деполяризаційними імпульсами від -40 до +20 мВ на частотах, що викликали стабільні альтернації Ca^{2+}. Імпульси УФ (355 нм) лазера (зображено символом блискавки) подавалися на початку деполяризаційного імпульсу (час 0 на рис. 1.13A) або через певні проміжки часу від 50 до 300 мс після початку деполяризації (рис. 1.13, B і C). Цей протокол використовувався двічі для виведення реакції на штучне збільшення кальцію з однаковою затримкою під час малого (перша серія, червоний сигнал) та великого транзієнту Ca^{2+} (друга серія, синій сигнал). До застосування імпульсу УФ-лазера для анкейджінгу проводили принаймні 10 деполяризаційних імпульсів для досягнення уніфікованого навантаження СР Ca^{2+}. На рис. 1.13A наведено приклад, де імпульс ультрафіолетового випромінювання подавався одночасно з імпульсом деполяризуючої напруги, під час альтернуючих Ca^{2+} транзієнтів. В обох серіях амплітуда транзієнту, викликаного комбінованим впливом деполяризаційного імпульсу та УФ-флеш спалаху, перевищувала амплітуду, спричинену лише деполяризацією мембрани (зазначимо, що деполяризація до +20 мВ призводила максимальну Ca^{2+}-відповідь при однакових експериментальних умовах; дані не представлені). Це безпосередньо свідчить про те, що кальцієвий струм ICa, який є фізіологічний тригер CICR, ICa, не вивільняє весь доступний Ca^{2+} з СР і що під час альтернації, коли відбувається невеликий транзієнт, у СР залишається достатня кількість Ca^{2+}. При цьому, при наявності достатньо сильного тригера, можливе подолання рефрактерності механізму вивільнення. Як зображено на рис. 1.13А, амплітуда транзієнту Ca^{2+}, викликаного комбінацією деполяризації мембрани і УФ-флеш спалаху, була вищою після малого транзієнту (очікуючи великий транзієнт, синя лінія) порівняно з тим після великого транзієнту (червона лінія). На рис. 1.13A,b ця відмінність оцінювалася за допомогою коефіцієнта альтернацій (AR), який визначався як відношення амплітуди малого до великого альтернуючих кальцієвих транзієнтів.

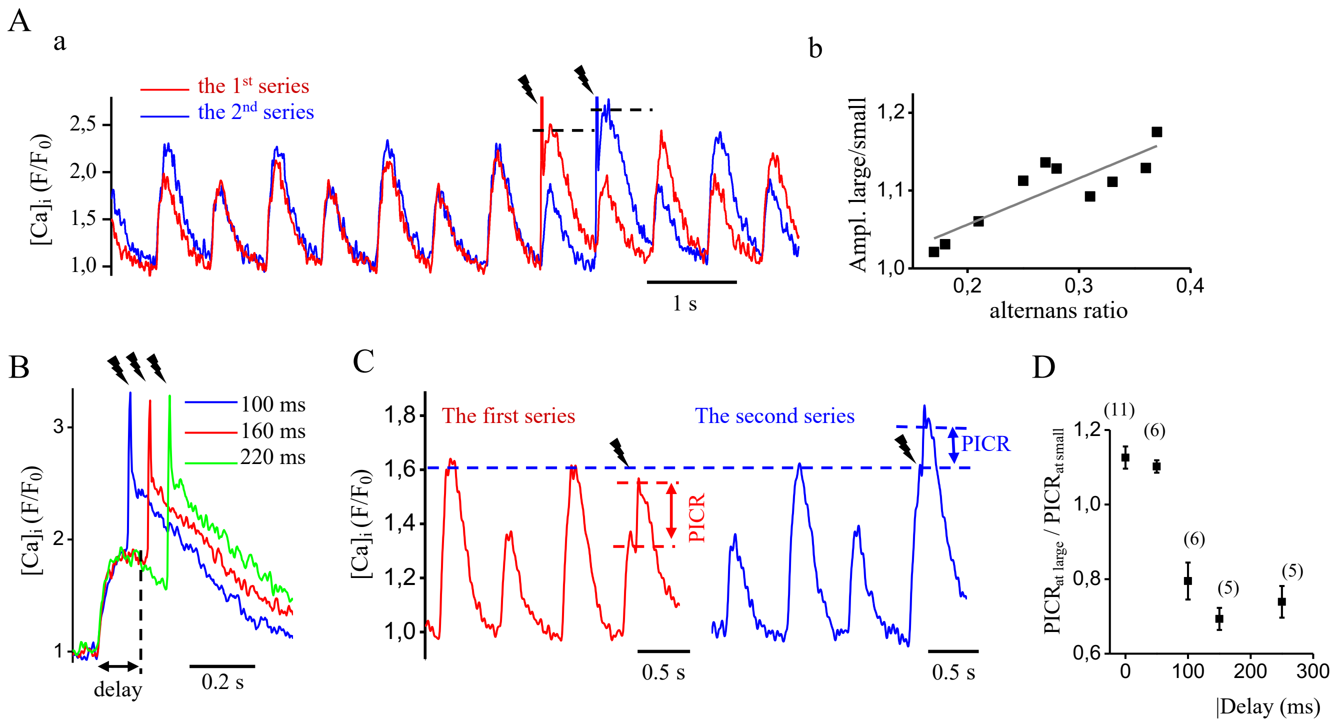

Рисунок 1.13. Рефрактерність вивільнення Ca^{2+} з СР під час Ca^{2+} альтернації, досліджена за допомогою вивільнення Ca^{2+}, індукованого фотолізом (PICR). (A) Дві серії Ca^{2+} альтернацій, викликані 100-мс імпульсами деполяризації до +20 мВ з початкового потенціалу в -40 мВ. (A,a) Ультрафіолетові (355 нм) лазерні імпульси (позначено блискавкою) були застосовані для фотолітичного вивільнення Ca^{2+} одночасно з початком деполяризаційного імпульсу при очікуваному малоамплітудному (червоний; перша серія) та великоамплітудному (синій; друга серія)

Ca^{2+}-транзієнтах. (A,b) Кореляція між AR, індукованою стимуляцією, і сигналом [Ca^{2+}], викликаним комбінацією деполяризації та CICR і УФ-флеш спалахом (PICR). (B) Три приклади PICR, застосовані із затримками 100, 160 та 220 мс під час деполяризаційних Ca^{2+}-транзієнтів. (C) Фотовивільнення зв'язаного Ca^{2+} під час малих (перша серія) та великих (друга серія) транзієнтів Ca^{2+} (з затримкою 150 мс після початку деполяризаційного імпульсу) та визначення амплітуди PICR. (D) Середнє співвідношення PICR під час великих і малих транзієнтів Ca^{2+} ($PICR_L/PICR_S$) як функція затримки між деполяризаційним імпульсом та УФ-флеш спалахом. Кількість досліджуваних клітин вказана у дужках.

Клітини з найвиразнішою AR для транзієнтів Ca^{2+}, викликаних деполяризацією мембрани, також демонстрували найбільшу розбіжність між амплітудами транзієнтів Ca^{2+}, викликаних комбінованою деполяризацією (CICR) та УФ-флеш імпульсом (PICR). Оскільки кінцевий діастолічний [Ca^{2+}] був однаковим перед подачею імпульсу (червона та синя лінії), а також враховуючи наше спостереження, що при [Ca^{2+}] $\geq$ 300 нМ сигнал вивільнення Ca^{2+} залишався сталим, можна припустити, що навантаження Ca^{2+} в кейджі було ідентичним. Таким чином, однакова кількість Ca^{2+} вивільнялася з клітини, незалежно від того, що [Ca^{2+}] коливався під час цитозольного Ca^{2+}-транзієнту. Отже, різниця в амплітуді [Ca^{2+}] виникала через відмінності у PICR. Чим більший коефіцієнт альтернації тім більше розбіжність між малим і великими транзієнтами викликаними комбінацією деполярізації та флеш-фотолізу, що свідчить про зміну рефрактерності при альтернаціях кальцію.

На рис. 1.13C наведено приклад, у якому УФ-флеш спалах був застосований через 150 мс після початку деполяризаційного імпульсу під час малого транзієнту Ca^{2+} (червона лінія) і великого транзієнту Ca^{2+} (синя лінія). Додаткове вивільнення Ca^{2+} через фотоліз DM-nitrophen (PICR) було більшим під час малого Ca^{2+} транзієнту ($\Delta F/F_0$ PICR становив 0.25 для малого та 0.17 для великого Ca^{2+} транзієнтів). Для кількісної оцінки кінетики відновлення вивільнення кальцію під час альтернацій ми порівнювали PICR, отримані під час малих та великих альтернантів Ca^{2+}, при різних часових затримках після деполяризації та фотолітичного вивільнення. Було побудовано графік, який відображає співвідношення PICR під час великого до малого транзієнтів ($PICR_L/PICR_S$) відносно затримки (див. рис. 1.13D). При цьому $PICR_L$ представлено у відсотках від $PICR_S$ для кожної конкретної затримки. Для УФ-флеш спалахів, поданих у момент часу 0 (без затримки) та із затримкою 50 мс, відношення $PICR_L/PICR_S$ перевищувало 1, свідчить про те, що під час великого транзієнту на початку деполяризації канали вивільнення RyRs були повністю доступні і могли активуватися максимально під впливом комбінації деполяризаційного імпульсу та УФ-флеш спалаху. Протягом інтервалу від піку Ca^{2+} транзієнту до його спаду (100-250 мс) відношення $PICR_L/PICR_S$ зменшувалося, досягаючи мінімуму приблизно через 150 мс. Ці результати свідчать про те, що під час альтернації частка RyRs, яка залучена до вивільнення Ca^{2+}, коливається з кожним новим стимулом. Під час великого транзієнту більша частина RyRs залучена до вивільнення, і, отже, більша частина каналів переходить у рефрактерний стан, стаючи тимчасово недоступними для подальшої активації. Протилежна ситуація спостерігається під час малого транзієнту. У підсумку, ці дані надають переконливі докази тому, що коливання властивостей реституції та кінетики механізму вивільнення Ca^{2+} відіграють ключову роль у формуванні Ca^{2+}-альтернацій.

Відновлення тривалості потенціалу дії, яке включає відновлення Ca^{2+}-каналів L-типу після потенціал- та Ca^{2+}-залежної інактивації, а також секвестрування Ca^{2+} (зокрема, зворотне захоплення Ca^{2+} в СР та відновлення Ca^{2+}-завантаження (Cutler et al., 2009, Xie et al., 2008)), є відомими факторами, що викликають електромеханічні та Ca^{2+}-альтернації. Ще однією можливою причиною може бути рефрактерність CICR або тимчасова недоступність RyRs після вивільнення, що може призводити до нестабільності вивільнення Ca^{2+} у серцевій м'язовій тканині. У даному дослідженні ми аналізували ряд параметрів, які безпосередньо або опосередковано взаємодіють з процесом реституції вивільнення Ca^{2+} з СР. Проведені експерименти підтвердили, що під час альтернацій кінетика рефрактерності вивільнення Ca^{2+} з СР збільшується після велико амплітудного транзієнту. Ми дійшли до висновку, що залежність від часу відновлення рефрактерністі та реституції вивільнення Ca^{2+} з СР є ключовими факторами для генерації Ca^{2+} альтернацій. Аналогічні висновки про важливість рефрактерності вивільнення Ca^{2+} з СР для виникнення альтернацій були отримані на основі досліджень ролі люмінального Ca^{2+} у вивільненні в інтактних клітинах серця миші (Kornyeyev et al., 2010), а також при спільній активності Ca^{2+} спалахів. У цих дослідженнях рефрактерність центрів вивільнення Ca^{2+} після Ca^{2+} спалаху була визначена як вирішальний фактор, що визначає появу серцевих альтернацій (Rovetti et al., 2010). Отже, ми підтвердили, що ключовим механізмом, що лежить в основі серцевих альтернацій, є залежні від часу властивості реституції та кінетика відновлення механізму вивільнення Ca^{2+} з СР.

Am J Physiol Heart Circ Physiol 302: H2310–H2320, 2012.
First published March 30, 2012; doi:10.1152/ajpheart.00079.2012.

Refractoriness of sarcoplasmic reticulum Ca^{2+} release determines Ca^{2+} alternans in atrial myocytes

Vyacheslav M. Shkryl, Joshua T. Maxwell, Timothy L. Domeier, and Lothar A. Blatter

Department of Molecular Biophysics and Physiology, Rush University Medical Center, Chicago, Illinois

Submitted 27 January 2012; accepted in final form 26 March 2012

Shkryl VM, Maxwell JT, Domeier TL, Blatter LA. Refractoriness of sarcoplasmic reticulum Ca^{2+} release determines Ca^{2+} alternans in atrial myocytes. *Am J Physiol Heart Circ Physiol* 302: H2310–H2320, 2012. First published March 30, 2012; doi:10.1152/ajpheart.00079.2012.—Cardiac alternans is a recognized risk factor for cardiac arrhythmia and sudden cardiac death. At the cellular level, Ca^{2+} alternans appears as cytosolic Ca^{2+} transients of alternating amplitude at regular beating frequency. Cardiac alternans is a multifactorial process but has been linked to disturbances in intracellular Ca^{2+} regulation. In atrial myocytes, we tested the role of voltage-gated Ca^{2+} current, sarcoplasmic reticulum (SR) Ca^{2+} load, and restitution properties of SR Ca^{2+} release for the occurrence of pacing-induced Ca^{2+} alternans. Voltage-clamp experiments revealed that peak Ca^{2+} current was not affected during alternans, and alternans of end-diastolic SR Ca^{2+} load, evaluated by application of caffeine or measured directly with an intra-SR fluorescent Ca^{2+} indicator (fluo-5N), were not a requirement for cytosolic Ca^{2+} alternans. Restitution properties and kinetics of refractoriness of Ca^{2+} release after activation during alternans were evaluated by four different approaches: measurements of *1*) the delay (latency) of occurrence of spontaneous global Ca^{2+} releases and *2*) Ca^{2+} spark frequency, both during rest after a large and small alternans Ca^{2+} transient; *3*) the magnitude of premature action potential-induced Ca^{2+} transients after a large and small beat; and *4*) the efficacy of a photolytically induced Ca^{2+} signal (Ca^{2+} uncaging from DM-nitrophen) to trigger additional Ca^{2+} release during alternans. The results showed that the latency of global spontaneous Ca^{2+} release was prolonged and Ca^{2+} spark frequency was decreased after the large Ca^{2+} transient during alternans. Furthermore, the restitution curve of the Ca^{2+} transient elicited by premature action potentials or by photolysis-induced Ca^{2+} release from the SR lagged behind after a large-amplitude transient during alternans compared with the small-amplitude transient. The data demonstrate that beat-to-beat alternation of the time-dependent restitution properties and refractory kinetics of the SR Ca^{2+} release mechanism represents a key mechanism underlying cardiac alternans.

calcium alternans; ryanodine receptor; refractoriness; sarcoplasmic reticulum calcium release

CARDIAC ALTERNANS is a recognized risk factor for cardiac arrhythmia and sudden cardiac death (58, 60, 61) and has been directly linked to atrial fibrillation (26, 42), the most common form of cardiac arrhythmia (43). At the cellular level, cardiac alternans is defined by cyclic, beat-to-beat variations in contraction amplitude (mechanical alternans), action potential (AP) duration (APD; electrical or APD alternans), and Ca^{2+} transient amplitude (Ca^{2+} alternans) at constant stimulation frequency (e.g., Ref. 65). A plethora of experimental conditions and interventions have been demonstrated to cause and modulate cardiac alternans, suggesting a multifactorial process. Nonetheless, it has become increasingly clear that alternans is ultimately linked to disturbances in myocardial Ca^{2+} homeostasis and impaired intracellular Ca^{2+} concentration ($[Ca^{2+}]_i$) regulation (for reviews, see Refs. 6, 11, 17, 19, 21, 22, 37, 41, and 48). Based on the theory of cardiac Ca^{2+} cycling, computational studies, and experimental data (for reviews and references, see Refs. 63 and 64), two parameters have emerged as critically relevant to the beat-to-beat regulation of $[Ca^{2+}]_i$ and the generation of alternans: fractional Ca^{2+} release and the efficiency of cytosolic Ca^{2+} sequestration. Fractional release of Ca^{2+} refers to the nonlinear relationship between the Ca^{2+} content of the sarcoplasmic reticulum (SR) and the amount of Ca^{2+} (or fraction of SR Ca^{2+} content) released by Ca^{2+}-induced Ca^{2+} release (CICR) with each cardiac cycle, where at a higher SR Ca^{2+} content a larger fraction is liberated upon activation of CICR (3). Ca^{2+} sequestration is a phenomenological parameter that refers to the net efficiency of clearing the cytosolic compartment of Ca^{2+} and includes Ca^{2+} reuptake into the SR via sarco(endo)plasmic reticulum Ca^{2+}-ATPase (SERCA), extrusion via the Na^+/Ca^{2+} exchanger (NCX) and plasmalemmal Ca^{2+}-ATPase, cytosolic buffering, mitochondrial uptake, and diastolic SR Ca^{2+} leak [via ryanodine receptor (RyR)-mediated SR Ca^{2+}-release channels or other pathways; see Ref. 69]. The nonlinear relationship between Ca^{2+} sequestration and fractional release determines the vulnerability to alternans (see Fig. 6 in Ref. 63). The relationship predicts that, in general, factors increasing Ca^{2+} load and fractional release promote alternans and factors increasing Ca^{2+} sequestration protect against alternans. Thus, under low Ca^{2+} sequestration conditions (e.g., because of reduced SERCA activity or enhanced diastolic SR Ca^{2+} leak) alternans can occur at relatively modest SR loads and small fractional releases, whereas at high sequestration rates higher Ca^{2+} loads and fractional release are required to induce alternans. The boundary between stability and instability (alternans) of Ca^{2+} cycling is not linear. The boundary is shallow in the low sequestration range and becomes steep at high sequestration rates. That is, at low sequestration rates the transition from stability to instability is dominated by changes in fractional release, whereas at higher sequestration rates small changes in Ca^{2+} sequestration become critical for the occurrence of alternans.

The beat-to-beat dynamics of both Ca^{2+} sequestration and fractional release are critically dependent on the restitution properties and refractory kinetics of the SR Ca^{2+}-release mechanism. The amount of Ca^{2+} released during a given heart beat, and thus the magnitude of the Ca^{2+} transient, is determined by the recovery of the trigger of CICR, SR Ca^{2+} load, and the release mechanism itself (RyRs and associated regulatory proteins) of the preceding beat. APD restitution (including the recovery of L-type Ca^{2+} channels from voltage- and

---

Address for reprint requests and other correspondence: L. A. Blatter, Dept. of Molecular Biophysics and Physiology, Rush Univ. Medical Center, 1750 W. Harrison St., Chicago, IL 60612 (e-mail: Lothar_Blatter@rush.edu).

Ca^{2+}-dependent inactivation) has been recognized as causative and/or contributing factors to electromechanical and Ca^{2+} alternans and may play a role, particularly at high heart rates (for reviews, see Refs. 63 and 64). The role of reuptake of Ca^{2+} into the SR and reestablishing Ca^{2+} load have been the subject of numerous investigations (12, 30, 68) together with the controversial question of whether cardiac alternans requires beat-to-beat alternations in SR Ca^{2+} content and end-diastolic SR filling (15) or not (28). While it has been suggested that instability in the beat-to-beat feedback control of SR content leads to Ca^{2+} alternans (18), direct dynamic measurements of Ca^{2+} concentration in the SR ($[Ca^{2+}]_{SR}$) revealed that alternans can readily occur without significant diastolic $[Ca^{2+}]_{SR}$ fluctuations (44). These results raise the intriguing possibility that factors other than SR Ca^{2+} load, such as the kinetics of restitution of SR Ca^{2+} release (or time dependence of the refractoriness of the Ca^{2+}-release mechanism) centrally underlie pacing-induced cardiac alternans. Indeed, recent findings have provided evidence that the recovery of CICR or refractoriness of RyR-mediated Ca^{2+} release may contribute to the instabilities of cardiac Ca^{2+} release and vulnerability to arrhythmias (56). Experimental studies on the recovery of Ca^{2+} transients as well as Ca^{2+} sparks (i.e., Ca^{2+} release at the local level of individual SR Ca^{2+}-release units) (7, 8, 47, 52, 55, 57) have raised the possibility that the recovery of RyR-dependent Ca^{2+} release may occur on a time scale that overlaps with the stimulation frequencies at which Ca^{2+} alternans occurs. The time-dependent recovery of SR Ca^{2+} release may become a critical factor for the occurrence of Ca^{2+} alternans when recovery is slowed, a mechanism we have proposed to contribute to alternans during inhibition of glycolysis (28).

Therefore, the goal of the present investigation was to test the hypothesis that beat-to-beat alternations in the restitution kinetics of SR Ca^{2+} release cause Ca^{2+} alternans in atrial tissue. The focus was placed on atrial myocytes for several reasons: *1*) atrial arrhythmias (particularly atrial fibrillation) are the most common and most prevalent form of cardiac arrhythmia (e.g., Ref. 43) and have been linked directly to alternans (26, 42); *2*) at the cellular level, due to the lack of a t-tubular membrane system and the special features of Ca^{2+} release during excitation-contraction coupling (27, 33, 39, 40, 53, 66), atrial myocytes are particularly susceptible to pacing and metabolically induced Ca^{2+} alternans (28, 34); and *3*) Ca^{2+} alternans can be subcellularly inhomogeneous (1, 2, 15, 24), which is again particularly pronounced in atrial tissue (28, 32). We have demonstrated subcellular transverse and longitudinal gradients of the degree of Ca^{2+} alternans and subcellular regions alternating out of phase. These pronounced and complex subcellular inhomogeneities and gradients provide a proarrhythmic substrate that renders atrial myocytes particularly vulnerable to spontaneous SR Ca^{2+} release and susceptible to propagating arrhythmogenic diastolic Ca^{2+} waves. The present study provides the first direct evidence that in atrial myocytes, beat-to-beat alternation of the restitution kinetics of SR Ca^{2+} release represents a key causative mechanism for the occurrence of electromechanical and Ca^{2+} alternans.

Part of this work has been previously presented in abstract form (54).

METHODS

Solutions and chemicals. All chemicals and reagents were purchased from Sigma-Aldrich (St. Louis, MO), unless otherwise stated. Tyrode solution contained (in mM) 135 NaCl, 4 KCl, 2 $CaCl_2$, 1 $MgCl_2$, 10 D-glucose, and 10 HEPES (pH 7.4 with NaOH).

Myocyte isolation. Atrial myocytes were isolated from New Zealand White rabbits (2.5 kg, Myrtle's Rabbitry, Thompsons Station, TN). Rabbits were anesthetized with pentobarbital sodium (50 mg/kg), and hearts were excised and mounted on a Langendorff apparatus. Hearts were retrogradely perfused with nominally Ca^{2+}-free Tyrode solution containing heparin (2 U/ml) for 5 min, followed by minimal essential medium Eagle (MEM) solution containing 20 μM Ca^{2+} and 45 μg/ml Liberase Blendzyme TH (Roche Applied Science, Indianapolis, IN) for 20 min at 37°C. MEM solution contained (in mM) 23.8 $NaHCO_3$, 2 Na-pyruvate, 10 Na-HEPES, 10 HEPES, 0.02 $CaCl_2$, and 8 taurine with 40 U/l insulin and 50,000 U/l penicillin-streptomycin (pH 7.35 with NaOH). Digested tissue was minced and washed in MEM solution containing 10 mg/ml BSA and 50 μM $CaCl_2$. Finally, isolated atrial cells were kept in MEM solution with 50 μM $CaCl_2$ and were used within 1–6 h after isolation. All experiments were performed at room temperature (22–24°C). Animal protocols were approved by the Institutional Animal Care and Use Committee.

Confocal microscopy and $[Ca^{2+}]_i$ measurements. Confocal microscopy was used for the measurements of intra-SR Ca^{2+}, cytosolic Ca^{2+} transients, Ca^{2+} sparks, and Ca^{2+} waves. To directly monitor $[Ca^{2+}]_{SR}$, the SR was loaded with the low-affinity Ca^{2+} indicator fluo-5N (Molecular Probes-Invitrogen, Carlsbad, CA) by incubation of atrial myocytes with 10 μM of membrane-permeable fluo-5N AM together with 0.25% Pluronic F-127 in nominally Ca^{2+}-free Tyrode solution for 2.5 h, followed by a 30-min wash (all at 37°C). For $[Ca^{2+}]_i$ measurements, intact atrial myocytes were incubated with 10 μM fluo-4 AM (Molecular Probes-Invitrogen) for 10 min, followed by a 15-min wash. Cells were placed on laminin-coated glass coverslips. $[Ca^{2+}]_i$ and $[Ca^{2+}]_{SR}$ were measured with fluorescence laser scanning confocal microscopy (Radiance 2000 MP, Bio-Rad). Fluo-4 and fluo-5N were excited using the 488-nm line of an argon ion laser, and emission signals were acquired at >500 nm. All line-scan images (3 ms/line, 0.1-μm pixel size) were recorded from a central focal plane, with the scan line positioned along the transverse axis of the cell, avoiding regions of the nucleus. This allowed recording of Ca^{2+} release simultaneously from the junctional SR (j-SR) in the cell periphery and the nonjunctional SR (nj-SR) in the cell center (27). Background-subtracted fluorescence emission signals (F) were normalized to baseline fluorescence (F_0), and changes of $[Ca^{2+}]_i$ are presented as changes of F/F_0 or $\Delta F/F_0$ (where $\Delta F = F - F_0$). SR Ca^{2+} load was assessed from the cytosolic fluo-4 signal in response to the rapid application of 10 mM caffeine. SR Ca^{2+} loads were quantified as the amplitude ($\Delta F/F_0$) of caffeine-induced cytosolic Ca^{2+} transient. Changes in $[Ca^{2+}]_{SR}$ measured with fluo-5N are expressed as $[Ca^{2+}]_{SR} = (F - F_{min})/(F_0 - F_{min})$, where F_0 is the baseline diastolic $[Ca^{2+}]_{SR}$ and F_{min} is the intra-SR fluorescence in the absence of Ca^{2+} obtained after complete emptying of SR Ca^{2+} with 10 mM caffeine.

Electrophysiology and photolysis of caged Ca^{2+}. Experiments involving photolysis of caged Ca^{2+} and simultaneous $[Ca^{2+}]_i$ and Ca^{2+} current (I_{Ca}) measurements were performed on voltage-clamped atrial myocytes. The patch pipette solution contained (in mM) 120 L-aspartate, 120 CsOH, 20 TEA-Cl, 20 HEPES, 1 L-gluthathione (reduced), 1 DM-nitrophen (EMD Chemicals, Philadelphia, PA), 0.8 K-ATP, 0.7 $CaCl_2$, and 0.05 fluo-4 pentapotassium salt (Molecular Probes-Invitrogen) (pH 7.2 with CsOH). Free $[Ca^{2+}]$ of the pipette solution was ~150 nM. Due to competition of Ca^{2+} and Mg^{2+} for binding to DM-nitrophen (20), Mg^{2+} was omitted from the pipette solution to achieve optimal loading of the cage with Ca^{2+}. In in vitro control experiments, we determined that under our experimental conditions at $[Ca^{2+}] \geq 300$ nM, the uncaging Ca^{2+} signal was constant and became independent of [Ca^{2+}] (data not shown). Low-Mg^{2+} conditions potentially affect RyR-dependent Ca^{2+} release due to decreased Mg^{2+} inhibition of the channel (e.g., Ref. 25). In our experiment, however, the pipette solution composition was constant and not expected to affect the comparison of Ca^{2+} signaling between the large- and small-amplitude alternans Ca^{2+} transient.

I_{Ca} was recorded with the patch-clamp technique in the whole cell configuration using an Axopatch 200A amplifier (Molecular Devices, Sunnyvale, CA). Atrial myocytes were voltage clamped and held at −40 mV. I_{Ca} was activated with 100-ms depolarization steps to +20 mV. I_{Ca} was low-pass filtered at 5 kHz and digitized at 10 kHz. Simultaneous [Ca^{2+}]$_i$ measurements were obtained with a Nipkow dual-disk-type confocal laser scanning unit (CSU10, Yokogawa Electric, Tokyo, Japan) attached to the side port of a Nikon Diaphot 300 inverted microscope equipped with a ×100 ultraviolet (UV)-transmitting oil objective lens (CF Fluor, numerical aperture: 1.3, Nikon). Fluo-4 was excited with the 488-nm line of an argon ion laser connected fiber optically to the confocal unit. [Ca^{2+}]$_i$-dependent fluo-4 signals were collected at >515 nm from single atrial myocytes using a photomultiplier tube. Photolysis of caged Ca^{2+} (DM-nitrophen) was achieved with single 355-nm light pulses (3–5 ns) from a Nd:YAG laser (Continuum Minilite II, Santa Clara, CA) connected via a single solid fused silica fiber to the epifluorescence port of the microscope. Synchronization of flash photolysis, I_{Ca}, and [Ca^{2+}]$_i$ measurements and data recording and digitization were achieved using pCLAMP 10.2 software and the Axon Digidata 1440A interface (Molecular Devices).

Ca^{2+} alternans. Ca^{2+} alternans was induced by incrementally increasing the pacing frequency until stable Ca^{2+} alternans was observed. Global Ca^{2+} transients were elicited by electrical stimulation via depolarization pulses in voltage-clamped myocytes or by electrical field stimulation of intact myocytes using a pair of platinum electrodes (voltage set at ~50% above the threshold for contraction). The frequency at which stable Ca^{2+} alternans was observed varied from cell to cell and ranged from >1 to 2.5 Hz. The degree of Ca^{2+} alternans was quantified as the alternans ratio (AR). The AR was defined as 1 − S/L, where S/L is the ratio of the small-amplitude Ca^{2+} transient (S) to the large-amplitude Ca^{2+} transient (L) during a pair of alternating Ca^{2+} transients (32, 67).

Data analysis and statistics. Ca^{2+} spark frequency [quantified as the number of sparks per second and 100 μm of scanned distance (sparks·s^{-1}·(100 μm)$^{-1}$)] was calculated using the SparkMaster algorithm (45). Results are reported as means ± SE of *n* cells. Statistical significance was evaluated using Student's *t*-test or Wilcoxon signed-rank test.

RESULTS

I_{Ca} and SR Ca^{2+} load during pacing-induced Ca^{2+} alternans. In an initial set of experiments, we tested the hypothesis of whether alternations in I_{Ca} or diastolic SR Ca^{2+} load are required for cytosolic Ca^{2+} alternans in atrial myocytes. Figure 1*A* shows simultaneous Ca^{2+} transients (*a*) and I_{Ca} (*b*) recordings from a voltage-clamped atrial myocyte. Ca^{2+} transients were evoked by membrane depolarization to +20 mV from a holding potential of −40 mV. In the example shown, stable Ca^{2+} alternans with an AR of 0.36 was observed at a stimulation frequency of 1 Hz. Peak I_{Ca} (Fig. 1*A*,*c*) was essentially identical during the large (−0.551 nA) and small (−0.559 nA) Ca^{2+} transients. On average, the ratio of I_{Ca} peak amplitude during the large transient divided by the small transient was 1.008 ± 0.011 ($n = 8$), i.e., the average beat-to-beat variation was <1%. Upon closer examination, inactivation of I_{Ca} was slightly faster during the large-amplitude Ca^{2+} transient (blue trace in Fig. 1*A*,*c*), consistent with a more pronounced Ca^{2+}-dependent inactivation of the current. Furthermore, the tail current observed after repolarization was larger after the large-amplitude alternans Ca^{2+} transient, consistent with larger Ca^{2+} release leading to enhanced Ca^{2+} removal across the surface membrane via NCX.

We addressed the question of whether SR Ca^{2+} content alternates during Ca^{2+} alternans with two separate experimental approaches. With the first assay, we rapidly applied 10 mM caffeine after the large and small Ca^{2+} transient during alternans while recording cytosolic [Ca^{2+}]$_i$. This approach allowed SR content to be measured with subcellular (subsarcolemmal j-SR vs. central nj-SR) resolution using laser scanning confocal microscopy (Fig. 1*B*,*a*). Figure 1*B*,*b* shows the average amplitudes of electrically evoked (field stimulation) Ca^{2+} transients for the j-SR and nj-SR. Average AR was 0.54 ± 0.03 for the JSR and 0.61 ± 0.04 for the nj-SR ($n = 10$). As shown in Fig. 1*B*,*c*, there were no differences in amplitude of the caffeine-induced Ca^{2+} transient (i.e., SR Ca^{2+} load) after the large and small transient, nor were there any differences between the j-SR and nj-SR. These results confirmed earlier measurements in atrial tissue (28).

With the second approach, we measured [Ca^{2+}]$_{SR}$ levels directly using the low-affinity Ca^{2+} indicator fluo-5N entrapped in the SR. As shown in Fig. 1*B*,*d* (*left*), the end-diastolic [Ca^{2+}]$_{SR}$ levels preceding a large SR depletion were identical to the [Ca^{2+}]$_{SR}$ levels immediately before a small transient ($n = 9$). Furthermore, the end-diastolic AR, expressed as the ratio of end-diastolic [Ca^{2+}]$_{SR}$ before a large and small SR Ca^{2+} depletion transient, was 1.003 ± 0.002 [Fig. 1*B*,*d* (*right*)], indicating that Ca^{2+} alternans could occur at constant end-diastolic [Ca^{2+}]$_{SR}$.

In conclusion, the data shown in Fig. 1 indicate that alternans of cytosolic Ca^{2+} transients occur in the absence of beat-to-beat alternations of the physiological trigger (I_{Ca}) for CICR during excitation-contraction coupling. Furthermore, alternations in end-diastolic [Ca^{2+}]$_{SR}$ are not required for Ca^{2+} alternans. Therefore, alternations in I_{Ca} and SR Ca^{2+} content can be excluded as the primary or sole determinants of cytosolic Ca^{2+} alternans under our experimental conditions. This is consistent with our previous findings in atrial and ventricular myocytes (28, 44). Therefore, in the following experiments, we focused on refractory kinetics and restitution of SR Ca^{2+} release and tested the hypothesis that alternans of refractoriness of RyR-dependent Ca^{2+} release is causally linked to cardiac alternans.

Propensity of spontaneous Ca^{2+} release during rest after alternans. To evaluate the availability or restitution of the Ca^{2+}-release mechanism after a Ca^{2+} transient during alternans, we induced Ca^{2+} alternans by pacing and measured the time to the occurrence (latency) of spontaneous global Ca^{2+} release (e.g., in the form of a Ca^{2+} wave or a spontaneous AP) during a period of rest after pacing. As shown in Fig. 2*A*,*a*, the occurrence of spontaneous global Ca^{2+} release was compared during rest periods after a small Ca^{2+} transient (*left*) and a large Ca^{2+} transient (*right*). The average latency of spontaneous global Ca^{2+} release (Fig. 2*A*,*b*) was 1.41 ± 0.24 s after the small transient and 2.12 ± 0.42 s after the large transient ($n = 6$, $P < 0.05$). The significantly shorter latency observed after the small Ca^{2+} transient during alternans suggests that refractoriness of the SR Ca^{2+}-release mechanism alternates and is

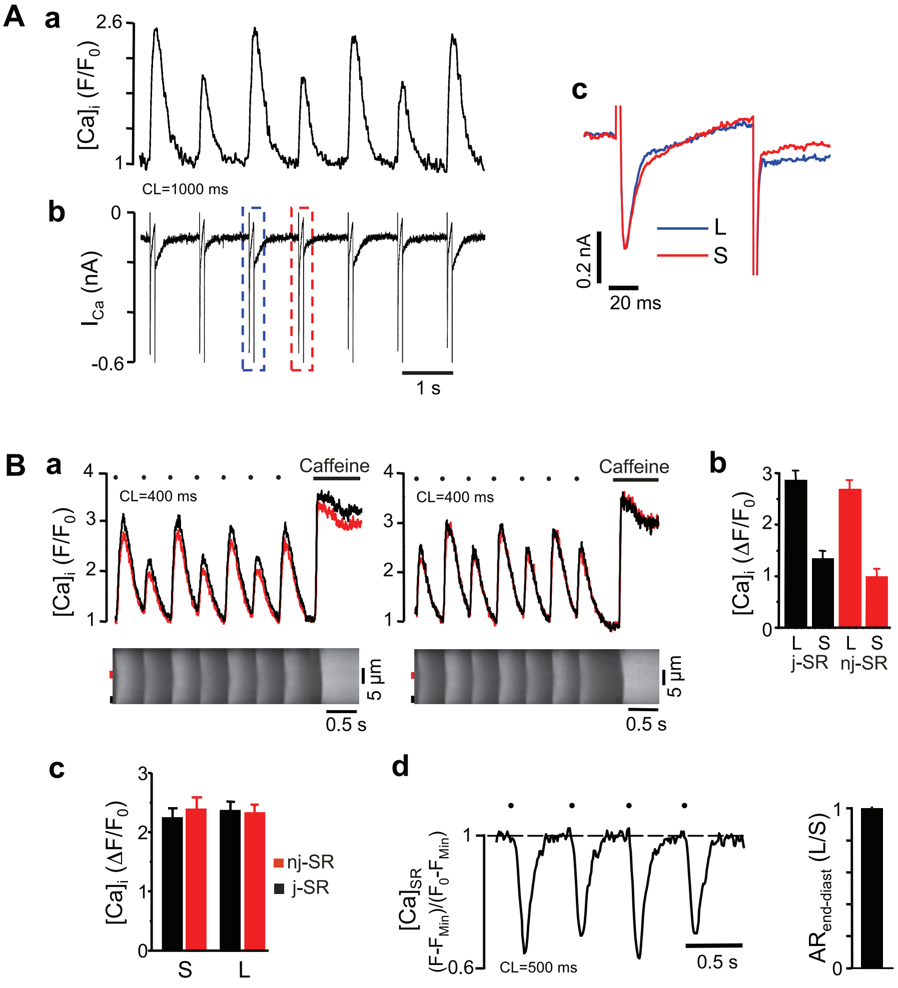

Fig. 1. Ca^{2+} current (I_{Ca}) and sarcoplasmic reticulum (SR) Ca^{2+} concentration ($[Ca]_{SR}$) during pacing-induced Ca^{2+} alternans. *A*: simultaneous measurements of intracellular Ca^{2+} concentration ($[Ca^{2+}]_i$; *a*) and I_{Ca} (*b*) in voltage-clamped rabbit atrial myocytes. *c*, Overlay of I_{Ca} measured during a large-amplitude Ca^{2+} transient (L; blue trace) and a small-amplitude Ca^{2+} transient (S; red trace). *B*: subcellular Ca^{2+} transients recorded from the junctional SR (j-SR; black) and nonjunctional SR (nj-SR; red) during pacing-induced Ca^{2+} alternans. *Top*, local Ca^{2+} transients; *bottom*: line-scan images. The black and red boxes mark the subcellular regions where local Ca^{2+} signals were recorded. *a*, SR Ca^{2+} load was calculated from the magnitude of the $[Ca^{2+}]_i$ signal induced by the rapid application of caffeine (10 mM) after a large (*left*) and small (*right*) Ca^{2+} transient during alternans. *b* and *c*, Average local Ca^{2+} transient amplitudes during alternans induced by pacing ($n = 10$; *b*) and caffeine (SR Ca load, $n = 14$ after a small transient and $n = 11$ after a large transient; *c*). *d*, $[Ca^{2+}]_{SR}$ during pacing-induced Ca alternans (*left*) and end-diastolic alternans ratio (AR; *right*), expressed as the ratio of end-diastolic $[Ca^{2+}]_{SR}$ before a large and small SR Ca^{2+} depletion transient ($n = 9$). Filled circles indicate electrical field stimulation pulses. CL, cycle length; F, fluorescence; F_0, initial fluorescence; ΔF, change in fluorescence or F-F_0; F_{Min}, minimum fluorescence.

significantly reduced after a small transient (or prolonged after a large transient).

We investigated this hypothesis further by evaluating the frequency of spontaneous elementary SR Ca^{2+}-release events [Ca^{2+} sparks (9)] during rest after pacing-induced alternans. Figure 2*B*,*a* shows spark recordings after a small transient (*left*) and after a large transient (*right*) from the same cell. Spark frequency was twofold higher after the small Ca^{2+} transient than after the large Ca^{2+} transient (after the small transient: 3.18 ± 0.86 sparks·s^{-1}·$(100\ \mu m)^{-1}$ and after the large transient: 1.62 ± 0.75 sparks·s^{-1}·$(100\ \mu m)^{-1}$, $n = 5$, $P < 0.002$; paired observation). Notably, in the example shown, early after the cessation of pacing a burst of Ca^{2+} sparks was observed after the small transient that was absent after the large transient.

In conclusion, the observation that the latency of spontaneous global Ca^{2+} release and abundance of spontaneous Ca^{2+} sparks during rest after alternans is critically dependent whether the rest period was preceded by a final small- or large-amplitude transient suggests that refractoriness of SR Ca^{2+} release plays a critical role in the Ca^{2+} alternans mechanism. The experiments shown in Fig. 2, however, only indirectly addressed the role of refractoriness for alternans because spontaneous Ca^{2+}-release events were evaluated after the cessation of electrical pacing. The following experiments were designed to address this question directly during alternans.

Refractoriness of Ca^{2+} release during alternans. Refractoriness of Ca^{2+} release during alternans was tested by applying premature electrical pulses at exactly defined time intervals during the Ca^{2+} transient induced by a regular pacing protocol. Premature stimuli were applied during large and small Ca^{2+} transients between 100 and 1,000 ms after the regular pulse. The magnitude of Ca^{2+} release induced by the premature stimulus was quantified as fractional release, i.e., the amplitude was normalized to SR Ca^{2+} load in each individual cell to account for cell-to-cell variability of SR Ca^{2+} content. SR load was measured as the amplitude of the Ca^{2+} signal elicited with the rapid application of 10 mM caffeine (the general protocol is shown in Fig. 3*A*). Figure 3*B* shows an example where the extra stimulus (black arrowhead) was applied 250 ms after the regular depolarization (filled circles) during alternans, after a small-amplitude Ca^{2+} transient (*a*), and after a large-amplitude Ca^{2+} transient (*b*). Release had partially recovered 250 ms after a small transient, whereas after the large transient additional Ca^{2+} release was barely detectable. As shown in Fig.

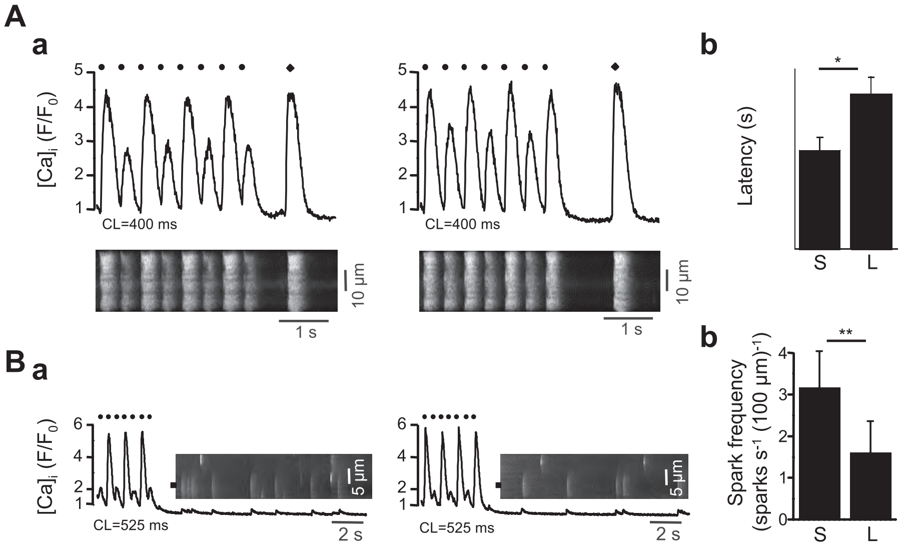

Fig. 2. Spontaneous Ca^{2+}-release events during rest after pacing-induced Ca^{2+} alternans. *A*: spontaneous global Ca^{2+}-release events (solid diamonds) during a 10-s rest period after a small (*left*) and large (*right*) alternans Ca^{2+} transient (*a*). *Top*, $[Ca^{2+}]_i$ averaged over the width of the cell; *bottom*: confocal line-scan image of $[Ca^{2+}]_i$. *b*, Average latency of spontaneous global Ca^{2+} release after a small and large transient during alternans ($n = 6$). *B*: local Ca^{2+} transient and Ca^{2+} sparks (*a*) during rest after a small (*left*) and large (*right*) alternans Ca^{2+} transient. Shown are local $[Ca^{2+}]_i$ changes recorded from the subcellular location marked by the black box and line-scan images. *b*, Average Ca^{2+} spark frequency after a large and small alternans Ca^{2+} transient ($n = 5$). Filled circles indicate electrical field stimulation pulses. Statistical significance: $*P < 0.05$ and $**P < 0.002$.

3*C*, in response to a stimulus applied after a 500-ms interval, Ca^{2+} release had fully recovered after the small- and almost completely after the large-amplitude alternans Ca^{2+} transients. The results are shown in Fig. 3*D*. During the small Ca^{2+} transient (dashed lines), SR Ca^{2+} release became partially available in <250 ms, whereas SR Ca^{2+} release during a large transient remained unavailable for >250 ms. The 50% recovery time (taken from the fit to the average data) during the small transient (dashed lines) was 230 ms for the j-SR and 260 ms for the nj-SR. In contrast, the 50% recovery time during the large transient (solid lines) was 350 ms for the j-SR and 450 ms for the nj-SR, i.e., restitution of Ca^{2+} release during the large Ca^{2+} transient was prolonged by nearly 65% and the recovery of release from the j-SR preceded the recovery of nj-SR release by 30–100 ms. The latter is largely explained by the fact that the activation of release in the cell center lagged behind activation in the cell periphery due to the lack of t-tubules in atrial cells and the time required for the propagation of CICR from the cell periphery to the cell center (33, 39, 40, 66). As shown previously, this delay amounts to 45–80 ms (27, 53).

Recovery of SR Ca^{2+} release from inactivation during alternans was further investigated with an experimental approach where step-like increases of $[Ca^{2+}]_i$ were imposed during alternans using a caged Ca^{2+} compound [DM-nitrophen (31)] and photolytical release of Ca^{2+}. Ca^{2+} released from the SR by uncaging of DM-nitrophen was termed photolysis-induced Ca^{2+} release (PICR). Atrial myocytes were voltage clamped and stimulated with 100-ms depolarization pulses from a holding potential of −40 to +20 mV at frequencies that elicited stable Ca^{2+} alternans. UV (355 nm) laser flashes (lightning symbol) were applied at the beginning of the depolarization pulse (*time 0* in Fig. 4*A*) or at defined intervals ranging from 50 to 400 ms after the beginning of the depolarization pulse (Fig. 4, *B* and *C*). This protocol was applied twice to deliver a UV flash of identical delay during a small Ca^{2+} transient (first series, red trace) and a large Ca^{2+} transient (second series, blue trace). The UV laser pulse was preceded by a minimum of 10 depolarization pulses to achieve reproducible Ca^{2+} loading of the SR. In the example shown in Fig. 4*A*, the UV flash was applied simultaneously with the voltage-clamp pulse. In both series, the amplitude of the transient elicited by the combined application of a depolarization step and UV flash was larger than elicited by membrane depolarization alone (note that depolarization to +20 mV elicited a maximal Ca^{2+} response under identical experimental conditions; data not shown). This demonstrates directly that the physiological trigger of CICR, I_{Ca}, does not release all available Ca^{2+} in the SR and that under alternans conditions during the small transient sufficient SR Ca^{2+} would be present, provided there is a sufficiently strong trigger that could overcome the refractoriness of the release mechanism. As shown in Fig. 4*A*, the amplitude of the Ca^{2+} transient elicited by the combination of membrane depolarization and UV flash was larger after a small transient (i.e., when a large transient is expected, blue trace) than after a large transient (red trace). As shown in Fig. 4*A*,*b*, this difference was graded with the AR. Cells with the largest AR of Ca^{2+} transients elicited by membrane depolarization also revealed the largest difference between the Ca^{2+} transient amplitudes elicited by the combined application of depolarization (CICR) and UV flash (PICR). Since end-diastolic $[Ca^{2+}]_i$ was identical before application of the pulse (red vs. blue trace) and based on our observation that at $[Ca^{2+}] \geq 300$ nM the uncaging Ca^{2+} signal was constant (see METHODS), we could assume that the Ca^{2+} loading of the caged compound was identical and therefore identical amounts of Ca^{2+} were released from the cage despite the fact that $[Ca^{2+}]_i$ changed during a cytosolic Ca^{2+} transient. Consequently, the difference in $[Ca^{2+}]_i$ amplitude was the result of differences in PICR.

Figure 4*B* shows an example where a UV flash was applied 150 ms after the beginning of the depolarization step during a small Ca^{2+} transient (red trace) and a large Ca^{2+} transient (blue trace). The extra amount of Ca^{2+} release by uncaging of Ca^{2+} from DM-nitrophen (PICR) was larger during the small Ca^{2+} transient ($\Delta F/F_0$ of PICR was 0.25 for the small Ca^{2+} transient and 0.17 for the large Ca^{2+} transient). Figure 4*C* shows the effect of the delay of UV flash application on the amplitude of PICR. UV flashes applied during identical Ca^{2+} transients but with increasing delays from the beginning of the transient revealed PICR of increasing magnitudes. This obser-

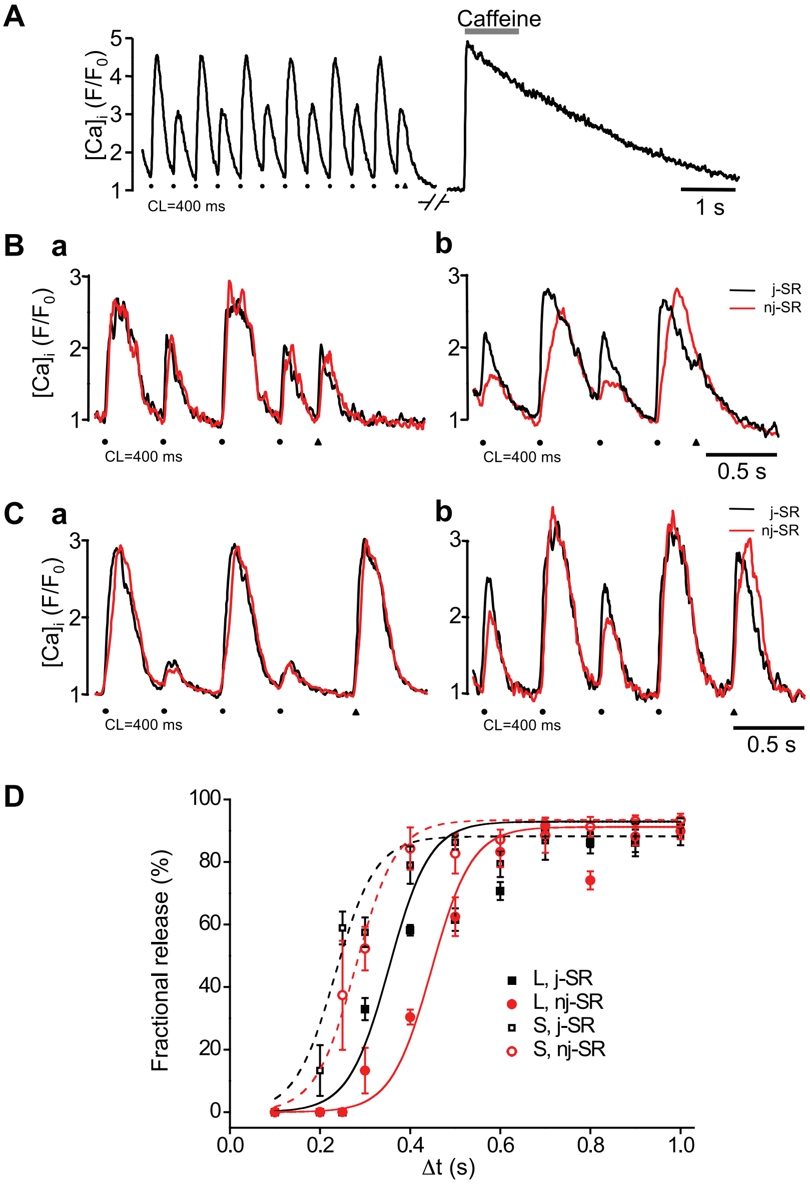

Fig. 3. Refractoriness of SR Ca^{2+} release during Ca^{2+} alternans probed by the application of extra electrical stimuli. *A*: experimental protocol. Extra stimuli were applied at defined intervals (100–1,000 ms) during pacing-induced (2.5 Hz) Ca^{2+} alternans during/after a small (shown) and large alternans Ca^{2+} transient. Filled circles indicate regular field stimulation pulses; extra stimuli are indicated by black arrowheads. In each experiment, SR Ca^{2+} load was subsequently measured by the application of caffeine (10 mM). *B* and *C*: subcellular (j-SR, black traces; nj-SR, red traces) Ca^{2+} transients and Ca^{2+} release induced by extra stimuli applied at 250 ms (*B*) and 500 ms (*C*) during a small (*a*) and large (*b*) alternans Ca^{2+} transient. *D*: Ca^{2+} release as a function of time interval between a regular stimulus and an extra stimulus, for small (open symbols) and large (filled symbols) transients, and for the j-SR (black) and nj-SR (red). Ca^{2+} release by extra stimuli is expressed as the percentage of fractional release (amplitude of the extra Ca^{2+}-release transient divided by the amplitude of the caffeine-induced Ca^{2+} signal). The data shown in *D* were obtained from a total of 80 myocytes. Δ*t*, time interval between regular electrical stimulus and extra stimulus.

vation indicates that with increasing time during the Ca^{2+} transient, a growing fraction of RyR Ca^{2+}-release channels had recovered and became available for activation by PICR. We now quantified the recovery kinetics during alternans by comparing PICR obtained during small and large alternans Ca^{2+} transients at variable delays. For this purpose, the ratio of PICR during a large and small transient ($PICR_L/PICR_S$) was plotted as a function of delay (Fig. 4*D*), i.e., $PICR_L$ is expressed as a percentage of $PICR_S$ for any given delay. For UV flashes applied at *time 0* (no delay between onset of the depolarization pulse and UV flash) and with a delay of 50 ms, $PICR_L/PICR_S$ was >1, indicating that, for the large transient, at the beginning of the depolarization RyR release channels are fully available and can be activated maximally by the combined application of a depolarization and UV flash pulse. During the time interval starting at the peak of the Ca^{2+} transient and ranging into its declining phase (100–250 ms), $PICR_L/PICR_S$ decreased and reached a minimum at 150 ms. At a delay of >400 ms, $PICR_L/PICR_S$ had recovered. These data indicate that during alternans, the fraction of RyRs that participate in Ca^{2+} release alternates in magnitude in a beat-to-beat fashion. During the large transient, more RyRs participate in release; consequently, a larger fraction of channels become refractory and are temporarily unavailable for further activation and release. The opposite applies to the small transient. Thus, taken together, these data provide strong evidence that beat-to-beat alternations in the restitution properties and kinetics of the Ca^{2+}-release mechanism play a fundamental role in generation of Ca^{2+} alternans.

Modulation of Ca^{2+} alternans by sensitization of RyRs. In the following set of experiments, we tested how increasing the sensitivity of RyRs to Ca^{2+} affects pacing-induced alternans. For this purpose, cells were paced at a constant frequency of 2.5 Hz. Under control conditions, this pacing frequency con-

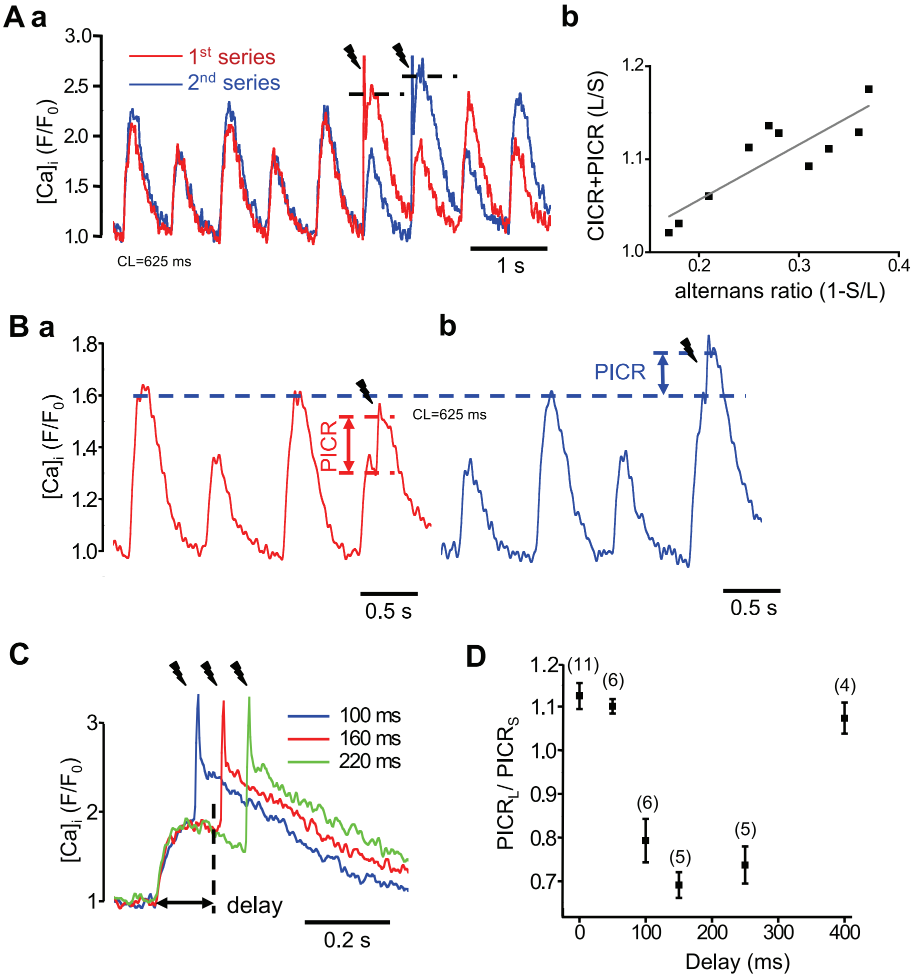

Fig. 4. Refractoriness of SR Ca^{2+} release during Ca^{2+} alternans probed by photolysis-induced Ca^{2+} release (PICR). *A*: two series of Ca^{2+} alternans elicited by 100-ms depolarization pulses to +20 mV from a holding potential of −40 mV. *a*, UV (355 nm) laser pulses (lightning bolt) were applied to photolytically uncage Ca^{2+} and coincided with the beginning of the depolarization pulse for an anticipated small-amplitude Ca^{2+} transient (red; first series) and a large-amplitude Ca^{2+} transient (blue; second series). *b*, Correlation between AR induced by pacing and $[Ca^{2+}]_i$ signal induced by the combination of depolarization [Ca^{2+}-induced Ca^{2+} release (CICR)] and UV flash (PICR). *B*: photorelease of caged Ca^{2+} during small (*a*) and large (*b*) alternans Ca^{2+} transients (delay: 100 ms) and determination of PICR amplitude. *C*, three examples of PICR applied with delays of 100, 160, and 220 ms during depolarization-induced Ca^{2+} transients of identical amplitude. *D*: average PICR ratios during large and small Ca^{2+} transients ($PICR_L$/$PICR_S$) as a function of the delay between the depolarization pulse and UV flash. Numbers in parentheses indicate numbers of cells tested.

sistently caused stable Ca^{2+} alternans (Fig. 5*A*). After stable alternans had been established, cells were exposed to a low dose (0.1 mM) of caffeine, which is well established to increase the Ca^{2+} sensitivity of the RyR (16, 59). As shown in Fig. 5*A*, caffeine normalized pacing-induced Ca^{2+} alternans within <10 beats. Upon closer inspection, the predominant effect of caffeine was on the small-amplitude Ca^{2+} transient, which increased substantially, whereas the amplitude of the large transient only slightly decreased. The increase in amplitude was particularly pronounced for release from the nj-SR. In addition to rescuing pacing-induced Ca^{2+} alternans, caffeine also shortened the time to the occurrence of a spontaneous global Ca^{2+} release during rest after pacing (Fig. 5*B*). The latency in the presence of caffeine was reduced to 1.30 ± 0.11 s (n = 12) compared with control conditions (Fig. 2*A*,*b*). Thus, sensitization of the RyR increased the threshold for pacing-induced alternans to >2.5 Hz and shortened refractoriness of the Ca^{2+}-release mechanism. Similar to caffeine, β-adrenergic stimulation with isoproterenol (10 μM) prevented the occurrence of Ca^{2+}

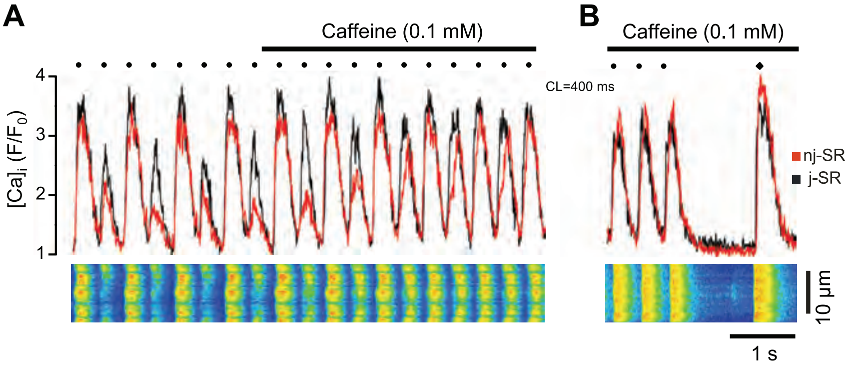

Fig. 5. Effect of ryanodine receptor sensitization on Ca^{2+} alternans and refractoriness of Ca^{2+} release. *A*: application of low-dose (0.1 mM) caffeine normalized pacing-induced Ca^{2+} alternans. *B*: spontaneous Ca^{2+} release (solid diamond) during rest in the presence of caffeine. Shown are subcellular Ca^{2+} signals from the j-SR (black) and nj-SR (red) (*top*) and line-scan images (*bottom*). Filled circles indicate electrical field stimulation pulses.

alternans at a pacing frequency of 2.5 Hz and reduced latency on average to 0.71 s (n = 6; data not shown).

Modulation of Ca^{2+} alternans by step-like increases of $[Ca^{2+}]_i$. Using photolysis of caged Ca^{2+} in voltage-clamped myocytes, we tested the effect of rapid step-like elevations of $[Ca^{2+}]_i$ on alternans threshold pacing frequency and the phase of alternans. UV flashes used to photolyse DM-nitrophen (lightning symbol in Fig. 6) were synchronized with the onset of the depolarization step (filled circles). When UV flashes were applied to cells with stable alternans at the time of an expected small-amplitude transient, two types of responses were observed. In one case, the large Ca^{2+} transient induced by PICR was followed by a normalization of the Ca^{2+} transients and the disappearance of alternans while pacing frequency remained unchanged (n = 4; Fig. 6*A*). In the other case, alternans continued after the PICR-induced Ca^{2+} transient, but the PICR-induced Ca^{2+} transient was followed by a small-amplitude transient, indicating a phase shift in alternans (n = 11; Fig. 6*B*). In contrast, when PICR coincided with a large-amplitude transient during stable alternans, alternans continued without a change in phase (n = 11; Fig. 6*C*). Finally, in nonalternating myocytes, PICR timed to coincided with a voltage-clamp pulse could initiate alternans at unchanged stimulation frequency (n = 6; Fig. 6*D*). In summary, these experiments show that interference with Ca^{2+} cycling during regular pacing by imposing step-like increases in $[Ca^{2+}]$ has profound effects on AR and the alternans phase that will be further discussed below.

DISCUSSION

In this investigation, we established direct evidence that beat-to-beat alternans of time-dependent restitution of the SR Ca^{2+}-release mechanism constitutes a key defining factor of cardiac alternans.

A key element toward a comprehensive understanding of cardiac alternans is the concept of bidirectional coupling of electrical and Ca^{2+} signaling, leading to the paradigm that alternans are either membrane voltage or $[Ca^{2+}]_i$ driven, and alternans has been linked to disturbances in both electrical and Ca^{2+} signaling (reviewed and discussed in Refs. 29, 51, 63, and 64). Led by the observation, however, that mechanical and Ca^{2+} alternans can occur in the absence of APD alternans (experimentally confirmed in voltage-clamp experiments) and with constant I_{Ca} (10, 14, 28, 62) (see also Fig. 1*A* in the present study), the focus has shifted (46) toward disturbances in Ca^{2+} signaling that might underlie alternans and APD alternans may be merely a consequence of Ca^{2+} alternans. As outlined in the Introduction, here the relationship between fractional SR Ca^{2+} release and cytosolic Ca^{2+} sequestration determines whether Ca^{2+} cycling is stable or undergoes alternans. The key question in this context is how does Ca^{2+} release during any given heart beat determine Ca^{2+} release and Ca^{2+} transient magnitude of the subsequent beat. The recovery of the Ca^{2+} transient (generally referred to as Ca^{2+} transient restitu-

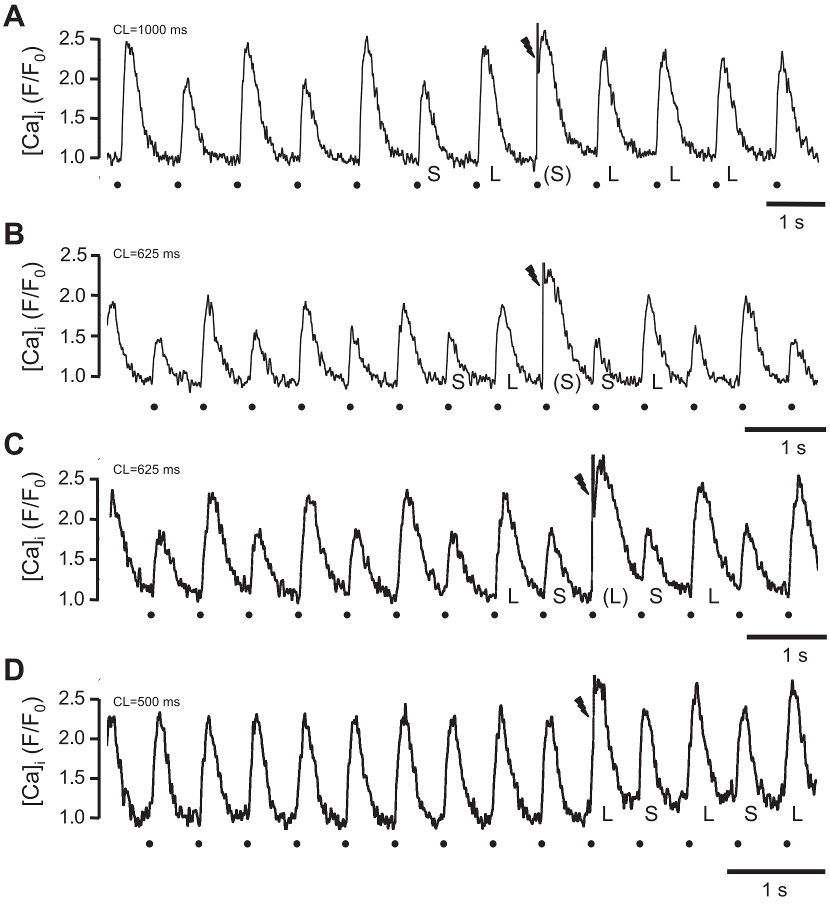

Fig. 6. Phase modulation of Ca^{2+} alternans by PICR. UV flashes (lightning bolts) were applied coincidently with a depolarization pulse in voltage-clamped myocytes during pacing induced Ca^{2+} alternans (*A*–*C*) and during regular Ca^{2+} transients (*D*). Filled circles indicate the electrical onset of depolarization pulses (100 ms, to +20 mV from a holding potential of −40 mV). Letters in parentheses indicate the anticipated Ca^{2+} transient amplitude.

tion) depends on the recovery of the trigger of CICR (I_{Ca}), SR Ca^{2+} load, and the release mechanism itself (RyRs). These three factors have been addressed directly in the present study.

As shown in Fig. 1*A*, when I_{Ca} was recorded from voltage-clamped atrial myocytes at stimulation frequencies that induced Ca^{2+} alternans, no beat-to-beat differences in peak current could be observed. I_{Ca} showed accelerated inactivation kinetics and enhanced tail currents during the large-amplitude Ca^{2+} transient, consistent with stronger Ca^{2+}-dependent inactivation and enhanced Ca^{2+} extrusion via NCX. The lack of alternans of peak I_{Ca} is consistent with our earlier observation (28) and is at variance with observations of alternating L-type I_{Ca} that triggers CICR and Ca^{2+} alternans (23, 38). Nonetheless, our observations exclude I_{Ca} alternans as the sole cause of cardiac alternans.

Clearly more controversial is the issue whether cardiac alternans require beat-to-beat alternations in SR Ca^{2+} content as a causative factor (15), and it has been suggested that instability in the beat-to-beat feedback control of SR content leads to Ca^{2+} alternans (18). We addressed this question experimentally with two different approaches. The first approach relied on measurements of SR Ca^{2+} load by quantifying the cytosolic Ca^{2+} signal in response to rapid SR depletion with caffeine. As shown in Fig. 1*B*, the caffeine-induced Ca^{2+} transients were identical after the large and small alternans Ca^{2+} transient, excluding alternating differences in diastolic SR Ca^{2+} load and confirming earlier findings made in atrial tissue (28). The second approach used a refined method of direct dynamic measurements of $[Ca^{2+}]_{SR}$ using a low-affinity Ca^{2+} indicator (fluo-5N) entrapped in the SR lumen. With this method, we demonstrated reliably that alternating end-diastolic SR Ca^{2+} content is not required for alternans to occur. These results confirmed our earlier observations in ventricular myocytes, where we showed that while diastolic $[Ca^{2+}]_{SR}$ fluctuations can occur during alternans, Ca^{2+} alternans can also readily occur without significant diastolic $[Ca^{2+}]_{SR}$ alternations (44), thus also eliminating SR Ca^{2+} load alternans as a mandatory prerequisite for cardiac alternans.

While APD restitution (including the recovery of L-type Ca^{2+} channels from voltage- and Ca^{2+}-dependent inactivation) and sequestering of Ca^{2+} [specifically reuptake of Ca^{2+} into the SR and reestablishment of Ca^{2+} load (12, 30, 68)] have been recognized as contributing factors to electromechanical and Ca^{2+} alternans, recent findings have provided evidence that refractoriness of CICR or temporary unavailability of RyRs after a release event may contribute to instabilities of cardiac Ca^{2+} release and vulnerability to arrhythmias (see the discussion in Ref. 56). Experimental studies on the recovery of whole cell Ca^{2+} transients as well as Ca^{2+} release at the level of individual Ca^{2+}-release units (Ca^{2+} sparks) after a preceding release event (7, 8, 47, 52, 55, 57) have shown that Ca^{2+} release is unavailable immediately after release due to RyR inactivation and requires several hundred milliseconds for full recovery. These restitution kinetics have raised the possibility that the recovery of RyR-dependent Ca^{2+} release may occur on a time scale that overlaps with stimulation frequencies at which Ca^{2+} alternans occurs and that the time-dependent recovery of SR Ca^{2+} release may be the critical factor for the occurrence of Ca^{2+} alternans. In the present study, we addressed this question using multiple experimental approaches. We tested four different parameters that are directly or indirectly related to SR Ca^{2+}-release restitution: the occurrence of Ca^{2+} sparks and spontaneous global Ca^{2+}-release events during rest after alternans (indirect parameters) and the availability of SR Ca^{2+} release elicited at defined intervals during and after a Ca^{2+} transient in response to a premature electrical stimulus or a step-like increase of $[Ca^{2+}]$ elicited by photorelease of caged Ca^{2+}. In all these experiments, these parameters were compared between large and small alternans Ca^{2+} transients. In summary, these experiments provided consistent results showing that during alternans, the restitution kinetics of SR Ca^{2+} release were prolonged after the large-amplitude transient. Thus, we conclude that time-dependent recovery from refractoriness and the restitution of SR Ca^{2+} release is a key factor for the generation of Ca^{2+} alternans. Similar conclusions on the importance of refractoriness of SR Ca^{2+} release for the occurrence of alternans were drawn from studies on the role of luminal Ca^{2+} for release in intact mouse hearts (36) and the collective behavior of Ca^{2+} sparks, where refractoriness of a Ca^{2+}-release unit after a Ca^{2+} spark was identified as one of the key determinant factors of cardiac alternans (49).

The nonlinear relationship described earlier between Ca^{2+} sequestration and fractional SR Ca^{2+} release that determines the vulnerability to alternans allows the prediction of how endogenous or exogenous perturbances of beat-to-beat Ca^{2+} cycling affect alternans. As shown in Fig. 5, sensitization of the RyR with low-dose caffeine (0.1 mM) rescued pacing-induced Ca^{2+} alternans and normalized Ca^{2+} transient amplitude, an observation also made in ventricular myocytes when alternans occurred as a consequence of spatially fragmented Ca^{2+} release (38). RyR sensitization to CICR is expected to have complex effects on the propensity for Ca^{2+} alternans. While low-dose caffeine will initially enhance fractional release, it will also enhance SR Ca^{2+} leak (4, 16) and thus diminishes Ca^{2+} sequestration, which favors alternans. The increased SR Ca^{2+} leak, however, also reduces Ca^{2+} load and, subsequently, fractional release. The latter would predict a decrease in alternans probability. Evidence in support of the sensitization of RyRs leading to alternans was found in a study (5) on postmyocardial infarction myoctes where hyperactivity of RyRs due to redox modification of the release channel was accompanied by an increased propensity to alternans. In the same study, however, an increase in fractional SR Ca^{2+} release, a condition favoring alternans, was also found, which potentially could outweigh the effect on increased sensitivity of the release channel. Furthermore, we propose an additional mechanism through which low-dose caffeine normalizes alternans. Sensitization of the RyR accelerates the prolonged restitution kinetics observed after a large-amplitude Ca^{2+} release during alternans and, therefore, more release channels are available for the next beat and, consequently, the Ca^{2+} transient amplitude increases. Consistent with our observation, low-dose caffeine has been found to accelerate the time-dependent refractoriness of Ca^{2+} sparks (47), and such a mechanism is further supported by our observation that low-dose caffeine primarily enhanced the amplitude of the small-amplitude transient and by this mechanism contributed to the normalization of Ca^{2+} alternans.

Similarly to low-dose caffeine treatment, we demonstrated that in atrial myocytes, β-adrenergic stimulation stabilized pacing-induced Ca^{2+} alternans. During β-adrenergic stimulation, SERCA activity and, consequently, SR Ca^{2+} uptake and load are increased, leading to enhanced fractional release, which tends to promote alternans. Increased SERCA activity, however, also increases the efficiency of Ca^{2+} sequestration, resulting in protection against alternans. Whether β-adrenergic stimulation favors (13) or protects against alternans and alternans-related arrhythmias, as observed here (see also Ref. 28), depends on which of the β-adrenergic effects predominate (sequestration or fractional release). Consistent with our results are the observations that β-adrenergic stimulation accelerated the restitution of Ca^{2+} sparks (47), and depletion of the intra-SR buffer calsequestrin resulted in an accelerated refilling of SR Ca^{2+}, a reduced refractoriness of Ca^{2+} release, and a decreased probability to develop Ca^{2+} alternans (35).

Extra beats and premature stimuli have been shown to be capable to induce and modulate the phase of cardiac alternans (for a discussion, see Refs. 50 and 63). In a series of experiments, we tested the effect of rapid and large increases of $[Ca^{2+}]_i$ that coincided in time with an electrical stimulus during regular pacing. Several interesting observations were made. A step-like elevation of $[Ca^{2+}]_i$ imposed by Ca^{2+} uncaging applied coincidently with a (expected) small-amplitude Ca^{2+} transient resulted in two different responses. It either eliminated Ca^{2+} alternans (Fig. 6*A*) or led to a phase shift where the next electrically induced Ca^{2+} transient was of small amplitude instead of the expected large amplitude (Fig. 6*B*). The latter (Fig. 6*B*) can be explained by the notion that the combination of electrical stimulation and photolysis of caged Ca^{2+} led to maximal SR Ca^{2+} release, leading to prolonged refractoriness. The observation that a similar disturbance (Fig. 6*B*) could eliminate alternans demands an alternative explanation. We hypothesize that in this case, the elevated $[Ca^{2+}]_i$ also increased SERCA (and possibly NCX) activity. Both favor the sequestration of cytosolic Ca^{2+}, which reduces the likelihood of alternans. Whether the cell responds in one way or the other critically depends on the intricate balance among $[Ca^{2+}]_i$, SR Ca^{2+} load, fractional release, and cytosolic Ca^{2+} sequestration. When photorelease of Ca^{2+} coincided with a large transient, the phase of Ca^{2+} alternans remained unchanged (Fig. 6*C*). This is explained by the fact that after a large transient refractoriness is already prolonged and the subsequent Ca^{2+} transient is expected to be of small amplitude. A preceding Ca^{2+} transient of excessively large amplitude (as induced here by combined CICR and PICR) would be expected to be followed by a transient of even smaller amplitude, and this effect was indeed observed experimentally (Fig. 6*C*). Finally, combined electrical stimulation and a step-like increase of $[Ca^{2+}]_i$ was able to induce Ca^{2+} alternans (Fig. 6*D*). We postulate that the additional stimulus imposed by Ca^{2+} uncaging enhanced CICR and increased fractional release. In this case, the effect of enhanced fractional release dominated over a Ca^{2+}-dependent enhancement of sequestration. The observation that diastolic $[Ca^{2+}]_i$ actually increased after Ca^{2+} uncaging suggests a reduced net clearance of cytosolic Ca^{2+}. According to our model, the combined result of all these effects was the occurrence of alternans.

In summary, we have demonstrated that beat-to-beat alternans in the time-dependent restitution properties and recovery kinetics of the SR Ca^{2+}-release mechanism represents a key mechanism underlying cardiac alternans.

ACKNOWLEDGMENTS

The authors thank Dr. Elisa Bovo and Dr. Stefanie Walther for assistance with myocyte isolation.

Present address of V. M. Shkryl: Dept. of General Physiology of Nervous System, A. A. Bogomoletz Institute of Physiology, Kiev, Ukraine.

Present address of T. L. Domeier: Dept. of Medical Pharmacology and Physiology, The University of Missouri School of Medicine, Columbia, MO.

GRANTS

This work was supported by National Heart, Lung, and Blood Institute Grants HL-62231, HL-80101, and HL-101235 and by the Leducq Foundation.

DISCLOSURES

No conflicts of interest, financial or otherwise, are declared by the author(s).

AUTHOR CONTRIBUTIONS

Author contributions: V.M.S., J.T.M., T.L.D., and L.A.B. conception and design of research; V.M.S., J.T.M., and T.L.D. performed experiments; V.M.S., J.T.M., T.L.D., and L.A.B. analyzed data; V.M.S., J.T.M., T.L.D., and L.A.B. interpreted results of experiments; V.M.S., J.T.M., T.L.D., and L.A.B. prepared figures; V.M.S., J.T.M., T.L.D., and L.A.B. drafted manuscript; V.M.S., J.T.M., T.L.D., and L.A.B. edited and revised manuscript; V.M.S., J.T.M., T.L.D., and L.A.B. approved final version of manuscript.

REFERENCES

1. **Aistrup GL, Kelly JE, Kapur S, Kowalczyk M, Sysman-Wolpin I, Kadish AH, Wasserstrom JA.** Pacing-induced heterogeneities in intracellular Ca^{2+} signaling, cardiac alternans, and ventricular arrhythmias in intact rat heart. *Circ Res* 99: e65–e73, 2006.
2. **Aistrup GL, Shiferaw Y, Kapur S, Kadish AH, Wasserstrom JA.** Mechanisms underlying the formation and dynamics of subcellular calcium alternans in the intact rat heart. *Circ Res* 104: 639–649, 2009.
3. **Bassani JW, Yuan W, Bers DM.** Fractional SR Ca release is regulated by trigger Ca and SR Ca content in cardiac myocytes. *Am J Physiol Cell Physiol* 268: C1313–C1319, 1995.
4. **Belevych A, Kubalova Z, Terentyev D, Hamlin RL, Carnes CA, Gyorke S.** Enhanced ryanodine receptor-mediated calcium leak determines reduced sarcoplasmic reticulum calcium content in chronic canine heart failure. *Biophys J* 93: 4083–4092, 2007.
5. **Belevych AE, Terentyev D, Viatchenko-Karpinski S, Terentyeva R, Sridhar A, Nishijima Y, Wilson LD, Cardounel AJ, Laurita KR, Carnes CA, Billman GE, Gyorke S.** Redox modification of ryanodine receptors underlies calcium alternans in a canine model of sudden cardiac death. *Cardiovasc Res* 84: 387–395, 2009.
6. **Blatter LA, Kockskamper J, Sheehan KA, Zima AV, Huser J, Lipsius SL.** Local calcium gradients during excitation-contraction coupling and alternans in atrial myocytes. *J Physiol* 546: 19–31, 2003.
7. **Brochet DX, Yang D, Di Maio A, Lederer WJ, Franzini-Armstrong C, Cheng H.** Ca^{2+} blinks: rapid nanoscopic store calcium signaling. *Proc Natl Acad Sci USA* 102: 3099–3104, 2005.
8. **Cheng H, Lederer MR, Lederer WJ, Cannell MB.** Calcium sparks and $[Ca^{2+}]_i$ waves in cardiac myocytes. *Am J Physiol Cell Physiol* 270: C148–C159, 1996.
9. **Cheng H, Lederer WJ, Cannell MB.** Calcium sparks: elementary events underlying excitation-contraction coupling in heart muscle. *Science* 262: 740–744, 1993.
10. **Chudin E, Goldhaber J, Garfinkel A, Weiss J, Kogan B.** Intracellular Ca^{2+} dynamics and the stability of ventricular tachycardia. *Biophys J* 77: 2930–2941, 1999.
11. **Clusin WT.** Mechanisms of calcium transient and action potential alternans in cardiac cells and tissues. *Am J Physiol Heart Circ Physiol* 294: H1–H10, 2008.
12. **Cutler MJ, Wan X, Laurita KR, Hajjar RJ, Rosenbaum DS.** Targeted SERCA2a gene expression identifies molecular mechanism and therapeutic target for arrhythmogenic cardiac alternans. *Circ Arrhythm Electrophysiol* 2: 686–694, 2009.
13. **de Diego C, Chen F, Xie LH, Dave AS, Thu M, Rongey C, Weiss JN, Valderrabano M.** Cardiac alternans in embryonic mouse ventricles. *Am J Physiol Heart Circ Physiol* 294: H433–H440, 2008.
14. **Diaz ME, Eisner DA, O'Neill SC.** Depressed ryanodine receptor activity increases variability and duration of the systolic Ca^{2+} transient in rat ventricular myocytes. *Circ Res* 91: 585–593, 2002.

15. **Diaz ME, O'Neill SC, Eisner DA.** Sarcoplasmic reticulum calcium content fluctuation is the key to cardiac alternans. *Circ Res* 94: 650–656, 2004.
16. **Domeier TL, Blatter LA, Zima AV.** Alteration of sarcoplasmic reticulum Ca^{2+} release termination by ryanodine receptor sensitization and in heart failure. *J Physiol* 587: 5197–5209, 2009.
17. **Eisner DA, Choi HS, Diaz ME, O'Neill SC, Trafford AW.** Integrative analysis of calcium cycling in cardiac muscle. *Circ Res* 87: 1087–1094, 2000.
18. **Eisner DA, Diaz ME, Li Y, O'Neill SC, Trafford AW.** Stability and instability of regulation of intracellular calcium. *Exp Physiol* 90: 3–12, 2005.
19. **Eisner DA, Li Y, O'Neill SC.** Alternans of intracellular calcium: mechanism and significance. *Heart Rhythm* 3: 743–745, 2006.
20. **Ellis-Davies GC.** DM-nitrophen AM is caged magnesium. *Cell Calcium* 39: 471–473, 2006.
21. **Euler DE.** Cardiac alternans: mechanisms and pathophysiological significance. *Cardiovasc Res* 42: 583–590, 1999.
22. **Florea SM, Blatter LA.** The role of mitochondria for the regulation of cardiac alternans. *Front Physiol* 1: 1–9, 2010.
23. **Fox JJ, McHarg JL, Gilmour RF Jr.** Ionic mechanism of electrical alternans. *Am J Physiol Heart Circ Physiol* 282: H516–H530, 2002.
24. **Gaeta SA, Bub G, Abbott GW, Christini DJ.** Dynamical mechanism for subcellular alternans in cardiac myocytes. *Circ Res* 105: 335–342, 2009.
25. **Gusev K, Niggli E.** Modulation of the local SR Ca^{2+} release by intracellular Mg^{2+} in cardiac myocytes. *J Gen Physiol* 132: 721–730, 2008.
26. **Hiromoto K, Shimizu H, Furukawa Y, Kanemori T, Mine T, Masuyama T, Ohyanagi M.** Discordant repolarization alternans-induced atrial fibrillation is suppressed by verapamil. *Circ J* 69: 1368–1373, 2005.
27. **Huser J, Lipsius SL, Blatter LA.** Calcium gradients during excitation-contraction coupling in cat atrial myocytes. *J Physiol* 494: 641–651, 1996.
28. **Huser J, Wang YG, Sheehan KA, Cifuentes F, Lipsius SL, Blatter LA.** Functional coupling between glycolysis and excitation-contraction coupling underlies alternans in cat heart cells. *J Physiol* 524: 795–806, 2000.
29. **Jordan PN, Christini DJ.** Characterizing the contribution of voltage- and calcium-dependent coupling to action potential stability: implications for repolarization alternans. *Am J Physiol Heart Circ Physiol* 293: H2109–H2118, 2007.
30. **Kameyama M, Hirayama Y, Saitoh H, Maruyama M, Atarashi H, Takano T.** Possible contribution of the sarcoplasmic reticulum Ca^{2+} pump function to electrical and mechanical alternans. *J Electrocardiol* 36: 125–135, 2003.
31. **Kaplan JH, Ellis-Davies GC.** Photolabile chelators for the rapid photorelease of divalent cations. *Proc Natl Acad Sci USA* 85: 6571–6575, 1988.
32. **Kockskamper J, Blatter LA.** Subcellular Ca^{2+} alternans represents a novel mechanism for the generation of arrhythmogenic Ca^{2+} waves in cat atrial myocytes. *J Physiol* 545: 65–79, 2002.
33. **Kockskamper J, Sheehan KA, Bare DJ, Lipsius SL, Mignery GA, Blatter LA.** Activation and propagation of Ca^{2+} release during excitation-contraction coupling in atrial myocytes. *Biophys J* 81: 2590–2605, 2001.
34. **Kockskamper J, Zima AV, Blatter LA.** Modulation of sarcoplasmic reticulum Ca^{2+} release by glycolysis in cat atrial myocytes. *J Physiol* 564: 697–714, 2005.
35. **Kornyeyev D, Petrosky AD, Zepeda B, Ferreiro M, Knollmann B, Escobar AL.** Calsequestrin 2 deletion shortens the refractoriness of Ca^{2+} release and reduces rate-dependent Ca^{2+}-alternans in intact mouse hearts. *J Mol Cell Cardiol* 52: 21–31, 2012.
36. **Kornyeyev D, Reyes M, Escobar AL.** Luminal Ca^{2+} content regulates intracellular Ca^{2+} release in subepicardial myocytes of intact beating mouse hearts: effect of exogenous buffers. *Am J Physiol Heart Circ Physiol* 298: H2138–H2153, 2010.
37. **Laurita KR, Rosenbaum DS.** Cellular mechanisms of arrhythmogenic cardiac alternans. *Prog Biophys Mol Biol* 97: 332–347, 2008.
38. **Li Y, Diaz ME, Eisner DA, O'Neill S.** The effects of membrane potential, SR Ca^{2+} content and RyR responsiveness on systolic Ca^{2+} alternans in rat ventricular myocytes. *J Physiol* 587: 1283–1292, 2009.
39. **Mackenzie L, Bootman MD, Berridge MJ, Lipp P.** Predetermined recruitment of calcium release sites underlies excitation-contraction coupling in rat atrial myocytes. *J Physiol* 530: 417–429, 2001.
40. **Mackenzie L, Roderick HL, Berridge MJ, Conway SJ, Bootman MD.** The spatial pattern of atrial cardiomyocyte calcium signalling modulates contraction. *J Cell Sci* 117: 6327–6337, 2004.
41. **Myles RC, Burton FL, Cobbe SM, Smith GL.** The link between repolarisation alternans and ventricular arrhythmia: does the cellular phenomenon extend to the clinical problem? *J Mol Cell Cardiol* 45: 1–10, 2008.
42. **Narayan SM, Bode F, Karasik PL, Franz MR.** Alternans of atrial action potentials during atrial flutter as a precursor to atrial fibrillation. *Circulation* 106: 1968–1973, 2002.
43. **Nattel S.** New ideas about atrial fibrillation 50 years on. *Nature* 415: 219–226, 2002.
44. **Picht E, DeSantiago J, Blatter LA, Bers DM.** Cardiac alternans do not rely on diastolic sarcoplasmic reticulum calcium content fluctuations. *Circ Res* 99: 740–748, 2006.
45. **Picht E, Zima AV, Blatter LA, Bers DM.** SparkMaster: automated calcium spark analysis with ImageJ. *Am J Physiol Cell Physiol* 293: C1073–C1081, 2007.
46. **Pruvot EJ, Katra RP, Rosenbaum DS, Laurita KR.** Role of calcium cycling versus restitution in the mechanism of repolarization alternans. *Circ Res* 94: 1083–1090, 2004.
47. **Ramay HR, Liu OZ, Sobie EA.** Recovery of cardiac calcium release is controlled by sarcoplasmic reticulum refilling and ryanodine receptor sensitivity. *Cardiovasc Res* 91: 598–605, 2011.
48. **Rosenbaum DS.** T wave alternans: a mechanism of arrhythmogenesis comes of age after 100 years. *J Cardiovasc Electrophysiol* 12: 207–209, 2001.
49. **Rovetti R, Cui X, Garfinkel A, Weiss JN, Qu Z.** Spark-induced sparks as a mechanism of intracellular calcium alternans in cardiac myocytes. *Circ Res* 106: 1582–1591, 2010.
50. **Rubenstein DS, Lipsius SL.** Premature beats elicit a phase reversal of mechanoelectrical alternans in cat ventricular myocytes. A possible mechanism for reentrant arrhythmias. *Circulation* 91: 201–214, 1995.
51. **Sato D, Shiferaw Y, Garfinkel A, Weiss JN, Qu Z, Karma A.** Spatially discordant alternans in cardiac tissue: role of calcium cycling. *Circ Res* 99: 520–527, 2006.
52. **Sham JS, Song LS, Chen Y, Deng LH, Stern MD, Lakatta EG, Cheng H.** Termination of Ca^{2+} release by a local inactivation of ryanodine receptors in cardiac myocytes. *Proc Natl Acad Sci USA* 95: 15096–15101, 1998.
53. **Sheehan KA, Blatter LA.** Regulation of junctional and non-junctional sarcoplasmic reticulum calcium release in excitation-contraction coupling in cat atrial myocytes. *J Physiol* 546: 119–135, 2003.
54. **Shkryl VM, Littwitz C, Domeier TL, Blatter LA.** Refractoriness of ryanodine receptors during calcium alternans in rabbit atrial myocytes. *Biophys J* 98: 103a, 2010.
55. **Sobie EA, Song LS, Lederer WJ.** Local recovery of Ca^{2+} release in rat ventricular myocytes. *J Physiol* 565: 441–447, 2005.
56. **Sobie EA, Song LS, Lederer WJ.** Restitution of Ca^{2+} release and vulnerability to arrhythmias. *J Cardiovasc Electrophysiol* 17, *Suppl* 1: S64–S70, 2006.
57. **Szentesi P, Pignier C, Egger M, Kranias EG, Niggli E.** Sarcoplasmic reticulum Ca^{2+} refilling controls recovery from Ca^{2+}-induced Ca^{2+} release refractoriness in heart muscle. *Circ Res* 95: 807–813, 2004.
58. **Ter Keurs HE, Boyden PA.** Calcium and arrhythmogenesis. *Physiol Rev* 87: 457–506, 2007.
59. **Trafford AW, Sibbring GC, Diaz ME, Eisner DA.** The effects of low concentrations of caffeine on spontaneous Ca release in isolated rat ventricular myocytes. *Cell Calcium* 28: 269–276, 2000.
60. **Walker ML, Rosenbaum DS.** Cellular alternans as mechanism of cardiac arrhythmogenesis. *Heart Rhythm* 2: 1383–1386, 2005.
61. **Walker ML, Rosenbaum DS.** Repolarization alternans: implications for the mechanism and prevention of sudden cardiac death. *Cardiovasc Res* 57: 599–614, 2003.
62. **Wan X, Laurita KR, Pruvot EJ, Rosenbaum DS.** Molecular correlates of repolarization alternans in cardiac myocytes. *J Mol Cell Cardiol* 39: 419–428, 2005.
63. **Weiss JN, Karma A, Shiferaw Y, Chen PS, Garfinkel A, Qu Z.** From pulsus to pulseless: the saga of cardiac alternans. *Circ Res* 98: 1244–1253, 2006.
64. **Weiss JN, Nivala M, Garfinkel A, Qu Z.** Alternans and arrhythmias: from cell to heart. *Circ Res* 108: 98–112, 2011.
65. **Wohlfart B.** Analysis of mechanical alternans in rabbit papillary muscle. *Acta Physiol Scand* 115: 405–414, 1982.
66. **Woo SH, Cleemann L, Morad M.** Spatiotemporal characteristics of junctional and nonjunctional focal Ca^{2+} release in rat atrial myocytes. *Circ Res* 92: e1–e11, 2003.
67. **Wu Y, Clusin WT.** Calcium transient alternans in blood-perfused ischemic hearts: observations with fluorescent indicator fura red. *Am J Physiol Heart Circ Physiol* 273: H2161–H2169, 1997.
68. **Xie LH, Sato D, Garfinkel A, Qu Z, Weiss JN.** Intracellular Ca alternans: coordinated regulation by sarcoplasmic reticulum release, uptake, and leak. *Biophys J* 95: 3100–3110, 2008.
69. **Zima AV, Picht E, Bers DM, Blatter LA.** Spark and non-spark mediated SR calcium leak in rabbit ventricular myocytes. *Biophys J* 94: 171, 2008.

РОЗДІЛ 2. ТРАНЗІЄНТІ ЗМІНИ ВНУТРІШНЬОКЛІТИННОГО КАЛЬЦІЮ У СКЕЛЕТНОМУ М’ЯЗІ ЗА РАХУНОК ВИВІЛЬНЕННЯ З САРКОПЛАЗМАТИЧНОГО РЕТИКУЛУМУ

2.1 Тунелювання Ca^{2+} від саркоплазмотичного ретикулуму до мітохондрій

Мітохондрії є однією з основних субклітинних структур у скелетних м’язах ссавців. Ключова роль яких полягає у виробництві АТФ (Gillis, 1997, Madsen et al., 1996, Sembrowich et al., 1985). Вважається, що константа дисоціації для мітохондріального поглинання Ca^{2+} є надто низькою, та мітохондрії не можуть обробити швидкі зміни рівню кальцію (Brini, 2003). Проте, дослідження показали, що ця органела може швидко реагувати на зміни вмісту кальцію під час не тільки тетанічних, а і поодиноких скорочень м’язів (Rudolf et al., 2004). Таким чином, має існувати тісний зв’язок між мітохондріями і СР, який забезпечує швидке поглинання кальцію.

Здатність мітохондрій скелетних м'язів секвеструвати Ca^{2+}, який вивільнюється з саркоплазматичного ретикулуму під час циклу м'язового скорочення-розслаблення, продовжує буди предметом дискусій. Ми провели аналіз функціональної взаємодії між сайтами вивільнення Ca^{2+} з СР та місцями поглинання Ca^{2+} мітохондріями у скелетних м'язах щурів, які характеризуються швидким і повільними скороченнями. Для цього ми порівнювали кофеїн-індуковані цитозольні та мітохондріальні транзієнти Ca^{2+} у присутності повільного (EGTA) та швидкого (BAPTA) Ca^{2+} буферів.

На рис. 2.1В представлені цитозольні та мітохондріальні транзієнти $[Ca^{2+}]$, зафіксовані в 0.5 мМ розчині EGTA. Пермеабілізовані волокна постійно перфузувались внутрішнім розчином на основі EGTA, і кофеїн (20 мМ) додавали короткочасно з інтервалом в 3 хвилини. Кожне застосування кофеїну викликало короткочасний приріст співвідношення флуоресценції Fura-2 через вивільнення Ca^{2+} з SR (верхня панель). Паралельно до цього спостерігалось істотне зростанням флуоресценції Mag-rhod-2 (нижня панель), що відповідає підвищенню концентрації кальцію у мітохондріях.

У цьому та 11 інших волокнах EDL амплітуда цитозольних Ca^{2+}-транзієнтів, виміряна як $\Delta(F_{340}/F_{380})$, дорівнювала 0.44±0.05. А усереднена амплітуда мітохондріальних Ca^{2+}-транзієнтів у величинах $\Delta F_{540}/F_0(540)$ становила 0.23±0.02. Для підтвердження того, що сигнал, виміряний за допомогою Mag-rhod-2, дійсно віддзеркалює зміни мітохондріального [Ca^{2+}], було вивчено вплив протонофору FCCP. Завдяки тому, що поглинання Ca^{2+} мітохондріями переважно регулюється електрогенним уніпортером Ca^{2+}, нейтралізація мембранного потенціалу мітохондрій повинна обмежити здатність органел секвеструвати Ca^{2+}, який вивільнюється з СР під дією кофеїну.

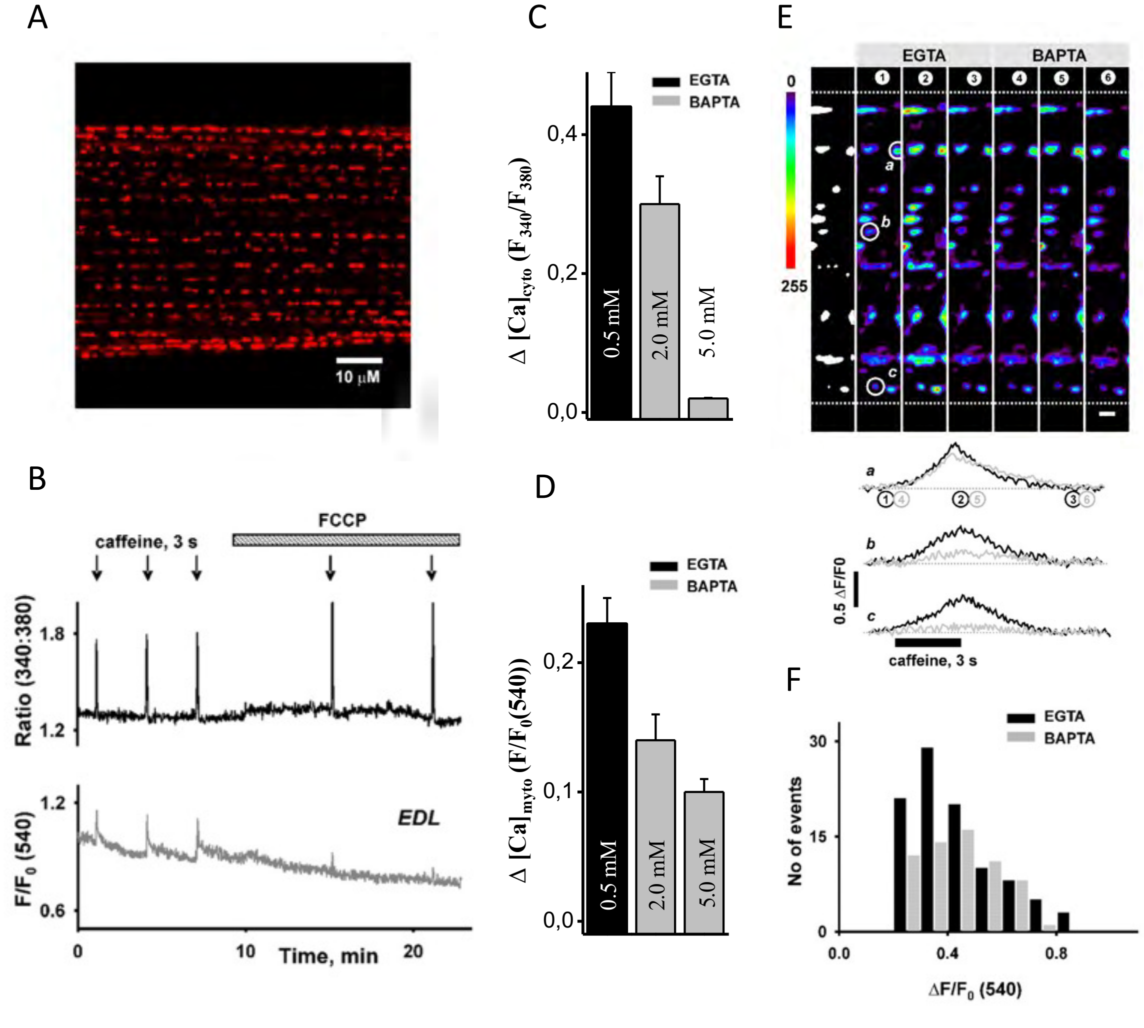

Рисунок 2.1. Структурні та функціональні взаємодії між мітохондріями та СР у м'язових волокнах. (A) Зображення м'язового волокна EDL, завантаженого Mag-rhod-2. (B) Цитозольні (верхні панелі) та мітохондріальні (нижні панелі) Ca^{2+} транзієнти в EDL, індуковані кофеїном, одночасно реєстровані за допомогою фотометра. Клітини навантажували мітохондріальним Ca^{2+} індикатором Mag-rhod-2, та потім пермеабілізовувалися сапоніном, та досліджували у внутрішньому розчині якій містив EGTA та Fura-2. Швидке застосування 20 мМ кофеїну (позначено стрілками) викликало синхронізовані цитозольні та мітохондріальні транзієнти Ca^{2+}. Амплітуди

цитозольних (C) та мітохондріальних (D) Ca^{2+}-транзієнтів, виміряна як $\Delta(F_{340}/F380)$ та $\Delta F540/F0(540)$ відповідно, у середовищах EGTA та BAPTA. (E) Середні амплітуди Ca^{2+}-транзієнтів індукованих кофеїном (зверху) та локальні зміни $\Delta[Ca^{2+}]m$ у середовищах EGTA та BAPTA (знизу). Крайня ліва панель демонструє бінарне зображення сегмента волокна для ділянок з $\Delta F/F_{0Bk} > 2$ S.D., де F_{0Bk} отримано усередненням інтенсивності флуоресценції по всіх пікселях зображення до застосування кофеїну. Псевдокольорові зображення демонструють моменти часу, вказані на графіку, що відображає транзієнт Ca^{2+} в мітохондріях, позначених кружечками. Графіки відображають транзієнти Ca^{2+} у середовищах EGTA (чорна лінія) і BAPTA (сіра лінія) в мітохондріях, позначених кружечками. Масштабна лінійка = 2 мкм. (F) Амплітудний розподіл локалізованих $\Delta[Ca^{2+}]m$. Враховувались лише сигнали, що перевищували рівень шуму на 3 S.D.; менш виражені сигнали були виключені.

Як і очікувалося, застосування 2.5 мкМ FCCP істотно знижувало флуоресценцію Mag-rhod-2 і майже повністю усував кофеїн-індуковані мітохондріальні Ca^{2+}-транзієнти в семи аналізованих клітинах. При цьому FCCP суттєво підвищував амплітуду цитозольних Ca^{2+} сигналів ($\Delta(F_{340}/F_{380})$, яка дорівнювала 0.40±0.06 до застосування та 0.48±0.07 після додавання препарату. Показано шо мітохондрії здатні секвеструвати кальцій який вивільнюються з СР.

Щоб дослідити близьке розташування між місцями вивільнення Ca^{2+} з СР та його поглинанням мітохондріями у скелетних м'язах щурів, ми провели експерименти з використанням швидкодіючого Ca^{2+} буфера BAPTA. Якщо просторове розташування між цими органелами є значним, що зумовлює необхідність дифузії Ca^{2+} з СР для його поглинання мітохондріями, тоді BAPTA має значно зменшити або навіть усунути як цитозольні, так і мітохондріальні Ca^{2+}-відповіді на кофеїн. Проте, якщо мітохондрії та СР розташовані дуже близько, формуючи мікродомени з високою концентрацією $[Ca^{2+}]$ під час вивільнення Ca^{2+} з СР, тоді BAPTA пригнічувала б тільки цитозольні сигнали Ca^{2+}, не впливаючи на мітохондріальні транзієнти. Це свідчило б про можливість тунелювання Ca^{2+} через такі мікродомени. В 11 клітинах EDL, інкубованих у 2 мМ BAPTA, середня амплітуда цитозольних транзієнтів Ca^{2+} в $\Delta(F_{340}/F_{380})$ дорівнювала 0.30±0.04, або 68.2% значення в EGTA. Схоже зменшення спостерігалося і в мітохондріальних транзієнтах Ca^{2+}. Усереднена амплітуда $\Delta[Ca^{2+}]m$ дорівнювала 0.14±0.02, або 60.9% контрольної амплітуди. При дослідженні волокон з вищою концентрацією BAPTA (5 мМ), результати відрізнялися. У шести клітинах EDL 5 мМ BAPTA майже повністю пригнічувала цитозольні транзієнти Ca^{2+} (середнє значення $\Delta(F_{340}/F_{380})$ було 0.02±0.001, або лише 4.5% від значення в EGTA), тоді як мітохондріальні відповіді на Ca^{2+} залишалися значущими (середнє значення $\Delta F_{540}/F_0(540)$ було 0.10±0.01, або 43.5% від контрольної амплітуди). Частина мітохондрій має бути розміщена на дуже близькій відстані від СР.

Щоб визначити, чи всі окремі мітохондрії скелетного м'яза рівномірно захоплюють Ca^{2+} та чи їх розташування сприяє цьому в умовах дії BAPTA, ми використали конфокальну мікроскопію для аналізу локальних змін $[Ca^{2+}]m$ у відповідь на аплікацію кофеїну.

На рис. 2.1E представлено скелетне м'язове волокно EDL, яке було навантажено Mag-rhod-2, пермеабілізоване та поміщене в розчині EGTA. Сегмент волокна (64 x 512 пікселів) було відскановано з частотою 11.7 Гц за допомогою конфокального сканера. У цьому та 21 інших волокнах EDL, що були досліджені в EGTA, кофеїн індукував підвищення рівня в майже всіх мітохондріях (454 з 461), які були ідентифіковані на зображеннях. У експериментах, де використовувались внутрішні розчини з 5 мМ BAPTA, прикладання кофеїну спричиняло зростання $[Ca^{2+}]m$ у приблизно 70% визначених мітохондрій (192 з 272) у 15 досліджених клітинах. Також, мітохондріальні транзієнти Ca^{2+}, індуковані кофеїном, були зафіксовані спочатку в EGTA, а потім у 5 мМ BAPTA. Зображення флуоресценції Mag-rhod-2 з волокна, отримані спочатку в EGTA (ліва панель) та потім в BAPTA (права панель), під час застосування 20 мМ кофеїну. В EGTA кофеїн викликав виразні транзієнти Ca^{2+} у всіх 18 ідентифікованих мітохондріях. Після зміни середовища на BAPTA, лише 10 мітохондрій продовжували секвеструвати Ca^{2+}. Лінійні діаграми внизу відображають зміни флуоресценції, асоційованої з Mag-rhod-2, у трьох окремих мітохондріях (вказані кружечками). На рис. 2.1F представлено розподіл амплітуд мітохондріальних транзієнтів Ca^{2+}, отриманих в EGTA та BAPTA для однієї й тієї ж групи мітохондрій. Усереднена максимальна амплітуда мітохондріальних транзієнтів становили 0.43±0.02 та 0.40±0.02 (в $\Delta F_{540}/F_0$ 540) після появи кофеїнової відповіді в EGTA та BAPTA, відповідно і ця різниця була статистично значущою.

У цілому, дані, представлені в цьому дослідженні, підтверджують існування двох різних типів структурно-функціональних взаємозв’язків між мітохондріями та СР у м'язових волокнах. Результати, отримані при низьких концентраціях BAPTA, свідчать, що деяка частина мітохондріальної популяції розташована на певній відстані від місць вивільнення Ca^{2+} з СР, і дифузія Ca^{2+}, ініційована відкриттям RyRs кофеїном, перешкоджає секвестрації Ca^{2+} цими віддаленими мітохондріями. З іншого боку, результати експериментів при високих концентраціях BAPTA вказують на наявність значної кількості мітохондрій, які мають прямий функціональний (і, імовірно, структурний) контакт із СР. У цих мітохондріях переважно відбувається пряме тунелювання Ca^{2+} між цими органелами. Оскільки ці мітохондрії також можуть поглинати Ca^{2+}, який дифундує від інших мітохондрій, висока концентрація BAPTA лише трохи знижує Ca^{2+} сигнали в цих органелах.

THE JOURNAL OF BIOLOGICAL CHEMISTRY VOL. 281, NO. 3, pp. 1547–1554, January 20, 2006

Transfer and Tunneling of Ca^{2+} from Sarcoplasmic Reticulum to Mitochondria in Skeletal Muscle*

Received for publication, May 6, 2005, and in revised form, September 6, 2005 Published, JBC Papers in Press, October 10, 2005, DOI 10.1074/jbc.M505024200

Vyacheslav M. Shkryl[1] **and Natalia Shirokova**[2]
From the Department of Pharmacology and Physiology, University of Medicine and Dentistry of New Jersey (UMDNJ), New Jersey Medical School, Newark, New Jersey 07103

The role of mitochondrial Ca^{2+} transport in regulating intracellular Ca^{2+} signaling and mitochondrial enzymes involved in energy metabolism is widely recognized in many tissues. However, the ability of skeletal muscle mitochondria to sequester Ca^{2+} released from the sarcoplasmic reticulum (SR) during the muscle contraction-relaxation cycle is still disputed. To assess the functional cross-talk of Ca^{2+} between SR and mitochondria, we examined the mutual relationship connecting cytosolic and mitochondrial Ca^{2+} dynamics in permeabilized skeletal muscle fibers. Cytosolic and mitochondrial Ca^{2+} transients were recorded with digital photometry and confocal microscopy using fura-2 and mag-rhod-2, respectively. In the presence of 0.5 mM slow Ca^{2+} buffer (EGTA (ethylene glycol-bis(2-aminoethylether)-*N,N,N′,N′*-tetraacetic acid)), application of caffeine induced a synchronized increase in both cytosolic and mitochondrial $[Ca^{2+}]$. 5 mM fast Ca^{2+} buffer (BAPTA (1,2-bis(2-aminophenoxy)ethane-*N,N,N′,N′*-tetraacetic acid)) nearly eliminated caffeine-induced increases in $[Ca^{2+}]_c$ but only partially decreased the amplitude of mitochondrial Ca^{2+} transients. Confocal imaging revealed that in EGTA, almost all mitochondria picked up Ca^{2+} released from the SR by caffeine, whereas only about 70% of mitochondria did so in BAPTA. Taken together, these results indicated that a subpopulation of mitochondria is in close functional and presumably structural proximity to the SR, giving rise to subcellular microdomains in which Ca^{2+} has preferential access to the juxtaposed organelles.

Mitochondria are one of the major subcellular structures in mammalian skeletal muscle. The key role of these organelles in muscle physiology was always considered to be the energy production via generation of ATP. In addition to this well documented function, more evidence has recently accumulated regarding the importance of mitochondrial Ca^{2+} transport in the intracellular Ca^{2+} homeostasis (*e.g.* Refs. 1–5). Some confirmation has also been obtained that mitochondrial Ca^{2+} uptake plays an important role in the regulation of Ca^{2+} signals during the contraction-relaxation cycle in mammalian skeletal muscle (*e.g.* Ref. 6, but see Ref. 7). Up to now, the most compelling data for a mitochondrial participation in excitation-contraction coupling of skeletal muscle was presented by Rudolf *et al.* (8). The authors reported rapid increases in mitochondrial $[Ca^{2+}]$ during single twitches or tetanic stimulation of mouse skeletal muscle *in vivo*. The increases in $[Ca^{2+}]_m$ were well synchronized with muscle contraction. These results are quite intriguing as the K_d for the mitochondrial Ca^{2+} uptake is believed to be too low and the kinetics of the uptake to be too slow to account for rapid mitochondrial Ca^{2+} transients during excitation-contraction coupling (for reviews, see *e.g.* Refs. 9 and 10). The apparent contradiction can be resolved, however, if a tight structural connection exists between mitochondria and the sarcoplasmic reticulum (SR)[3] in skeletal muscle. The latter would favor the existence of highly localized microdomains of elevated $[Ca^{2+}]$ during the SR Ca^{2+} release, which include both SR Ca^{2+} release sites and mitochondrial Ca^{2+} uptake sites (for a review, see Ref. 11).

Currently available morphological data, although revealing a close proximity of mitochondria to the SR in skeletal muscle (*e.g.* Ref. 12), place the organelles on the side of the SR/t-tubule junctions opposite to that where SR Ca^{2+} release takes place. The latter makes it somewhat difficult to conceptualize the intimate functional link between SR Ca^{2+} release and mitochondrial Ca^{2+} uptake during excitation-contraction coupling. The apparent discrepancies mentioned above underscore the need for additional functional and structural studies of the cross-talk between the two organelles. In the present study, we evaluated the functional proximity of the SR Ca^{2+} release sites and mitochondrial Ca^{2+} uptake sites in fast- and slow-twitch skeletal muscles of rat by comparing caffeine-induced cytosolic and mitochondrial Ca^{2+} transients in the presence of slow (EGTA) and fast (BAPTA) Ca^{2+} buffers.

EXPERIMENTAL PROCEDURES

Preparation of Skeletal Muscle Fibers and Solutions—Rats (Sprague-Dawley, 175–200 g) were killed by cervical dislocation under deep anesthesia induced by intraperitoneal injection of sodium pentobarbital (100–200 mg/kg of body weight). The Institutional Animal Care and Use Committee at UMDNJ-New Jersey Medical School approved the use and the method of euthanasia of animals in this study. The extensor digitorum longus (EDL) or soleus muscle was removed and pinned in a dissecting chamber. Small fiber segments were cut (as described in Refs. 13 and 14), transferred to an experimental chamber, and pushed down against the coverslip floor of the chamber. Segments were first loaded with 5 μM mag-rhod-2 AM for 20 min at room temperature and then washed, permeabilized with saponin (as in Ref. 4), and immersed into one of the "internal solutions." The total volume of solution in the chamber was ~500 μl.

"EGTA" internal solution contained (in mM): potassium L-glutamate (140), HEPES (10), EGTA (0.5), sodium phosphocreatine (5), Mg-ATP (5), and $CaCl_2$ (0.155) for a nominal $[Ca^{2+}]$ of 150 nM and $[Mg^{2+}]$ of 380 μM. "BAPTA" solutions had 2 or 5 mM BAPTA instead of EGTA. Nom-

---

* This work was supported by grants from the Muscular Dystrophy Association and NIAMS National Institutes of Health (Grant R01 AR45690). The costs of publication of this article were defrayed in part by the payment of page charges. This article must therefore be hereby marked "*advertisement*" in accordance with 18 U.S.C. Section 1734 solely to indicate this fact.

[1] Present address: A. A. Bogomoletz Institute of Physiology, Ukrainian National Academy of Sciences, Bogomoletz Street 4, Kiev, 01024, Ukraine.

[2] To whom correspondence should be addressed: Dept. of Pharmacology and Physiology, UMDNJ, New Jersey Medical School, 185 South Orange Ave., Newark, NJ 07103. Tel.: 973-972-8877; Fax: 973-972-7950; E-mail: nshiroko@umdnj.edu.

[3] The abbreviations used are: SR, sarcoplasmic reticulum; EGTA, ethylene glycol-bis-(2-aminoethylether)-*N,N,N′,N′*-tetraacetic acid; BAPTA, 1,2-bis(2-aminophenoxy)-ethane-*N,N,N′,N′*-tetraacetic acid; EDL, extensor digitorum longus; FCCP, carbonyl cyanide *p*-trifluoromethoxyphenylhydrazone.

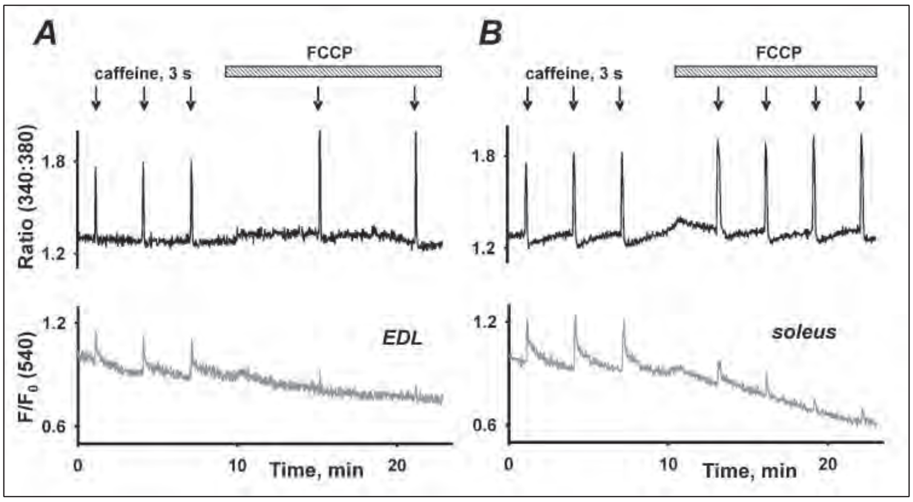

FIGURE 1. **Caffeine-induced cytosolic (*top panels*) and mitochondrial (*bottom panels*) Ca^{2+} transients simultaneously recorded with a photometer either in EDL (*A*) or in soleus (*B*) muscle fibers.** Cells were loaded with the mitochondrial Ca^{2+} indicator mag-rhod-2, permeabilized with saponin, and studied in EGTA internal solution containing fura-2. The rapid application of 20 mM caffeine (*arrows*) elicited synchronized cytosolic and mitochondrial Ca^{2+} transients. Note that 2.5 μM FCCP markedly attenuates $\Delta[Ca^{2+}]_m$ and increases $\Delta[Ca^{2+}]_c$, confirming the mitochondrial origin of the mag-rhod-2 signals.

inal $[Ca^{2+}]$ and $[Mg^{2+}]$ were also adjusted to 150 nM and 380 μM, respectively. Dissociation constants were taken from the National Institute of Standards and Technology (NIST) Critically Selected Stability Constants of Metal Complexes Database 46 (U. S. Department of Commerce, Technology Administration, NIST, Gaithersburg, MD). Both solutions contained a low concentration of the fluorescent Ca^{2+} indicator fura-2 (2 μM; potassium salt) and 20 μM *N*-benzyl-*p*-toluene sulfonamide to minimize the contraction of fast-twitch EDL fibers. To reduce movement artifacts fibers were also stretched to about 3.5 mm sarcomere length. pH was adjusted to 7.0 with KOH, and osmolality was 300 mosmol/kg.

Fluorescence Measurements—To study the mutual relationship between ligand-stimulated cytosolic and mitochondrial $[Ca^{2+}]$ transients, we modified the technique introduced by Duke and Steele (15). Throughout the experimental protocol, the permeabilized fiber preloaded with mag-rhod-2 was continuously perfused with internal solution containing fura-2 at a rate of ~0.5 ml/min. Waste solution was collected at the outlet pool. Solutions containing 20 mM caffeine were rapidly applied (~2 ml/min) for a duration of 3 s via a dedicated inlet pipette. Cytosolic Ca^{2+} transients were recorded as ratiometric fura-2 signals. At the same time, changes in mitochondrial $[Ca^{2+}]$ were estimated from the mag-rhod-2 signals. Mag-rhod-2 fluorescence decreased by about 50% after permeabilization, suggesting that most of the dye initially trapped in the cytoplasm was washed out. The rest of the dye was accumulated in mitochondria (as shown in Ref. 4).

Fluorescence measurements were carried out with a RatioMaster M-40 fluorescence photometer (Photon Technology International, Lawrenceville, NJ) mounted on a Zeiss Axiovert 200 microscope (Zeiss Inc., Oberkochen, Germany) equipped with a quartz ×40, 1.25 NA, glycerol immersion objective (Partec GmbH, Münster, Germany). The fiber was illuminated with light of 340 or 380 nm (for fura-2) and 540 nm (for mag-rhod-2) at 1 ÷ 20 Hz. The fluorescence emission was detected through a rectangular pinhole placed in the center of the fiber. Cytosolic Ca^{2+} transients are presented as the excitation ratio (340:380 nm) of light intensities emitted above 500 nm. Mitochondrial transients are presented in arbitrary units as light intensities emitted above 570 nm.

Imaging Local Changes in $[Ca^{2+}]$ within Individual Mitochondria—Mitochondria labeled with mag-rhod-2 (as described above) were imaged with a confocal laser scanning microscope (Radiance 2000; Bio-Rad) mounted on a Zeiss Axiovert 100 inverted microscope equipped with a ×63, 1.2 NA, water immersion lens (Zeiss Inc., Oberkochen, Germany). Mag-rhod-2 was excited with the 543 nm line of a HeNe laser. The emitted light was collected above 570 nm.

Chemicals and Statistics—Fura-2 was obtained from Biotium (Hayard, CA). Mag-rhod-2 was purchased from Molecular Probes (Eugene, OR). Other chemicals were from Sigma. Values are presented as means ± S.E., and *n* represents the number of analyzed cells or mitochondria. Student's *t* test was used for comparing paired observations. $p < 0.05$ was considered significant.

RESULTS

Cytosolic and Mitochondrial $[Ca^{2+}]$ Transients in 0.5 mM EGTA—Fig. 1*A* show cytosolic and mitochondrial Ca^{2+} transients recorded at the same time from EDL muscle fiber at 1 Hz. In this series of experiments, fibers were constantly perfused with EGTA internal solution, and caffeine (20 mM) was briefly applied at 3-min intervals. Each caffeine application resulted in a transient increase in the fura-2 fluorescence ratio due to SR Ca^{2+} release (*upper panel*). Under our experimental conditions, each 3-s exposure to 20 mM caffeine produced a Ca^{2+} transient of maximal amplitude as more prolonged application of caffeine did not substantially increase the amplitude of the response. From *in situ* calibration experiments, we know that this was not due to saturation of fura-2 ($R_{340/380\,\max} = 4.68$, $R_{340/380\,\min} = 0.74$, $K_d = 386$ nM). Increasing the time interval between caffeine pulses also had no effect on the amplitude of caffeine-induced transients, suggesting that SR was completely reloaded with Ca^{2+} between the caffeine pulses. In this and 11 other EDL fibers, the amplitude of the cytosolic Ca^{2+} transients expressed in $\Delta R_{340/380}$ was 0.44 ± 0.05. In Fig. 1*A*, the *bottom panel* illustrates that the release of Ca^{2+} from the SR also resulted in a substantial increase in the mag-rhod-2 fluorescence. The averaged amplitude of the mitochondrial Ca^{2+} transients in units of $\Delta F_{540}/F_{0\,540}$ was 0.23 ± 0.02. To show that the signal measured with mag-rhod-2 indeed reflects changes in mitochondrial $[Ca^{2+}]$, the effect of the protonophore FCCP was examined. Since Ca^{2+} uptake into mitochondria is largely governed by an electrogenic Ca^{2+} uniporter, dissipation of mitochondrial membrane potential should impair the ability of the organelles to sequester Ca^{2+} released from the SR by caffeine. As expected, the application of 2.5 μM FCCP significantly decreased the mag-rhod-2 fluorescence and nearly eliminated caffeine-induced mitochondrial Ca^{2+} transients in seven cells studied. At the same time, FCCP significantly increased the amplitude of cytosolic Ca^{2+} signals in five out of seven

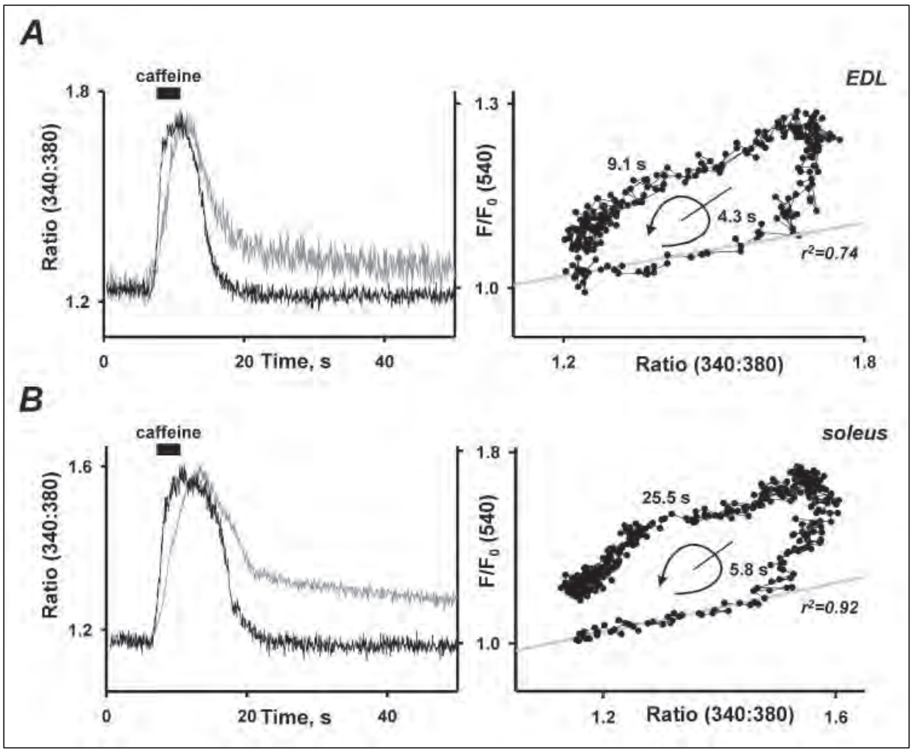

FIGURE 2. **Temporal characteristics of caffeine-induced cytosolic and mitochondrial Ca^{2+} transients.** *Left panels* show superimposed cytosolic and mitochondrial Ca^{2+} transients in EDL (*A*) and soleus (*B*) fibers, respectively. *Right panels* plot fura-2 ratio *versus* mag-rhod-2 fluorescence from the traces on the *left*. The *curved counterclockwise arrow* gives an approximation of the time course for each phase of the response. Although during the first 2.5 s both signals changed in a synchronized fashion (as indicated by the *gray regression lines*), the mitochondrial signal lagged behind the cytosolic Ca^{2+} transient during later phases of the signal.

cells ($\Delta R_{340/380}$ was 0.40 ± 0.06 and 0.48 ± 0.07, respectively, before and after the drug was added).

Fig. 1*B* illustrates a similar set of experiments carried out on 12 permeabilized soleus muscle fibers. The application of caffeine produced substantial cytosolic ($\Delta R_{340/380}$ was 0.34 ± 0.03) and mitochondrial ($\Delta F_{540}/F_{0\ 540}$ was 0.42 ± 0.07) Ca^{2+} transients. Similar to the experiments with EDL cells, 2.5 μM FCCP progressively eliminated caffeine-induced mitochondrial Ca^{2+} transients, gradually reduced mitochondrial $[Ca^{2+}]$, and significantly increased the amplitude of cytosolic Ca^{2+} transients (from 0.34 ± 0.05 to 0.50 ± 0.04, $n = 4$, in units of $\Delta R_{340/380}$).

In Fig. 2, the *left panels* represent superimposed records of cytosolic (*black lines*) and mitochondrial (*gray lines*) Ca^{2+} signals recorded in EDL (*panel A*) and soleus (*panel B*) muscle cells at 20 Hz. The caffeine-induced cytosolic Ca^{2+} transients exhibited a relatively slow time course. The maximal increase in $\Delta[Ca^{2+}]_c$ was reached 4.1 and 4.9 s after the onset of the application of caffeine in EDL and soleus fibers, respectively. The Ca^{2+} transients then decreased to the resting value with a half-time ($t_{1/2}$) of 3.2 and 5.8 s for EDL and soleus cells, respectively. Cytosolic transients were closely accompanied by the mitochondrial Ca^{2+} signals. The kinetics of mitochondrial transients was somewhat slower than that of cytosolic signals. The maximal increase in $[Ca^{2+}]_m$ occurred 5.2 and 7.2 s after caffeine application, and $t_{1/2}$ was 3.4 and 6.4 s in EDL and soleus fibers, correspondingly. However, mitochondrial $[Ca^{2+}]$ started to increase immediately after cytosolic $[Ca^{2+}]$ rose above the resting level. This is clearly seen in Fig. 2 (*right panels*), in which $\Delta[Ca^{2+}]_m$ *versus* $\Delta[Ca^{2+}]_c$ are plotted on an expanded time scale. The *gray regression lines* show a strong positive correlation between the transients at the initial phase of their development.

On average, the maximal increase in $\Delta[Ca^{2+}]_c$ occurred 3.40 ± 0.23 s ($n = 12$) after the onset of the 3-s application of caffeine in EDL fibers and 5.05 ± 0.48 s ($n = 12$) after the onset in soleus cells. $[Ca^{2+}]_c$ decreased to its resting value with a half-time of 3.78 ± 0.37 and 4.78 ± 0.42 s, in EDL and soleus cells, respectively. In the same set of experiments, the time to both the maximal increase in $[Ca^{2+}]_m$ and the $t_{1/2}$ were significantly longer (4.97 ± 0.28 and 6.84 ± 0.51 s; 4.93 ± 0.89 and 6.8 ± 0.82 s in EDL and soleus cells, respectively).

Cytosolic and Mitochondrial $[Ca^{2+}]$ Transients in 2 and 5 mM BAPTA—To probe the functional proximity of Ca^{2+} release sites and mitochondrial Ca^{2+} uptake sites in fast- and slow-twitch skeletal muscles of rat, we repeated the same type of experiments as illustrated in Figs. 1 and 2, in the presence of the fast Ca^{2+} buffer BAPTA. If the organelles are substantially separated in space such that mitochondrial Ca^{2+} uptake requires diffusion of Ca^{2+} released from the SR, then BAPTA would dramatically attenuate (or even eliminate) both caffeine-induced cytosolic and mitochondrial Ca^{2+} transients. However, if mitochondria and SR are in sufficiently close spatial proximity, this could result in the formation of microdomains of high $[Ca^{2+}]$ during SR Ca^{2+} release. Ca^{2+} could then reach the mitochondria by "tunneling" via these microdomains and could not be intercepted by BAPTA. As a consequence, BAPTA (at a suitable concentration) would only suppress the cytosolic Ca^{2+} signals but not eliminate mitochondrial Ca^{2+} transients.

In our experiments, 2 mM BAPTA partially suppressed both cytosolic and mitochondrial Ca^{2+} signals produced by the application of caffeine. Furthermore, 5 mM BAPTA nearly eliminated cytosolic but did not further substantially reduce mitochondrial transients. Fig. 3 shows representative caffeine-induced $\Delta[Ca^{2+}]_c$ and $\Delta[Ca^{2+}]_m$ signals recorded from EDL (*A*) and soleus (*B*) fibers incubated in 5 mM BAPTA solution. In both fibers, the cytosolic Ca^{2+} indicator fura-2 failed to detect substantial increases in $[Ca^{2+}]_c$ following the application of caffeine, whereas mag-rhod-2 reported considerable $\Delta[Ca^{2+}]_m$.

In 11 EDL cells bathed in 2 mM BAPTA, the average amplitude of cytosolic Ca^{2+} transients in $\Delta R_{340/380}$ units was 0.30 ± 0.04, which constitutes 68.2% of the value obtained in EGTA. A comparable

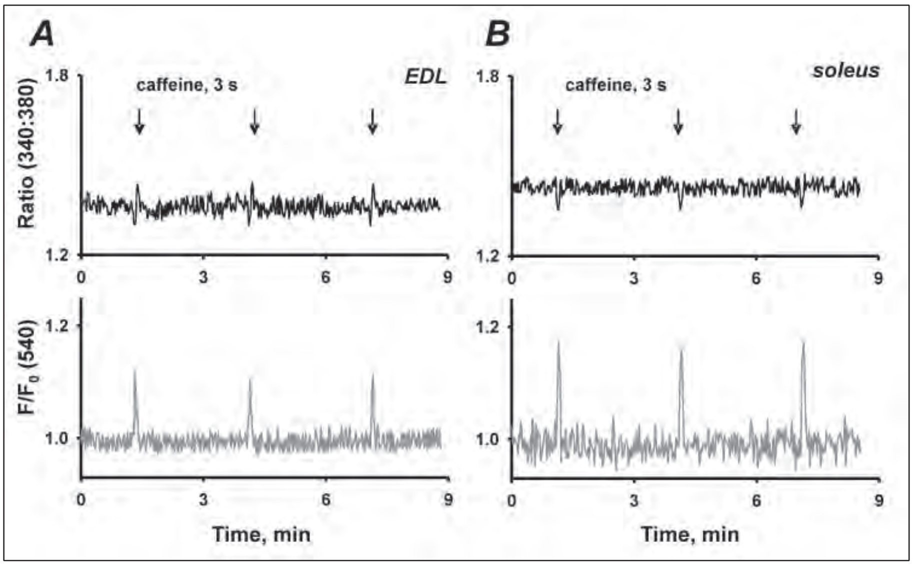

FIGURE 3. **Caffeine-induced $\Delta[Ca^{2+}]_c$ and $\Delta[Ca^{2+}]_m$ in 5 mM BAPTA.** *A* and *B*, cytosolic (*top panels*) and mitochondrial (*bottom panels*) Ca^{2+} transients simultaneously recorded in the presence 5 mM BAPTA in EDL (*A*) and soleus (*B*) fibers. Although the cytosolic Ca^{2+} signals were completely suppressed by the rapid Ca^{2+} buffer BAPTA, the mitochondrial transients remained clearly visible, suggesting preferential access or tunneling of SR Ca^{2+} into the mitochondria. The small deflections in the cytosolic traces during the application of caffeine result from small motion artifacts and/or from slight quenching of fura-2 signal by caffeine.

decrease was also observed in mitochondrial Ca^{2+} transients with respect to control (EGTA). The averaged amplitude of $\Delta[Ca^{2+}]_m$ expressed in units of $\Delta F_{540}/F_{0\,540}$ was 0.14 ± 0.02, which is 60.9% of the control amplitude. In addition, whereas 2 mM BAPTA did not substantially change the kinetics of cytosolic Ca^{2+} transients (time to the peak was 3.81 ± 0.18 when compared with 3.40 ± 0.23 s in EGTA), it significantly sped up mitochondrial transients (time to the peak was 3.86 ± 0.16 when compared with 4.97 ± 0.28 s in EGTA).

A similar observation was also made in 11 soleus fibers. The averaged amplitudes of $\Delta[Ca^{2+}]_c$ and $\Delta[Ca^{2+}]_m$ in 2 mM BAPTA were 0.20 ± 0.02 and 0.21 ± 0.03, respectively, which correspond to 58.8 and 52.5% of the control values obtained in EGTA. The kinetics of mitochondrial but not cytosolic transients was also significantly faster in 2 mM BAPTA (see Table 1 for details).

When fibers were studied at a higher concentration of BAPTA (5 mM), quantitatively different results were obtained. In six EDL cells, 5 mM BAPTA nearly eliminated cytosolic Ca^{2+} transients (averaged $\Delta R_{340/380}$ was 0.02 ± 0.001, or only 4.5% of the value obtained in EGTA). At the same time, the mitochondrial Ca^{2+} responses remained substantial (the averaged $\Delta F_{540}/F_{0\,540}$ was 0.10 ± 0.01, which is 43.5% of the control amplitude). A similar observation was also made in six soleus fibers. Although no caffeine-induced cytosolic Ca^{2+} signals could be detected in BAPTA, corresponding mitochondrial Ca^{2+} transients were still recorded. The averaged amplitude of $\Delta[Ca^{2+}]_m$ was 0.15 ± 0.02, or 37.5% of that measured in EGTA. It also turned out that in both fiber types, the kinetics of $\Delta[Ca^{2+}]_m$ in high BAPTA was not significantly different from the kinetics of $\Delta[Ca^{2+}]_c$ in EGTA (time to the peak was 3.81 ± 0.48 and 5.08 ± 0.74 s, for EDL and soleus cells, correspondingly).

Local Changes in $[Ca^{2+}]_m$ in EGTA—To establish whether all individual mitochondria in skeletal muscle pick up Ca^{2+} in the same way and whether they are all strategically positioned to do so in BAPTA, we employed confocal imaging and studied local changes in $[Ca^{2+}]_m$ in response to caffeine applications. Fig. 4*A* shows an EDL skeletal muscle fiber, which has been loaded with mag-rhod-2, permeabilized, and immersed in EGTA solution. The subcellular organization of the organelles was very similar to that observed when tetramethylrhodamine ethyl ester fluorescence or NADH autofluorescence was used to monitor mitochondrial membrane potential or mitochondrial redox state (4, 5).

A fiber segment (64 × 512 pixels) was imaged at 11.7 Hz with a confocal scanner. Mitochondria were identified with an automatic digital image-processing algorithm similar to that used for spark detection (16). They are shown as binary masks on the *left* in *panel B*. *Panel B* also represents pseudocolor images of raw fluorescence obtained from the same location within the fiber before, during, and after application of 20 mM caffeine. Averaged fluorescent signals emitted by mag-rhod-2 trapped inside identified mitochondria were determined at every image of the series, normalized to the corresponding mag-rhod-2 fluorescence values before the application of caffeine, and plotted against time. The line plot on the *bottom* represents changes in mag-rhod-2-related fluorescence within a mitochondrion (or small groups of mitochondria) indicated by a *circle*. $\Delta[Ca^{2+}]_m$ reached its peak of 0.49 (in $\Delta F_{540}/F_{0\,540}$) 3.68 s after onset of caffeine application.

In this and 21 other EDL fibers studied in EGTA, caffeine produced increases in almost all (454 out of 461) mitochondria identified on the images. Fig. 3, *C* and *D*, summarize amplitudes and spatial characteristics of local mitochondrial transients recorded in EGTA. Only transients with an amplitude of $\Delta F/F_0 > 3$ S.D. were analyzed. They varied substantially in their peak amplitude and temporal onsets. Similarly to those recorded from a whole cell, caffeine-induced mitochondrial transients were relatively slow (with a time to the peak after the onset of caffeine pulse corresponding to 4.32 ± 0.02 s) and reached maximal amplitude of 0.47 ± 0.01 (in $\Delta F_{540}/F_{0\,540}$).

Local Changes in $[Ca^{2+}]_m$ in 5 mM BAPTA—In this group of experiments, we studied localized mitochondrial Ca^{2+} transients in EDL fibers incubated in 5 mM BAPTA. Fiber segments were imaged with a fast confocal scanner. Mitochondria were identified on the images obtained before caffeine pulses were applied. Local Ca^{2+} transients in individual or small groups of mitochondria were analyzed in the same way as in the experiments with EGTA.

Fig. 5*A* represents pseudocolor images of raw fluorescence obtained from the same location within a fiber before, during, and after caffeine was applied. On the *left* is a mask image of identified mitochondria. In this particular fiber, caffeine produced substantial (with an amplitude $\Delta F/F_0 > 3$ S.D.) Ca^{2+} transients in 6 out of 14 mitochondria. The line plots on the *bottom* illustrate changes in mag-rhod-2-related fluorescence within two different mitochondria with contrast responses to caffeine.

TABLE 1

Amplitudes and temporal characteristics of caffeine-induced cytosolic and mitochondrial Ca^{2+} transients in EDL and soleus fibers

	$\Delta[Ca^{2+}]_c$		$\Delta[Ca^{2+}]_m$	
	Amplitude	Time to the peak	Amplitude	Time to the peak
	$\Delta R_{340/380}$	*s*	$\Delta F_{540}/F_{0\ 540}$	*s*
EDL fibers				
0.5 EGTA, *n* = 12	0.44 ± 0.05	3.40 ± 0.23	0.23 ± 0.02	4.97 ± 0.28
2 BAPTA, *n* = 11	0.30 ± 0.04	3.81 ± 0.18	0.14 ± 0.02	3.86 ± 0.16
5 BAPTA, *n* = 6	0.02 ± 0.001	NA	0.10 ± 0.01	3.81 ± 0.48
Soleus fibers				
0.5 EGTA, *n* = 12	0.34 ± 0.03	5.05 ± 0.48	0.42 ± 0.07	6.84 ± 0.51
2 BAPTA, *n* = 11	0.20 ± 0.02	5.40 ± 0.79	0.21 ± 0.03	5.45 ± 0.72
5 BAPTA, *n* = 6	NA	NA	0.15 ± 0.02	5.08 ± 0.74

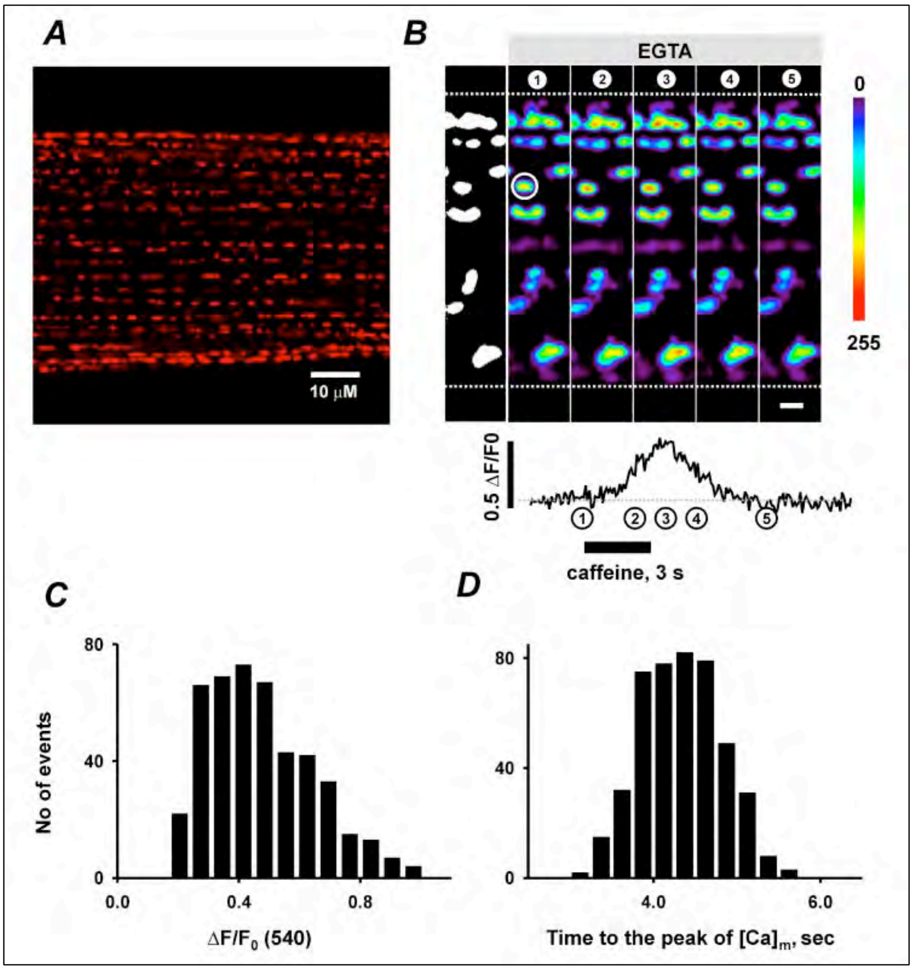

FIGURE 4. **Local mitochondrial Ca^{2+} transients in EGTA.** *A*, image of EDL muscle fiber loaded with mag-rhod-2. *B*, subcellular changes in $\Delta[Ca^{2+}]_m$ elicited by the application of caffeine. The *leftmost panel* shows a binary image of the fiber segment for the regions with $\Delta F/F_{0Bk} > 2$ S.D., where F_{0Bk} was obtained by averaging fluorescence intensity in all pixels on the image before a caffeine pulse. Pseudocolor images were obtained at the times indicated on the plot, which represents a Ca^{2+} transient within the mitochondria indicated by the *circle*. The *scale bar* corresponds to 2 μm. *C* and *D*, amplitude distribution and temporal characteristics of localized $\Delta[Ca^{2+}]_m$.

In 15 cells, the application of caffeine produced an increase in $[Ca^{2+}]_m$ in ~70% of the identified mitochondria (192 out of 272). Mitochondrial transients reached a maximal amplitude of 0.39 ± 0.01 (in $\Delta F_{540}/F_{0\ 540}$) 4.20 ± 0.04 s after the onset of the caffeine pulse (Fig. 5, *B* and *C*).

Local Changes in $[Ca^{2+}]_m$ in EGTA and 5 mM BAPTA in the Same Population of Mitochondria—Mag-rhod-2 is a non ratiometric Ca^{2+} indicator. Its concentration inside different mitochondria may vary. The latter, in principle, could contribute to the heterogeneity of mitochondrial Ca^{2+} responses observed in our experiments. Although the analysis revealed no correlation between the amplitude of mitochondrial Ca^{2+} transients and resting mag-rhod-2 fluorescence, both in EGTA and in BAPTA (regression coefficients r^2 were 0.004 and −0.001, respectively), we used an additional approach to clarify this issue. EDL cells were loaded with mag-rhod-2, and caffeine-induced mitochondrial Ca^{2+} transients from the same group of mitochondria were recorded first in EGTA and then in 5 mM BAPTA internal solutions. Fig. 6*A* represents images of fluorescence obtained from a fiber first in EGTA (*left panel*) and then in BAPTA (*right panel*) during the application of 20 mM caffeine. In EGTA, caffeine produced substantial Ca^{2+} transients in all 18 identified mitochondria. After the fiber was immersed in BAPTA, only 10 mitochondria remained capable of sequestering Ca^{2+}. The line plots on the *bottom* illustrate changes in mag-rhod-2-related fluorescence within three different mitochondria (indicated by *circles*).

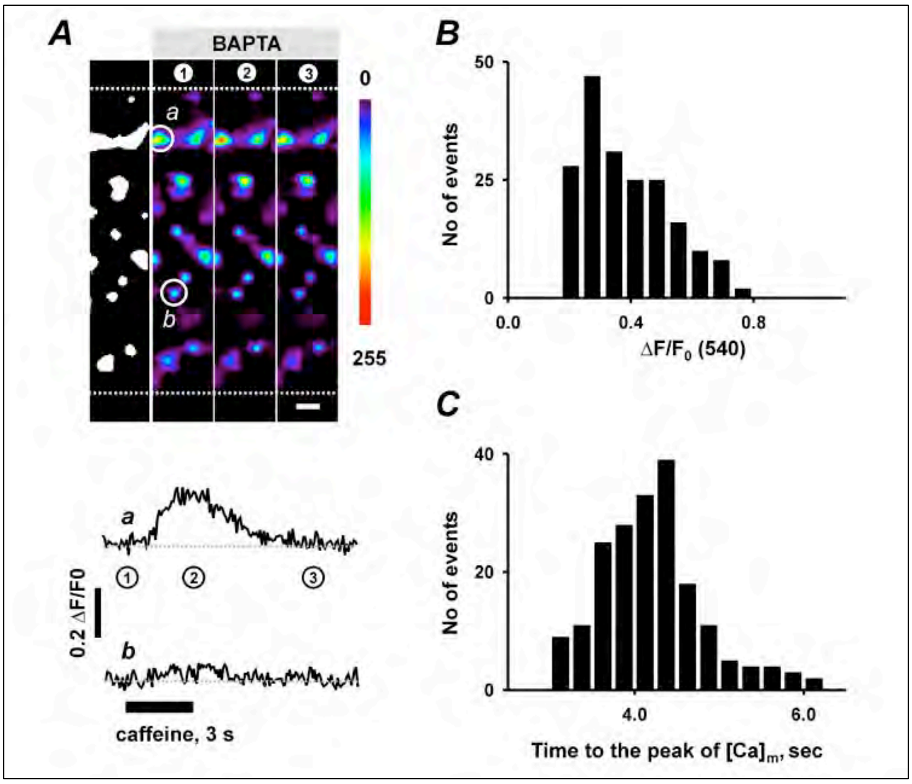

FIGURE 5. **Local mitochondrial Ca^{2+} transients in 5 mM BAPTA.** *A*, caffeine-induced subcellular changes in Δ[Ca^{2+}]$_m$. The *leftmost panel* shows a binary image of the detected mitochondria (*white*). Confocal images were obtained at the times indicated on the plots, which represent Ca^{2+} transients within mitochondria indicated by *circles*. The *scale bar* corresponds to 2 μm. *B* and *C*, amplitude distribution and temporal characteristics of localized Δ[Ca^{2+}]$_m$. Only signals larger than 3 S.D. above noise (*e.g. panel A, a*) were analyzed, and smaller signals were excluded (*e.g. panel A, b*).

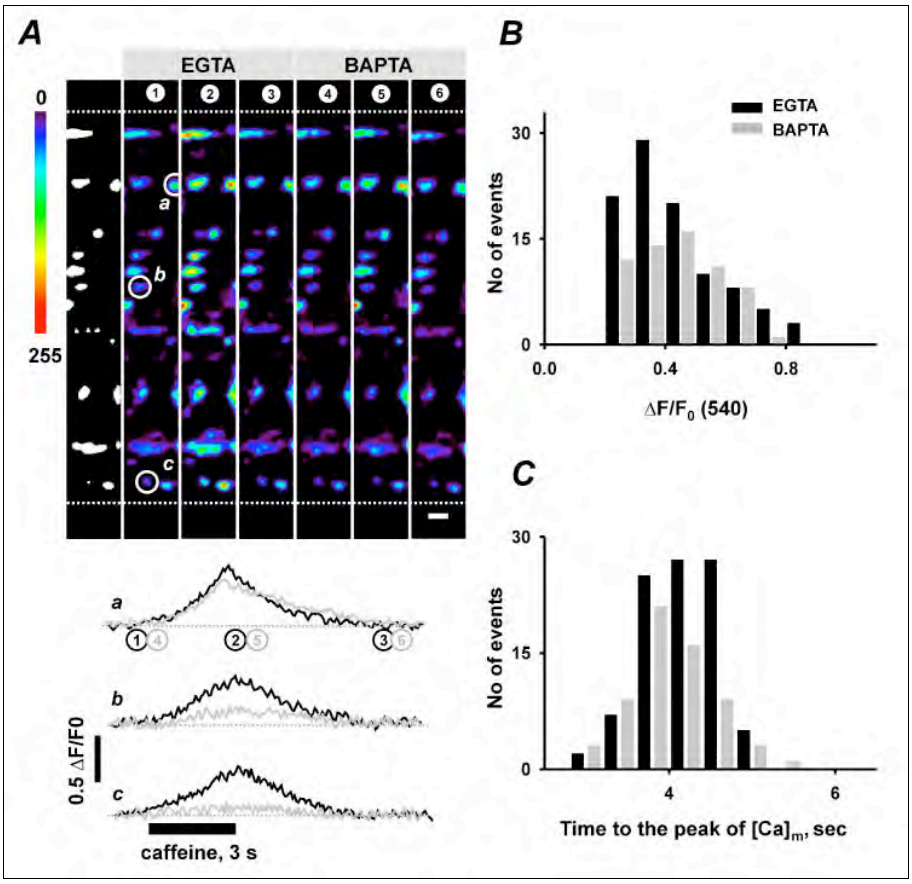

FIGURE 6. **Local mitochondrial Ca^{2+} transients in EGTA and BAPTA.** *A*, caffeine-induced local changes in Δ[Ca^{2+}]$_m$ in EGTA and BAPTA. Confocal images were obtained from one cell at the times indicated on the plots shown at the *bottom*. Plots represent Ca^{2+} transients in EGTA (*black line*) and BAPTA (*gray line*) within mitochondria indicated by *circles*. The *scale bar* corresponds to 2 μm. *B* and *C*, amplitude distribution, and temporal characteristics of localized Δ[Ca^{2+}]$_m$. Only signals larger than 3 S.D. above noise were analyzed, and smaller signals were excluded.

In BAPTA, caffeine elicited Ca^{2+} transients in ~70% (64 out of 92, $n = 6$ cells) of mitochondria that initially picked up Ca^{2+} in EGTA. Fig. 6, *B* and *C*, summarize amplitudes and temporal characteristics of mitochondrial transients obtained in EGTA and BAPTA in the same group of mitochondria. On average, mitochondrial transients reached maximal amplitude of 0.43 ± 0.02 and 0.40 ± 0.02 (in $\Delta F_{540}/F_{0\ 540}$) 4.15 ± 0.05 and 4.00 ± 0.06 s after the onset of the caffeine pulse in EGTA and BAPTA, respectively.

Studies with High Affinity Mitochondrial Ca^{2+} Indicators—Here we performed several crucial tests to prove the adequacy of the experimental procedure (and the probe) we used to measure mitochondrial Ca^{2+} signals. Mag-rhod-2 is a low affinity Ca^{2+} indicator with *in vitro* K_d of about 70 μM. If some mitochondria have $[Ca^{2+}]$ below the dynamic range of the indicator, they would not report any transients during a caffeine pulse. Therefore, some experiments were repeated using the higher affinity mitochondrial Ca^{2+} indicators rhod-2 ($K_d = 570$ nM) and rhod-2FF ($K_d = 19$ μM). In five EDL cells studied in EGTA with digital photometry, rhod-2 did not report any caffeine-induced Ca^{2+} signals, whereas fura-2 reported cytosolic transients of normal amplitude (0.85 ± 0.17 in units of $\Delta R_{340/380}$). In 10 EDL cells studied in EGTA with confocal microscopy, rhod-2FF reported tiny 0.23 ± 0.01 (in $\Delta F_{540}/F_{0\ 540}$) transients only in 16% of mitochondria (42 out of 263) detected on the images. At the same time, in five fibers studied in parallel with mag-rhod-2, all 70 identified mitochondria picked up Ca^{2+} released from the SR by caffeine with an averaged amplitude of 0.52 ± 0.02 in $\Delta F_{540}/F_{0\ 540}$. These experiments indicated that resting $[Ca^{2+}]_m$ in permeabilized skeletal muscle is much higher than in the majority of previously studied cell types and is probably ~100 μM. The results also suggested that an intrinsic variability of the mitochondrial capability to sequester Ca^{2+} is accountable for the phenomena described in this study.

Taken together, the data presented in this study were consistent with the existence of two distinctive types of structural and functional connections between mitochondria and SR in fast- and slow-twitch muscle fibers. The findings obtained with low concentrations of BAPTA suggest that a fraction of the mitochondrial population is located at some distance from the SR Ca^{2+} release sites, and diffusion of Ca^{2+} released by caffeine precedes Ca^{2+} sequestration by those more distant mitochondria. On the other hand, the results from experiments with high BAPTA concentrations indicate that a substantial number of mitochondria have a tight functional (and therefore most likely also structural) contact with the SR. Within this population of mitochondria, there is a preferential transfer or tunneling of Ca^{2+} between the organelles. Because these mitochondria are also likely to take up Ca^{2+} diffusing from spatially distant mitochondria, high BAPTA somewhat reduced the Ca^{2+} signals in these organelles.

DISCUSSION

Tight structural association between the SR (or endoplasmic reticulum) and mitochondria has been described in many cell types (*e.g.* Refs. 17–19). Multiple pathways have been implicated for a functional interaction between the organelles. In particular, there are several lines of evidence indicating that mitochondria are involved in shaping spatiotemporal characteristics of intracellular Ca^{2+} signals during cell activation (reviewed by Refs. 9, 11, and 20). One of the involved mechanisms is believed to be mitochondrial Ca^{2+} uptake. It is likely that strategic positioning of mitochondria in close proximity to the Ca^{2+} release sites optimizes the transfer of released Ca^{2+} to mitochondria, making the organelles an effective and fast Ca^{2+} buffer *in vivo* in many tissues.

However, in skeletal muscle, the issue of an involvement of mitochondrial Ca^{2+} transport in the regulation of physiological Ca^{2+} signals remains unclear, especially during the rapid and large Ca^{2+} signals in excitation-contraction coupling. It has been shown that mitochondria of skeletal muscle myotubes are capable of Ca^{2+} accumulation in response to depolarizations or caffeine applications (21–23). Moreover, there are some findings suggesting that increases in $[Ca^{2+}]_m$ up-regulate mitochondrial ATP synthesis in myotubes and therefore adjust muscle metabolism to the physiological demands (24). As to the mitochondrial sequestration of Ca^{2+} released from the SR during a single twitch or during a tetanic stimulation of mature skeletal muscle, the data are somewhat contradictory. Using the mitochondrial Ca^{2+} indicator rhod-2, Bruton *et al.* (6) showed substantial Ca^{2+} accumulation in skeletal muscle mitochondria of EDL and soleus muscle fibers of mice during electrical stimulation. However, the same group of investigators failed to detect any increases in $[Ca^{2+}]_m$ in fast-twitch flexor digitorum brevis muscle fibers isolated from mice (7). On the other hand, Rudolf *et al.* (8), using a genetically expressed "cameleon" Ca^{2+} sensor, demonstrated fast mitochondrial Ca^{2+} transients during stimulation of contraction in fast-twitch mouse tibialis anterior muscle *in vivo*.

Studies of parvalbumin knock-out mice provide additional support for a Ca^{2+} buffering function of skeletal muscle mitochondria. Chen *et al.* (25) found that the fractional volume of mitochondria in the fast-twitch EDL muscle is almost doubled in parvalbumin knock-out mice when compared with the wild type. The fatigue resistance of the muscle increased, and removal of cytosolic Ca^{2+} after electrical stimulation was substantially accelerated. These observations were interpreted to suggest that by increasing the mitochondrial volume and mitochondrial Ca^{2+} buffering capacity, the EDL muscle tries to compensate for the lack of cytoplasmic Ca^{2+} buffer parvalbumin.

Unfortunately, the present shortage of comprehensive ultrastructural studies, in particular regarding the three-dimensional subcellular arrangement of the organelles, does not help to resolve the contradiction revealed by functional probing of the Ca^{2+} cross-talk between SR and mitochondria. According to Ogata and Yamasaki (12), there are two major subpopulations of mitochondria, which have very different subcellular organization. The first group is comprised of "I-band limited mitochondria." They are located on both sides of the Z-line and seem to wrap the terminal cisternae of the SR, although on the side opposite to the SR/t-tubule junction. The second group consists of mitochondria forming columns in the intermyofibrillar or subsarcolemmal space. The organelles of this group have much fewer contacts with the SR.

The results reported in this study represented strong additional evidence for a close functional connection between the SR and mitochondria in adult fast- and slow-twitch skeletal muscle. For a long time, the mobile calcium buffers EGTA and BAPTA have been elegant tools to test temporal and spatial functional compartmentalization of calcium signals within living cells. In particular, the two buffers were used in functional studies of microdomains of high $[Ca^{2+}]$ between Ca^{2+} release channels and mitochondrial Ca^{2+} uptake sites in smooth and cardiac muscle cells (19, 26). In these microdomains, $[Ca^{2+}]$ readily reaches levels of many tens of micromoles to activate low affinity processes, such as mitochondrial Ca^{2+} uptake. Buffers tend to shape up steep Ca^{2+} gradients in the close vicinity of release channels because the microdomains dissipate depending on the concentration, chemical kinetics, and diffusional mobility of the buffers (*e.g.* Refs. 27–29). In general, EGTA, having a relatively slow binding rate to Ca^{2+}, is not effective in buffering Ca^{2+} within the microdomains; thus Ca^{2+} can travel hundreds of nm before being captured by the buffer. In contrast, BAPTA has much faster on-rate kinetics. As a result, it is much more effective in spatially confining microdomains of high [Ca^{2+}] to several dozens of nm from the source.

In our experiments, 5 mM BAPTA was not able to eliminate mitochondrial Ca^{2+} transients while nearly abolishing cytosolic signals. In other words, BAPTA, at this concentration, successfully interrupted Ca^{2+} binding to fura-2 but was not able to interfere with mitochondrial Ca^{2+} buffering, suggesting some sort of Ca^{2+} tunneling from the SR to the mitochondria. Therefore, our data not only supported the ability of mitochondria in both slow- and fast-twitch muscle fibers to sequester Ca^{2+} *in situ*, but they strongly suggested that at least a subpopulation of mitochondrial Ca^{2+} uptake sites is located in close proximity to the SR Ca^{2+} release sites, within a microdomain of high [Ca^{2+}] during SR Ca^{2+} release. These functional studies call for an additional morphological investigation of mutual spatial positioning of the SR and mitochondria in skeletal muscle.

Acknowledgments—We thank Drs. Ernst Niggli, John Reeves and Roman Shirokov for helpful discussions and critical reading of the manuscript.

REFERENCES

1. Sembrowich, W. L., Quintinskie, J. J., and Li, G. (1985) *J. Appl. Physiol.* **59,** 137–141
2. Madsen, K., Ertbjerg, P., Djurhuus, M. S., and Pedersen, P. K. (1996) *Am. J. Physiol.* **271**, E1044–E1050
3. Gillis, J. M. (1997) *J. Muscle Res. Cell Motil.* **18,** 473–483
4. Isaeva, E. V., and Shirokova, N. (2003) *J. Physiol.* (*Lond.*) **547,** 453–462
5. Isaeva, E. V., Shkryl, V. M., and Shirokova, N. (2005) *J. Physiol.* (*Lond.*) **565,** 855–872
6. Bruton, J., Tavi, P., Aydin, J., Westerblad, H., and Lannergren, J. (2003) *J. Physiol.* (*Lond.*) **551,** 179–190
7. Lannergren, J., Westerblad, H., and Bruton, J. D. (2001) *J. Muscle Res. Cell Motil.* **22,** 265–275
8. Rudolf, R., Mongillo, M., Magalhaes, P. J., and Pozzan, T. (2004) *J. Cell Biol.* **166,** 527–536
9. Duchen, M. R. (2000) *J. Physiol.* (*Lond.*) **529,** 57–68
10. Brini, M. (2003) *Cell Calcium* **34,** 399–405
11. Rizzuto, R., Duchen, M. R., and Pozzan, T. (2004) *Sci. STKE 2004,* re1
12. Ogata, T., and Yamasaki, Y. (1985) *Cell Tissue Res.* **241,** 251–256
13. Garcia, J., and Schneider, M. F. (1993) *J. Physiol.* (*Lond.*) **463,** 709–728
14. Shirokova, N., Garcia, J., Pizarro, G., and Rios, E. (1996) *J. Gen. Physiol.* **107,** 1–18
15. Duke, A. M., and Steele, D. S. (1998) *Pfluegers Arch. Eur. J. Physiol.* **436,** 104–111
16. Cheng, H., Song, L. S., Shirokova, N., Gonzalez, A., Lakatta, E. G., Rios, E., and Stern, M. D. (1999) *Biophys. J.* **76,** 606–617
17. Rizzuto, R., Pinton, P., Carrington, W., Fay, F. S., Fogarty, K. E., Lifshitz, L. M., Tuft, R. A., and Pozzan, T. (1998) *Science* **280,** 1763–1766
18. Simpson, P. B., and Russell, J. T. (1998) *Brain Res. Brain Res. Rev.* **26,** 72–81
19. Sharma, V. K., Ramesh, V., Franzini-Armstrong, C., and Sheu, S. S. (2000) *J. Bioenerg. Biomembr.* **32,** 97–104
20. Csordas, G., Thomas, A. P., and Hajnoczky, G. (2001) *Trends Cardiovasc. Med.* **11,** 269–275
21. Brini, M., De Giorgi, F., Murgia, M., Marsault, R., Massimino, M. L., Cantini, M., Rizzuto, R., and Pozzan, T. (1997) *Mol. Biol. Cell* **8,** 129–143
22. Challet, C., Maechler, P., Wollheim, C. B., and Ruegg, U. T. (2001) *J. Biol. Chem.* **276,** 3791–3797
23. Robert, V., Massimino, M. L., Tosello, V., Marsault, R., Cantini, M., Sorrentino, V., and Pozzan, T. (2001) *J. Biol. Chem.* **276,** 4647–4651
24. Jouaville, L. S., Pinton, P., Bastianutto, C., Rutter, G. A., and Rizzuto, R. (1999) *Proc. Natl. Acad. Sci. U. S. A.* **96,** 13807–13812
25. Chen, G., Carroll, S., Racay, P., Dick, J., Pette, D., Traub, I., Vrbova, G., Eggli, P., Celio, M., and Schwaller, B. (2001) *Am. J. Physiol.* **281,** C114–C122
26. Gurney, A. M., Drummond, R. M., and Fay, F. S. (2000) *Cell Calcium* **27,** 339–351
27. Stern, M. D. (1992) *Cell Calcium* **13,** 183–192
28. Smith, G. D., Wagner, J., and Keizer, J. (1996) *Biophys. J.* **70,** 2527–2539
29. Naraghi, M., and Neher, E. (1997) *J. Neurosci.* **17,** 6961–6973

2.2 Окисно-відновний стан мітохондрій та Ca^{2+}-спалахи в пермеабілізованому скелетному м'язі ссавців

Розуміння складних біофізичних процесів, пов’язаних зі змінами концентрації кальцію в скелетних м’язах та виявлення причин гальмування кальцій індукованого вивільнення кальцію у м’язових клітинах ссавців за фізіологічних умов є важливою задачею. Процес пермеабілізації, коли мембрана стає проникною, може порушити певні механізми, які зазвичай стримують CICR у непошкоджених клітинах.

У наступній частині роботи було досліджено механізми, які визначають появу Ca^{2+}-спалахів у пермеабілізованих волокнах, виділених з м'язів з різною метаболічною ємністю. Спонтанні Ca^{2+}-спалахи виявляли за допомогою Fluo-3 та однофотонної конфокальної мікроскопії; мітохондріальний редокс-потенціал визначали за сигналом мітохондріального NADH, зареєстрованим за допомогою двофотонної конфокальної мікроскопії.

За фізіологічних умов Ca^{2+}-спалахи майже не фіксується в інтактних скелетних м'язових волокнах дорослих ссавців (Conklin et al., 1999), але виявляються в хімічно або механічно ушкоджених клітинах (Kirsch et al., 2001). Ця відмінність дала підстави припустити, що процес пермеабілізації може порушувати певні механізми, які зазвичай стримують CICR в непошкоджених клітинах. Було встановлено, що частота Ca^{2+}-спалахів у пермеабілізованих волокнах визначається метаболічним станом клітини (Isaeva and Shirokova, 2003). Як підтверджено дослідженнями, мітохондрії розташовані в стратегічно вигідних місцях поруч із зонами вивільнення Ca^{2+} з СР і, імовірно, модулюють CICR, виконуючи контрольний негативний зворотний зв'язок.

Після пермеабілізації волокна поміщали у внутрішньоклітинний розчин та вивчали появу спонтанних явищ вивільнення Ca^{2+} з СР за рахунок відкриття RyRs. При цьому, відзначалась затримка перед появою спонтанних Ca^{2+}-спалахів. Для аналізу того, чи корелює час появи Ca^{2+}-спалахів з метаболічною ємністю певного типу клітин, ми вибрали м'язи з волокнами, що мають різний вміст та субклітинну локалізацію мітохондрій. Підошовний м'яз щура (soleus) має переважно волокна І типу (див., наприклад, (Ariano et al., 1973)). Скелетний м'яз EDL щура має приблизно 60% волокон IIa типу (Ariano et al., 1973). Приблизно 70% волокон м'язів FDB миші є типу IIX. Окислювальна ємність цих волокон зростає в наступному порядку: IIX, IIa і I. Варто відзначити, що відносний об'єм мітохондрій у волокнах soleus типу I майже удвічі перевищує аналогічний показник у клітинах EDL типу IIa (Gonzalez et al., 2003).

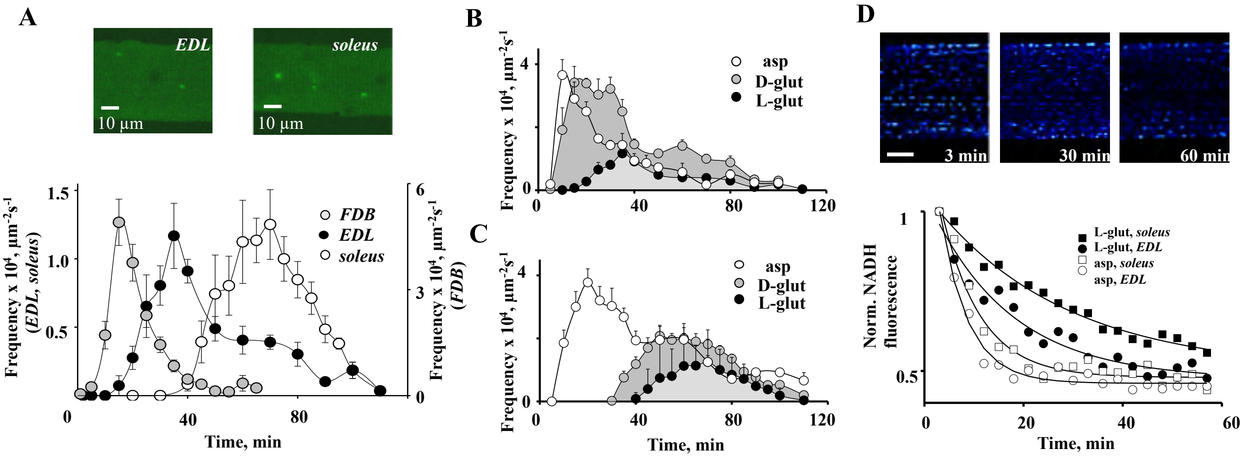

Рисунок 2.2. Вплив мітохондріальних субстратів на появу Ca^{2+} спалахів. (A) Верхні панелі: конфокальні флуоресцентні зображення EDL та soleus волокон. Нижня панель: часова залежність частоти Ca^{2+} спалахів у 36 FDB, 17 EDL та 17 soleus волокнах. Ліва вертикальна вісь відповідає клітинами EDL та soleus, тоді як права вісь для клітинам FDB. (B) Вплив мітохондріальних субстратів на часовий перебіг появи Ca^{2+} спалахів у EDL. (C) Той самий вплив, але для soleus м'язів. (D) Верхні панелі: зображення флуоресценції NADH, отримані з EDL в різний час після пермеабілізації волокна. Волокно інкубували в розчині L-глутамату. Масштабна лінійка відповідає 10 мкм. Нижня панель: затухання сигналів NADH в EDL і soleus м'язах інкубованих в розчини аспартату і L-глутамату.

На рис. 2.2A представлено часову залежність появи Ca^{2+} спалахів у 17 м'язових волокнах EDL та 17 м'язових волокнах soleus та 36 м'язових волокнах FDB волокон миші, досліджених за однаковими умовами експерименту. Ca^{2+} спалахи у волокнах soleus розвивалися значно пізніше, ніж у EDL: час до першого зафіксованого спалаху складав 47±2.3 хв порівняно з 21±1.1 хв у клітинах soleus та EDL відповідно. Крім того, час, необхідний для досягнення максимальної частоти спалахів, був істотно довшим у волокнах soleus — 67±2.2 хв, порівняно з 35±1.4 хв у EDL волокнах. Загалом дані, отримані з різних типів м'язових волокон, вказують на те, що час появи Ca^{2+} спалахів у пермеабілізованих волокнах тісно корелює з кількістю мітохондрій у цих волокнах.

Скелетні м’язи генерують активні форми кисню за допомогою низки цитозольних та мембрано-зв’язуючих ферментів, включаючи ксантиноксидазу, NAD(P)H оксидази (NOXs), мітохондріальний дихальний ланцюг, синтазу оксиду азоту (NOS) тощо (Reid, 2001b, Stamler and Meissner, 2001).

У наступній серії експериментів була досліджена роль мітохондрій у розвитку спонтанної Ca^{2+}-активності. Ми поміщали скелетні м'язові волокна різної метаболічної активності (FDB, EDL та soleus) у внутрішні розчини на основі L-глутамату, D-глутамату чи аспартату. Варто відзначити, хоча L-глутамат є субстратом циклу Кребса, D-глутамат не виконує цієї ролі. Якщо додавання субстратів до внутрішнього розчину має активізувати мітохондріальний метаболізм, то їх відсутність може призвести до його зниження. Передбачається, що аспартат, як продукт циклу Кребса, інгібує окислювальний метаболізм сильніше, ніж D-глутамат.

У всіх трьох досліджуваних типах волокон найбільший час до виникнення Ca^{2+} спалахів після початку пермеабілізації спостерігався в розчині, збагаченому L-глутаматом. Для 17 клітин EDL, які були поміщені в розчин L-глутамату, пікова частота Ca^{2+} спалахів досягалася через 35±1.4 хв після пермеабілізації волокон (див. рис. 2.2B). У випадку, коли клітини знаходилися у розчині D-глутамату, пік частоти спалахів реєструвався раніше — через 20±1.4 хв (n=11). Спалахи з'являлися ще швидше у волокнах, які були піддані впливу розчину з аспартатом — 11±0.7 хв (n=9). Подібні часові залежності розвитку спалахів від субстратів спостерігалися також в м'язових волокнах soleus (див. рис. 2.2C).

У наступному етапі дослідження ми використали двофотонну конфокальну флуоресцентну мікроскопію для відстеження локальних змін у флуоресценції NADH. М'язові волокна EDL та soleus були пермеабілізовані та знаходились у розчині з L-глутаматом або аспартатом. На верхній панелі рис. 2.2D представлені три зображення флуоресценції NADH, отримані відразу після пермеабілізації волокон EDL (3 хв), а також через 30 та 60 хв після інкубації у розчині L-глутамату. Ми визначили сигнал флуоресценції, випромінюваний молекулами NADH у декількох групах мітохондрій на кожному зображенні, а потім провели його усереднення. Отримані значення були нормалізовані відносно початкового рівня NADH. Результати представлені на нижній панелі рис. 2.2D у вигляді графіка відносно часу. Динаміка спаду флуоресценції NADH у цьому досліді та в ще шести інших дослідженнях EDL найкраще апроксимується експоненційною функцією (лінія на графіку), із середнім часом спаду τ, який становить 14.8±0.81 хв. У волокнах soleus, досліджених аналогічним методом, динаміка була повільнішою ($\tau = 21.1 \pm 1.72$ хв, n= 9). У волокнах обох типів, коли їх інкубували у розчині аспартату, динаміка зміни сигналу NADH була значно швидшою порівняно з L-глутаматом (EDL: $\tau = 6.3 \pm 0.64$ хв, n= 11; soleus: $\tau = 7.4 \pm 0.61$ хв, n= 9). Загалом, час виникнення Ca^{2+} спалахів у цих волокнах корелював зі швидкістю зміни мітохондріального окислювально-відновного потенціалу (і метаболізму) відповідного волокна.

Можливий механізм впливу мітохондрій на цитоплазматичні сигнали Ca^{2+} пов'язаний з утворенням активних форм кисню (ROS). Під час аеробного дихання, для синтезу АТФ у мітохондріях, відбувається витік електронів, що регулярно спричиняє формування мітохондріальних супероксидних аніонів, які надалі перетворюються на H_2O_2 за допомогою марганцевої супероксиддисмутази. H_2O_2 виступає як одна з ключових молекул-месенджерів в окислювально-відновлювальних сигнальних шляхах (див. огляди (Brookes et al., 2004, Reid, 2001a)). Оскільки СР розташований дуже близько до мітохондрій, його функції можуть бути модифіковані ROS, які виділяються з цих органел. Послаблення захисних механізмів мітохондрій від ROS, а отже і посилення вивільнення ROS у цитоплазму, може модулювати активність RyRs, що спричиняє появу Ca^{2+} спалахів.

Для перевірки припущення про те, що ROS можуть спричинити появу Ca^{2+} спалахів у пермеабілізованих м'язових клітинах ссавців, ми спробували модулювати активність RyRs за рахунок ROS через застосування екзогенних поглиначів. На рис. 2.3A представлено результати експериментів, де м'язові волокна EDL інкубувалися у розчині на основі аспартату, а також у розчині аспартату із додаванням 600 ОД/мл супероксиддисмутази (SOD) чи комбінованим додаванням 600 ОД/мл SOD і 500 ОД/мл каталази. Порівнюючи волокна під різними умовами, було виявлено, що час до першого зареєстрованого спалаху і час до досягнення максимальної частоти спалахів становили 7.9±1.01 хв і 11.4±1.80 хв (n=7) відповідно. Вплив лише SOD суттєво затримав розвиток Ca^{2+} спалахів (11.0±1.00 хв до першого спалаху та 18.0±1.22 хв до піку частоти, n=5). Застосування двох поглиначів разом ще більше інгібувало розвиток спалахів, затримуючи їхню появу порівняно з контрольною групою (11.3±1.25 хв до першого спалаху і 18.3±1.17 хв до піку частоти, n=4).

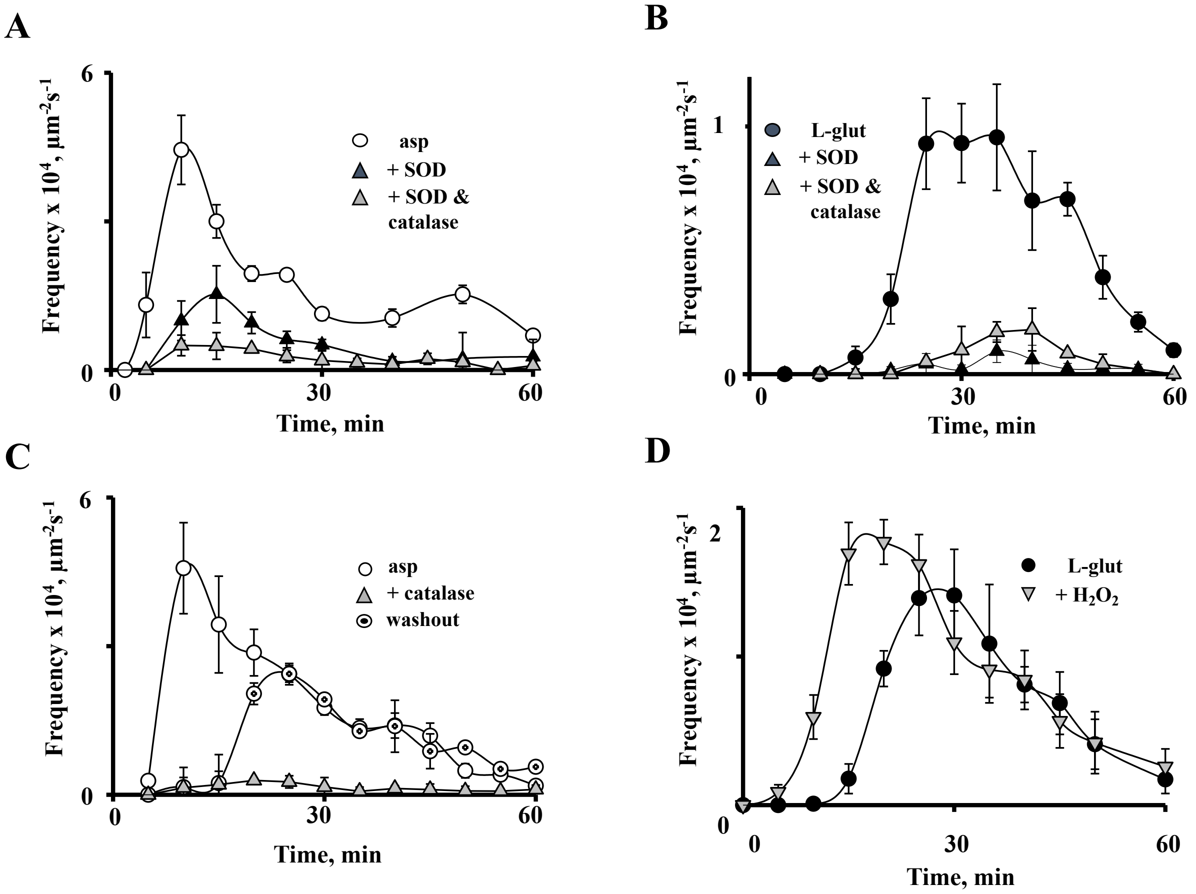

Рисунок 2.3. Вплив ROS та їх поглиначів на Ca^{2+} спалахи в м'язових волокнах EDL. (A) Поява Ca^{2+} спалахів в розчині аспартату з додаванням SOD або комбінації SOD та каталази. (B) Поява Ca^{2+} спалахів в розчині L-глутамату. (C) Час виникнення спалахів у розчині аспартату з додаванням каталази, а також після її видалення з розчину через 15 хв. (D) Спалахи у контрольних умовах (L-глутамат) порівняно з присутністю 50 мкМ H_2O_2.

Рисунок 2.3B ілюструє результати експериментів із застосуванням поглиначів ROS, SOD і каталази, у м'язових волокнах EDL у внутрішньому розчині на основі L-глутамату. Час до першого виявленого спалаху та його максимальна частота склали 28.8±1.25 хв та 36.3±2.39 хв (n=4) для SOD, 37.7±5.05 хв та 46.7±2.89 хв (n=3) для комбінації SOD і каталази, тоді як контрольні значення склали 18.8±1.25 хв та 30.0±1.64 хв (n=8).

На рис. 2.3C представлено результати впливу каталази на Ca^{2+} спалахи. Трикутники відображають результати шести експериментів, у яких волокна пермеабілізували та інкубували у розчині аспартату з додаванням 500 ОД/мл каталази. За таких умов спостерігалися дуже рідкі спалахи. Окремо каталазу відмивали з розчину через 15 хв після початку інкубації (пунктирні кружечки). Це призводило до відновлення спалахів до контрольних показників (відкриті кружечки). Всі експерименти виконували паралельно на волокнах однієї групи щурів для зниження варіабельності між окремими тваринами.

Нарешті ми перевірили, чи призведе додавання ROS до розчину, для інкубації волокон, до ефекту, протилежному ефекту поглиначів ROS (див. рис. 2.3D). При додаванні 50 мкМ H_2O_2 спостерігалась протилежна реакція щодо появи спалахів у м'язових волокнах EDL. Додавання H_2O_2 до розчинів на основі L-глутамату незначно підвищувало максимальну частоту спалахів, але пришвидшувало їхній часовий початок. Як час до першого виявлення спалаху, так і час досягнення максимальної частоти спалахів значно зменшилися (8.1±0.91 хв та 17.5±1.33 хв, n=8 порівняно з 15.6±1.13 хв та 30.6±1.12 хв, n=8, для L-глутамату з додаванням 50 мкМ H_2O_2 і без нього відповідно).

Під час усіх експериментів найбільша затримка появи Ca^{2+} спалахів спостерігалася у повільно скорочувальних окислювальних волокнах. Проміжний час виникнення спалахів характеризував швидко скорочувальні гліколітично-окислювальні волокна, тоді як найкоротший час затримки спостеригався у швидко скорочувальних гліколітичних клітинах. Частота Ca^{2+} спалахів відзначалася колоколоподібним розподілом. Максимальна частота спалахів досягалася повільно в волокнах, багатих на мітохондрії, і швидко — в волокнах із низьким вмістом мітохондрій. Існуюча кореляція появи спонтанних Ca^{2+} спалахів корелює з окислювально-відновним потенціалом мітохондрій. Застосування поглиначів активних форм кисню, таких як супероксиддисмутаза і каталаза, істотно і зворотно зменшувало частоту спалахів, при цьому затримуючи їхню появу. Навпаки, інкубація волокон з 50 чи 200 мкМ H_2O_2 стимулювала розвиток Ca^{2+} спалахів і підвищувала їхню частоту. Ці дані свідчать про залежність появи Ca^{2+} спалахів у пермеабілізованих м'язових волокнах від їх окислювальної активності. Дисбаланс між продукцією мітохондріальних ROS та антиоксидантною здатністю волокон, ймовірно, викликає активацією RyRs за рахунок ROS, що призводить до появи Ca^{2+} спалахів у пермеабілізованих препаратах, скелетних м’язів ссавців.

J Physiol 565.3 (2005) pp 855–872

Mitochondrial redox state and Ca^{2+} sparks in permeabilized mammalian skeletal muscle

Elena V. Isaeva, Vyacheslav M. Shkryl and Natalia Shirokova

Department of Pharmacology and Physiology, University of Medicine and Dentistry of New Jersey, New Jersey Medical School, 185 South Orange Avenue, Newark, NJ 07103, USA

Intact skeletal muscle fibres from adult mammals exhibit neither spontaneous nor stimulated Ca^{2+} sparks. Mechanical or chemical skinning procedures have been reported to unmask sparks. The present study investigates the mechanisms that determine the development of Ca^{2+} spark activity in permeabilized fibres dissected from muscles with different metabolic capacity. Spontaneous Ca^{2+} sparks were detected with fluo-3 and single photon confocal microscopy; mitochondrial redox potential was evaluated from mitochondrial NADH signals recorded with two-photon confocal microscopy, and Ca^{2+} load of the sarcoplasmic reticulum (SR) was estimated from the amplitude of caffeine-induced Ca^{2+} transients recorded with fura-2 and digital photometry. In three fibre types studied, there was a time lag between permeabilization and spark development. Under all experimental conditions, the delay was the longest in slow-twitch oxidative fibres, intermediate in fast-twitch glycolytic–oxidative fibres, and the shortest in fast-twitch glycolytic cells. The temporal evolution of Ca^{2+} spark frequencies was bell-shaped, and the maximal spark frequency was reached slowly in mitochondria-rich oxidative cells but quickly in mitochondria-poor glycolytic fibres. The development of spontaneous Ca^{2+} sparks did not correlate with the SR Ca^{2+} content of the fibre, but did correlate with the redox potential of their mitochondria. Treatment of fibres with scavengers of reactive oxygen species (ROS), such as superoxide dismutase (SOD) and catalase, dramatically and reversibly reduced the spark frequency and also delayed their appearance. In contrast, incubation of fibres with 50 μM H_2O_2 sped up the development of Ca^{2+} sparks and increased their frequency. These results indicate that the appearance of Ca^{2+} sparks in permeabilized skeletal muscle cells depends on the fibre's oxidative strength and that misbalance between mitochondrial ROS production and the fibre's ability to fight oxidative stress is likely to be responsible for unmasking Ca^{2+} sparks in skinned preparations. They also suggest that under physiological and pathophysiological conditions the appearance of Ca^{2+} sparks may be, at least in part, limited by the fine-tuned equilibrium between mitochondrial ROS production and cellular ROS scavenging mechanisms.

(Resubmitted 7 March 2005; accepted after revision 12 April 2005; first published online 21 April 2005)

Corresponding author N. Shirokova: Department of Pharmacology and Physiology, UMDNJ, New Jersey Medical School, 185 South Orange Avenue, Newark, NJ 07103, USA. Email: nshiroko@umdnj.edu

Skeletal muscle depends on ATP supply to meet its energy demands. There are three major sources of ATP in muscle: creatine phosphate, anaerobic glycolysis and oxidative phosphorylation. The relative contribution of each ATP source varies among muscle fibre types. Type I (slow-twitch, oxidative) and type IIa (fast-twitch, glycolytic–oxidative) fibres are rich in mitochondria. They rely for their ATP production on oxidative phosphorylation. In contrast, type IIb (fast-twitch, glycolytic) fibres, are mitochondria-poor and have a very effective glycolytic ATP synthesis. Thus, muscle mitochondrial content is a reflection of the relative importance of mitochondria to the energy budget of each fibre type.

In addition to the pivotal role in cell energy metabolism, mitochondria are also involved in other cellular processes of key importance. In particular, it has been suggested that these organelles participate in the control of intracellular Ca^{2+} homeostasis. It has been shown that mitochondrial Ca^{2+} uptake can modify the intracellular Ca^{2+} transients in a variety of cell lines and some tissues. On the other hand, $[Ca^{2+}]$ in the mitochondrial matrix ($[Ca^{2+}]_m$) controls the metabolism, as three major dehydrogenases of the

---

E. V. Isaeva and V. M. Shkryl contributed equally to this work.

DOI: 10.1113/jphysiol.2005.086280

mitochondrial tricarboxylic acid (TCA) cycle are Ca^{2+} sensitive. The increase in $[Ca^{2+}]_m$ enhances the production of nicotinamide adenine dinucleotide (NADH), electron transport, proton leak, ATP synthesis and the production of reactive oxygen species (ROS) (for recent reviews see Duchen, 2000; Hajnóczky *et al.* 2000; Rizzuto *et al.* 2004) . All these Ca^{2+}-dependent mechanisms, in turn, can exert positive and negative feedback effects on cytoplasmic Ca^{2+} signals. Therefore, calcium homeostasis, metabolism, and bioenergetics are intimately interconnected in living cells.

Release of Ca^{2+} from the sarcoplasmic reticulum (SR) is a required step in skeletal muscle excitation–contraction coupling (ECC). It is initiated during the depolarization of the transverse tubular membrane via an allosteric interaction between the voltage sensors of ECC (dihydropyridine receptors; DHPRs) and the associated SR Ca^{2+} release channels (ryanodine receptors; RyRs) (Schneider & Chandler, 1973; Ríos *et al.* 1993; Nakai *et al.* 1996). It has been proposed that the initial voltage-activated increase in local $[Ca^{2+}]$ at the triad opens the RyRs, which are not allosterically coupled with DHPRs, via Ca^{2+}-induced Ca^{2+} release (CICR) (Ríos & Pizarro, 1988; Shirokova *et al.* 1996). However, the existence of CICR in mammalian skeletal muscle has been questioned. No Ca^{2+} sparks, the elementary events of CICR, were found in mammalian muscle cells during electrical stimulation (Shirokova *et al.* 1998; Conklin *et al.* 1999; Csernoch *et al.* 2004). This observation suggests the existence of some inhibitory mechanisms that suppress regenerative CICR *in vivo*.

In Shirokova *et al.* (1999), we proposed that a functional interaction between DHPRs and RyRs prevents RyRs from being activated by Ca^{2+}. However, this idea was challenged by Kirsch *et al.* (2001), who demonstrated the abundance of sparks in mechanically skinned fibres, where the physical coupling between DHPRs and RyRs is presumably preserved (Lamb, 2002). In Isaeva & Shirokova (2003), we suggested that mitochondria, being in close proximity to Ca^{2+} release sites, are capable of interfering with Ca^{2+} released from the SR, thereby inhibiting CICR by a not yet established mechanism. It is conceivable that wash out of cytosolic constituents, which inevitably follows all chemical or mechanical skinning procedures, can impair mitochondrial function and relieve their inhibitory effect on CICR, thus allowing Ca^{2+} sparks to appear. The results we present in this paper provide further support for this hypothesis by correlating the appearance of Ca^{2+} sparks with the functional state of the mitochondria in skeletal muscle fibres of different metabolic strength.

Methods

Preparation of muscle fibres

Female rats (Sprague-Dawley, 175–200 g) and mice (Swiss Webster, 25–30 g) were killed by cervical dislocation under deep anaesthesia induced by intraperitoneal injection of sodium pentobarbital (100–200 mg (kg body weight)$^{-1}$). Single fibres from rat extensor digitorum longus (EDL) or soleus muscles were manually dissected as described by García & Schneider (1993) and Shirokova *et al.* (1996). Single fibres from mouse flexor digitorum brevis (FDB) muscle were enzymatically dissociated by a procedure detailed in Wang *et al.* (1999). Fibres were transferred to an experimental chamber, pushed down against the coverslip floor of the chamber, permeabilized with saponin (as in Isaeva & Shirokova, 2003) and immersed into one of the 'internal solutions' (see below). The Institutional Animal Care and Use Committee at UMDNJ–New Jersey Medical School approved the use and killing method of all animals in this study.

Solutions

The L-glutamate internal solution contained (mM): potassium L-glutamate (140), Hepes (10), EGTA (0.5), sodium phosphocreatine (5), Mg-ATP (5) and $CaCl_2$ (0.155) for nominal $[Ca^{2+}]$ of ~150 nM and $[Mg^{2+}]$ of ~380 μM. The D-glutamate-based solution contained 140 mM of potassium D-glutamate, instead of potassium L-glutamate. In aspartate-based solution, potassium L-glutamate was replaced with potassium aspartate, and nominal $[Ca^{2+}]$ and $[Mg^{2+}]$ were adjusted to 150 nM and 380 μM, respectively. Dissociation constants were taken from the NIST Critically Selected Stability Constants of Metal Complexes Database 46 (US Department of Commerce, Technology Administration, NIST, Gaithersburg, MD, USA). Calculations were performed assuming 1 : 1 stoichiometry for Mg-ATP. For all solutions pH was adjusted to 7.0 and osmolality to 300 mosmol kg^{-1}.

Confocal imaging and image processing

Local changes in cytoplasmic $[Ca^{2+}]$ were measured with the fluorescent Ca^{2+} indicator fluo-3 (penta-potassium salt, 50 μM) added to internal solutions. Mitochondrial membrane potential was monitored with the potentiometric dye tetramethyl rhodamine ethyl ester (TMRE; 10 nM). A laser scanning confocal microscope Radiance 2000 (Bio-Rad, Hercules, CA, USA) connected to a Zeiss Axiovert 100 inverted microscope equipped with a × 63, 1.2 NA, water immersion lens (Zeiss Inc., Oberkochen, Germany) was used to acquire confocal images of fluo-3 or TMRE-related fluorescence. Fluo-3 was excited with the 488 nm line of an argon laser and TMRE was excited with the 543 nm line of a He–Ne laser. The emitted light was collected above 500 nm (fluo-3) or above 570 nm (TMRE). Fibres were imaged in the XY mode at 500 lines s^{-1}. As a rule, series of 40 images (102.8 by 102.8 μm) were acquired at 1 Hz at random locations within fibres. Discrete events of Ca^{2+} release were identified with an automatic detection method (Cheng *et al.* 1999) modified for localization of events in XY images, as previously described in Isaeva & Shirokova (2003). Because XY images carry no information about event morphology, we call all of them Ca^{2+} sparks.

The two-photon confocal scanner Radiance 2001 MP (Bio-Rad, Hercules, CA, USA) attached to a Nikon Eclipse TE 2000 microscope equipped with a × 60, 1.2 NA, water immerssion objective (Nikon, Tokyo, Japan) was used to monitor local changes in mitochondrial NADH autofluorescence. For two-photon excitation, a Ti:Sapphire laser (MIRA 900F, Coherent, Santa Clara, CA, USA) pumped with a frequency-doubled (Nd:YVO4) solid-state diode laser (Verdi-10 W, Coherent) provided the 80 MHz mode-locked laser pulses with 730 nm wavelength. The emitted light between 410 and 490 nm was collected with a direct (non-descanned) detector. Series of 20 images (101.2 by 101.2 μm) were acquired every 5 min from a fixed location within the fibre.

Digital photometry

To estimate the Ca^{2+} content of the sarcoplasmic reticulum in permeabilized skeletal muscle fibres under different experimental conditions, we adapted a technique developed by Duke & Steele (1998). For this purpose, permeabilized segments of muscle fibres were mounted into a two-Vaseline gap chamber. The chamber was designed with the middle pool to function as a flow chamber that allowed for rapid changes of the solution. The middle pool, which usually corresponds to the voltage-clamped compartment, was connected to small inlet and outlet pools at both ends, where the perfusion and suction lines were attached (more details are in Shirokova & Ríos, 1996). Throughout the experimental protocol, the middle segment of the fibre was continuously perfused with internal solution containing the Ca^{2+} indicator fura-2 (potassium salt, 2 μM) at a rate of ~0.5 ml min^{-1}. Waste solution was collected continuously at the outlet pool. Solutions containing 20 mM caffeine were rapidly applied (~2 ml min^{-1}) for a duration of 2 s via a dedicated inlet pipette. To minimize contraction of fast-twitch fibres, 20 μM of *N*-benzyl-*p*-toluene sulphonamide (BTS; Cheung *et al.* 2002) was added. Both EDL and soleus fibres were stretched to about 3.5 μm per sarcomere length.

Dual-excitation recordings of intracellular Ca^{2+}-related fluorescence in fura-2-loaded fibres were performed with a RatioMaster M-40 high-speed fluorescence photometer (PTI, Lawrenceville, NJ, USA) mounted on a Zeiss Axiovert 200 microscope (Zeiss Inc., Oberkochen, Germany) equipped with a quartz × 40, 1.25 NA, glycerol-immersed objective (Partec GmbH, Münster, Germany). The quartz objective is designed specifically to optimize fluorescence measurements with probes excitable in the UV range of light wavelengths. The fibre was illuminated with light of 340 and 380 nm at 50 Hz. The fluorescence emission in the centre section of fibre was detected through a rectangular pinhole (20 × 40 μm). Ca^{2+} transients are presented as the ratio of light intensities emitted above 500 nm. The SR Ca^{2+} load was estimated from the amplitude of caffeine-induced cytoplasmic Ca^{2+} transients.

Whole-cell NADH fluorescence signals were imaged with a CH1 CCD camera (Photometrics, Tucson, AZ, USA), as previously described by Hajnóczky *et al.* (1999) and also by Isaeva & Shirokova (2003). Fibres were excited at 360 nm and the light emitted above 420 nm was recorded. A single series of 300 images at 0.33 Hz was acquired in each experiment.

Statistics

Values are presented as means ± S.E.M., and *n* represents the number of analysed cells. Student's *t* test was used for comparing paired observations. $P < 0.05$ was considered significant.

Chemicals

Fluo-3 and fura-2 were obtained from Biotium (Hayward, CA, USA). MitoTracker Green FM and TMRE were purchased from Molecular Probes (Eugene, OR, USA). Other chemicals were from Sigma (St Louis, MO, USA).

Results

Although Ca^{2+} sparks are rarely recorded in intact adult mammalian skeletal muscle fibres (Conklin *et al.* 1999), they are readily observed in chemically and mechanically skinned cells (Kirsch *et al.* 2001). This apparent controversy led to the suggestion that the permeabilization procedure impairs some of the mechanisms that normally inhibit CICR in intact cells. Our recent studies indicate that the frequency of Ca^{2+} sparks in permeabilized fibres is tightly regulated by the metabolic state of the cell (Isaeva & Shirokova, 2003). We suggested that mitochondria, being located strategically close to the SR Ca^{2+} release sites, exert negative control over CICR. Now we tested further implications of this hypothesis by examining several features of spontaneous Ca^{2+} sparks in skeletal muscle fibres with different mitochondrial content.

Time course of appearance of Ca^{2+} sparks correlates with the fibre's mitochondrial content

In our previous studies (Isaeva & Shirokova, 2003) we noticed that, after fibres were permeabilized with saponin and immersed into the internal solution, it took some time for spontaneous Ca^{2+} sparks to appear. We speculated that the delay in the appearance of sparks is related to the degradation of cellular metabolic pathways. To test this hypothesis we designed a number of experiments that correlate the onset of the appearance of Ca^{2+} sparks with changes in cellular metabolism.

In the first set of experiments, we examined whether the time course of Ca^{2+} spark appearance correlates with the metabolic capacity of the particular cell type. In this study we used muscles that contain fibres with different mitochondrial content and subcellular localization of the organelles. Rat soleus muscle contains mostly type I cells (e.g. Ariano *et al.* 1973). EDL skeletal muscle of rat contain ~60% of type IIa fibres (Ariano *et al.* 1973). About 70% of the fibres from mouse FDB muscle are of the IIX type (Gonzalez *et al.* 2003). The oxidative capacity of these fibres increases in the order: IIX, IIa and I. In particular, the relative volume of mitochondria in soleus type I fibres is almost two times larger than that in EDL type IIa cells (Eisenberg, 1983). The larger the mitochondrial content, the more mitochondria are generally targeted to the I-bands, close to the junctional SR, where they are able to interfere with Ca^{2+} release (Ogata & Yamasaki, 1985).

Because each muscle contains fibres of different types, we first tested whether fibres we selected from rat EDL and soleus muscles during the dissection procedure indeed differed in mitochondrial content. To visualize mitochondria, cells were permeabilized and immersed into L-glutamate solution. The mitochondrial NADH autofluorescence was imaged with a two-photon excitation laser-scanning confocal microscope 10 min after fibre permeabilization (top panels in Fig. 1*A* and *B*). For a more quantitative analysis, mitochondria were identified with an automatic digital image processing algorithm similar to that used for spark detection. The detected mitochondria are shown as binary masks in two middle panels. The 'mitochondrial content' was estimated as the ratio (*r*) of the number of pixels occupied by mitochondria to the total number of pixels occupied by the fibre. The ratio was significantly larger in soleus fibres (Fig. 1*C*). Obviously, the analysis we used here is not very precise, as the algorithm is somewhat sensitive to the average NADH signal intensity. However, similar results were also obtained with the potential sensitive dye TMRE (lower two panels) and with the mitochondria-targeted fluorescent indicator MitoTracker Green FM (data not shown).

Figure 2 represents the time course of Ca^{2+} spark appearance in an EDL muscle fibre incubated in L-glutamate solution. Sets of 40 sequential fluorescence images of fluo-3 were acquired at different times after fibre permeabilization. A typical image is shown in Fig. 2*A*. Sparks were identified in each image of the set and all together are presented as cumulative masks (Fig. 2*B*). For

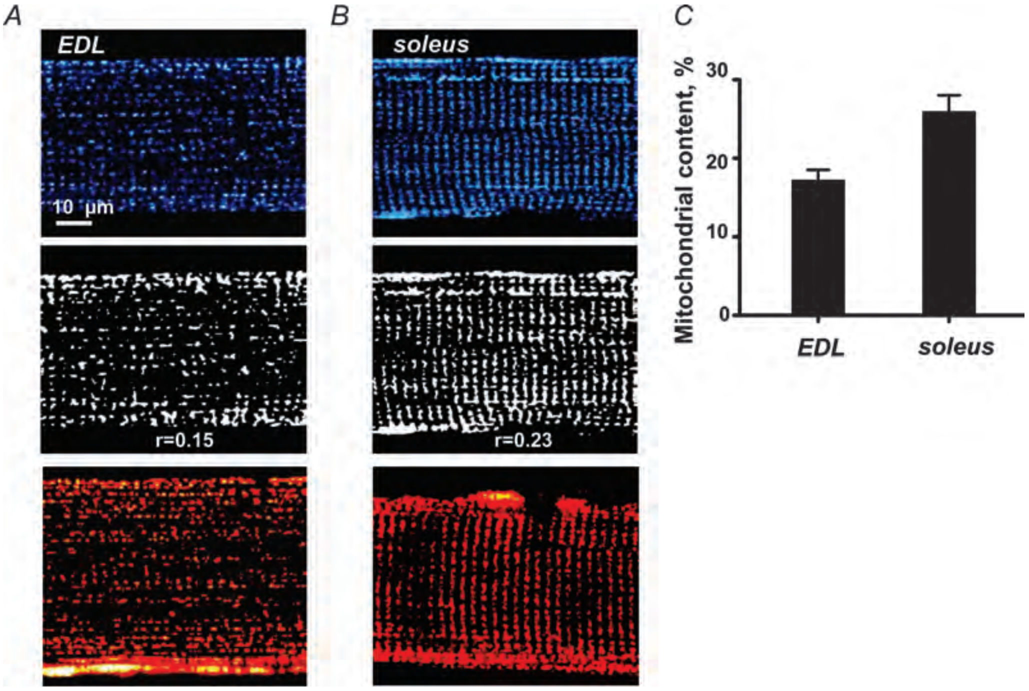

Figure 1. Visualization of mitochondria in EDL and soleus muscle

A and *B*, top panels, images of NADH fluorescence obtained from EDL (*A*) and soleus (*B*) cells, immersed into L-glutamate solution. Middle panels, corresponding binary images for the regions with $\Delta F/F_0 > 2$ S.D. (Cells 080604-EDL8 and 080503-soleus6.) Bottom panels, representative images of TMRE fluorescence obtained from the two fibre types. (Cells 091902-EDL1 and 091802-soleus1.) *C*, 'mitochondrial content' of EDL ($n = 15$) and soleus ($n = 16$) fibres.

each set, the spark frequency was determined as the mean number of events per unit area and time. The values are plotted against time in Fig. 2*C*. The frequency varied somewhat from frame to frame within each series of images, but also exhibited a characteristic time course over longer times. In this particular fibre, Ca^{2+} sparks developed 15 min after permeabilization. In general, the time course of the frequency of spontaneous Ca^{2+} sparks was bell-shaped with a maximum reached about 30 min after chemical skinning.

Figure 3 illustrates a similar experiment carried out on a soleus muscle fibre. As in the experiments with EDL cells, the fibre was permeabilized and immersed into L-glutamate solution. Again, the frequency of Ca^{2+} sparks was determined at different times. In the soleus fibre, the lag in spark appearance was substantially longer than that observed in EDL cells. It took about 40 min for the first Ca^{2+} spark to be recorded. The maximal frequency of Ca^{2+} sparks in this preparation was reached 60 min after permeabilization, after which the number of events declined over another 40 min.

Figure 4 summarizes data on the time dependence of appearance of Ca^{2+} sparks for 17 EDL and 17 soleus muscle fibres studied with similar experimental protocols. Figure 4*A* represents the time dependencies of the averaged spark frequencies, and Fig. 4*B* shows corresponding normalized cumulative frequencies. Ca^{2+} sparks developed much later in soleus than in EDL fibres (time to the first spark recording was 47 ± 2.3 min *versus* 21 ± 1.1 min, in soleus and EDL cells, respectively). In addition, time to the maximal frequency was significantly longer in soleus muscle (67 ± 2.2 min *versus* 35 ± 1.4 min, respectively). It should be stated that, whereas the maximal frequency of sparks varied substantially between different fibres of the same type, the time course of spark appearance was remarkably similar. Time-dependent changes in the frequency of Ca^{2+} sparks did not correlate with fibre diameter and with the time needed for diffusion and equilibration of fluo-3 (and similarly sized molecules) in the fibre. During the experiments with EDL and soleus muscle cells summarized in Fig. 4, the average resting fluo-3 fluorescence within the fibres did not increase significantly (Fig. 4*C*).

In a separate set of experiments, FDB muscle fibres were isolated from mice and studied under conditions identical to those described above. The majority of mouse FDB cells are glycolytic and have much fewer mitochondria than rat EDL or soleus fibres. Averaged spark frequencies determined at different times after permeabilization in 36 FDB cells are represented in Fig. 4 by black diamonds. As expected, the onset of Ca^{2+} sparks in these fibres was more rapid than in rat EDL and soleus cells. Maximal frequency

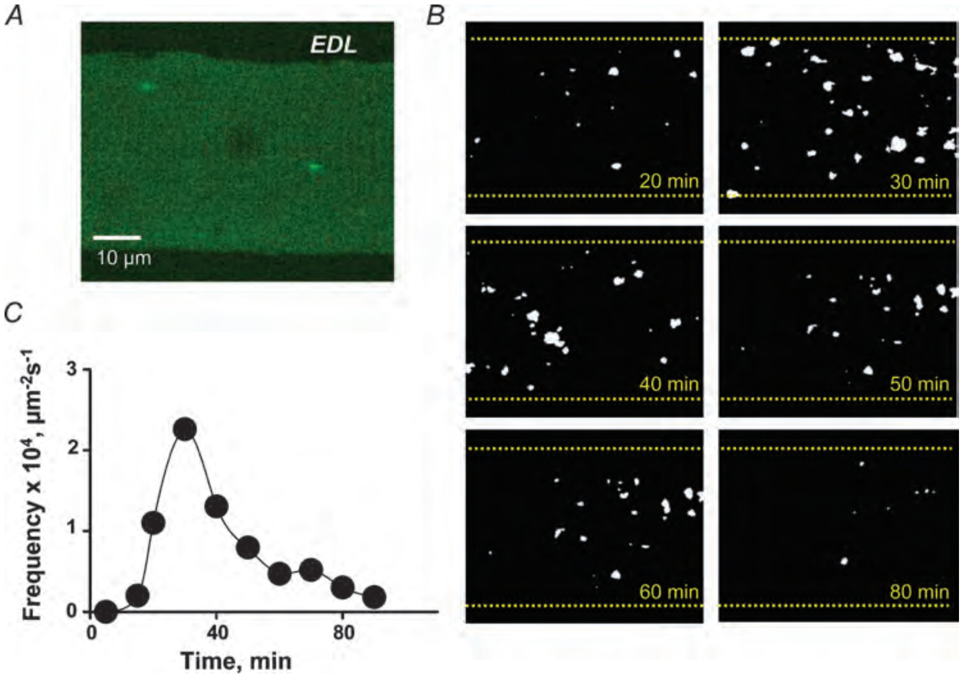

Figure 2. Appearance of Ca^{2+} sparks in EDL muscle
A, confocal image of Ca^{2+}-related fluorescence in an EDL fibre showing Ca^{2+} sparks. *B*, binary images of cumulative masks of sparks identified in sets of 40 images acquired at different times after fibre permeabilization (detection criterion $\Delta F/F_0 > 3$ S.D.). *C*, frequencies of Ca^{2+} sparks determined at different times during the experiment. (Fibre 20302-EDL2.)

of sparks was reached at 21 ± 0.8 min after skinning and the delay to the first spark detection was 9 ± 0.7 min (see also Table 1).

Taken together, the results obtained from different fibre types revealed that the temporal onset of Ca^{2+} sparks in permeabilized muscle fibres correlates well with the fibre's mitochondrial content.

Temporal onset of Ca^{2+} sparks depends on the SR Ca^{2+} load

Several lines of evidence suggest that luminal $[Ca^{2+}]$ regulates the activity of RyR Ca^{2+} release channels. In particular, it has been shown that SR Ca^{2+} overload stimulates SR Ca^{2+} release in cardiac muscle cells by increasing Ca^{2+} spark frequency and also their magnitude (DelPrincipe *et al.* 1999; Lukyanenko *et al.* 2001). Studies on skeletal muscle also suggest the existence of some, although not well defined yet, luminal mechanisms that regulate Ca^{2+} release from the SR (e.g. Donoso *et al.* 1995; Zhou *et al.* 2004). The average Ca^{2+} content of the SR is known to be different between fibre types (e.g. Fryer & Stephenson, 1996). This can affect the temporal onset of Ca^{2+} sparks. Therefore, it is important to monitor the Ca^{2+} loading state of the SR in our experiments.

We probed the SR Ca^{2+} load in permeabilized EDL and soleus muscle fibres by brief applications of caffeine. On each experimental day, both types of fibres were obtained from the same animal and studied in parallel. Figure 5*A* and *B* shows representative recordings of the 340 : 380 fura-2 fluorescence ratio from saponin-permeabilized fibres. In these experiments, cells were continuously perfused with L-glutamate solution containing 2 μM fura-2. Caffeine (20 mM) was briefly (2 s) applied at 5 min intervals (indicated by arrows). Caffeine application produced a transient increase in fluorescence ratio due to release of Ca^{2+} from the SR. Figure 5*C* shows two superimposed traces of caffeine-induced Ca^{2+} transients recorded at about 30 min after permeabilization in EDL and soleus fibres. It can be seen that the decaying phases of the transients were markedly different, being much slower in the soleus than in the EDL fibre. This may reflect differences in the molecular makeup of the system that is responsible for the removal of Ca^{2+} from the cytoplasm, following its release from the SR. In particular, compared to EDL muscle fibres, soleus cells contain virtually no parvalbumin, a soluble myoplasmic Ca^{2+} and Mg^{2+} binding protein (Celio & Heizmann, 1982). The amplitude of the caffeine-induced Ca^{2+} transients (ΔR) was determined at different times after

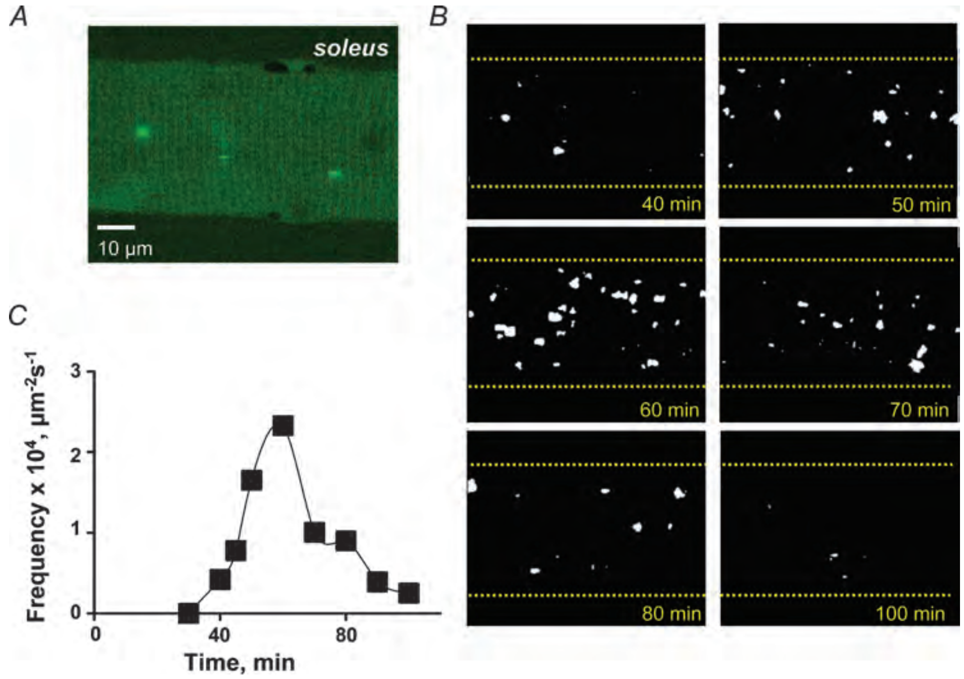

Figure 3. Development of Ca^{2+} sparks in soleus muscle
A, confocal fluorescent image of a soleus fibre. *B*, binary masks of sparks identified in sets of 40 images acquired at different times (detection criterion $\Delta F/F_0 > 3$ S.D.). *C*, time dependency of the Ca^{2+} spark frequency. (Fibre 010603-soleus1.)

fibre permeabilization. It was considered to be an estimate of SR Ca^{2+} content. This assumption is also supported by the observation that under our conditions, more prolonged application of caffeine did not increase the amplitude of cytosolic Ca^{2+} transients. Figure 5*D* presents averaged data compiled from 16 EDL and 18 soleus cells. It shows that in both fibre types, refilling of the SR with Ca^{2+} was complete and reached a steady-state within 20 min after the cells were permeabilized and immersed in the internal solution with slightly elevated $[Ca^{2+}]$ (150 nM). A subtle decrease in the amplitude of the caffeine-induced Ca^{2+} transients after ~40 min of incubation indicates a partial decline in SR Ca^{2+} load towards the end of such prolonged experiments.

The somewhat larger Ca^{2+} transients in soleus fibres also indicated that the SR of these fibres is more loaded with Ca^{2+} than that of EDL cells. Taking into account that the relative cell volume occupied by the SR is only half in soleus muscle with respect to EDL (Eisenberg, 1983), we can estimate that under our experimental conditions the SR of soleus fibres is about two times more loaded with Ca^{2+}. This is in agreement with the results by Fryer & Stephenson (1996) who also reported an about twofold difference in the SR load of rat fast- and slow-twitch fibres.

The experiments shown in Fig. 6 were designed to assess how SR Ca^{2+} load affects the onset of Ca^{2+} sparks. For this, EDL cells were incubated in L-glutamate solution supplemented with 1 μM 2′,5′-di(tert-butyl)-1,4-benzohydroquinone (TBQ) or 1 μM cyclopiazonic acid (CPA), two different potent inhibitors of SR Ca^{2+}-ATPase. The drugs, at these concentrations, did not completely deplete the SR but reduced caffeine-induced Ca^{2+} transients (e.g. SR Ca^{2+} load) by more than 50% (ΔR was reduced from 0.64 ± 0.09 to 0.29 ± 0.03, $n = 6$, by TBQ; and from 0.35 ± 0.03 to 0.15 ± 0.02, $n = 5$, by CPA). The examination of the temporal onset of spontaneous Ca^{2+} sparks under conditions of reduced SR Ca^{2+} load revealed that the delay to the first detection of Ca^{2+} sparks and the time to the maximal frequency of sparks were significantly prolonged (52 ± 3.7 min and 81 ± 2.4 min, $n = 5$, correspondingly in the presence of TBQ, and 54 ± 5.1 min and 85 ± 4.5 min,

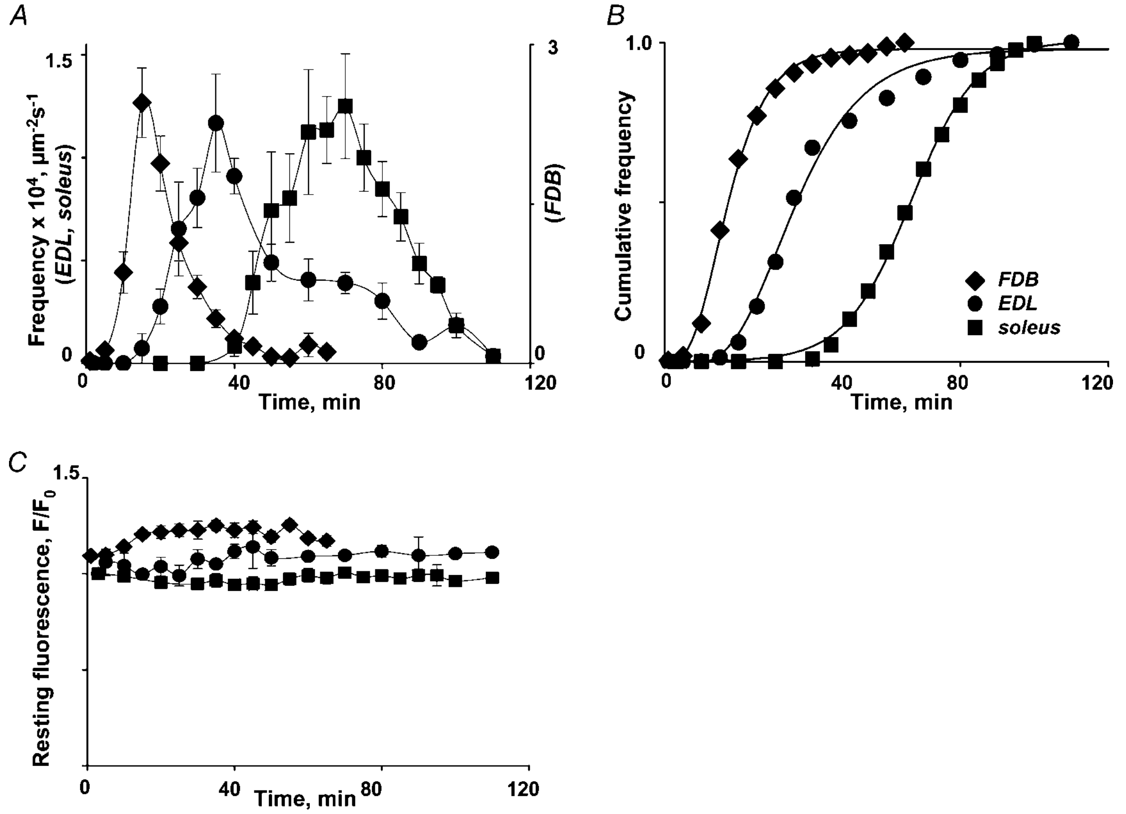

Figure 4. Appearance of Ca^{2+} sparks in permeabilized FDB, EDL and soleus skeletal muscle fibres in L-glutamate solution

A, time dependence of Ca^{2+} spark frequency in 36 FDB (◆), 17 EDL (●) and 17 soleus (■) fibres. Left vertical axis corresponds to EDL and soleus cells, right axis corresponds to FDB cells. *B*, cumulative frequencies of events. *C*, changes in resting fluorescence within fibres.

$n = 5$, in CPA). Therefore, the slower temporal onset of Ca^{2+} sparks in soleus fibres in respect to EDL cells cannot be explained by the observed difference in luminal SR $[Ca^{2+}]$.

Washout of cytoplasmic GSH does not promote sparks

It has been shown that cytoplasmic redox state, mainly determined by the ratio of GSSG/GSH, tightly influences the activity of RyR (Feng *et al.* 2000). In mammalian muscle cells, the cytoplasmic GSSG/GSH ratio is about 1 : 30 (5 mM total). Thus, under normal physiological conditions RyRs are functioning in a reduced cytosolic environment. According to Feng *et al.* (2000), oxidation of the cytoplasm enhances the activity of RyRs. It is conceivable that the washout of GSH from the cytosol may underlie the appearance of sparks in skinned cells. However, this possibility is less likely because the addition of 5 mM GSH into the L-glutamate solution, in order to compensate for cytosol oxidation during the washout, did not have a significant effect either on the time course of appearance of sparks, or on their maximal frequencies. In seven EDL muscle fibres studied in the presence of GSH, time to the first spark recording, time to the maximal frequency of sparks and the maximal frequency of sparks were 15.6 ± 3.4 min, 30.0 ± 2.8 min, and $2.3 \pm 0.3 \times 10^4\ \mu m^{-2}\ s^{-1}$, respectively. The numbers are not significantly different from that obtained in eight fibres studied in parallel in L-glutamate (18.2 ± 2.8 min, 33.6 ± 3.1 min, and $2.5 \pm 0.3 \times 10^4\ \mu m^{-2}\ s^{-1}$, respectively).

Mitochondrial substrates delay the appearance of Ca^{2+} sparks

Results of the experiments illustrated in Figs 2–4 suggested the involvement of mitochondria in the development of spontaneous Ca^{2+} activity in permeabilized skeletal muscle cells. In the next set of experiments, we further examine this possibility. For this purpose, skeletal muscle fibres of different metabolic strength (FDB, EDL and soleus) were immersed into internal solutions based on L- or D-glutamate or aspartate. While L-glutamate is a substrate of the TCA cycle, D-glutamate is not. Whereas the addition of substrates into the internal solution is supposed to stimulate mitochondrial metabolism, their

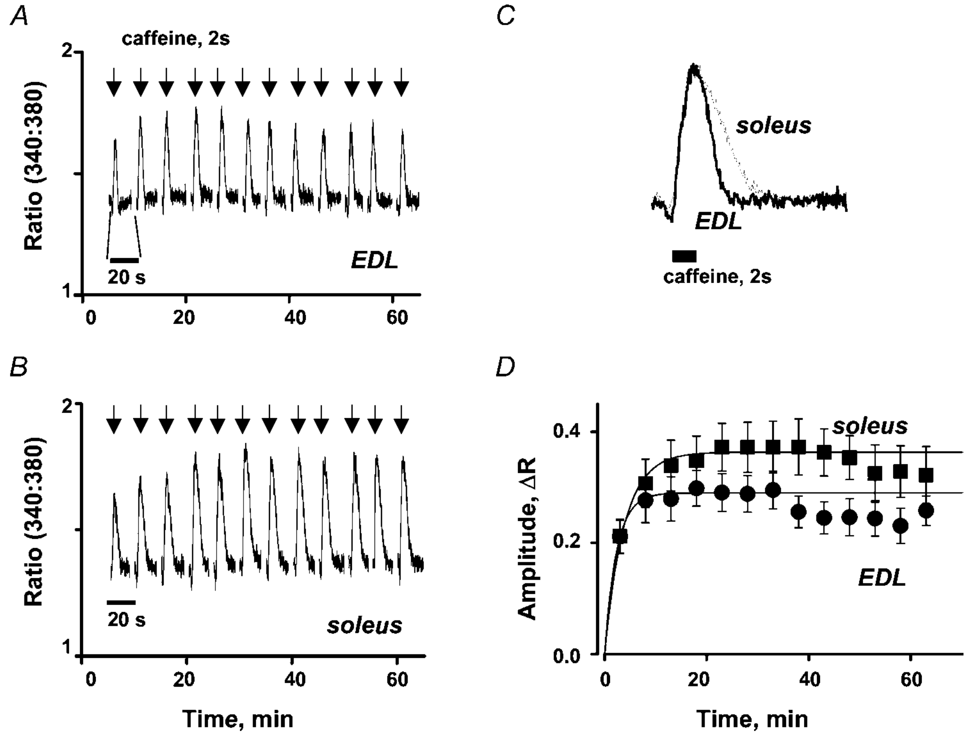

Figure 5. Estimates of SR Ca^{2+} load in EDL and soleus skeletal muscle fibres
A and *B*, caffeine-induced Ca^{2+} transients in EDL (*A*) and soleus (*B*) fibres. Individual transients of each set are represented in the expanded (20 s) time scale. *C*, superimposed transients obtained in EDL (thick line) and soleus (thin line) fibres 30 min after permeabilization. (Fibres 121102-EDL2 and 121102-soleus2.) *D*, averaged data from 16 EDL (●) and 18 soleus (■) fibres.

removal would slow it down. Aspartate, being a product of the TCA cycle, is expected to inhibit oxidative metabolism even more than D-glutamate.

The inset in Fig. 7*A* shows representative changes in NADH fluorescence recorded in EDL cells when L-glutamate-based solution was subsequently replaced with one based on D-glutamate and aspartate. These measurements provided us with information about the redox state of the mitochondrial NAD system, which in turn reflects mitochondrial metabolism. Images were acquired every 10 s. Whole-cell NADH fluorescence was measured with digital photometry as described in Methods. It was spatially averaged over the region of interest corresponding to the fibre. The signal is represented in arbitrary units on the plot. The NADH fluorescence slowly decreased when the fibre was incubated in L-glutamate solution. It diminished more rapidly after L-glutamate solution was replaced with one based on D-glutamate. Replacement of D-glutamate solution with one based on aspartate led to a dramatic oxidation of the mitochondrial NADH pool, indicating a massive impairment of the mitochondrial metabolism under this experimental condition. Addition of 20 μM rotenone, an inhibitor of NADH dehydrogenase, partially restored NADH fluorescence. Similar results were obtained in four EDL fibres.

In the three fibre types studied, the temporal onset of Ca^{2+} sparks after skinning was most delayed in a 'substrate-rich' L-glutamate solution. In 17 EDL cells immersed in L-glutamate solution, the maximal frequency of Ca^{2+} sparks was reached 35 ± 1.4 min after fibre permeabilization (Fig. 7*C*). When cells were exposed to D-glutamate solution, the peak of the spark frequency was recorded earlier (20 ± 1.4 min, $n = 11$). Sparks developed even faster when fibres were exposed to aspartate-containing solution (11 ± 0.7, $n = 9$). The difference in the time course of spark appearance in various experimental solutions is clearly seen on a cumulative frequency plot in Fig. 7*D*. Similar dependencies of the time course of spark appearance on substrates were

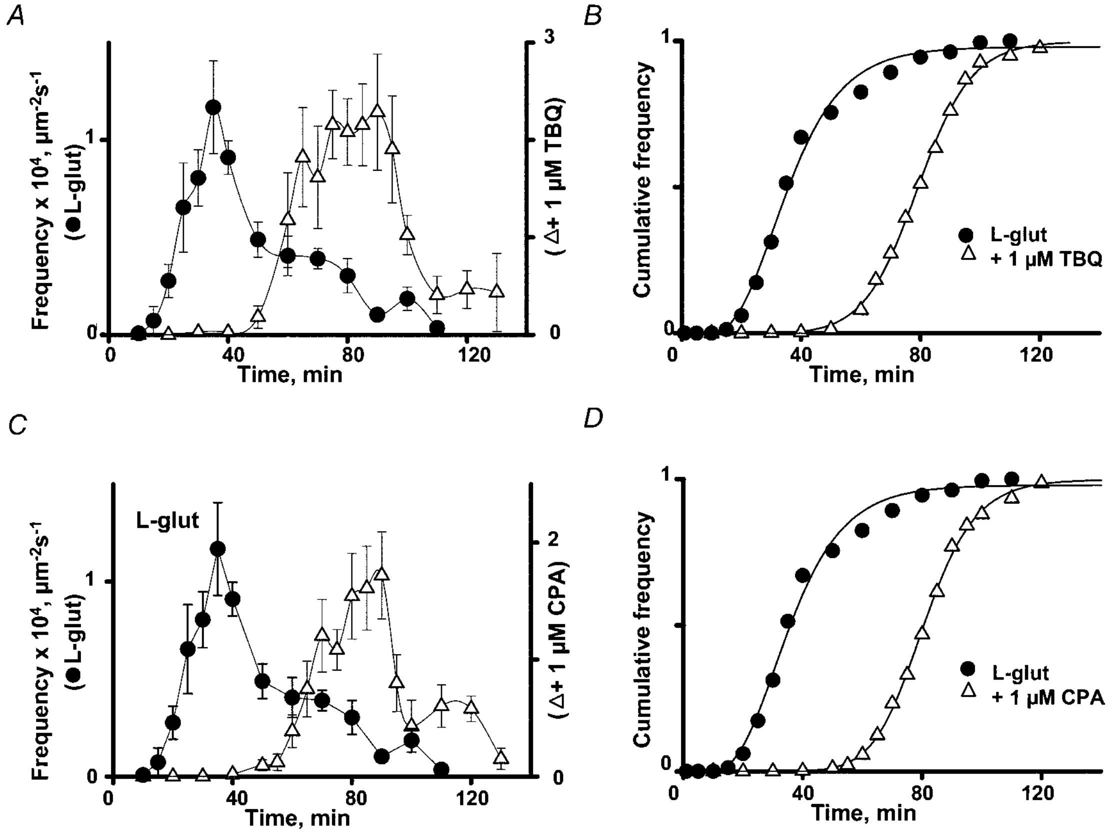

Figure 6. Effects of SR Ca^{2+} load on the time course of spark appearance in EDL muscle
A, effect of TBQ on the tempotal onset of Ca^{2+} sparks. Triangles (Δ) show averaged frequency of sparks recorded in 5 fibres at different times after they were immersed into solution containing 1 μM TBQ. Circles (●) represent control data taken from Fig. 4. Right axis corresponds to the experiments in TBQ. Left axis corresponds to data in control. *B*, cumulative frequencies of sparks in control and in TBQ. *C*, effect of 1 μM CPA on time course of Ca^{2+} sparks under control conditions (●) and in CPA (Δ, $n = 5$). *D*, cumulative frequencies of sparks in control and in CPA.

observed in FDB and soleus muscle fibres (Fig. 7*A*, *B*, *E* and *F*, correspondingly, and also Table 1). Interestingly, under each experimental condition (L- or D-glutamate, or aspartate), Ca^{2+} sparks developed fastest in fibres poor in mitochondria (FDB) and slowest in cells rich in mitochondria (soleus).

Mitochondrial redox state correlates with Ca^{2+} spark activity

The experiment illustrated in the inset of Fig. 7*A* revealed that mitochondrial NADH fluorescence gradually declined after fibre permeabilization. It also showed that the rate of the NADH oxidation depends on the composition of

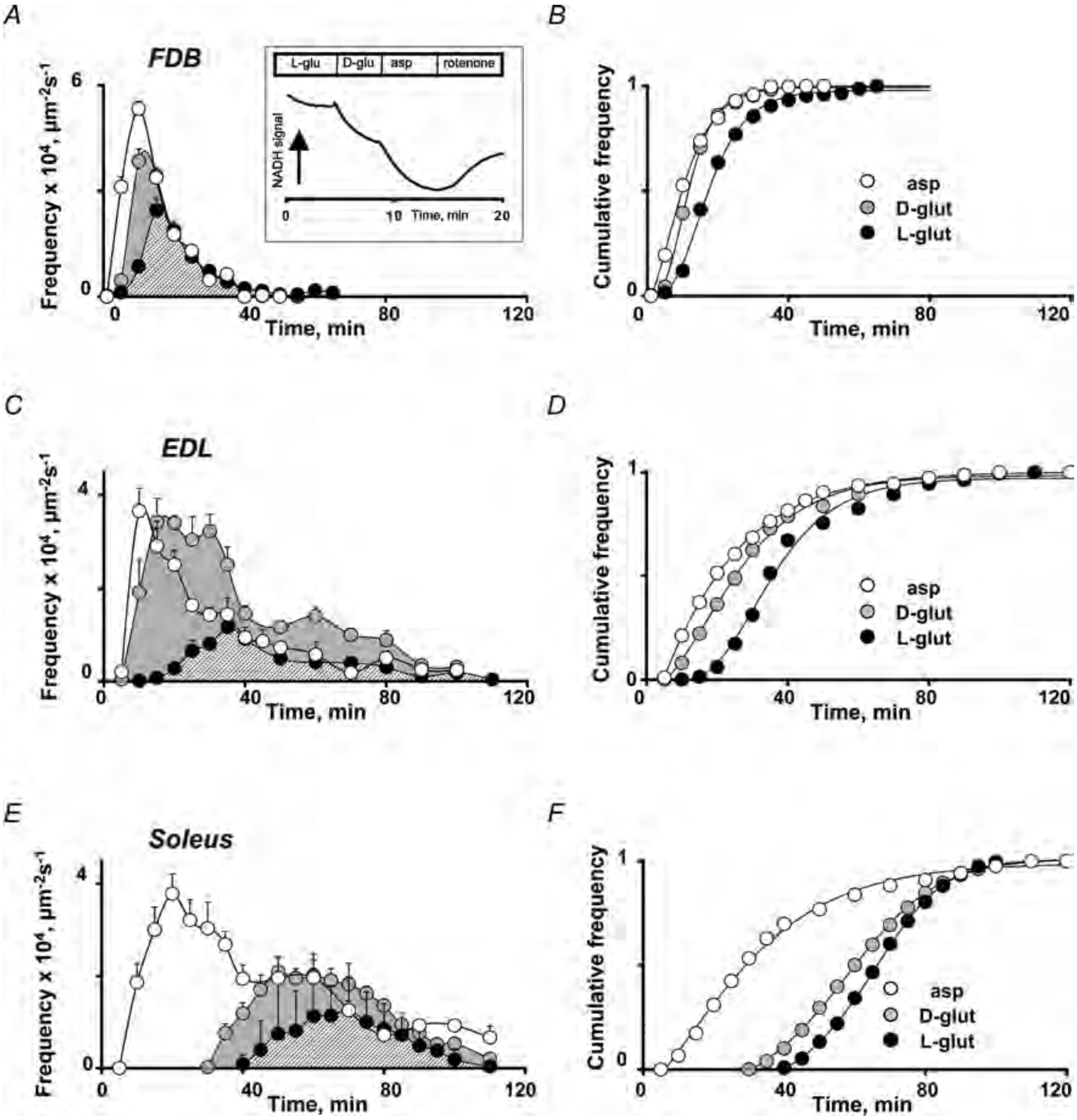

Figure 7. Effects of mitochondrial substrates on the frequency of Ca^{2+} sparks in FDB, EDL and soleus muscles

A and *B*, time course of the appearance of sparks in FDB fibres, immersed in various bathing solutions. Inset shows changes in mitochondrial NADH signal when an EDL fibre was consequently exposed to L- or D-glutamate or aspartate solutions and after rotenone was added. *C* and *D*, temporal onset of sparks in EDL fibres. *E* and *F*, spark development in soleus muscle fibres.

Table 1. Evolution of Ca^{2+} sparks in different fibre types

	L-Glutamate	D-Glutamate	Aspartate
Time to the maximal Ca^{2+} spark frequency			
FDB	21.2 ± 0.78 (36)	18.6 ± 0.97 (14)	10.6 ± 1.13 (8)
EDL	35.0 ± 1.39 (17)	20.1 ± 1.40 (11)	11.1 ± 0.73 (9)
Soleus	66.8 ± 2.20 (17)	55.0 ± 2.31 (14)	15.0 ± 1.50 (6)
Time to the first spark detection			
FDB	9.3 ± 0.65 (36)	8.6 ± 0.94 (14)	6.3 ± 0.81 (8)
EDL	20.9 ± 1.11 (17)	10.6 ± 0.61 (11)	7.0 ± 1.23 (9)
Soleus	47.1 ± 2.29 (17)	38.9 ± 1.42 (14)	11.5 ± 1.07 (6)

Data are mean ± S.E.M. for the number of experiments carried out in each group (*n*), shown in parentheses. Values are in minutes.

solutions the fibres were bathed in. The rate of decay of the NADH signal appeared to be the slowest in substrate-rich L-glutamate solution and the fastest in aspartate solution. This correlates with the time course of Ca^{2+} spark development under similar experimental conditions.

In the following series of experiments, we applied two-photon fluorescence microscopy to monitor local changes in NADH fluorescence. EDL and soleus muscle fibres were permeabilized and exposed to either L-glutamate or aspartate solutions. The NADH signal was recorded every 3 min from the same confocal plane within the fibre during 1 h. Figure 8*A* shows three images of NADH fluorescence acquired right after EDL fibre permeabilization (3 min) and also 30 and 60 min after the cell had been incubated in L-glutamate solution. The fluorescence signal emitted by NADH molecules within several small groups of mitochondria was determined on every image and then averaged. The values were normalized to the NADH value at the beginning of the experiment. They are plotted in Fig. 8*B* against time (filled circles). The decay of NADH fluorescence in this and six other EDL cells was fitted with a single exponential function (line on the plot) yielding an average τ of decay of 14.8 ± 0.81 min. The time course of decay was significantly slower in soleus fibres studied in the same way ($\tau = 21.1 \pm 1.72$ min, $n = 9$). When fibres of both types were examined in aspartate solution, the NADH signal had diminished significantly faster compared with that in L-glutamate (EDL: $\tau = 6.3 \pm 0.64$ min, $n = 11$; soleus: $\tau = 7.4 \pm 0.61$ min, $n = 9$). In general, the temporal onset of Ca^{2+} sparks in these fibre types correlated well with the rate of decay of mitochondrial redox potential (and mitochondrial metabolism) of the respective fibre.

Coupling mitochondrial redox state to intracellular Ca^{2+} homeostasis

There are many mechanisms by which mitochondria can influence intracellular Ca^{2+} homeostasis: via ATP synthesis, accumulation of Ca^{2+}, generation of superoxide radicals, etc. Disruption of mitochondrial functions due to a collapse of the mitochondrial redox potential can subsequently alter the pattern of intracellular Ca^{2+} signalling.

One obvious pathway through which mitochondria can affect cytosolic Ca^{2+} signals is via generation of ATP. Reduction in metabolically produced ATP can, in general, affect the function of two major molecules involved in intracellular Ca^{2+} homeostasis: RyR Ca^{2+} release channels and SR Ca^{2+}-ATPases. However, this mechanism is unlikely to influence the temporal onset of sparks because: (1) all bathing solutions contained 5 mM ATP to minimize the contribution of metabolically generated ATP; and (2) incubation of EDL cells in L-glutamate solution with 2.5 μM oligomycin, an inhibitor of the F_1/F_0 ATP synthase, did not modify the time course of spark appearance. In seven fibres studied in the presence of oligomycin, time to the first spark recording, time to the maximal frequency of sparks and the maximal frequency of sparks were 21.2 ± 1.4 min, 35.1 ± 2.1 min, and $1.1 \pm 0.1 \times 10^4\ \mu\text{m}^{-2}\ \text{s}^{-1}$, respectively. The numbers are not significantly different from that obtained in 15 fibres studied in parallel in L-glutamate (19.1 ± 1.7 min, 32.1 ± 2.2 min, and $1.1 \pm 0.2 \times 10^4\ \mu\text{m}^{-2}\ \text{s}^{-1}$, respectively).

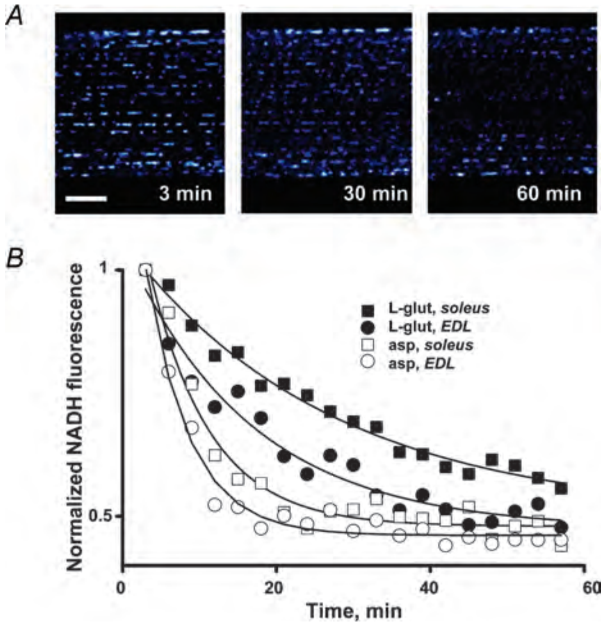

Figure 8. Effects of mitochondrial substrates on mitochondrial redox potential

A, images of NADH fluorescence recorded in permeabilized EDL muscle fibre at different times after permeabilization. Fibre was incubated in L-glutamate solution. Scale bar corresponds to 10 μm. (Cell 043004-EDL2.) *B*, decay of NADH signals in EDL and soleus muscles immersed in aspartate and L-glutamate solutions. (Fibres 060904-soleus2 (L-glu), 043004-EDL2 (L-glu), 061704-soleus4 (asp), 043004-EDL1 (asp).)

Previously we have suggested that mitochondrial Ca^{2+} uptake plays a significant role in the modulation of spontaneous Ca^{2+} sparks in permeabilized mammalian muscle fibres (Isaeva & Shirokova, 2003). We have shown that oxidation of the mitochondrial NADH pool is accompanied by a decrease in the driving force for Ca^{2+} uptake via the electrogenic Ca^{2+} uniporter. It is possible that a gradual impairment of mitochondrial Ca^{2+} uptake after fibre permeabilization and wash out of the cytosol may influence the temporal pattern of Ca^{2+} spark appearance. Unfortunately, most of the mitochondrial Ca^{2+} uniporter inhibitors are not specific and are likely to affect cytosolic Ca^{2+} transients by multiple interconnected pathways (e.g. via direct inhibition of Ca^{2+} release channels, generation of ROS, etc.). In addition, Ru360, the most specific blocker of the uniporter, appears to have a poor stability (Wang & Thayer, 2002; also Dr A. P. Thomas, personal communication). We were not able to prevent oxidation of Ru360 in long-lasting experiments. Therefore, up to date, we have no adequate experimental tools to explore to what extent mitochondrial Ca^{2+} buffering is involved in unmasking sparks in skinned preparations. Consequently, we cannot rule out the mitochondrial Ca^{2+} uptake as the mechanism that is at least in part responsible for the phenomena described above.

Another possible way for mitochondria to affect cytoplasmic Ca^{2+} signals is via generation of ROS. During aerobic respiration to generate ATP in mitochondria, leakage of electrons regularly produces mitochondrial superoxide anions that are later reduced to H_2O_2 by manganese superoxide dismutase. H_2O_2 appears to be one of the primary messenger molecules in the redox signalling pathway (e.g. reviewed by Reid, 2001; Brookes *et al.* 2004). It can travel somewhat to interact with remote targets, even though its life time is short because of its rapid metabolism. However, since the SR lies very close to mitochondria, it may well be influenced by ROS released by these organelles. Every cell has a set of potent ROS scavengers to prevent oxidative damage. As one of the major targets for ROS, mitochondria have their own defence instrument. Because catalase is not detected in the mitochondria of mammalian tissues except heart (Radi *et al.* 1991), mitochondrial glutathione peroxidase plays a key role in metabolizing hydrogen peroxide. Therefore, reduced glutathione (GSH), required for the activity of mitochondrial glutathione peroxidase, is the potential free radical scavenger. GSH is synthesized in the cytosol and transported into mitochondria (Griffith & Meister, 1985; Martensson *et al.* 1990). However, oxidized glutathione disulphide (GSSG) in the mitochondria cannot be exported back to the cytosol (Olafsdottir & Reed, 1988) for conversion to GSH. Therefore, mitochondrial NADPH is a required reducing equivalent for the regeneration of GSH from GSSG. A reduction of the mitochondrial redox potential can consequently lead to a depletion of the mitochondrial GSH pool, weakening the mitochondrial defence against ROS and finally increasing the leak of ROS to the cytoplasm. This, in turn, can have effects on the RyRs and result in Ca^{2+} sparks.

To test whether ROS indeed can account for the development of Ca^{2+} sparks in permeabilized mammalian muscle cells, we first studied the time course of spark appearance under experimental conditions where exogenous scavengers chelated ROS. Figure 9*A* and *B* illustrates the experiments in which EDL muscle fibres were exposed to aspartate-based internal solutions, and to aspartate solution supplemented with 600 U ml^{-1} of superoxide dismutase (SOD) or with a combination of 600 U ml^{-1} of SOD and 500 U ml^{-1} of catalase. Fibres were studied in parallel under all three conditions. The temporal onset of Ca^{2+} spark appearance in aspartate was similar to that listed in Table 1 (time to the first spark detection and time till the maximal frequency of sparks was reached were 7.9 ± 1.01 min and 11.4 ± 1.80 min, $n = 7$, respectively). SOD alone substantially inhibited Ca^{2+} sparks and delayed their temporal onset (corresponding times were 11.0 ± 1.00 min and 18.0 ± 1.22, $n = 5$). Two scavengers, used in combination, further suppressed sparks and significantly delayed their appearance compared with that in control (times were 11.3 ± 1.25 and 18.3 ± 1.17 min, $n = 4$).

Figure 9*C* and *D* shows that the effect of scavengers was reversible. The triangles summarize the results of six experiments when fibres were permeabilized and bathed in aspartate solution containing 500 U ml^{-1} of catalase. Very few sparks could be detected under this condition. In another set of experiments (dotted circles), catalase was removed from the bath 15 min after recording started. Catalase washout led to a restoration of spark frequency and their temporal onset to control levels (open circles). All three groups of experiments were performed in parallel on fibres isolated from the same group of rats to minimize the variability in spark frequencies often observed between different animals.

Finally, we tested whether the introduction of ROS into the bathing solution produces an effect opposite to that of scavengers (Fig. 9*E* and *F*). H_2O_2 at 50 μM added to the aspartate solution somewhat increased the maximal Ca^{2+} spark frequency, but only slightly accelerated their appearance. It is possible that the changes in the temporal onset of sparks were difficult to detect because the onset is very fast in aspartate. Interestingly, the effects of H_2O_2 appeared to be concentration dependent. While 50–200 μM H_2O_2 promoted sparks, 10 mM H_2O_2 completely inhibited them (data not shown).

Figure 10 illustrates the experiments with ROS scavengers, SOD and catalase, carried out in EDL muscle cells in D-glutamate (Fig. 10*A* and *B*) or in L-glutamate (Fig. 10*C* and *D*) containing internal solutions. In D-glutamate, SOD and SOD in combination with catalase dramatically reduced the Ca^{2+} spark frequency and also substantially delayed the spark appearance. Time to the first spark detection and time when the maximal frequency of sparks was recorded were 23.8 ± 1.25 min and 33.8 ± 1.57 min, $n = 8$, and 36.7 ± 6.01 min and 46.7 ± 1.67 min, $n = 3$, in SOD and SOD and catalase, respectively. These times were significantly longer than those recorded in the control experiments (no scavengers added) carried out in parallel (13.3 ± 2.04 min and 23.9 ± 2.32 min, $n = 8$). Similar results were obtained in L-glutamate. Addition of scavengers not only decreased the spark frequency, but also delayed their temporal onset. Times to the first spark detection and to their maximal frequency were 28.8 ± 1.25 min and 36.3 ± 2.39 min, $n = 4$, and 37.7 ± 5.05 min and 46.7 ± 2.89 min, $n = 3$, in SOD and SOD and catalase, respectively, and

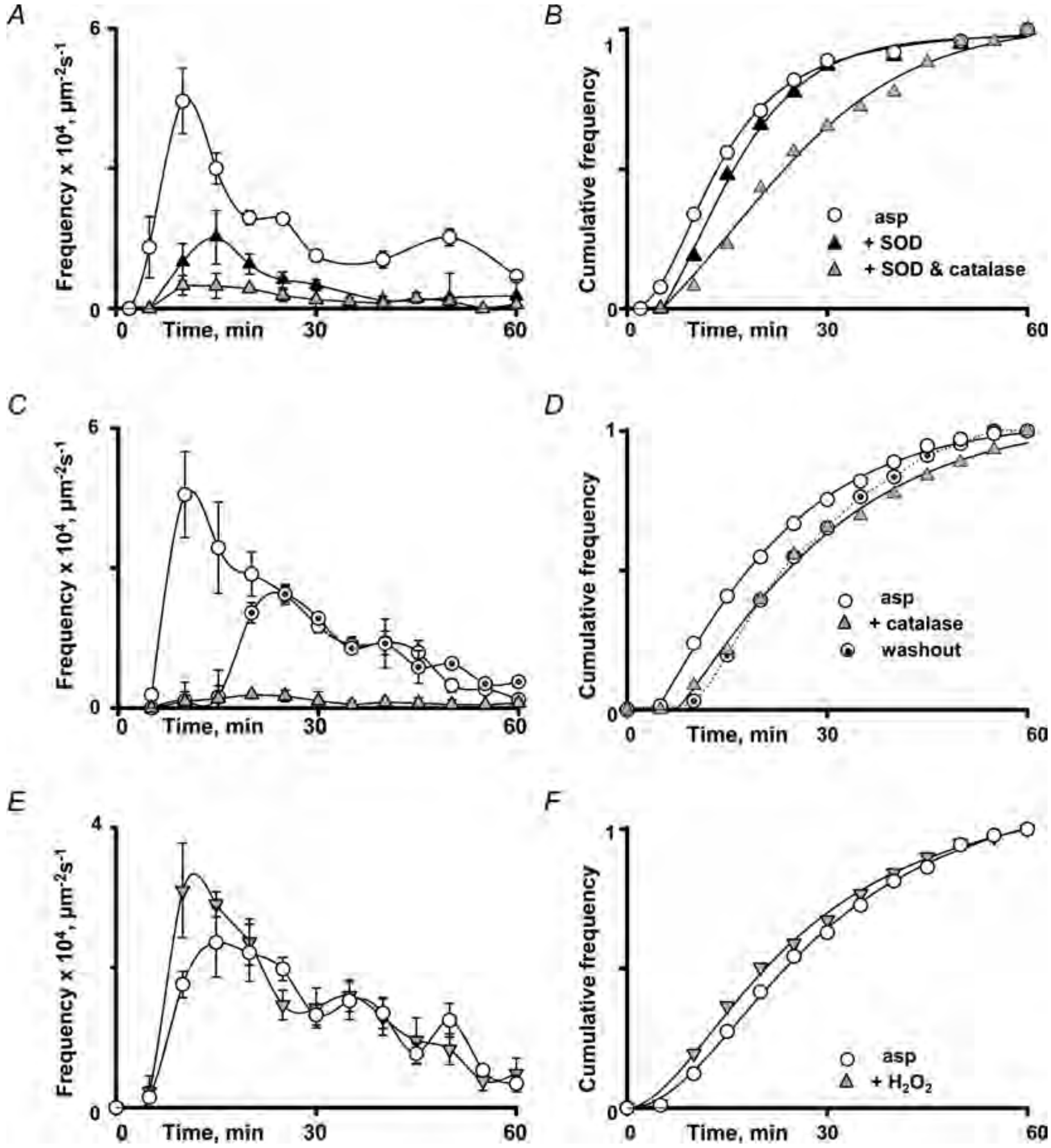

Figure 9. Effects of ROS scavengers and ROS on Ca^{2+} sparks in EDL muscle fibres bathed in aspartate solution

A and *B*, development of Ca^{2+} sparks in aspartate solution (○, $n = 7$), in aspartate solution supplemented with SOD (▲, $n = 5$), or SOD and catalase (Δ, $n = 4$). *C* and *D*, temporal onset of sparks in aspartate solution (○, $n = 6$), in the presence of catalase (Δ, $n = 6$), and when catalase was removed from the bathing solution after 15 min (dotted circles, $n = 6$). *E* and *F*, sparks in control conditions (L-glutamate, ○, $n = 4$) and in the presence of 50 μM H_2O_2 (Δ, $n = 7$).

corresponding times recorded in the control group of experiments were 18.8 ± 1.25 min and 30.0 ± 1.64 min, $n = 8$).

Figure 11 further summarizes experiments with $50\ \mu\text{M}$ H_2O_2. ROS scavengers and H_2O_2 had opposite effects on the appearance of sparks in EDL muscle fibres. Addition of H_2O_2 to D- and L-glutamate internal solutions somewhat increased the maximal spark frequency and sped up their temporal onset. Both time to the first spark detection and time when the maximum frequency of sparks was observed were significantly shortened (6.7 ± 1.05 min and 16.7 ± 1.67 min, $n = 9$, and 11.7 ± 1.44 min and 21.6 ± 2.04 min, $n = 8$, in D-glutamate supplemented with $50\ \mu\text{M}$ H_2O_2 and D-glutamate, respectively; 8.1 ± 0.91 min and 17.5 ± 1.33 min, $n = 8$, and 15.6 ± 1.13 min and 30.6 ± 1.12 min, $n = 8$, in L-glutamate with $50\ \mu\text{M}$ H_2O_2 and L-glutamate, respectively).

Discussion

Intact skeletal muscle fibres from adult mammals exhibit neither spontaneous nor stimulated Ca^{2+} sparks. Surprisingly, skinning procedures have been reported to unmask them. The study presented here was aimed to clarify mechanisms that determine their appearance in permeabilized mammalian muscle fibres of different oxidative strength. We present the following findings: (1) the time course of Ca^{2+} spark appearance was the fastest in glycolytic and the slowest in oxidative fibres; (2) addition of mitochondrial substrates to bathing solutions delayed the appearance of spontaneous Ca^{2+} sparks; (3) larger SR Ca^{2+} load could not account for the slower appearance of sparks in slow-twitch muscle cells; (4) Ca^{2+} sparks appeared in parallel with the reduction in the fibre's mitochondrial redox potential; (5) ROS scavengers (SOD and catalase) dramatically decreased spark frequency and significantly delayed their appearance; (6) micromolar concentrations of H_2O_2 promoted sparks and sped up their appearance. Taken together, these data suggest that under physiological conditions mitochondria are actively involved in the suppression of spontaneous Ca^{2+} sparks in mammalian muscle fibres.

Ca^{2+} sparks in skeletal muscle cells

The discovery of Ca^{2+} sparks in cardiac myocytes by Cheng *et al.* (1993) constituted an important advance in our understanding of the control of Ca^{2+} release in muscle

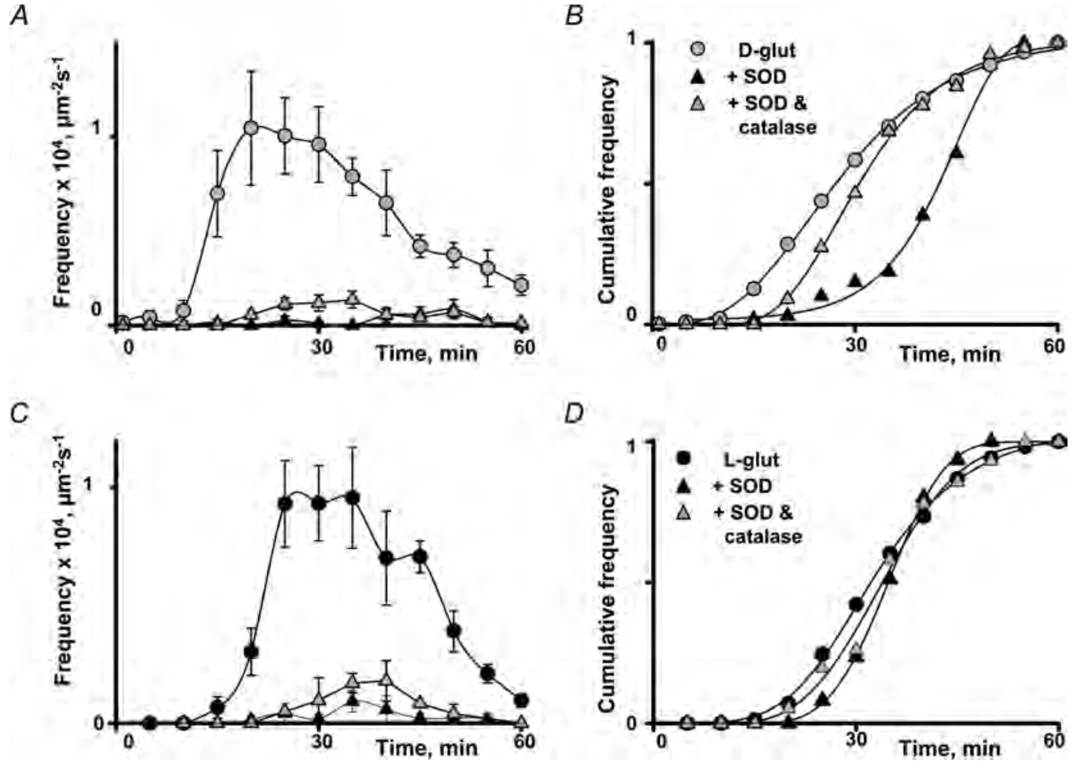

Figure 10. Effects of ROS scavengers on Ca^{2+} sparks in EDL muscle fibres
A and *B*, temporal onset of sparks in D-glutamate solution (●, $n = 8$) or in the presence of ROS scavengers (SOD, Δ, $n = 8$; SOD + catalase, ▲, $n = 3$). *C* and *D*, sparks in control conditions (L-glutamate, ●, $n = 8$) and in the presence of ROS chelators (SOD, Δ, $n = 4$; SOD + catalase, ▲, $n = 3$).

cells. Ca^{2+} sparks are often referred to as elementary events of CICR. Infrequent appearance of Ca^{2+} sparks in adult mammalian skeletal muscle fibres was considered as an indication of a less prominent role of CICR in mammalian ECC, compared to amphibian muscle. Several explanations for this difference have already been considered but most have been rejected. One possibility to account for the inhibited CICR in mammals was envisaged in the molecular makeup of the muscle fibres themselves. Most adult mammalian muscles express only the RyR1 isoform, whereas amphibian skeletal muscle and embryonic mammalian muscle, in which sparks were found, express two RyR isoforms, RyR α and RyR β or RyR1 and RyR3, respectively (for reviews see Sutko & Airley, 1996; Franzini-Armstrong & Protasi, 1997). Naturally, it has been suggested that RyR3 may be necessary for skeletal muscle to produce Ca^{2+} sparks. However, this hypothesis did not sustain experimental challenge: spontaneous Ca^{2+} sparks were detected in developing skeletal muscle from RyR3-knockout mice (Shirokova *et al.* 1999; Conklin *et al.* 2000). In addition, in developing skeletal muscle, Ca^{2+} sparks were found to be spatially segregated and mutually exclusive with the homogeneous Ca^{2+} release induced by membrane depolarization. This observation led to the suggestion that an allosteric negative feedback interaction between DHPRs and RyRs prevents CICR (Shirokova *et al.* 1999). However, the latter hypothesis was again questioned by the work of Kirsch *et al.* (2001) who demonstrated the abundance of sparks in mechanically skinned muscle cells. Our recent studies (Isaeva & Shirokova, 2003) added a new twist to this complicated story. Our results suggested that mitochondria, being in close proximity to the Ca^{2+} release sites, also play an important role in inhibiting CICR.

The present results on the temporal onset of the appearance of Ca^{2+} sparks in different fibre types lend further support for the notion that spontaneous Ca^{2+} activity in permeabilized cells is suppressed by mitochondria. The time lag between fibre permeabilization and first recordings of Ca^{2+} sparks suggests that a gradual degradation of physiological processes within the cell accounts for the appearance of sparks. The match between a fibre's mitochondrial content and the temporal onset of sparks, the relationship between oxidative strength of the bathing solution and spark appearance, and the correlation between spark development and the dissipation of the mitochondrial redox potential indicate that disruption

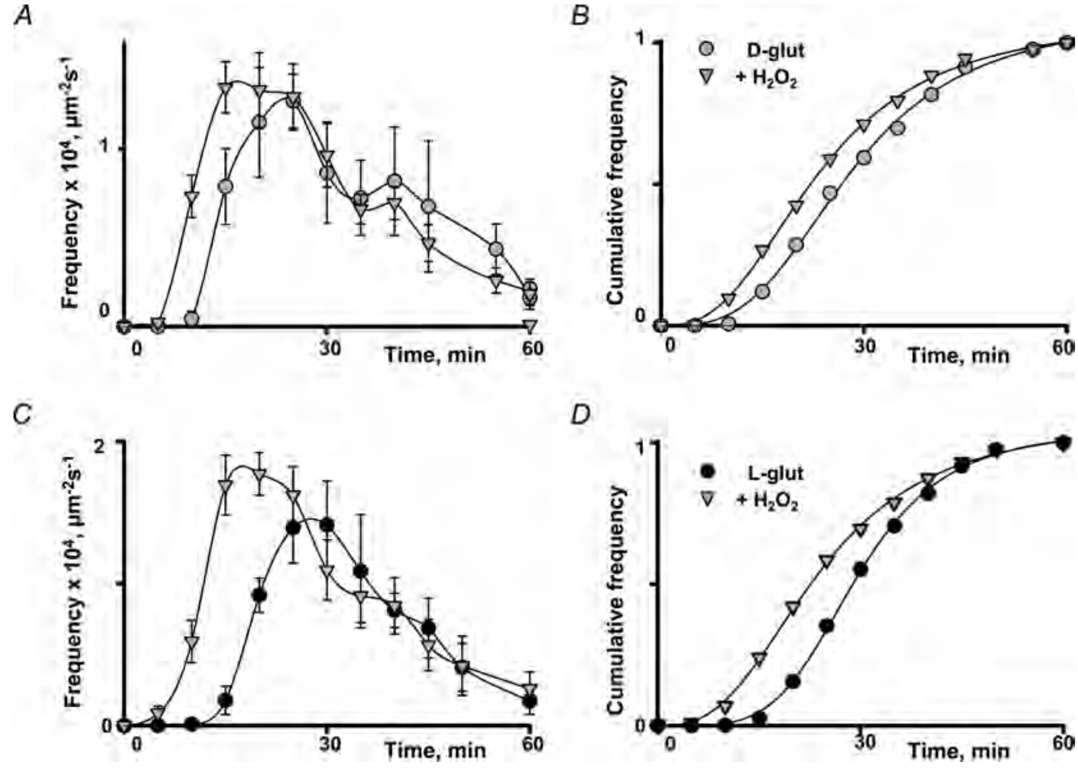

Figure 11. Effects of ROS on Ca^{2+} sparks in EDL muscle fibres
A and *B*, temporal onset of sparks in D-glutamate solution (○, $n = 8$) or in the presence of 50 µM of H_2O_2 (Δ, $n = 9$). *C* and *D*, sparks in L-glutamate (●, $n = 8$) and in the presence of 50 µM of H_2O_2 (Δ, $n = 8$).

of mitochondrial functions during the cytosol washout can be one of the possible reasons for the relief of CICR inhibition.

Intracellular Ca^{2+} signalling and mitochondria

Mitochondria exert a multifactorial influence on a variety of cell functions. First, these organelles produce ATP through oxidative metabolism to supply energy. Second, mitochondria can accumulate Ca^{2+} whenever the local cytoplasmic [Ca^{2+}] rises above a critical 'set point'. Third, the mitochondrial respiratory chain is a major site for generation of superoxide radicals. Fourth, mitochondria can disrupt the fine balance between reduced and oxidized forms of cellular major redox couples, GSSG/GSH and NAD^+/NADH, thus disturbing the cytosolic redox potential and consequently the activity of various redox-sensitive molecules. Most likely mitochondria have many more cellular and signalling functions, also depending on the cell type. Each of these functions is influenced by and can in turn influence the intracellular Ca^{2+} homeostasis.

It has been demonstrated in a large number of functional studies that mitochondrial Ca^{2+} uptake can participate in shaping global and local Ca^{2+} signals in a variety of cell types. For example, inhibiting the mitochondrial Ca^{2+} uniporter increased the frequency of spontaneous Ca^{2+} sparks in cardiac muscle cells (Pacher *et al.* 2002) and in mammalian skeletal muscle fibres (Isaeva & Shirokova, 2003), and, on the other hand, inhibited Ca^{2+} sparks in smooth muscle cells (Cheranov & Jaggar, 2004). This suggests that, at least in cardiac and skeletal muscle, mitochondrial Ca^{2+} uptake normally leads to suppression of RyR channel activity. Unfortunately, we were not able to test here to what extent the gradual decline of Ca^{2+} uptake via the Ca^{2+} uniporter, resulting from the oxidation of the mitochondrial NADH pool and consequent depolarization of the mitochondrial membrane, is responsible for the delayed development of sparks. So, this possibility is yet to be investigated.

The reduction of the mitochondrial redox potential not only leads to a lower driving force for the Ca^{2+} uniporter, but also results in a partial oxidation of the mitochondrial GSH pool. This, in turn, reduces the mitochondrial protection against ROS generated during oxidative phosphorylation, and presumably increases the escape of ROS (mostly H_2O_2) into the cytosol. Although the effect of ROS on SR Ca^{2+} release in skeletal muscle is still controversial (Brotto & Nosek, 1996; Andrade *et al.* 1998; Plant *et al.* 2002; Posterino *et al.* 2003), it has been shown that H_2O_2 increases the activity of RyRs incorporated into artificial bilayers (Boraso & Williams, 1994; Favero *et al.* 1995) and impairs the function of the Ca^{2+}-ATPase in SR vesicle preparations (Xu *et al.* 1997). In addition, Posterino *et al.* (2003) found that treatment with H_2O_2 markedly potentiated caffeine-induced Ca^{2+} release in mechanically skinned skeletal muscle fibres isolated from rats. In our experiments, ROS scavengers (SOD and catalase) dramatically altered the pattern of appearance of Ca^{2+} sparks by reducing their maximal frequency and delaying their appearance. In contrast, H_2O_2 in the micromolar range promoted sparks and sped up their appearance. These data indicate ROS can be responsible for unmasking sparks in skinned preparations. They also suggest that weakening of the mechanisms protecting the cell against oxidation results from cytosol washout after permeabilization. Apparently, when ROS production exceeds the cell's capacity to chelate free radicals, CICR inhibition can be removed and sparks can appear. In addition, based on the experiments with 10 mM H_2O_2, we can also speculate that accumulation of ROS in the cytosol above a certain level may be responsible for complete shutdown of spark activity seen later on in the experiments.

In summary, our results show that the temporal onset of the appearance of spontaneous Ca^{2+} sparks in permeabilized mammalian muscle cells is closely associated with the redox state of mitochondria. We suggest that a misbalance between mitochondrial ROS generation and the cell's ability to counteract and neutralize oxidative stress is most likely responsible for the collapse of the physiological CICR inhibition and the subsequent manifestation of Ca^{2+} sparks. Out data also indicate that under physiological conditions (i.e. before skinning) mitochondrial ROS production and cellular ROS chelating are well balanced and in equilibrium, which keeps the number of spontaneous Ca^{2+} sparks minimal. However, we cannot exclude the possibility that other unknown diffusible factors produced in mitochondria (Ørtenblad & Stephenson, 2003), mitochondrial Ca^{2+} uptake, or some rearrangement in the structural environment of RyR channels caused by permeabilization and cellular swelling can also contribute to the described phenomena.

References

Andrade FH, Reid MB, Allen DG & Westerblad H (1998). Effect of hydrogen peroxide and dithiothreitol on contractile function of single skeletal muscle fibres from the mouse. *J Physiol* **509**, 565–575.

Ariano MA, Armstrong RB & Edgerton VR (1973). Hindlimb muscle fiber populations of five mammals. *J Histochem Cytochem* **21**, 51–55.

Boraso A & Williams AJ (1994). Modification of the gating of the cardiac sarcoplasmic reticulum Ca^{2+}-release channel by H_2O_2 and dithiothreitol. *Am J Physiol* **267**, H1010–H1016.

Brookes PS, Yoon Y, Robotham JL, Anders MW & Sheu SS (2004). Calcium, ATP, and ROS: a mitochondrial love-hate triangle. *Am J Physiol Cell Physiol* **287**, C817–C833.

Brotto MA & Nosek TM (1996). Hydrogen peroxide disrupts Ca^{2+} release from the sarcoplasmic reticulum of rat skeletal muscle fibers. *J Appl Physiol* **81**, 731–737.

Celio MR & Heizmann CW (1982). Calcium-binding protein parvalbumin is associated with fast contracting muscle fibres. *Nature* **297**, 504–506.

Cheng H, Lederer WJ & Cannell MB (1993). Calcium sparks: elementary events underlying excitation-contraction coupling in heart muscle. *Science* **262**, 740–744.

Cheng H, Song LS, Shirokova N, González A, Lakatta EG, Ríos E & Stern MD (1999). Amplitude distribution of calcium sparks in confocal images: theory and studies with an automatic detection method. *Biophys J* **76**, 606–617.

Cheranov SY & Jaggar JH (2004). Mitochondrial modulation of Ca^{2+} sparks and transient K_{Ca} currents in smooth muscle cells of rat cerebral arteries. *J Physiol* **556**, 755–771.

Cheung A, Dantzig JA, Hollingworth S, Baylor SM, Goldman YE, Mitchison TJ & Straight AF (2002). A small-molecule inhibitor of skeletal muscle myosin II. *Nat Cell Biol* **4**, 83–88.

Conklin MW, Ahern CA, Vallejo P, Sorrentino V, Takeshima H & Coronado R (2000). Comparison of Ca^{2+} sparks produced independently by two ryanodine receptor isoforms (type 1 or type 3). *Biophys J* **78**, 1777–1785.

Conklin MW, Barone V, Sorrentino V & Coronado R (1999). Contribution of ryanodine receptor type 3 to Ca^{2+} sparks in embryonic mouse skeletal muscle. *Biophys J* **77**, 1394–1403.

Csernoch L, Zhou J, Stern MD, Brum G & Ríos E (2004). The elementary events of Ca^{2+} release elicited by membrane depolarization in mammalian muscle. *J Physiol* **557**, 43–58.

DelPrincipe F, Egger M & Niggli E (1999). Calcium signalling in cardiac muscle: refractoriness revealed by coherent activation. *Nat Cell Biol* **6**, 323–329.

Donoso P, Prieto H & Hidalgo C (1995). Luminal calcium regulates calcium release in triads isolated from frog and rabbit skeletal muscle. *Biophys J* **68**, 507–515.

Duchen MR (2000). Mitochondria and calcium: from cell signalling to cell death. *J Physiol* **529**, 57–68.

Duke AM & Steele DS (1998). Effects of cyclopiazonic acid on Ca^{2+} regulation by the sarcoplasmic reticulum in saponin-permeabilized skeletal muscle fibres. *Pflugers Arch* **436**, 104–111.

Eisenberg BA (1983). Quantitative ultrastructure of mammalian skeletal muscle. In *Handbook of Physiology*, section 10, *Skeletal Muscle*, ed. Peachey LD, p. 95 American Physiological Society, Bethesda, MD, USA.

Favero TG, Zable AC & Abramson JJ (1995). Hydrogen peroxide stimulates the Ca^{2+} release channel from skeletal muscle sarcoplasmic reticulum. *J Biol Chem* **270**, 25557–15563.

Feng W, Liu G, Allen PD & Pessah IN (2000). Transmembrane redox sensor of ryanodine receptor complex. *Biol Chem* **275**, 35902–35907.

Franzini-Armstrong C & Protasi F (1997). Ryanodine receptors of striated muscles: a complex channel capable of multiple interactions. *Physiol Rev* **77**, 699–729.

Fryer MW & Stephenson DG (1996). Total and sarcoplasmic reticulum calcium contents of skinned fibres from rat skeletal muscle. *J Physiol* **493**, 357–370.

García J & Schneider MF (1993). Calcium transients and calcium release in rat fast-twitch skeletal muscle fibres. *J Physiol* **463**, 709–728.

Gonzalez E, Messi ML, Zheng Z & Delbono O (2003). Insulin-like growth factor-1 prevents age-related decrease in specific force and intracellular Ca^{2+} in single intact muscle fibres from transgenic mice. *J Physiol* **552**, 833–844.

Griffith OW & Meister A (1985). Origin and turnover of mitochondrial glutathione. *Proc Natl Acad Sci U S A* **82**, 4668–4672.

Hajnóczky G, Csordas G, Madesh M & Pacher P (2000). The machinery of local Ca^{2+} signalling between sarco-endoplasmic reticulum and mitochondria. *J Physiol* **15**, 69–81.

Hajnóczky G, Hager R & Thomas AP (1999). Mitochondria suppress local feedback activation of inositol 1,4,5-trisphosphate receptors by Ca^{2+}. *J Biol Chem* **274**, 14157–14162.

Isaeva EV & Shirokova N (2003). Metabolic regulation of Ca^{2+} release in permeabilized mammalian skeletal muscle fibres. *J Physiol* **547**, 453–462.

Kirsch WG, Uttenweiler D & Fink RH (2001). Spark- and ember-like elementary Ca^{2+} release events in skinned fibres of adult mammalian skeletal muscle. *J Physiol* **537**, 379–389.

Lamb GD (2002). Excitation-contraction coupling and fatigue mechanisms in skeletal muscle: studies with mechanically skinned fibres. *J Muscle Res Cell Motil* **23**, 81–91.

Lukyanenko V, Viatchenko-Karpinski S, Smirnov A, Wiesner TF & Gÿorke S (2001). Dynamic regulation of sarcoplasmic reticulum Ca^{2+} content and release by luminal Ca^{2+}-sensitive leak in rat ventricular myocytes. *Biophys J* **81**, 785–798.

Martensson J, Lai JC & Meister A (1990). High-affinity transport of glutathione is part of a multicomponent system essential for mitochondrial function. *Proc Natl Acad Sci U S A* **87**, 7185–7189.

Nakai J, Dirksen RT, Nguyen HT, Pessah IN, Beam KG & Allen PD (1996). Enhanced dihydropyridine receptor channel activity in the presence of ryanodine receptor. *Nature* **380**, 72–75.

Ogata T & Yamasaki Y (1985). Scanning electron-microscopic studies on the three-dimensional structure of mitochondria in the mammalian red, white and intermediate muscle fibers. *Cell Tissue Res* **241**, 251–256.

Olafsdottir K & Reed DJ (1988). Retention of oxidized glutathione by isolated rat liver mitochondria during hydroperoxide treatment. *Biochim Biophys Acta* **964**, 377–382.

Ørtenblad N & Stephenson DG (2003). A novel signalling pathway originating in mitochondria modulates rat skeletal muscle membrane excitability. *J Physiol* **548**, 139–145.

Pacher P, Thomas AP & Hajnóczky G (2002). Ca^{2+} marks: miniature calcium signals in single mitochondria driven by ryanodine receptors. *Proc Natl Acad Sci U S A* **99**, 2380–2385.

Plant DR, Lynch GS & Williams DA (2002). Hydrogen peroxide increases depolarization-induced contraction of mechanically skinned slow twitch fibres from rat skeletal muscles. *J Physiol* **539**, 883–891.

Posterino GS, Cellini MA & Lamb GD (2003). Effects of oxidation and cytosolic redox conditions on excitation–contraction coupling in rat skeletal muscle. *J Physiol* **547**, 807–823.

Radi R, Turrens JF, Chang LY, Bush KM, Crapo JD & Freeman BA (1991). Detection of catalase in rat heart mitochondria. *J Biol Chem* **266**, 22028–22034.

Reid MB (2001). Invited Review: redox modulation of skeletal muscle contraction: what we know and what we don't. *J Appl Physiol* **90**, 724–731.

Ríos E, Karhanek M, Ma J & González A (1993). An allosteric model of the molecular interactions of excitation-contraction coupling in skeletal muscle. *J General Physiol* **102**, 449–481.

Ríos E & Pizarro G (1988). Voltage sensors and calcium channels of excitation-contraction coupling. *News Physiol Sci* **3**, 223–227.

Rizzuto R, Duchen MR & Pozzan T (2004). Flirting in little space: the ER/mitochondria Ca^{2+} liaison. *Sci STKE* **215**, re1.

Schneider MF & Chandler WK (1973). Voltage dependent charge movement of skeletal muscle: a possible step in excitation-contraction coupling. *Nature* **242**, 244–246.

Shirokova N, García J, Pizarro G & Ríos E (1996). Ca^{2+} release from the sarcoplasmic reticulum compared in amphibian and mammalian skeletal muscle. *J General Physiol* **107**, 1–18.

Shirokova N, García J & Ríos E (1998). Local calcium release in mammalian skeletal muscle. *J Physiol* **512**, 377–384.

Shirokova N & Ríos E (1996). Activation of Ca^{2+} release by caffeine and voltage in frog skeletal muscle. *J Physiol* **493**, 317–339.

Shirokova N, Shirokov R, Rossi D, González A, Kirsch WG, García J, Sorrentino V & Ríos E (1999). Spatially segregated control of Ca^{2+} release in developing skeletal muscle. *J Physiol* **521**, 483–495.

Sutko J & Airley J (1996). Ryanodine receptor Ca^{2+} release channels: does diversity in form equal diversity in function? *Physiol Rev* **76**, 1027–1071.

Wang ZM, Messi ML & Delbono O (1999). Patch-clamp recording of charge movement, Ca^{2+} current, and Ca^{2+} transients in adult skeletal muscle fibers. *Biophys J* **77**, 2709–2716.

Wang GJ & Thayer SA (2002). NMDA-induced calcium loads recycle across the mitochondrial inner membrane of hippocampal neurons in culture. *J Neurophysiol* **87**, 740–749.

Xu KY, Zweier JL & Becker LC (1997). Hydroxyl radical inhibits sarcoplasmic reticulum Ca^{2+}-ATPase function by direct attack on the ATP binding site. *Circ Res* **80**, 76–81.

Zhou J, Launikonis BS, Rios E & Brum G (2004). Regulation of Ca^{2+} sparks by Ca^{2+} and Mg^{2+} in mammalian and amphibian muscle. An RyR isoform-specific role in excitation-contraction coupling? *J General Physiol* **124**, 409–428.

Acknowlegements

This work was supported by grants from the Muscular Dystrophy Association and NIAMS NIH (R01 AR45690). We thank Drs Lothar Blatter, Larry Gaspers, Ernst Niggli, Roman Shirokov and Andrew Thomas for helpful comments on the manuscript.

Author's permanent address

E. V. Isaeva and V. Shkryl: A. A. Bogomoletz Institute of Physiology, Ukrainian National Academy of Sciences, Bogomoletz Street 4, Kiev, 01024, Ukraine.

2.3 Вплив активних форм кисню на Ca^{2+} - сигнали, спричинені осмотичним шоком у інтактних скелетних м'язових волокнах миші

Як було показано вище, дисбаланс між продукцією та поглинанням ROS у пермеабілізованих клітинах скелетних м'язів ссавців відіграє ключову роль у появі Ca^{2+} спалахів. У цьому розділі роботи ми перевіряли гіпотезу, згідно з якою подібний механізм може спричинити виникнення Ca^{2+} спалахів в інтактних волокнах після осмотичного стресу.

Wang та співавтори (Wang et al., 2005) виявили, що осмотичний шок, прикладений до інтактних м'язових волокон ссавців, індукує транзиторну активність внутрішньоклітинних Ca^{2+} сигналів, які схожі на спалахи. При цьому Ca^{2+} спалахи, індуковані осмотичним стресом, локалізуються у субсарколемальній зоні.

Рисунок 2.4 демонструє результати аналогічних експериментів, проведених в рамках нашого дослідження. Клітини були завантажені за допомогою Fluo-4 AM і візуалізувалися під час гіпоосмотичного стресу. Після 2-хвилинного впливу низькоосмотичного розчину і подальшого повернення до ізотонічного стану у 81% волокон (18 з 22) спостерігалися дискретні внутрішньоклітинні Ca^{2+} сигнали. Типова відповідь представлена на рис. 2.4А. У 16 досліджених клітинах стрес-індуковані Ca^{2+} спалахи локалізувалися в області приблизно 10 мкм від плазматичної мембрани. Ці події відбувалися протягом усього періоду запису (25 хв), проте їхня частота зменшувалася із часом (див. гістограму на рис. 2.4С).

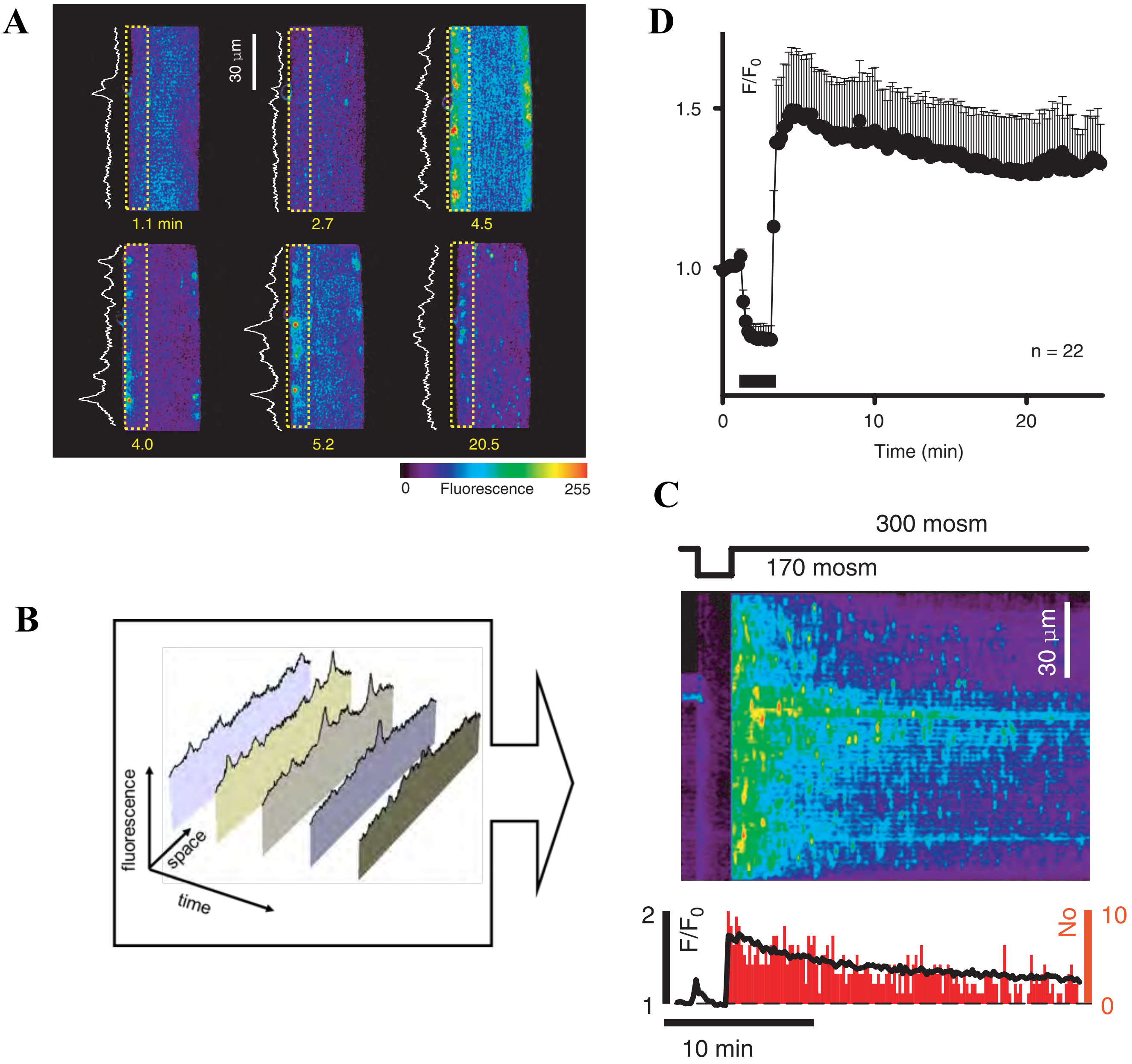

Рисунок 2.4. Внутрішньоклітинні Ca^{2+} сигнали, викликані осмотичним шоком. (A) Зображення Ca^{2+}-залежної Fluo-4 флуоресценції в клітині після осмотичного шоку. (B) Методика, перетворення для кількісної оцінки та порівняння даних між різними групами клітин. Для кожного з 150 зображень серії визначалася середня інтенсивність флуоресценції (F) у районі 10 мкм під сарколемою вздовж усієї довжини волокна; ці сигнали відображено як лінійні графіки в частині A. Далі 150 таких ліній були розташовані послідовно і перетворені на двовимірне зображення "лінійного сканування" (див. частину C). Лінійний графік у нижній частині C демонструє просторово усереднену інтенсивність флуоресценції, нормалізовану до значення, зареєстрованого на початку експерименту (F/F_0). (C) Об'єднані дані згідно з цим протоколом для 22 волокон. Відмітка внизу ілюструє час застосування гіпотонічного розчину.

Для реєстрації змін ROS використовувався флуоресцентній барвник CM-H2DCFDA (DCF). На рис. 2.5A представлені репрезентативні зображення флуоресценції CM-H2DCFDA (DCF) у волокні: до застосування гіпоосмотичного шоку (зображення на 1 хвилині), під час його дії (зображення на 6 хвилині) та після нього. Рисунок 2.5B ілюструє усереднені зміни нормалізованої флуоресценції DCF. У контрольних клітинах (до яких осмотичний шок не застосовувався, відкриті кружечки) сигнал, асоційований з ROS, монотонно зростав, ймовірно, через ендогенне формування ROS, яке призводило до окиснення індикатора.

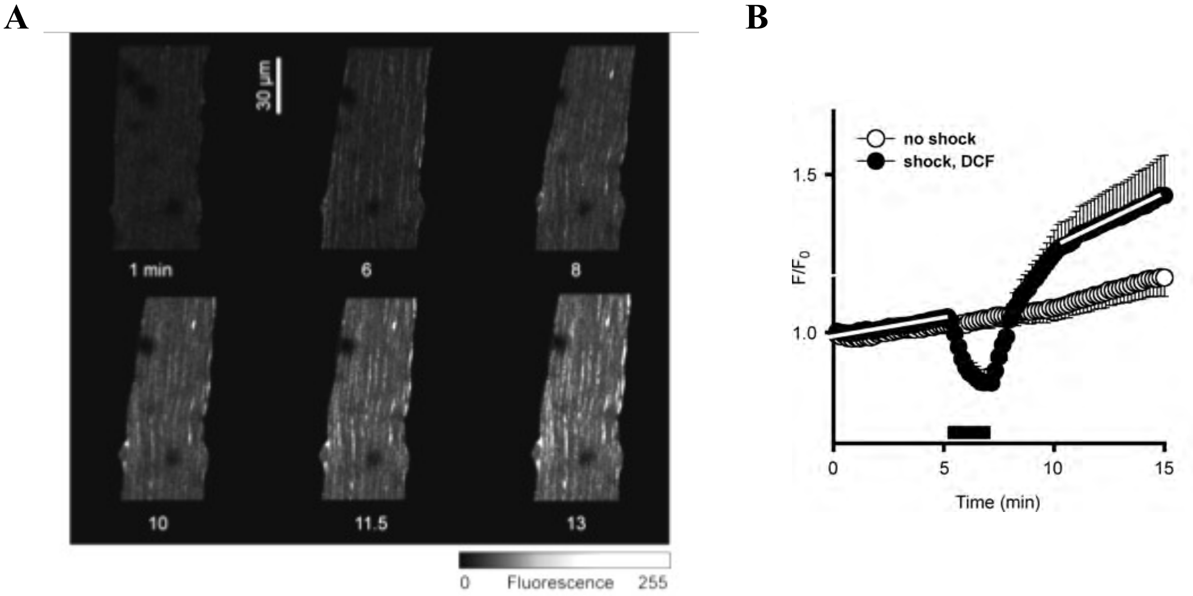

Рисунок 2.5. Зміни у внутрішньоклітинному виробництві ROS під впливом стресу. Для кількісного аналізу продукції ROS, волокна завантажувались CM-H2DCFDA (DCF) і сканувались кожні 10 секунд. При цьому потужність лазера встановлювалась на мінімум, щоб знизити фотопродукцію ROS. (А) Зображення флуоресценції DCF, що корелює з ROS, в волокні під час осмотичного шоку. (B) Усереднені зміни в нормалізованих сигналах DCF в клітинах під час осмотичного шоку (зафарбовані кружечки) порівняно із змінами в нормалізованих сигналах DCF у контрольних клітинах, де шок не застосовувався (незафарбовані кружечки).

Осмотичний шок істотно підвищував продукцію ROS, що відображається на збільшенні нахилу кривої після шоку (див. зафарбовані кружечки). У середньому, після шоку спостерігалося значне підвищення крутизни кривої: з 0.01±0.003 до 0.05±0.01 (у одиницях $d(F/F_0)/d$(хв); $P<0.01$, $n=11$). Оскільки нахил кривої для DCF-сигналу відображає швидкість генерації ROS, отримані дані свідчать про збільшення виробництва ROS після осмотичного шоку.

Якщо механізми, що залежать від ROS, сприяють генерації спалахів у непошкоджених волокнах під час осмотичного шоку, тоді поглиначі ROS можуть запобігти їхній появі. В наступному етапі дослідження ми аналізували стрес-індуковані внутрішньоклітинні Ca^{2+} відповіді в умовах контролю (без поглиначів) та після 30 або 60 хв преінкубації з трьома широко використовуваними мембранопроникними поглиначами ROS, які мають різну хімічну структуру, механізми дії та можливі побічні ефекти (наприклад, гасіння флуоресценції або буферизація Ca^{2+}; див. (Ghosh et al., 2002)). MnTBAP і Mn-cpx3 діють як імітатори SOD. MnTBAP є також потужним каталізатором розпаду пероксинітриту, у той час як TIRON переважно поглинає супероксидний аніон. Зазначимо, що інкубація з поглиначами, використаними в нашому дослідженні (або їхнє гостре застосування), не викликало суттєвих змін флуоресценції у спокою в волокнах, завантажених Fluo-4 AM.

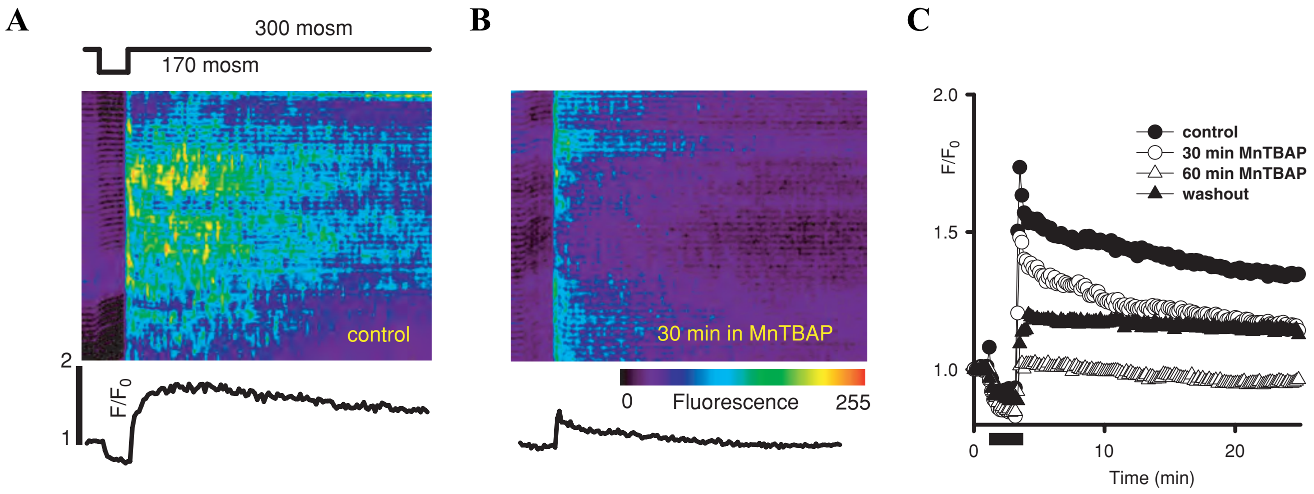

Рисунок 2.6. Пригнічення стрес-індукованих Ca^{2+} спалахів за допомогою MnTBAP. Лінійне сканування в часі від серій зображень, отриманих в клітинах після осмотичного шоку, у контрольних умовах (без додавання поглинача, див. частину А) та після 30 хв інкубації з 50 мкМ MnTBAP (див. частину В). Лінії відображають відносні зміни усередненої субсарколемної флуоресценції. (С) Середні значення нормалізованої флуоресценції протягом 6 хв після осмотичного шоку в присутності та за відсутності MnTBAP.

Рисунок 2.6 демонструє характерні стрес-індуковані Ca^{2+}-відповіді. Після 30-хвилинної інкубації з 50 мкМ MnTBAP інтенсивність внутрішньоклітинних транзієнтів Ca^{2+}, ініційованих осмотичним шоком, знижується порівняно із контролем. На рис. 2.6С відображено середні зміни нормалізованої флуоресценції в субсарколемального шару на фоні осмотичного шоку, як у присутності, так і при відсутності MnTBAP. Середнє значення флуоресценції суттєво знизилося з 1.51±0.08 (n = 4) у контрольній групі (без поглинача) до 1.34±0.06 (n = 4) та 1.01±0.01 (n = 5) після 30 та 60 хв інкубації з MnTBAP відповідно. Після відмивання препарату флуоресценція частково відновлювалася, досягаючи 1.21±0.04 (n = 3).

Щоб виключити можливі побічні ефекти, що можуть викликатися поглиначами, було застосовано ще дві сполуки з різною хімічною структурою та/або профілем поглинання: Mn-cpx 3 (4 мкМ) та TIRON (10 мМ). У експериментах з осмотичним шоком середня флуоресценція після застосування Mn-cpx 3 складала 1.3±0.03 (n = 5) та 1.16±0.01 (n = 5) після 30 і 60 хв інкубації, відповідно, з порівнянням до 1.62±0,06 (n = 6) у контролі. Після відмивання препарату флуоресценція частково відновилася (1.27±0.04, n = 5). У випадку застосування TIRON відповідні показники становили 1.79±0.02 (n = 5) в контролі, 1.51±0.06 (n = 5) після 30 хв, 1.16±0.03 (n = 4) після 60 хв і 1.60±0.04 (n = 3) після вимивання.

Отримані результати свідчать про те, що ROS сприяють аномальній активності Ca^{2+} у скелетних м'язах ссавців під час осмотичного стресу. Припускаємо, що Ca^{2+} спалахи, залежні від ROS, є ключовим компонентом адаптивних та неадаптивних реакцій у скелетних м'язах у різноманітних патологічних станах, зокрема при ексцентричному розтягненні, осмотичних змінах під час ішемії та реперфузії, а також у випадку деяких м'язових захворювань.

J Physiol 586.1 (2008) pp 197–210

Reactive oxygen species contribute to Ca^{2+} signals produced by osmotic stress in mouse skeletal muscle fibres

Adriano S. Martins, Vyacheslav M. Shkryl, Martha C. Nowycky and Natalia Shirokova

Department of Pharmacology and Physiology, University of Medicine and Dentistry of New Jersey, New Jersey Medical School, 185 South Orange Avenue, Newark, NJ 07103, USA

Ca^{2+} sparks, localized elevations in cytosolic [Ca^{2+}], are rarely detected in intact adult mammalian skeletal muscle under physiological conditions. However, they have been observed in permeabilized cells and in intact fibres subjected to stresses, such as osmotic shock and strenuous exercise. Our previous studies indicated that an excess in cellular reactive oxygen species (ROS) generation over the ROS scavenging capabilities could be one of the up-stream causes of Ca^{2+} spark appearance in permeabilized muscle fibres. Here we tested whether the cytosolic ROS balance is compromised in intact skeletal muscle fibres that underwent osmotic shock and whether this misbalance contributes to unmasking Ca^{2+} sparks. Spontaneous Ca^{2+} sparks and the rate of ROS generation were assessed with single photon confocal microscopy and fluorescent indicators fluo-4, CM-H_2DCFDA and MitoSOX Red. Osmotic shock produced spontaneous Ca^{2+} sparks and a concomitant significant increase in ROS production. Preincubation of muscle cells with ROS scavengers (e.g. MnTBAP, Mn-cpx 3, TIRON) nearly eliminated Ca^{2+} sparks. In addition, inhibitors of NAD(P)H oxidase (DPI and apocynin) significantly reduced ROS production and suppressed the appearance of Ca^{2+} sparks. Taken together, the data suggest that ROS contribute to the abnormal Ca^{2+} spark activity in mammalian skeletal muscle subjected to osmotic stress and also indicate that NAD(P)H oxidase is a possible source of ROS. We propose that ROS-dependent Ca^{2+} sparks are an important component of adaptive/maladaptive muscle responses under various pathological conditions such as eccentric stretch, osmotic changes during ischaemia and reperfusion, and some muscle diseases.

(Resubmitted 12 October 2007; accepted after revision 25 October 2007; first published online 1 November 2007)

Corresponding author N. Shirokova: Department of Pharmacology and Physiology, UMDNJ, New Jersey Medical School, 185 South Orange Avenue, Newark, NJ 07103, USA. Email: nshiroko@umdnj.edu

Sarcoplasmic reticulum (SR) Ca^{2+} release channels (ryanodine receptors; RyRs) are key molecules involved in skeletal muscle excitation–contraction coupling (ECC) as muscle contraction is initiated by Ca^{2+} released from the SR through RyR channels. The trigger for activation of RyRs comes through allosterical interaction with voltage-operated dihydropyridine receptors (DHPRs) located in the T-tubular membrane (Rios *et al.* 1991). The initial Ca^{2+} release is thought to be subsequently amplified by means of Ca^{2+}-induced Ca^{2+} release (CICR), which is also mediated by RyRs. However, in mammalian skeletal muscle CICR was found to be very limited under physiological conditions (Shirokova *et al.* 1996). In particular, mammalian skeletal muscle does not produce Ca^{2+} sparks (Shirokova *et al.* 1998) under normal circumstances. Ca^{2+} sparks were first observed in cardiomyocytes (Cheng *et al.* 1993) and are believed to be elementary events of CICR (reviewed by Berridge, 1997). Several manipulations, however, have been shown to remove the physiological inhibition of CICR in mammalian muscle cells and to uncover sparks. These interventions so far include mechanical or chemical permeabilization of the plasmalemmal membrane (Kirsch *et al.* 2001) and disruption of mitochondrial functions (Isaeva & Shirokova, 2003; Isaeva *et al.* 2005). It has also been demonstrated that osmotic shock induces Ca^{2+} sparks in intact muscle cells (Wang *et al.* 2005), and that this Ca^{2+} response is altered by strenuous exercise, during muscle disease (e.g. muscular dystrophy) or ageing (Weisleder *et al.* 2006). The observation of sparks under various stress conditions, suggests that Ca^{2+} sparks, although not the mediators of Ca^{2+} signalling in normal ECC of mammals, may play an important role in muscle pathology. Molecular mechanisms uncovering CICR (and Ca^{2+} sparks) in mammalian muscle are still unclear.

A. S. Martins and V. M. Shkryl contributed equally to this work.

DOI: 10.1113/jphysiol.2007.146571

Understanding these mechanisms is a prerequisite to understanding the various aspects of the muscle pathology mentioned above.

Our recent work implicated changes in ROS and in the intracellular redox environment in the development of Ca^{2+} sparks in permeabilized mammalian muscle cells (Isaeva *et al.* 2005). Both the intracellular ROS balance and the redox potential are likely to be compromised following osmotic shock, strenuous exercise, or muscle disease. Skeletal muscle generates reactive oxygen and nitrogen species (ROS and RNS, respectively) by a number of cytosolic and membrane-bound enzymes including xanthine oxidase (XO), NAD(P)H oxidases (NOXs), mitochondrial respiratory chain, nitric oxide synthase (NOS), etc. (Reid, 2001; Stamler & Meissner, 2001). The biological activity of ROS/NOS is effectively controlled by various scavenging molecules under physiological conditions. However, a variety of factors, e.g. strenuous exercise, muscle injury during ischaemia–reperfusion or stretch, inflammation, certain diseases and ageing, increase ROS/RNS production to the extent that they are not rapidly buffered by endogenous antioxidants anymore (reviewed by Clanton *et al.* 1999). This results in either a transient rise of intracellular ROS/RNS or in sustained oxidative stress.

ROS/RNS have been implicated in the regulation of various signalling events in skeletal muscle such as Ca^{2+} homeostasis and muscle contraction (Andrade *et al.* 1998; Posterino *et al.* 2003; Pattwell & Jackson, 2004). It is currently believed that ROS/RNS affect intracellular Ca^{2+} signalling through redox modulation of several major Ca^{2+}-handling proteins, including RyR (Trimm *et al.* 1986; Marengo *et al.* 1998; Feng *et al.* 2000; Sun *et al.* 2001). It has been shown that oxidative/nitrosative modifications of RyRs increase channel activity (reviewed by Waring, 2005). In addition, it seems that oxidation/nitrosylation reduces the coupling of RyRs with the accessory proteins calstabin and calmodulin, which normally inhibit RyR functions (Aracena *et al.* 2005). Increased activity of RyRs due to oxidation of the intracellular environment may, at least in part, be responsible for uncovering CICR (and sparks) in stressed muscle. Therefore, in the present study we directly tested whether ROS/RNS-dependent mechanisms are responsible for the development of Ca^{2+} sparks in skeletal muscle undergoing osmotic shock.

Methods

Fibre isolation

Single skeletal muscle fibres from flexor digitorum brevis (FDB) muscle were isolated from 4- to 6-week-old male mice (Swiss Webster from the Jackson Laboratory, Bar Harbor, ME, USA). Mice were killed by cervical dislocation under deep anaesthesia induced by intraperitoneal injection of sodium pentobarbital (100 mg (kg body weight)$^{-1}$). The Institutional Animal Care and Use Committee at UMDNJ-New Jersey Medical School approved the use and killing method of all animals in this study. FDB muscles were mechanically dissected and incubated with 2 mg ml^{-1} of collagenase (type I, Sigma, St Louis, MO, USA) in a shaker incubator at 37°C for 40 min. Fibre bundles were then transferred to serum-supplemented medium (Dulbecco's modified Eagle's medium (DMEM), Sigma; with 10% fetal bovine serum, Invitrogen, Carlsbad, CA, USA), teased apart and separated by gentle trituration. Intact single fibres were plated on the laminin-covered coverslips in serum-supplemented media and incubated overnight in a 5% CO_2 incubator at 37°C to allow attachment of only viable fibres.

Solutions

Most chemicals were obtained from Sigma. ROS scavengers, MnTBAP and Mn-cpx 3, NOX inhibitors, diphenyleneiodonium (DPI) and apocynin, were purchased from Calbiochem (San Diego, CA, USA). Ryanodine was from Alomone Laboratories (Jerusalem, Israel). An isotonic Ringer solution contained (mM): 140 NaCl, 5 KCl, 2.5 $CaCl_2$, 1 $MgCl_2$, 10 Hepes, 10 glucose. The osmolality of the solution was ~300 mosmol kg^{-1} and pH was 7.0. A hypotonic Ringer solution contained (mM): 70 NaCl, 5 KCl, 2.5 $CaCl_2$, 1 $MgCl_2$, 10 Hepes, 10 glucose. The osmolality was ~170 mosmol kg^{-1} and pH was 7.0. 'Zero Ca^{2+}' external solution had 1 mM EGTA and no Ca^{2+} added.

Confocal imaging

Local changes in cytosolic [Ca^{2+}] and ROS production were monitored with fluorescent indicators fluo-4 AM (acetoxymethyl ester form of fluo-4; 5 μM), 5-(and -6)-chloromethyl-2′,7′-dichlorodihydrofluorescein diacetate (CM-H_2DCFDA; 10 μM), and MitoSOX Red (10 μM), respectively. Probes were purchased from Invitrogen. A laser scanning confocal microscope (Radiance 2000; Bio-Rad, Hercules, CA, USA) connected to a Zeiss Axiovert 100 inverted microscope equipped with a ×63, 1.2 NA, water immersion lens (Zeiss Inc., Oberkochen, Germany) was used to acquire images. Fluo-4 and CM-H_2DCFDA were excited with the 488 nm line of an argon laser. The emitted light was collected above 500 nm. MitoSOX was excited with 514 nm of the argon laser, and the fluorescent signal was detected with a 570 LP filter. Fibres were imaged in the XY mode at 500 lines s^{-1}. As a rule, a series of 100 or 150 images (102.8 μm by 102.8 μm) were acquired every 10 s at the same locations within fibres. Because XY imaging does not provide sufficient information about the morphology of discrete events of Ca^{2+} release, we arbitrarily referred to them as Ca^{2+} sparks.

Data analysis

Analysed data are represented as mean ± s.e.m. Where stated, statistical significance was determined by using Student's *t* test. In the figures * indicates $P < 0.05$, ** indicates $P < 0.01$.

Results

Our previous work suggested a misbalance between ROS production and scavenging in permeabilized mammalian skeletal muscle cells as an upstream cause for the development of Ca^{2+} sparks. In this study we tested the hypothesis that a similar mechanism contributes to the appearance of Ca^{2+} sparks in intact fibres subjected to osmotic shock.

Stress-induced sparks in intact muscle fibres

Recently, Wang *et al.* (2005) reported that osmotic shock induces a transient activity of intracellular Ca^{2+} signals reminiscent of sparks in intact mammalian muscle fibres. They showed that in cells isolated from wild-type mice these Ca^{2+} sparks are localized to the subsarcolemmal region. Figure 1 illustrates the results of similar experiments carried out in our laboratory. Cells were loaded with fluo-4 by exposure to the AM-ester indicator, and imaged while being subjected to hyposmotic shock. Return to isotonic solution after 2 min of low osmolarity produced discrete intracellular Ca^{2+} signals in 81% of fibres (18 out of 22). A typical response is illustrated in Fig. 1*A*. In 16 cells, stress-induced Ca^{2+} sparks were localized to a ~10 μm band below the plasmalemmal membrane. The events were observed during the entire duration of the recording (25 min), although their frequency gradually decreased with time (see bar plot in Fig. 1*B*). In two cells (or in 9% of responding cells), however, sparks propagated into the cell centre within 65 ± 20 s and were sustained for the entire 25 min recording time.

Figure 1*B* illustrates the procedure we used to quantify and compare the data between different groups of cells. For each of the 150 images in a series, average fluorescence (*F*) was determined within 10 μm under the sarcolemma along the fibre length. Signals are represented as line plots in Fig. 1*A*. One hundred and fifty lines were then arranged in series and converted to a two-dimensional 'line-scan' image (Fig. 1*B*). Thus, the 'sparky' image illustrates average fluorescence changes in the subsarcolemmal region of the cell for the entire duration of the experiment. The line plot on the bottom shows spatially averaged fluorescence normalized to the signal recorded at the beginning of the experiment (F/F_0). This dependence was determined for all fibres studied and then averaged. It is represented in Fig. 1*C*. The bar plot in Fig. 1*B* illustrates changes in the frequency of hypotonicity-induced sparks. Both average fluorescence and the spark frequency have a similar time course.

Osmotic shock increases ROS/RNS generation in muscle fibre

It has been reported that some interventions, such as strenuous exercise or muscle injury due to mechanical stretch, enhance ROS/RNS production in skeletal muscle (e.g. Bejma & Ji, 1999; Clanton *et al.* 1999). Recently, it has been shown that osmotic shock is associated with a delayed mechanical deformation of the transverse tubules and nearby Ca^{2+} release sites (Apostol *et al.* 2007). It has also been reported that hyposmotic swelling increases oxidative stress in astrocytes (Reinehr *et al.* 2007). Here we tested whether osmotic shock increases the production of ROS/RNS in skeletal muscle cells.

For the quantification of ROS production, fibres were loaded with CM-H_2DCFDA and imaged every 10 s while laser power was minimized to reduce the photoproduction of ROS. CM-H_2DCFDA is hydrolysed to DCFH in the cell, and DCFH is oxidized to form highly fluorescent DCF in the presence of the appropriate oxidant (e.g. hydrogen peroxide or peroxynitrite). ROS/RNS generation was detected as a result of DCFH oxidation. Figure 2*A* shows representative images of DCF fluorescence in a fibre before (image at 1 min), during (image at 6 min) and after hyposmotic shock was applied. Figure 2*B* represents averaged changes in normalized DCF fluorescence. In control cells (no osmotic shock was applied, open circles), the ROS/RNS-related signal monotonically increased, presumably due to endogenous generation of ROS/RNS, which led to oxidation of the indicator. Osmotic shock significantly increased the ROS/RNS production (note increased slope of the curve after the shock, filled circles). The slope was steeper immediately after the shock was applied, which correlates with the increased Ca^{2+} spark activity during this period. A steeper slope can also be, at least in part and for a short time, due to water loss upon return to the isotonic solution and consequent increase in CM-H_2DCFDA concentration. Therefore, the data were fitted with a linear function before and later after osmotic shock was applied (lines on the plot). On average, the steepness significantly increased following the shock, from 0.01 ± 0.003 to 0.05 ± 0.01 (in units of $d(F/F_0)/d(\min)$, $P < 0.01$, $n = 11$) (Fig. 2*C*, filled bars). Because the slope of the DCF signal reflects the rate of ROS/RNS production and depends much less on cell loading with the dye, these results suggest an increase in ROS/RNS generation subsequent to osmotic shock.

Exogenous ROS scavengers inhibit stress-induced Ca^{2+} sparks

Our previous work revealed a causal relationship between ROS and Ca^{2+} sparks in permeabilized mammalian fibres. If ROS/RNS-dependent mechanism(s) are involved in the generation of sparks in intact fibres subjected to osmotic shock, we would expect that ROS/RNS scavengers prevent their appearance. Here we compared stress-induced intracellular Ca^{2+} responses in control conditions (no scavengers added), with those after 30 or 60 min preincubation with three widely used membrane-permeable ROS/RNS scavengers with different chemical structures, mechanisms of action and possible side-effects

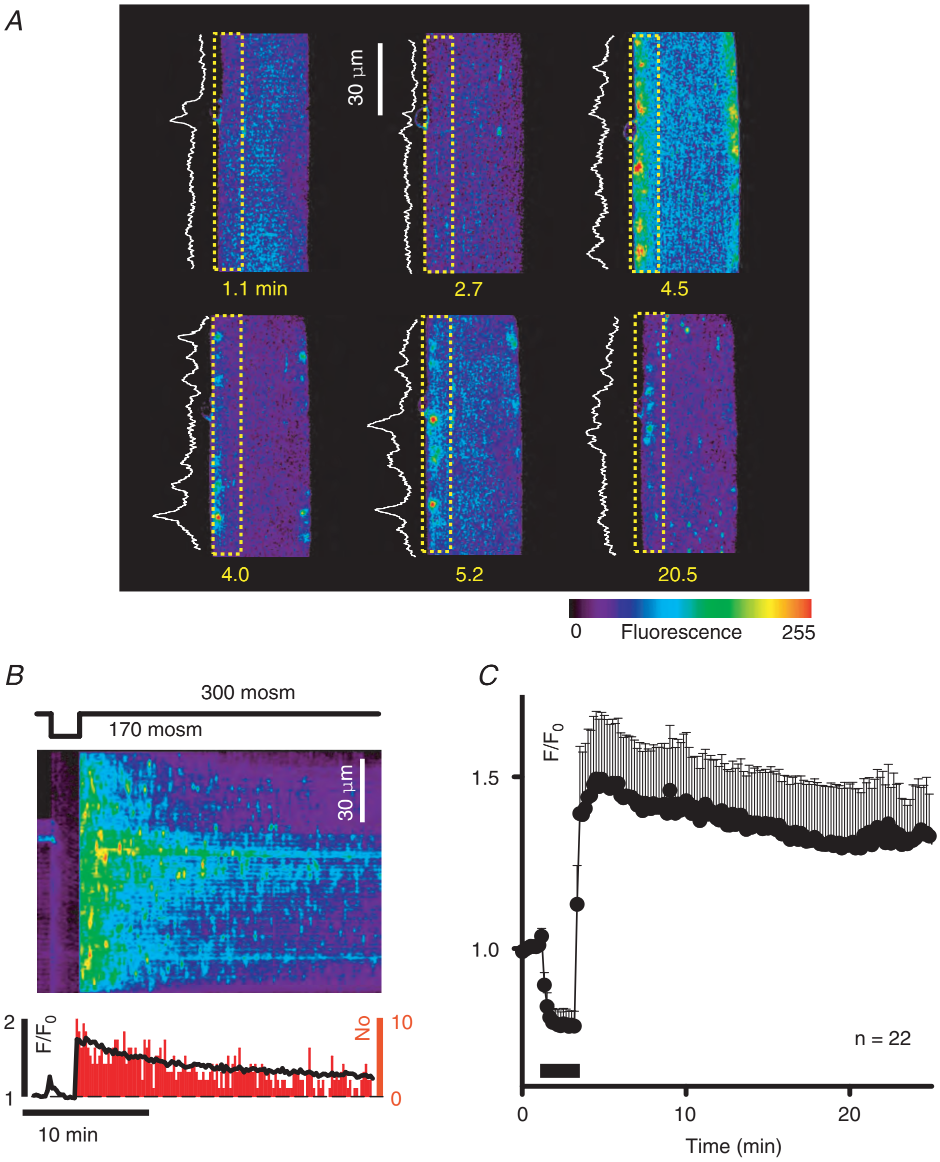

Figure 1. Intracellular Ca^{2+} signals produced by osmotic shock in skeletal muscle fibres
A, images of Ca^{2+}-related fluorescence (fluo-4) obtained in a cell subjected to osmotic shock. *B*, image is a 'line-scan' representation of the time series acquired from cell in *A*. Averaged fluorescence was determined within 10 μm under the sarcolemma along the fibre length and converted to a two-dimensional image. Line at the bottom represents normalized changes in the averaged subsarcolemmal fluorescence. Bar plot represents corresponding changes in the frequency of sparks ('No', number of sparks per image). Line on the top illustrates the protocol by which extracellular solutions were changed. *C*, pooled data from this protocol in 22 fibres. The bar on the bottom marks time during which hypotonic solution was applied.

(e.g. fluorescence quench or Ca^{2+} buffering; Ghosh *et al.* 2002). MnTBAP and Mn-cpx 3 are superoxide dismutase (SOD) mimetics. MnTBAP is also a potent peroxynitrite decomposition catalyst, whereas TIRON scavenges mostly superoxide anion. It should be mentioned that incubation with all of the scavengers used in our studies (or acute application of the scavengers) did not significantly change resting fluorescence in the fibres loaded with fluo-4 AM.

Figure 3*A* illustrates typical stress-induced Ca^{2+} responses in four different cells studied as described above. After 30 min incubation with 50 μM MnTBAP, intracellular Ca^{2+} transients produced by osmotic shock were substantially reduced. After 60 min incubation with the scavenger stress-induced Ca^{2+} signals were nearly eliminated. The inhibition was partially reversible. The bottom right panel shows Ca^{2+} signals in a cell that was washed out for 30 min after 1 h incubation with the drug. Figure 3*B* summarizes the results of several similar experiments. It represents the averaged changes in normalized fluorescence in the subsarcolemmal region

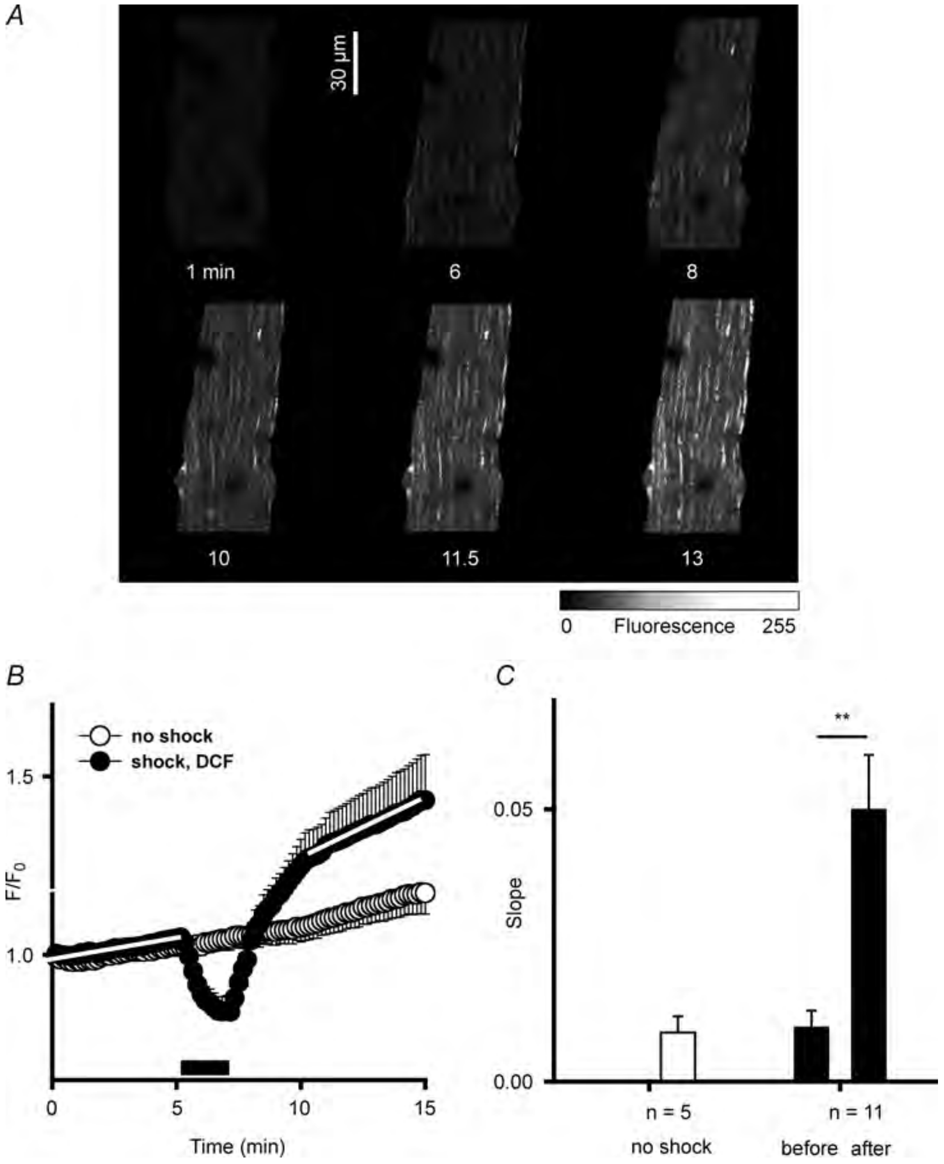

Figure 2. Stress-induced changes in intracellular ROS/RNS production
A, images of ROS/RNS-related DCF fluorescence in a fibre exposed to osmotic shock. *B*, averaged changes in normalized DCF signals in cells subjected to osmotic shock (filled circles) and changes in normalized DCF fluorescence in cells imaged in control, when no shock was applied (open circles). *C*, averaged slopes of DCF signals in control (open bar) and before and after application of osmotic shock (filled bars).

in response to the osmotic shock in the presence and absence of MnTBAP. Figure 3*C* illustrates the mean fluorescence signal determined during the first 6 min after returning to the isosmotic solution in all cells studied. It was significantly smaller in the presence of MnTBAP (note that in this and several following figures a F/F_0 of 1.0 after the shock indicates that the Ca^{2+} signalling response was completely suppressed).

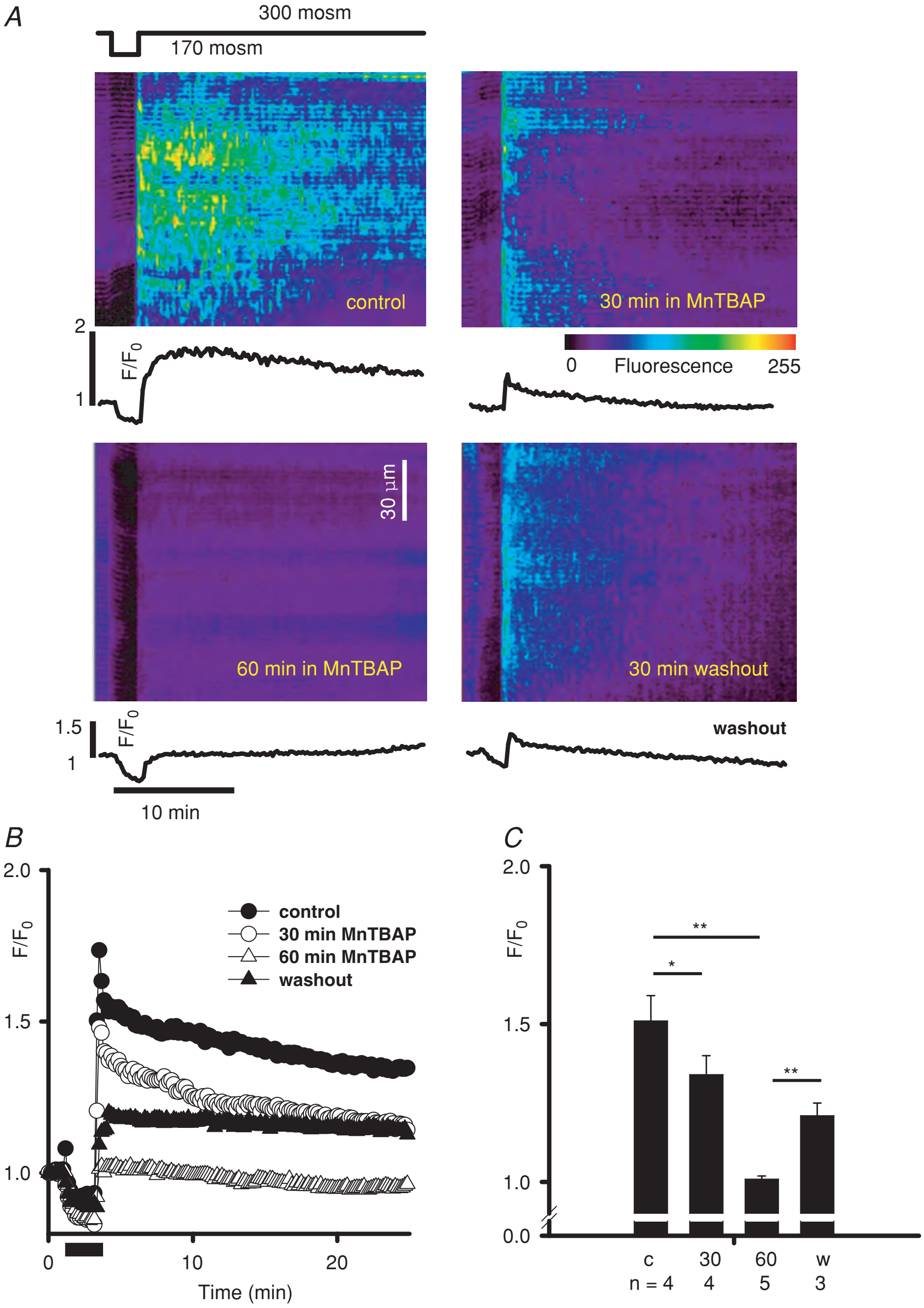

Figure 3. MnTBAP suppresses stress-induced Ca^{2+} sparks
A, line-scan representations of time series of images obtained in 4 different cells subjected to osmotic shock under control conditions (no scavenger added, top left panel), 30 min (top right panel) and 60 min (bottom left panel) of incubation with 50 μM MnTBAP, and 30 min after drug washout (bottom right). Lines represent relative changes in the averaged subsarcolemmal fluorescence. *B*, pooled data from these protocols. *C*, mean values of normalized fluorescence during 6 min after the osmotic shock in the presence and absence of MnTBAP. Note that an F/F_0 of 1.0 corresponds to a complete suppression of the response.

The mean fluorescence significantly decreased from 1.51 ± 0.08 ($n = 4$) in control (no scavenger added) to 1.34 ± 0.06 ($n = 4$) and 1.01 ± 0.01 ($n = 5$) after 30 and 60 min of incubation with MnTBAP, respectively. The fluorescence partially recovered after the drug was washed out (1.21 ± 0.04, $n = 3$).

It should be mentioned that, as expected from its scavenging properties, MnTBAP also gradually reduced the magnitude of the DCF signal (data not shown). Moreover, it also reduced the change of the signal slope before and after osmotic shock. The slope had changed from (in $d(F/F_0)/dt$) 0.04 ± 0.02 ($n = 4$) to 0.035 ± 0.01 ($n = 5$) and 0.02 ± 0.005 ($n = 5$), and from 0.07 ± 0.06 to 0.05 ± 0.03 and 0.03 ± 0.01, after 30 and 60 min in MnTBAP, respectively. This group of experiments provides evidence that MnTBAP effectively reduces cytosolic [ROS/RNS].

In order to rule out possible side-effects introduced by the scavengers, two additional compounds with different chemical structure and/or scavenging profile were employed: Mn-cpx 3 (4 μM) and TIRON (10 mM). The data are summarized in Fig. 4. Both Mn-cpx 3 (Fig. 4*A* and *B*) and TIRON (Fig. 4*C* and *D*) gradually and reversibly inhibited osmotic shock-induced Ca^{2+} signals in a manner

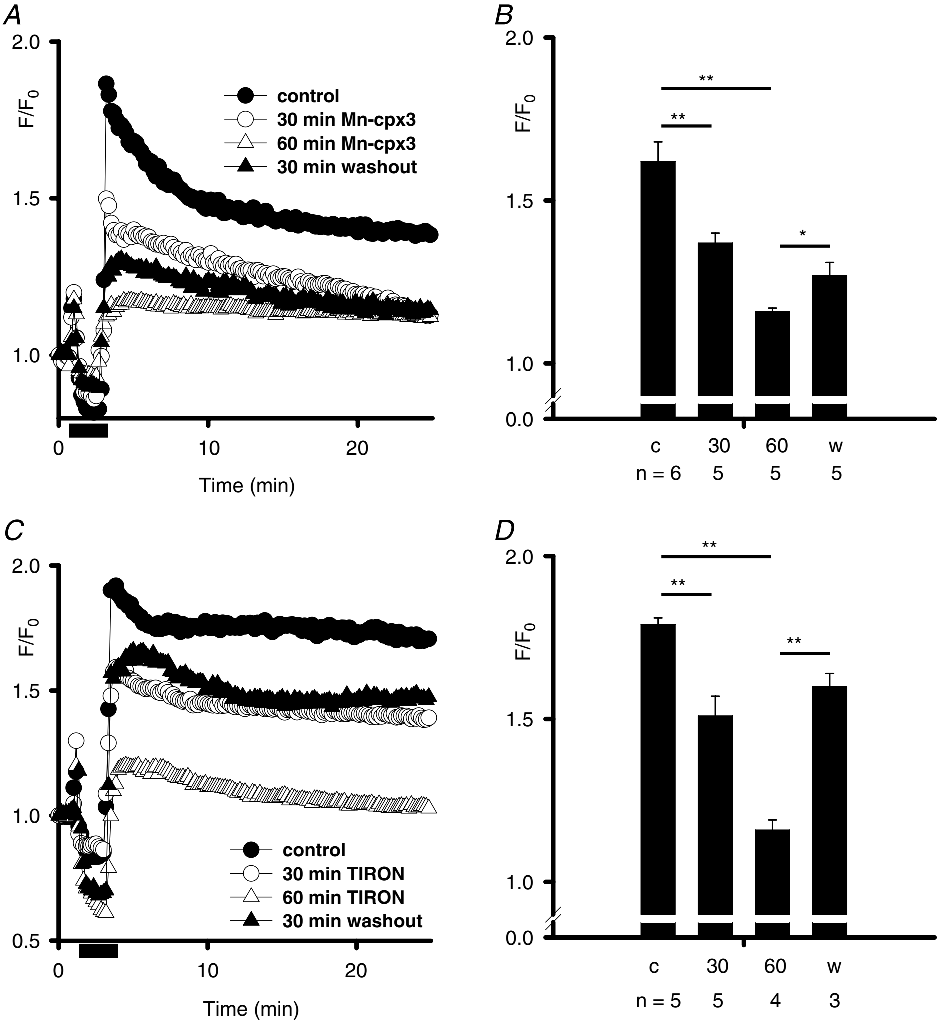

Figure 4. ROS/RNS scavengers inhibit cytosolic Ca^{2+} responses to osmotic shock
A and *C*, averaged subsarcolemmal fluorescence signals in the presence and absence of 4 μM Mn-cpx 3 and 10 mM TIRON, respectively. *B* and *D*, mean values of normalized fluorescence during an interval of 6 min after the osmotic shock in the absence of the scavengers, after 30 min and 60 min preincubation, and 30 min after drug washout. The mean fluorescence decreased from 1.62 ± 0.06 ($n = 6$) in control (no Mn-cpx 3 added) to 1.37 ± 0.03 ($n = 5$) and 1.16 ± 0.01 ($n = 5$) after 30 and 60 min of incubation with Mn-cpx 3, respectively. The fluorescence partially recovered after the drug was washed out (1.27 ± 0.04, $n = 5$). In the experiments with TIRON, the corresponding numbers were 1.79 ± 0.02 ($n = 5$), 1.51 ± 0.06 ($n = 5$), 1.16 ± 0.03 ($n = 4$) and 1.60 ± 0.04 ($n = 3$) in control, after 30 and 60 min in TIRON and upon its washout, respectively.

similar to MnTBAP. Taken together our experiments with a variety of ROS/RNS scavengers indicate that ROS (and possibly RNS)-dependent mechanisms are involved in the generation of Ca^{2+} sparks in mammalian muscle fibres challenged by osmotic shock.

Activation of NAD(P)H oxidase accounts for stress-induced ROS production and cytosolic Ca^{2+} signals

ROS/RNS generation in response to various pathophysiological conditions, including excessive mechanical forces, may originate from several sources such as mitochondria, NOX, NOS and XO (reviewed in Reid, 2001; Cave *et al.* 2006; Pacher *et al.* 2007). Here we test whether and to what extent different sources of ROS/RNS are involved in an enhanced ROS production in skeletal muscle following the osmotic shock.

Recently, the increase in ROS production in response to a hyposmotic shock in cultured astrocytes and brain slices has been attributed to the activation of NOX (Reinehr *et al.* 2007). NOX is expressed in skeletal muscle cells (Hidalgo *et al.* 2006). In order to investigate the involvement of NOX in the cellular responses we observed subsequent to osmotic shocks, fibres were incubated for 30 min with two different NOX inhibitors: DPI (10 μM) and apocynin (0.5 mM). Figure 5*A* (grey and open circles) and *B* (grey and open bars) shows that both DPI and

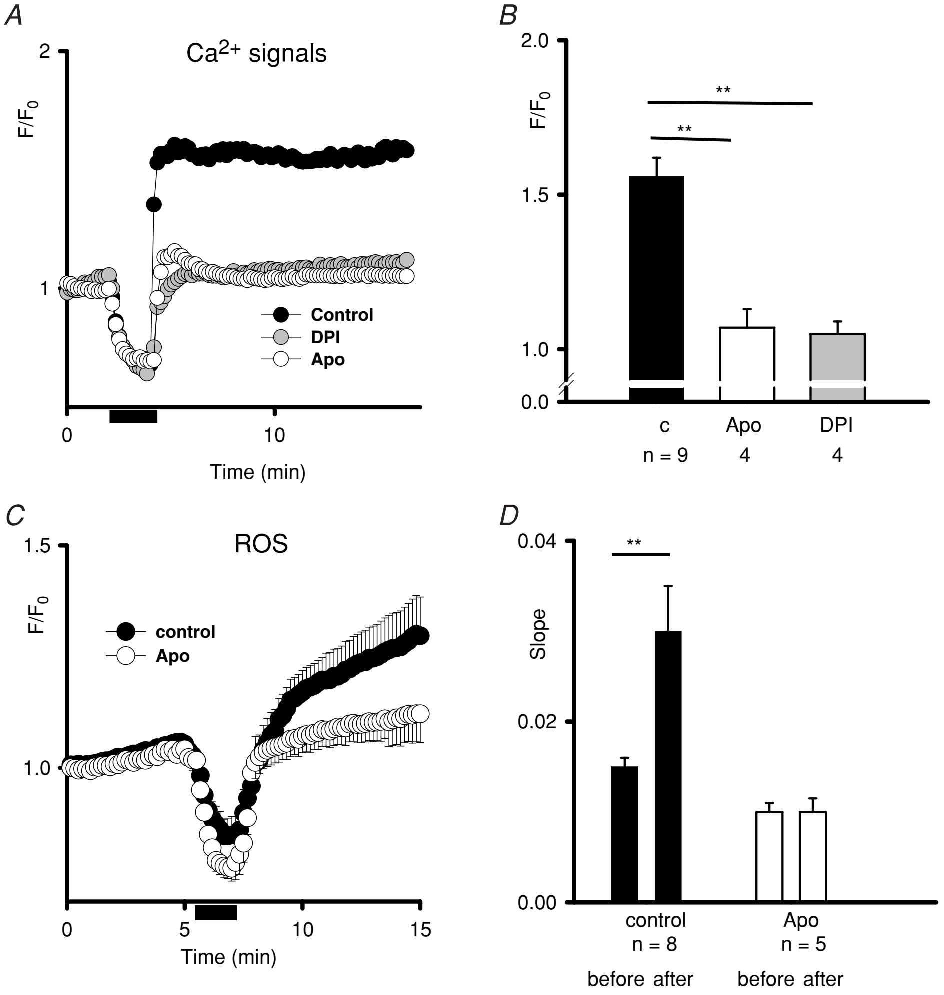

Figure 5. NOX inhibitors suppress stress-induced ROS production and Ca^{2+} sparks
A, averaged normalized changes in subsarcolemmal fluorescence following the osmotic shock under control conditions (no inhibitors added, black circles) and after 30 min of incubation with 200 μM DPI (grey circles) or 0.5 mM apocynin (Apo; open circles). *B*, mean values of normalized fluorescence during an interval of 6 min after the osmotic shock in the presence and absence of a NOX inhibitor. *C*, averaged changes in normalized DCF signal in cells subjected to osmotic shock under control conditions (no NOX inhibitors, black circles) and after 30 min of incubation with 0.5 mM apocynin (open circles). *D*, averaged slopes of DCF signals before and after application of osmotic shock in control (filled bars) and in the presence of apocynin (open bars).

apocynin nearly, but not completely, eliminated intracellular Ca^{2+} signals induced by osmotic shock. The mean fluorescence determined during the first 6 min after returning to the isosmotic solution significantly decreased from 1.56 ± 0.06 ($n = 9$) in control (no inhibitors added) to 1.07 ± 0.06 ($n = 4$) and 1.05 ± 0.04 ($n = 4$) after cells were pretreated with apocynin and DPI, respectively. This is most likely a consequence of the NOX inhibition, which suppresses the increase in ROS production upon return to isotonic solution (Fig. 5*C*). Whereas the slope of the ROS-related fluorescence curve increased by ~2-fold (from (in $d(F/F_0)/dt$) 0.015 ± 0.002 to 0.03 ± 0.005, $P < 0.01$, $n = 8$; Fig. 5*D*, filled bars) under control conditions (no inhibitors applied), it did not change significantly in the presence of apocynin (Fig. 5*D*, open bars). These results indicate that NOX is the source of acute ROS production in skeletal muscle fibres following osmotic shock.

In a parallel series of experiments, we also tested the roles of other potential sources of ROS such as NOS and XO (Fig. 6*A* and *B*). Inhibitors of NOS (L-NAME, 1 mM) and XO (allopurinol, 100 μM) did not have a significant effect on osmotic shock-induced cytosolic Ca^{2+} signals, suggesting that NOS and XO play a minor role. The mean fluorescence was 1.41 ± 0.06 ($n = 11$) in control (no inhibitors added) and 1.32 ± 0.05 ($n = 12$)

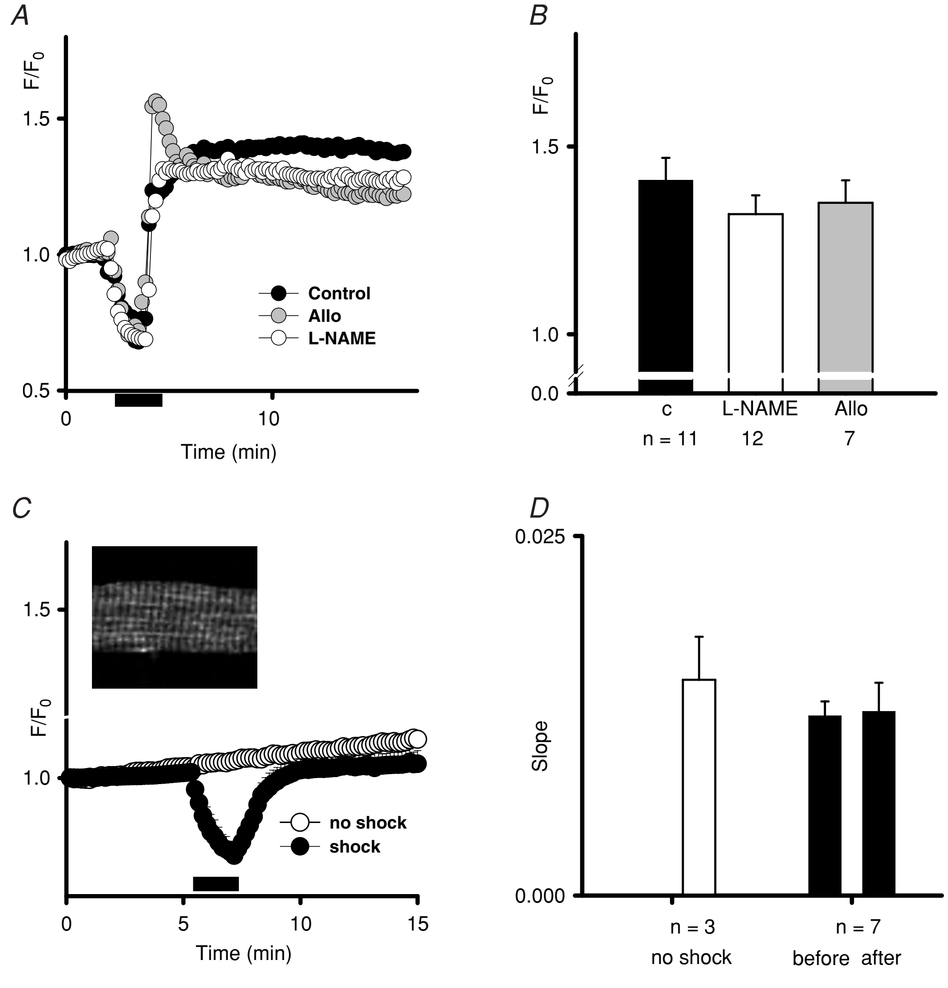

Figure 6. NO, NOS and mitochondria do not contribute to cytosolic Ca^{2+} responses and/or ROS production in response to osmotic shock

A, averaged fluo-4 fluorescence under control conditions (no inhibitors added, black circles) and after 30 min of incubation with 100 μM allopurinol (Allo; grey circles) or 1 mM L-NAME (open circles). *B*, mean values of normalized fluo-4 fluorescence after the osmotic shock in the presence and absence of the inhibitors. *C* and *D,* changes in MitoSOX signal in control (no osmotic shock applied, open circles and bar) and following osmotic shock (filled circles and bars). No significant change in MitoSOX fluorescence was observed (averaged slopes of the signal were 0.0125 ± 0.001 and 0.0128 ± 0.002 ($n = 7$) before and after the osmotic shock). Inset in *C* illustrates the mitochondrial localization of the dye (box width ~50 μm).

and 1.35 ± 0.06 ($n = 7$) in the presence of L-NAME and allopurinol, respectively.

To determine the contribution of mitochondria to the increased ROS/RNS signals, we had to use a different experimental approach. Unfortunately, interfering with the mitochondrial respiratory chain with various pharmacological tools inevitably produces additional ROS. Ru360, a blocker of mitochondrial Ca^{2+} uptake has a poor chemical stability which precludes its use over prolonged times (Wang & Thayer, 2002). Therefore, here we directly measured the mitochondrial ROS generation with MitoSOX Red, a novel fluorescent probe, which selectively detects superoxide in the mitochondria of live cells (Robinson *et al.* 2006; Abramov *et al.* 2007; Mukhopadhyay *et al.* 2007). No significant changes in MitoSOX fluorescence in response to hyposmotic shock were observed (Fig. 6*C* and *D*), suggesting a rather limited role of mitochondria in the augmented ROS production.

Ca^{2+} is needed for a substantial activation of NAD(P)H oxidase

A recent report (Abramov *et al.* 2007) suggested that activation of NOX is Ca^{2+} dependent in astrocytes. Longitudinal stretch of muscle fibres, as well as mechanical stress associated with osmotic shock, may produce transient ruptures of sarcolemma and open stretch-activated channels that would, in turn, lead to local increases in $[Ca^{2+}]$ in the subsarcolemmal region. The latter can contribute to both the activation of NOX and spark production. Figure 7 summarizes the results

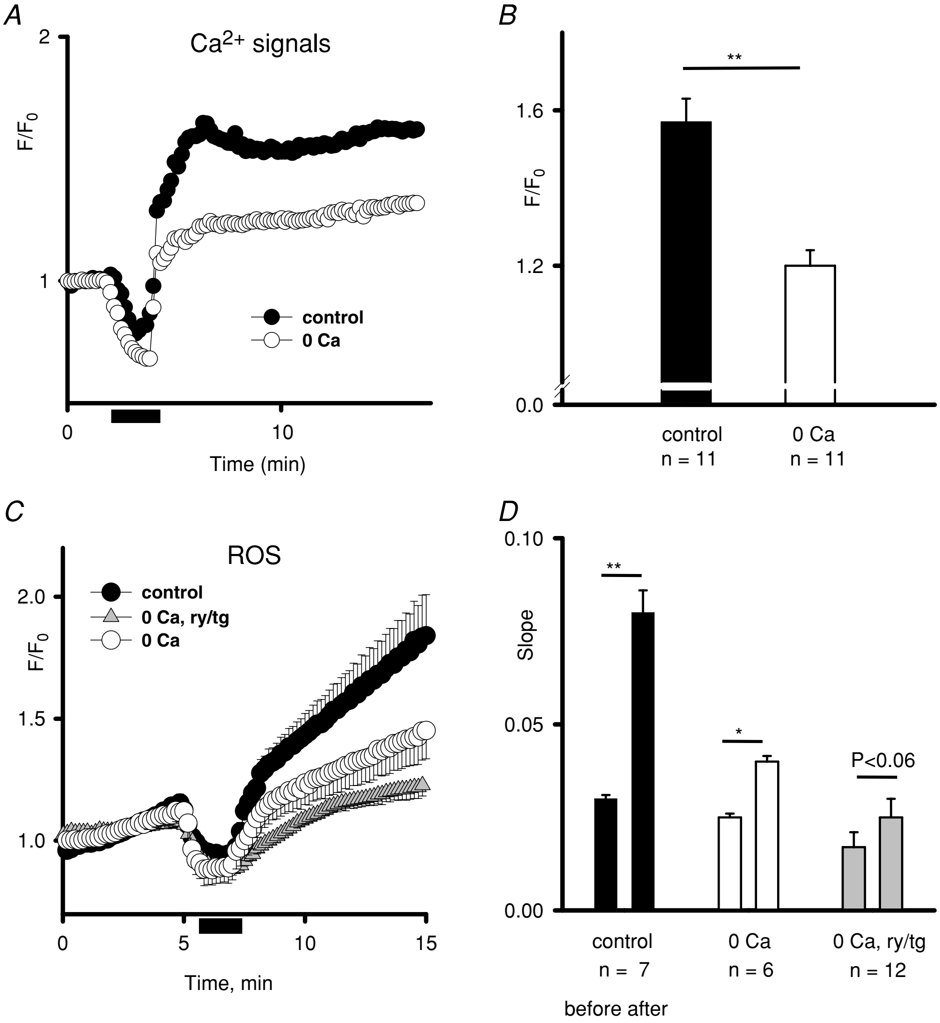

Figure 7. Ca^{2+} dependence of mechanisms of NOX activation

A and *B,* averaged cytosolic Ca^{2+} response to osmotic shock in control and in the absence of extracellular Ca^{2+}. *C* and *D*, changes in ROS/RNS production in control (black circles and bars), in the absence of extracellular Ca^{2+} (open circles and bars), and after incubation with 20 μM ryanodine (ry) and 1 μM thapsigargin (tg) (grey triangles and bars).

of experiments when osmotic shock-induced changes in intracellular Ca^{2+} transients and ROS production were monitored in control (1.2 mM Ca^{2+}) and zero Ca^{2+} (0 mM Ca^{2+}, 1 mM EGTA) external solutions. Removal of Ca^{2+} from extracellular media significantly inhibited (but did not completely eliminate) cytosolic Ca^{2+} responses (open circles and bars in Fig. 7*A* and *B*). The mean fluorescence decreased from 1.57 ± 0.06 ($n = 11$) in 1.2 mM Ca^{2+} to 1.20 ± 0.04 ($n = 11$) in zero Ca^{2+}. This intervention also blunted the increase in ROS production (open circles and bars in Fig. 7*C* and *D*). Whereas in 1.2 mM Ca^{2+}, the steepness of DCF fluorescence signal increased following the shock by ~3-fold (from 0.03 ± 0.001 to 0.08 ± 0.006 ($n = 7$), $P < 0.01$), in zero Ca^{2+} the increase was significantly smaller (from 0.025 ± 0.001 to 0.04 ± 0.001 ($n = 7$), $P < 0.05$). Thus, there seems to be a 'residual' increase in the ROS signal (and therefore presumably NOX activity) that is independent of the influx of Ca^{2+} during or following osmotic shock. There are two, not mutually exclusive, possibilities to account for this: (1) NOX is activated via Ca^{2+}-independent mechanisms (reviewed in Cave *et al.* 2006; Bedard & Krause, 2007), or (2) NOX is activated by Ca^{2+} released from the SR, possibly because of the disturbed resting state inhibition of RyRs by DHPRs. This suppression mediated by an allosteric coupling process may be relieved directly by mechanical force (as proposed by Wang *et al.* 2005). To distinguish between these two possibilities, we performed experiments in the presence of the RyR blocker ryanodine (20 μM) and the inhibitor of the SR Ca^{2+}-ATPase thapsigargin (1 μM). Fibres were preincubated with the drugs, exposed to several caffeine pulses (20 mM, 1 s) to ensure successful Ca^{2+} depletion of the SR and studied in zero Ca^{2+} external solution. Figure 7*C* and *D* (grey triangles and bars) shows that there was still a small but not highly significant ($P < 0.6$) increase in DCF fluorescence in response to the osmotic shock under these conditions. Taken together, these results suggest a predominant but not exclusive role of Ca^{2+}-dependent mechanisms for NOX activation following osmotic shock.

Discussion

This study provides initial evidence for the involvement of ROS/RNS in the acute generation of spontaneous Ca^{2+} sparks in intact mammalian skeletal muscle in response to mechanical challenge, applied as osmotic shock. In this paper we demonstrate that this stress induces robust localized cytosolic Ca^{2+} transients (aka Ca^{2+} sparks) in the majority of skeletal muscle fibres and that these sparks are effectively and reversibly inhibited by exogenous ROS/RNS scavengers. We also show that osmotic stress increases cellular ROS/RNS production. Furthermore, inhibitors of NOX (but not NOS and XO) substantially reduce osmotic shock-induced increases in ROS/RNS and suppress cytosolic Ca^{2+} responses to stress, implying that NOX is a possible source of acute ROS generation following the stress.

Ca^{2+} sparks in health and disease

Ca^{2+} sparks, microscopic events of CICR, are scarce in adult mammalian skeletal muscle fibres under physiological conditions. In mammals, depolarization induces events ('embers'), which are of much lower amplitude, narrower in space, and of much longer duration than Ca^{2+} sparks. Such events are likely to result from the opening of a single RyR channel and do not involve CICR (Csernoch *et al.* 2004). In addition to the absence of Ca^{2+} sparks elicited by depolarizations, spontaneous Ca^{2+} sparks are also rare in adult mammalian muscle (Conklin *et al.* 2000; Chun *et al.* 2003). Currently it is generally accepted that CICR is less important for healthy mammalian skeletal muscle than for amphibians, where sparks are readily observed. Mammalian fibres have two triadic junctions per sarcomere whereas lower animals have only one. Ca^{2+} released from the SR in mammals needs to travel a shorter distance to activate the contractile machinery of the muscle. Therefore, a further amplification of the initial voltage-induced Ca^{2+} signals by CICR may not be necessary. Under stress, however, a moderate augmentation of cytosolic Ca^{2+} signals may be required for muscle adaptation and for this purpose the physiological inhibition of CICR may be relieved. Under pathophysiological conditions acute and exaggerated Ca^{2+} spark activity could lead to deterioration of muscle function, activation of Ca^{2+}-dependent proteases and later even to necrotic or apoptotic cell death. Therefore, Ca^{2+} sparks in mammalian skeletal muscle are more likely to be a response to stress or disease rather than to physiological stimuli. Understanding the mechanisms that facilitate CICR and Ca^{2+} sparks in mammalian muscle will provide important insights into muscle physiology and pathology.

Possible mechanisms for physiological suppression of CICR in mammalian muscle

Some evidence indicates that the physiological allosteric interaction between DHPRs and RyRs contributes to the basal inhibition of CICR and Ca^{2+} sparks in mammalian muscle. For example, in skeletal muscle myotubes, Ca^{2+} sparks are spatially segregated from depolarization-induced 'spark-less' release, suggesting that in regions where the interaction between DHPRs and RyRs is established, CICR is inhibited (Shirokova *et al.* 1999). In developing myotubes and dedifferentiating adult muscle fibres, spontaneous sparks are more likely to occur in the regions where T-tubules are not yet developed

(Zhou *et al.* 2006) or already disorganized (Brown *et al.* 2007). Appearance of sparks in chemically skinned cells or in fibres subjected to osmotic shock could therefore be attributed, at least in part, to the disrupted interaction between DHPRs and RyRs due to mechanical deformation of sarcolemmal and SR membranes (Chawla *et al.* 2001). However, work on mechanically skinned fibres indicates that this is not the only possibility. After mechanical skinning, T-tubules are resealed, presumably preserving physiological contact between DHPRs and RyRs (Lamb, 2002). Nevertheless, spontaneous Ca^{2+} sparks were observed in this preparation, although at a lower frequency (Kirsch *et al.* 2001). In addition, osmotic shock-induced Ca^{2+} sparks were recently found in dysgenic myotubes lacking the $\alpha 1$ subunit of DHPR (Apostol *et al.* 2007). Taken together these observations indicate that the appearance of Ca^{2+} sparks after skinning is not only a consequence of mechanical cell alterations but rather also results from a change of the intracellular milieu.

Our recent work suggested an additional mechanism that contributes to the physiological repression of CICR in mammalian muscle. We found in saponized muscle fibres that an alteration of either one of two mitochondria-related mechanisms, Ca^{2+} buffering and ROS production, lead to the development of Ca^{2+} sparks (Isaeva & Shirokova, 2003; Isaeva *et al.* 2005). More specifically, based on these observations, we suggested that sparks occur when the concentration of ROS increases in the cytosol as a result of reduced cellular ROS scavenging capacity. In line with this previous findings, our present results shows that ROS-related mechanisms are also involved in the initiation of Ca^{2+} activity in intact muscle cells exposed to osmotic stress.

NOX as a possible source of ROS in mammalian muscle fibres undergoing osmotic shock

ROS/RNS are produced by a number of cellular oxidative metabolic processes, involving mitochondria, NOX, XO, NOS, etc. Various physiological and pathophysiological stimuli promote generation of ROS/RNS by one or several ROS/RNS-generating components, thus changing the intracellular redox environment and affecting function of several proteins involved in Ca^{2+} signalling and ECC (Andrade *et al.* 1998; Marengo *et al.* 1998; Feng *et al.* 2000; Sun *et al.* 2001; Posterino *et al.* 2003; Pattwell & Jackson, 2004; Aracena *et al.* 2005).

NOX appeared to be a likely source for the stress-dependent production of ROS, as this enzyme has been recently shown to be activated by mechanical stretch, including osmotic shock (Hwang *et al.* 2003; Reinehr *et al.* 2007). NOX is a family of enzymes first described in phagocytes but now known to be expressed much more widely. The phagocytic NOX is composed of the membrane-bound cytochrome b_{558}, three cytosolic subunits ($p47^{phox}$, $p67^{phox}$, $p40^{phox}$), and the small GTPase Rac2. It appears that NOX could increase their ROS production in response to specific stimuli, such as various metabolic factors, hypoxia, membrane depolarization, mechanical forces, osmotic shock, Ca^{2+}, etc. (reviewed by Cave *et al.* 2006; Geiszt, 2006). Molecular steps of NOX activation are not yet clear. They may vary for different stimuli and may involve Ca^{2+}-dependent phosphorylation of the cytosolic subunit $p47^{phox}$ by PKC, the prenylation and translocation of Rac, etc. (Cave *et al.* 2006; Bedard & Krause, 2007).

Recently the presence of cytochrome b_{558} components ($gp91^{phox}$ and $p22^{phox}$) as well as cytoplasmic regulatory subunits ($p47^{phox}$ and $p67^{phox}$) of NAD(P)H oxidase has been reported in skeletal muscle (Javesghani *et al.* 2003; Hidalgo *et al.* 2006). These subunits have been shown to be localized in T-tubular membranes close to SR Ca^{2+} release sites, and have been found in isolated triads. Furthermore, it has been reported that NOX-dependent ROS production can be stimulated by membrane depolarization or field stimulation in skeletal muscle myotubes (Espinosa *et al.* 2006). Our results with NOX inhibitors suggest that NOX activity indeed increases following application of osmotic shocks. Moreover, its activation pathways are largely but not exclusively Ca^{2+} dependent. It seems that NOX-produced ROS play an important role in the augmented osmotic stress-induced Ca^{2+} signals in skeletal muscle as the inhibition of the enzyme almost completely prevents the appearance of Ca^{2+} sparks. Removal of extracellular Ca^{2+} significantly inhibited the increase in detectable ROS and Ca^{2+} signals, suggesting that Ca^{2+} influx into the cell during or after osmotic stretch is governing the activation of NOX and sparks to a large extent. The remaining NOX activation appears to be partly driven by Ca^{2+} release from the SR, since the combined application of thapsigargin and ryanodine reduced it further. Such SR Ca^{2+} release could result from a stress-induced mechanical perturbation of the inhibitory molecular interaction between DHPRs and RyRs across the dyadic cleft, as proposed by Wang *et al.* (2005). However, at present we cannot exclude the possibility of a Ca^{2+}-independent mechanism for some NOX activation, because of the limited sensitivity of our ROS detection.

Taken together, these results suggest a predominant but not exclusive role of Ca^{2+}-dependent mechanisms for NOX activation following osmotic shock. Ca^{2+} coming from the extracellular space during or after osmotic shock, together with Ca^{2+} released from the SR as a result of a disrupted DHPRs/RyRs interaction, facilitates activation of NOX leading to the increase in ROS production. The latter, in turn, exerts a strong positive feedback on intracellular Ca^{2+} signalling by further activation of RyRs and CICR, e.g. via oxidative modification and sensitization of RyRs.

Cross-talk between CICR and ROS/RNS

CICR and ROS/RNS generation are two signalling pathways that each exhibit a high degree of positive feedback. The low ROS/RNS levels present under normal conditions are essential for muscle contraction. The basal cytosolic redox state optimizes the function of several proteins involved in muscle ECC (Reid, 2001). For example, ROS/RNS could affect RyR functions by oxidative/nitrosative modifications of the channel. Whereas increasing levels of RyR oxidation is known to enhance its response to Ca^{2+} (Marengo *et al.* 1998), highly reduced RyR channels respond poorly to Ca^{2+} activation. This phenomenon may be at least in part responsible for complete inhibition of osmotic shock-induced Ca^{2+} sparks after 60 min of incubation with ROS/RNS scavengers (Figs 3 and 4). On the other hand, Ca^{2+} is required for the activation of various ROS/RNS-producing pathways, including NOX (as discussed above). Therefore dramatic decrease in cytosolic [Ca^{2+}] can inhibit cellular ROS/RNS production. Either CICR or ROS/RNS generation could lead to the observed massive Ca^{2+} signals. However, the combination of both pathways being activated in a concerted way may have even more severe consequences, as both pathways exhibit cross-talk with each other. Taken together, even a moderate but simultaneous activation of these two signalling pathways with mutually synergistic positive feedback loops leads to escalated Ca^{2+} signals.

To conclude, our results suggest that, although not a signature of physiological ECC, ROS-induced Ca^{2+} sparks are a manifestation of an adaptive/maladaptive muscle response under various pathophysiological conditions, including eccentric stretch or osmotic challenges, such as during ischaemia and reperfusion, and other muscle diseases.

References

Abramov AY, Scorziello A & Duchen MR (2007). Three distinct mechanisms generate oxygen free radicals in neurons and contribute to cell death during anoxia and reoxygenation. *J Neurosci* **27**, 1129–1138.

Andrade FH, Reid MB, Allen DG & Westerblad H (1998). Effect of hydrogen peroxide and dithiothreitol on contractile function of single skeletal muscle fibres from the mouse. *J Physiol* **509**, 565–575.

Apostol S, Ursu D & Melzer W (2007). Local calcium release and changes in T-system volume during osmotic challenges of mammalian skeletal muscle. 2007 Biophysical Society Meeting Abstracts. *Biophys J* (Suppl.), 79a, 368-Pos.

Aracena P, Tang W, Hamilton SL & Hidalgo C (2005). Effects of *S*-glutathionylation and *S*-nitrosylation on calmodulin binding to triads and FKBP12 binding to type 1 calcium release channels. *Antioxid Redox Signal* **7**, 870–881.

Bedard K & Krause KH (2007). The NOX family of ROS-generating NADPH oxidases: physiology and pathophysiology. *Physiol Rev* **87**, 245–313.

Bejma J & Ji LL (1999). Aging and acute exercise enhance free radical generation in rat skeletal muscle. *J Appl Physiol* **87**, 465–470.

Berridge MJ (1997). Elementary and global aspects of calcium signalling. *J Physiol* **499**, 291–306.

Brown LD, Rodney GG, Hernandez-Ochoa E, Ward CW & Schneider MF (2007). Ca^{2+} sparks and T tubule reorganization in dedifferentiating adult mouse skeletal muscle fibers. *Am J Physiol Cell Physiol* **292**, C1156–C1166.

Cave AC, Brewer AC, Narayanapanicker A, Ray R, Grieve DJ, Walker S & Shah AM (2006). NADPH oxidases in cardiovascular health and disease. *Antioxid Redox Signal* **8**, 691–728.

Chawla S, Skepper JN, Hockaday AR & Huang CL (2001). Calcium waves induced by hypertonic solutions in intact frog skeletal muscle fibres. *J Physiol* **536**, 351–359.

Cheng H, Lederer WJ & Cannell MB (1993). Calcium sparks: elementary events underlying excitation–contraction coupling in heart muscle. *Science* **262**, 740–744.

Chun LG, Ward CW & Schneider MF (2003). Ca^{2+} sparks are initiated by Ca^{2+} entry in embryonic mouse skeletal muscle and decrease in frequency postnatally. *Am J Physiol Cell Physiol* **285**, C686–C697.

Clanton TL, Zuo L & Klawitter P (1999). Oxidants and skeletal muscle function: physiologic and pathophysiologic implications. *Proc Soc Exp Biol Med* **222**, 253–262.

Conklin MW, Ahern CA, Vallejo P, Sorrentino V, Takeshima H & Coronado R (2000). Comparison of Ca^{2+} sparks produced independently by two ryanodine receptor isoforms (type 1 or type 3). *Biophys J* **78**, 1777–1785.

Csernoch L, Zhou J, Stern MD, Brum G & Rios E (2004). The elementary events of Ca^{2+} release elicited by membrane depolarization in mammalian muscle. *J Physiol* **557**, 43–58.

Espinosa A, Leiva A, Pena M, Muller M, Debandi A, Hidalgo C, Carrasco MA & Jaimovich E (2006). Myotube depolarization generates reactive oxygen species through NAD(P)H oxidase; ROS-elicited Ca^{2+} stimulates ERK, CREB, early genes. *J Cell Physiol* **209**, 379–388.

Feng W, Liu G, Allen PD & Pessah IN (2000). Transmembrane redox sensor of ryanodine receptor complex. *J Biol Chem* **275**, 35902–35907.

Geiszt M (2006). NADPH oxidases: new kids on the block. *Cardiovasc Res* **71**, 289–299.

Ghosh M, Wang HD & McNeill JR (2002). Tiron exerts effects unrelated to its role as a scavenger of superoxide anion: effects on calcium binding and vascular responses. *Can J Physiol Pharmacol* **80**, 755–760.

Hidalgo C, Sanchez G, Barrientos G & Aracena-Parks P (2006). A transverse tubule NADPH oxidase activity stimulates calcium release from isolated triads via ryanodine receptor type 1 *S*-glutathionylation. *J Biol Chem* **281**, 26473–26482.

Hwang J, Saha A, Boo YC, Sorescu GP, McNally JS, Holland SM, Dikalov S, Giddens DP, Griendling KK, Harrison DG & Jo H (2003). Oscillatory shear stress stimulates endothelial production of O_2^- from $p47^{phox}$-dependent NAD(P)H oxidases, leading to monocyte adhesion. *J Biol Chem* **278**, 47291–47298.

Isaeva EV & Shirokova N (2003). Metabolic regulation of Ca^{2+} release in permeabilized mammalian skeletal muscle fibres. *J Physiol* **547**, 453–462.

Isaeva EV, Shkryl VM & Shirokova N (2005). Mitochondrial redox state and Ca^{2+} sparks in permeabilized mammalian skeletal muscle. *J Physiol* **565**, 855–872.

Javesghani D, Hussain SN, Scheidel J, Quinn MT & Magder SA (2003). Superoxide production in the vasculature of lipopolysaccharide-treated rats and pigs. *Shock* **19**, 486–493.

Kirsch WG, Uttenweiler D & Fink RH (2001). Spark- and ember-like elementary Ca^{2+} release events in skinned fibres of adult mammalian skeletal muscle. *J Physiol* **537**, 379–389.

Lamb GD (2002). Voltage-sensor control of Ca^{2+} release in skeletal muscle: insights from skinned fibers. *Front Biosci* **7**, d834–842.

Marengo JJ, Hidalgo C & Bull R (1998). Sulfhydryl oxidation modifies the calcium dependence of ryanodine-sensitive calcium channels of excitable cells. *Biophys J* **74**, 1263–1277.

Mukhopadhyay P, Rajesh M, Yoshihiro K, Hasko G & Pacher P (2007). Simple quantitative detection of mitochondrial superoxide production in live cells. *Biochem Biophys Res Commun* **358**, 203–208.

Pacher P, Beckman JS & Liaudet L (2007). Nitric oxide and peroxynitrite in health and disease. *Physiol Rev* **87**, 315–424.

Pattwell DM & Jackson MJ (2004). Contraction-induced oxidants as mediators of adaptation and damage in skeletal muscle. *Exerc Sport Sci Rev* **32**, 14–18.

Posterino GS, Cellini MA & Lamb GD (2003). Effects of oxidation and cytosolic redox conditions on excitation–contraction coupling in rat skeletal muscle. *J Physiol* **547**, 807–823.

Reid MB (2001). Nitric oxide, reactive oxygen species, and skeletal muscle contraction. *Med Sci Sports Exerc* **33**, 371–376.

Reinehr R, Gorg B, Becker S, Qvartskhava N, Bidmon HJ, Selbach O, Haas HL, Schliess F & Haussinger D (2007). Hypoosmotic swelling and ammonia increase oxidative stress by NADPH oxidase in cultured astrocytes and vital brain slices. *Glia* **55**, 758–771.

Rios E, Ma JJ & Gonzalez A (1991). The mechanical hypothesis of excitation-contraction (EC) coupling in skeletal muscle. *J Muscle Res Cell Motil* **12**, 127–135.

Robinson KM, Janes MS, Pehar M, Monette JS, Ross MF, Hagen TM, Murphy MP & Beckman JS (2006). Selective fluorescent imaging of superoxide in vivo using ethidium-based probes. *Proc Natl Acad Sci U S A* **103**, 15038–15043.

Shirokova N, Garcia J, Pizarro G & Rios E (1996). Ca^{2+} release from the sarcoplasmic reticulum compared in amphibian and mammalian skeletal muscle. *J Gen Physiol* **107**, 1–18.

Shirokova N, Garcia J & Rios E (1998). Local calcium release in mammalian skeletal muscle. *J Physiol* **512**, 377–384.

Shirokova N, Shirokov R, Rossi D, Gonzalez A, Kirsch WG, Garcia J, Sorrentino V & Rios E (1999). Spatially segregated control of Ca^{2+} release in developing skeletal muscle of mice. *J Physiol* **521**, 483–495.

Stamler JS & Meissner G (2001). Physiology of nitric oxide in skeletal muscle. *Physiol Rev* **81**, 209–237.

Sun J, Xu L, Eu JP, Stamler JS & Meissner G (2001). Classes of thiols that influence the activity of the skeletal muscle calcium release channel. *J Biol Chem* **276**, 15625–15630.

Trimm JL, Salama G & Abramson JJ (1986). Sulfhydryl oxidation induces rapid calcium release from sarcoplasmic reticulum vesicles. *J Biol Chem* **261**, 16092–16098.

Wang GJ & Thayer SA (2002). NMDA-induced calcium loads recycle across the mitochondrial inner membrane of hippocampal neurons in culture. *J Neurophysiol* **87**, 740–749.

Wang X, Weisleder N, Collet C, Zhou J, Chu Y, Hirata Y, Zhao X, Pan Z, Brotto M, Cheng H & Ma J (2005). Uncontrolled calcium sparks act as a dystrophic signal for mammalian skeletal muscle. *Nat Cell Biol* **7**, 525–530.

Waring P (2005). Redox active calcium ion channels and cell death. *Arch Biochem Biophys* **434**, 33–42.

Weisleder N, Brotto M, Komazaki S, Pan Z, Zhao X, Nosek T, Parness J, Takeshima H & Ma J (2006). Muscle aging is associated with compromised Ca^{2+} spark signaling and segregated intracellular Ca^{2+} release. *J Cell Biol* **174**, 639–645.

Zhou J, Yi J, Royer L, Launikonis BS, Gonzalez A, Garcia J & Rios E (2006). A probable role of dihydropyridine receptors in repression of Ca^{2+} sparks demonstrated in cultured mammalian muscle. *Am J Physiol Cell Physiol* **290**, C539–C553.

Acknowledgements

This study was supported by grants from the Muscular Dystrophy Association (to N.S. and M.C.N.) and from UMDNJ Foundation (to N.S.). We thank Drs Larry Gaspers, Ernst Niggli, Jakob Ogrodnik, Roman Shirokov and Andrew Thomas for discussions.

Author's present address

V. M. Shkryl: Department of Physiology, Loyola University Chicago, Stritch School of Medicine, 2160 S First Ave, Maywood, IL 60153, USA.

2.4 Взаємне посилення сигналів ROS та Ca^{2+} під час стресу в дистрофічних м'язових волокнах скелетних м'язів

М'язові дистрофії відносяться до найбільш серйозних спадкових захворювань м'язової тканини. Причиною їх виникнення є мутація гена дистрофіну — цитоскелетного білка, який забезпечує захист м'язових клітин від механічного пошкодження. Механічний стрес, спричинений осмотичним шоком, викликає аномальне підвищення Ca^{2+} у вигляді спалахів у скелетних м'язових волокнах миші з дефіцитом дистрофіну (лінії миші mdx; (Wang et al., 2005)). Як було показано вище, що між змінами внутрішньоклітинного окисно-відновного балансу та виникненням Ca^{2+} спалахів у звичайних скелетних м'язах ссавців існує зв'язок. У цьому дослідженні ми аналізували, чи пов'язані збільшені Ca^{2+} відповіді у волокнах mdx з оксидативним стресом.

Як було показано в наших попередніх дослідженнях (Wang et al., 2005, Martins et al., 2008) при осмотичному шоці, в клітинах WT Ca^{2+} спалахи переважно локалізувалися в області приблизно 10 мкм від сарколеми, то у волокнах миші лінії mdx такий Ca^{2+} сигнал розповсюджувалася по всьому цитозолю.

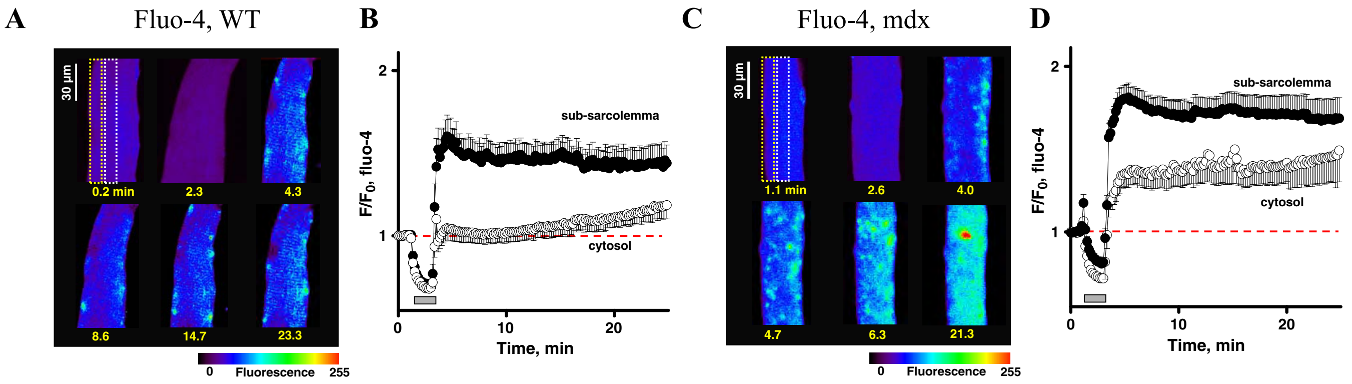

Рисунок 2.7. Цитозольні Ca^{2+} сигнали, індуковані гіпоосмотичним шоком у м'язових волокнах mdx порівняно з нормальними (WT). Вибрані зображення флуоресценції Fluo-4 у волокнах mdx (C) та WT (A) до (зображення на 1.1 та 0.2 хв відповідно), під час (зображення на 2.6 та 2.3 хв) та після дії гіпоосмотичного шоку. Вставки показують ділянки, в яких була визначена середня флуоресценція. (D) та (B) показують усереднені субсарколемальні (чорні кружечки) та цитозольні (білі кружечки) Ca^{2+} відповіді у 34 mdx та дев'яти WT-клітинах на гіпоосмотичний шок.

На рис. 2.7 представлено зображення волокна mdx до (на 1.1 хв), під час (на 2.6 хв) та після (на 4.0, 4.7, 6.3 та 21.3 хв) дії гіпоосмотичного шоку. У 97% м’язових волокон mdx (33 з 34 волокон з N=11 особин) осмотичний шок ініціював Ca^{2+} спалахи. У дев'яти з цих клітин (або 38% реагуючих клітин) Ca^{2+} спалахи швидко розповсюджувалися вглиб волокна, досягаючи його центру в середньому за 34.4±8.5 с (як це ілюстровано на частині C та D). Це суттєво відрізняється від відповідей у клітинах WT, де Ca^{2+} спалахи переважно були обмежені субсарколемальною зоною (див. частини A та B).

Як було показано в попередньому розділі, осмотичний шок спричиняє підвищення продукції ROS у клітинах WT. У рамках поточного дослідження ми розглянули два ключові питання: чи перевищує "базова" продукція ROS у дистрофічних м'язових волокнах миші лінії mdx рівні, характерні для клітин WT; а також чи сприяє осмотичний шок інтенсифікації генерації ROS. Волокна завантажували CM-H2DCFDA та досліджували дію осмотичного шоку. На рисунку 2.8A показані усереднені нормалізовані зміни DCF-сигналів у семи волокнах mdx під час осмотичного шоку (сірі кружечки). Чорні кружечки відображають відповідні зміни в DCF-флуоресценції восьми клітинах WT. DCF-сигнал підвищувався в обох типах клітин. Для кожної клітини ми апроксимували зміни DCF лінійними функціями до і після застосування шоку. Загалом, виявлено зростання "базової" генерації ROS у волокнах mdx порівняно з WT, а також збільшення її під час осмотичного шоку. В середньому крутизна сигналу перед шоком була достовірно вищою ($P < 0.01$) у клітинах mdx (представлено сірими стовпчиками) порівняно з клітинах WT (чорні стовпчики): 0.06±0.01 проти 0.02±0.003 відповідно. Після осмотичного шоку крутизна сигналу значно зросла, досягаючи значень 0.13±0.02 для клітин mdx і 0.04±0.01 для клітин WT. Враховуючи, що нахил сигналу DCF корелює зі швидкістю генерації ROS, ці дані свідчать про те, що: збільшено базову генерацію вільних радикалів у волокнах mdx; наявна інтенсифікація генерації ROS під впливом осмотичного шоку у волокнах mdx порівняно з клітинами лінії миші WT.

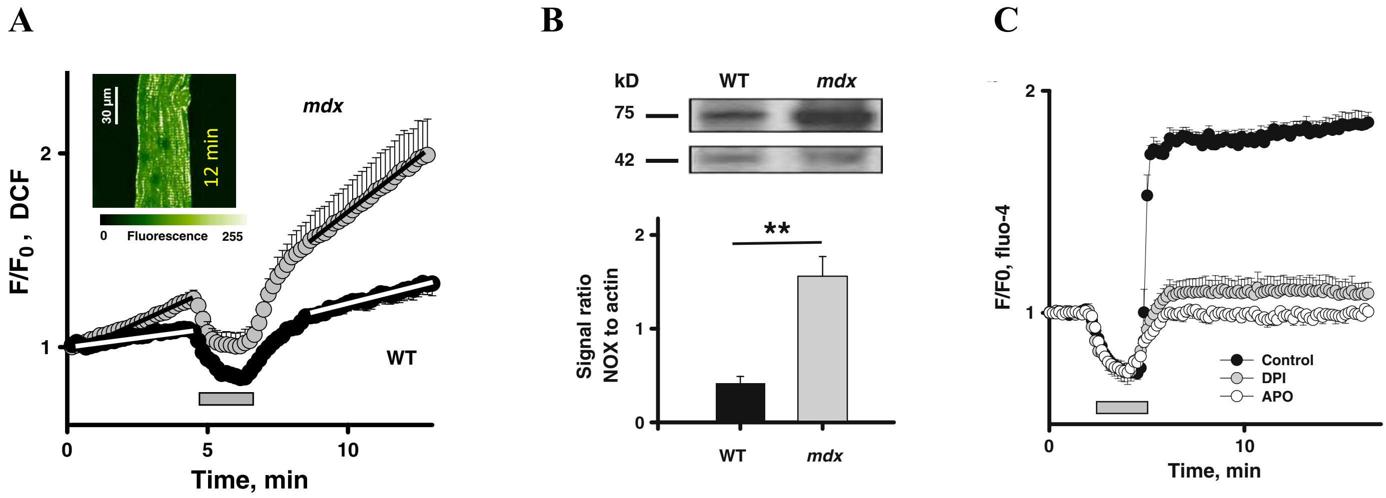

Рисунок 2.8. Продукція ROS у скелетних м'язових волокнах миші лінії mdx. (A) Усереднена флуоресценція DCF для 7 клітин mdx (сірі кружечки) порівняно з 8 волокнами м'язів з миші лінії WT (чорні кружечки). Вставка на підграфіці A демонструє зображення флуоресценції DCF у м'язі з миші лінії mdx на 12 хв після застосування осмотичного шоку. (B) Верхня частина зображення показує вестерн-блот, де відображені рівні білків NOX та актину для м'язових волокнах mdx та WT. Нижній блок представляє співвідношення інтенсивностей сигналів gp91^{phox} до актину для м'язових волокон mdx (сірий стовпець) та дикого типу (чорний стовпець). (C) Усереднені відповіді цитозольного Ca^{2+} на осмотичний шок у волокнах mdx за контрольних умов (без додавання препаратів, чорні кружечки) та після інкубації з інгібіторами NOX: апоциніном (0.5 мМ, білі кружечки) та DPI (10 мкМ, сірі кружечки).

Збільшена продукція ROS у м'язових волокнах миші лінії mdx, відображена на рис. 2.8A, може бути обумовлена (1) підвищеною активністю або експресією NAD(P)H-оксидази; або (2) активацією додаткових джерел ROS, які відіграють менш важливу роль у волокнах WT. Ми застосовували вестерн-блот для аналізу можливої зміни рівня експресії NAD(P)H-оксидази в скелетних м'язах mdx. Як ілюструється на рис. 2.8B, рівень експресії gp91^{phox} у скелетних м'язах mdx (N = 7) зріс більше ніж утричі порівняно з контролем (N = 3, P < 0.01). Було виявлено значне збільшення рівня експресії у волокнах м'язів з миші лінії mdx порівняно з контрольними клітинами.

У скелетних м'язах NAD(P)H-оксидаза розташована в сарколемі та мембрані T-трубочок. Її може бути активовано як за допомогою Ca^{2+}-залежного, так і Ca^{2+}-незалежного механізму (Hidalgo et al., 2006). В рамках наступного експерименту волокна завантажували флуоресцентним Ca^{2+} індикатором Fluo-4, а потім інкубували протягом 30 хв з двома різними інгібіторами NAD(P)H-оксидази: апоциніном (0.5 мМ) та DPI (10 мкМ). Згідно з даними на рис. 2.8B, кожен з препаратів суттєво знижував цитозольні Ca^{2+}-відповіді на осмотичний шок. Середнє значення флуоресценції після повернення до ізотонічного розчину знизилося з 1.8±0.04 в контрольній групі (n=8, N=6) до 1.25±0.06 (n=4, N=3) та 1.07±0.06 (n=5, N=3) при застосуванні DPI та апоциніну відповідно. Таким чином, NAD(P)H-оксидаза є основним фактором, що сприяє підвищенню активності ROS та посиленню Ca^{2+}-відповідей на осмотичний шок у скелетних м'язових волокнах миші лінії mdx.

Мітохондрії служать додатковим потенційним джерелом ROS у скелетних м'язах. Відомо, що м'язові клітини генерують ROS як побічний продукт дихального ланцюга. Посилене поглинання мітохондріального Ca^{2+} може стимулювати продукцію мітохондріального АТФ та ROS (див. огляд (Brookes et al., 2004)). Існує гіпотеза, що цитозольний Ca^{2+}, який збільшується через стрес, може бути секвестрований мітохондріями. Це може сприяти збільшенню продукції ROS мітохондріями, що призводить до витоку ROS в цитозоль, і подальшого посилення цитозольних Ca^{2+}-сигналів.

Дистрофічні FDB клітини mdx та нормальні FDB м'язові волокна навантажували низькоафінним Ca^{2+} індикатором Mag-rhod-2 у формі його AM-ефіру. Рисунок 2.9A ілюструє розподіл мітохондріального Mag-rhod-2 у клітині mdx. У 7 з 10 волокон mdx (N = 5) осмотичний шок індукував поступове та істотне підвищення флуоресценції Mag-rhod-2 на 33±6 % (див. рис. 2.9B). На противагу цьому, в клітинах нормальних мишей істотне збільшення мітохондріального сигналу Mag-rhod-2 спостерігалося значно менше (лише у двох з 12 клітин, N = 4). Цей сигнал був нижчим, ніж у клітинах mdx, і в основному зосереджувався у субсарколемальних межах. Середнє значення флуоресценції Mag-rhod-2 зросло з 69.2±1.6 на початку до 73.6±2.1 (в а.о.) або 6±0.1%.

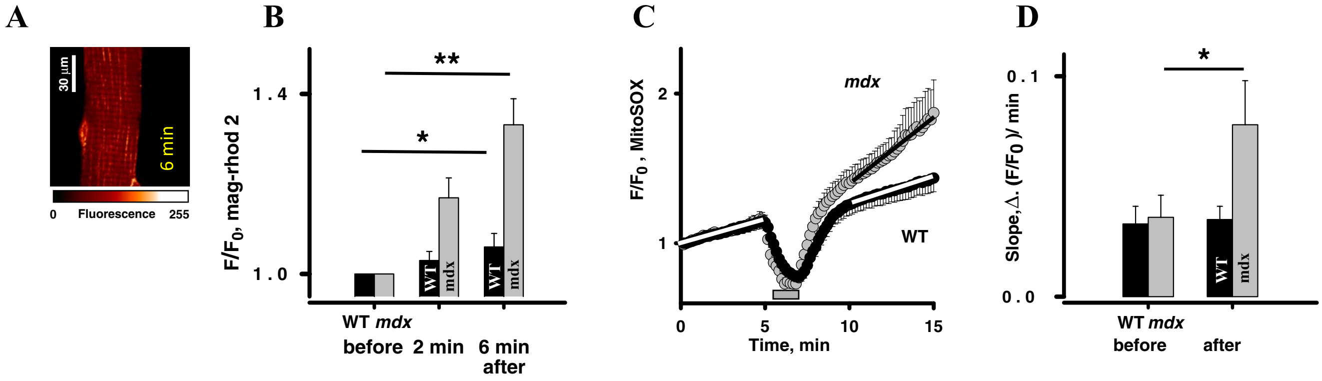

Рисунок 2.9. Мітохондріальні сигнали після осмотичного шоку. (A) Вибране зображення флуоресценції Mag-rhod-2 у клітині mdx через 6 хв після застосування осмотичного шоку. (B) Усереднені значення зростання мітохондріальної Ca^{2+}-пов'язаної флуоресценції після осмотичного шоку у волокнах mdx (сірі стовпчики) та WT (чорні стовпчики) в різний час експерименту. (C) Усереднені значення флуоресценції MitoSOX у 8 клітин mdx (сірі кружки) та 9 волокнах нормальних мишей (чорні кружки) за умов осмотичного шоку. (D) Усереднені значення нахилів сигналів MitoSOX до і після осмотичного шоку в клітинах mdx (сірі стовпчики) і клітинах дикого типу (чорні стовпчики).

Використовуючи люмінесцентні екворини, що локалізувалися в мітохондріях та СР, Robert та співавтори (Robert et al., 2001) виявили збільшення мітохондріальних сигналів Ca^{2+} відповідно до цитозольних транзиєнтів Ca^{2+} у міотрубках від mdx, порівняно з WT. Це свідчить про посилене поглинання Ca^{2+} у клітинах mdx. Що і було підтверджено нашими дослідженями.

Одним із наслідків помірної секвестрації Ca^{2+} мітохондріями є посилення мітохондріального метаболізму, оскільки декілька ферментів циклу Кребса залежить від Ca^{2+}. Було виміряно продукцію мітохондріального ROS у клітинах mdx та дикого типу. Волокна навантажували мітохондріальним супероксидним флуоресцентним зондом MitoSOX red і візуалізували в умовах гіпоосмотичного шоку.

На рис. 2.9C зображено усереднену нормалізовану флуоресценцію MitoSOX для 8 волокон mdx (сірі кружечки). Динаміку флуоресценції MitoSOX було апроксимовано лінійною функцією до та після осмотичного шоку. Згідно з результатами вимірювання MitoSOX, було зафіксовано значне збільшення нахилу кривої (з 0.04±0.01 до 0.08±0.02, $P<0.05$), вказуючи на посилення утворення мітохондріального ROS під час осмотичного шоку. Для клітин WT (чорні кружечки, n = 9) зміни в нахилі сигналу MitoSOX були незначними: від 0.033±0.008 до 0.035±0.006. Важливо зауважити, що базова продукція ROS мітохондріями, яка відображається початковим нахилом, була трохи вищою в клітинах mdx порівняно з WT. Ці дані свідчать, що мітохондрії можуть бути вторинним джерелом оксидативного стресу в дистрофічних м'язах, особливо під час механічного стресу. Гіпоосмотичний шок викликав аномальну та стійку активність Ca^{2+} спалахів, які були пригнічені агентами, що знижують формування ROS, та інгібіторами NAD(P)H-оксидази. Ці Ca^{2+} сигнали призводили до накопичення мітохондріального Ca^{2+} у волокнах mdx та додаткового збільшення клітинного та мітохондріального утворення ROS. Отримані дані свідчать про існування взаємозв'язку між надмірним утворенням ROS та активацією аномальних Ca^{2+}-сигналів. Ці два процеси можуть взаємно посилювати дію один одного, утворюючи замкнений цикл патологічних подій. Цей механізм, ймовірно, відіграє ключову роль у підвищеній чутливості до стресу в дистрофічних скелетних м'язах.

Pflugers Arch - Eur J Physiol (2009) 458:915–928
DOI 10.1007/s00424-009-0670-2

MUSCLE PHYSIOLOGY

Reciprocal amplification of ROS and Ca^{2+} signals in stressed *mdx* dystrophic skeletal muscle fibers

Vyacheslav M. Shkryl · Adriano S. Martins ·
Nina D. Ullrich · Martha C. Nowycky · Ernst Niggli ·
Natalia Shirokova

Received: 27 November 2008 / Revised: 26 March 2009 / Accepted: 31 March 2009 /

Abstract Muscular dystrophies are among the most severe inherited muscle diseases. The genetic defect is a mutation in the gene for dystrophin, a cytoskeletal protein which protects muscle cells from mechanical damage. Mechanical stress, applied as osmotic shock, elicits an abnormal surge of Ca^{2+} spark-like events in skeletal muscle fibers from dystrophin deficient (*mdx*) mice. Previous studies suggested a link between changes in the intracellular redox environment and appearance of Ca^{2+} sparks in normal mammalian skeletal muscle. Here, we tested whether the exaggerated Ca^{2+} responses in *mdx* fibers are related to oxidative stress. Localized intracellular and mitochondrial Ca^{2+} transients, as well as ROS production, were assessed with confocal microscopy. The rate of basal cellular but not mitochondrial ROS generation was significantly higher in *mdx* cells. This difference was abolished by pre-incubation of *mdx* fibers with an inhibitor of NAD(P)H oxidase. In addition, immunoblotting showed a significantly stronger expression of NAD(P)H oxidase in *mdx* muscle, suggesting a major contribution of this enzyme to oxidative stress in *mdx* fibers. Osmotic shock produced an abnormal and persistent Ca^{2+} spark activity, which was suppressed by ROS-reducing agents and by inhibitors of NAD(P)H oxidase. These Ca^{2+} signals resulted in mitochondrial Ca^{2+} accumulation in *mdx* fibers and an additional boost in cellular and mitochondrial ROS production. Taken together, our results indicate that the excessive ROS production and the simultaneous activation of abnormal Ca^{2+} signals amplify each other, finally culminating in a vicious cycle of damaging events, which may contribute to the abnormal stress sensitivity in dystrophic skeletal muscle.

Keywords Ca^{2+} sparks · Skeletal muscle · *mdx* mice · ROS · Confocal microscopy

Introduction

Dystrophinopathies are a category of muscle diseases that result from mutations of the dystrophin gene. This gene is located on chromosome Xp21 and encodes the protein dystrophin, which links the cytoskeleton with the extracellular matrix. The lack of dystrophin is thought to make the sarcolemma of skeletal muscle fibers and cardiac myocytes more fragile and more vulnerable to mechanical stress during contraction or eccentric stretch [19, 23]. Duchenne Muscular Dystrophy (DMD) is the most common muscular dystrophy. It is characterized by progressive muscle weakness, deterioration of skeletal and cardiac muscle function, and premature death. *mdx* mice completely lack dystrophin and recapitulate several of the pathophysiological features of DMD. Skeletal muscle from *mdx* mice shows signs of extensive muscle degeneration at the age of

---

Drs. V.M. Shkryl and A.S. Martins contributed equally to this work.

V. M. Shkryl · A. S. Martins · M. C. Nowycky ·
N. Shirokova (✉)
Department of Pharmacology and Physiology,
University of Medicine and Dentistry of New Jersey,
New Jersey Medical School, 185 South Orange Avenue,
Newark, NJ 07103, USA
e-mail: nshiroko@umdnj.edu

N. D. Ullrich · E. Niggli
Department of Physiology, University of Bern,
Bühlplatz 5,
Bern 3012, Switzerland

Present Address:
V. M. Shkryl
Department of Molecular Biophysics and Physiology,
Rush University,
Chicago 60612, USA

4–12 weeks. The skeletal muscle performance is later improved, at least to some extent, in older animals, presumably because of the upregulation and redistribution of utrophin, another cytoskeletal protein which can partly substitute for dystrophin [13]. The cardiac manifestations of the disease, however, become progressively more severe with age, finally resulting in dilated cardiac hypertrophy in ~10–12 month old animals [37]. *mdx* mice are widely used to elucidate the cellular mechanisms underlying the development of skeletal and cardiac muscle dysfunction in DMD and also to test possible therapeutic approaches to treat the disease [9, 32, 51, 52].

Several studies on muscle fibers from *mdx* mice indicated a disproportionate stretch-induced Ca^{2+} influx and abnormal intracellular Ca^{2+} homeostasis. It has been suggested that the lack of dystrophin results in an exaggerated fragility of the sarcolemma and in excessive Ca^{2+} influx via a number of voltage-independent pathways, such as "leak" channels" [31], stretch-activated channels (SAC, [53]), store operated channels (SOC, [49]) and microruptures [52]. However, although stretch-induced Ca^{2+} influx is greater in *mdx* cells than in cells from wild-type mice, it is still relatively small [12, 26]. This modest Ca^{2+} influx by itself does not appear to be sufficient to explain the excessive and potentially damaging intracellular Ca^{2+} signals evoked by mechanical stress, applied as osmotic shock in both *mdx* skeletal muscle fibers and in *mdx* ventricular cardiac myocytes [26, 49]. Therefore, it is likely that additional mechanisms are involved in the generation and further amplification of intracellular Ca^{2+} signals which ultimately lead to activation of Ca^{2+} dependent proteases and cell death (reviewed in [2]).

There are indications that oxidative stress (alone or in combination with mechanical load) can contribute to dystrophinopathy (reviewed in [46]). In both muscle fibers from DMD patients and *mdx* mice, the levels of most antioxidant enzymes and antioxidants are significantly elevated [4, 16]. Basal or background generation of reactive oxygen species (ROS) and reactive nitrogen species (RNS) seem to be elevated as well [51]. Oxidative stress is already present in young animals when muscle damage cannot yet be detected [14], suggesting that oxidative stress precedes the development of the disease. In addition, in vivo treatment of *mdx* mice with antioxidants, such as green tea extract [9] or *N*-acetylcysteine [51], improves skeletal muscle pathology and partially restores muscle force production.

Ca^{2+} entry via any of the suspected pathways mentioned above may stimulate production of ROS and RNS by several cellular mechanisms, including mitochondria [34], NAD(P)H oxidase [30], nitric oxide syntase (NOS) etc. Undue ROS production and accumulation may in turn lead to additional Ca^{2+} influx by increasing sarcolemmal Ca^{2+} permeability via lipid peroxidation, or by oxidation of proteins involved in other Ca^{2+} influx pathways, such as TRP channels (possible constituents of SAC and SOC [2, 21, 48]. ROS/RNS can also promote the release of Ca^{2+} from the sarcoplasmic reticulum (SR) via Ca^{2+} release channels (ryanodine receptors, RyRs), which are subject to oxidative/nitrositive modifications [29, 45]. Ca^{2+} released from the SR can subsequently further amplify the production of ROS thus establishing another intracellular positive feedback loop for damaging Ca^{2+} and ROS signals.

Our recent studies indicate that ROS contribute to the development of intracellular Ca^{2+} signals (reminiscent of Ca^{2+} sparks) induced by osmotic stress in normal mammalian skeletal muscle [30]. Ca^{2+} sparks are highly localized signals that are created by the opening and closing of a small group of RyRs. They are believed to reflect activation of RyRs by Ca^{2+}, and therefore represent "elementary events" of Ca^{2+}-induced Ca^{2+} release [35]. Unlike many other muscle types, mammalian skeletal muscle does not generate spontaneous Ca^{2+} sparks under physiological conditions [42]. The release of Ca^{2+} from the SR during excitation–contraction coupling (ECC) appears to be exclusively under the control of the voltage sensors (a.k.a., dihydropyridine receptors, DHPRs). Pathophysiological stimuli, however, such as strenuous exercise or mechanical stretch of the sarcolemma caused by osmotic shock, uncover spontaneous Ca^{2+} signals reminiscent of Ca^{2+} sparks. Compared to cells from healthy control animals, this activity seems to be abnormally augmented in muscle fibers dissected from *mdx* mice [49]. Here, we addressed the following questions: (1) is excessive "Ca^{2+} spark" activity in dystrophic *mdx* muscle fibers associated with, and possibly caused by, an enhanced ROS/RNS production? (2) Can ROS scavengers inhibit stress-induced "Ca^{2+} sparks"? (3) What are the sources of ROS/RNS in *mdx* skeletal muscle fibers?

Preliminary results of these studies have been published as an abstract [43].

Materials and methods

Fiber preparation

Male *mdx* (C57BL/10ScSn-*mdx*) mice at 4–8 weeks of age were purchased from Jackson Laboratory (Bar Harbor, Main, USA) or were provided by Drs. M. Rüegg (Biozentrum, University of Basel, Switzerland) and U. Rüegg (University of Geneva, Switzerland). Muscle fibers were enzymatically isolated from *flexor digitorium brevis* (FDB) muscle as previously described [30]. Briefly, mice were killed by cervical dislocation under deep anesthesia induced by intra-peritoneal injection of sodium pentobarbital (100 mg kg body weight^{-1}). FDB muscle was mechanically dissected and incubated in a modified Tyrode solution (in mM, 145 NaCl, 5 KCl, 1 $CaCl_2$, 10 HEPES, 10 glucose, pH=7.0) supplemented with 2 mg ml^{-1} collagenase (Type I, Sigma, St. Louis, MO, USA) at 37°C for 40 min. Single fibers were obtained by gentle trituration of the digested muscles. They were plated on laminin-coated coverslips and studied 2–8 h after isolation. The procedure conforms with the *Guide for the Care and Use of Laboratory Animals* published by the US National Institutes of Health (NIH Publication No. 85-23, revised 1996).

Solutions

The isotonic external solution contained in mM, 140 NaCl, 5 KCl, 2.5 $CaCl_2$, 1 $MgCl_2$, 10 HEPES, 10 glucose. Its osmolality was ~300 mosmol kg^{-1} and pH of 7.0. The hypotonic solution contained in mM: 70 NaCl, 5 KCl, 2.5 $CaCl_2$, 1 $MgCl_2$, 10 HEPES, 10 glucose, with osmolality of ~170 mosmol kg^{-1}, and pH of 7.0. Most chemicals were obtained from Sigma (St. Louis, MO, USA). MnTBAP and Mn-cpx3, and NAD(P)H oxidase inhibitor diphenyleneiodonium (DPI) were from Calbiochem (EMD Chemicals, Gibbstown, NJ, USA).

Confocal imaging

To monitor microscopic intracellular Ca^{2+} transients, fibers were loaded with 10 μM fluorescent Ca^{2+} indicator fluo-4 AM (acetoxymethyl form of fluo-4) for 40 min. To follow local changes in intracellular and/or mitochondrial ROS/RNS production, cells were loaded with either 10 μM CM-H_2DCFDA (5-(and-6)-chloromethyl-2′,7′-dichlorodihydrofluorescein diacetate) or 5 μM MitoSOX red for 30 min. To examine changes in mitochondrial Ca^{2+} load, fibers were incubated with 10 μM mag-rhod-2 for 30 min. Voltage-sensitive indicators JC-1 (2 μM, 60 min) and TMRE (100 nM, 30 min) were used to monitor mitochondrial membrane potential. All probes were obtained from Molecular Probes (Invitrogen, Carlsbad, CA, USA). The fluorescence images (*X–Y* scans) were acquired with a laser-scanning confocal microscope (Radiance 2000; BioRad) connected to a Zeiss Axiovert 100 inverted microscope equipped with a 63x, 1.2 N.A. water immersion lens (Zeiss Inc., Oberkochen, Germany). Fluo-4, CM-H_2DCFDA and JC-1 were excited with the 488 nm and MitoSOX with the 514 nm lines of an Argon laser. Fluorescence emission was collected with 500 LP and 590/70 BP filters for fluo-4 and CM-H_2DCFDA, respectively. The relative contribution of red (aggregated) and green (monomeric) forms of JC-1 was determined as a ratio of fluorescence signals detected with 515/30 BP and 570 LP emission filters. Mag-rhod-2 and TMRE were excited with a HeNe laser at 543 nm. The emitted light was collected above 570 nm. In all experiments, the laser power was minimized and detection sensitivity was maximized in order to reduce the laser-light-induced production of ROS. In most experiments, 100 or 150 images (102.8 μm by 102.8 μm) were collected from the same spatial locus within a fiber at 0.1 Hz. Even though *X–Y* imaging does not provide sufficient information about the temporal properties of discrete events of Ca^{2+} release, we referred to them as Ca^{2+} sparks.

Sample preparation and Western blotting

Protein expression studies were conducted on explanted striated muscles from control and *mdx* mice as described previously [17]. Samples were snap-frozen in liquid nitrogen. After mechanical homogenization, tissue samples were lysed in SB20 (0.1 M Tris–HCl, pH 6.8, 20% SDS, 10 mM EDTA) and sonicated. Protein content was assayed using the Micro BCA protein assay kit (Pierce Biotechnology, Rockford, IL, USA). All samples were stored at −20°C. For immunoblotting, 20 μg of total protein were loaded per lane. Samples were run on 10% SDS-polyacrylamide gels and electrophoretically transferred to PVDF membranes (0.45 μM, Immobilon-P, Millipore, Bedford, MA, USA). Membranes were blocked in 5% non-fat dry milk in Tris-buffered saline-Tween 20, and then incubated with primary antibody against human NAD(P)H oxidase (rabbit anti-human gp91-phox, 1:200, Millipore, Bedford, MA, USA). Horseradish peroxidase (HRP) conjugated goat anti-rabbit IgG (1:1,000, Millipore, Bedford, MA, USA) was used as secondary antibody. Immunoreactivity of blots was detected using enhanced chemiluminescence (BioRad, Hercules, CA, USA). Immunoreaction against actin (goat polyclonal IgG, sc-1615, 1:2000, and HRP-conjugated donkey anti-goat IgG, sc-2020, 1:2000, Santa Cruz Biotechnology, CA, USA) served as internal control for protein expression levels. Quantification of Western blots was done by densitometric analysis of the membranes. Data are expressed as the mean signal ratio of NAD(P)H oxidase and actin in control and *mdx* tissue.

Statistical analysis

Data analysis is presented as mean±SEM. Statistical significance was determined by using Student's *t* test. In the figures * indicates $p<0.05$, ** indicates $p<0.01$. *n* and *N* indicate number of cells and animals studied in each group of experiments.

Results

Dystrophic skeletal muscle exhibits more pronounced intracellular Ca^{2+} signals in response to osmotic shock than muscle from control animals. Our previous results had suggested a close link between the intracellular level of ROS and the development of Ca^{2+} sparks in both permeabilized and intact skeletal muscle fibers isolated from normal animals [24, 25, 30]. Here, we tested the hypothesis that sustained and/or transient oxidative stress in *mdx* muscle fibers underlies their more prominent intracellular Ca^{2+} responses triggered by mechanical challenges involving osmotic shocks. We also determined possible sources responsible for the increased generation of ROS, and possibly RNS, in *mdx* muscle fibers.

Stress-induced sparks often propagate inside the *mdx* muscle fibers

Wang et al. [49] recently reported that both hypo- and hyper-osmotic shock produced a long-lasting surge of Ca^{2+} sparks in skeletal muscle fibers from *mdx* mice. In contrast to the general responses observed in normal (a.k.a., wild type, WT) cells, where Ca^{2+} sparks were mostly restricted to a narrow space ~10 μm beneath the sarcolemma, response in *mdx* fibers propagated gradually throughout the entire cytosol. Figure 1a illustrates images from an *mdx* fiber before (image at 1.1 min), during (image at 2.6 min) and after (images at 4.0, 4.7, 6.3, and 21.3 min) a hypo-osmotic shock was applied. In 97% of *mdx* fibers (33 out of 34 fibers from $N=11$ animals) studied in this group, the osmotic shock triggered Ca^{2+} sparks. In nine cells (or in 38% of the responding cells), Ca^{2+} sparks rapidly propagated inside the fiber, reaching the center on average within 34.4±8.5 s (as seen on panel a). This is significantly different from the responses obtained in wild-type cells, where Ca^{2+} sparks were mostly localized to the sub-sarcolemmal region ([30] and Fig. 1c). It should be mentioned, that the pattern of intracellular Ca^{2+} responses

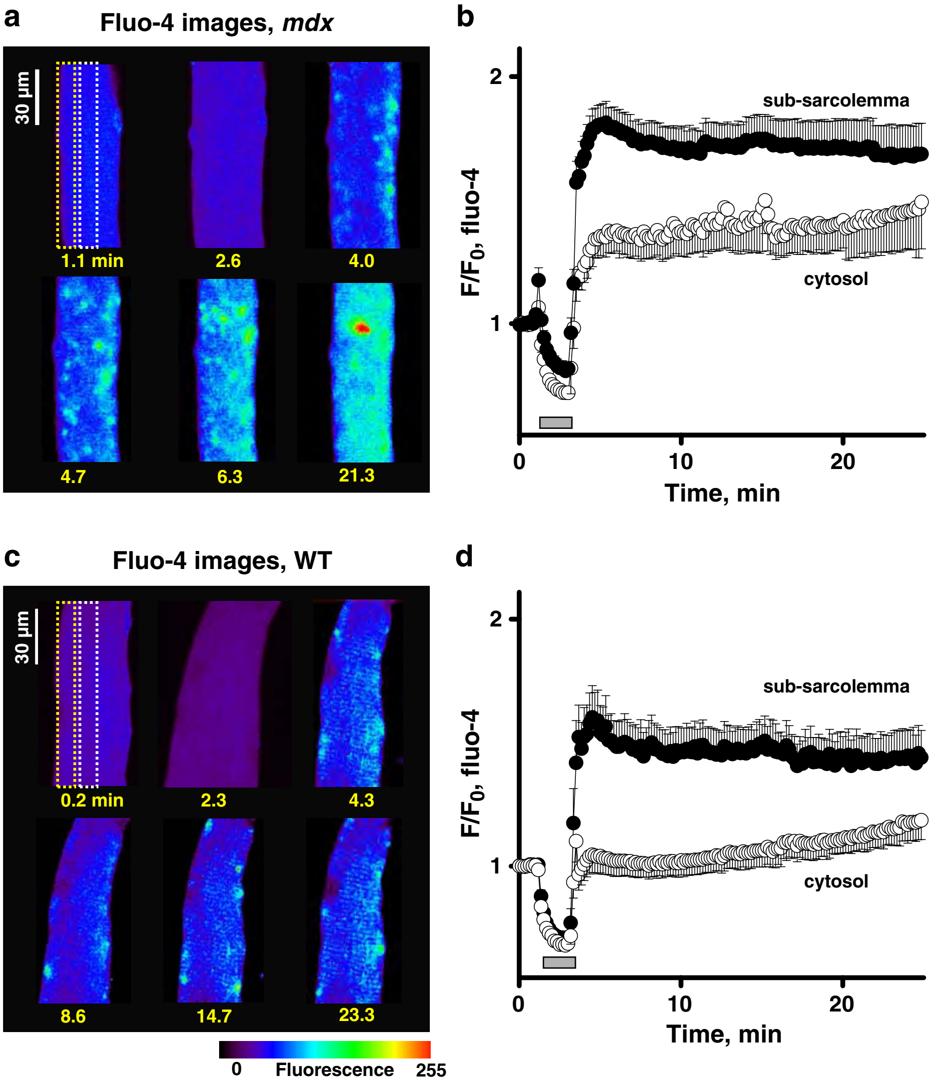

Fig. 1 Cytosolic Ca^{2+} signals elicited by hyposmotic shock in *mdx* and normal (*WT*) muscle fibers. Selected images of fluo-4 fluorescence in *mdx* (**a**) and WT (**c**) fiber before (images at 1.1 and 0.2 min, respectively) during (images at 2.6 and 2.3 min) and after osmotic shock was applied. *Boxes* indicate the regions where the average fluorescence was determined. **b**, **d** Averaged sub-sarcolemmal (*black circles*) and cytosolic (*white circles*) Ca^{2+} responses of 34 *mdx* and nine WT cells to osmotic shock

to stress (propagation or no propagation) varied in *mdx* fibers isolated from the same animal, probably because fibers are heterogeneously affected by the disease. To quantify and compare data obtained in different cells, we determined the spatial average fluorescence within 10 µm under the sarcolemma (yellow dashed box in panel a) or inside the fiber (white box) for each image in a series ($F(t)$). Then we normalized these signals to the average signal recorded before the osmotic shock was applied ($F(t)/F_0$). The corresponding $F(t)/F_0$ function represents the time dependence of changes in fluorescence in the selected region of interest. Figure 1b and d illustrate the averaged Ca^{2+} responses in the sub-sarcolemmal region (black circles) and in the center (white circles) of 34 *mdx* and nine WT muscle fibers studied in this series.

ROS/RNS generation is greater in *mdx* cells

In the literature, there are several reports of sustained oxidative stress in *mdx* skeletal muscle [16, 46, 51]. In addition, our previous data suggest that osmotic shock increases ROS production in wild-type cells [30]. Here, we tested (1) whether the "basal" production of ROS/RNS is elevated in dystrophic muscle fibers in *mdx*, compared with wild-type cells, and (2) whether an osmotic shock further increased ROS/RNS generation.

Fibers were loaded with CM-H_2DCFDA and imaged while being subjected to an osmotic shock. Inside the cell, CM-H_2DCFDA is hydrolysed to DCFH, which is oxidized by hydrogen peroxide or peroxynitrite to form the highly fluorescent compound DCF. Therefore, changes (i.e., increases) in DCF fluorescence are directly related to elevations in ROS/RNS concentration within a cell. Figure 2a shows images of DCF fluorescence in an *mdx* muscle fiber before (image at 1 min), during (image at 6 min) and after a hypo-osmotic (images at 8, 9, 10 and 12 min) shock was applied. Please note that the increase in fluorescence was initially mostly visible in the sub-sarcolemmal regions (images at 8 and 9 min) but later became more pronounced inside the fiber. Figure 2b represents averaged normalized changes in DCF signals in seven *mdx* fibers ($N=3$) subjected to osmotic shock (gray

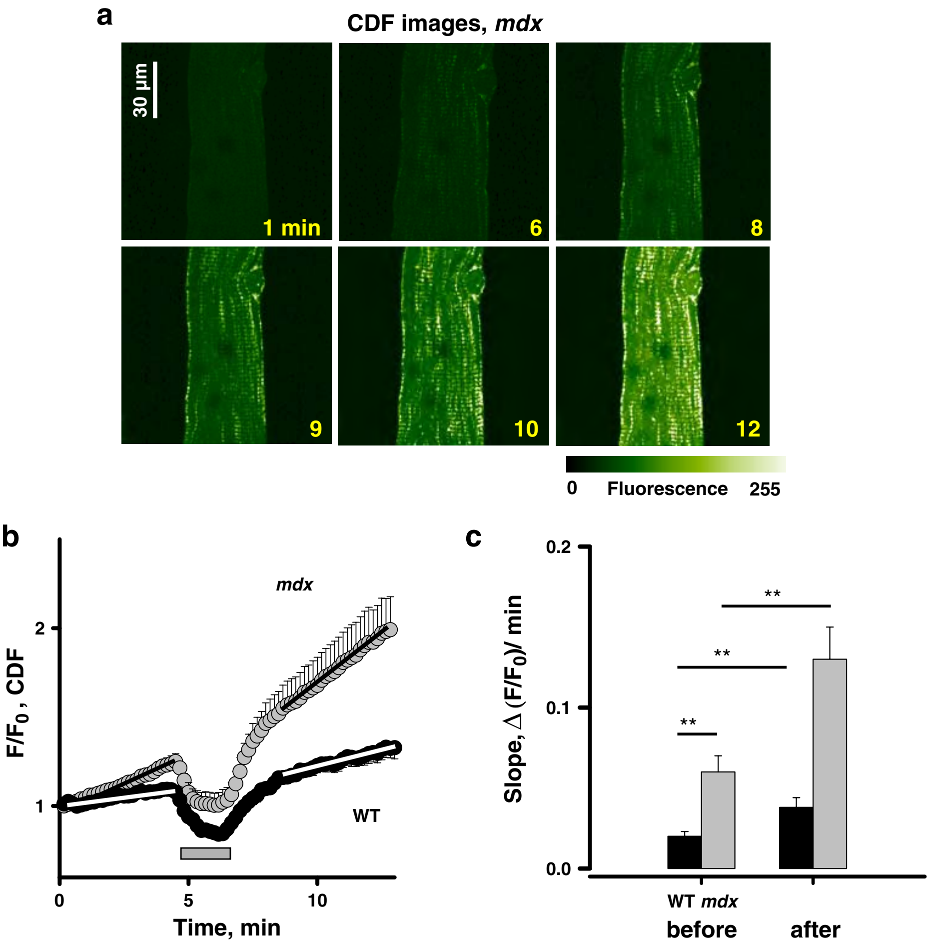

Fig. 2 Basal and stress-induced generation of ROS/RNS in skeletal muscle. **a** Selected images of DCF fluorescence in *mdx* fiber before (image at 1 min), during (image at 6 min) and after (images at 8, 9, 10, and 12 min) osmotic shock was applied. **b** Averaged DCF fluorescence from seven *mdx* cells (gray circles) and eight fibers from WT mice (*black circles*). **c** Averaged slopes of DCF signals before and after osmotic shock in *mdx* (*gray bars*) and WT cells (*black bars*). Steeper slopes indicate larger production of ROS/RNS in *mdx*

circles). Black circles represent changes in DCF fluorescence in eight cells from normal mice ($N=4$) studied in parallel with the same experimental protocol and confocal microscope settings. During these experiments, the DCF signal increased in both types of cells. The slope of the DCF fluorescence before the shock was applied reflects the rate of basal or endogenous generation of free radicals that lead to the oxidation of the indicator. The slope was significantly steeper after the shock suggesting an additional increase in ROS/RNS production. For each cell, the DCF recordings were fitted with linear functions before and after the osmotic shock was applied. The results are summarized in Fig. 2c. On average, the steepness before the shock was significantly ($P<0.01$) larger in *mdx* (gray bars) compared with WT (black bars) cells (0.06±0.01 and 0.02±0.003, respectively). The steepness significantly increased following the shock (0.13±0.02 and 0.04±0.01 in *mdx* and WT cells, respectively). The change of slope was somewhat more pronounced in *mdx* fibers (the slope ratios after/before were 2.16±0.01 and 2.00±0.01 in *mdx* and control cells, respectively). Because the slope of the DCF signal reflects the rate of generation of ROS/RNS, these results suggest (1) increased basal generation of free radicals and (2) greater increase in ROS/RNS production caused by osmotic challenge in *mdx* fibers compared with normal cells.

ROS/RNS scavengers inhibit intracellular Ca^{2+} responses to osmotic shock

As already mentioned, our previous studies suggested a link between ROS and the development of Ca^{2+} sparks in both permeabilized and intact mammalian muscle fibers [24, 25, 30]. The findings described above indicate a higher level of background and inducible ROS/RNS generation in *mdx* skeletal muscle fibers. Since ROS/RNS can make the RyRs more Ca^{2+} sensitive, they may be responsible for the excessive intracellular Ca^{2+} responses in *mdx* fibers. Here, we tested whether pre-incubation of *mdx* fibers with exogenous ROS/RNS scavengers or SOD mimetics suppresses Ca^{2+} sparks induced by osmotic shock in *mdx* muscle.

Changes in sub-sarcolemmal fluo-4 fluorescence were monitored in a control group of *mdx* fibers (no scavengers added), in fibers following 30 and 60 min incubation with MnTBAP (50 μM), Mn-cpx 3 (4 μM) and TIRON (10 mM) and in cells 30 min after wash out of drugs. Previously [30], we showed that incubation of fibers from normal mice with MnTBAP significantly reduced the basal ROS/RNS levels and decreased ROS/RNS production following osmotic stress. Here, we used three different compounds with distinct chemical structures and scavenging profiles to ensure that the results obtained are not associated with possible non-specific actions of these scavengers.

Figure 3a illustrates averaged changes in fluorescence in *mdx* fibers studied in control ($n=6$, $N=3$), after 30 ($n=7$, $N=3$) and 60 ($n=5$, $N=3$) min of incubation with 50 μM MnTBAP, and 30 min after washout of the scavenger ($n=6$, $N=3$). The mean fluorescence signal was determined during the first 6 min after returning to the isotonic solution in each group of fibers. As shown in Fig. 3b, the abnormal Ca^{2+} activity was significantly ($P<0.01$) suppressed by the drug (from F/F_0 of 1.47±0.06 to 1.28±0.03 after 30 min pre-incubation and further to 1.02±0.005 after 60 min of pre-incubation), and was partially restored after washout of MnTBAP (to 1.21±0.04), confirming reversibility of the inhibition.

Qualitatively similar results were also obtained with the two other scavengers. Figure 3c and d show that both Mn-cpx3 and TIRON effectively and reversibly inhibited cytosolic Ca^{2+} responses to osmotic shock in *mdx* muscle.

Contribution of NAD(P)H oxidase to elevated ROS/RNS level and excessive intracellular Ca^{2+} responses to osmotic shock in mdx muscle

There are several intracellular sources producing ROS/RNS in skeletal muscle. Mitochondria, NAD(P)H oxidase (NOX), xanthine oxidase (XO), and nitric oxide synthase (NOS) are among them (reviewed in [40]). Our previous studies suggested a pivotal role of NAD(P)H oxidase in the increased ROS production after osmotic shock in WT mammalian skeletal muscle fibers. They also suggested a rather limited role of mitochondria, NOS and XO [30].

The larger ROS production in *mdx* cells seen in Fig. 2 can be explained (1) by an increased activity and/or expression of NAD(P)H oxidase, or (2) by the recruitment of additional sources of ROS, which are of limited importance in wild-type fibers. Our results support both possibilities.

First, we examined whether NAD(P)H oxidase expression is higher in *mdx* skeletal muscle. Western blotting was performed on lysates of control and *mdx* skeletal muscle. At equal protein loading, immunoreactivity of a protein with an apparent molecular mass of 75 kDa corresponding to a transmembrane subunit of the NAD(P)H oxidase ($gp91^{phox}$, or NOX2 in the most recent terminology) showed a dramatic increase in expression levels and reached near maximal reactivity in *mdx* compared with control samples. To ascertain whether the increase in immunoreactivity of this band of 75 kDa corresponded indeed to an increase in the actual expression levels of the protein, we performed simultaneous immunoprecipitation studies using anti-actin antibody on the same protein lysates. Assuming that the expression of actin, which precipitates at ~42 kDa, is unchanged in *mdx* when compared with control tissue, this test served as an internal control for quantification of the NAD(P)H oxidase signal responses. Signal ratios of

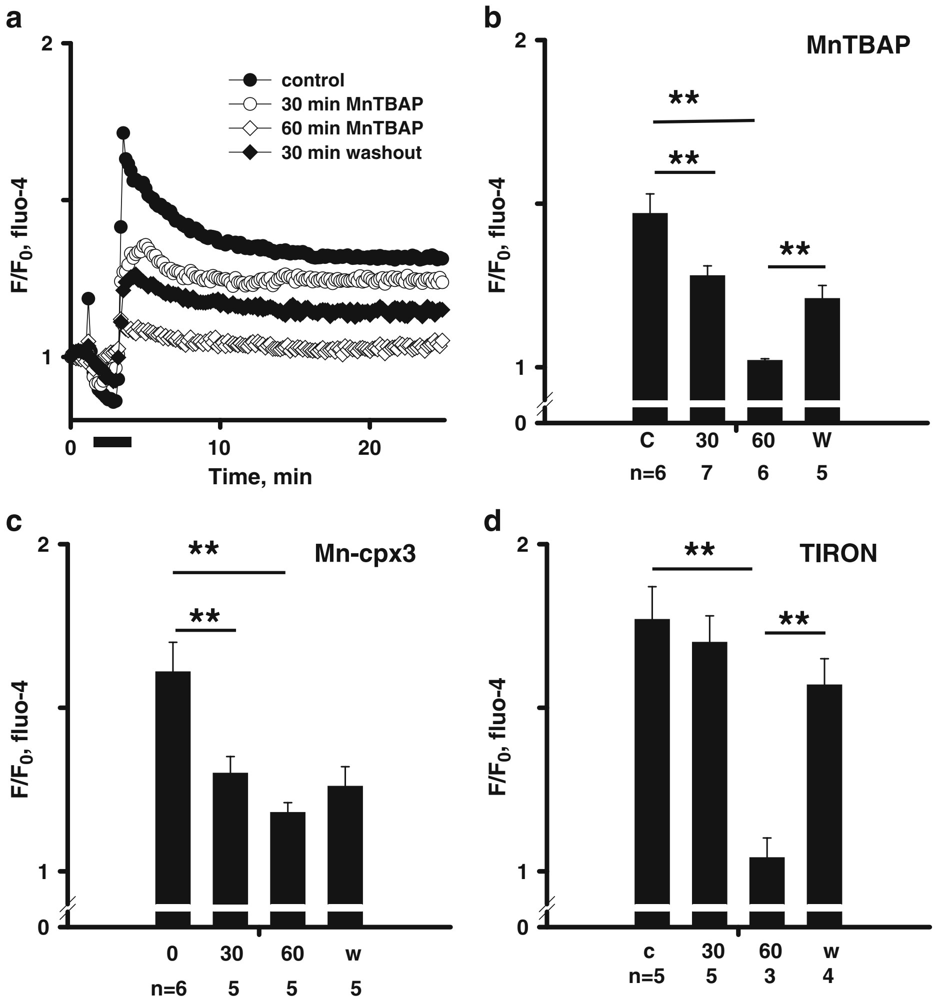

Fig. 3 ROS/RNS scavengers inhibit cytosolic Ca^{2+} responses to osmotic shock. **a** Average changes in normalized fluo-4 fluorescence in *mdx* fibers studied under control condition (no drugs added, *black circles*), 30 (*white circles*) and 60 min (*white diamonds*) after incubation with 50 μM MnTBAP, and after washout (*black diamonds*). **b** The mean fluorescence determined during the first 6 min after returning to the isotonic solution in each group of the experiments. **c**, **d** Summary of similar experiments but with Mn-cpx3 (4 μM) and TIRON (10 mM)

background-subtracted band intensities for gp91^{phox} (at ~75 kDa) and actin (at ~42 kDa) in each lane were used for analysis. As shown in Fig. 4a, the expression of gp91^{phox} is increased more than three fold in *mdx* skeletal muscle (N=7) when compared with control (N=3, P<0.01).

In skeletal muscle NAD(P)H oxidase is localized to the sarcolemma and T-tubular membrane and can be activated in a Ca^{2+}-dependent and Ca^{2+}-independent manner [22, 30]. Thus, NAD(P)H oxidase may be exposed to a microdomain of high [Ca^{2+}], which is established under the cell membrane by abnormal Ca^{2+} influx during regular mechanical activity of dystrophic muscle as well as during eccentric stretch. Therefore, ROS production by this enzyme can contribute to both the elevated basal level of ROS and the enhanced generation of free radicals following more severe mechanical challenges such as osmotic shock. Using CM-H_2DCFDA, we examined the rate of basal and stress-induced ROS generation in *mdx* cells pre-incubated for 30 min with 0.5 mM apocynin, an inhibitor of NAD(P)H oxidase. Apocynin significantly (P<0.05) reduced the basal level of ROS production (slopes of DCF curves before the shock were 0.03±0.005, n=10, N=4, in control, and 0.01± 0.002, n=7, N=3, in apocynin, data not shown). The drug also nearly eliminated the increase in ROS generation by osmotic shock (slopes of DCF curves were 0.01±0.002 and 0.014±0.001, before and after the shock, respectively, data not shown). The variability in the baseline values of ROS/RNS levels in different groups of experiments is likely to be due to heterogeneity in the disease phenotype.

In the next group of experiments, fibers were loaded with the fluorescent Ca^{2+} indicator fluo-4 and incubated for 30 min with two different NAD(P)H oxidase inhibitors: apocynin (0.5 mM) and DPI (10 μM). As seen in Fig. 4b and c, both drugs significantly diminished cytosolic Ca^{2+} responses to osmotic shock. The mean fluorescence after returning to the isotonic solution was reduced from 1.8±0.04 in the control (n=8, N=6) to 1.25±0.06 (n=4, N=3) and 1.07±0.06 (n=5, N=3) in DPI and apocynin, respectively.

In Martins et al. [30], we suggested that activation of NOS and XO are not likely to account for stress-induced

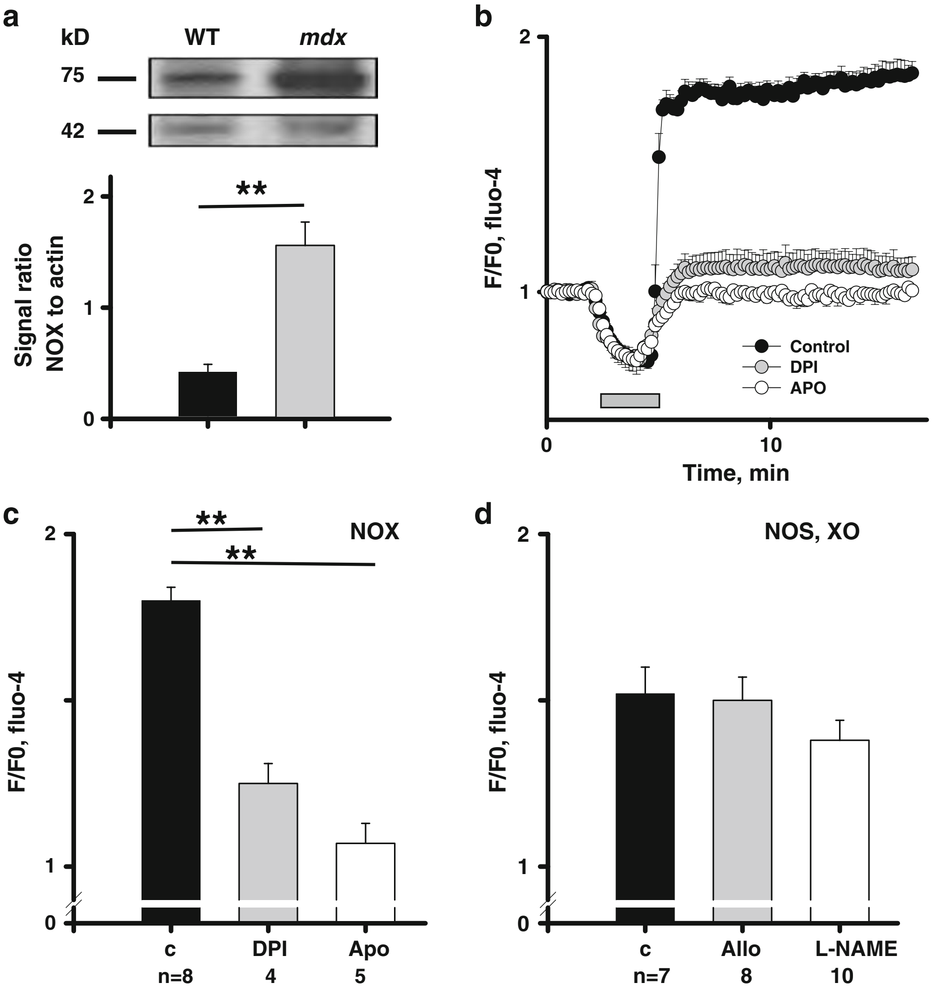

Fig. 4 NOX is a major contributor to the increased ROS production in *mdx* skeletal muscle. **a** Expression of NOX and actin in *mdx* and WT mice. *Top panel*, Western blots demonstrating protein levels of NOX and actin in two types of muscles. *Bottom level*, signal ratios of band intensities for gp91^{phox} and actin in *mdx* (*gray bar*) and wild-type (*black bar*) muscles (n=3 animals for wild type, seven for *mdx*). **b** Average cytosolic Ca^{2+} responses to osmotic challenge in *mdx* fibers studied under control condition (no drugs added, *black circles*), and after incubation with NOX inhibitors apocynin (0.5 mM, *white circles*) and DPI (10 μM, *gray circles*). **c** The mean fluorescence determined during the first 6 min after returning to the isotonic solution in each group of the experiments illustrated in **b**. **d** The mean fluorescence after osmotic shock in control group fibers (*black bars*) and in cells pre-incubated with allopurinol (100 μM) and L-NAME (1 mM)

ROS production and cytosolic Ca^{2+} signals in normal muscle cells. Here, we also assessed the role of these sources in *mdx* muscle fibers. Figure 4d shows that the XO inhibitor allopurinol (100 μM) did not significantly change intracellular Ca^{2+} transients elicited by osmotic stress. The non-specific NOS inhibitor L-NAME (1 mM) somewhat reduced cytosolic Ca^{2+} responses but the reduction was not highly significant. The mean fluorescence was 1.52±0.08 (n=5, N=3) in control, 1.50±0.07 (n=8, N=5) after 30 min of incubation in XO inhibitor allopurinol and 1.38±0.06 (n=10, N=4) after 30 min exposure of fibers to NOS inhibitor L-NAME.

Overall, these data indicate that most likely NOX is the major contributor to the increase in ROS/RNS and augmented Ca^{2+} responses to osmotic shock in *mdx* skeletal muscle fibers.

Osmotic stress increases mitochondrial Ca^{2+} loading

Mitochondria are another potential source of ROS in skeletal muscle. It is known that muscle cells continuously generate ROS, as a byproduct of the respiratory chain, and that enhanced mitochondrial Ca^{2+} uptake stimulates further mitochondrial ATP and ROS production (reviewed in [8]). It is possible that stress-generated cytosolic Ca^{2+} is sequestered by mitochondria. In turn, this would stimulate mitochondrial ROS production, increase leakage of ROS to the cytosol and thus further amplify cytosolic Ca^{2+} signals. Here, we tested (1) whether and to what extent osmotic shock increases the mitochondrial Ca^{2+} load, and (2) whether the increase is different in *mdx* and wild-type muscle fibers.

Dystrophic *mdx* and normal muscle fibers were loaded with the low affinity Ca^{2+} indicator mag-rhod-2 in its AM ester form. Mag-rhod-2 is a charged molecule that preferentially partitions into the mitochondria. The dye has been demonstrated to be useful in studies of mitochondrial Ca^{2+} uptake in skeletal muscle, where the resting mitochondrial Ca^{2+} load seems to be quite high [44]. Figure 5a shows the mitochondrial mag-rhod-2 distribution and the fluorescence signal in an *mdx* cell before (image at 1 min), during (image at 4 min) and after the shock (images

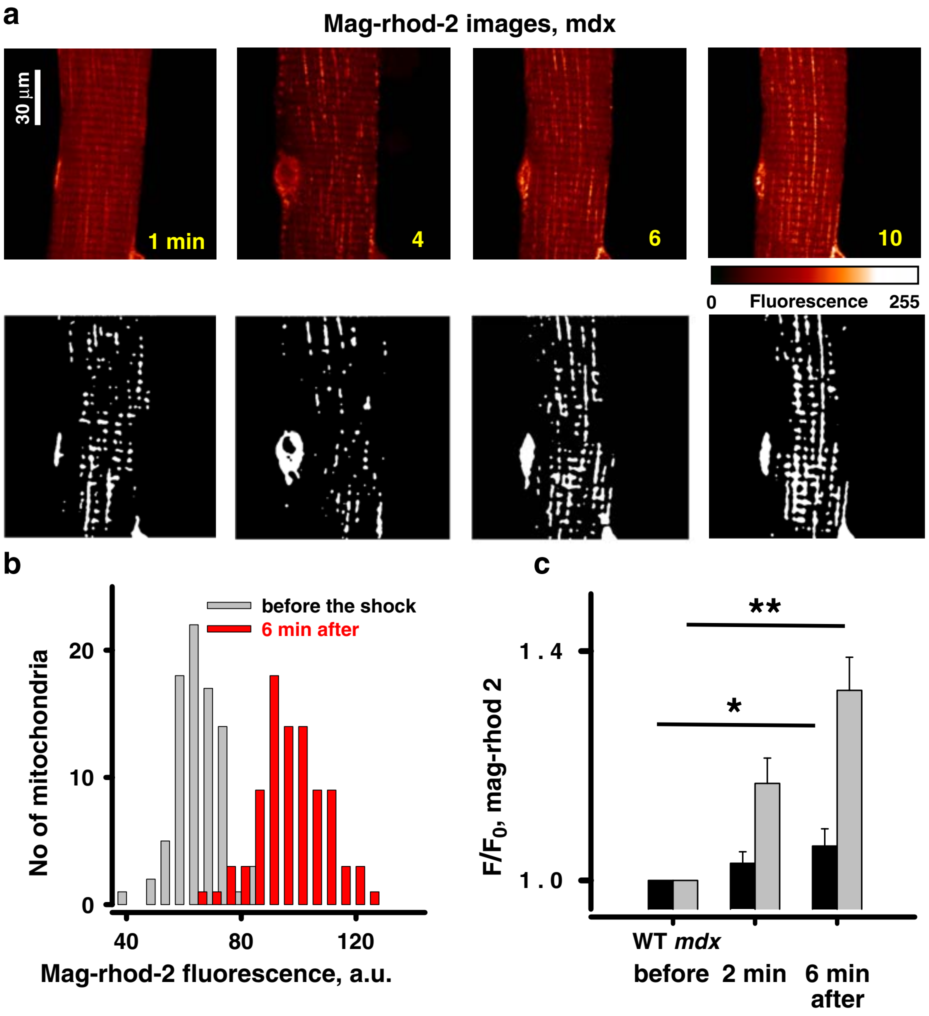

Fig. 5 Excessive cytosolic Ca^{2+} is taken up by mitochondria. **a** *Top panels* represent selected images of mag-rhod-2 fluorescence in an *mdx* cell before (image at 1 min), during (image at 4 min), and after (images at 6 and 10 min) osmotic shock was applied. *Bottom panels* show binary masks of mitochondria identified on corresponding mag-rhod-2 images. **b** Histogram of averaged fluorescence in the identified organelles before (*gray bars*) and 6 min after (*red bars*) osmotic shock was applied. **c** Average increase in mitochondrial Ca^{2+} related fluorescence after osmotic shock in *mdx* (*gray bars*) and wild-type (*black bars*) fibers

at 6 and 10 min). Mitochondria were identified in each image (as seen on binary masks at the bottom of panel a) and their average fluorescence was determined. Figure 5b shows the histogram of averaged fluorescence in the organelles before and 6 min after the osmotic shock was applied. In this particular fiber, the averaged mag-rhod-2 fluorescence (in a.u.) increased significantly ($P<0.01$) from 64.5±0.9 at resting conditions to 80.7±1.5 and 94.2±1.2 two and six min after the stress, respectively. Overall, in seven out of ten *mdx* fibers ($N=5$) osmotic shock produced a gradual and significant increase in mag-rhod-2 fluorescence (1.33± 0.06 in units of F/F_0) at the end of the experiments (Fig. 5c). In contrast, in cells from normal mice, a significant increase in mitochondrial mag-rhod-2 signal was observed much less frequently (two out of 12 cells, $N=4$). It was substantially smaller than in *mdx* cells and preferentially detected in subsarcolemmal regions. The averaged mag-rhod-2 fluorescence increased from 69.2±1.6 at the beginning to 73.6±2.1 (in a.u.) at the end of experiments ($P<0.05$).

The larger mitochondrial Ca^{2+} accumulation in dystrophic fibers can be a direct consequence of enhanced cytosolic Ca^{2+} signals in these cells (as seen in Fig. 1), but also due to more sensitive mitochondrial Ca^{2+} uptake mechanism(s). Using mitochondrial and SR-targeted luminescent aequorins, Robert et al. [41] showed augmented mitochondrial Ca^{2+} signals resulting from similar cytosolic Ca^{2+} transients in *mdx* developing myotubes compared to WT, suggesting enhanced uptake in the *mdx* cells. As described below, our experiments support this possibility. Mag-rhod-2 is not a ratiometric fluorescent Ca^{2+} indicator. Therefore, direct quantitative comparison of the effectiveness of mitochondrial Ca^{2+} uptake is not feasible under our experimental conditions. Instead, we measured mitochondrial potential with the voltage-sensitive probe JC-1. JC-1 is an indicator that exhibits potential-dependent accumulation in mitochondria accompanied by a fluorescence emission shift from green to red. Muscle fibers were isolated from *mdx* and WT mice on the same day, loaded with 2 µM JC-1 for 60 min to

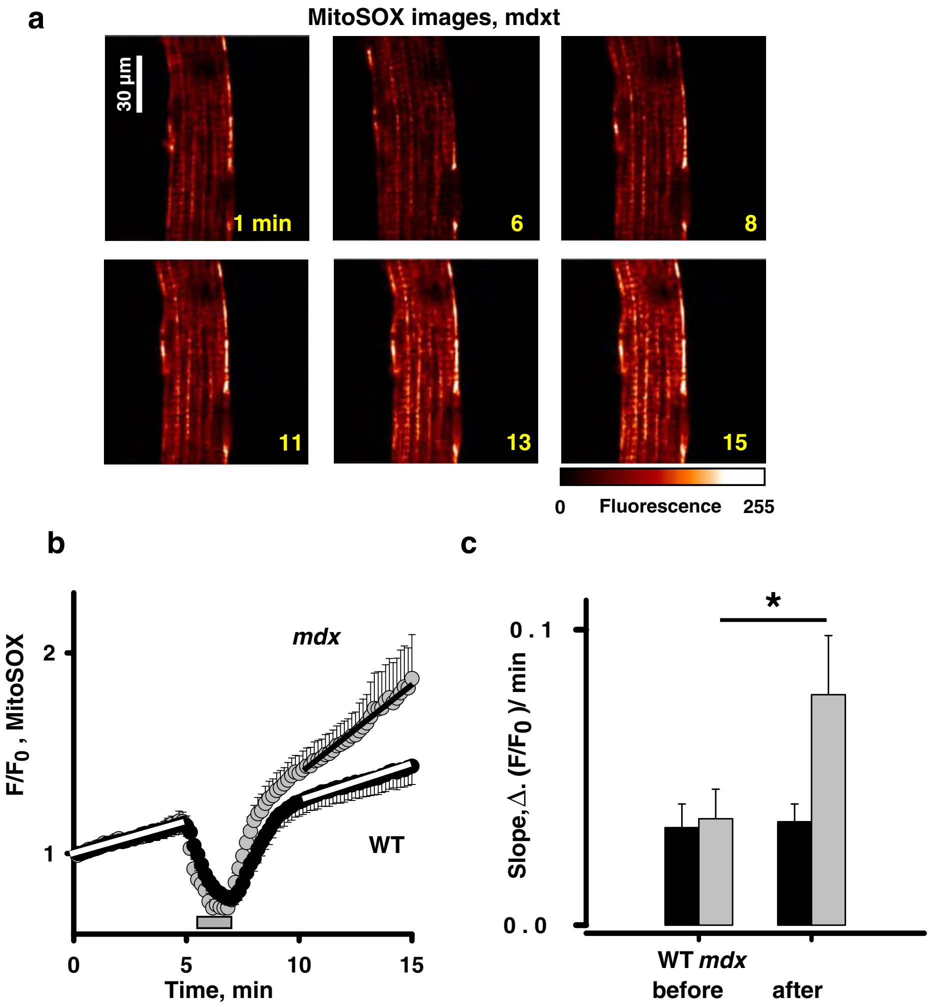

Fig. 6 Mitochondrial ROS production. **a** Selected images of MitoSOX fluorescence in an *mdx* cell before (image at 1 min), during (image at 6 min), and after (images at 8, 11, 13, and 15 min) osmotic shock was applied. **b** Averaged MitoSOX fluorescence from eight *mdx* cells (*gray circles*) and nine fibers from normal mice (*black circles*). **c** Averaged slopes of MitoSOX signals before and after osmotic shock in *mdx* (*gray bars*) and wild-type cells (*black bars*)

equilibrate dye distribution within the cell and studied in parallel. The red to green fluorescent ratio was significantly larger in *mdx* fibers (0.8±0.07, *n*=19, *N*=7 and 0.6±0.06, *n*=23, *N*=7 in *mdx* and WT cells, respectively), indicating that mitochondria in dystrophic fibers are hyperpolarized compared with those in WT. A larger potential gradient across the mitochondrial membrane could lead to stimulation of the electrogenic mitochondrial Ca^{2+} uniporter resulting in augmented mitochondrial Ca^{2+} accumulation in *mdx* skeletal muscle of this age group.

Osmotic stress increases mitochondrial ROS production

One of the consequences of moderate mitochondrial Ca^{2+} sequestration can be an enhancement of mitochondrial metabolism, as the activity of several enzymes of the TCA cycle depends on Ca^{2+}. Here, we directly measured mitochondrial ROS production in *mdx* and wild-type cells under identical experimental conditions. Fibers were loaded with the mitochondrial superoxide fluorescent probe MitoSOX red and imaged while subjected to hypo-osmotic shock. Because targeting of MitoSOX (and therefore the fluorescence signal intensity) is driven by the mitochondrial membrane potential, we also tested whether osmotic shocks can change this potential. As JC-1 is not very reliable for dynamic measurements, we used TMRE at a concentration of 100 nM, which we previously found to result in a non-quenching behavior in both skeletal muscle fibers and in cardiac myocytes [24, 26]. No significant changes of the TMRE fluorescence were elicited by osmotic shocks, neither in WT (*n*=5, *N*=3) nor in *mdx* (*n*=7, *N*=3) fibers, suggesting that the mitochondrial membrane potential did not change noticeably and that the MitoSOX signals reliably reflect mitochondrial ROS production. Figure 6a represents images of MitoSOX fluorescence in an *mdx* fiber before (image at 1 min) during (image at 6 min) and after (images at 8, 11, 13, and 15 min) a shock was applied. Averaged normalized MitoSOX fluorescence from eight *mdx* (*N*=6) fibers is shown on panel b (gray circles). As in the experiments with CM-H_2DCFDA, the MitoSOX curve was fitted with a linear function before and after the shock was applied. As expected based on the results with mitochondrial Ca^{2+} measurements, there was a significant increase ($P<0.05$) in the slope of the curve (from 0.04±0.01 to 0.08±0.02). The increase clearly indicates an enhanced mitochondrial ROS generation resulting from the osmotic shock. Consistent with limited mitochondrial Ca^{2+} accumulation, no significant change in slope of the MitoSOX signal was detected in wild-type cells (black circles and bars, $n=9$, $N=4$). The slope only slightly changed from 0.033±0.008 to 0.035±0.006. Interestingly, the initial slope, which reflects the basal production of ROS by mitochondria, was slightly (but not significantly) larger in *mdx* cells. This suggests that, in contrast to NOX, mitochondria are likely to be minor contributor to basal oxidative stress in dystrophic skeletal muscle. However, they contribute to the increased ROS production in response to mechanical stress.

Discussion

Mechanical stress applied as an osmotic shock triggers a surge of Ca^{2+} spark-like events in intact skeletal muscle fibers. These events are not observed in intact mammalian muscle cells at rest or during physiological ECC. The extent of stress-induced intracellular Ca^{2+} activity is much greater in muscle fibers from *mdx* mice, but the reason for this difference is still elusive. Our previous studies on normal mammalian muscle strongly suggested a close link between overproduction of ROS/RNS and appearance of sparks in both permeabilized and intact fiber preparations. Here, we tested whether the exaggerated Ca^{2+} responses to osmotic challenges in dystrophic muscle are associated with (and presumably caused by) oxidative/nitrosative stress.

The present study revealed an elevated basal level of ROS in skeletal muscle fibers isolated from *mdx* mice, which is presumably mostly due to an enhanced ROS production by NOX. Our findings also revealed further consequences of this phenomenon. Challenging *mdx* fibers with mechanical stress, applied as osmotic shock, initiates several positive feedback loops. The mechanical challenge initially increases ROS production by NOX even further and triggers extensive intracellular Ca^{2+} transients. Subsequently, these large cytosolic Ca^{2+} responses lead to mitochondrial Ca^{2+} accumulation in *mdx* fibers and an additional boost in both NOX and mitochondrial ROS production which finally can again amplify cytosolic Ca^{2+} signals. Overall, our results suggest an important role for an abnormal production of ROS by NOX and mitochondria and consequent impaired Ca^{2+} homeostasis in pathological responses of dystrophic skeletal muscle to mechanical stress. Taken together, the present study shows that the near-simultaneous activation of several mutually synergistic feedback loops can culminate in a vicious cycle that may have damaging consequences for the affected muscle cells.

Oxidative/nitrosative stress and muscular dystrophy

In normally functioning healthy skeletal muscle, the basal production of ROS/RNS is balanced by various scavenging molecules and enzymes. Overproduction of free radicals and/or reduced ability of cellular defense mechanisms to neutralize them can eventually lead to sustained oxidative/nitrosative stress. Oxidative/nitrosative stress is involved in the pathogenesis of many skeletal muscle disorders and chronic diseases, such as muscle atrophy, fatigue, aging, diabetes, central core disease, malignant hyperthermia, etc. [18, 33].

Our present data show an increased basal level of ROS/RNS production in *mdx* muscle fibers (Fig. 2). We suggest that this is in large part due to the enhanced ROS generation by NAD(P)H oxidase. There are also some reports in the literature supporting the possibility that oxidative stress contributes to the pathology of muscular dystrophy. In particular, it has been reported that in dystrophic skeletal muscle (1) the levels of several antioxidant defense components such as catalase, glutathione peroxidase and superoxide dismutase are elevated; (2) the ROS concentration is increased [51]; and (3) levels of products of lipid peroxidation are higher (reviewed in [46]). In addition, although the expression of nNOS and, consequently, the production of NO have been found to be reduced in dystrophy [11, 50], the expression of iNOS has been recently shown to be increased [7]. Moreover, in vivo treatment of *mdx* mice with antioxidants can improve muscle function [9, 51]. Nevertheless, it is not yet clear to what extent oxidative/nitrosative stress determines the pathology of muscular dystrophy and what molecular pathways are involved. On one hand, levels of antioxidant enzymes are elevated in dystrophic muscle prior to the onset of muscle degeneration, suggesting that oxidative stress precedes the development of the disease [14]. On the other hand, these levels are also higher in extraocular skeletal muscle, which is spared from *mdx* pathology, and in dystrophic muscle already undergoing active regeneration [38, 39]. It is possible that oxidative/nitrosative stress itself does not drive muscle degeneration in dystrophy but rather acts synergistically with other factors, such as elevated resting Ca^{2+} concentrations, abnormal Ca^{2+} influx during repetitive muscle contraction and mechanical stress, to drive the pathological responses (e.g., [15]).

NOX as one of the major sources of oxidative stress in muscular dystrophy

A misbalance between the production of ROS/RNS and their elimination by various cellular scavenging systems may contribute to oxidative stress in dystrophy. Although the levels of major antioxidants are higher in dystrophic muscle, they seem to be insufficient to prevent extensive ROS production by ROS-producing sources.

Our data suggest that NAD(P)H oxidase is likely to be one of the major sources of ROS behind the oxidative stress in dystrophy. NAD(P)H oxidase is a multimolecular complex containing two major transmembrane subunits (NOX and p22^{phox}) and several cytosolic regulatory subunits (p47^{phox}, p40^{phox}, p67^{phox} and the small G proteins Rac1 or Rac2), which have to be translocated to the membrane to activate the oxidase. Skeletal muscle mostly expresses two isoforms of NOX, NOX2, and NOX4 [6, 10, 20]. Our results revealed that (1) expression of NOX2 (a.k.a. gp91^{phox}) is more than threefold higher in dystrophic skeletal muscle compared to normal mice and (2) incubation of dystrophic fibers with NOX inhibitors brings basal ROS production down close to the levels found in normal animals (Fig. 4). It seems that NOX, but not XO and NOS, is a primary source of ROS in response to the osmotic shock in muscle, as incubation of fibers with NOX inhibitors nearly eliminated the increase in ROS and cytosolic Ca^{2+} responses caused by the shock.

In Martins et al. [30] we had shown that activation of NOX following the mechanical challenge is partly governed by Ca^{2+}. Both NOX2 and NOX4 isoforms do not have an EF-hand like Ca^{2+} binding domains and therefore are unlikely to be directly activated by the increase in cytosolic [Ca^{2+}]. However, it has been suggested that Ca^{2+} can affect the activity of the NOX2 isoform indirectly via several pathways which are not mutually exclusive, involving Ca^{2+}-sensitive PKC isoforms, Ca^{2+}-dependent phospholipase A$_2$, association with S100 proteins, etc. (e.g., [1, 6, 10]). The activity of the NOX4 isoform does not seem to be regulated by Ca^{2+} [5], however more studies are needed to substantiate this conclusion.

Our experiments also revealed that in dystrophic cells, mitochondria are an important source of ROS generated subsequent to stress, in contrast to the situation in wild-type muscle. This is probably due to more severe cytosolic Ca^{2+} responses to osmotic shock in *mdx* fibers. Larger Ca^{2+} influx during mechanical stretch, increased resting [Ca^{2+}]$_c$ and/or increased sensitivity of RyR1 to be activated by Ca^{2+} as a result of oxidative/nitrosative stress (see below) can be responsible for this difference. Our results show that in *mdx* cells Ca^{2+} is eventually taken up by mitochondria (Fig. 5), stimulating ROS production by the organelles (Fig. 6).

Oxidative stress, Ca^{2+} influx, and intracellular Ca^{2+} homeostasis in muscular dystrophy

ROS/RNS have multiple targets in the sarcolemma and also inside the muscle cells. An increased level of free radicals can promote abnormal influx of Ca^{2+} into the muscle cells during muscle contraction or eccentric stretch by facilitating several possible Ca^{2+} influx pathways. Increased production of ROS may cause lipid peroxidation [14], and consequently may lead to additional Ca^{2+} influx via sarcolemmal membrane microruptures. Recently, some TRP channels have been shown to be sensitive to the cytosolic redox potential [21, 36]. As TRP channels are potential molecular components of SAC and SOC [2, 48], the oxidation of the cytosol may stimulate additional Ca^{2+} influx into the stressed cells via these channels as well.

ROS/RNS can also stimulate the release of Ca^{2+} from the SR via RyR1, as this molecule is a well-known target of oxidative/nitrosative modifications [45]. Increased levels of ROS/RNS may “hypersensitize” RyR1 making it more susceptible for activation by agonists, such as Ca^{2+}. In addition, *S*-nitrosylation and/or *S*-glutathionylation of RyR1 are likely to reduce binding of calstabin1 and calmodulin to RyR1, thereby relieving the inhibitory feedback on RyR1 exerted by these proteins [3, 7].

Taken together, production of ROS/RNS can intensify several mechanisms which deliver Ca^{2+} to the cytosolic space, both from the SR and from the extracellular space. This cytosolic Ca^{2+} load may, in turn, lead to additional production of ROS, thereby creating cross-talk to another positive feedback loop. For example, NOX can be further activated by Ca^{2+} [6, 10]. In addition, we found that mitochondria take up some of the extra Ca^{2+} load, which subsequently leads to an elevated generation of ROS by the mitochondria themselves.

Ca^{2+} overload and ROS production may have downstream consequences ranging far beyond the initial signaling events. For example, they may activate Ca^{2+}-dependent proteases, such as calpain, resulting in proteolysis of cellular constituents. In addition, they may lead to opening of the mitochondrial transition pore, allowing the efflux of proapoptotic mediators into the cytosol. Apoptotic and/or necrotic cell death may be one of the mechanisms leading to muscle wasting and fibrosis in patients with muscle dystrophy [47]. Sustained Ca^{2+} overload can eventually lead to the impaired mitochondrial oxidative phosphorylation reported in older *mdx* mice and DMD patients [27]. In addition, ROS can directly affect the contractile properties of muscle cells [28], also decreasing the force production in dystrophy.

In summary, one of the key findings of our study is that the near-simultaneous activation of two signaling systems triggers early events which synergistically contribute to the excessive stress sensitivity of dystrophic muscle. Based on this observation, one could consider the possibility to concurrently target both pathways, the Ca^{2+} signaling and the ROS generation, with pharmacological or other therapeutic approaches.

Acknowledgments This study was supported by the grants from NIH (to N.S.), Muscular Dystrophy Association (to N.S. and M.C.N.), Swiss Foundation for Research on Muscle Diseases (to E.N. and N.S.), Swiss National Science Foundation (to E.N.) and UMDNJ and Sigrist Foundations (to N.S). We thank Dr. Philippe Beauchamp for technical help, and Drs. John Reeves, Roman Shirokov and Andrew Thomas for discussions.

References

1. Abramov AY, Jacobson J, Wientjes F, Hothersall J, Canevari L, Duchen MR (2005) Expression and modulation of an NADPH oxidase in mammalian astrocytes. J Neurosci 25:9176–9184
2. Allen DG, Whitehead NP, Yeung EW (2005) Mechanisms of stretch-induced muscle damage in normal and dystrophic muscle: role of ionic changes. J Physiol 567:723–735
3. Aracena P, Tang W, Hamilton SL, Hidalgo C (2005) Effects of *S*-glutathionylation and *S*-nitrosylation on calmodulin binding to triads and FKBP12 binding to type 1 calcium release channels. Antioxid Redox Signal 7:870–881
4. Austin L, de Niese M, McGregor A, Arthur H, Gurusinghe A, Gould MK (1992) Potential oxyradical damage and energy status in individual muscle fibres from degenerating muscle diseases. Neuromuscul Disord 2:27–33
5. Banfi B, Molnar G, Maturana A, Steger K, Hegedus B, Demaurex N, Krause KH (2001) A Ca^{2+}-activated NADPH oxidase in testis, spleen, and lymph nodes. J Biol Chem 276:37594–37601
6. Bedard K, Krause KH (2007) The NOX family of ROS-generating NADPH oxidases: physiology and pathophysiology. Physiol Rev 87:245–313
7. Bellinger AM, Reiken S, Carlson C, Mongillo M, Liu X, Rothman L, Matecki S, Lacampagne A, Marks AR (2009) Hypernitrosylated ryanodine receptor calcium release channels are leaky in dystrophic muscle. Nat Med 15:325–330
8. Brookes PS, Yoon Y, Robotham JL, Anders MW, Sheu SS (2004) Calcium, ATP, and ROS: a mitochondrial love-hate triangle. Am J Physiol Cell Physiol 287:C817–C833
9. Buetler TM, Renard M, Offord EA, Schneider H, Ruegg UT (2002) Green tea extract decreases muscle necrosis in *mdx* mice and protects against reactive oxygen species. Am J Clin Nutr 75:749–753
10. Cave AC, Brewer AC, Narayanapanicker A, Ray R, Grieve DJ, Walker S, Shah AM (2006) NADPH oxidases in cardiovascular health and disease. Antioxid Redox Signal 8:691–728
11. Chang WJ, Iannaccone ST, Lau KS, Masters BS, McCabe TJ, McMillan K, Padre RC, Spencer MJ, Tidball JG, Stull JT (1996) Neuronal nitric oxide synthase and dystrophin-deficient muscular dystrophy. Proc Natl Acad Sci USA 93:9142–9147
12. De Backer F, Vandebrouck C, Gailly P, Gillis JM (2002) Long-term study of Ca^{2+} homeostasis and of survival in collagenase-isolated muscle fibres from normal and *mdx* mice. J Physiol 542:855–865
13. Deconinck AE, Rafael JA, Skinner JA, Brown SC, Potter AC, Metzinger L, Watt DJ, Dickson JG, Tinsley JM, Davies KE (1997) Utrophin–dystrophin-deficient mice as a model for Duchenne muscular dystrophy. Cell 90:717–727
14. Disatnik MH, Dhawan J, Yu Y, Beal MF, Whirl MM, Franco AA, Rando TA (1998) Evidence of oxidative stress in *mdx* mouse muscle: studies of the pre-necrotic state. J Neurol Sci 161:77–84
15. Dudley RW, Danialou G, Govindaraju K, Lands L, Eidelman DE, Petrof BJ (2006) Sarcolemmal damage in dystrophin deficiency is modulated by synergistic interactions between mechanical and oxidative/nitrosative stresses. Am J Pathol 168:1276–1287
16. Dudley RW, Khairallah M, Mohammed S, Lands L, Des Rosiers C, Petrof BJ (2006) Dynamic responses of the glutathione system to acute oxidative stress in dystrophic mouse (mdx) muscles. Am J Physiol Regul Integr Comp Physiol 291:R704–R710
17. Dupont E, Matsushita T, Kaba RA, Vozzi C, Coppen SR, Khan N, Kaprielian R, Yacoub MH, Severs NJ (2001) Altered connexin expression in human congestive heart failure. J Mol Cell Cardiol 33:359–371
18. Durham WJ, Aracena-Parks P, Long C, Rossi AE, Goonasekera SA, Boncompagni S, Galvan DL, Gilman CP, Baker MR, Shirokova N, Protasi F, Dirksen R, Hamilton SL (2008) RyR1 S-nitrosylation underlies environmental heat stroke and sudden death in Y522S RyR1 knockin mice. Cell 133:53–65
19. Ervasti JM, Campbell KP (1993) Dystrophin and the membrane skeleton. Curr Opin Cell Biol 5:82–87
20. Espinosa A, Leiva A, Pena M, Muller M, Debandi A, Hidalgo C, Carrasco MA, Jaimovich E (2006) Myotube depolarization generates reactive oxygen species through NAD(P) H oxidase; ROS-elicited Ca^{2+} stimulates ERK, CREB, early genes. J Cell Physiol 209:379–388
21. Hara Y, Wakamori M, Ishii M, Maeno E, Nishida M, Yoshida T, Yamada H, Shimizu S, Mori E, Kudoh J, Shimizu N, Kurose H, Okada Y, Imoto K, Mori Y (2002) LTRPC2 Ca^{2+}-permeable channel activated by changes in redox status confers susceptibility to cell death. Mol Cell 9:163–173
22. Hidalgo C, Sanchez G, Barrientos G, Aracena-Parks P (2006) A transverse tubule NADPH oxidase activity stimulates calcium release from isolated triads via ryanodine receptor type 1 S -glutathionylation. J Biol Chem 281:26473–26482
23. Hoffman EP, Brown RH Jr, Kunkel LM (1987) Dystrophin: the protein product of the Duchenne muscular dystrophy locus. Cell 51:919–928
24. Isaeva EV, Shirokova N (2003) Metabolic regulation of Ca^{2+} release in permeabilized mammalian skeletal muscle fibres. J Physiol 547:453–462
25. Isaeva EV, Shkryl VM, Shirokova N (2005) Mitochondrial redox state and Ca^{2+} sparks in permeabilized mammalian skeletal muscle. J Physiol 565:855–872
26. Jung C, Martins AS, Niggli E, Shirokova N (2008) Dystrophic cardiomyopathy: amplification of cellular damage by Ca^{2+} signalling and reactive oxygen species-generating pathways. Cardiovasc Res 77:766–773
27. Kuznetsov AV, Winkler K, Wiedemann FR, von Bossanyi P, Dietzmann K, Kunz WS (1998) Impaired mitochondrial oxidative phosphorylation in skeletal muscle of the dystrophin-deficient *mdx* mouse. Mol Cell Biochem 183:87–96
28. Lamb GD, Posterino GS (2003) Effects of oxidation and reduction on contractile function in skeletal muscle fibres of the rat. J Physiol 546:149–163
29. Marks A, Vianna DM, Carrive P (2009) Non-shivering thermogenesis without interscapular brown adipose tissue involvement during conditioned fear in the rat. Am J Physiol Regul Integr Comp Physiol 296:R1239–1247
30. Martins AS, Shkryl VM, Nowycky MC, Shirokova N (2008) Reactive oxygen species contribute to Ca^{2+} signals produced by osmotic stress in mouse skeletal muscle fibres. J Physiol 586:197–210
31. McCarter GC, Steinhardt RA (2000) Increased activity of calcium leak channels caused by proteolysis near sarcolemmal ruptures. J Membr Biol 176:169–174
32. Millay DP, Sargent MA, Osinska H, Baines CP, Barton ER, Vuagniaux G, Sweeney HL, Robbins J, Molkentin JD (2008) Genetic and pharmacologic inhibition of mitochondrial-dependent necrosis attenuates muscular dystrophy. Nat Med 14:442–447
33. Moylan JS, Reid MB (2007) Oxidative stress, chronic disease, and muscle wasting. Muscle Nerve 35:411–429
34. Nethery D, Callahan LA, Stofan D, Mattera R, DiMarco A, Supinski G (2000) PLA2 dependence of diaphragm mitochondrial formation of reactive oxygen species. J Appl Physiol 89:72–80

35. Niggli E, Shirokova N (2007) A guide to sparkology: the taxonomy of elementary cellular Ca^{2+} signaling events. Cell Calcium 42:379–387
36. Poteser M, Graziani A, Rosker C, Eder P, Derler I, Kahr H, Zhu MX, Romanin C, Groschner K (2006) TRPC3 and TRPC4 associate to form a redox-sensitive cation channel. Evidence for expression of native TRPC3-TRPC4 heteromeric channels in endothelial cells. J Biol Chem 281:13588–13595
37. Quinlan JG, Hahn HS, Wong BL, Lorenz JN, Wenisch AS, Levin LS (2004) Evolution of the mdx mouse cardiomyopathy: physiological and morphological findings. Neuromuscul Disord 14:491–496
38. Ragusa RJ, Chow CK, Porter JD (1997) Oxidative stress as a potential pathogenic mechanism in an animal model of Duchenne muscular dystrophy. Neuromuscul Disord 7:379–386
39. Ragusa RJ, Chow CK, St Clair DK, Porter JD (1996) Extraocular, limb and diaphragm muscle group-specific antioxidant enzyme activity patterns in control and *mdx* mice. J Neurol Sci 139:180–186
40. Reid MB (2001) Redox modulation of skeletal muscle contraction: what we know and what we don't. J Appl Physiol 90:724–731
41. Robert V, Massimino ML, Tosello V, Marsault R, Cantini M, Sorrentino V, Pozzan T (2001) Alteration in calcium handling at the subcellular level in mdx myotubes. J Biol Chem 276:4647–4651
42. Shirokova N, Garcia J, Rios E (1998) Local calcium release in mammalian skeletal muscle. J Physiol 512:377–384
43. Shkryl VM, Shirokova N (2006) ROS scavengers inhibit stress-induced Ca^{2+} sparks in skeletal muscle fibers. Biophys J:67a
44. Shkryl VM, Shirokova N (2006) Transfer and tunneling of Ca^{2+} from sarcoplasmic reticulum to mitochondria in skeletal muscle. J Biol Chem 281:1547–1554
45. Stamler JS, Meissner G (2001) Physiology of nitric oxide in skeletal muscle. Physiol Rev 81:209–237
46. Tidball JG, Wehling-Henricks M (2007) The role of free radicals in the pathophysiology of muscular dystrophy. J Appl Physiol 102:1677–1686
47. Tidball JG, Albrecht DE, Lokensgard BE, Spencer MJ (1995) Apoptosis precedes necrosis of dystrophin-deficient muscle. J Cell Sci 108:2197–2204
48. Vandebrouck A, Sabourin J, Rivet J, Balghi H, Sebille S, Kitzis A, Raymond G, Cognard C, Bourmeyster N, Constantin B (2007) Regulation of capacitative calcium entries by alpha1-syntrophin: association of TRPC1 with dystrophin complex and the PDZ domain of alpha1-syntrophin. FASEB J 21:608–617
49. Wang X, Weisleder N, Collet C, Zhou J, Chu Y, Hirata Y, Zhao X, Pan Z, Brotto M, Cheng H, Ma J (2005) Uncontrolled calcium sparks act as a dystrophic signal for mammalian skeletal muscle. Nat Cell Biol 7:525–530
50. Wehling M, Spencer MJ, Tidball JG (2001) A nitric oxide synthase transgene ameliorates muscular dystrophy in *mdx* mice. J Cell Biol 155:123–131
51. Whitehead NP, Pham C, Gervasio OL, Allen DG (2008) N-Acetylcysteine ameliorates skeletal muscle pathophysiology in *mdx* mice. J Physiol 586:2003–2014
52. Yasuda S, Townsend D, Michele DE, Favre EG, Day SM, Metzger JM (2005) Dystrophic heart failure blocked by membrane sealant poloxamer. Nature 436:1025–1029
53. Yeung EW, Whitehead NP, Suchyna TM, Gottlieb PA, Sachs F, Allen DG (2005) Effects of stretch-activated channel blockers on $[Ca^{2+}]i$ and muscle damage in the mdx mouse. J Physiol 562:367–380

2.5 Кальцій-індукована активація RyRs та вивільнення Ca^{2+} з саркоплазматичного ретикулуму у скелетних м'язах

Сигналом для скорочення м'язів є різке збільшення цитозольної концентрації Ca^{2+}, що вимагає координованого відкриття ріанодинові рецептори у саркоплазматичному ретикулумі. Внесок Ca^{2+}-індукованого вивільнення Ca^{2+} у ініціацію скелетного м'язового скорочення залишається предметом дискусій. Кальцій індуковане вивільнення кальцію має бути здійснено тільки завдяки кальцію, без одночасно залучення інших процесів (Endo, 2009).

Для з’ясування механізму залучення CICR при активації RyRs кальцієм у скелетних м’язах ссавців та амфібій ми використовували двофотонне фотовивільнення Ca^{2+} з нітродибензофурану NDBF-EGTA для отримання штучного локалізованого підвищення концентрації [Ca^{2+}] (SLICs). Таке збільшення [Ca^{2+}] може бути згенерованим безпосередньо за межами пермеабілізованої плазматичної мембрани. SLICs дозволили швидко та зворотно збільшити цитозольний [Ca^{2+}] до 8 мкМ, до рівнів, подібних до тих, що досягаються під час фізіологічної активності.

На рис. 2.10А зображено SLICs у двовимірному режимі x-y. SLICs було отримано шляхом опромінення розчину, який містив 3 мМ NDBF-EGTA, згідно дослідженню (Momotake et al., 2006). NDBF-EGTA має дві ключові особливості: він має низьку афінність до Mg^{2+}, що дозволяє незалежно модифікувати концентрацію Mg^{2+}, а також відзначається підвищеною двофотонною афінністю, завдяки якій можливе звільнення великої кількості Ca^{2+} при рівнях опромінення, які є безпечними для клітин. Зображення флуоресценції Fluo-4FF були отримані за допомогою LSM 5 LIVE з частотою 3.47 мс на зображення. На рисунку показано кожний другий кадр до 41-го в серії з 200 кадрів. Спалах для фотоактивації відбувся приблизно за 2 мс до третього представленого кадру. На рис. 2.10В відображено значення [Ca^{2+}] у центрі SLICs для кожного кадру.

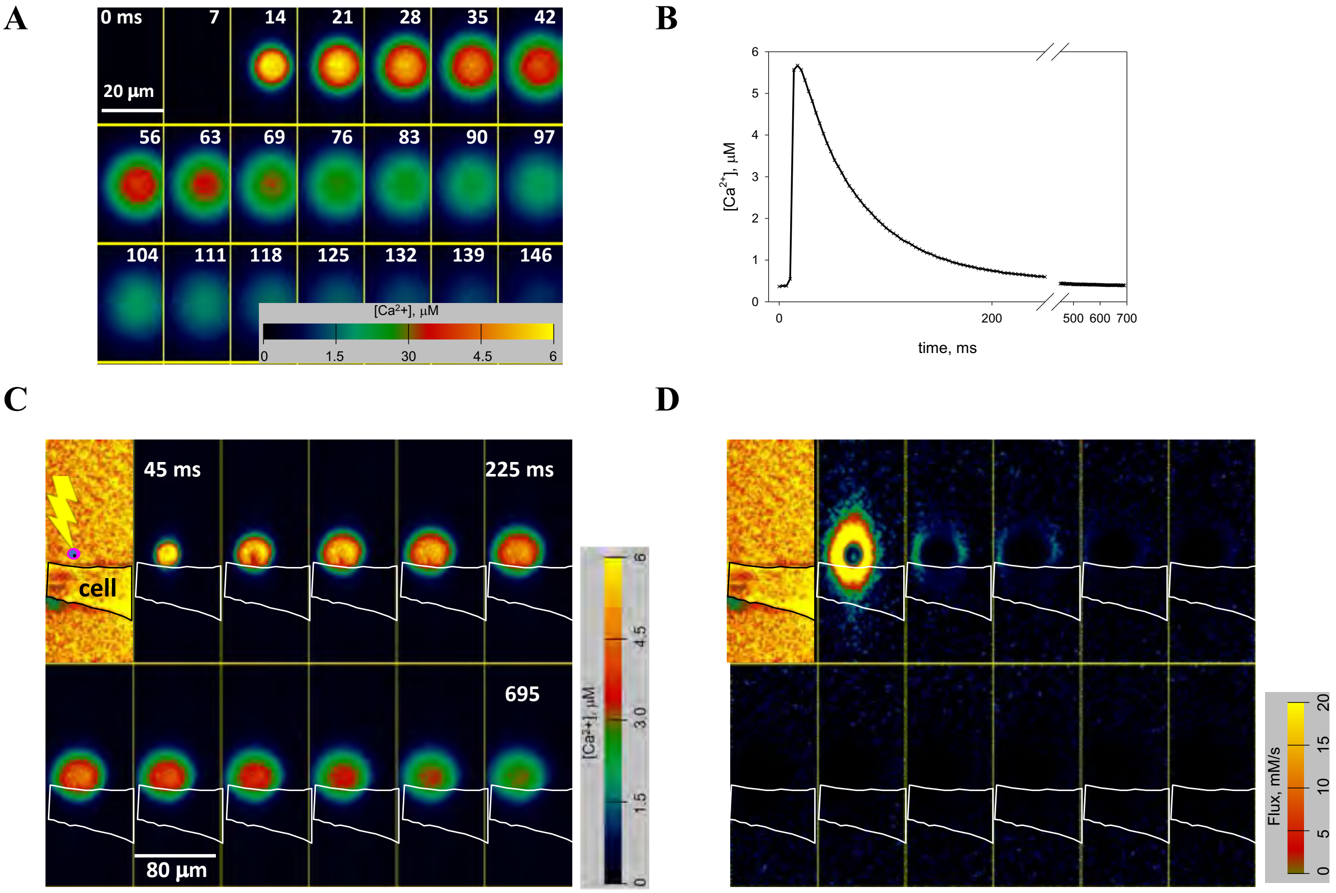

Рисунок 2.10. Скелетний м'яз миші в нормі не здатні до CICR. (A) Фрагменти F(x,y,t) транзієнта, згенерованого за рахунок SLICs, отриманого точковим опроміненням тривалістю 0.1 мс у краплі внутрішньоклітинного розчину, що містить 3 мМ NDBF-EGTA, із вимірюваним вмістом вільного [Ca^{2+}] = 0.374 мкМ. Зображення SLICs було отримано у двовимірному просторі, з частотою 3.47 мс на кадр і 0.44 мкм на піксель. Наведено кожні два з перших 42 кадрів з 100-кадрової серії. Час фіксації кожного кадру вказано приблизно в мілісекундах. ІЧ-спалах застосовано за 2 мс до третього продемонстрованого кадру. Для моніторингу Ca^{2+} використовували 100 мкМ Fluo-4FF. (B) Концентрація вільного кальцію, побудована для зображень з частини A, та усереднена в центральних 25 пікселях SLICs. (C) Зображення [Ca^{2+}] (x,y,t) пермеабілізованого волокна миші, збалансованого розчином, що містить 3 мМ NDBF-EGTA і 0.3 мкМ вільного [Ca^{2+}], у відповідь на SLICs на відстані 3 мкм від клітини. На першому кадрі зображено положення клітини, контури якої позначено білою лінією на двох верхніх зображеннях. Представлено одне зображення з кожних п'яти кадрів з серії, отриманої з інтервалом 9 мс. (D) Потік Ca^{2+}, розрахований на основі відповідних кадрів [Ca^{2+}] (x,y,t) з частини C. Зверніть увагу на повну відсутність вивільнення Ca^{2+} всередині клітини.

SLICs також застосовували до окремих скелетних волокон FDB, які були ферментативно дисоційовані з миші. Клітини пермеабілізовували та балансували за допомогою внутрішнього середовища. Репрезентативний експеримент наведено на рис. 2.10C. На першому кадрі зображено клітину як F(x,y); контур клітини виділений на інших фреймах. Як видно, SLICs не ініціювали вивільнення Ca^{2+} в клітинах миші. Аналіз потоку (див. рис. 2.10D) свідчить про повну відсутність вивільнення Ca^{2+} в цих клітинах. Умови експерименту, при яких не спостерігалося жодної реакції, включали концентрації Mg^{2+} від 0.045 до 3 мМ, вільного $[Ca^{2+}]$ в покої від 0.05 до 2 мкМ, а також великі концентрації "кейджу" (або NDBF-EGTA, або DM-nitrophen). Ці "кейджі" фотолізували у формі плям або спіралей при високій інтенсивності лазерного випромінювання, і цей процес повторювався до 10 разів, досягаючи рівнів Ca^{2+} до 8 мкМ у точці контакту з клітиною. Експерименти за високого цитозольного $[Ca^{2+}]$ проводилися з метою стимулювання CICR шляхом збільшення вільного та загального навантаження Ca^{2+} у СР, проте результати значно не відрізнялися.

Канали RyR1 активуються іонами Ca^{2+} з цитозольного боку (див. огляд (Fill and Copello, 2002)). Така властивість характерна для всіх ізоформ. Відомо, що чутливість до активації Ca^{2+} більш виражена у β субодиниці порівняно з α субодиницею RyRs [Murayama, 2001 #132] і у RyR3 порівняно з RyR1 [Murayama, 2004 #133]. Однак залишається несподіваним абсолютна нездатність клітин миші відповідати in situ на наші Ca^{2+}-стимули. Дійсно, вивільнення Ca^{2+} не спостерігалося, навіть коли рівень тригерних імпульсів був у 20 разів вищим, ніж той, що необхідний для викликання відповіді в м'язових клітинах жаби (див. нижче). І це при концентраціях $[Mg^{2+}]$, що є нижчими за найнижчі оцінені значення K_D інгібіторної ділянки каналу (Copello et al., 2002, Laver et al., 1997).

В наступному експерименті досліджувалась здатність до CICR, за рахунок каналів RyR1 при певних нефізіологічних умовах – низький вміст $[Mg^{2+}]$ (лише 0.045 мМ). Ця умова була перевірена у 33 експериментах на 8 клітинах, при яких тригерний $[Ca^{2+}]$ досягав 3.2 мкМ, проте не призводив до очікуваної реакції. Ми також використовували SLICs для клітин миші у присутності речовин, відомих своєю здатністю стимулювати активність каналів. Зокрема, ми використовували кофеїн і 4-CMC (Westerblad et al., 1998) – хімічні агенти, які сприяють відкриттю каналів, і, принаймні у випадку кофеїну, підвищують чутливість каналів до Ca^{2+}. Зазначені речовини вводили в концентраціях, які самостійно не призводили до вивільнення Ca^{2+}. Концентрацію [Mg^{2+}] тримали на рівні 0.3 або 0.5 мМ.

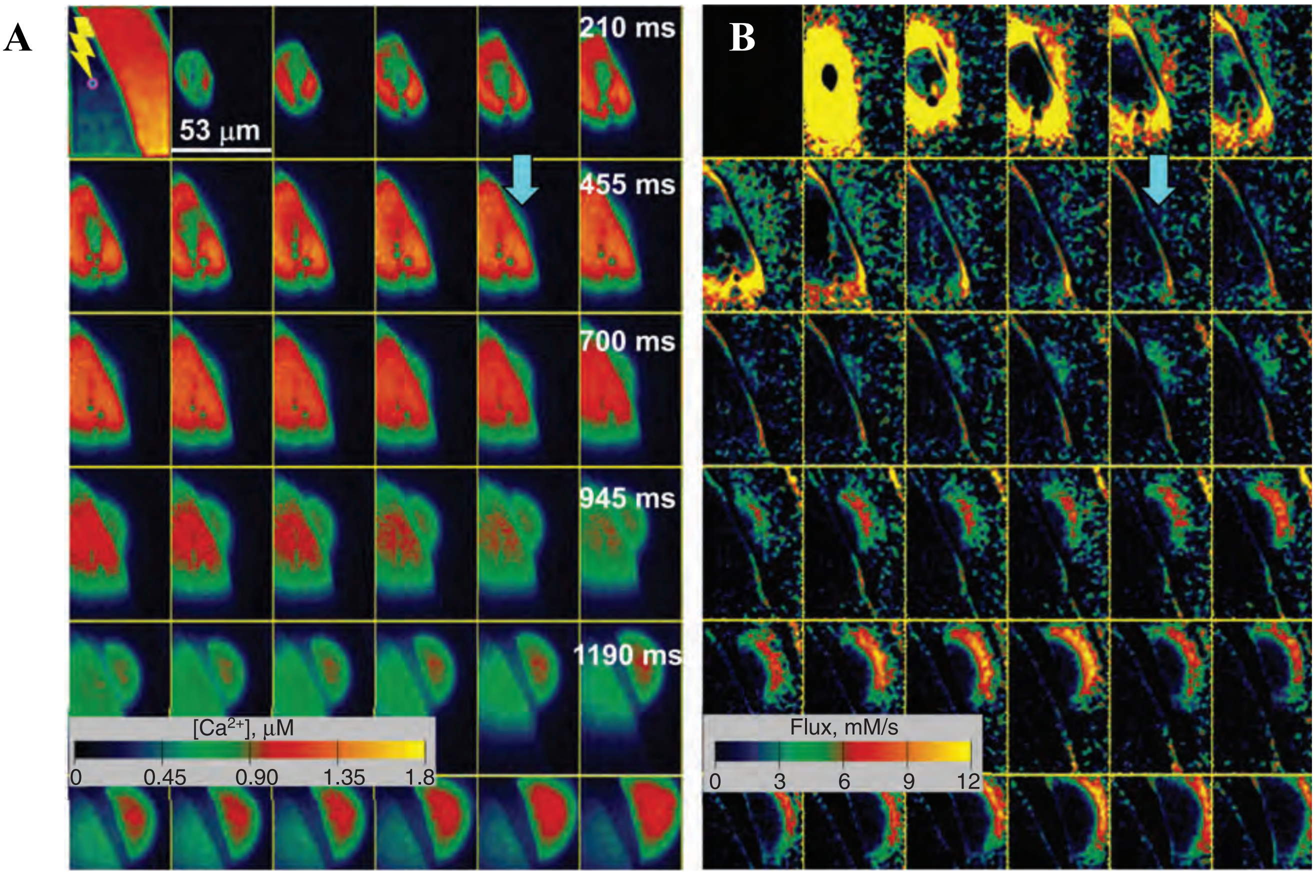

Рисунок 2.11. Ca^{2+}-сенсибілізуючі речовини підсилюють розповсюдження вивільнення кальцію у скелетних м'язових волокнах миші. (A) [Ca^{2+}] (x,y,t) з пермеабілізованого волокна FDB, яке було врівноважено внутрішнім розчином із 0.4 мМ 4-CMC та 1.8 мМ кофеїну (0.08 мкМ вільного Ca^{2+} та 0.5 мМ вільного Mg^{2+}). В якості стимулу використовувався макро SLICs великої амплітуди та тривалості, згенерований ззовні клітини. Макро SLICs викликав поширену відповідь у волокні. (B) Потік Ca^{2+} (x,y), отриманий із зображень [Ca^{2+}] в частині A. Периферійна хвиля вивільнення стає відчутною на 400-500 мс (вказано стрілкою).

У клітинах, які перебували у розчині із 1 мМ кофеїну та 0.1 мМ 4-CMC, ані зовнішні SLICs, ані застосовані безпосередньо у межах клітин, не викликали реакції. Ми реєстрували відповіді на SLICs, коли кофеїн та 4-CMC були присутні одночасно у концентраціях 1.8 мМ та 0.4 мМ відповідно. Приклад наведено на рис. 2.11, де периферійна хвиля утворювалась та поширювалася без затухання. Хвиля формувалася повільно із тривалою фазою зростання, яка розпочиналася лише після того, як макро SLICs існував близько 500 мс (точка старту та приблизний час показані стрілками на панелях А та В). Середнє значення потоку кальцію, який вивільнюється з СР в м'язах ссавців при використанні сенсибілізуючих речовин ріанодинових рецепторів складали 15.1±1.2 мМ/с, з середньою швидкістю поширення хвилі 46.6±7.7 мкм/с (13 клітин). Висновок з цих експериментів полягає в тому, що скелетні м'язи миші можуть демонструвати CICR, але це можливо лише за фармакологічної стимуляції відкриття каналів, тобто поза фізіологічними умовами.

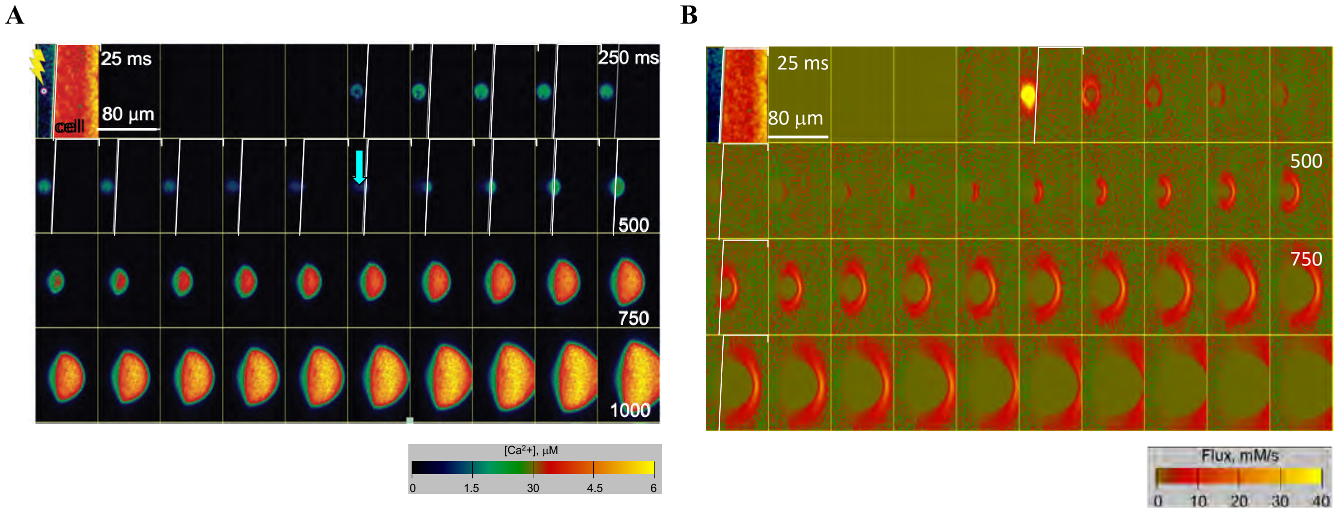

Рисунок 2.12. Розподілена відповідь на SLICs у м'язовій клітині жаби. (А) Зображення зміну Ca^{2+} у скелетному м'язі жаби. Перший кадр демонструє флуоресценцію в режимі покою та положення клітини. З 6-го кадру, межі клітини позначено білою лінією. Місце ІЧ-випромінювання, що було застосовано для створення SLICs, відзначено спалахом (під час отримання 6-го кадру). З 16-го кадру, відзначеного стрілкою, всередині клітини можна спостерігати реакцію. Початкова концентрація $[Ca^{2+}]$, визначена як значення, зафіксоване безпосередньо за межами клітини на кадрі, де була зафіксована перша клітинна відповідь, була приблизно 0.7 мкМ (див. 2-гу стрілку поряд з відповідним значенням на кольоровій шкалі). (В) Потік Ca^{2+} (x,y,t), виведений з послідовності $[Ca^{2+}]$(x,y,t), представленої в частині А. Потік вивільнення представляє собою радіальну хвилю, що виходить від початкової точки. Зверніть увагу на анізотропію хвилі потоку: вона має вищий пік, але вузький просторовий профіль та трохи меншу швидкість поширення на "екваторі" (горизонтально на рисунку).

Наступне дослідження SLICs як стимулів, проведене на скелетних м'язових клітинах жаби, представлено на рис. 2.12. Після пермеабілізації плазматичної мембрани за допомогою сапоніну, клітини були врівноважені розчином з NDBF-EGTA та Fluo-4 FF. У скелетних м'язах жаби SLICs викликали реакції, що мали характеристики CICR. Поріг [Ca^{2+}] для ініціації відповіді вивільнення Ca^{2+} з СР при відкритті RyRs каналів був приблизно 0.5 мкМ. Оскільки це значення значно менше концентрацій, що спостерігаються поблизу каналів під час звичайної активності, це свідчить на користь участі CICR у фізіологічному регулюванні скорочення м'язів амфібій. Аналіз потоків (рис. 2.12В) виявив постійне вивільнення Ca^{2+} у клітині. Вивільнення потоків кальцію мало різні швидкості, від 9 до 55 мМ/с (середнє значення 22.7±1.6), та відрізнялося швидкістю поширення від 30 до 300 мкм/с (середнє значення 98.9±10.2) у 16 вивчених клітинах. Реакція клітини на CICR зазвичай починалася з початкового підвищення амплітуди, досягала піку і залишалася стабільною під час поширення хвилі по клітині до моменту виходу за межі зображення.

У м'язах жаби збільшення Ca^{2+} викликало активацію RyRs, із вивільнення даного іону з СР, які мали характеристики CICR. Поріг [Ca^{2+}] в цих клітинах для запуску RyRs опосередкованого вивільнення, що розповсюджувалась вдовж клітини, становив 0.5 мкМ. Оскільки ця величина набагато нижча за концентрації, які можна спостерігати біля каналів під час нормальної активності, результат підтверджує участь CICR у фізіологічному контролі скорочення в м'язах амфібій.

Навпаки, скелетні м'язові волокна миші не реагували на збільшення концентрації кальцію аж до 8 мкМ, якщо препарати, що відкривають RyRs канали, не були присутні у значних концентраціях, що суперечить фізіологічному залученню CICR у процесі збудження-скорочення у скелетних м’язах ссавців. У м'язах миші хвиля кальцію, що поширюється, мала значно менший потік вивільнення кальцію, що разом із вищим порогом активації каналів RyRs обумовлює відсутність розповсюдження відповіді, якщо відсутні препарати що полегшують відкриття RyRs.

Скелетні м'язи дорослих ссавців мають переважно ізоформу RyR1. Але м'язи жаби експресують майже однакову кількість двох ізоформ RyRs, які називаються α- та β-RyR (Murayama and Ogawa, 1992, Olivares et al., 1991). RyR1 у своїй первинній структурі є гомогенній до субодиниці α RyR та опосередковує вивільнення Ca^{2+}, спричинене лише деполяризацією – датчиком напруги (Ottini et al., 1996). Відомо, що чутливість до активації Ca^{2+} більш виражена у β субодиниці порівняно з субодиницею α RyRs (Murayama and Ogawa, 1992), тобто β -RyR опосередковує кальцій-індуковане вивільнення Ca^{2+} у скелетних м'язах не ссавців.

За структурними ознаками дорослі м'язи не ссавців мають додаткову ізоформу RyR, β (дивись огляд (Sutko and Airey, 1996)), яка є гомологічною до "мозкової" ізоформи 3, RyR3 ссавців і займає парафункціональну позицію на поверхні СР (Felder and Franzini-Armstrong, 2002), що знаходиться поза межами прямого контролю DHPR. З функціональних міркувань було показано, що вивільнення Ca^{2+} у м'язах жаб складається з спалахів Ca^{2+}, тоді як ефект відсутній у ссавців, якщо тільки вони не експресують екзогенний RyR3 (Pouvreau et al., 2007). На цій основі припускають, що вивільнення Ca^{2+} у м'язах жаб має специфічний CICR-компонент, опосередкований RyR β, який здебільшого має форму спалаху (Stern et al., 1997, Shirokova and Ríos, 1997), але цей механізм відсутній у дорослих м'язах миш і щурів. Важливо зауважити, що ізоформа RyR β є гомогенною до RyR3, які розповсюджені у нервових клітинах (Ottini et al., 1996, Oyamada et al., 1994). Іншими словами, ріанодинові рецептори нервових клітин мають можливість активуватися за рахунок CICR.

J Physiol 590.6 (2012) pp 1389–1411

The Journal of Physiology

Synthetic localized calcium transients directly probe signalling mechanisms in skeletal muscle

Lourdes Figueroa[1], Vyacheslav M. Shkryl[1], Jingsong Zhou[1], Carlo Manno[1], Atsuya Momotake[2], Gustavo Brum[3], Lothar A. Blatter[1], Graham C. R. Ellis-Davies[4] and Eduardo Ríos[1]

[1] *Section of Cellular Signaling, Department of Molecular Biophysics and Physiology, Rush University, 1750 W. Harrison St, Chicago, IL 60612, USA*
[2] *Tsukuba University, Ibaraki, Japan*
[3] *Department of Biophysics, School of Medicine, Universidad de la República, Montevideo, Uruguay*
[4] *Department of Neuroscience, Mount Sinai School of Medicine, New York, NY 10029-6574, USA*

Key points

- The signal for skeletal muscle contraction is a rapid increase in cytosolic Ca^{2+} concentration, which requires the coordinated opening of ryanodine receptor (RyR) channels in the sarcoplasmic reticulum.
- Channel opening is controlled by voltage-sensing dihydropyridine receptors (DHPRs) of plasma membrane and T tubules. Whether or not their signal is amplified by Ca^{2+}-induced Ca^{2+} release (CICR) is controversial.
- We used two-photon lysis of an advanced Ca^{2+} cage to produce local Ca^{2+} concentration transients that were large, fast, reproducible and quantifiable, while monitoring the cellular response with a dual confocal laser scanner.
- Single frog muscle cells in physiological solutions responded to transients greater than 0.28 μM with propagated CICR waves.
- Mouse cells did not respond to stimuli up to 8 μM, unless channel opening drugs were present.
- We conclude that CICR contributes to physiological Ca^{2+} release in frog but not mouse muscle.
- Mice and presumably other mammals do have a capability for CICR that is normally inhibited. It could be manifested under special circumstances, including diseases.

Abstract The contribution of Ca^{2+}-induced Ca^{2+} release (CICR) to trigger muscle contraction is controversial. It was studied on isolated muscle fibres using synthetic localized increases in Ca^{2+} concentration, SLICs, generated by two-photon photorelease from nitrodibenzofuran (NDBF)-EGTA just outside the permeabilized plasma membrane. SLICs provided a way to increase cytosolic $[Ca^{2+}]$ rapidly and reversibly, up to 8 μM, levels similar to those reached during physiological activity. They improve over previous paradigms in rate of rise, locality and reproducibility. Use of NDBF-EGTA allowed for the separate modification of resting $[Ca^{2+}]$, trigger $[Ca^{2+}]$ and resting $[Mg^{2+}]$. In frog muscle, SLICs elicited propagated responses that had the characteristics of CICR. The threshold $[Ca^{2+}]$ for triggering a response was 0.5 μM or less. As this value is much lower than concentrations prevailing near channels during normal activity, the result supports participation of CICR in the physiological control of contraction in amphibian muscle. As SLICs were applied outside cells, the primary stimulus was Ca^{2+}, rather than the radiation or subproducts of photorelease. Therefore the responses qualify as 'classic' CICR. By contrast, mouse muscle fibres did not respond unless channel-opening drugs were present at substantial concentrations, an observation contrary to the physiological involvement of CICR in mammalian excitation–contraction coupling. In mouse muscle, the propagating wave had a

DOI: 10.1113/jphysiol.2011.225854

substantially lower release flux, which together with a much higher threshold justified the absence of response when drugs were not present. The differences in flux and threshold may be ascribed to the absence of ryanodine receptor 3 (RyR3) isoforms in adult mammalian muscle.

(Received 6 December 2011; accepted after revision 1 February 2012; first published online 6 February 2012)

Corresponding author E. Ríos: Section of Cellular Signaling, Department of Molecular Biophysics and Physiology, Rush University School of Medicine, 1750 W. Harrison St, Suite 1279JS, Chicago, IL 60612, USA. Email: erios@rush.edu

Abbreviations CICR, Ca^{2+}-induced Ca^{2+} release; DICR, depolarization-induced Ca^{2+} release; DHPR, dihydropyridine receptor; EC, excitation–contraction; FDB, flexor digitorum brevis; NDBF, nitrodibenzofuran; 2P, two-photon; RyR, ryanodine receptor; SERCA, sarcoplasmic reticulum Ca^{2+}-ATPase; SLIC, synthetic localized increase in Ca^{2+} concentration; SR, sarcoplasmic reticulum; T tubules, transverse tubules.

Introduction

In both cardiac and skeletal muscle, contraction is mediated by a transient increase in cytosolic calcium ion concentration, $[Ca^{2+}]_c$, which requires the release of a large amount of calcium from the sarcoplasmic reticulum (SR). In fast skeletal muscles fluxes of as much as 300 mmol l^{-1} of myoplasmic water per second have been measured (Pape *et al.* 1993; Baylor & Hollingworth, 2003).

Such high flux levels are reached by near-simultaneous opening of ryanodine receptor (RyR) channels clustered in T tubule–SR junctions. The high synchronicity is insured first by the fast propagation down T tubules of membrane depolarization, which is translated by dihydropyridine receptors (DHPRs; Fosset *et al.* 1983) into signals that cause RyR channels to open. In cardiac cells, DHPRs open to allow entry of a small amount of trigger Ca^{2+}, which inside the cells causes Ca^{2+} release channels to open and amplify the signal (reviewed by Bers, 2002). The phenomenon, named Ca^{2+}-induced Ca^{2+} release or CICR, was first described in skeletal muscle 41 years ago (Ford & Podolsky, 1970; Endo *et al.* 1970). This historical fact is surprising because in skeletal muscle DHPRs (Ríos & Brum, 1987; Tanabe *et al.* 1987) pass the opening signal to RyRs by mechanical transmission (Schneider & Chandler, 1973; Nakai *et al.* 1996) in a process that does not require Ca^{2+} as a messenger (Armstrong *et al.* 1972).

DHPRs, however, are not in mechanical contact with every release channel. To constitute a functional unit (called the couplon; Stern *et al.* 1997), they align with RyR1 in a strict 1:2 stoichiometry, appearing to come in contact with alternate channels in a checkered array (Block *et al.* 1988). On this basis, it was proposed that RyRs not directly overlapping with DHPRs could be activated by Ca^{2+} (Ríos & Pizarro, 1988). A role of CICR in Ca^{2+} release was later supported by work on cut fibres of the frog under voltage clamp (Jacquemond *et al.* 1991) and skinned fibres of a crustacean (Launikonis & Stephenson, 2000).

The view that CICR contributes to physiological Ca^{2+} release in skeletal muscle, however, remains controversial. As authoritatively formulated by Endo (2009), two main observations argue against it: one is that presumably physiological Ca^{2+} fluxes measured in intact or voltage-clamped cells (reviewed in Royer *et al.* 2008) are enormously greater than the maximum rates of CICR measured in skinned fibres and SR fractions (Murayama *et al.* 2000). The other is that to qualify as CICR, Ca^{2+} release must be induced by Ca^{2+} alone, without the simultaneous action of other processes. Thus, for example, Ca^{2+} sparks, which in cardiac muscle are considered a paradigm of CICR (Cheng *et al.* 1993), in skeletal muscle may not be a clean manifestation of CICR because they are initiated by the DHPR voltage sensor and can also be cut short by repolarization (Lacampagne *et al.* 2000).

An intermediate possibility has been frequently considered, that CICR contributes to activation, but only in non-mammalian species. On structural grounds, non-mammalian adult muscle has an additional isoform of RyR, β (reviewed by Sutko & Airey, 1996), which is homologous to the 'brain' isoform 3, RyR3, of mammals and occupies a parajunctional position on the SR surface (Felder & Franzini-Armstrong, 2002), beyond the reach of direct control by DHPR. On functional grounds it has been shown that the Ca^{2+} release of frog muscle is composed of Ca^{2+} sparks, while that of mammals is not, unless they express exogenous RyR3 (Pouvreau *et al.* 2007). On this basis it is proposed that Ca^{2+} release in frog muscle has a specific CICR component mediated by RyR β, which largely takes the form of sparks (Shirokova & Ríos, 1997; Stern *et al.* 1997) and is absent in adult wild-type muscle of mice and rats.

However, two sets of observations cast some doubt on a species-specific operation of CICR. Initial comparisons showed that the time course of release flux (under voltage clamp depolarization or in trains of action potentials), which is characterized by an early peak followed by a lower slowly varying level, had a proportionally much greater peak component in the frog (Shirokova *et al.* 1996). The excess peak and its peculiar voltage dependence were attributed to the CICR portion of the activity. However, later measurements demonstrated large early peaks in mouse muscle as well (e.g. Ursu *et al.* 2005). Additionally, there is evidence, both from experiments on bilayer-reconstituted channels (Tripathy & Meissner

1996 – but see Liu *et al.* 2010) and frog cells (Fénelon & Pape, 2002) that channels experience activation and prolongation of openings by their own permeating Ca^{2+}. Such autoregulatory CICR cannot be disproved by classic tests of CICR (like suppression by a fast acting Ca^{2+} buffer) and therefore these tests do not constitute decisive tools for comparisons between species.

Two controversial issues are therefore addressed in the present work: whether or not there is a contribution by CICR to physiological Ca^{2+} release and whether this contribution is different in mammals and amphibians. As first done by Lipp & Niggli (1998) to probe the response of cardiac myocytes, we test these possibilities directly, by introducing as stimuli synthetic localized increases of Ca^{2+}, called SLICs for brevity, produced by 2-photon (2P) release of caged Ca^{2+}. SLICs are local, of very rapid onset and termination, of controllable magnitude, and indefinitely repeatable. Their use as stimuli offers one way to overcome the first of Endo's objections. Indeed, the large discrepancy existing between depolarization-induced release flux and measured CICR rates could be evidence not of CICR's irrelevance but of inadequacy of the protocols used for its measurement. It is possible that the ability of SR fractions and skinned fibres to release Ca^{2+} is comparatively degraded, and it is likely that the techniques used to synchronize their channels might not be sufficiently rapid, allowing inactivation to interfere. By contrast, SLICs can be made to reach concentrations of several micromolar in less than a millisecond.

Additionally, SLICs applied as we do here provide a nearly pure increase in $[Ca^{2+}]$, which does not include other changes. This satisfies the second requirement of a test of true CICR. Finally, they can be applied with identical characteristics to similarly prepared muscle cells from different species, therefore being ideally suited for objective comparisons of frogs and mice.

Two technical advances allowed us to improve on earlier uses of localized photorelease (Lipp & Niggli, 1998; Lindegger & Niggli, 2005): one is the availability of a dual scanner, namely, two laser scanners of fluorescence converging on one microscope and preparation (Noguchi *et al.* 2005), whereby Ca^{2+} ions can be photoreleased by light from one scanner (the 'actuator'), while the other is used to image a Ca^{2+} monitor. This advance allowed for x–y imaging of the cellular response and for triggers of extremely brief onset and termination. An additional novelty is the use of NDBF-EGTA (Momotake *et al.* 2006), a Ca^{2+} cage with the dual advantage of an increased 2P cross-section that enabled efficient local production of Ca^{2+} and a low affinity for Mg^{2+}. Mg^{2+}, a major physiological inhibitor of CICR, could therefore be present at physiological concentrations (Blatter, 1990; Westerblad & Allen, 1992) and independently varied in the present studies.

SLICs have time course, flux and spatial features reminiscent of biological sparks. The aim of their use in this work, however, is not to test whether actual sparks would induce a response, but whether Ca^{2+} release can be triggered by a Ca^{2+} transient similar to that produced by the primary response (depolarization-induced Ca^{2+} release, DICR) to depolarization. A simulation of such transients (in the Appendix) shows that SLICs are appropriate for this test.

Methods

Ethical approval

All experiments performed in this study were in compliance with the NIH Guide for the Care and Use of Laboratory Animals, and were approved by the Institutional Animal Care and Use Committee (IACUC) of the Rush University Medical Center.

Preparation of cells

Experiments were performed in segments of fibres from semitendinosus muscle of *Rana pipiens* dissected manually or in fibres separated enzymatically from flexor digitorum brevis (FDB) of 7- to 12-week-old mice (*Mus musculus*, Swiss Webster). In brief, frogs were killed by double pithing under deep anesthesia, achieved by immersion for 10 min in an aqueous solution of MS-222 (500 mg l^{-1}, pH 7.0–7.5). Frog fibres were dissected in a relaxing solution (Zhou *et al.* 2004), fixed to the glass bottom of a 50 μl Lucite chamber, and moderately stretched to sarcomere length of 2.5–3.2 μm. FDB muscles were enzymatically digested by 2 mg ml^{-1} collagenase Type I (Sigma-Aldrich Co., USA) in MEM-alpha medium (Invitrogen, USA), plus 10% fetal bovine serum (FBS) for 45 min at 37°C. About 10–20 dissociated single fibres were transferred with normal Tyrode solution directly to the glass bottom of the chamber, leaving them sticking to it for at least 10 min before the experiment. On the stage of the microscope, fibres were membrane-permeabilized by 2 min exposure to 0.004% saponin. After saponization, fibres were equilibrated in an internal solution containing a calcium cage, usually NDBF-EGTA and occasionally DM-nitrophen, and a calcium monitor, Fluo-4 FF. We used the laser scanning confocal microscope Zeiss LSM 5 DUO (Carl Zeiss, Oberkochen, Germany) consisting of two scanners converging simultaneously in an inverted microscope (Axio Observer.Z1 SP) equipped with a 40×, 1.2 NA water-immersion objective. The Zeiss LSM 5 DUO confocal microscope unites the LSM 510 scanner, used to photorelease calcium by 2P excitation with microsecond time resolution, with the LSM 5 LIVE scanner, used for imaging calcium at high speed.

Solutions

To simplify comparison with earlier work, we used experimental solutions described by Zhou *et al.* (2003, 2004). For reasons discussed by Zhou *et al.* (2003), largely a beneficial effect on frequency and stability of sparks in mammalian muscle, internal solutions were sulfate based. Their composition was (in mM): K_2SO_4 75 (frog) or 85 (mouse), NDBF-EGTA 3.0–3.5, Fluo-4 FF (pentapotassium salt; Invitrogen, Carlsbad, CA, USA) 0.1, Na_2-phosphocreatine 5, Na_2ATP 5, glucose 10, Hepes 10 and BTS 0.075 (*N*-benzyl-*p*-toluene sulphonamide), plus dextran 8%. The nominal [Ca^{2+}] and [Mg^{2+}], which varied in the range 0.05–2 μM and 0.045–3 mM, respectively, were set by addition of chloride salts, in quantities calculated by the program winmaxc32 version 2.51 (maxchelator.stanford.edu; *Bers et al.* 2010) taking into account the relevant ligands and assuming a temperature of 20°C and an ionic strength calculated from the final composition of each solution as 0.170 N (frog) or 0.188 N (mouse). All internal solutions were titrated to pH 7.2 and adjusted with K_2SO_4 to 265 ± 5 mosmol kg^{-1} (frog) or 320 ± 5 mosmol kg^{-1} (mouse). Experiments were performed at room temperature (19–22°C). Pharmacological conditioning experiments in FDB fibres were performed in internal solutions containing well-known activators of RyR activity (reviewed in Endo, 2009) at concentrations that do not cause visible Ca^{2+} release: 1 to 2 mM of caffeine, 0.1 to 0.4 mM of 4-CMC (4-chloro-3-methylphenol (also known as *p*-chlorocresol)), and 1.5 to 4.5 mM of clofibrate (2-(*p*-chlorophenoxy)-methylpropionic acid). In every case the experiment was followed by application of the drugs at greater concentrations (20, 4 and 20 mM, respectively). This application invariably resulted in massive release. All drugs were purchased from Sigma-Aldrich Co. (St Louis, MO, USA).

Photorelease of caged Ca^{2+}

Cells were equilibrated with an internal solution containing 3–3.5 mM of the cage NDBF-EGTA and a range of [Ca^{2+}] between 0.05 and 2 μM, or in some cases a solution with 15 mM of the cage DM-nitrophen (tetrasodium salt; Calbiochem, La Jolla, CA, USA). Infrared (IR) light of 720 nm was applied in 2P excitation mode by a Ti–sapphire femtosecond tunable laser (MaiTai, Newport Co. Spectra Physics, Irvine, CA, USA) dispersion-compensated for enhanced 2P efficiency by a DeepSee attachment (Newport Co. Spectra Physics). Most SLICs were obtained with spot irradiation of 0.1 ms duration and variable intensity. Other durations were possible but were not used here. In some cases we applied much greater transients, which we will refer to as macro SLICs. These were generated by a series of 25 spots, applied during a 2.5 ms lapse, forming a small scribble or 'whorl' of ~3 μm in diameter. To increase the magnitude and duration of macro SLICs the whorl was iterated up to 10 times.

At pH 7.2, the measured K_D for Ca^{2+} was 25 nM for NDBF-EGTA and 5 nM for DM-nitrophen. Photolysis results in products with a $K_D \approx 1$ mM at pH 7.5, an approximately 140,000-fold increase, which is similar to that of DM-nitrophen (Momotake *et al.* 2006). At 350 nm the extinction coefficient of NDBF-EGTA is 15,400 $M^{-1}\ cm^{-1}$, about 4 times greater than that of DM-nitrophen, and the measured quantum efficiency of photolysis is 0.7 (that of DM-nitrophen is 0.18). These features, and a 2P cross-section measured at 0.6 GM, resulted in a greatly increased efficiency of photorelease compared with DM-nitrophen (Momotake *et al.* 2006). This was verified in our scanner by showing that the amplitude of SLICs induced by similar 2P flashes was approximately equal for solutions with 3 mM NDBF-EGTA or 15 mM DM-nitrophen when both cages were essentially saturated with Ca^{2+}. The diffusion coefficients, used in calculations of Ca^{2+} flux (see below), were given values of $1.4 \times 10^{-6}\ cm^2\ s^{-1}$ for NDBF-EGTA and $1.47 \times 10^{-6}\ cm^2\ s^{-1}$ for DM-nitrophen, derived from the value measured for ATP (Kushmerick & Podolsky, 1969) and an inverse relationship with molecular radius, which was calculated from the molecular weight.

SLICs could be produced with amplitudes and spatio-temporal parameters variable in a wide range, which depended on parameters of irradiation, cage and Ca^{2+} concentration, and the presence of extrinsic buffers. Two examples of SLICs in aqueous solutions are presented in Results (Fig. 1). The SLICs in the present study, elicited by irradiation of 0.1 ms at a single spot, had peak amplitudes ($\Delta F/F_0$) that varied monotonically with light intensity, ranging from the detectability limit (~0.05) to 40. The maximum [Ca^{2+}] calculated at the peak was 15 μM (but when applied as stimuli outside cells, the maximum [Ca^{2+}] at the point of contact with the cell was 8 μM). FWHM at peak amplitude increased slightly with amplitude; for the SLICs used in the present experiments it was on average 5.9 μm. Narrower SLICs, of FWHM as low as 3 μm, were generated in solutions of lower free [Ca^{2+}]. Macro SLICs were produced in a wide range of parameters, including peak amplitude up to 50 and FWHM up to 52 μm.

Monitoring of free Ca^{2+}

[Ca^{2+}] was monitored by imaging the fluorescence of the dye Fluo-4 FF. The intermediate affinity of this dye ($K_D = 9.7\ \mu$M, reported by the supplier) and its high dynamic range ($(F_{max} - F_{min})/F_{min} = 170$, measured in our setup, makes it suitable for reporting [Ca^{2+}] reached in large SLICs and details of the cellular transient at the same time. Fluo-4 FF was excited at 489 nm and its fluorescence (F) collected at 530 nm (with 40 nm half-intensity bandwidth). Scanning of F was by a high speed 'slit' confocal scanner (LSM 5 LIVE) in either linescan or x–y mode.

Calculation of [Ca^{2+}] and Ca^{2+} release flux

Cytosolic calcium concentration, $[\mathrm{Ca}^{2+}]_c$, and the flux of Ca^{2+} release, a function of space coordinates and time, were derived from first principles, by solving the differential diffusion–reaction equations relating concentrations of Ca^{2+} and its ligands B_j, which could be diffusible or (in the case of components inside cells) fixed. As an approximation, the SR Ca^{2+}-ATPase (SERCA), was included in this formalism as an additional ligand.

The diffusion–reaction equations are

$$\frac{\partial[\mathrm{Ca}^{2+}]}{\partial t} = D_{\mathrm{Ca}}\nabla^2[\mathrm{Ca}^{2+}] + \mathrm{flux} - \sum_j \left([\mathrm{Ca}^{2+}][B_j]k_{j,\mathrm{on}} + [\mathrm{Ca}^{2+}:B_j]\,k_{j,\mathrm{off}}\right) \tag{1}$$

$$\frac{\partial[\mathrm{Ca}^{2+}:B_j]}{\partial t} = D_{\mathrm{Ca}B_j}\nabla^2[\mathrm{Ca}^{2+}:B_j] + [\mathrm{Ca}^{2+}][B_j]k_{j,\mathrm{on}} - [\mathrm{Ca}^{2+}:B_j]\,k_{j,\mathrm{off}} \tag{2}$$

$$\frac{\partial[B_j]}{\partial t} = D_{B_j}\nabla^2[B_j] - [\mathrm{Ca}^{2+}][B_j]k_{j,\mathrm{on}} + [\mathrm{Ca}^{2+}:B_j]\,k_{j,\mathrm{off}} \tag{3}$$

The laplacian operator ∇^2 of a function $C(x,y,z)$ is

$$\nabla^2 C = \frac{\partial^2 C}{\partial x^2} + \frac{\partial^2 C}{\partial y^2} + \frac{\partial^2 C}{\partial z^2}.$$

Here we approximate it by its x and y components. In Supplemental Fig. S1 we put an upper bound on the error incurred by this approximation and conclude that it does not compromise the conclusions reached, which are qualitative in nature.

There is one equation like eqns (2) and (3) for every Ca^{2+} ligand present. If the diffusion coefficients for Ca:B_j and B_j are equal, then the total concentration of ligand, $[B_j]_\mathrm{T}$, is constant, $[B_j] = [B_j]_\mathrm{T} - [\mathrm{Ca}{:}B_j]$ and eqn (3) can be eliminated.

$[\mathrm{Ca}^{2+}]\ (x,y,t)$ is calculated by solving eqn (2) above for $[\mathrm{Ca}^{2+}]$ when the ligand is the dye:

$$[\mathrm{Ca}^{2+}] = \frac{\dfrac{\partial[\mathrm{Ca}^{2+}\!:\mathrm{Dye}]}{\partial t} - D_{\mathrm{CaDye}}\nabla^2[\mathrm{Ca}^{2+}\!:\mathrm{Dye}] + [\mathrm{Ca}^{2+}\!:\mathrm{Dye}]\,k_{\mathrm{off}}}{([\mathrm{Dye}_\mathrm{T}] - [\mathrm{Ca}^{2+}\!:\mathrm{Dye}])k_{\mathrm{on}}} \tag{4}$$

k_{on} was assumed equal to that measured by Shirokova *et al.* (1996) for Fluo-3 in frog cells ($0.8 \times 10^{-8}\ \mathrm{M}^{-1}\ \mathrm{s}^{-1}$). k_{off} was set at 776 s^{-1}, by multiplying the value measured in the same paper, 90 s^{-1}, by the ratio of the K_Ds of Fluo-4 FF and Fluo-3 (9.7/1.125).

Introducing the basic relationship between fluorescence and dye saturation

$$F = F_{\max}\left[\mathrm{Ca}:\mathrm{Dye}\right] + F_{\min}\left(\left[\mathrm{Dye}\right]_\mathrm{T} - \left[\mathrm{Ca}:\mathrm{Dye}\right]\right) \tag{5}$$

a useful expression is derived:

$$[\mathrm{Ca}^{2+}] = \frac{\dfrac{\partial F}{\partial t} - D_{\mathrm{CaDye}}\nabla^2 F + (F - F_{\min})\,k_{\mathrm{off}}}{(F_{\max} - F)k_{\mathrm{on}}} \tag{6}$$

This is solved numerically by the method of Euler, using custom routines programmed in the IDL environment (ITT Visual Information Solutions, Boulder, CO, USA) and tested with simulations done with the symbolic and numeric environment Macsyma (Macsyma Ing., Arlington, MA, USA). Examples of $[\mathrm{Ca}^{2+}](x, y)$ calculated from fluorescence images start with Fig. 3. Examples of flux in cellular responses start with Fig. 6.

Supplemental material

Supplemental narrative and Fig. S1 present an estimation of the error incurred in the calculation of release flux from series $F(x,y,t)$, which contain no information regarding fluorescence and [Ca^{2+}] in the z dimension. Supplemental narrative and Fig. S2 illustrate a propagated wave with a gradual start, which is extreme for lasting hundreds of milliseconds. During this time, speed and flux increased progressively over a greater than 10-fold range in an approximately proportional manner. Supplemental narrative 3 provides a list of videos, associated with Figs 2, 3, 4, 6 and 11.

Results

The goal of the present work is to test the ability of skeletal muscle cells of amphibians and mammals to respond with Ca^{2+} release to a transient increase in $[\mathrm{Ca}^{2+}]_c$. The underlying question is whether Ca^{2+} release channels can contribute to the functional excitation–contraction (EC) coupling signal even if they are not directly operated by a voltage sensor (as seems to be the case for every other RyR1 in a skeletal muscle couplon; Block *et al.* 1988).

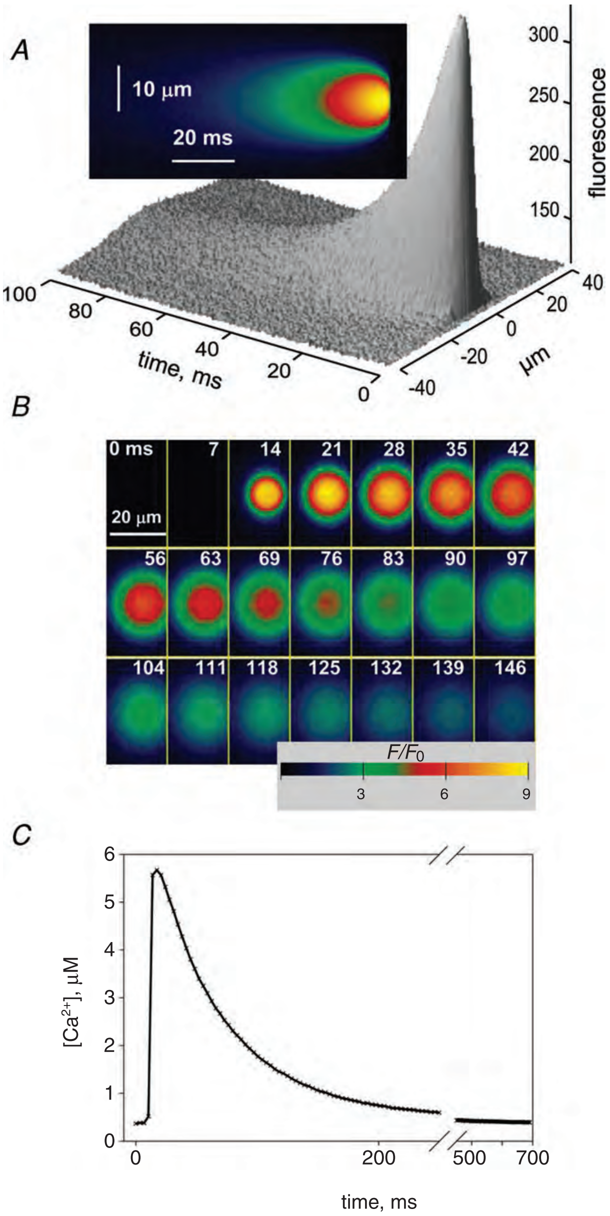

Figure 1. Features of synthetic localized increases of Ca^{2+} (SLICs) monitored in different dimensions
A, line scan image *F*(*x*,*t*) of the SLIC produced by 0.1 ms spot irradiation in a droplet of internal solution with 15 mM DM-nitrophen and a measured free $[Ca^{2+}]$ of 1.25 μM. The increase in fluorescence had amplitude of 2.6 and FWHM of 6.1 μm at the time of the peak. $[Ca^{2+}]$, calculated by a one-dimensional version of eqn (6), peaked at 8.6 μM. *B*, frames *F*(*x*,*y*) of the transient generated by a similar spot irradiation as in *A*, of an internal solution with 3 mM of NDBF-EGTA and a measured free $[Ca^{2+}]$ of 0.374 μM. The SLIC was imaged two-dimensionally, at 3.47 ms per frame and 0.44 μm per pixel. Shown are one of every two of the first 42 frames acquired in a 100 frame series. The time of acquisition of each frame is indicated approximately in milliseconds. The IR flash was applied 2 ms before the third frame shown. In the 3rd panel the amplitude (peak $\Delta F/F_0$) was 7.85 and the FWHM in the *x* direction was 7.5 μm. In both cases, 100 μM of Fluo-4FF was used as Ca^{2+} monitor. *C*, free calcium concentration, $[Ca^{2+}](t)$, calculated by eqn (6) from the images in *B* and averaged in the central 25 pixels of the SLIC. $[Ca^{2+}]$ peaked at 6.07 μM. Note the high quality of the signal (apparent in its dynamic range, temporal resolution and low noise). ID: 110909 series 12 and 071911 series 7.

The strategy is to test on cells the effect of a Ca^{2+} transient within the range likely to be reached by the primary response to depolarization. In a simulation presented in the Appendix (Fig. A1), it is shown that the channels that are placed next to open RyRs in a couplon of an SR with a luminal free $[Ca^{2+}]$ of 0.5 mM are unlikely to face a $[Ca^{2+}]$ greater than 15 μM. Given the large variance reported in the levels of $[Ca^{2+}]_{SR}$ (Rudolf *et al.* 2006; Canato *et al.* 2010; Jiménez-Moreno *et al.* 2010; Ziman *et al.* 2010; Sztretye *et al.* 2011*b*), the concentration will often be less than half as much.

SLICs of up to 8 μM were produced with 2P photolysing irradiation of cells equilibrated with a solution containing caged Ca^{2+} and a Ca^{2+} monitoring dye. Figure 1 illustrates SLICs produced in solution, with two cages and two forms of image acquisition. In panel *A* is a SLIC produced by irradiation (with IR light delivered by one of the scanning modules of a dual laser scanner) of an internal solution with 15 mM DM-nitrophen, and a free $[Ca^{2+}]$ that saturated the cage. While the solution was irradiated, fluorescence of the low-affinity Ca^{2+} monitor Fluo-4 FF was being acquired in line-scan mode by the second scanning module (LSM 5 LIVE) of the dual scanner. The scanning line exactly intercepted the irradiation spot, so that the SLIC was recorded in focus. The spot irradiation lasted 0.1 ms and the scanning frequency was 5 kHz (200 μs per line, 0.22 μm per pixel). (Unlike what is implied in the manufacturer's publications, the two scanners of the Zeiss Dual Scanner are not truly mutually independent. Even though the instrument is capable of higher scanning frequencies, 5 kHz, as demonstrated in the figure, is the highest scanning rate compatible with a simultaneous irradiation of 0.1 ms. Attempts at a higher rate resulted in unpredictable performance.)

Figure 1*B* illustrates a SLIC imaged in two dimensions (*x*–*y* mode). The SLIC was produced by irradiation of a solution containing 3 mM of NDBF-EGTA (Momotake *et al.* 2006), a cage with two major advantages: a low affinity for Mg^{2+}, so that the Mg^{2+} concentration may be independently changed, and a substantially greater 2P cross-section, so that large quantities of Ca^{2+} can be released with levels of irradiation that cells can tolerate well. The images are of fluorescence of Fluo-4 FF, acquired by the LSM 5 LIVE at 3.47 ms per frame – the highest frequency used in the present study. The figure shows one of every two frames, up to the 41st in a series of 200 frames. Acquisition times are listed. The photoreleasing flash occurred approximately 2 ms before the third frame shown. Figure 1*C* plots the value of $[Ca^{2+}]$ (calculated by eqn (6)) at the centre of the SLIC in every frame. As shown with these examples, peak $[Ca^{2+}]$ reached with 3 mM of NDBF-EGTA were comparable with the levels produced with 15 mM DM-nitrophen under similar conditions of irradiation and Ca^{2+} saturation of the cages. Morphometric parameters of SLICs are given in Methods.

SLICs elicit a propagated increase of $[Ca^{2+}]_c$ in frog skeletal muscle cells

A first test of SLICs as stimuli, done in frog muscle cells, is illustrated in Fig. 2 After permeabilization of the plasma membrane by saponin the cells were equilibrated with a solution containing the cage NDBF-EGTA and Fluo-4 FF. The first panel in Fig. 2 shows the distribution of fluorescence at rest. Due to binding of dye to cellular structures the fluorescence is greater inside the cell, even though $[Ca^{2+}]_c$ is the same as outside in these membrane-permeabilized conditions. Note that in all multiframe figures the frames are oriented so that the longitudinal scanning axis (x, which in experiments with frog fibres is aligned with the fibre axis) is vertical on the page and the transversal axis (y) is horizontal. In response to a 'flash' of 2P excitation lasting 100 μs the cell responded with a propagated Ca^{2+} transient, a wave that rapidly expanded to the full thickness and length of the cell. The Discussion will show that this wave of Ca^{2+} release is mediated by Ca^{2+}, constituting a CICR response. (The phenomenon, as well as all events captured in series of images, is seen best in associated Supplemental video 1 Fig. 2, in the present case.)

Two problems arise in the interpretation of these results. One is the possibility that the intracellular irradiation causes damage. An indication of damage is the dark area that remains at the spot where light was applied. In later images, not shown, the spot had disappeared, which indicates that it reflected local bleaching, later restored by diffusion of fresh dye. In other cases, an area of elevated fluorescence appeared after the bleached monitor was restored. This is evidence of damage to the SR, which causes a local increase in $[Ca^{2+}]_c$.

An additional problem arises from the overlap in space and time of trigger Ca^{2+} and Ca^{2+} supplied by release from the SR. Because of this overlap it is not possible to measure the concentration that triggered the release response.

The alternative approach illustrated in Fig. 3 circumvents both problems. It consists of applying the photoreleasing irradiation at a spot that, as indicated in the first frame, is outside the cell but close to it, 3–5 μm away from the permeabilized plasma membrane. As the photoreleasing light is applied outside the cell, it causes no damage or dye bleaching. It is also possible to determine with precision the triggering $[Ca^{2+}]$, that is, the one recorded at the initiation site immediately before the time when the first cellular response was detected.

Starting with Fig. 3, $[Ca^{2+}]_c$, derived from the fluorescence images by eqn (6), is illustrated. In these images $[Ca^{2+}]$ is nearly linear with F, due to the low affinity and rapid reaction of the monitoring dye. As in the previous figure, the dynamics of this experiment are best appreciated in the associated video (Supplemental video 2 Fig. 3). The triggering $[Ca^{2+}]$ can be evaluated directly on these images as the value present at the surface of the cell at the time when the first cellular response was detected (the measurement was done on the outside, as close as possible to the membrane, in the frame marked by the arrow).

In the example the triggering $[Ca^{2+}]$ was 0.7 μM. To find the *threshold* $[Ca^{2+}]$ for eliciting CICR the intensity of the IR flash was progressively reduced so that lower

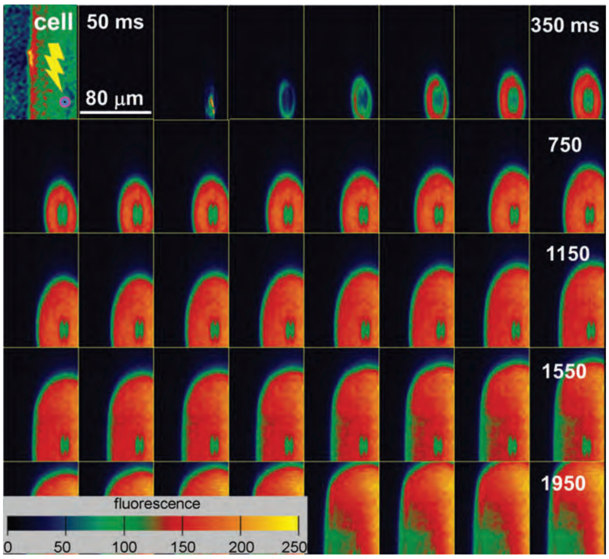

Figure 2. Propagated response to a SLIC applied inside a frog muscle cell

Successive images of raw fluorescence, $F(x,y)$, of a frog fibre subjected to a SLIC. The fibre had been membrane-permeabilized by saponin and equilibrated with an internal solution containing 0.05 μM free Ca^{2+}, 0.3 mM free Mg^{2+}, the cage (NDBF-EGTA), the indicator (Fluo-4FF) and BTS as suppressor of movement (details given in Methods). The first frame shows in a highly expanded colour scale the distribution of fluorescence at rest, with the cell delineated as a region of greater intensity. The locus of infrared irradiation (which lasted 0.1 ms) is indicated by a target in the same frame. Frames were acquired at 25 ms intervals and shown at 50 ms intervals (that is, skipping every other frame). Note a persistent area of loss of fluorescence at the spot where light was applied. It reflects bleaching of the dye, which recovered after several seconds (not shown). ID: 080309, series 33. The corresponding calcium dynamics of this figure is shown as a video (Supplemental video 1).

triggers were applied until finding one that did not cause a response. The results for this particular fibre are summarized in Fig. 3*B*. The intensity of the flash is plotted against the trigger [Ca^{2+}] measured in the same application. Symbols representing successive trials, at 3 min intervals, are joined by line segments. Red symbols represent triggers that elicited a propagated response. It can be seen that flashes of energy below 45% failed, a result that sets the threshold at ~0.28 μM. In some cells the minimum successful trigger increased after a propagated response – a transient inhibition. In those cases a threshold was more difficult to define, but responses to Ca^{2+} triggers below 1 μM were still common. The trigger [Ca^{2+}] attained next to the membrane ranged between 0.18 and 6 μM (higher triggers, reaching 8 μM, were used in experiments with mouse cells). No correlation was found between suprathreshold trigger [Ca^{2+}] and speed or intensity of the response, but there was an apparent non-monotonic relationship, described in the next sub-section, between triggering [Ca^{2+}] and success rate of the response.

An additional type of response to local increase in [Ca^{2+}]$_c$

Often cells responded to SLICs in a manner that we call 'frustrated'. An example is in Fig. 4. After the trigger Ca^{2+} reaches the cell, a local increase in [Ca^{2+}]$_c$ is observed, which gains strength and expands but fails to propagate the full length of the cell (see also Supplemental video 3 Fig. 4). The extent and intensity of these responses was variable. Some cells exhibited full propagated responses, then frustrated responses, and later recovered the full phenomenon.

As the trigger Ca^{2+} was increased, the fraction of fully propagated and frustrated responses varied in a suggestive manner. These fractions are represented in the bar diagram of Fig. 5*A*, where the ranges of trigger [Ca^{2+}] are indicated on the *x* axis, under each bar. As can be seen, the fraction of positive responses (either full or frustrated) increased with trigger [Ca^{2+}] up to about 1 μM, then decreased as trigger [Ca^{2+}] increased up to the highest values used. A statistical analysis of the significance of the observed

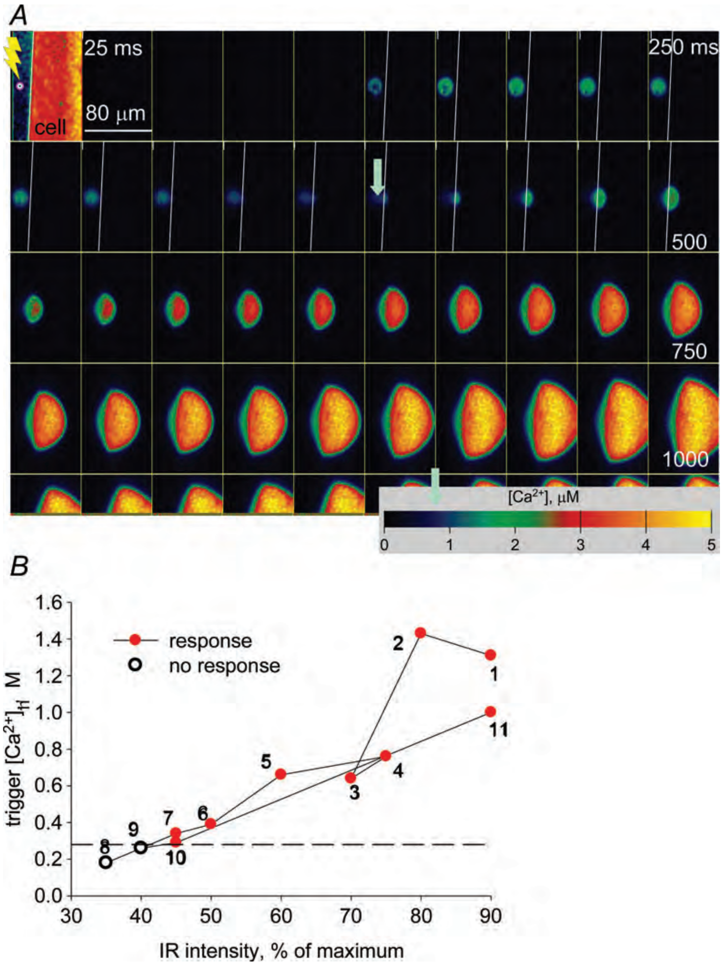

Figure 3. Propagated response to a SLIC applied outside a frog muscle cell
A, images of [Ca^{2+}](x,y) derived from $F(x,y)$ by eqn (6), in a frog cell prepared as in Fig. 2. The first frame shows resting fluorescence and position of the cell. Starting with the 6th frame, the border of the cell is indicated by a line in white. The target shows the place where IR was applied (during acquisition of the 6th frame) to generate a SLIC. Starting with the 16th frame, indicated by an arrow, a response is visible inside the cell. The triggering [Ca^{2+}], defined as the value present immediately outside the cell in the frame where the first cellular response was detected, was ~0.7 μM (see 2nd arrow, at the corresponding value on colour scale bar). A video of this event is available as supplemental material (Supplemental video 2 Fig. 3). ID: 080309 series 5. *B*, intensity of the photolyzing radiation (% of maximum) is plotted against the trigger [Ca^{2+}] measured in the same application. Intensity of the flash was progressively reduced in the same cell until finding one that did not cause a response, and the sequence of stimuli was then continued at increasing intensities. Symbols representing successive trials, at an interval of 3 min, are joined by a line. Red symbols represent triggers that elicited the propagated response. Note that flashes of energy below 45% failed, revealing a threshold of ~0.28 μM in this fibre. ID: 080309 series 3, 5, 7, 10–16.

decrease in success rate with trigger [Ca^{2+}] was done by testing the null hypothesis that the concentration of trigger Ca^{2+} did not have any effect on the type of response beyond the 2nd bin in the graph (0.6–0.99 μM). Under this assumption, the probability of response could be calculated by averaging the success frequency over all bins, which was 0.67. Assuming that the number of successful trials had Poisson distribution, the probabilities that random variation would account for the above-average number of responses in the 2nd bin (where they amounted to 80% of the trials), and that they would be only 50% in the last bin, were calculated, respectively, at 0.32 and 0.16. The joint probability of both deviations in the null hypothesis was 0.053; therefore the hypothesis could not be rejected at a $P < 0.05$. In spite of the limited significance, the observation suggests that the feedback actions of Ca^{2+} include an inactivation component, in addition to CICR. Given the number of experiments that would be necessary to substantially improve the power of the test, and the limited supply of NDBF-EGTA, we did not pursue further the investigation of this interesting result.

The propagated response of frog muscle was abolished in high [Mg^{2+}]$_c$

One of the well-understood characteristics of CICR is the involvement of a cytosolic site (or sites) where Mg^{2+} acts as a competitive antagonist. To probe this feature, and taking advantage of the lack of affinity of NDBF-EGTA for Mg^{2+}, the level of this ion was varied between 0.3 and 3 mM in the experiments on frog muscle cells. Conditions and results are summarized in the diagram of Fig. 5*B*. In agreement with expectations for CICR, there was a clear decrease in the rate of induction of propagated responses as [Mg^{2+}] increased between 0.3 and 3 mM; in fact, no responses were ever observed in solutions with 3 mM [Mg^{2+}].

The flux of Ca^{2+} release underlying cellular responses

Often it was difficult to decide whether a given Ca^{2+} transient resulted simply from photorelease or was increased by release from the cell. The decisive procedure for this purpose was to calculate the release flux underlying the combined Ca^{2+} signals from cage and cellular store. The calculation of flux also provided insights to the nature and mechanism of the response.

Release flux $\dot{R}(x,y)$ was calculated from sequences of images of fluorescence by generalizing the 'backward' method originally introduced for line scans (Ríos *et al.* 1999). The generalized algorithm is described in Methods. The result of the calculation for the propagated response illustrated in Fig. 3*A* is shown in Fig. 6. To demonstrate the spatial relationship between flux and [Ca^{2+}] a portion of the frames of [Ca^{2+}]$_c$ calculated for Fig. 3*A* is superimposed on the flux images. The release flux is a centrifugal wave, diverging from the point of origin (see also Supplemental video 4 Fig. 6). It is obvious from inspection that the flux wave is anisotropic, with a higher peak and narrower spatial profile at the 'equator' of the growing ellipsoid.

A one-dimensional snapshot of the flux in the y direction is obtained as illustrated in Fig. 6*B*, by averaging flux in a narrow range of values of x at the equator of the wave. Thus, a function $\dot{R}(y)$ is generated for every x–y frame. By stacking together these functions for successive frames, a function $\dot{R}(y, t)$ is obtained, which is represented as a surface plot in Fig. 6*C*. We refer to this function as the 'transversal flux wave'. A similar description of the flux wave is possible in any angular direction of propagation.

The transversal flux wave (in Fig. 6*C*) has several features that are observed in most experiments. The first large transient, at low values of y and t, is of photorelease flux, outside the cell. The cellular CICR response usually develops with an initial phase of increasing amplitude, and then reaches a peak that remains steady as the wave propagates across the cell until it goes out of the frame.

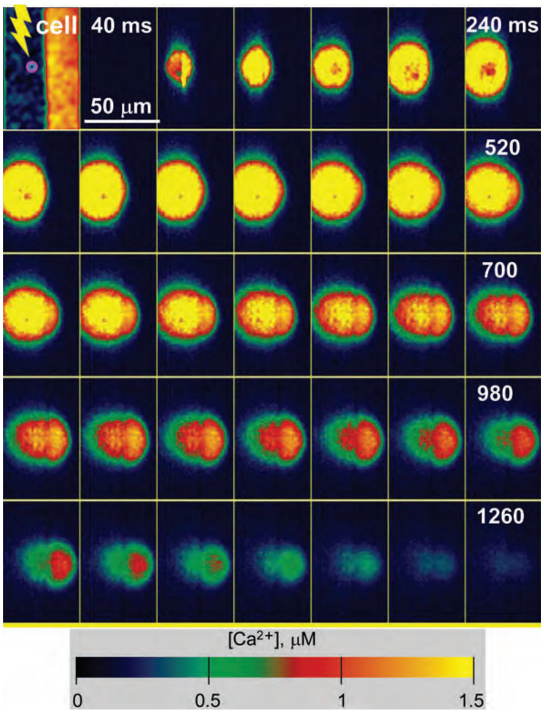

Figure 4. A 'frustrated' response to local increase in [Ca^{2+}]$_c$
Images [Ca^{2+}](*x*,*y*) of a permeabilized frog fibre prepared as in the previous figure, responding to a SLIC generated outside the cell (at 3rd frame). Frames acquired at 20 ms intervals, and shown every 40 ms. The first frame, resting fluorescence at a highly amplified scale, shows location of the cell. The response propagates but fails to reach the full width and length of the cell (Supplemental video 3 Fig. 4). Further analysis of this response is illustrated in Fig. 7. ID: 073109 series 7.

Fluxes reached values in a range of 9–55 mM s^{-1} ($n = 16$). This stable phase is characterized by a constant speed of propagation, which can be derived proportionally from the cotangent of the angle φ between the line of peaks of flux and the x axis. This angle is measurable accurately on a top view of $\dot{R}(y,t)$ (Fig. 6*D*). The propagation speed varied between 30 and 300 $\mu\mathrm{m\ s}^{-1}$ in 16 cells. A peculiarity of these plots is the difference of noise level, which is greater after the flux wave; this is a consequence of the non-linearity of the flux calculations, which results in different levels of noise when operating on widely different levels of $[\mathrm{Ca}^{2+}]_\mathrm{c}$.

The Ca^{2+} release flux underlying frustrated responses

The release flux $\dot{R}(x,y)$ calculated from the $[\mathrm{Ca}^{2+}]_\mathrm{c}$ frames in of the frustrated response in Fig. 4 is illustrated in Fig. 7. A centrifugal flux wave develops and propagates, but loses strength after ~1 s. This evolution is clearly seen in the transversal flux wave $\dot{R}(x,t)$, shown from two perspectives in panels *B* and *C*. The wave propagates across the cell, but decays and stops near the edge of the frame. The top view (panel *C*) demonstrates a consistent feature of frustrated responses; their speed of propagation (measurable on tangents AA, BB and CC) decreases as the wave propagates. Amplitude, speed and extent of propagation varied greatly even in different instances of frustrated waves in the same cell.

The three characteristic features, peak flux, speed and extent of propagation, could be followed in successive responses of some cells. Their relationships and evolution are indicative of underlying mechanisms. An example is in Fig. 8, a scatter plot of these three features in 11 successive responses to an artificial spark of the same magnitude (applied at 3 min intervals, always at ~4 μm from the cell surface). The symbols plot peak flux, propagation speed and propagation range or extent. Symbols in red represent fully propagated responses (plotted at range = 40 μm, i.e.

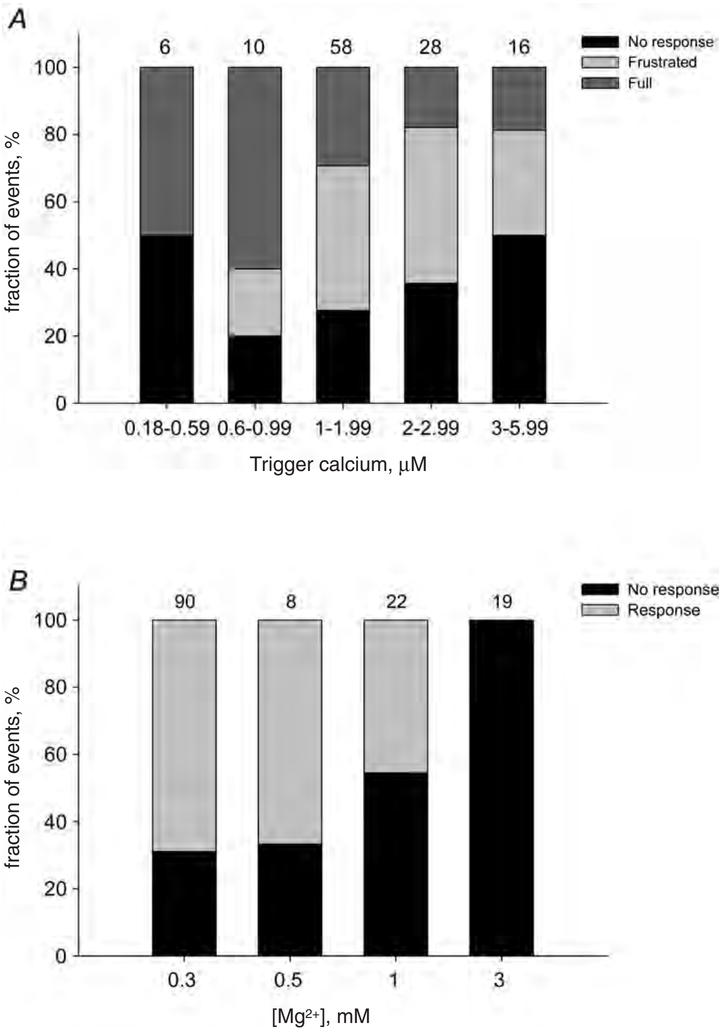

Figure 5. The dependence of stimulus success rate on trigger $[\mathrm{Ca}^{2+}]$ and cytosolic $[\mathrm{Mg}^{2+}]$
A, bars plot the fraction of trial stimuli that did not (black) or did elicit a response (dark grey: full; light grey: frustrated) *vs.* the magnitude of the stimulus ($[\mathrm{Ca}^{2+}]$ at the point of contact). Nominal $[\mathrm{Mg}^{2}]$ varied from 0.3 to 0.5 mM. As the trigger Ca^{2+} was increased, the fraction of fully propagated and frustrated responses varied non-monotonically. The fraction of positive responses (either full or frustrated) increased with trigger $[\mathrm{Ca}^{2+}]$ up to about 1 μM, then decreased. The significance of the decrease was marginal (detailed in text). The number of trials is listed above the bars; the number of cells per range was 2, 2, 8, 6 and 5, respectively. *B*, fraction of trials with successful responses (including frustrated and fully propagated) at different concentrations of Mg^{2+}. Number of cells was 9, 2, 6, and 4, respectively. Total number of trials are listed. The trials used similar Ca^{2+} triggers at every $[\mathrm{Mg}^{2+}]$, variable in the range 0.8–3 μM.

the width of the frame). In this and other examples fully propagated responses (no. 1 and 8 in the sequence) were followed by a number of frustrated responses. Within the sequence of frustrated responses there was a trend, whereby successive responses had increasing flux, speed and range, all three features being positively correlated. We suggest that this trend reflects a gradual recovery of the ability to respond, which underwent a sudden reduction after the first full response. The sudden decay after the full response is probably a consequence of the SR depletion associated with it. If that was the case, then the recovery could be due to gradual reuptake of the lost Ca^{2+}.

The correlation between peak flux and speed can be seen inside single waves, and is clearly displayed by the waves

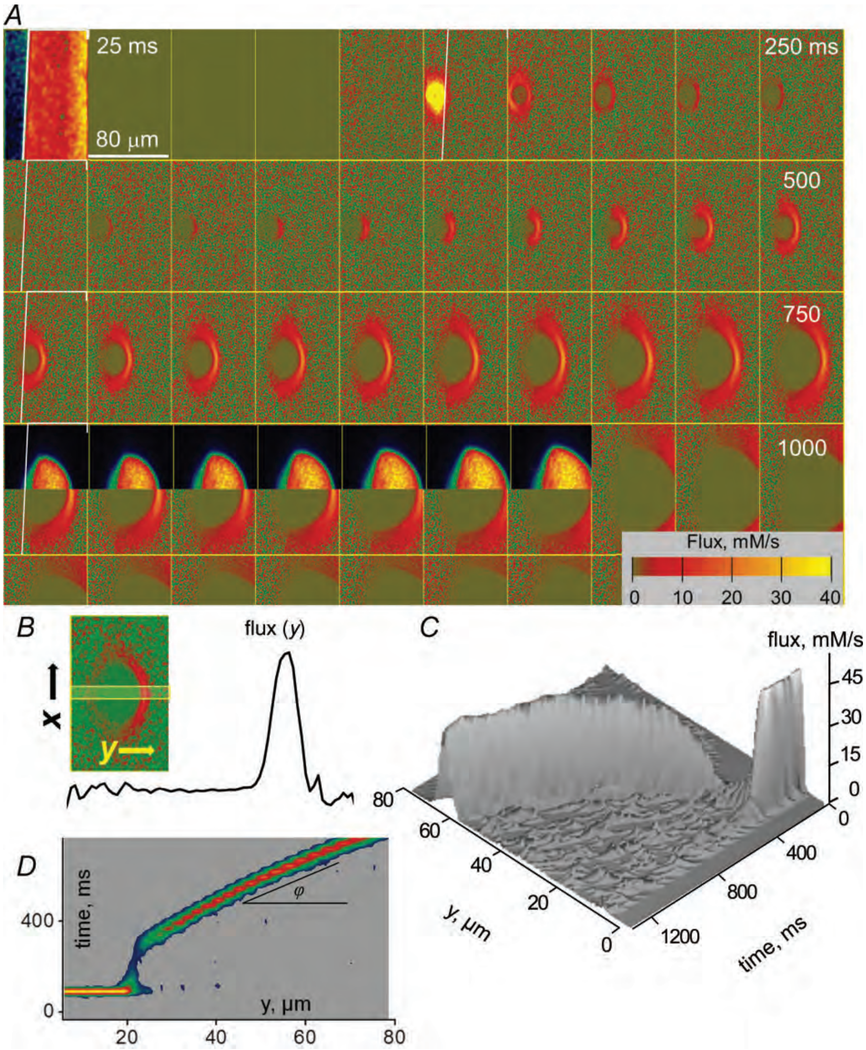

Figure 6. The flux of Ca^{2+} release underlying cellular responses
A, flux, $\dot{R}(x,y)$, derived from the [Ca^{2+}](x,y) series presented in Fig. 3*A* as described in Methods. A portion of the frames of [Ca^{2+}]$_c$ calculated for Fig. 3*A* is superimposed on the flux images, to demonstrate the spatial relationship between flux and [Ca^{2+}]. The release flux is a centrifugal wave, diverging from the point of origin. Note that the flux wave is anisotropic, with a higher peak but a narrower spatial profile and slightly lower speed of propagation at the ‘equator’ (horizontal on the page). See also Supplemental video 4 Fig. 6. ID: 080309 series 5. *B*, in every frame the flux was averaged along the longitudinal axis of the fibre (the x coordinate) in a narrow ‘slit’ region at the equator of the wave, to yield the function $\dot{R}(y)$, in black trace. *C*, two-dimensional function $\dot{R}(y,t)$ (the transversal flux wave) obtained by stacking $\dot{R}(y)$ from every frame in *A*. The first large transient, at low values of y and t, is of photorelease flux, outside the cell. *D*, a top view of $\dot{R}(y, t)$ from *B*. The propagation speed is proportional to the cotangent of the angle φ between the line of peaks and the x axis. During the early development of the propagated wave the speed increases as the wave gains in amplitude. The stable phase of the flux is characterized by a constant speed of propagation, which in this case is ∼130 μm s^{-1}. ID: 080309 series 5.

in Figs 6 and 7. This correlation applies over a wide range of speeds and fluxes; it applies in either direction, during the early development of propagating waves (Fig. 6) or during termination of a frustrated wave (Fig. 7). Illustrated in Supplemental Fig. S2 is a remarkable case in which approximately linearly correlated speed and flux at the start of the propagating wave increased gradually by one order of magnitude.

A summary of this relationship in different cells and conditions is in Fig. 9. Different dates (which correspond to different animals) are represented by different colours; data from the same cell are represented by symbols linked by a line. Approximately one third of the symbols correspond to frustrated responses. It can be seen that a nearly proportional relationship applies across different cells, different waves of the same cell (full or frustrated) and different times during a wave.

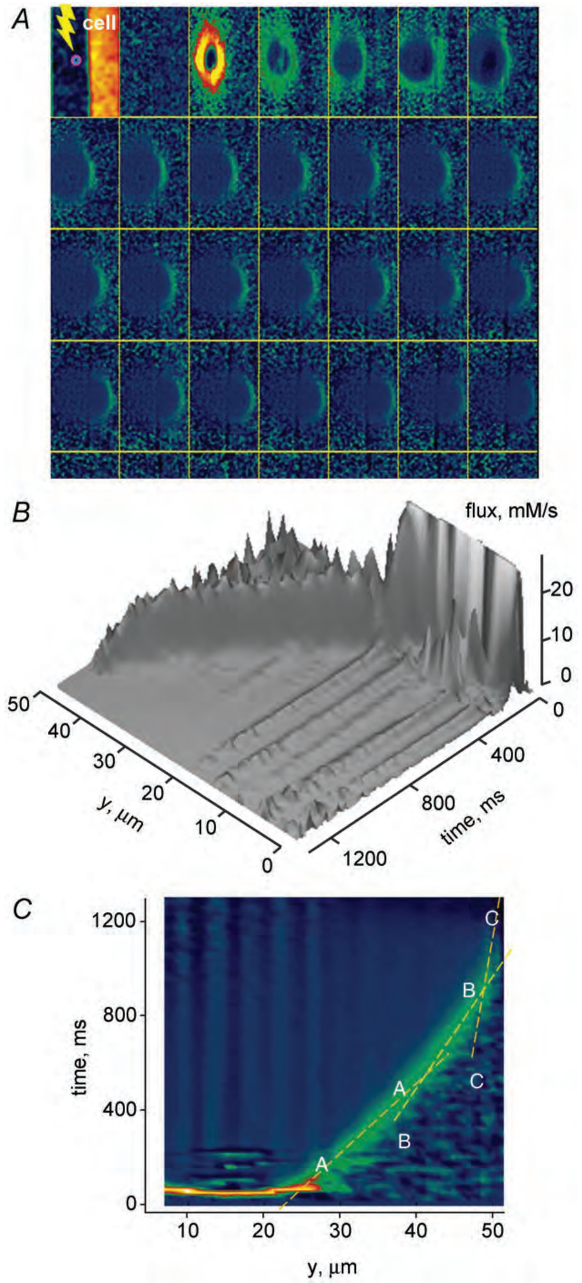

Figure 7. Ca^{2+} release flux underlying frustrated responses
A, $\dot{R}(x,y)$ calculated from the $[Ca^{2+}]_c$ frames in Fig. 4. The wave propagates nearly throughout the width of the cell, but decays and stops near the edge of the frame. *B*, transversal flux wave, $\dot{R}(y,t)$, calculated as described in Fig. 6, from frames in *A*. *C*, a top view of the transversal wave demonstrates the association between peak flux and speed of propagation (measurable on tangents AA, BB and CC, drawn for illustration purposes). ID: 073109 series 7. *D*, $\dot{R}(y,t)$ from a second frustrated response in the same cell. Peak flux and speed decay after ∼500 ms. ID: 073109 series 14.

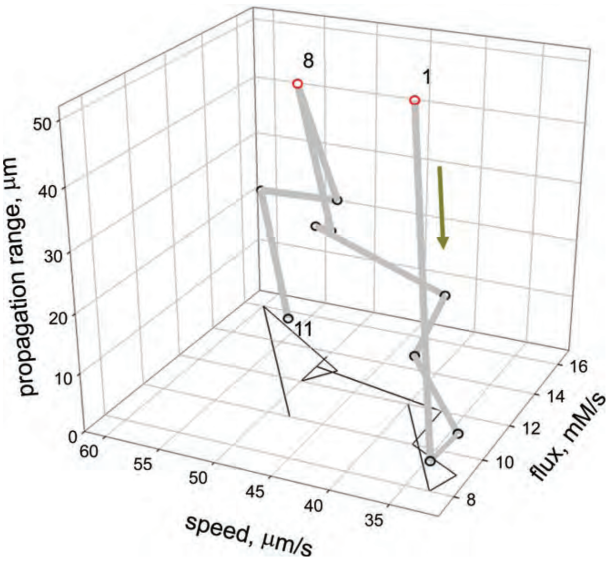

Figure 8. Quantitative features of the propagating wave are correlated
Peak flux, speed and propagation range (all in transversal direction) in 11 successive responses to an artificial spark of the same magnitude in the same frog fibre. The fibre had been equilibrated with an internal solution containing 0.05 μM free Ca^{2+} and 0.3 mM free Mg^{2+} (details given in Methods). The artificial sparks were applied at 3 min intervals, at 4 μm from the cell surface. Symbols in red represent fully propagated responses (no. 1 and 8 in the sequence). Propagated responses were followed by a number of frustrated responses (black symbols). The black line at the bottom of the graph joins the projections of the data points in the flux–speed plane. Note a trend within the sequence of frustrated responses, whereby successive responses had increasing flux, speed and range. ID: 073109 series 4 to 14.

Mouse muscle is normally incapable of CICR

SLICs were also applied to single skeletal fibres enzymatically dissociated from the FDB of young adult mice. The cells were permeabilized and equilibrated with an internal solution similar to that used for frogs, and except for the method of cell separation, the experimental procedures and conditions were nearly identical. A representative experiment is summarized in Fig. 10. The cell is visible in the first frame of the figure, representing $F(x,y)$; the cell's contour is marked in other frames. These much smaller cells could not be moved individually and lay at random angles, no longer aligned with the x scanning axis. As shown, SLICs within the range of $[Ca^{2+}]$ and durations that elicited propagated responses in the frog failed to cause Ca^{2+} release in mouse cells. The analysis of flux (Fig. 10*B*) demonstrated complete absence of release within the cells. The conditions in which no responses were obtained, which are listed in Table 1, included concentrations of Mg^{2+} between 0.045 and 3 mM, resting free $[Ca^{2+}]_c$ between 0.05 and 2 μM, and large concentrations of cage (either NDBF-EGTA or DM-nitrophen), photolized with spots or whorls at high laser intensity and iterated up to 10 times, causing levels of trigger Ca^{2+} up to 8 μM at the point of contact with the cell. The SR of all cells tested was shown to be loaded and capable of releasing Ca^{2+} by exposure to a high concentration of caffeine and 4-CMC. Trials at high $[Ca^{2+}]_c$ were done in an attempt to achieve CICR by increasing free and total Ca^{2+} SR load, but the results were not different.

For a more radical testing of the ability of murine muscle for CICR, we used spot irradiation inside the cell. In several cases the flash was so intense that it caused lasting damage, reflected in a persistent increase in local fluorescence. None of these attempts caused propagated Ca^{2+} release.

Pharmacological conditioning makes propagated responses possible in mouse cells

RyR1 channels are activated by cytosolic-side Ca^{2+} when reconstituted in bilayers (reviewed by Fill & Copello, 2002). This property is shared by all isoforms. While we knew that the Ca^{2+} sensitivity of activation favours β over α RyRs (Murayama & Ogawa, 2001) and RyR3 over RyR1 (Murayama & Ogawa, 2004), we were still surprised by the absolute inability of mouse cells to respond *in situ* to our Ca^{2+} stimuli. Indeed, Ca^{2+} release was not observed even with triggers 20 times greater than those needed to elicit the response in frog muscle, and at $[Mg^{2+}]$ below the lowest estimates of K_D of the channel's inhibitory 'I' site (Laver *et al.* 1997*a*,*b*; Copello *et al.* 2002).

A relevant question is whether a CICR ability can be demonstrated at all using the present approach for RyR1 channels inside cells. To answer it we used drastic means, including un-physiologically low $[Mg^{2+}]$ (as low as 0.045 mM including 33 trials in 8 cells, in which trigger $[Ca^{2+}]$ reached 3.2 μM), which as stated before failed to enable responses. We also applied SLICs to mouse cells in the presence of drugs known to favour channel activity. We used caffeine (Rousseau *et al.* 1988) and 4-CMC (Zorzato *et al.* 1993; Westerblad *et al.* 1998) – chemicals that promote channel opening and, at least in the case of caffeine, do it by increasing the channels' sensitivity to Ca^{2+}. In an alternative pharmacological approach we used clofibrate, an anion that promotes the response of the channels to activation via the voltage sensor (Ikemoto & Endo, 2001). The drugs were applied at concentrations that did not directly cause Ca^{2+} release. $[Mg^{2+}]$ was set at 0.3 or 0.5 mM. The tests with SLICs were always followed by application of the drugs at a suprathreshold concentration; the application caused a direct response in every case, showing that the cells were in a release-capable state.

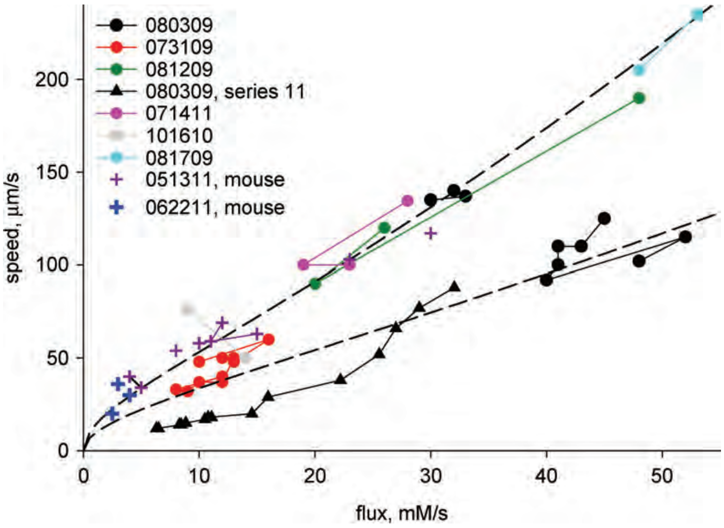

Figure 9. Speed of propagation and release flux in cells from frogs and mice

Free $[Ca^{2+}]$ and $[Mg^{2+}]$ in internal solutions varied in the range 0.05–0.2 μM and 0.3–1 mM, respectively. Different dates (which correspond to different animals) are represented by different colours. Data from the same cell are represented by symbols linked by a line. The black triangles represent values of speed and peak flux at different times during the evolution of a single wave, more fully represented in Supplemental Fig. S2. Data represented by crosses are from experiments in mice, either in the presence of 1.8 mM caffeine and 0.4 mM 4-CMC (purple) or 1.5 mM clofibrate (blue). The dashed traces plot eqn (8) with $k^{+} = 2.5\ 10^{8}\ M^{-1}\ s^{-1}$, $C_0 = 0.5\ \mu M$, $D = 4\ 10^{-6}\ cm^2\ s^{-1}$, $D_B = 10^{-7}\ cm^2\ s^{-1}$, and $K_D = 1\ \mu M$. *B* was 250 μM for the lower trace and 150 μM for the upper one.

In cells immersed in solution containing 1 mM caffeine and 0.1 mM 4-CMC, neither extracellular SLICs nor photorelease applied directly inside the cells were able to elicit a response. We did observe responses to SLICs when caffeine and 4-CMC were present together, at 1.8 mM and 0.4 mM, respectively. In 6 of 13 cells studied the responses took the form of frustrated waves, like those illustrated in Fig. 4. In four cells there were fully propagated responses. An example is shown in Fig. 11, where a centrifugal wave develops and propagates without decrement. In this example, the stimulus was an extensive macro SLIC. The wave developed slowly, with a protracted rising phase, which only started after the macro SLIC had been sustained for about 500 ms (the initiation spot and approximate time are indicated by an arrow in both panels *A* and *B*). The quantitative properties of this and other responses in the mouse are represented in the collective plot of Fig. 9 by purple crosses. On average, the propagated waves in the mouse had a lower peak flux and velocity of propagation than those of the frog (Table 1). The phenomenon is also illustrated in Supplemental video 5 Fig. 11*A* and video 6 Fig. 11*B*).

When the release-promoting anion clofibrate was present at 1.5 mM, a concentration that does not directly cause Ca^{2+} release, a small frustrated response to large SLICs was also detected. Similar to the responses observed with caffeine and 4-CMC, the ones in clofibrate were small in flux, of low velocity and limited propagation range (Table 1). An individual fibre responses to clofibrate are represented by blue crosses in Fig. 9.

The conclusion from this set of experiments is that murine skeletal muscle is capable of CICR, but only under pharmacological promotion of channel opening. Under these conditions, the responses are qualitatively similar but quantitatively substantially different from those of the amphibian.

Although both caffeine and 4-CMC are agonists of RyR1 (e.g. Zorzato *et al.* 1993), their potency, affinity and site of action on the channel are different (Choisy *et al.* 2000; Treves *et al* 2002). Moreover, 4-CMC is

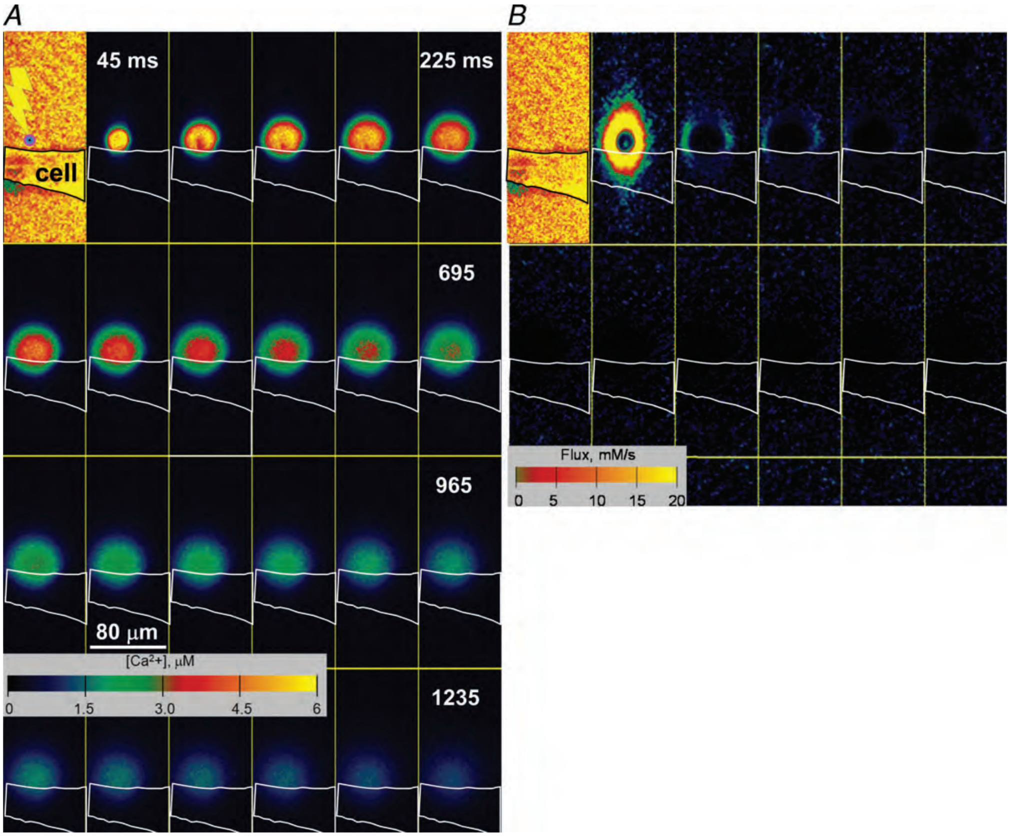

Figure 10. Mouse muscle is normally incapable of CICR
A, images of $[Ca^{2+}]$ (*x*,*y*) of a permeabilized mouse fibre equilibrated with solution containing 3 mM NDBF-EGTA and 0.3 μM free $[Ca^{2+}]$, responding to a SLIC originated 3 μm away from the cell. The first frame shows position of the cell, the contour of which is marked by a white line in the top two rows. One of every five frames is shown in a series acquired at 9 ms intervals. *B*, $\dot{R}(x, y)$ calculated from the corresponding $[Ca^{2+}]_c$ frames in *A*. Note the complete absence of release within the cell. ID: 071210 series 10.

Table 1. CICR responses in frog and mouse muscle fibres

	Enhancer	Trigger [Ca^{2+}] (range, μM)	[Mg^{2+}] (range, mM)	Success rate	Flux (mM s^{-1})	Velocity (μm s^{-1})	*N* Trials	Cells	Mice
Frog	None	0.28–6	0.3–1	0.65	22.7 ± 1.6	98.9 ± 10.2	145	16	10
Mouse	None	0.18–8	0.045–3	0	n.a.	n.a.	150	42	12
	Caffeine + 4-CMC	0.5–2	0.3–0.5	0.52	$15.1 \pm 1.2^*$	$46.6 \pm 7.7^*$	31	13	3
	Clofibrate	1.5–3	0.3	0.31	$3.3 \pm 0.5^*$	$26.1 \pm 3.0^*$	51	9	3

The 2nd column lists drugs present, including caffeine, which was present at 1.8 mM together with 4-CMC at 0.4 mM, and clofibrate, present at 1.5 mM. Triggering [Ca^{2+}], in column 3, was measured at the point of contact of SLICs and cell at the time of initiation of the response. Column 4 lists ranges of [Mg^{2+}]. Column 5 lists the fraction of propagated responses, which include full and frustrated ones, over total trials. Note that in mouse cells propagated responses were only seen in the presence of drugs. Columns 6 and 7 list average flux and velocity (± SEM) of fully propagated responses. Details of internal solution composition are in Methods. In those experiments where release responses were observed, free [Ca^{2+}] in internal solution varied in the range 0.05–0.2 μM without correlation with results. In attempts to elicit response on mouse cells without enhancer drugs, resting free [Ca^{2+}] as high as 2 μM were also used. $^*P < 0.05$ Student's paired *t* test between frog and mouse flux and velocity values.

known to affect other targets inside muscle cells (Biggs, 1965; Al-Moussa & Michelangeli, 2009). We did not carry out tests in the presence of caffeine or 4-CMC alone. Therefore, while the drugs are facilitating the response of the channel to Ca^{2+}, we do not know whether any singular effects of 4-CMC are necessary for inducing CICR in the mammal.

Discussion

The aim of this work was to directly probe the ability of muscle cells to respond to Ca^{2+} transients with Ca^{2+} release. For this purpose and taking advantage of technical innovations in scanning and Ca^{2+} caging we were able to apply SLICs to fast-twitch muscle cells of frogs and mice. The key features that made these synthetic Ca^{2+} events valuable in the present application were rapid time course, arbitrarily adjustable amplitude and quantitative reproducibility. Their limited spatial width was also useful, in allowing precise placement at short distances from the plasma membrane and for avoiding wholesale destruction of dye and cage upon repeated trials.

Frog muscle fibres reacted with a wave of Ca^{2+} release when SLICs were placed either inside the cells or on the outside, 3 to 5 μm from the (permeabilized) plasma membrane. These responses were absent in the mammal, except under pharmacologically altered conditions.

The responses have the hallmarks of 'classic' CICR

As defined by M. Endo (e.g. 2009), a key requirement for a CICR response is that it be elicited by a pure stimulus, involving only an increase in [Ca^{2+}]. The stimulus that gives rise to the response documented here requires direct application of infrared light and production of chemical species other than Ca^{2+} upon cage photolysis. To reduce the complexity of the stimulus we applied the flash outside the cell. This approach constituted a crucial improvement. Indeed, it removed direct irradiation, it either removed or reduced the concentration of photoproducts (which have demonstrated side effects in the case of a chemically related probe, Allen *et al.* 1999) and allowed for accurate determination of the triggering [Ca^{2+}]. The responses observed thus satisfy the definition of CICR, as presumably little else but the trigger Ca^{2+} changes inside cells. The probe was also ideal for comparing abilities across taxa, as amphibian and mammalian cells could be tested under essentially the same conditions.

An additional property of the response that identifies it as classic CICR in skeletal muscle is its inhibition by Mg^{2+}. This ion inhibits CICR by direct action on the RyR, demonstrated on SR fractions and bilayer-reconstituted channels. Mg^{2+} inhibits at the activation site (Laver *et al.* 1997*a*,*b*, 2004) and at the low-affinity I site (Meissner *et al.* 1986; Laver *et al.* 1997*a*). The actions of Mg^{2+} on skeletal muscle at the cellular level were quantitatively reconciled in the frog with this two-site picture by Lacampagne *et al.* (1998), who showed that the steep negative correlation observed between [Mg^{2+}] and frequency of spontaneous sparks could result from increasing occupancy by Mg^{2+} of the I site. The concentration dependence of the inhibition observed here is roughly consistent with that reported by Lacampagne *et al.* (1998). Together, these two works suggest that the present responses and Ca^{2+} sparks have CICR as common mechanism.

While these results endorse the contribution of CICR to Ca^{2+} release in the frog, we seldom found spontaneous Ca^{2+} sparks, which are an established manifestation of CICR. The conditions were not ideal for their detection, as the monitoring dye, Fluo-4 FF, has an affinity at most 10 times lower than the dyes favoured for imaging sparks. In any case, the edge of the propagating waveform seemed smooth, free of sparks. This may reflect a consequence of the powerful synchronization of CICR that is produced by the propagating wave.

The quantitative properties of CICR flux

The Ca^{2+} flux underlying the CICR responses was calculated from the fluorescence images by generalizing to the two-dimensional case, the so-called backward calculation developed for the analysis of line scans (Ríos *et al.* 1999). As scanning was limited to two dimensions of space, the absence of information about the distribution of Ca^{2+} in the *z* direction required a simplifying hypothesis. The probable errors associated with this simplification are estimated, by a simulation presented as Supplemental Fig. S1, to be no greater than 30%.

The main properties of the flux underlying the propagating Ca^{2+} wave are summarized in Fig. 9. Fluxes were found to reach 55 mM s^{-1}, which is somewhat less than the highest values calculated in frog cells activated by voltage clamp depolarization (reviewed by Ríos & Pizarro, 1991), but is sufficiently large to suggest that the CICR response involves a substantial fraction of the release resources of the cell. Waves started at the cell surface, at the point of contact with the stimulating SLIC and, when frustrated, stopped in different regions, some near

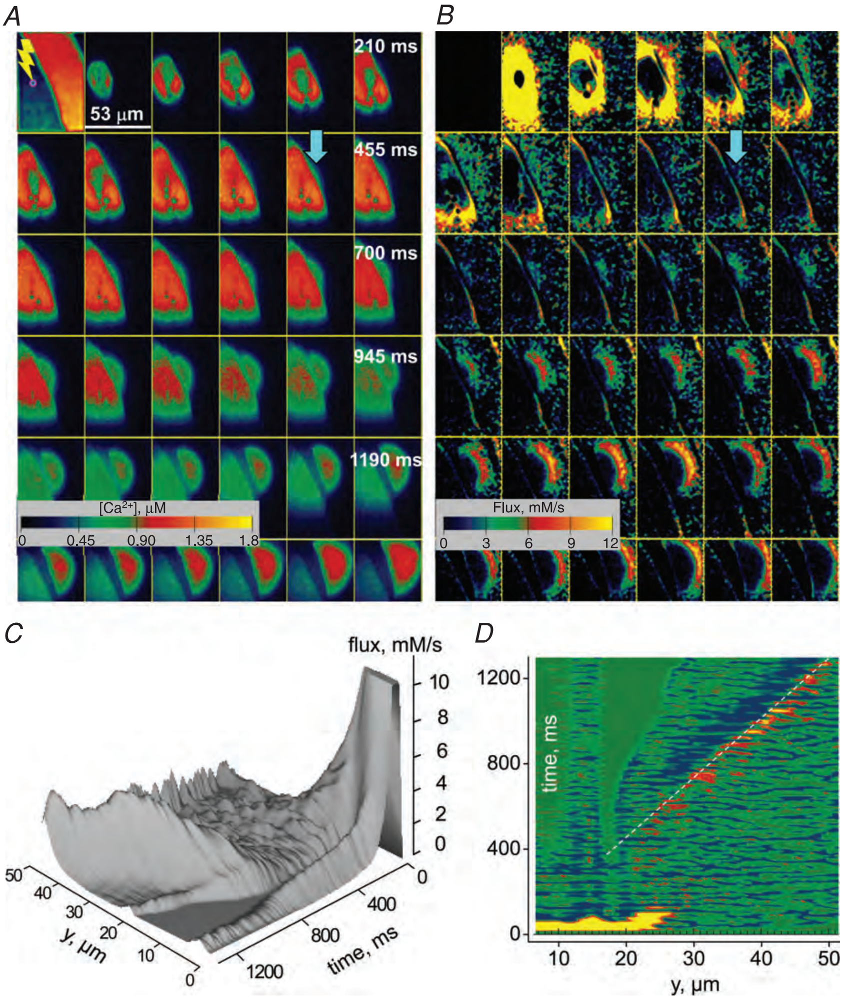

Figure 11. Ca^{2+}-sensitizing drugs promote propagated responses in the mouse
A, $[Ca^{2+}]$ (*x*,*y*) from a permeabilized FDB fibre equilibrated in an internal solution containing 0.4 mM 4-CMC and 1.8 mM caffeine (0.08 µM free Ca^{2+} and 0.5 mM free Mg^{2+}). The stimulus was a macro SLIC of large size and very long duration, originated outside the cell. The macro SLIC triggered a propagated response (see also Supplemental video 5 Fig.11*A*). *B*, $\dot{R}(x,y)$, derived from the $[Ca^{2+}]$ images in *A*. A centrifugal release wave becomes noticeable at 400 to 500 ms (arrow, see also Supplemental video 6 Fig. 11*B*). *C*, transversal flux wave $\dot{R}(y,t)$. *D*, top view of $\dot{R}(y,t)$. Colour scale is modified for convenience of visualization. Flux parameters for mouse cells in the presence of caffeine and 4-CMC are represented in Fig. 9 by purple crosses. ID: 051311 series 54.

the surface, and others near the cell axis. Gradual changes in peak flux were observed at both start (an increase in flux) and end of the propagation (a decrease). That these changes occurred at both ends of the wave implies that the changes were neither a consequence of the different geometry or limitations to diffusion imposed by the cell boundary nor a result of the rapid decrease in curvature that a developing wave experiences near its point of origin. In other words, an intrinsic ability to produce waves of different flux and speed is present in all regions of the cell, near the plasmalemma and away from it.

There is, likewise, a positive three-way correlation among flux, speed and extent of propagation. The good correlation applied both across cells with all-or-none responses, which typically display a constant speed and peak of release flux, and within cells with responses that were graded, either at the beginning or end of the wave. This again identifies the correlation as a property not linked to gross geometry but emanating from fundamental aspects of the process, aspects or features that must be reproducible anywhere in the cell.

These quantitative features were roughly consistent with predictions made by a simple theory of Ca^{2+} waves. We use a formulation by Kupferman *et al.* (1997), representative of results consistent with continuous and discrete models (De Young & Keizer, 1992; Tang & Othmer, 1994; Ponce-Dawson *et al.* 1999). In a continuum of sources with two states (open and closed), a fixed release flux, J_0, a SR pump of rate constant Γ and a fixed threshold concentration for source opening, C_0, the speed v of a wave is

$$v = \left(\frac{DJ_0}{C_0}\right)^{1/2} \frac{1-2\gamma}{(1-\gamma)^{1/2}} \tag{7}$$

where $\gamma = \Gamma C_0/J_0$.

The second fraction in eqn (7), a dimensionless scale factor smaller than 1, represents the slowing associated with removal by the SR pump. γ is typically 0.1 or less; therefore the scale factor is not much smaller than 1 and can be ignored for most purposes. The characteristic time of the system (the time it takes for the flux to build the threshold concentration) is $\tau = C_0/J_0$.

Equation (7) applies when there are no buffers. Clearly, it does not provide a good description of the observations, as it predicts a square-root dependence of speed on flux.

Kupferman *et al.* (1997) also provide analytical expressions for the relationship in the presence of buffers. When one buffer, present at concentration B and having a binding rate constant k^+, is dominant (so that other buffers can be neglected) and fast (implying that $k^+B >> \tau^{-1}$) the wave speed is given by

$$v = \left(\frac{D_{\mathrm{eff}} J_{\mathrm{eff}}}{C_0}\right)^{1/2} \left(1 + \frac{J_0}{2C_0 k^+ B}\right) \tag{8}$$

D_{eff} is an effective diffusion coefficient, reduced by binding to the buffer, defined as

$$D_{\mathrm{eff}} = \frac{D + D_{\mathrm{B}}(\bar{\kappa} - 1)}{\bar{\kappa}}$$

where $\bar{\kappa}$ is the buffer capacity B/K_{D}. The dashed curves in Fig. 9, which approximately 'bracket' the values observed experimentally, were obtained using eqn (8) with $B = 150\ \mu\mathrm{M}$ (upper curve) or $250\ \mu\mathrm{M}$. Other parameters are listed in the figure legend.

The essence of the phenomenon is therefore captured by the simple excitable medium of Kupferman *et al.* (1997), with one buffer, and concentrations and fluxes of Ca^{2+} within a reasonable range. The model suggests reasons for failure of CICR in the mammal. Note that the waves in the mammal are described well with the same parameters that fit the frog data, including threshold C_0, but flux and propagation speed are lower in the mammal. As the response in the mouse required priming with channel-opening drugs (like caffeine, which sensitizes RyRs to activation by Ca^{2+}; reviewed by Lamb *et al.* 2001) one can conclude that in the absence of drugs C_0 is greater in the mammal. Therefore, mouse skeletal muscle cells fail to have CICR due to the combination of a lower release flux and a higher threshold for channel opening by cytosolic Ca^{2+}. Both differences can be ascribed to the absence of RyR3. Indeed, the expression of exogenous RyR3 in adult mouse muscle has been shown to increase flux (Pouvreau *et al.* 2007; Legrand *et al.* 2008) and associate with the presence of Ca^{2+} sparks, spontaneous or in response to voltage clamp depolarization (Pouvreau *et al.* 2007). The drastic changes brought about by the presence of RyR3 need not reflect intrinsic differences among isoforms, as there is evidence that the low sensitivity of RyR1 channels *in situ* to activation by Ca^{2+} is associated at least in part with the presence of the T membrane voltage sensor (Shirokova *et al.* 1999; Zhou *et al.* 2006).

Additionally, we observed a positive correlation between flux, wave speed and the spatial extent of frustrated propagation. Given that the propensity of release channels to open is increased by SR load (Donoso *et al.* 1995; Lamb *et al.* 2001; Sztretye *et al.* 2011*a*), this correlation can be explained simply by assuming that propagation failure results from a decaying flux, consequent to local inhomogeneity of loading and/or an increased threshold, which could also result from local variations in load. Conversely, a greater load would translate to greater release flux, which would result both in faster propagation and a greater safety factor – excess flux over that necessary to reach threshold – which in turn would prevent or delay failures due to local inhomogeneities, and therefore extend the propagation range.

In addition to these straightforward correlations between parameters of the response, there was an indication of negative feedback, namely the non-monotonic dependence of the response rate on trigger [Ca^{2+}], documented in Fig. 5*A*. This dependence was of borderline statistical significance, but it is consistent with the known features of the actions of Ca^{2+}, which include a negative component (e.g. Baylor & Hollingworth, 1988; Simon *et al.* 1991; Hollingworth *et al.* 1992), generally attributed to binding to site I on the channel.

An intriguing property of the propagating flux wave was a slight anisotropy (visible in any of the panels of Fig. 6*A*), whereby the wave was more compact (i.e. had a lesser spatial width), a slightly higher peak and lower speed in the equator, where it propagated orthogonally to the fibre axis. The anisotropic speed in particular is not an artifact of the 'slit' scanning mechanism (which is known to result in a slightly greater optical spread in the x direction) because the SLIC images (e.g. in Fig. 1*B*) are approximately radially symmetrical. The theory of propagation in media with discrete sources predicts a slowing of the speed when sources are separated by longer distances (Kupferman *et al.* 1997; Ponce-Dawson *et al.* 1999). In frog striated muscle, which has one triad junction per sarcomere, the distances between discrete couplons are greater in the longitudinal direction (e.g. Franzini-Armstrong, 1999; Franzini-Armstrong *et al.* 1999); this structural feature might account for the more compact character of the wave at the equator. The greater speed in the longitudinal direction, however, is inconsistent with the greater separation between couplons. According to eqn (8) it could reflect the greater diffusion coefficient of Ca^{2+} and its diffusible ligands in the axial direction (e.g. Kinsey *et al.* 1999).

CICR in physiological Ca^{2+} release

The present observations were made in a less than physiological condition, as the plasma membrane was permeabilized, which both alters the internal medium and modifies the state of the T membrane voltage sensor and other potentially important membrane molecules. In spite of this limitation, which is common to most studies of regulation by Ca^{2+}, the fact that SLICs of [Ca^{2+}] as low as 0.28 μM elicit a response – in the frog – in the presence of physiological [Mg^{2+}] suggests that this mechanism contributes to physiological EC coupling. The present work is therefore consistent with earlier evidence of the involvement of Ca^{2+} in the activation of Ca^{2+} release channels (Klein *et al.* 1996; Pouvreau *et al.* 2007; Legrand *et al.* 2008).

In fact, the present results pose a reverse question: given the apparent ease with which these responses are elicited, what prevents these CICR waves under physiological conditions? There may be two reasons: first, the physiological response involves synchronous release in the whole cell; this in turn results in transient depression of excitability. Second, the propensity of these cells to respond with waves may be exaggerated by saponin permeabilization, in a way similar to the increase of spark size and frequency observed in cut *vs.* intact muscle fibres (Baylor *et al.* 2002; Chandler *et al.* 2003) or the appearance of spark-like events in mammalian muscle cells when they are peeled or saponized (Kirsch *et al.* 2001).

To summarize, the observation of propagated CICR in response to Ca^{2+} transients as low as 0.28 μM is consistent with a contribution by CICR to physiological EC coupling. As the threshold is so much lower than [Ca^{2+}] levels reached near open channels, the mechanism is likely to be activated even if the susceptibility to CICR in intact cells is much lower than in these chemically permeabilized fibres.

CICR is unlikely to contribute to EC coupling in mammalian muscle

As revealed by the present work, the capabilities for CICR of amphibian and mammalian muscle are drastically different. A simulation presented in the Appendix shows that a channel located within an active couplon at a distance of 28 nm from an open channel may face a peak [Ca^{2+}] in the range 6–16 μM. The present experiments could only probe the low end of this range (up to 8 μM). However, the range 6–16 μM was calculated assuming unitary currents of 0.15–0.25 pA, which are the values derived by Kettlun *et al.* (2003) from measurements in bilayers, for currents driven by a luminal-side Ca^{2+} concentration of 0.5 mM. Since recent measurements place [Ca^{2+}]$_{SR}$ at or below 0.5 mM (Rudolf *et al.* 2006; Sztretye *et al.* 2011*b*) and [Ca^{2+}]$_{SR}$ is known to drop during sustained activity (Allen *et al.* 2011), the peak [Ca^{2+}] available for triggering in physiological situations should easily drop below 8 μM, which, as shown here, fails to elicit a response.

Of additional interest is the failure to trigger responses at [Mg^{2+}] as low as 0.045 mM. At this concentration, a substantial fraction of channels should be free of Mg^{2+} at their inhibitory site (according to K_I values reported by Laver *et al.* 1997*a*,*b* or Copello *et al.* 2002). Therefore, the absence of CICR in the mouse is probably not due to inhibition by Mg^{2+} at the I site.

The evidence therefore indicates that CICR may only occasionally, if at all, contribute to physiological EC coupling in the mammal. Caveats apply, because cells have been enzymatically treated and membrane permeabilized, thus permitting many components of the cytosol to diffuse away. Still, the differences between frog and mouse muscle cannot be attributed to the preparation process, which was the same for both animals. That responses occur in mouse muscle when stimulant drugs are present indicates that the channel's ability to respond is still present, albeit severely depressed. The inferred absence of CICR leaves unsettled the mechanism of activation of RyR1 channels not directly facing T tubule voltage sensors.

In conclusion, synthetic localized increases of Ca^{2+} applied in the near-vicinity of cells with permeabilized plasma membrane proved valuable for the study of the functional effects of Ca^{2+} on EC coupling. Use of the Ca^{2+} cage NDBF-EGTA additionally allowed for the separate modification of resting [Ca^{2+}], trigger [Ca^{2+}] and resting [Mg^{2+}], therefore permitting a more physiological environment and a search for the signature dependence of CICR on [Mg^{2+}]. Thus, SLICs provide a new avenue for the exploration of the roles of Ca^{2+} in skeletal muscle, which improves over previous protocols in rate of rise, locality and reproducibility. In frog muscle, SLICs elicited propagated responses that had the hallmarks of CICR. In cells equilibrated with physiological internal solutions the threshold [Ca^{2+}] was 0.5 μM or less. As this value is much lower than concentrations prevailing near channels during normal activity, the result is evidence of Ca^{2+}-dependent activation of Ca^{2+} release during physiological EC coupling. As the primary stimulus was Ca^{2+} rather than the radiation or subproducts of photo-release, the present responses qualify as CICR. By contrast, fibres of mouse skeletal muscle did not respond unless Ca^{2+} channel opener drugs were present at substantial concentrations, an observation contrary to the possibility of a physiological contribution of CICR in the mammal. Lower flux and higher threshold [Ca^{2+}] of the propagating wave explain the absence of CICR in the mouse under normal conditions. In turn the differences in flux and threshold may be ascribed to the different endowment of RyR isoforms in these two taxa.

Appendix

Local [Ca^{2+}] in a working couplon

To compare Ca^{2+} transients that could occur physiologically with the SLICs used as stimuli in the present work, we calculated the stationary increase in local cytosolic [Ca^{2+}] due to the activation of a linear array of channels, or couplon (Stern *et al.* 1997), with the geometry described by Franzini-Armstrong *et al.* (1999) for rat muscle (illustrated in Fig. A1). The goal in this Appendix is to calculate the free Ca^{2+} concentration facing a channel when the nearest neighbour is assumed to be open and the rest of the couplon is in a state between typical and maximal physiological activation.

Repeating the implementation by Rengifo *et al.* (2002) of an analytical solution to the linearized diffusion problem provided by Pape *et al.* (1995), local [Ca^{2+}] was calculated as

$$[\mathrm{Ca}^{2+}](r) = [\mathrm{Ca}^{2+}]_{\mathrm{R}} + \Delta[\mathrm{Ca}^{2+}]_{\mathrm{p}}(r) + \Delta[\mathrm{Ca}^{2+}]_{\mathrm{c}}. \quad \text{(A1)}$$

[Ca^{2+}]$_{\mathrm{R}}$ is resting [Ca^{2+}], Δ[Ca^{2+}]$_{\mathrm{p}}$ is the contribution due to the 'central' channel – the one assumed to be open – and is a function of the distance *r* from said channel. Δ[Ca^{2+}]$_{\mathrm{c}}$ is the sum of individual contributions of the other channels in the couplon.

The steady state increase $\Delta[\mathrm{Ca}^{2+}]_{\mathrm{p}}(r)$ due to one channel was calculated as

$$\Delta[\mathrm{Ca}^{2+}]_{\mathrm{p}}(r) = \frac{\phi}{2\pi n_{A'} D_{\mathrm{Ca}}\, r} + \sum_{i=1}^{m} c_i y_i / r$$
$$\equiv \Phi/r + \sum_{i=1}^{m} c_i y_i / r \quad \text{(A2)}$$

ϕ is the unitary flux in ions s^{-1}, set to 0.62×10^6 s^{-1} (0.2 pA) to match the measured unitary current through channels reconstituted in bilayers separating solutions of near-physiological composition (Kettlun *et al.* 2003) when [Ca^{2+}]$_{\mathrm{SR}}$ is 0.5 mM (Sztretye *et al.* 2011*b*). D_{Ca} is the Ca^{2+} diffusion coefficient (3.5×10^{-6} cm^2 s^{-1}), $n_{A'}$ is the number of ions in 1 one-thousandth of a mol. There is one additive term, of index *i*, for each of *m* mobile buffers. y_i are elements of the column vector

$$\mathbf{UDe} - \Phi\mathbf{A}^{-1}\mathbf{f}$$

A is a $m \times m$ matrix of elements $\mathrm{A}_{ii} = a_i + b_i$ and $\mathrm{A}_{ij} = a_i\, c_j / c_i$, with $a_i = k_i\, L_i / D_{\mathrm{Ca}}$, k_i the forward Ca^{2+}-binding

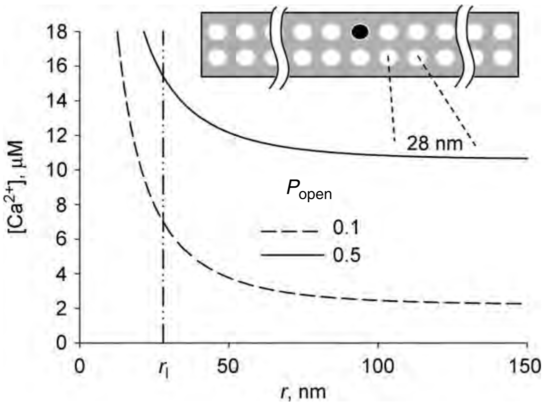

Figure A1. Concentrations of Ca^{2+} within an active couplon
The couplon geometry is represented in the inset. The 'central' channel (black) is assumed to be open. The state of the other channels in the couplon is described by an average open probability. Calcium concentration, calculated by eqn (A1), is plotted *vs.* distance from the central channel. The two curves correspond to two values of p_{open}, 0.1 and 0.5, which are believed to span the physiological range. The vertical line marks the distance r_1 (= 28 nm) separating centres of neighbouring channels. [Ca^{2+}] facing the nearest neighbour to an open channel is therefore between 6 and 16 μM. As argued in the text, this calculation applies regardless of the position of the open channel within the couplon. 8 μM is the highest value of the trigger [Ca^{2+}] reached in the present experiments. These triggers never elicited a response in mouse cells, unless channel opening drugs were present.

rate constant of buffer i, L_i its concentration, $b_i = (k_i [\mathrm{Ca}^{2+}]_\mathrm{R} + k_i^-)/D_i$, $[\mathrm{Ca}^{2+}]_\mathrm{R}$ is resting $[\mathrm{Ca}^{2+}]$, and k_i^- the backward rate constant. **U** is the matrix of unit eigenvectors of **A** in column, **f** the column vector of elements a_i/c_i, and **e** the column vector of terms $e^{-r/\sqrt{\lambda_j}}$, where λ_j are the eigenvalues of **A**. Finally **D** is a diagonal $m \times m$ matrix, the diagonal terms of which form the column vector Φ**JCf** and **J** is the Jordan form of **A**.

Because the situation is stationary, fixed buffers do not enter the calculation. In the conditions thought to prevail in a working cell the contributions by mobile buffers other than ATP will be small. Therefore the calculation was limited to a two-buffer case ($m = 2$). It took into account ATP and merged the other diffusible buffers into a 'generic' mobile buffer, assumed to be present at a concentration of 100 μM. i is 1 for ATP and 2 for the generic buffer, c_i is D_i/D_Ca. D_1 is 1.4×10^{-6} cm^2 s^{-1} and D_2 is 0.7×10^{-6} cm^2 s^{-1} for the generic buffer. For ATP:Ca the rate constants were 1.36×10^7 M^{-1} s^{-1} and 3×10^4 s^{-1}. For the generic buffer the rate constants were set at 5×10^8 M^{-1} s^{-1} and 50 s^{-1}, for a K_D of 0.1 μM. Given the high concentration of ATP, the results are not strongly dependent on the assumptions for the generic buffer. The general form of the equations allow for easy extension of the calculation to more complex buffering conditions.

The contribution due to the other channels in the couplon was calculated as

$$\Delta[\mathrm{Ca}^{2+}]_\mathrm{c}(r) = p_\mathrm{open} \sum_j \Delta[\mathrm{Ca}^{2+}]_\mathrm{p}(r_j), \qquad \text{(A3)}$$

a sum of terms of the form given by eqn (A2), scaled down by a p_open that represents the average open fraction of the other channels in the couplon, which was estimated as follows. The maximum flux, corresponding to a unitary current of 0.2 pA (Kettlun *et al.* 2003) and a concentration of channels of 0.27 mM (a calculation of Baylor *et al.* 1983, made for the frog but roughly applicable to the mammal, which has twice the number of couplons but lacks parajunctional channels) is 169 mM s^{-1}. Royer *et al.* (2008) measured on average 45 mM s^{-1} in mouse FDB fibres maximally activated by voltage clamp, consistent with a p_open of 0.25. As the individual contributions fall precipitously with distance, only the nearest three to four channels add appreciably to $\Delta[\mathrm{Ca}^{2+}]_\mathrm{c}$. This property makes $\Delta[\mathrm{Ca}^{2+}]_\mathrm{c}$ effectively independent of r, equal at all channel positions, except those less than three to four channels removed from the ends of the couplon. The property also makes the calculation independent of couplon size beyond a certain small bound.

Calcium concentration, calculated by eqn (A1), is plotted *vs.* distance in Fig. A1. The two curves correspond to two values of p_open, 0.1 and 0.5, considered to span the range of possibilities. The vertical line marks the distance r_1 (= 28 nm) between the channel that is assumed open and a nearest neighbour. This neighbour, therefore, faces a $[\mathrm{Ca}^{2+}]$ estimated between 6 and 16 μM. The Ca^{2+} triggers used in the present experiments, which reached up to 8 μM, never elicited a response in mouse cells, unless channel opening drugs were present.

References

Al-Mousa F & Michelangeli F (2009). Commonly used ryanodine receptor activator, 4-chloro-m-cresol (4CmC), is also an inhibitor of SERCA Ca^{2+} pumps. *Pharmacol Rep* **61**, 838–842.

Allen DG, Clugston E, Petersen Y, Roder IV, Chapman BE & Rudolf R (2011). Interactions between intracellular calcium and phosphate in intact mouse muscle during fatigue. *J Appl Physiol* **111**, 358–366.

Allen DG, Lannergren J & Weserblad H (1999). The use of cage adenine nucleotides and caged phosphate in intact skeletal muscle fibres of the mouse. *Acta Physiol Scand* **166**, 341–347.

Armstrong CM, Bezanilla FM & Horowicz P (1972). Twitches in the presence of ethylene glycol bis(-aminoethyl ether)-N,N'-tetracetic acid. *Biochem Biophys Acta* **267**, 605–608.

Baylor SM, Chandler WK & Marshall MW (1983). Sarcoplasmic reticulum release in frog skeletal muscle fibres estimated from arsenazo III calcium transients. *J Physiol* **344**, 625–666.

Baylor SM & Hollingworth S (1988). Fura-2 calcium transients in frog skeletal muscle fibers. *J Physiol* **403**, 151–192.

Baylor SM, Hollingworth S & Chandler WK (2002). Comparison of simulated and measured calcium sparks in intact skeletal muscle fibers of the frog. *J Gen Physiol* **120**, 349–368.

Baylor SM & Hollingworth S (2003). Sarcoplasmic reticulum calcium release compared in slow-twitch and fast-twitch fibres of mouse muscle. *J Physiol* **551**, 125–138.

Bers DM (2002). Cardiac excitation-contraction coupling. *Nature* **415**, 198–205.

Bers DM, Patton CW & Nuccitelli R (2010). A practical guide to the preparation of Ca^{2+} buffers. *Methods Cell Biol* **99**, 1–26.

Biggs DF (1965). Experiments on the mechanism of action of chlorocresol and caffeine. *Br J Pharmacol Chemother* **24**, 510–518.

Blatter LA (1990). Intracellular free magnesium in frog skeletal muscle studied with a new type of magnesium-selective microelectrode: interactions between magnesium and sodium in the regulation of $[\mathrm{Mg}]_\mathrm{i}$. *Pflugers Arch* **416**, 238–246.

Block BA, Imagawa T, Campbell KP & Franzini-Armstrong C (1988). Structural evidences for direct interaction between the molecular components of the transverse tubule/sarcoplasmic reticulum junction in skeletal muscle. *J Cell Biol* **107**, 2587–2600.

Canato M, Scorzeto M, Giacomello M, Protasi F, Reggiani C & Stienen GJ (2010). Massive alterations of sarcoplasmic reticulum free calcium in skeletal muscle fibers lacking calsequestrin revealed by a genetically encoded probe. *Proc Natl Acad Sci U S A* **107**, 22326–22331

Chandler WK, Hollingworth S & Baylor SM (2003). Simulation of calcium sparks in cut skeletal muscle fibers of the frog. *J Gen Physiol* **121**, 311–324.

Cheng H, Lederer WJ & Cannell MB (1993). Calcium sparks: elementary events underlying excitation-contraction coupling in heart muscle. *Science* **262**, 740–744.

Choisy S, Huchet-Cadiou C & Léoty C (2000). Differential effects of 4-chloro-m-cresol and caffeine on skinned fibers from rat fast and slow skeletal muscles. *J Pharmacol Exp Ther* **294**, 884–893.

Copello JA, Barg S, Sonnleitner A, Porta M, Diaz-Sylvester P, Fill M, Schindler H & Fleischer S (2002). Differential activation by Ca^{2+} ATP and caffeine of cardiac and skeletal muscle ryanodine receptors after block by Mg^{2+}. *J Membr Biol* **187**, 51–64.

De Young GW & Keizer J (1992). A single-pool inositol 1,4,4-trisphosphate-receptor-based model for agonist-stimulated oscillations in Ca^{2+} concentration. *Proc Natl Acad Sci U S A* **89**, 9895–9899.

Donoso P, Prieto H & Hidalgo C (1995). Luminal calcium regulates calcium release in triads isolated from frog and rabbit skeletal muscle. *Biophys J* **68**, 507–515.

Endo M (2009). Calcium-induced calcium release in skeletal muscle. *Physiol Rev* **89**, 1153–1176.

Endo M, Tanaka M & Ogawa Y (1970). Calcium induced release of calcium from the sarcoplasmic reticulum of skinned skeletal muscle fibres. *Nature* **228**, 34–36.

Felder E & Franzini-Armstrong C (2002). Type 3 ryanodine receptors of skeletal muscle are segregated in a parajunctional position. *Proc Natl Acad Sci U S A* **99**, 1695–1700.

Fénelon K & Pape PC (2002). Recruitment of Ca^{2+} release channels by calcium-induced Ca^{2+} release does not appear to occur in isolated sites in frog skeletal muscle. *J Physiol* **544**, 777–791.

Fill M & Copello JA (2002). Ryanodine receptor calcium release channels. *Physiol Rev* **82**, 893–922.

Ford LE & Podolsky RJ (1970). Regenerative calcium release within muscle cells. *Science* **167**, 58–59.

Fosset M, Jaimovich E, Delpont E & Lazdunski M (1983). $[^3H]$nitrendipine receptors in skeletal muscle. *J Biol Chem* **258**, 6086–6092.

Franzini-Armstrong C (1999). The sarcoplasmic reticulum and the control of muscle contraction. *FASEB J* **13**, S266–S270.

Franzini-Armstrong C, Protasi F & Ramesh V (1999). Shape, size, and distribution of Ca^{2+} release units and couplons in skeletal and cardiac muscles. *Biophys J* **77**, 1528–1539.

Hollingworth S, Harkins AB, Kurebayashi N, Konishi M & Baylor SM (1992). Excitation-contraction coupling in intact frog skeletal muscle fibers injected with mmol concentrations of Fura-2. *Biophys J* **63**, 224–234.

Ikemoto T & Endo M (2001). Properties of Ca^{2+} release induced by clofibric acid from sarcoplasmic reticulum of mouse skeletal muscle fibres. *Br J Pharmacol* **134**, 719–728.

Jacquemond V, Csernoch L, Klein MG & Schneider MF (1991). Voltage-gated and calcium-gated calcium release during depolarization of skeletal muscle fibers. *Biophys J* **60**, 867–873.

Jiménez-Moreno R, Wang ZM, Messi ML & Delbono O (2010). Sarcoplasmic reticulum Ca^{2+} depletion in adult skeletal muscle fibres measured with the biosensor D1ER. *Pflugers Arch* **459**, 725–735.

Kettlun G, Gonzalez A, Ríos E & Fill M (2003). Unitary Ca^{2+} current through mammalian cardiac and amphibian skeletal muscle ryanodine receptor channels under near-physiological ionic conditions. *J Gen Physiol* **122**, 407–417.

Kinsey ST, Locke BR, Penke B & Moerland TS (1999). Diffusional anisotropy is induced by subcellular barriers in skeletal muscle. *NMR Biomed* **12**, 1–7.

Kirsch WG, Uttenweiler D & Fink RH (2001). Spark- and ember-like elementary Ca^{2+} release events in skinned fibres of adult mammalian skeletal muscle. *J Physiol* **537**, 379–389.

Klein MG, Cheng H, Santana LF, Jiang YH, Lederer WJ & Schneider MF (1996). Two mechanism of quantized calcium release in skeletal muscle. *Nature* **379**, 455–458.

Kupferman R, Mitra PP, Hohenberg PC & Wang S (1997). Analytical calculation of intracellular calcium wave characteristics. *Biophys J* **72**, 2430–2444.

Kushmerick MJ & Podolsky RJ (1969). Ion mobility in muscle cells. *Science* **166**, 1297–1298.

Lacampagne A, Klein MG & Schneider MF (1998). Modulation of the frequency of spontaneous sarcoplasmic reticulum Ca^{2+} release events (Ca^{2+} sparks) by myoplasmic $[Mg^{2+}]$ in frog skeletal muscle. *J Gen Physiol* **111**, 207–224.

Lacampagne A, Klein MG, Ward CW & Schneider MF (2000). Two mechanisms for termination of individual Ca^{2+} sparks in skeletal muscle. *Proc Natl Acad Sci U S A* **97**, 7823–7828.

Lamb GD, Cellini MA & Stephenson DG (2001). Different Ca^{2+} releasing action of caffeine and depolarisation in skeletal muscle fibres of the rat. *J Physiol* **31**, 715–728.

Launikonis BS& Stephenson DG (2000). Effects of Mg^{2+} on Ca^{2+} release from sarcoplasmic reticulum of skeletal muscle fibres from yabby (crustacean) and rat. *J Physiol* **526**, 299–312.

Laver DR, Baynes TM & Dulhunty AF (1997*a*). Magnesium inhibition of ryanodine-receptor calcium channels: evidence for two independent mechanism. *J Membr Biol* **156**, 213–229.

Laver DR, O'Neill ER & Lamb GD (2004). Luminal Ca^{2+}-regulated Mg^{2+} inhibition of skeletal RyRs reconstituted as isolated channels or coupled clusters. *J Gen Physiol* **124**, 741–758.

Laver DR, Owen VJ, Junankar PR, Taske NL, Dulhunty AF & Lamb GD (1997*b*). Reduced inhibitory effect of Mg^{2+} on ryanodine receptor-Ca^{2+} release channels in malignant hyperthermia. *Biophys J* **73**, 1913–1924.

Legrand C, Giacomello E, Berthier C, Allard B, Sorrentino V & Jacquemond V (2008). Spontaneous and voltage-activated Ca^{2+} release in adult mouse skeletal muscle fibres expressing the type 3 ryanodine receptor. *J Physiol* **586**, 441–457.

Lindegger N & Niggli E (2005). Paradoxical SR Ca^{2+} release in guinea-pig cardiac myocytes after β-adrenergic stimulation revealed by two-photon photolysis of caged Ca^{2+}. *J Physiol* **565**, 801–813.

Lipp P & Niggli E (1998). Fundamental calcium release events revealed by two-photon excitation photolysis of caged calcium in guinea-pig cardiac myocytes. *J Physiol* **508**, 801–809.

Liu Y, Porta M, Quin J, Ramos J, Nani A, Shannon TR & Fill M (2010). Flux regulation of cardiac ryanodine receptor channels. *J Gen Physiol* **135**, 15–27.

Meissner G, Darling E & Eveleth J (1986). Kinetics of rapid Ca^{2+} release by sarcoplasmic reticulum. Effects of Ca^{2+}, Mg^{2+}, and adenine nucleotides. *Biochemistry* **25**, 236–244.

Momotake A, Lindegger N, Niggli E, Barsotti RJ & Ellis-Davies GC (2006). The nitrodibenzofuran chromophore: a new caging group for ultra-efficient photolysis in living cells. *Nat Methods* **3**, 35–40.

Murayama T, Kurebayashi N & Ogawa Y (2000). Role of Mg^{2+} in Ca^{2+}-induced Ca^{2+} release through ryanodine receptors of frog skeletal muscle: modulations by adenine nucleaotides and caffeine. *Biophys J* **78**, 1810–1824.

Murayama T & Ogawa Y (2001). Selectively suppressed Ca^{2+}-induced Ca^{2+} release activity of α-ryanodine receptor (α-RyR) in frog skeletal muscle sarcoplasmic reticulum: potential distinct modes in Ca^{2+} release between α- and β-RyR. *J Biol Chem* **276**, 2953–2960.

Murayama T & Ogawa Y (2004). RyR1 exhibits lower gain of CICR activity than RyR3 in the SR: evidence for selective stabilization of RyR1 channel. *Am J Physiol Cell Physiol* **287**, C36–C45.

Nakai J, Dirksen RT, Nguyen HT, Pessah IN, Beam KG & Allen PD (1996). Enhanced dihydropyridine receptor channel activity in the presence of ryanodine receptor. *Nature* **380**, 72–75.

Noguchi J, Matsuzaki M, Ellis-Davies GC & Kasai H (2005). Spine-neck geometry determines NMDA receptor-dependent Ca^{2+} signaling in dendrites. *Neuron* **46**, 609–622.

Pape PC, Jong DS & Chandler WK (1995). Calcium release and its voltage dependence in frog cut muscle fibers equilibrated with 20 mM EGTA. *J Gen Physiol* **106**, 259–336.

Pape PC, Jong DS, Chandler WK & Baylor SM (1993). Effect of Fura-2 on action potencial-stimulated calcium release in cut twitch fibers from frog muscle. *J Gen Physiol* **102**, 295–332.

Ponce-Dawson S, Keizer J & Pearson J (1999). Fire-diffuse-fire model of dynamics of intracellular calcium waves. *Proc Natl Acad Sci U S A* **96**, 6060–6063.

Pouvreau S, Royer L, Yi J, Brum G, Meissner G, Ríos E & Zhou J (2007). Ca^{2+} sparks operated by membrane depolarization require isoform 3 ryanodine receptor channels in skeletal muscle. *Proc Natl Acad Sci U S A* **104**, 5232–5240.

Rengifo J, Rosales R, Gonzalez A, Cheng H, Stern MD & Ríos E (2002). Intracellular Ca^{2+} release as irreversible Markov process. *Biophys J* **83**, 2511–2521.

Ríos E & Brum G (1987). Involvement of dihidropiridine receptors in excitation-contraction coupling in skeletal muscle. *Nature* **325**, 717–720.

Ríos E & Pizarro G (1988). Voltage sensors and calcium channels of excitation-contraction coupling. *News Physiol Sci* **3**, 223–227.

Ríos E & Pizarro G (1991). Voltage sensor of excitation-contraction coupling in skeletal muscle. *Physiol Rev* **71**, 849–908.

Ríos E, Stern MD, Gonzalez A, Pizarro G & Shirokova N (1999). Calcium release flux underlying Ca^{2+} sparks of frog skeletal muscle. *J Gen Physiol* **114**, 31–48.

Rosseau E, Ladine J, Liu QY & Meissner G (1988). Activation of the Ca^{2+} release channel of skeletal muscle sarcoplasmic reticulum by caffeine and related compounds. *Arch Biochem Biophys* **267**, 75–86.

Royer L, Pouvreau S & Ríos E (2008). Evolution and modulation of intracellular calcium release during long-lasting depleting depolarization in mouse muscle. *J Physiol* **586**, 4609–4629.

Rudolf R, Magalhães PJ & Pozzan T (2006). Direct *in vivo* monitoring of sarcoplasmic reticulum Ca^{2+} and cytosolic cAMP dynamics in mouse skeletal muscle. *J Cell Biol* **173**, 187–193.

Schneider MF & Chandler WK (1973). Voltage dependent charge movement of skeletal: a possible step in excitation-contraction coupling. *Nature* **242**, 244–246.

Shirokova N, Garcia J, Pizarro G & Ríos E (1996). Ca^{2+} release from the sarcoplasmic reticulum compared in amphibian and mammalian skeletal muscle. *J Gen Physiol* **107**, 1–18.

Shirokova N & Ríos E (1997). Small event Ca^{2+} release: a probable precursor of Ca^{2+} sparks in frog skeletal muscle. *J Physiol* **502**, 3–11.

Shirokova N, Shirokov R, Rossi D, González A, Kirsch WG, García J, Sorrentino V & Ríos E (1999). Spatially segregated control of Ca^{2+} release in developing skeletal muscle of mice. *J Physiol* **521**, 483–495.

Simon BJ, Klein MG & Schneider MF (1991). Calcium dependence of inactivation of calcium release from the sarcoplasmic reticulum in skeletal muscle fibers. *J Gen Physiol* **97**, 437–471.

Stern MD, Pizarro G & Ríos E (1997). Local control model of excitation-contraction coupling in skeletal muscle. *J Gen Physiol* **110**, 415–440.

Sutko JL Airey JA (1996). Ryanodine receptor Ca^{2+} release channels: does diversity in form equal diversity in function? *Physiol Rev* **76**, 1027–1071.

Sztretye M, Yi J, Figueroa L, Zhou J, Royer L, Allen PD, Brum G & Ríos E (2011*a*). Measurement of RyR permeability reveals a role of calsequestrin in termination of SR Ca^{2+} release in skeletal muscle. *J Gen Physiol* **138**, 231–247.

Sztretye M, Yi J, Figueroa L, Zhou J, Royer L & Ríos E (2011*b*). D4cpv-calsequestrin: a sensitive ratiometric biosensor targeted to the calcium store of skeletal muscle. *J Gen Physiol* **138**, 211–229.

TanabeT, Takeshima H, Mikami A, Flockerzi V, Takahashi H, Kangawa K, Kojima M, Matsuo H, Hirose T & Numa S (1987). Primary structure of the receptor for calcium channel blockers from skeletal muscle. *Nature* **328**, 313–318.

Tang Y & Othmer Y (1994). A model of calcium dynamics in cardiac myocytes based on the kinetics of ryanodine-sensitive calcium channels. *Biophys J* **67**, 2223–2235.

Treves S, Pouliquin R, Moccagatta L & Zorzato F (2002). Functional properties of EGFP-tagged skeletal muscle calcium-release channel (ryanodine receptor) expressed in COS-7 cells: sensitivity to caffeine and 4-chloro-m-cresol. *Cell Calcium* **31**, 1–12.

Tripathy A & Meissner G (1996). Sarcoplasmic reticulum luminal Ca^{2+} has access to cytosolic activation and inactivation sites of skeletal muscle Ca^{2+} release channel. *Biophys J* **70**, 2600–2615.

Ursu D, Schuhmeier RP & Melzer W (2005). Voltage-controlled Ca^{2+} release and entry flux in isolated adult muscle fibres of the mouse. *J Physiol* **562**, 347–365.

Westerblad H & Allen D (1992). Myoplasmic free Mg^{2+} concentration during repetitive stimulation of single fibres from mouse skeletal muscle. *J Physiol* **453**, 413–434.

Westerblad H, Andrade FH & Allen D (1998). Effects of ryanodine receptor agonist 4-chloro-*m*-cresol on myoplasmic free Ca^{2+} concentration in mouse skeletal muscle. *Cell Calcium* **24**, 105–115.

Zhou J, Brum G, Gonzalez A, Launikonis B, Stern MD & Ríos E (2003). Ca^{2+} sparks and embers of mammalian muscle. Properties of the sources. *J Gen Physiol* **122**, 95–114.

Zhou J, Launikonis BS, Ríos E & Brum G (2004). Regulation of Ca^{2+} sparks by Ca^{2+} and Mg^{2+} in mammalian and amphibian muscle. An RyR isoform-specific role in excitation-contraction coupling? *J Gen Physiol* **124**, 409–428.

Zhou J, Yi J, Royer L, Launikonis BS, González A, García J & Ríos E (2006). A probable role of dihydropyridine receptors in repression of Ca^{2+} sparks demonstrated in cultured mammalian muscle. *Am J Physiol Cell Physiol* **290**, C539–C553

Ziman AP, Ward CW, Rodney GG, Lederer WJ & Bloch RJ (2010). Quantitative measurement of Ca^{2+} in the sarcoplasmic reticulum lumen of mammalian skeletal muscle. *Biophys J* **99**, 2705–2714

Zorzato F, Scutari E, Tegazzin V, Clementi E & Treves S (1993). Chlorocresol: an activator of ryanodine receptor-mediated Ca^{2+} release. *Mol Pharmacol* **44**, 1192–11201.

Author's present address

V. M. Shkryl: Department of General Physiology of Nervous System, A. A. Bogomoletz Institute of Physiology, Kiev, Ukraine.

Author contributions

Experiments were carried out in the laboratories of the Section of Cellular Signaling at Rush University, Chicago. Synthesis and initial testing of NDBF-EGTA was carried out in the Department of Pharmacology and Physiology, Drexel University, Philadelphia. L.F. carried out most experiments, data collection and initial analysis. Contributed to design, interpretation, preparation of figures, writing and revising. V.M.S. contributed to assembly of experimental set-up, carried out data collection, analysis, and contributed to the preparation of figures. J.Z. contributed to initial assembly, experiments and data collection. C.M. contributed to assembly and testing of experimental set-up, and collection of data in mouse muscle. A.M. synthesized the cage and contributed critical discussion of results. G.B. contributed to initial set-up assembly, testing, experimental design, collection and analysis of data. L.A.B. to planning of experimental approach, set-up assembly, experimental design, data analysis and interpretation, drafting and critical editing. G.C.R.E.-D. synthesized the cage, contributed to experimental design, data analysis, interpretation, and drafting of the article. E.R. planned, designed and realized experiments, analysed and interpreted data, and contributed figure preparation and writing. All authors approved the final version.

Acknowledgements

This work was supported by grants from the National Center for Research Resources, Rush University's Hasterlik Philanthropic Fund and the National Institute of Arthritis and Musculoskeletal and Skin Diseases, NIAMS, (AR049184 and AR032808) to E. Ríos, the National Institute of General Medical Sciences (GM53395) to GCRE-D, the National Heart and Lung Institute (HL62231, HL80101 and HL101235) and the Leducq Foundation to L. Blatter, and the NIAMS (AR057404) and the Muscular Dystrophy Association of America (MDA-4351) to J. Zhou. GCRE-D and AM have filled a preliminary patent on the synthesis of nitrodibenzyl caging chromophores.

РОЗДІЛ 3. ЗМІНА КАЛЬЦІЄВО СИГНАЛУ У НЕЙРОНАХ

3.1 Внутрішньоклітинні потоки кальцію у збудливих клітинах

Одним із важливих завдань сучасної клітинної біології є визначення не лише концентрацій різних внутрішньоклітинних іонів, зокрема кальцію, але і динаміки змін цих параметрів. Визначення концентрацій кальцію всередині клітини або навіть її окремих органел є можливим із використанням декількох експериментальних підходів – електронної мікроскопії, електрофізіологічних, флуоресцентно-оптичних методів і низки інших. Кальцій у клітині знаходиться у вільному (іонізованому) і зв’язаному стані. Локальні швидкі зміни рівня Ca^{2+} в певних локусах є індивідуальними квантами інтегрального осциляторного кальцієвого сигналу, що визначає багато функцій клітини. З’ясування розподілу кальцієвих потоків у різних клітинних компартментах і з’ясування ролі низки кальцієвих рецепторів і каналів у плазматичний мембрані та мембранах внутрішньоклітинних органел, дозволяє наблизитися до визначення внеску відповідних подій у регуляцію фізіологічних функцій клітини, наприклад синаптичної пластичності нейрона. В даному огляді описані методичні підходи для визначення концентрації кальцію та величини його потоків, що дозволяє охарактеризувати окремі компоненти кальцієвої сигналізації та виявити їх роль у регуляції різних функцій збудливих клітин.

DOI 10.1007/s11062-018-9698-2
Neurophysiology, Vol. 49, No. 5, October, 2017

REVIEWS

Intracellular Calcium Fluxes in Excitable Cells

V. M. Shkryl[1]

Received: February 10, 2016

The estimation of not only concentrations of different intracellular ions (calcium in particular), but also of the dynamics of changes in these parameters, is one of the most important tasks in today cell biology. The measurements of calcium concentrations in the cell and even in its separate organelles are possible with the use of several experimental approaches (electron microscopy, electrophysiological techniques, fluorescent/optic methods, and others). Calcium is present in the cell in free (ionized) and bound states. Local rapid changes in the Ca^{2+} level in definite cell sites are individual quanta of an integral oscillatory calcium signal determining numerous cell functions. Separation of calcium fluxes in different cell compartments and evaluation of the role of calcium receptors and channels in the plasma membrane and membranes of the intracellular organelles allows experimenters to begin estimation of contributions of the respective events to the regulation of physiological functions of the cell, e.g., of synaptic plasticity of the neuron. This review describes some methodic approaches for the measurements of concentrations of calcium and characteristics of its fluxes; this makes it possible to characterize separate components of calcium signaling and to determine the roles of these components in the regulation of different functions of excitable cells.

Keywords: Ca^{2+}, calcium fluxes, fluorescent indicators, microscopy, neuron.

INTRODUCTION

Calcium is the most important ion in cell signaling, and changes in its concentration provide the regulation of a number of cell processes (excitation, muscle contraction, transmitter release, synaptic plasticity, gene expression, apoptosis, etc.). The characteristics of calcium signals are determined by the functioning of an integral complex of the molecular mechanisms, namely ion channels, calcium-binding proteins, channels providing calcium release from the intracellular stores, and also exchangers (or pumps) providing calcium removal from the cell cytosol. Intracellular structures responsible for translocations of calcium ions play significant roles in the transmission of calcium signals. In excitable cells (neurons, muscle cells, and secretory cells), a depolarization-induced calcium entry initiates an additional increase in the concentration of its ions due to calcium release from the calcium stores, and this exerts strong regulatory effects on the corresponding cell functions both in a local mode and in the cell as the whole [1, 2]. From the most general aspect, calcium is frequently considered an agent affecting intracellular processes via changes in the intracellular concentration of an ionized form of this element ($[Ca^{2+}]_i$), i.e., of free calcium. This index changes from about 50 nM in the resting state to approximately 10 μM at the peaks of a few physiological signals [3]. In the course of realization of various physiological processes and after stimulations of a different nature, short-lasting (transient) significant increases in the $[Ca^{2+}]_i$ occur.

The entry of Ca^{2+} from the extracellular environment is realized due to activation of voltage-gated Ca^{2+} channels (VGCCs), channels of ionotropic glutamate NMDA receptors and acetylcholine receptors, and also of channels of the transient receptor potential (TRPV channels) in the plasma membrane. The endoplasmic reticulum (ER) is the main intracellular structure that receives and processes calcium signals coming from calcium channels in the plasma membrane. The corresponding structure in muscle fibers is called the sarcoplasmic reticulum (SR). The release of

---

[1] Bogomolets Institute of Physiology of the NAS of Ukraine, Kyiv. Ukraine
Correspondence should be addressed to V. M. Shkryl
(e-mail: slava@biph.kiev.ua)

calcium from the intracellular stores appears as oscillations; it depends on the channel activity in the membranes of calcium-binding cell organelles (ER, SR, mitochondria, Golgi apparatus, and nucleus). An additional increase in the cytosol concentration of calcium by its release from the ER/SR is realized due to opening of the channels of inositol-3-phosphate rectors (IP_3Rs) and/or ryanodine receptors (RyRs). This process can be divided into two stages. The first stage is RyR- or IP_3R-mediated local release of calcium from the ER/SR induced by the rapid entry of calcium ions via VGCCs or NMDA receptors of the plasma membrane. The second stage corresponds to a process of spreading of the calcium signal along the entire cell due to activation of neighboring channels (e.g., of RyRs) under the action of diffusing calcium itself. This results in more global effects, namely in increase in the $[Ca^{2+}]_i$ within the entire cell or separate cell compartments [4].

In the cell, three calcium pools should be distinguished; these are free (ionized) calcium (Ca^{2+}), chelated (bound to proteins) calcium, and that contained in the intracellular organelles. Such a term as the total calcium concentration (that of free + + bound Ca) is used in some cases.

It should be emphasized that Ca^{2+}, after its entry into the cell or release from the Ca^{+2} stores, is intensely bound with cytosol proteins, such as troponin, parvalbumin, calmodulin, calretinin, calcineurin, and others. Adenosine triphosphate also possesses a significant buffer calcium capacity and is capable of binding considerable amounts of calcium ions. Calcium is stored in the cell organelles (mostly ER and SR) due to the activity of sarco/endoplasmic ATPase (SERCA), and this process needs energy expenditure; the respective energy is produced in the course of ATP hydrolisis. In the organelles, Ca^{2+} also can be bound with buffer proteins, calsequestrin and calreticulin. The sodium/calcium exchanger is an additional mechanism maintaining low $[Ca^{2+}]_i$ values; it extrudes Ca^{2+} ions from the cytoplasm using the energy of a sodium electrochemical gradient.

Calcium signals at the periphery and in the center of the cell (or in the cell organelles) can significantly differ from each other; this is why it is rather important not only to estimate the Ca^{2+} concentration in one locus or another but also to measure the spatial and time characteristics of the respective calcium fluxes.

We describe below some methodical approaches allowing experimenters to estimate calcium concentrations in the cell in general and in certain separate intracellular organelles.

Estimation of Calcium Concentrations by the Means of Electron Microscopy. Electron microscopy, EM, allows one, using wave- or energy-dispersion consoles, to estimate the concentration of a certain ion or atom by X-ray spectral analysis. There is the following physical regularity: upon bombardment of an object by an electron beam, the length of the wave and energy of the initiated X-ray radiation are determined by the atomic number of the element and structure of the electron shells of its atoms. This regularity is the basis of X-ray microanalysis. Under the action of the above-mentioned irradiation, electrons are eliminated from the inner electron shell of the atom. Electrons of the outer shell “jump” on the vacant sites; they release the excessive energy as a quantum of X-ray radiation or transmit this energy to another electron on the outer shells. According to values of the energy and number of quanta released in the course of such processes, the qualitative and quantitative composition of the analyzed substance can be evaluated. Quantitative analysis is carried out by comparison of the number of released X-ray quanta to that obtained from the standard specimen (definite material). Electron microscopy gives only a static pattern (the time resolution is absent), but the above-described approach allows one to record, in some way, changes accompanying one or another physiological process. This can be provided by rapid cryofixation of the examined material. The described method has certain limitations; in this case, the concentration of total calcium, but not that of free or bound calcium, is measured. There are a few variants of the above-described technique.

Energy-dispersive X-ray spectroscopy (EDXS) is a technique of elemental analysis of a substance based on measurements of the emission energy of its X-ray spectrum. Within the framework of this technique, the wavelengths and intensity of radiation are measured using a spectrometer. As a standard source of X-ray radiation, an analyzer crystal (mica, quartz, or lithium fluoride) is used; in this case, it is possible to detect characteristic radiations from a large number of elements, from sodium to uranium. This allows researchers to quantitatively estimate both total concentrations of calcium and other elements (e.g., sodium and potassium) and their distribution across cell compartments [5–9].

The mean value of the total calcium concentration in the ER of CNS neurons measured using these techniques was 5.1 ± 1.1 mmol/kg of dry mass, or 1.3 ± 0.3 μM (if we assume that the water content is 85%) [10]. After stimulation of such cells by bursts of high-frequency stimuli, the Ca^{2+} concentration in the ER of these cells increased to 3.7 mM [10]. The mean value of the total calcium concentration in the cytosol was equal to 0.7 mmol/kg of dry mass, which corresponds to 120 μM [8]. As is known, the concentration of free calcium (Ca^{2+}) in most neurons in the resting state is about 100 nM [3]. According to these data, it is possible to calculate the ratio of the concentration of total calcium vs. concentration of free calcium; this is about 1200. In the active state of the cell (e.g., after intense stimulation), the level of free Ca^{2+} increases to about 1 μM, while the content of total cytosol calcium is about 0.8 μM [10]; thus, the above ratio is 800. In other studies, comparable values were obtained. For example, it was mentioned that the ratio of bound vs. free calcium is about 1000 [11]; it should be taken into account that this value is not constant. Therefore, after estimation of the content of total calcium using EDXS, it is possible to obtain an approximate estimate of the concentration of free calcium (the first index should be divided by 10^3).

Another approach is *electron energy loss spectroscopy* (EELS) [12]. This method is three or four times more sensitive than EDSX; it allows one to estimate calcium levels within a 0.2 to 20 mM range [13] and provides a better spatial resolution.

Measurements of the Concentration of Calcium Using its Radioactive Isotope. Concentrations of calcium in the cell or even in separate organelles of the latter can be estimated by measurements of the activity of its radioactive isotope, ^{45}Ca. Analysis of the kinetics of ^{45}Ca absorption and/or desaturation curves allows researchers to obtain information on the distribution of this element in various cell compartments and to estimate the rate of its redistribution between such compartments. The respective studies should be carried out in the stationary states. Measurements of rapid changes in calcium fluxes related to the entry of calcium in the cells and its release from the latter with the use of the above method can be provided by fractional analysis. In this case, it is possible to estimate the amplitude and kinetic parameters of the calcium signal, but the actual rate of the calcium fluxes cannot be measured because of time restrictions [14, 15]. The use of the above methods is accompanied by an error related to the difficulties of determination of the concrete compartment in which changes in the calcium level occur. The fact that it is impossible to accurately identify the anatomical structure of the object imposes certain restrictions on the capabilities of the respective measurements.

Measurements of $[Ca^{2+}]_i$ Using a Ca-Sensitive Electrode. The concentration of free calcium in the cell can be measured potentiometrically using a Ca-sensitive electrode. The sensitivity of such electrodes is within a 1 nM to 100 mM range. This method can be successfully used for the measurements of $[Ca^{2+}]_i$ under stationary conditions, in particular in calibration solutions. The time of a reaction of the above-mentioned electrode to changes in $[Ca^{2+}]_i$ is about 1 sec; this is why this technique also cannot be used for investigations of rapid changes in the calcium concentrations. The construction of the Ca-sensitive electrode is, in general, based on a lipophilic membrane that separates two aqueous compartments. In one of latter, there is a standard solution with the known Ca^{2+} concentration, while another compartment contains the examined solution. Calcium ions from the latter compartment enter another compartment (standard), which results in the generation of a potential on the membrane, and this potential is proportional to the concentration difference. The value of this potential can be calculated according to the Nernst equation: $\Delta V = 28 \log (c/c_{ref})$, where ΔV is the potential difference, c_{ref} is the concentration of Ca^{2+} in the standard (reference) solution, and c is the respective parameter in the examined solution [16]. From the constructive aspect, the Ca-sensitive electrode can be made as a microelectrode with the 0.5- to 10-μM-thick tip. The existence of considerable noise overlapping the useful signal is a negative aspect of the properties of such microelectrode; beside this, there are noticeable problems with calibration [17].

Measurements of $[Ca^{2+}]_i$ Using a Patch-Clamp Technique. The current determined by the movement of ions through a channel of the plasma membrane can be measured by a patch-clamp technique, i.e., by fixation of the potential on a mictropatch of the membrane and recording of the current. If the value of the current is known in this case, the local calcium concentration can be measured as $\int 1/c_f \cdot I_{Ca} \cdot dt$, where c_f is the Faraday constant and I_{Ca} is the current through calcium channels of the cell. This approach was used for calibration of Ca-sensitive fluorescent indicators. In particular, the fluorescent probe Fluo-4 was calibrated according to the results of electrophysiological measurements of the calcium current through a unitary calcium channel of the L type in myocytes of the myocardium (ventricle). This allowed experimenters to obtain precise values of the magnitude of a miniature calcium signal using a confocal scanning microscope [18]. A low-affinity calcium probe can be used for optical measurements of the calcium current in a presynaptic ending; this has been demonstrated by comparison of values of the optic signal and channel current [19].

Measurements of $[\mathrm{Ca}^{2+}]_i$ Using Fluorescent Microscopy. If a sufficiently high time resolution is necessary in studies of calcium signaling in the cell, a fluorescent microscope and calcium fluorescent probes are used. In this case, it is possible to use a standard fluorescent microscope supplied with a photoelectric multiplier and a CCD-camera or a high-speed scanning confocal microscope.

The fluorescent technique does not allow one to obtain a direct value of the $[\mathrm{Ca}^{2+}]_i$; this technique reflects the amount of Ca^{2+} ions, which is bound to the dye. The concentration of free Ca^{2+} is calculated according to the value of intensity of fluorescence of the dye using the formula shown below. When the measured signal is linked to the region of Ca^{2+} release from the intracellular store or to the site of entry of this ion through the plasma membrane, the dynamics of free Ca^{2+} and value of calcium fluxes in separate compartments of the neuron can be characterized. When calculating the $[\mathrm{Ca}^{2+}]_i$, it is necessary to take into account accessory calcium fluxes that are not related to the reaction with the dye; an additional differential component should be included in the respective calculations.

The equation for calculation of the concentration of free calcium for a single-wave technique of excitation of the dye with the involvement of the above-mentioned additional differential component looks as follows:

$$[\mathrm{Ca}^{2+}]_i = \frac{\frac{1}{k_{on}}\cdot\frac{d[\mathrm{Ca{:}dye}]}{dt} + K_\mathrm{D}\cdot[\mathrm{Ca{:}dye}]}{[\mathrm{dye}]-[\mathrm{Ca{:}dye}]}, \quad (1)$$

where [dye] is the dye concentration, [Ca:dye] is the concentration of the dye bound to calcium, K_D is the dissociation constant of the dye, and k_{on} is the coefficient of binding of calcium with the dye. The process of diffusion of dye molecules from the region of recording should also be taken into account. In this case, Eq. (1) has the following pattern:

$$[\mathrm{Ca}^{2+}]_i = \frac{\frac{1}{k_{on}}\cdot\frac{d[\mathrm{Ca{:}dye}]}{dt} - D\cdot\Delta[\mathrm{Ca{:}dye}] + K_\mathrm{D}\cdot[\mathrm{Ca{:}dye}]}{[\mathrm{dye}]-[\mathrm{Ca{:}dye}]}, \quad (2)$$

where D is the diffusion coefficient of the dye, and Δ is the vector differential operator.

The expression describing the fluorescent signal looks as follows:

$$F = \frac{[Ca:dye]\cdot F_{\max}}{[dye]} + \frac{([dye]-[Ca:dye])\cdot F_{\min}}{[dye]}, \quad (3)$$

where $F_{\max}$ and $F_{\min}$ correspond to the maximum and minimum intensities of fluorescence measured in calibration of the dye, and [Ca:dye] corresponds, in fact, to the value of the fluorescent signal F. Then, an equation for measurement of the concentration of free calcium with respect to the fluorescence intensity of the dye can be written as follows:

$$[\mathrm{Ca}^{2+}]_i = \frac{\frac{dF}{dt} - D\cdot\Delta F + \left(F - F_{\min}\right)k_{off}}{\left(F_{\max} - F\right)\cdot k_{on}}, \quad (4)$$

where F is the current intensity of fluorescence. Using Eq. (4), it is possible to measure the concentration of free calcium in the solution according to the change in the fluorescence intensity of the calcium probe, e.g., when using Fluo-4.

Upon applications of physiological stimuli, the calcium signal changes in a transient mode; this is why not only the absolute value of the Ca^{2+} concentration, but also the dynamics of its changes should be evaluated. The latter is provided by determination of the magnitude and rate of fluxes for the calcium signal in definite cell regions, e.g., in a zone of the channel or of the calcium store.

Measurement of the Calcium Flux Value. The flux value is the main quantitative characteristic used for the description of changes in the ion concentration, e.g., on the transfer of this ion through the membrane. The flux of ions Φ through the area S is measured by the number of the particles crossing this area within a time unit. Calculation of the flux value is reduced, in fact, to determination of the first derivative of the calcium signal with respect to time. Several approaches have been proposed for the determination of the time characteristics and amplitude of the Ca^{2+} flux upon the release of these ions from the intracellular stores [20–25]. The main complexity in this case is that it is necessary to calculate several parameters and to determine not only the value of the free calcium concentration, but also to calculate the concentrations of calcium bound in the organelles and with the endogenous buffers, and also to estimate the amount of calcium released from the cell. For this, it is necessary to obtain a system of nonlinear differential equations with known concentration of free calcium and with taking into account of each process involved in $[Ca^{2+}]_i$ changes. The kinetic parameters for calcium-sensitive components of the cell can be estimated in the course of additional experiments or determined in the course of analysis of the calcium signal.

In the simplest case, where the buffer capacity for Ca is absent, the calcium flux can be calculated using a rather simple formula:

$$\Phi = \frac{d[\mathrm{Ca}^{2+}]_i}{dt}.$$

In such calculations, Brum and colleagues first used in 1988 the term “input flux” and demonstrated that, in skeletal muscle, this flux is equal to the “release flux” [21]. This condition, however, is not performed in other cells, cardiomyocites, smooth muscle fibers, and neurons; this is why using the term “removal” is more correct in these cases.

$$\frac{d[\mathrm{Ca}^{2+}]_i}{dt} = \text{flux} - \text{removal} \quad (5).$$

There are two methods for calculation of removal, a theoretical one based on the known values of Ca^{2+} flux [26] and an empirical one [27]. Brum et al. combined these two methods, and the combined method is being used at present. Blatter et al. used an original method of analysis of the calcium macrosignal recorded from the cell [24, 26, 27] and adapted this technique for the analysis of local calcium microsignals in cardiomyocites; these signals were related to calcium release from the SR.

In calculations of the value of calcium flux, it is necessary to set accurately the buffer components, such as binding to cytoplasmic proteins (e.g., troponin), ATP, and EGTA, capturing of calcium by the mitochondria, contribution of the SERCA, release of Ca^{2+} from the cell, etc. [28].

Equations that describe changes in the calcium concentration ($[Ca^{2+}]$) for a few buffer systems (B_i) when diffusion is taken into account, will look as follows:

$$\frac{[\mathrm{Ca}^{2+}]}{dt} = D_{\mathrm{Ca}^{2+}} \cdot \Delta[\mathrm{Ca:dye}] + \Phi - \sum_i \left([\mathrm{Ca}^{2+}] \cdot [B_i] \cdot k_{on}^i + [\mathrm{Ca}:B_i] \cdot k_{off}^i \right), \quad (6)$$

$$\frac{[\mathrm{Ca}:B_i]}{dt} = D_{\mathrm{Ca}^{2+}} \cdot \Delta[\mathrm{Ca:dye}] + \sum_i \left([\mathrm{Ca}^{2+}] \cdot [B_i] \cdot k_{on}^i - [\mathrm{Ca}:B_i] \cdot k_{off}^i \right), \quad (7)$$

$$\frac{[B_i]}{dt} = D_{B_i} \cdot \Delta[B_i] - \sum_i \left([\mathrm{Ca}^{2+}] \cdot [B_i] \cdot k_{on}^i + [\mathrm{Ca}:B_i] \cdot k_{off}^i \right), \quad (8)$$

where D is the corresponding diffusion coefficient, B_i represents various calcium-binding buffer components, $[Ca:B]$ is the concentration of calcium bound with the buffer, and k_{on} and k_{off} are the coefficients of binding with the given buffer and dissociation of calcium ions from the latter. If the diffusion coefficients for $[Ca:B]$ and $[B]$ are equal to each other and $[B]$ is the constant, correspondingly, Eq. (8) can be excluded. By solving of these equations for the selected calcium binding components (calcium concentrations are calculated according to Eq. (4)), it is possible to estimate the value of the calcium flux Φ.

Error in recalculation of the calcium flux. The process of reconstruction of the flux rate was developed initially for single-dimension confocal scanning (modes *x-t* or *y-t*) of the calcium signal in a radial symmetry approximation. In the case of scanning in a two-dimensional space (*x-y-t*), recalculation of the calcium flux becomes more complicated because of the absence of radial symmetry and existing limitations within the axial plane *z*; for the latter, there is no complete information on the calcium signal. The error can be estimated using simulation of the preset calcium flux for definite experimental conditions. In particular, in the case of simulation of the preset calcium signal with a vertical resolution of 1 μm (which is comparable to the confocal resolution in the axial direction, *z*), the error corresponded to 20% of the preset calcium flux [29]. Thus, recording in the *x-y-t* coordinates and recalculation of the calcium signal by the flux value involve a systematic underestimation error equal to about 20%. Such a situation, however, may be acceptable in the description of physiological processes related to changes in the $[Ca^{2+}]_i$ in the cell.

Example of calculation of the calcium flux upon opening of a group of RyR channels. The quantitative characteristics of the calcium flux were described in detail in the course of studies of coupling between excitation and contraction in myocytes of the myocardium. Initially, calcium enters the cell trough VGCCs of the L type. This, in turn, initiates an additional increase in the Ca^{2+} concentration at the expense of activation of RyRs and release of calcium from the intracellular stores. Single discrete events of Ca^{2+} release related to the opening of RyRs were visualized using confocal fluorescent microscopy; these events were called calcium *sparks* [30, 31]. These sparks reflect activation of several RyRs in the SR (or ER) and correspond to individual blocks (quanta) of the integral calcium signal. The probe fluorescence at such sparks remains local, which may be a good object for the description and characterization of the calcium fluxes. Such calcium entry events, but mediated by IP_3Rs, were called *puffs*; these calcium events were first observed in *Xenopus* oocytes [32]. IP_3Rs may be activated with increase in the calcium level provided not only by the expense of ions entering the cell via channels of these receptors but also due to additional modulation of the calcium amount localized in the cytosol in close proximity to the receptor. When the calcium release possesses a more global character, local signals are merged and can spread along the cytosol as a self-supporting wave.

The above-described method of calculation of the calcium flux in the course of calcium release from the intracellular store requires estimation of the concentration and kinetic parameters of calcium binding with definite molecules and also of the action of the systems of calcium extrusion [33, 34]. Among seven main processes modulating a calcium spark, the reaction of Ca^{2+} binding to ATP and diffusion of this ion from the examined site are the crucial ones. The contribution of other buffer processes, such as (in the order of decreasing importance) binding of Ca^{2+} with the probe dye, EGTA, SERCA, and troponin, and, finally, activity of the sarcolemmal sodium/calcium exchanger does not exceed 10% [34]. The calculated maximum density of the flux (at the peak of the calcium spark) is equal to 53 mM/sec, which is equivalent to 11 pA of the current. When these values were taken into account, it became possible to calculate the number of opened RyR channels. The obtained estimate corresponded to 20–30 (value of the current through a single channel was 0.3–0.5 pA at the peak of the calcium spark) [36]. In another study, the value of the above mentioned current was somewhat smaller (8 pA) [35].

Therefore, calculation of calcium fluxes allows researchers to characterize the role of various buffer systems, systems of calcium extrusion from the cell, and systems involved in the formation of the calcium signal upon the release of these ions from the stores; it is not less important that the dynamics of the above processes can be estimated. Using such approach, it is possible to determine when calcium release from the store was initiated or terminated. This cannot be done based only on the estimates of changes in the absolute values of the free calcium concentration [34].

Calcium Signaling in Neurons. A rather low intracellular concentration of free calcium (50 to 100 nM) is typical of most neurons in the resting state. This index can increase up to 10 µM upon intense electrical activity of the cell [3]. In particular, the calcium level in the dendrites could increase to 5 µM during the development of synaptically induced calcium waves [37, 38]. Thus, the range of changes in the $[Ca^{2+}]_i$ is rather wide. If we consider this, estimating of precise values of the calcium fluxes is a rather complex but necessary task in studies of specific mechanisms of calcium signaling in neurons. Information on the spatial distribution of the respective channels and receptors is rather limited; it is obvious, however, that molecular mechanisms and patterns of Ca^{2+} release in different regions of the cell and in neurons of different types differ significantly from each other [39].

Calcium signals based on the release of this element from the intracellular stores were found in neurons subjected to various physiological stimulations [40–42]. As is well known, Ca^{2+} release from the ER occurs under conditions of opening of the IP_3R and RyR channels [43]. The IP_3-mediated release of calcium from the dendrites is initiated most frequently by the action of neurotransmitters (e.g., of glutamate) [44], while RyRs can be activated by an increase in the Ca^{2+} concentration in the cytosol. The entry of calcium ions through VGCCs activates RyRs via a calcium-mediated process that obtained, at present, the generally known designation "calcium-induced calcium release" (CICR). This process can promote significant intensification of the calcium flux evoked by generation of a single or a few action potentials in the neuronal soma [45, 46]. The functioning of intracellular receptors of both types (IP_3Rs and RyRs) is regulated by a variety of intracellular factors, in particular by the calcium level *per se* [47]. Calcium ions can affect the above-mentioned channels from both luminal and cytosol sides of the membrane. Such calcium regulation provides, in fact, the functioning of a feedback loop that coordinates the inflow of Ca^{2+} from the intracellular store to the cytosol. In the case of IP_3, such a mechanism can play an important role in the generation of dendritic calcium waves. The latter are initiated in cortical and hippocampal pyramidal neurons and cells of some other types by synaptic activation [37, 48]. In presynaptic terminals, the Ca^{2+} entry switches on the process of exocytosis of synaptic vesicles containing neurotransmitter molecules [49, 50]. In turn, transient increases in the calcium levels in proximity to the postsynaptic membrane of the dendrites modulate the development of synaptic plasticity [51].

Local calcium events, such as calcium sparks and puffs, were not found for a long time in the neuronal soma; it was believed that such events in the soma are absent or extremely rare. This conclusion, probably, was related to the absence of clusterization of RyRs and IP_3Rs in the nerve cells (in contrast to fibers of the skeletal muscles and cardiomyocites), low magnitudes of the corresponding signals, and a relatively high noise level. Later on, however, such events were successfully detected in the PC12 cells after their differentiation under the action of neural growth factor [52] and also in the dendrites of pyramidal neurons in hippocampal slices [42]. In the membrane of dendritic spines, RyRs are distributed relatively evenly. The sharp rise in the calcium concentration resulting from Ca^{2+} entry through channels of NMDA receptors and VDCCs induces the calcium release from the ER [4]. In this case, calcium events are mostly mediated by the RyR activity, while that of IP_3Rs is also involved to a certain extent.

"Fast" fluorescent microscopy allows researchers to perform analysis of calcium signaling in excitable cells. From this aspect, examination of rapid local calcium events, both sparks and puffs, is rather urgent. Such phenomena have at present been found in a number of excitable cells.

In the studies of calcium signaling in neurons, strict differentiation of the contributions of RyRs and IP_3Rs in the course of calcium release from the intracellular store is obviously important. The patterns and functional role of spatial distribution of local calcium events (both sparks and puffs) in the neuronal dendrites have not been elucidated until now. Examination of IP_3R-mediated local events is complicated by the necessity of initiation of synaptic activity for the manifestation of such events; naturally, such initiation results in activation of these cell receptors themselves. Therefore, studies of the above-mentioned calcium events are, at present, rather difficult not only from the technical aspect, but also because of the structural basis of these events.

The appearance of novel fluorescent dyes characterized by a high sensitivity and of novel detectors with low levels of noise (which allows one to detect even separate photons) will allow experimenters to record extremely small calcium events. This will open certain possibilities for more adequate qualification of the roles of RyRs and IP_3Rs in calcium signaling in neurons and other excitable cells.

Thus, studies of changes in the $[Ca^{2+}]_i$ in general, distribution of calcium within the cell borders, and fluxes determining redistribution of these ions have been initiated with the use of a number of various approaches. Some of them have been described above. Each of these methods possesses certain advantages, limitations, and deficiencies. It is quite natural that several different approaches can be simultaneously used in studies of calcium signaling in the cell.

Elucidation of the mechanisms of intracellular calcium signaling is extremely important for the understanding of cellular and molecular mechanisms of functioning of neurons and other excitable cells. Calcium ions perform a unique role as the main component in the system of intracellular signaling. Detailed adequate interpretation of such processes allows researchers to identify possible defects in such signaling; these defects are important or even main pathogenetic factors in a number of various pathologies of the cell or of the entire organism.

This is a review paper; therefore, confirmation of the accordance with the existing ethical standarts for experimental studies is not necessary.

The author of this study, V. M. Shkryl, confirms that he had no conflict of interest pertinent to commercial or financial relations and relations with organizations or persons somehow or other related to the study.

REFERENCES

1. M. J. Berridge, "Neuronal calcium signaling," *Neuron*, **21**, 13-26 (1998).
2. T. Pozzan, R. Rizzuto, P. Volpe, and J. Meldolesi, "Molecular and cellular physiology of intracellular calcium stores," *Physiol. Rev.*, **74**, 595-636 (1994).
3. M. J. Berridge, P. Lipp, and M. D. Bootman, "The versatility and universality of calcium signalling," *Nat. Rev. Mol. Cell Biol.*, **1**, 11-21 (2000).
4. D. Futagi, and K. Kitano, "Ryanodine-receptor-driven intracellular calcium dynamics underlying spatial association of synaptic plasticity," *J. Comput. Neurosci.*, **39**, 329-347 (2015).
5. A. V. Somlyo, H. Shuman, and A. P. Somlyo, "Composition of sarcoplasmic reticulum in situ by electron probe X-ray microanalysis," *Nature*, **268**, 556-558 (1977).
6. T. A. Hall, and B. L. Gupta, "The localization and assay of chemical elements by microprobe methods," *Q. Rev. Biophys.*, **16**, 279-339 (1983).
7. S. B. Andrews, R. A. Buchanan, and R. D. Leapman, "Quantitative dark-field mass analysis of ultrathin cryosections in the field-emission scanning transmission electron microscope," *Scanning Microsc. Suppl.*, **8**, 13-23; discussion 23-14 (1994).
8. R. A. Buchanan, R. D. Leapman, M. F. O'Connell, et al., "Quantitative scanning transmission electron microscopy of ultrathin cryosections: subcellular organelles in rapidly frozen liver and cerebellar cortex," *J. Struct. Biol.*, **110**, 244-255 (1993).
9. R. D. Leapman, and S. B. Andrews, "Analysis of directly frozen macromolecules and tissues in the field-emission STEM," *J. Microsc.*, **161**, 3-19 (1991).
10. L. D. Pozzo-Miller, N. B. Pivovarova, J. A. Connor, et al., "Correlated measurements of free and total intracellular calcium concentration in central nervous system neurons," *Microsc. Res. Tech.*, **46**, 370-379 (1999).
11. E. Neher, "The use of fura-2 for estimating Ca buffers and Ca fluxes," *Neuropharmacology*, **34**, 1423-1442 (1995).
12. R. D. Leapman, S. Q. Sun, J. A. Hunt, and S. B. Andrews, "Biological electron energy loss spectroscopy in the field-emission scanning transmission electron microscope," *Scanning Microsc. Suppl.*, **8**, 245-258; discussion 258-249 (1994).
13. H. Shuman, and A. P. Somlyo, "Electron energy loss analysis of near-trace-element concentrations of calcium," *Ultramicroscopy*, **21**, 23-32 (1987).
14. A. B. Borle, "An overview of techniques for the measurement of calcium distribution, calcium fluxes, and cytosolic free calcium in mammalian cells," *Environ. Health Perspect.*, **84**, 45-56 (1990).
15. T. Uchikawa, and A. B. Borle, "Studies of calcium-45 desaturation from kidney slices in flow-through chambers," *Am. J. Physiol.*, **234**, R34-38 (1978).
16. A. Takahashi, P. Camacho, J. D. Lechleiter, and B. Herman, "Measurement of intracellular calcium," *Physiol. Rev.*, **79**, 1089-1125 (1999).
17. S. Baudet, L. Hove-Madsen, and D. M. Bers, "How to make and use calcium-specific mini- and microelectrodes," *Methods Cell Biol.*, **40**, 93-113 (1994).
18. S. Q. Wang, L. S. Song, E. G. Lakatta, and H. Cheng, "Ca^{2+} signalling between single L-type Ca^{2+} channels and ryanodine receptors in heart cells," *Nature*, **410**, 592-596 (2001).
19. B. L. Sabatini, and W. G. Regehr, "Optical measurement of presynaptic calcium currents," *Biophys. J.*, **74**, 1549-1563 (1998).
20. S. M. Baylor, W. K. Chandler, and M. W. Marshall, "Calcium release and sarcoplasmic reticulum membrane potential in frog skeletal muscle fibres," *J. Physiol.*, **348**, 209-238 (1984).
21. G. Brum, E. Rios, and E. Stefani, "Effects of extracellular calcium on calcium movements of excitation-contraction coupling in frog skeletal muscle fibres," *J. Physiol.*, **398**, 441-473 (1988).
22. O. Delbono, and G. Meissner, "Sarcoplasmic reticulum Ca^{2+} release in rat slow- and fast-twitch muscles," *J. Membr. Biol.*, **151**, 123-130 (1996).
23. J. Garcia, and M. F. Schneider, "Calcium transients and calcium release in rat fast-twitch skeletal muscle fibres," *J. Physiol.*, **463**, 709-728 (1993).
24. W. Melzer, E. Rios, and M.F. Schneider, "A general procedure for determining the rate of calcium release from the sarcoplasmic reticulum in skeletal muscle fibers," *Biophys. J.*, **51**, 849-863 (1987).
25. N. Shirokova, J. Garcia, G. Pizarro, and E. Rios, "Ca^{2+} release from the sarcoplasmic reticulum compared in amphibian and mammalian skeletal muscle," *J. Gen. Physiol.*, **107**, 1-18 (1996).
26. S. M. Baylor, W. K. Chandler, and M. W. Marshall, "Sarcoplasmic reticulum calcium release in frog skeletal muscle fibres estimated from Arsenazo III calcium transients," *J. Physiol.*, **344**, 625-666 (1983).
27. W. Melzer, E. Rios, and M. F. Schneider, "Time course of calcium release and removal in skeletal muscle fibers," *Biophys. J.*, **45**, 637-641 (1984).
28. E. Rios, M. D. Stern, A. Gonzalez, et al., "Calcium release flux underlying Ca^{2+} sparks of frog skeletal muscle," *J. Gen. Physiol.*, **114**, 31-48 (1999).
29. L. Figueroa, V. M. Shkryl, J. Zhou, et al., "Synthetic localized calcium transients directly probe signalling mechanisms in skeletal muscle," *J. Physiol.*, **590**, 1389-1411 (2012).
30. H. Cheng, W. J. Lederer, and M. B. Cannell, "Calcium sparks: elementary events underlying excitation-contraction coupling in heart muscle," *Science*, **262**, 740-744 (1993).
31. A. Tsugorka, E. Rios, and L.A. Blatter, "Imaging elementary events of calcium release in skeletal muscle cells," *Science*, **269**, 1723-1726 (1995).
32. I. Parker, and I. Ivorra, "Localized all-or-none calcium liberation by inositol trisphosphate," *Science*, **250**, 977-979 (1990).
33. D. J. Santiago, J. W. Curran, D. M. Bers, et al., "Ca sparks do not explain all ryanodine receptor-mediated SR Ca leak in mouse ventricular myocytes," *Biophys. J.*, **98**, 2111-2120 (2010).

34. V. M. Shkryl, L. A. Blatter, and E. Rios, “Properties of Ca^{2+} sparks revealed by four-dimensional confocal imaging of cardiac muscle,” *J. Gen. Physiol.*, **139**, 189-207 (2012).
35. C. H. Kong, D. R. Laver, and M. B. Cannell, “Extraction of sub-microscopic Ca fluxes from blurred and noisy fluorescent indicator images with a detailed model fitting approach,” *PLoS Comput. Biol.*, **9**, e1002931 (2013).
36. C. Kettlun, A. Gonzalez, E. Rios, and M. Fill, “Unitary Ca^{2+} current through mammalian cardiac and amphibian skeletal muscle ryanodine receptor channels under near-physiological ionic conditions,” *J. Gen. Physiol.*, **122**, 407-417 (2003).
37. M. E. Larkum, S. Watanabe, T. Nakamura, et al., “Synaptically activated Ca^{2+} waves in layer 2/3 and layer 5 rat neocortical pyramidal neurons,” *J. Physiol.*, **549**, 471-488 (2003).
38. L. D. Pozzo Miller, J. J. Petrozzino, G. Golarai, and J. A. Connor, “Ca^{2+} release from intracellular stores induced by afferent stimulation of CA3 pyramidal neurons in hippocampal slices,” *J. Neurophysiol.*, **76**, 554-562 (1996).
39. A. Verkhratsky, “Physiology and pathophysiology of the calcium store in the endoplasmic reticulum of neurons,” *Physiol. Rev.*, **85**, 201-279 (2005).
40. I. Llano, J. Gonzalez, C. Caputo, et al., “Presynaptic calcium stores underlie large-amplitude miniature IPSCs and spontaneous calcium transients,” *Nat. Neurosci.*, **3**, 1256-1265 (2000).
41. C. Lohmann, A. Finski, and T. Bonhoeffer, “Local calcium transients regulate the spontaneous motility of dendritic filopodia,” *Nat. Neurosci.*, **8**, 305-312 (2005).
42. S. Manita, and W. N. Ross, “Synaptic activation and membrane potential changes modulate the frequency of spontaneous elementary Ca^{2+} release events in the dendrites of pyramidal neurons,” *J. Neurosci.*, **29**, 7833-7845 (2009).
43. R. Rizzuto, and T. Pozzan, “Microdomains of intracellular Ca^{2+}: molecular determinants and functional consequences,” *Physiol. Rev.*, **86**, 369-408 (2006).
44. C. M. Niswender, and P. J. Conn, “Metabotropic glutamate receptors: physiology, pharmacology, and disease,” *Annu. Rev. Pharmacol. Toxicol.*, **50**, 295-322 (2010).
45. M. Kano, O. Garaschuk, A. Verkhratsky, and A. Konnerth, “Ryanodine receptor-mediated intracellular calcium release in rat cerebellar Purkinje neurones,” *J. Physiol.*, **487**, 1-16 (1995).
46. R. W. Tsien, and R. Y. Tsien, “Calcium channels, stores, and oscillations,” *Annu. Rev. Cell Biol.*, **6**, 715-760 (1990).
47. M. J. Berridge, “Inositol trisphosphate and calcium signalling,” *Nature*, **361**, 315-325 (1993).
48. T. Nakamura, J. G. Barbara, K. Nakamura, and W. N. Ross, “Synergistic release of Ca^{2+} from IP3-sensitive stores evoked by synaptic activation of mGluRs paired with backpropagating action potentials,” *Neuron*, **24**, 727-737 (1999).
49. E. Neher, and T. Sakaba, “Multiple roles of calcium ions in the regulation of neurotransmitter release,” *Neuron*, **59**, 861-872 (2008).
50. C. Grienberger, and A. Konnerth, “Imaging calcium in neurons,” *Neuron*, **73**, 862-885 (2012).
51. R. S. Zucker, “Calcium- and activity-dependent synaptic plasticity,” *Curr. Opin. Neurobiol.*, **9**, 305-313 (1999).
52. S. Koizumi, M. D. Bootman, L. K. Bobanovic et al., “Characterization of elementary Ca^{2+} release signals in NGF-differentiated PC12 cells and hippocampal neurons,” *Neuron*, **22**, 125-137 (1999).

3.2 Корекція похибки через віднімання фону при раціометричних вимірюваннях кальцію за допомогою ПЗЗ-камери

Раціометричний метод часто застосовується для флуоресцентного барвника Fura-2. Для перерахунку флуоресценції у концентрацію вільного Ca^{2+} зазвичай використовується формула Гринкевича (Grynkiewicz, 1985). Однак віднімання фонового рівня може вносити суттєву похибку в раціометричних вимірюваннях кальцію, при використанні ПЗЗ-камери як детектору сигналу. Якщо похибка виникає внаслідок цього віднімання, відношення флуоресценції при збудженні в 340 нм до сигналу при 380 нм може перевищувати дійсне значення удвічі. Важливо також враховувати, що при нерегульованій інтенсивності збудження для забезпечення однорідної пропускної здатності об'єктива для ультрафіолетового освітлення барвника може відбутися нерівномірне знебарвлення для каналів з довжиною хвилі 340 нм та 380 нм. Це, у свою чергу, може призвести до додаткових похибок у визначенні концентрації Ca^{2+}.

Запис сигналів двовимірної інформації у формі зображення (x, y) або динамічного запису в часі (x-y-t) реєструвався за допомогою ПЗЗ-камери. Необхідне віднімання фонового сигналу з кожного пікселя зображень масиву x-y при збудженні світлом 340 нм та 380 нм може мати від'ємне або нульове значення, що може призвести до помилки в розрахунку $[Ca^{2+}]$. Так, у 8 досліджуваних клітин, без віднімання фону, базальні рівні флуоресцентних сигналів у сомі нейрона становили 261.8±12.7 при 380 нм та 226.4±8.0 при 340 нм. Пікове значення Ca^{2+}-транзієнту становило 178.5±5.7 при 380 нм і 279.3±12.9 при 340 нм. У випадку віднімання фону по піксельно, сигнал при збудженні на 380 нм має більшу тенденцію до від'ємного або нульового значення і може призводити до помилок у розрахунку реального сигналу Ca^{2+} не тільки на рівні спокою, але й на піку Ca^{2+}-транзієнту, що призводить до помилки у визначенні його амплітуди. Щоб отримати результат без помилок, необхідно спершу усереднити по площі клітини або ROI, а потім відняти фоновий рівень.

Функцію знебарвлення барвника (γ) можна знайти як усереднену різницю між нормалізованими сигналами F_{340} і F_{380}:

$$\gamma = \frac{1}{2}\left(\left(\frac{\mathrm{F}_{340}}{\mathrm{F}_{340}(0)}\right)^{C_0} + \frac{\mathrm{F}_{380}}{\mathrm{F}_{380}(0)}\right) \qquad (1)$$

коефіцієнт C_0 можна визначити: $$C_0 = \frac{\ln\left(2 - \frac{\mathrm{F}_{380}(1)}{\mathrm{F}_{380}(0)}\right)}{\ln\frac{\mathrm{F}_{340}(1)}{\mathrm{F}_{340}(0)}} \qquad (2)$$

де $F_{380}(0)$ і $F_{340}(0)$ - початкова флуоресценція; $F_{340}(1)$ і $F_{380}(1)$ - значення Ca^{2+}-транзиту на максимумі (або визначеного[Ca^{2+}]).

Для сигналу F_{340}, швидкість ефекту знебарвлення барвника може бути математично скоригована за допомогою степеневої функції з коефіцієнтом втраченої енергії збудження C_0, який можна обчислити за рівнянням (2) з умов калібрування.

Нормовані сигнали, скомпенсовані на знебарвлення для двох довжин хвиль можна записати у вигляді:

$$\mathrm{F} = \mathrm{F}_{340}(0)\cdot\left(\frac{1}{2}\left(\left(\frac{\mathrm{F}_{340}}{\mathrm{F}_{340}(0)}\right)^{C_0} - \frac{\mathrm{F}_{380}}{\mathrm{F}_{380}(0)}\right) + 1\right)$$

$$\mathrm{F} = \mathrm{F}_{380}(0)\cdot\left(\frac{1}{2}\left(\frac{\mathrm{F}_{340}}{\mathrm{F}_{340}(0)} - \left(\frac{\mathrm{F}_{380}}{\mathrm{F}_{380}(0)}\right)^{1/C_0}\right) + 1\right) \qquad (3)$$

Рівняння 3 обчислює флуоресцентний сигнал від F_{340} і F_{380} з компенсацією ефекту знебарвлення барвника, та використати для двохвильового методу збудження з барвником Fura-2 або його аналогами.

Рівняння для розрахунку вільного Ca^{2+} для однієї довжини хвилі може бути представлене наступним чином:

$$[\mathrm{Ca}^{2+}] = K_d\,\frac{(\mathrm{F}-\mathrm{F}_{\mathrm{min}})}{(\mathrm{F}_{\mathrm{max}}-\mathrm{F})} \qquad (4)$$

Концентрацию вільного Ca^{2+} можна визначити за допомогою рівняння 4. Похибка, пов'язана з відніманням фону і яка була виявлена для ратіометричного сигналу, відсутня для флуоресценції F, отриманої за допомогою рівняння 3. Застосування рівняння 3 дозволяє перевести двохвильове вимірювання на одну довжину хвилі без похибок віднімання фону і з компенсованим ефектом знебарвлення барвника.

У даній частині викладено покращений метод обчислення [Ca^{2+}] на основі ратіометричної флуоресценції барвника Fura-2, реєстрованої ПЗЗ-камерою. Даний метод розроблено з метою оптимізації вимірювань [Ca^{2+}] та забезпечення корекції фотознебарвлення без похибок, пов'язаних з відніманням фону. Додатково пропонується математичний підхід для корекції занижених значень флуоресценції на довжині хвилі збудження 340 нм. Цей підхід також компенсує швидкість фотознебарвлення для обох каналів (з довжинами хвиль 340 нм та 380 нм) за допомогою степеневої функції.

Heliyon 6 (2020) e04180

Contents lists available at ScienceDirect

Heliyon

journal homepage: www.cell.com/heliyon

Research article

Error correction due to background subtraction in ratiometric calcium measurements with CCD camera

Vyacheslav M. Shkryl [*]

Department of Biophysics of Ion Channels, Bogomoletz Institute of Physiology, 4 Bogomoletz Street, Kyiv, 01024, Ukraine

ARTICLE INFO

Keywords:
Neuroscience
Mathematical modeling
Biophysics
Cellular neuroscience
Physiology
Fluorescence
Ca^{2+}
Ratiometric method
Fura-2
Grynkiewitz's formula
CCD camera
Neuron

ABSTRACT

Background: Ca^{2+} plays an important role in many physiological processes and an accurate study of these signals is important. In modern fluorescence microscopy, a charge-coupled device (CCD) camera is widely deployed for calcium imaging. The ratiometric method is used for the fluorescence dye Fura-2 and Grynkiewitz's formula (Grynkiewicz et al., 1985) is commonly used to convert fluorescence to free Ca^{2+} concentration ($[Ca^{2+}]$). But the need to subtract the background signal can lead to a big error in ratiometric calcium measurements. When the error due to background subtraction occurs, the fluorescence ratio of 340 nm divided by 380 nm lights may be twice as large as the actual value. Under conditions when the excitation intensity is not adjusted to ensure the same throughput of the objective lens for ultraviolet dye illumination, the indicator does not gradually bleach out for channels with a wavelength of 340 nm and 380 nm light, which lead to an additional error in determining the concentration of Ca^{2+}.

New method: Here we present a new approach for calculating $[Ca^{2+}]$ from the ratiometric fluorescence of Fura-2 dye imaged by a CCD camera. It is designed to optimize $[Ca^{2+}]$ measurements with photobleaching correction without background subtraction error. A mathematical method is also provided for removing the existing underestimated value of fluorescence at an excitation wavelength of 340 nm and compensating for the bleaching rate for both channels with wavelengths of 340 nm and 380 nm using a power function.

Results: In cultured neurons, the calculations of the free Ca^{2+} concentration during Ca^{2+} transients estimated by the old and new methods, determine it to the same extent. This comparison was made under conditions without errors through background subtraction. If there is this error, the old method calculates $[Ca^{2+}]$ with a much higher, rather than the actual value.

Conclusions: We present a modified Grynkiewitz's formula for calculation $[Ca^{2+}]$ for ratiometric dye, such as Fura-2 imaged by a CCD camera, with photobleaching correction without background subtraction error.

1. Introduction

The calcium ion (Ca^{2+}) is a common second messenger that regulates different physiological pathways as secretion, fertilization, gene transcription, and apoptosis (Berridge et al., 2000; Pozzan et al., 1994). Tsien et al. were introduced Ca^{2+} fluorescent indicators for studies of Ca^{2+} signaling (Tsien et al., 1982). Studies of cellular Ca^{2+} signaling have been greatly facilitated by the availability of fluorescent Ca^{2+} indicators, which suitable to monitor Ca^{2+} signals inside a cell. In its simple form, the measurement of $[Ca^{2+}]$ using a fluorescent indicator requires only an appropriate light source and a photomultiplier tube (PMT) detector. A PMT was used for many years and still used when high sensitivity, fast measuring are needed. The contemporary imaging system uses a low-light intensified charge-coupled device (CCD) camera, with an array of isolated elements (or pixels), attached to the fluorescence microscope. Currently, two approaches are widely used to assess the dynamics of free intracellular Ca^{2+}: single-wavelength and two-wavelength (ratiometric) methods. The ratiometric method is used not only for quantitative measurements of the concentration of free Ca^{2+} ($[Ca^{2+}]$) but also for qualitative analysis, such as single-wavelength techniques, valuable for relative changes in Ca^{2+} (Grynkiewicz et al., 1985; Minta et al., 1989). Processing the ratio data of two-wavelength emission considerably reduces the effects of uneven dye loading, dye leakage, and photobleaching.

Fura-2 is a ratiometric fluorescence indicator of Ca^{2+}. The largest dynamic range was detected at an excitation wavelength of 340 nm and

---

[*] Corresponding author.
E-mail address: slava@biph.kiev.ua.

https://doi.org/10.1016/j.heliyon.2020.e04180
Received 8 October 2019; Received in revised form 21 October 2019; Accepted 5 June 2020

380 nm that make the wavelengths preferred for [Ca^{2+}] measurements. The Grynkiewitz's formula is commonly used to convert PMT ratiometric fluorescence into [Ca^{2+}] for the dye Fura-2 (Grynkiewicz et al., 1985).

Continuous excitatory illumination often leads to irreversible destruction or photobleaching of the fluorophore. Loss of fluorescence during data acquisition (photobleaching or bleaching) results in an error in determining the concentration of free Ca^{2+} (Scheenen et al., 1996). Using the ratiometric method, the effect of photobleaching is solved by dividing the fluorescence at 340 nm by the correspondent signal at 380 nm light. The background should be also subtracted from each excitation wavelength before determining the final ratio. Using the Grynkiewitz's formula, subtracting the background value from an individual element of the *x-y* fluorescence images can lead to a large error in determining the concentration of free Ca^{2+}.

In this work, we verify the Grynkiewicz's formula of calculation of [Ca^{2+}] for CCD cameras when background subtraction error appears. And a new approach was proposed for calculating the concentration of the free calcium ions with photobleaching correction, using fluorescent excitation channels at 340 and 380 nm lights, which can be used for the ratiometric dye as the Fura-2.

2. Materials and methods

All experimental procedures were performed in accordance with international principles of the European Convention for the protection of vertebrate animals used for experimental and other scientific purposes (European convention, Strasburg, 1986); the Law of Ukraine “On protection of animals from cruelty” and approved by the Animal Care Committee of Bogomoletz Institute of Physiology.

2.1. Cell culture and solutions

All experiments were performed on cultured neurons of the hippocampus of newborn Wistar rats. The primary culture of hippocampal neurons was prepared as previously reported (Shkryl et al., 1999). Ca^{2+} imaging studies were carried out in 7–14 days of cultivation. A cover glass with cells was placed in the solution included in mM: NaCl – 140.0; KCl – 2.0; CaCl$_2$ – 2.0; MgCl$_2$ - 2.0; HEPES – 10.0; pH = 7.4. To induce Ca^{2+} transient was used as a depolarization solution. Depolarization solution containing 50.0 mM KCl was equivalent to bath solution described above except that part of NaCl was replaced by KCl. All chemicals were obtained from Sigma-Aldrich (St. Louis, MO).

Before the experiment, the cells were loaded with 5 μM Fura-2 acetoxymethyl ester (Fura-2 AM) for 30 min at 37 °C and an additional 20 min for deesterification of the dye. For [Ca^{2+}] calculation we used vitro value of Fura-2 Kd = 224 nM (Grynkiewicz et al., 1985). Ca^{2+} transients were induced by a 5-seconds application of the depolarization solution with high potassium solution thereby opening voltage-sensitive Ca^{2+} channels in the cell membrane. To apply solutions we used a perfusion system, controlled by a computer and synchronized by data acquisition software.

2.2. Calcium imaging

In our study, we used a CCD camera (Olympus XM10) mounted on an Olympus IX71 inverted microscope equipped with an Olympus LUCPlanFFN 20x/0.45 lens and MT10 illumination system that includes a filter wheel exchanger (340 and 380 nm) and 150W xenon arc burner. Cell M software (Olympus, Japan) was used for data collection. The acquisition speed for one data point (340 nm and 380 nm) was 1.3 Hz.

2.3. Data analysis

Data analysis was performed using the IDL programming environment (ITT Visual Information Solutions). In the recorded images with excitation of 340 nm and 380 nm lights, the region of interest (ROI) was selected based on the criteria for the signal difference at the peak of Ca^{2+} transient and at its basal level. This allows us to make a good selection of the soma area. For the subsequent analyses, ROI was selected on the soma of a neuron without a nuclear region. All experiments were performed at room temperature (22–25 °C). Data are presented as mean ± SEM.

3. Results

The emission fluorescence from the Fura-2 indicator does not have a linear relationship to the [Ca^{2+}] and the dye fluorescence provides a relative indication of the magnitude of the Ca^{2+} signal, but can be calibrated. The Grynkiewicz formula with taking into account the background level is:

$$\left[\mathrm{Ca}^{2+}\right] = K_d \frac{\left(\frac{\mathrm{F}_{340}-\mathrm{Bgr}}{\mathrm{F}_{380}-\mathrm{Bgr}} - \mathrm{R}_{\min}\right)}{\left(\mathrm{R}_{\max} - \frac{\mathrm{F}_{340}-\mathrm{Bgr}}{\mathrm{F}_{380}-\mathrm{Bgr}}\right)} \frac{\mathrm{F}_{380}^{max} - \mathrm{Bgr}}{\mathrm{F}_{380}^{min} - \mathrm{Bgr}} \tag{1}$$

where $\mathrm{R}_{\min} = \frac{\mathrm{F}_{340}^{min}-\mathrm{Bgr}}{\mathrm{F}_{380}^{max}-\mathrm{Bgr}}$;$\mathrm{R}_{\max} = \frac{\mathrm{F}_{340}^{max}-\mathrm{Bgr}}{\mathrm{F}_{380}^{min}-\mathrm{Bgr}}$; K_d – dissociation constant; Bgr – background level; F_{340}, F_{380} – fluorescence at 340 nm and 380 nm excitation wavelength; F_{340}^{min} and F_{340}^{max}or F_{380}^{min} and F_{380}^{max}- minimal and maximal values of F_{340} and F_{380} respectively (Grynkiewicz et al., 1985). From this equation is clear that the real value of calcium concentration could be correctly determined then $\mathrm{F}_{380} - \mathrm{Bgr} > 0$.

Using CCD camera signals are recorded of two-dimensional information as an image (*x, y*) or dynamic recording in time array (*x-y-t*). The size of the PMD detector and one CCD pixel is three orders of magnitude, making the probability of detecting a signal at the level of one CCD pixel much lower than that of the PMT. On the other hand, the quantum efficiency is better for scientific CCDs to compare to PMT, especially those with semiconductor photo-cathodes, can detect single photons. CCDs are not capable of doing that. Unlike the signal recorded using a PMT, the CCD camera, at an individual pixel, records the reduced amount of photons with a high noise level at each data point of the *x-y* image (Heintzmann, 2006; Jerome, 2011). The necessary subtraction of the background signal, performed from each pixel of the *x-y* array images at excitation of 340 and 380 nm lights, can have the resulting values as a negative or a value of zero, which may cause an error in calculating of [Ca^{2+}].

A background signal can be caused by endogenous compounds that are unevenly distributed in the cell, such as collagen fibers, pyridine nucleotides, which absorb and emit light at wavelengths very similar to Ca^{2+} indicators (Bootman et al., 2013a). Using 50–100 μM Fura-2 autofluorescence of the cell may be as large as 5% - 10 % of total fluorescence after dye loading (Neher, 2013). During ratiometric measurements, the background subtraction is an important step for the correctly estimating of [Ca^{2+}] (Bootman et al., 2013a). Figure 1 shows an experiment in which Fura-2-loaded cells recorded in resting conditions. Figure 1A demonstrates a selected grayscale *x-y* image of a fluorescent signal at 380 nm light.

The histogram of the intensity distribution of F_{380} at one frame is shown in Figure 1B. The minimum value of F_{380} was 117 a. u., and for F_{340} was 120 a. u. The mean background level of 133 a. u. in the given image area (dashed line) was subtracted from each pixel of the *x-y* image. After subtracting the background level, the histogram of the signal intensity distribution was obtained, which is shown in Figure 1C. The peak of the histogram was -2.9 intensity values. As can be seen, after subtracting the background level, the fluorescent signal had both negative and zero values. After subtracting the background level, the image of the ratio of 340 nm–380 nm signals ($\frac{\mathrm{F}_{340}}{\mathrm{F}_{380}}$) is shown in Figure 1D. As you can see, the signal is highly distorted and many values have infinity values (white pixels) since division by zero occurred. After background subtraction, the ratio ($\frac{\mathrm{F}_{340}}{\mathrm{F}_{380}}$) was distorted. The background value was also measured inside the soma of neurons before Fura-2 loading cells with the

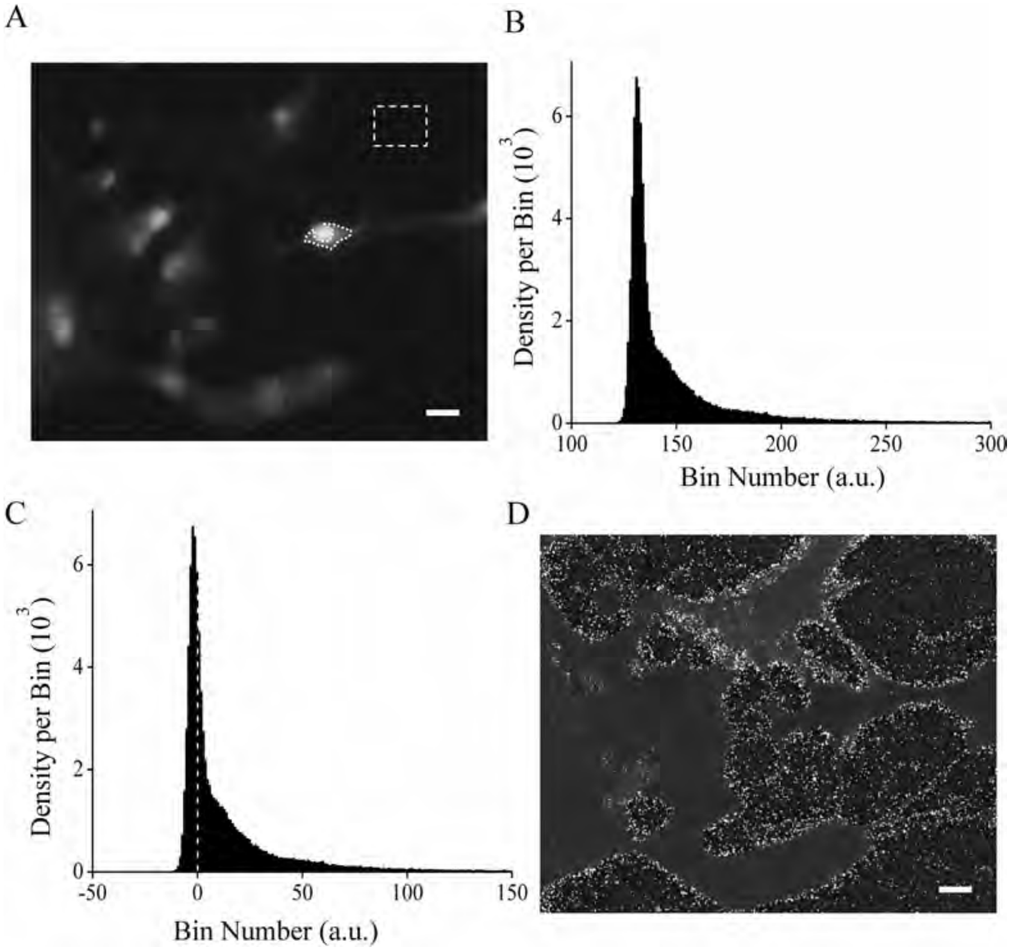

Figure 1. Intracellular Ca^{2+} measurement using the Fura-2 dye in cultured neurons of the hippocampus. A: Grayscale image displays the Fura-2 emission signal at 380 nm excitation wavelength (F_{380}) in rest. The neuron ROI (dotted white line) was selected on the soma of the neuron without a nuclear region. The dashed rectangle represents the place outside the neuron where the background level was obtained. The histogram of F_{380} pixel intensity distribution before and after subtracting the background is shown in Fig. 1B and 1C, respectably. The dashed line represents the zero value. D: Grayscale image of the distorted ratio of F_{340}/F_{380} fluorescence obtained after the background subtraction. Scale bar is 20 μm.

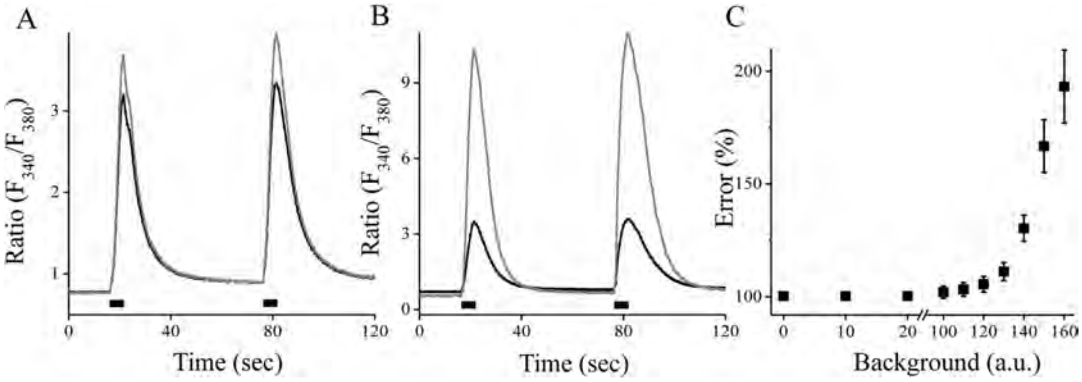

Figure 2. The appearance of an error in the ratio of F_{340}/F_{380} signals after subtracting the background level. The figure shows an experiment in which Fura-2-loaded hippocampal neurons. A, B: representative traces of the Fura-2 ratio ($\frac{F_{340}}{F_{380}}$) of Ca^{2+} transients under the condition of subtracting the background of 140 units (111114_c13#1) and 180 units (111114_c7#1), respectively. The gray line corresponds to the condition when the background value was subtracted from each pixel of fluorescence of *x-y* image; the black line – the background value was subtracted from averaged value from selected ROI of the neuron. The black rectangular indicates the application of a depolarization solution for 5 s. C: The error in determining the value of the ratio ($\frac{F_{340}}{F_{380}}$) on the value of the background. The error was calculated in 8 cells as a percentage value of Ca^{2+} transient amplitude (dR) obtained with each pixel subtraction divided on dR with averaged subtraction of the background level.

same conditions and fluorescence setting. It was 130.7 ± 0.6 at 340 nm and 133.7 ± 0.9 at 380 nm (n = 6) excitation wavelengths.

We consider two scenarios for subtracting the background level: the value is subtracted from each data point (pixel) of an *x-y* array of images for 340 nm and 380 nm fluorescence (each-pixel subtraction) or the average signal at selected ROI on the images (the averaged subtraction). The averaged subtraction is analogous to the measurement of a PMT detector. To show this consequence we check the value of the ratio signal recorded in cultured neurons loaded with Fura-2, AM dye. Two Ca^{2+} transients were recorded at soma area of neuron caused by 5-seconds application of the depolarization solution. The ratio $\frac{F_{340}-Bgr}{F_{380}-Bgr}$ is obtained then the background of 140 units was subtracted at each-pixel (a gray line) and form the averaged signal from the ROI (a black line), shown in Figure 2A. For each recording, the ratios were calculated from the same cell area. The value of 140 units was obtained at a site outside of the cell. Figure 2B shows another recording and the ratio with subtracting the background level of 180 units. As can be seen, the signals differ even at a lower background level and considerably by 180 units. As can be seen from the presented experimental data, the subtraction of the background level, from each pixel, leads to an error in determining the value of the ratio of fluorescence of 340 nm to 380 nm excitation wavelengths. According to the histogram of the distribution of the pixel intensity (Figure 1B), the signal at light of 380 nm was not underestimated. To describe the error in ratio that appears then the background is subtracted, the amplitude of Ca^{2+} transient for various background values were calculated. The amplitude of the first Ca^{2+} transient (*dR*) was calculated as the amplitude of the ratio at the peak of the transient from the base level when using each-pixel and the average background subtraction methods. How can we see from Figure 2C that the significant error occurs when the background level is above 120 a. u. This value is lower for the background level outside the cell that was 133.7 ± 0.4 units (n = 8). To reduce the difference in signals level, all the data presented in this experiment were obtained on the same day using the same settings of a fluorescent system, as well as and the exposure time and intensity of excitation. Of the 8 tested cells, without background subtraction, the basal levels of fluorescent signals at soma of neuron were 261.8 ± 12.7 at 380 nm and 226.4 ± 8.0 at 340 nm. The peak value of Ca^{2+} transient was 178.5 ± 5.7 at 380 nm and 279.3 ± 12.9 at 340 nm correspondently. In the case of each-pixel background subtraction signal at 380 nm excitation has a greater tendency towards a negative or zero value and can lead to errors in calculating the real Ca^{2+} signal not only at resting level but also at peak Ca^{2+} transient, that produce an error to determine the amplitude of it. To get the result without the error, it is necessary to average over the cell area or ROI of it and only then subtract the background level.

As mentioned earlier, $[Ca^{2+}]$ can be determined by a single wavelength method, but there will be no online dye bleaching correction. The calibration equation for a single wavelength can be written as:

$$\left[Ca^{2+}\right] = K_d\frac{(F - F_{min})}{(F_{max} - F)} \tag{2}$$

where F_{min} and F_{max} minimal and maximal fluorescence values (Grynkiewicz et al., 1985).

For ratiometric imaging, additional adjustment is required. It is that the excitation intensity at each wavelength is adjusted to match the resultant fluorescence to the bit-depth of the system (Bootman et al., 2013a). Using a chamber with indicator dye or some fluorescence grass, the fluorescence intensities for both wavelengths can be adjusted so that they are the same, attenuating the power level for excitation light at 380 nm. In our experiment, it was found that such conditions correspond to a 2.5-fold decrease in the light intensity at 380 nm compared with excitation at 340 nm.

A wavelength at < 360 nm, fluorescence increases when the Ca^{2+} ion binds to the dye, and decreases at > 360 nm. A fluorophore such as Fura-2 when excited at 340 nm and 380 nm wavelengths should have similar kinetic properties. Are the relative change values of these signals the same or different? It is well known that upon Ca^{2+} binding to the Fura-2 dye molecule the fluorescence emission differs mirror-like at excitation wavelengths of 340 and 380 nm, which are represented by Ca^{2+} transient (Figure 3A).

To compare relative change in fluorescence the signal at 380 nm is represented as the normalized signal $2 - \frac{F_{380}}{F_{380}(0)}$ and compared with the normalized signal at 340 nm as $\left(\frac{F_{340}}{F_{340}(0)}\right)^{C_0}$, where $F_{380}(0)$ and $F_{340}(0)$ are the initial, baseline fluorescence; where C_0 is the coefficient of the lost excitation power energy during the passage of light through the objective lens at a wavelength of 340 nm compared to 380 nm. Under the condition when fluorescent outputs coincide C_0 is 1. Interestingly, these signals are almost identical, except for the distorted part due to the dye bleaching effect (Figure 3B).

A dye bleaching function (γ) can be found as the averaged difference between these normalized signals added to 1:

$$\gamma = \frac{1}{2}\left(\left(\frac{F_{340}}{F_{340}(0)}\right)^{C_0} + \frac{F_{380}}{F_{380}(0)}\right) \tag{3}$$

The coefficient C_0 can be determined under specified boundary. Then for the given values of F_{340} and F_{380}, we can write: $\left(\frac{F_{340}(1)}{F_{340}(0)}\right)^{C_0} + \frac{F_{380}(1)}{F_{380}(0)} = 2$, where $F_{340}(1)$ and $F_{380}(1)$ is the value of Ca^{2+} transient at peak (or defined $[Ca^{2+}]$). Then we can find the coefficient as:

$$C_0 = \frac{\ln\left(2 - \frac{F_{380}(1)}{F_{380}(0)}\right)}{\ln\frac{F_{340}(1)}{F_{340}(0)}} \tag{4}$$

In case when the excitation intensity at each wavelength does not match the resultant fluorescence to the bit-depth of the fluorescence system the bleaching functions for a wavelength of 340 nm and 380 nm lights can be different. Figure 4 shows the kinetics of fluorescence emission at the two wavelengths with continuous illumination. At the beginning of the experiment, the fluorescence intensity for both at wavelengths was normalized to 100%. Figure 4A shows record without any intervention, just how the fluorescence drop-in time. The 380 traces dropped more rapidly than the 340 traces in both cases with a low and high bleaching rate. The best way to correct the fluorescence difference is power 340 trace with the power C_0 as $\left(\frac{F_{340}}{F_{340}(0)}\right)^{C_0}$. The resulting signals much bleaching rate with 380 traces in both records. Figure 4B presents another record during the recording of Ca^{2+} transient. In this example bleaching rate of F_{340} (black square line) and F_{380} (red triangle line) was differed significantly, but after correction as $\left(\frac{F_{340}}{F_{340}(0)}\right)^{C_0}$ bleaching rate much both wavelengths excitation (red and blue triangle lines). As can be seen from this figure the green trace (the dye bleaching function, obtained by formula 3) reflects the decrease in the traces of fluorescence of light at 380 nm and corrected 340 nm. The rate of bleaching effect can be simple mathematically corrected for 340 traces using power function with the coefficient of the lost excitation power energy C_0 which can be calculated by Eq. (4) with a calibration.

The bleaching-free normalized signals for two wavelengths can be presented as: $F1\ (340) = \frac{1}{\gamma}\left(\frac{F_{340}}{F_{340}(0)}\right)^{C_0}$ and $F2\ (380) = \left(2 - \frac{F_{380}}{F_{380}(0)\cdot\gamma}\right)$. As can be seen from Figure 3C, the normalized signals F1 and F2 are almost identical. The bleaching function γ obtained by Eq. (3) removes the component of the bleaching dye. The bleaching-free signals can be

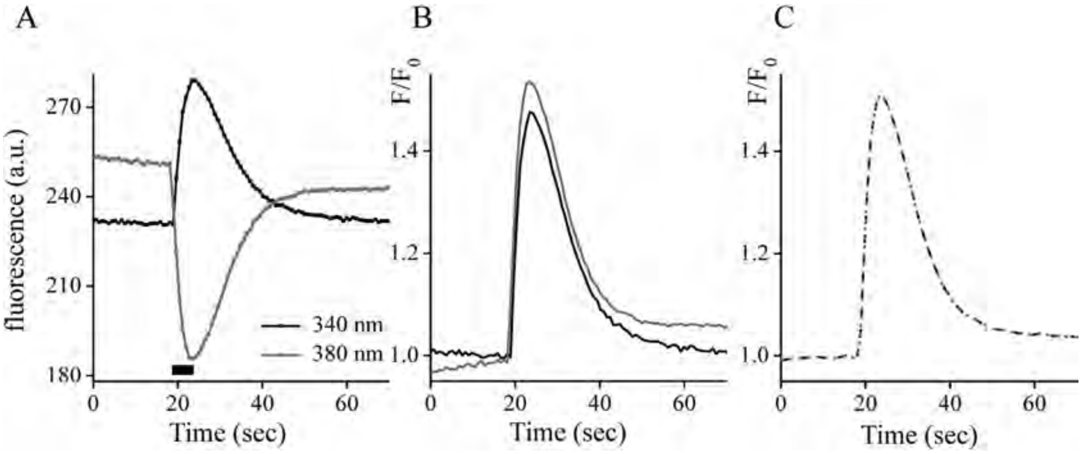

Figure 3. Fluorescence of Fura-2-loaded cells recorded during Ca^{2+} transient. Panel A depicts the measurement of fluorescence at excitation wavelengths of 340 nm (black line) and 380 nm (gray line). The black rectangular indicates the application of a depolarization solution. B: normalized fluorescent signals at both excitation wavelength, see the main text for additional explanations. A black line corresponds normalized fluorescence at 340 nm excitation wavelengths; a gray line – at 380 nm. C: normalized bleaching-free signal at excitation wavelengths of 340 nm (black dash) and 380 nm (gray short dash). The coefficient of the lost excitation power energy, C_0 was equal to 1.01. Ca^{2+} transient was caused by the 5-seconds application of the depolarization solution.

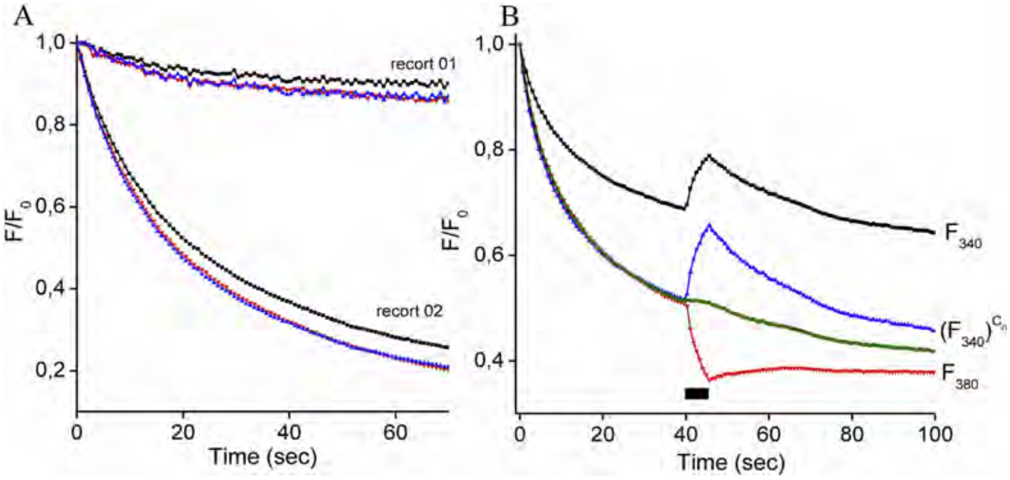

Figure 4. Bleached fluorescence of Fura-2-loaded cells. Panel A presents two cell recordings of the fluorescence emission at excitation wavelengths of 340 nm (black square line) and 380 nm (red triangle line) upon continuous illumination. During record 02, power energy of emission light at 340 nm and 380 nm was increased compared to the record 01. For both records, the blue triangle line presents the fluorescence emission at F_{340} recalculated as $\left(\frac{F_{340}}{F_{340}(0)}\right)^{C_0}$ with $C_0 = 1.35$ for the record 01 and $C_0 = 1.15$ for the record 02. The fluorescence was normalized to 1 at the starting point of experiments (time $= 0$ s). Panel B depicts the fluorescence at excitation wavelengths of 340 nm (black square line) and 380 nm (red triangle line) during Ca^{2+} transient. The blue triangle line presents the fluorescence emission at F_{340} recalculated as $\left(\frac{F_{340}}{F_{340}(0)}\right)^{C_0}$ with $C_0 = 1.77$. The green line is the bleaching function obtained by Eq. (3). Black rectangular indicates the application of a depolarization solution. Ca^{2+} transient was caused by the 5-seconds application of the depolarization solution.

found as: $\frac{(F_{340})^{C_0}}{\gamma}$ and $\frac{F_{380}}{\gamma}$ at 340 nm and 380 nm of excitation wavelength respectively.

Averaging $\left(\frac{F_{340}}{F_{340}(0)}\right)^{C_0}$ and $\left(2 - \frac{F_{380}}{F_{380}(0)}\right)$signals compensates the dye bleaching effect. Also, the resulting bleaching free fluorescence can be found by the next equation:

$$F = \frac{1}{2}\left(\left(\frac{F_{340}}{F_{340}(0)}\right)^{C_0} - \frac{F_{380}}{F_{380}(0)}\right) + 1 \tag{5}$$

Multiplying Eq. (5) by $F_{340}(0)$ or $F_{380}(0)$ allows comparing the fluorescent signals from other cells.

$$\begin{aligned} F &= F_{340}(0)\cdot\left(\frac{1}{2}\left(\left(\frac{F_{340}}{F_{340}(0)}\right)^{C_0} - \frac{F_{380}}{F_{380}(0)}\right) + 1\right), \text{or} \\ &= F_{380}(0)\cdot\left(\frac{1}{2}\left(\frac{F_{340}}{F_{340}(0)} - \left(\frac{F_{380}}{F_{380}(0)}\right)^{1/C_0}\right) + 1\right) \end{aligned} \tag{6}$$

The coefficient of the lost excitation power energy, C_0 could be found using Eq. (4). There is an option to use Fura-2 just at 380 nm (>360 nm) as a single wavelength method.

Rewrite formula 2 in condition as$F = 2 - \frac{F_{380}}{F_{380}(0)}$, $F_{max} = 2 - \frac{F_{380}^{min}}{F_{380}(0)}$, and $F_{min} = 2 - \frac{F_{380}^{max}}{F_{380}(0)}$ then:

$$[\mathrm{Ca}^{2+}] = \frac{(\mathrm{F}_{380}^{max} - \mathrm{F}_{380})}{(\mathrm{F}_{380} - \mathrm{F}_{380}^{min})} K_d \tag{7}$$

The formula 7 can be used to calculate the concentration of free Ca^{2+} for excitation wavelength >360 nm.

Eq. (6) calculates a new fluorescent signal from F_{340} and F_{380} with compensation for the bleaching dye effect. It can be used for a two-wave excitation method with Fura-2 dye or its analogs. The concentration of free Ca^{2+} can be obtained using Eq. (2) for fluorescence <360 nm or Eq. (7) for >360 nm excitation wavelength. The error through background subtraction that was found for the ratiometric signal is missing for the fluorescence F obtained by Eq. (6). Delivered Eq. (6) collapses the ratio measurement onto a single wavelength without background subtraction error. To calculate $[\mathrm{Ca}^{2+}]$ using Eq. (2) or 7, the background subtraction step can be skipped, as this value is equally excluded in the numerator and denominator of Eq. (2) or 7.

Figure 5A a represents an *x-y* grayscale image showing the Fura-2 emission signal at 340 nm light at rest before any manipulation. As can be seen in Figure 5B, the gray trace (the dye bleaching function, obtained by formula 3) reflects the decrease in the black trace of fluorescence of light at 340 nm and well defines the Fura-2 bleaching effect. In Figure 5C shows fluorescence at an excitation wavelength of 340 nm, obtained by Eq. (6). It is free bleaching fluorescence signal. Figure 5Ab and 5Ac show pseudo-color images of the two-dimensional signal obtained by Eq. (6) at rest and the peak of the first Ca^{2+} transient. These are not destroyed signals.

Under conditions without an error due to background subtraction, the calculation of the concentration of free Ca^{2+} using the Grynkiewicz formula 1 and the new technique presented in this paper, formula 6 and 2, should have the same result. For these comparisons, a background value was subtracted from F_{340} and F_{380} by the averaged subtraction circumstance. For both methods, the boundary values of the signals were

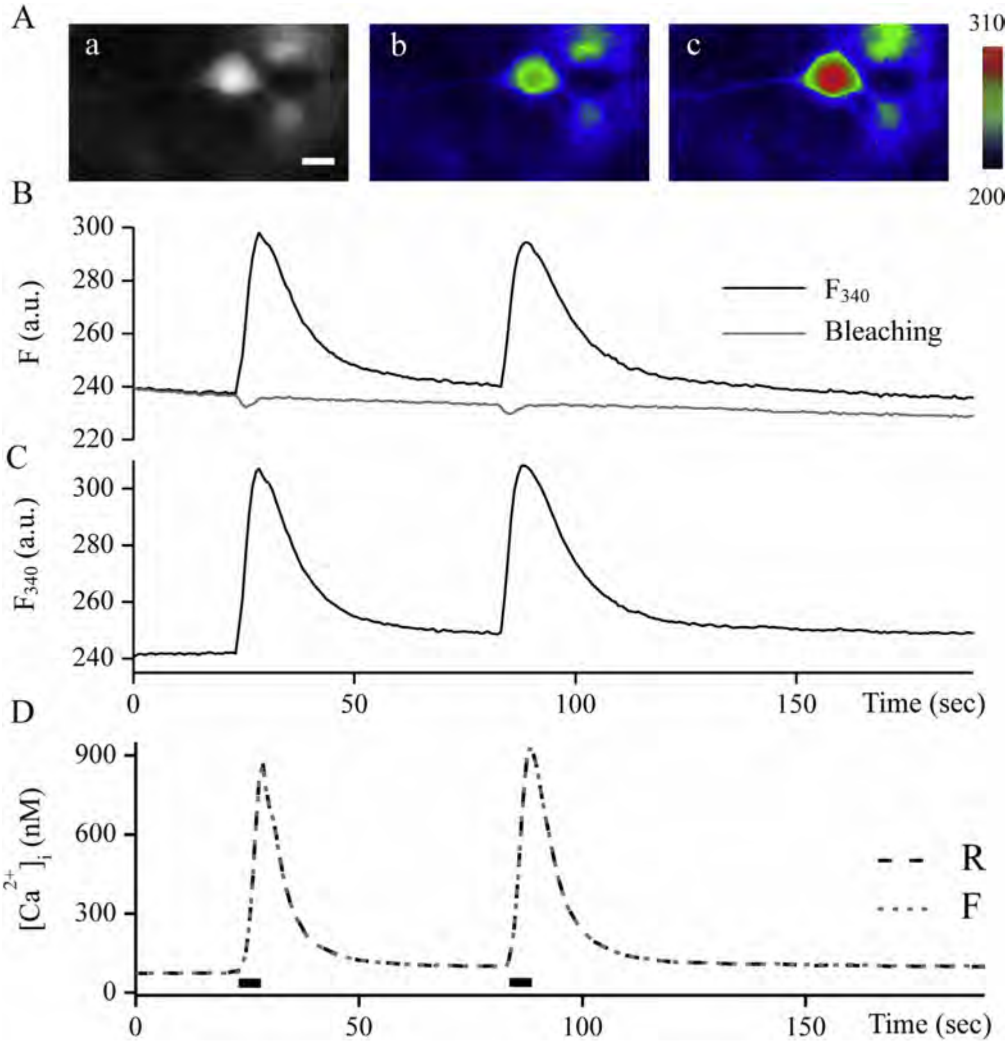

Figure 5. F_{340} and bleaching signals of Fura-2-loaded a hippocampal neuron. Aa: a part of the original fluorescent image at 340 nm light, at rest. It shows a pyramidal neuron. Ab and Ac are pseudocolor fluorescent images obtained by formula 6 at resting condition and at time of the peak of the first Ca^{2+} transient respectively. The color scale represents arbitrary fluorescence intensity values. B: The black line of the trace represents an original fluorescence signal at 340 nm excitation wavelength recorded from the soma of the neuron during two Ca^{2+} transients. The gray line is the bleaching function obtained by Eq. (3). C: The fluorescence at 340 nm light after bleaching correction obtained by Eq. (6). D: The concentration of free Ca^{2+} during two Ca^{2+} transients calculated using formulas 1 for the ratio of $\mathrm{F}_{340}/\mathrm{F}_{380}$ (R; black line) and fluorescence F obtained by formula 6 and 2 (gray line). Ca^{2+} transients were caused by the 5-seconds application of the depolarization solution. The black rectangular indicates the application of the depolarization solution. Scale bar is 20 μm.

obtained, as shown in AppendixA. F_{340}^{min} was 74.9 and $F_{340}^{max} = 195.5$; $F_{380}^{min} = 20.7$ and $F_{380}^{max} = 169.4$. The values of R_{min} and R_{max} were calculated, which amounted to 0.44 and 9.44, respectively. From the same data record, substituting these values into formula 2 for the resulting fluorescence F and Grynkiewicz formula 1 for the ratio signal R concentration of free Ca^{2+} was plotted in Figure 5D. As can be seen, both calculations equally determine $[Ca^{2+}]$.

A dye bleaching function can be also written as.

$$\gamma = \frac{{F_{340}}^{C} + F_{380}}{{F_{340}}^{C}(0) + F_{380}(0)} \tag{8}$$

where C is the coefficient of the lost excitation power energy for fluorescence F_{340} compare to F_{380}. This coefficient can be determined under given boundary conditions of $F_{340}(1)$ and $F_{380}(1)$ at given $[Ca^{2+}]$ or peak of Ca^{2+} transient. From Eqs. (3) and (8), we can write the equation to obtain a value of C:

$$2 \cdot F_{340}^{C}(1) + 2 \cdot F_{380}(1) + \left(\left(\frac{F_{340}(1)}{F_{340}(0)} \right)^{C_0} + \frac{F_{380}(1)}{F_{380}(0)} \right) \cdot \left(F_{340}^{C}(0) - F_{380}(0) \right) = 0 \tag{9}$$

where C_0 can be determined by Eq. (4) under the same conditions. The coefficient C can be empirically estimated by substituting a value from 0.5 to 2 units in Eq. (9).

The coefficient C can be used to calculate ratio value with compensation of different power energy lost during the passage of light through the objective lens at a wavelength of 340 nm compared to 380 nm.

$$R = \frac{{F_{340}}^{C}}{F_{380}} \tag{10}$$

The ratio obtained by Eq. (10) does not affect the lost excitation power for a wavelength of 340 nm light. The ratio should be used to compare the fluorescence ratio of Ca^{2+} signals from different recordings.

4. Calculation of $[Ca^{2+}]$ without error due to background subtraction

- The excitation intensity at each wavelength need to be adjusted to match the resultant fluorescence to the bit-depth of the system (Bootman et al., 2013a);
- Imaging data is acquired as a time series and must be saved into two image sequences separated into data at 340 nm and 380 nm excitation wavelengths (F_{340} and F_{380});
- Finding a background value at noncellular region;
- Make time profile of fluorescence for two channels $F_{340}(t)$ and $F_{380}(t)$ at selected ROI of a cell where need to calculate $[Ca^{2+}]$;
- Subtract the background from F_{340} and F_{380} signals. The background value must be subtracted from the averaged value of the fluorescence at selected ROI of the cell;
- Obtain ratio of F_{340} and F_{380};
- Using boundary values of fluorescence with the background subtraction (obtained how described in (Barreto-Chang and Dolmetsch, 2009; Bootman et al., 2013b)) calculate $[Ca^{2+}]$ by Grynkiewicz formula 1.

To obtain two-dimensional data of $[Ca^{2+}]$ (x-y), the following protocol can be used:

- Get fluorescence x-y image at an excitation wavelength of 340 nm or 380 nm with compensating the effect of bleaching of the dye under Eq. (6);
- Do not need to subtract the background value;
- Using fluorescence boundary values, calculate $[Ca^{2+}]$ by Eq. (2) or 7 for wavelengths of 340 nm or 380 nm respectively;

If excitation intensity at the excitation wavelength of 340 nm and 380 nm lights does not correspond to the resulting fluorescence to the bit-depth of the system, mathematical manipulation using a power function removes the difference in bleaching function and fluorescence value at excitation wavelength 340 nm. The coefficient C_0 and C can be calculated during calibration under boundary conditions using Eqs. (4) and (9).

The obtained x-y image $[Ca^{2+}]$ can be used for flux analyses, the protocol of which is described in detail in (Neher, 1995; Rios et al., 1999; Shkryl, 2017).

5. Discussion

The Fura-2 indicator, developed by Roger Tsien and co-authors (Grynkiewicz et al., 1985), was cited in thousands of scientific papers and is commonly used to study the role of calcium in cell regulation. As mentioned above, the ability to make ratio measurements with Fura-2 allows us to accurately measure the intracellular Ca^{2+} concentration. The ratiometric method removes the photobleaching of the dye and reduces the effect of the uneven loading of the dye. Without the ratiometric method, this is almost impossible online, however, some bleaching function can be obtained by an additional record that can be applied to the data or simply mathematically corrected because it follows a predictable exponential decay (Thomas et al. 2000). In this paper, we obtain Eq. (3), which finds the photobleaching function γ from F_{340} and F_{380} signals. This function can be used to obtain bleaching free fluorescence. In our experiments, the best bleaching curve approximation was achieved by power function x^c. A x^c curve fitting was performed from the baseline value using $\gamma = 1 - a \cdot x^b$, where b depends on the amount of excitation power, in our experimental conditions takes a value around 0.8. (data is not shown). As can be seen from Figure 5 before Ca^{2+} transient begins to increase there is a slight decrease in the level with a subsequent increase of the bleaching function γ. These changes are due to the slow temporal resolution, which was 0.76 s, while when fluorescence changes during Ca^{2+} transient signal F_{380} are ahead of the F_{340}. To reduce this artifact and noise before applying the bleaching function it can be approximated by $1 - a \cdot x^b$ generated to the same experimental condition.

As mentioned above, background subtraction is an important step for the ratiometric method. Unlike the signal recorded using a PMT, the CCD camera, at an individual pixel, records the reduced amount of photons with a high noise level at each data point of the x-y image (Heintzmann, 2006; Jerome, 2011). Also subtracting the background level directly from each pixel of the x-y image may be cases where the value is negative or even zero, which naturally leads to distortion of the ratio of signals at 340 nm to 380 nm excitation wavelengths and can lead to a significant error in determining the concentrations of free Ca^{2+} using the Grynkiewicz formula (formula 1 (Grynkiewicz et al., 1985);) that was shown here. When an error occurs due to background subtraction, the ratio may be twice as large as the actual value (Figure 2D). Barreto-Chang O.L. and Dolmetsch R.E. described the protocol of calcium imaging where the procedure of background value subtraction applied from each pixel in the field. They apply an additional step to reduce noise need to adjust the threshold values for each wavelength to generate a ratio image that includes only the cells and not the background and that is not noisy in the region close to the edges of the cells (Barreto-Chang and Dolmetsch, 2009). In the protocol described in this work using a CCD camera to reduce noise and eliminate the error requires averaging the signal from ROI before subtracting the background. To obtain a two-dimensional image of $[Ca^{2+}]$ need to use the fluorescence obtained by formula 6.

The resulting fluorescence F obtained by formula 6 is the average value of the normalized signals for the excitation lights of the dye at 340 nm and 380 nm. Due to the different bandwidths of the objective lens for these wavelengths, the normalized fluorescence may differ slightly for 340 nm and 380 nm. Also, the difference between the signals can be because the excitation and emission peak of NADH is 340 nm and 440–470 nm, respectively (Harbig et al., 1976; Paddle, 1985) and its fluorescence contaminates the true UV-exited Fura-2 indicator fluorescence.

Becker and Fay had shown that a bleached form of Fura-2 is still fluorescent and it is not sensitive to calcium over the same range as Fura-2 and ratio method are not completely remove proportional decreasing the concentration of dye (Becker and Fay, 1987). They suggested that to minimize photodegradation, one should decrease the illumination dose and O_2 concentration. In this way, some errors can appear in calcium concentration measurements. Significant photodegradation of the fluorescence dye leads to an underestimation of the analyze concentrations depending on the intensity and duration of illumination. Scheenen et all shown that the problem can be avoided by including cell-permeant antioxidants such as Trolox in the bathing solution (Scheenen et al., 1996).

During ratiometric Ca^{2+} imaging, in conditions when excitation intensity at each wavelength is not adjusted to match the resultant fluorescence to the bit-depth of the system, UV illumination of a dye not gradually bleaches the indicator for both excitation channels (Becker and Fay, 1987; Bootman et al., 2013a). In this work, it was shown that the existing difference in the dye bleaching function for F_{340} and F_{380} can be mathematically eliminated (by power function) both with a low and high power intensity of the dye excitation and with a significant difference in the dye bleaching rate. The coefficient of the lost excitation power energy, C_0 could be simply calculated by Eq. (4) during calibration with known $[Ca^{2+}]$ or at a value of baseline and peak value of Ca^{2+} transient. It will help to analyses data if an adjustment of excitation intensity both ratio channels was not much the resultant fluorescence to the bit-depth of the fluorescence system. It removes one trace drooped more rapidly for resulting in not distorted the fluorescence ratio.

Another problem that arises due to the poor performance in fluorescent imaging through ultraviolet excitation is the distortion of the ratio of the F_{340} to F_{380} signals, which restricts comparing this ratio for the different fluorescent settings. Using the coefficient C, calculated according to Eq. (9), we can calculate the fluorescence ratio using formula 10 without the limitation.

The advantage of Fura-2 is that it has a good cross-section for two-photon calcium imaging (Wokosin et al., 2004). The Eq. (2) could be used to calculate $[Ca^{2+}]$ for two-photon at 680 nm (or <360 nm at a single wavelength excitation). The new Eq. (7) can be used for the two-photon excitation method at 760 nm (or with single wavelength at 380 nm light) and allow you to use Fura-2 (>360 nm) as a dye with excitation at a single wavelength and can serve as an alternative to fluorescent systems with weak UV transmission lens.

6. Conclusions

In this paper, we present a modified formula for calculation of free Ca^{2+} concentration for ratiometric dye, such as Fura-2, which recalculates the fluorescence of two channels, imaged by a CCD camera, at excitation wavelengths of 340 nm and 380 nm into fluorescence with photobleaching correction without an error due to background subtraction. The resulting fluorescence can be converted into a concentration of free Ca^{2+}. Also, a mathematical elimination technique using the power function is provided to remove existing differences in the dye bleaching rate and fluorescence intensity. It helps compensate the signal at a wavelength of 340 nm light if the excitation intensity is not adjusted to ensure the same an objective lens transmittance for ultraviolet dye illumination. This is an important preference for a fluorescence system that uses CCD cameras.

Declarations

Author contribution statement

Vyacheslav M. Shkryl: Conceived and designed the experiments; Performed the experiments; Analyzed and interpreted the data; Contributed reagents, materials, analysis tools or data; Wrote the paper.

Funding statement

This work was supported by the National Academy of Sciences of Ukraine.

Competing interest statement

The authors declare no conflict of interest.

Additional information

Supplementary content related to this article has been published online at https://doi.org/10.1016/j.heliyon.2020.e04180.

References

Barreto-Chang, O.L., Dolmetsch, R.E., 2009. Calcium imaging of cortical neurons using Fura-2 AM. J. Vis. Exp. 23, e1067.

Becker, P.L., Fay, F.S., 1987. Photobleaching of fura-2 and its effect on determination of calcium concentrations. Am. J. Physiol. 253, C613–C618.

Berridge, M.J., Lipp, P., Bootman, M.D., 2000. The versatility and universality of calcium signalling. Nat. Rev. Mol. Cell Biol. 1, 11–21.

Bootman, M.D., Rietdorf, K., Collins, T., Walker, S., Sanderson, M., 2013a. Ca^{2+}-sensitive fluorescent dyes and intracellular Ca^{2+} imaging. Cold Spring Harb. Protoc. 2013, 83–99.

Bootman, M.D., Rietdorf, K., Collins, T., Walker, S., Sanderson, M., 2013b. Converting fluorescence data into Ca^{2+} concentration. Cold Spring Harb. Protoc. 2013, 126–129.

European convention, Strasburg, 1986. European Convention for the Protection of Vertebrate Animals used for Experimental and other Scientific Purposes. https://www.coe.int/en/web/conventions/full-list/-/conventions/treaty/123.

Grynkiewicz, G., Poenie, M., Tsien, R.Y., 1985. A new generation of Ca^{2+} indicators with greatly improved fluorescence properties. J. Biol. Chem. 260, 3440–3450.

Harbig, K., Chance, B., Kovach, A.G., Reivich, M., 1976. In vivo measurement of pyridine nucleotide fluorescence from cat brain cortex. J. Appl. Physiol. 41, 480–488.

Heintzmann, R., 2006. Structured illumination methods. In: Pawley, J.B. (Ed.), Handbook of Biological Confocal Microscopy. Springer US, Boston, MA, pp. 265–279.

Jerome, W.G., 2011. Digital image capture for confocal microscopy. In: Price, R.L., Jerome, W.G. (Eds.), Basic Confocal Microscopy. Springer, New York, pp. 133–155. New York, NY.

Minta, A., Kao, J.P., Tsien, R.Y., 1989. Fluorescent indicators for cytosolic calcium based on rhodamine and fluorescein chromophores. J. Biol. Chem. 264, 8171–8178.

Neher, E., 2013. Quantitative aspects of calcium fluorimetry. Cold Spring Harb. Protoc. 2013, 918–924.

Neher, E., 1995. The use of fura-2 for estimating Ca buffers and Ca fluxes. Neuropharmacology 34, 1423–1442.

Paddle, B.M., 1985. A cytoplasmic component of pyridine nucleotide fluorescence in rat diaphragm: evidence from comparisons with flavoprotein fluorescence. Pflueg. Arch. Eur. J. Physiol. 404, 326–331.

Pozzan, T., Rizzuto, R., Volpe, P., Meldolesi, J., 1994. Molecular and cellular physiology of intracellular calcium stores. Physiol. Rev. 74, 595–636.

Rios, E., Stern, M.D., Gonzalez, A., Pizarro, G., Shirokova, N., 1999. Calcium release flux underlying Ca^{2+} sparks of frog skeletal muscle. J. Gen. Physiol. 114, 31–48.

Scheenen, W.J., Makings, L.R., Gross, L.R., Pozzan, T., Tsien, R.Y., 1996. Photodegradation of indo-1 and its effect on apparent Ca^{2+} concentrations. Chem. Biol. 3, 765–774.

Shkryl, V.M., 2017. Intracellular calcium fluxes in excitable cells. Neurophysiology 49, 384–392.

Shkryl, V.M., Nikolaenko, L.M., Kostyuk, P.G., Lukyanetz, E.A., 1999. High-threshold calcium channel activity in rat hippocampal neurones during hypoxia. Brain Res. 833, 319–328.

Thomas, D., Tovey, S.C., Collins, T.J., Bootman, M.D., Berridge, M.J., Lipp, P., 2000. A comparison of fluorescent Ca^{2+} indicator properties and their use in measuring elementary and global Ca^{2+}signals. Cell Calcium 28, 213–223.

Tsien, R.Y., Pozzan, T., Rink, T.J., 1982. Calcium homeostasis in intact lymphocytes: cytoplasmic free calcium monitored with a new, intracellularly trapped fluorescent indicator. J. Cell Biol. 94, 325–334.

Wokosin, D.L., Loughrey, C.M., Smith, G.L., 2004. Characterization of a range of fura dyes with two-photon excitation. Biophys. J. 86, 1726–1738.

3.3 Просторово-часові властивості кальцієвих транзієнтів у пірамідних нейронах гіпокампу in vitro

Інформація про участь RyRs у кальцієвій сигналізації в нейронах є суперечливою. Особливі питання стосуються локалізації місця вивільнення Ca^{2+} з ендоплазматичного ретикулума (ЕР) та його взаємодії з сигналами Ca^{2+} під час короткочасної та тривалої стимуляції. Проте визнається, що молекулярні механізми та патерни вивільнення Ca^{2+} у різних ділянках різних нейронів можуть істотно відрізнятися (Verkhratsky, 2005). Як зазначалося вище, ізоформа RyR β є гомогенною до RyR3 домінуючих в нервових клітинах (Ottini et al., 1996, Oyamada et al., 1994). Тобто, видається переконливим, що нервові клітини мають можливість активувати ріанодинові рецептори за рахунок кальцію.

В даній роботі, просторово-часові характеристики кальцієвих сигналів були досліджені на культивованих пірамідних нейронах гіпокампу щурів за допомогою двовимірної флуоресцентної мікроскопії та ратіометричного барвника Fura-2. Додатково, з метою отримання детальної інформації про участь ріанодинових рецепторів у кальцієвій сигналізації нейронів, ми аналізували дані сигнали при впливі різних стимулів: стимуляції електричним полем (EFS), деполярізуючим розчином з високою концентрацією K+, кофеїну та дантролену на культивованих пірамідних нейронах CA1 гіпокампу щурів.

На рисуноку 3.1A наведені репрезентативні дані, які відображають зміну співвідношення Fura-2 (F_{340}/F_{380}; Ca^{2+} сигнали), спричинену двома серіями по 50 імпульсів EFS (використаних для завантаженням Ca^{2+} до ЕР), а також подальшим застосуванням 10 мМ кофеїну протягом 5 с для вивільнення Ca^{2+} з ЕР за участю RyRs. Для завантаження кальцієм ЕР було застосовано додатковий EFS та 5 с аплікацію деполяризуючого розчину.

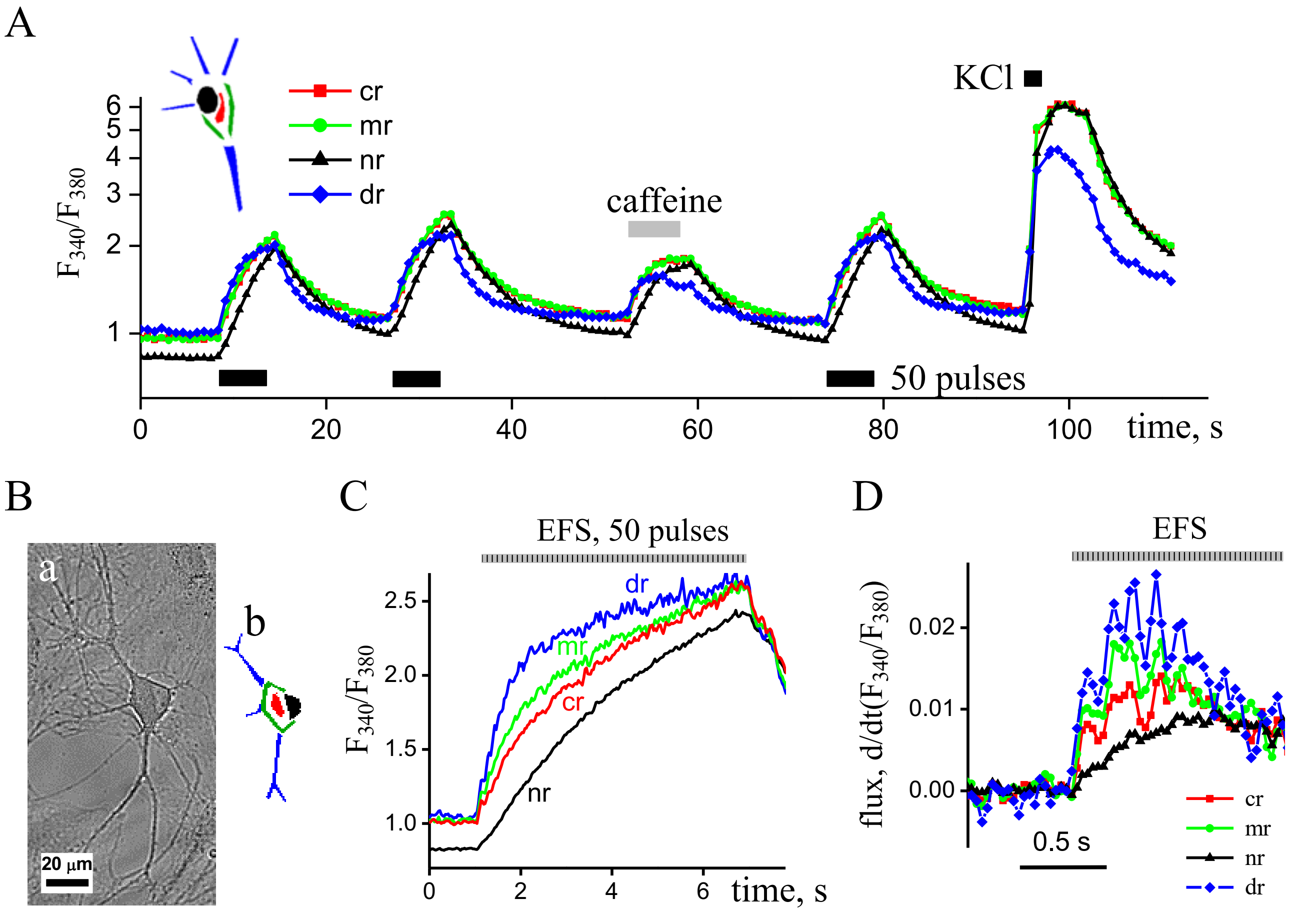

Рисунок 3.1. Ca^{2+}-відповіді в різних ділянках інтересу пірамідних нейронів гіпокампу. (A) Транзієнтні збільшення внутрішньоклітинної концентрації кальцію викликані двома серіями по 50 імпульсів EFS (чорний прямокутник, 9 Гц) з подальшим застосуванням кофеїну (caffeine, світло-сірий прямокутник; 10 мМ і 5 с) і серією з 50 імпульсів EFS і деполяризуючого розчину з 50 мМ KCL (KCl, чорний квадрат, 5 с). Відношення F_{340}/F_{380} представлені в натуральному логарифмічному масштабі. У лівому верхньому куті наведено схему аналізованих зон. (B,a) Зображення клітини, отримане при прямому освітленні. (B,b) Різні ділянки інтересу нейрона позначені кольором. (C) Розподіл співвідношень F_{340}/F_{380} нейрона з 50 EPS, у вигляді часових профілів. (D) $d(F_{340}/F_{380})/dt$ (с$^{-1}$), перша похідна сигналу Ca^{2+}. Поточні дані були отримані з даних, представлених у частині (C). Ca^{2+}-відповіді реєстрували в центральній ділянці (cr; червона лінія), субмембрані (mr; зелена лінія), дендритному дереві (dr; синя лінія) та ядрі (nr; чорна лінія) культивованих нейронів гіпокампу, навантажених флуоресцентним Ca^{2+}-індикатором Fura-2.

Значення базального вільного Ca^{2+} було значно знижено в ядрі клітини нейрона, на 15% менше порівняно з центральною ділянкою (61 нМ проти 85 нМ, $n = 30$; $P < 0.001$). Сигнал Ca^{2+} у дендритній ділянці у відповідь на стимуляцію з'являвся швидше порівняно з іншими ділянками, але мав найменшу амплітуду під час EFS, деполяризації KCl та застосування кофеїну. Амплітуда Ca^{2+}-транзієнту в дендритному дереві нейронів пірамідної форми у відповідь на EFS становила 1.18±0.09 (207 нМ, n = 19), що було значно менше порівняно з субмембранною ділянкою — 1.62±0.17 (303 нМ, n = 19; $P < 0.05$), центральною ділянкою — 1.73±0.18 (329 нМ, n = 19; $P < 0.01$) та ядрі — 1.66±0.17 (300 нМ, n = 19; $P < 0.05$). У дендритному дереві амплітуда Ca^{2+}-транзієнту, спричиненого деполяризацією розчином з високою концентрацією KCl, також значно знижувалася: 3.43±0.41 (0.87 мкМ, n = 24) порівняно з субмембранною ділянкою — 4.76±0.39 (1.65 мкМ, n = 24; $P < 0.05$), центральною ділянкою — 4.98±0.38 (1.84 мкМ, n = 24; $P < 0.01$) та ядрі — 5.06±0.39 (1.81 мкМ, n = 24; $P < 0.01$). Клітинна відповідь на кофеїн свідчить про наявність та навантаження кальцієм ЕР депо, а вивільнення цього іону відбувається за рахунок RyRs. Пікові значення кальцієвих сигналів, індуковані 10 мМ кофеїну (як вивільнення Ca^{2+} з ЕР), значно зменшувалися в ділянці дендритного дерева до 1.88±0.08 (225 нМ, n = 19) в порівнянні з 2.31±0.11 (310 нМ, n = 19; $P < 0.01$) у субмембранній ділянці, центральній ділянці — 2.43±0.13 (336 нМ, n = 19; $P < 0.001$) та ядрі — 2.17±0.12 (283 нМ, n = 19; $P < 0.05$) пірамідних нейронів.

У наступній серії експериментів ми досліджували просторово-часову організацію Ca^{2+}-транзієнтів у різних ділянках пірамідоподібних нейронів, зареєстрованих на частоті 30 Гц. Ми окремо реєстрували транзієнти Ca^{2+}, індуковані стимуляцією ESP на довжинах хвиль збудження 340 та 380 нм. Ці дані були синхронізовані з ESP і розділеними в часі. Перший зареєстрований транзієнт Ca^{2+} був з довжиною хвилі збудження 340 нм. Після затримки в 2 хвилини був зроблений додатковий запис при 380 нм, використовуючи аналогічні параметри стимуляції та умови запису, дозволяючи генерувати сигнал співвідношення F_{340}/F_{380} (рис. 3.1C).

Швидка двовимірна реєстрація транзієнтів Ca^{2+} під час деполяризації виявила асинхронне зростання концентрації вільного Ca^{2+}. EFS спричиняв збільшення Ca^{2+} сигналів, які спочатку з'являлися в дендритах, потім у субмембранній, центральній і, нарешті, в ядерній ділянках клітини. На рис. 3.1D представлена перша похідна сигналу $[Ca^{2+}]$ $[d(F_{340}/F_{380})/dt]$, яка відображає потік Ca^{2+}. Потік Ca^{2+} у субмембранній та центральній ділянках характеризується зростаючим та спадаючим ступенями, що відображає індуковані EFS кальцієві транзієнти. Максимальний потік у субмембранній та центральній ділянках спостерігався через 0.2 с після ініціації і поступово зменшувався. У ядерній ділянці нейрона потік з'являвся з затримкою, досягаючи піка через 0.6 с після початку, але з меншою амплітудою порівняно з іншими ділянками. Максимальна швидкість потоку спостерігалася в ділянці дендритного дерева (0.028±0.004, n = 8), знижувалася в субмембранній (0.018±0.002, n = 8) і центральній (0.015±0.004, n = 8) ділянках нейрона, і була найменшою в ядрі (0.010±0.001, n = 8) нейрона.

Двовимірна візуалізація Ca^{2+}-сигналів виявила асинхронну затримку при збільшенні концентрації вільного Ca^{2+} у ядрі в порівнянні з примембранними, центральними чи дендритними ділянками. Сигнал Ca^{2+} в цих пірамідних нейронах спочатку з’являвся на периферії клітини в примебранній області та дентритах, а потім у центрі нейрона. Він мав подібні ознаки розповсюдження кальцієвого сигналу, яке спостерігається в міоцитах передсердь. Як зазначено вище, у цих клітинах сигнал Ca^{2+} під час електричної стимуляції спочатку виникає на периферії міоцита, а потім розповсюджується до центру клітини.

Вивільнення Ca^{2+} з ЕР відбувається при відкритті RyRs та IP_3Rs (Rizzuto and Pozzan, 2006). Вивільнення кальцію через IP_3Rs з дендритів зазвичай ініціюється дією нейромедіаторів, таких як глутамат (Niswender and Conn, 2010). У свою чергу, RyRs активуються при зростанні концентрації Ca^{2+} в цитозолі (Shkryl and Blatter, 2013, Blatter, 2017) через кальцій-опосередковану активацію RyRs відомою як CICR (Fabiato, 1983). В наступних експериментах ми зосередились на дослідженні функціонування ЕР-сховищ у пірамідних нейронах гіпокампу. Для індукції вивільнення Ca^{2+} з ЕР, ми застосували кофеїн — агоністу RyRs, який раніше виявляв здатність підвищувати цитозольні концентрації Ca^{2+}. З метою завантаження депо ЕР ми використовували ESP.

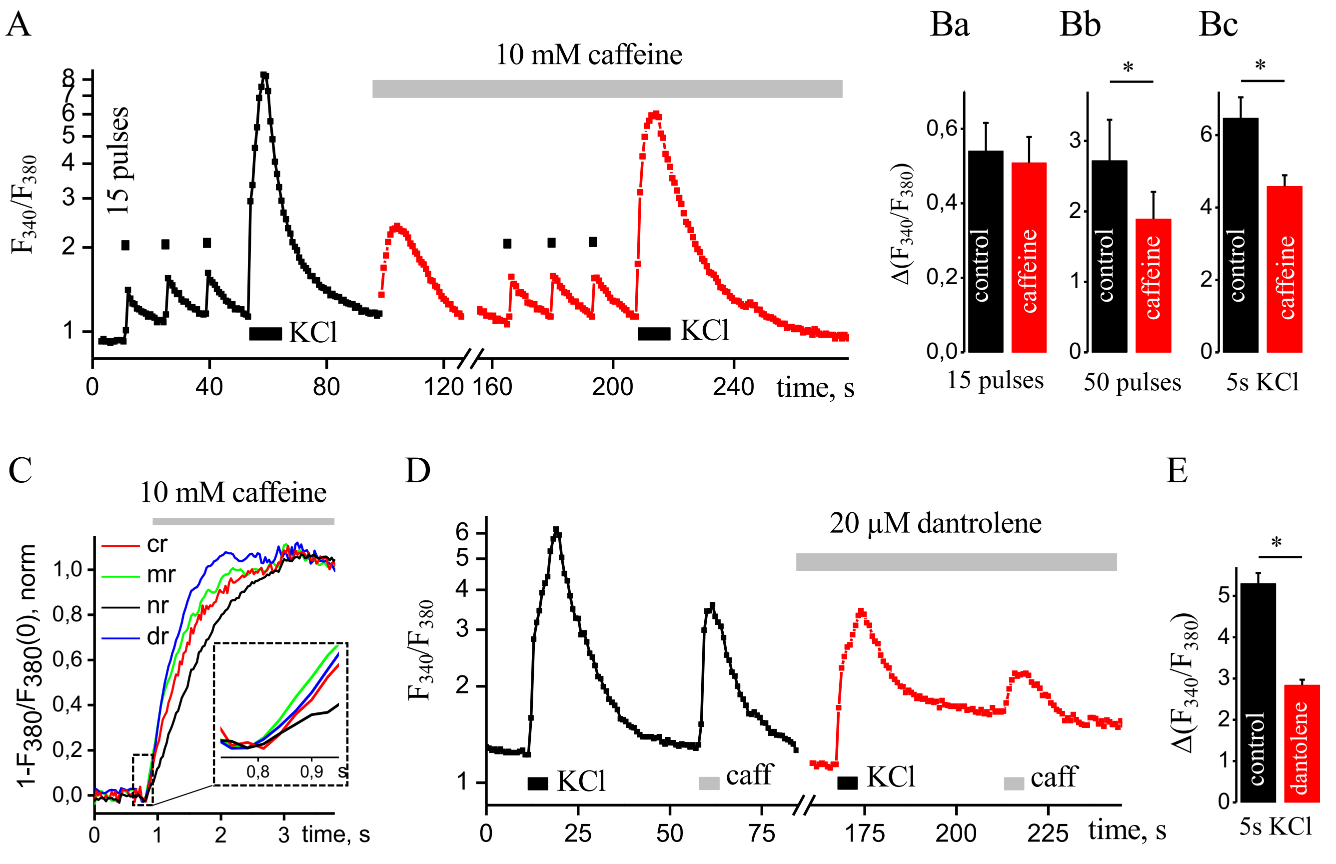

Рисунок 3.2. Транзієнти Ca^{2+} в умовах впливу агоніста та інгібітора RyRs. (А) Транзієнтне збільшення [Ca^{2+}], викликане трьома серіями по 15 імпульсів EFS (чорний квадрат; 1 с) з наступним застосуванням деполяризуючого розчину (KCl, чорний прямокутник, 5 с) у контролі (лінія з чорними квадратами) та при повторних стимуляціях у присутності 10 мМ кофеїну (caffeine; лінія з червоними квадратами), для блокування вивільнення кальцію з ЕР. (B) Середні значення амплітуди другого транзієнту Ca^{2+}, викликаного 15 (a) або 50 (b) імпульсами EFS, та транзієнту Ca^{2+} в умовах дії розчину великим вмістом KCl (c), у контролі та при додаванні 10 мМ кофеїну. (С) Нормалізовані транзієнти Ca^{2+} реєстровані за допомогою одного-хвильового методу (33 мс на зображення і довжина хвилі збудження 380 нм) у різних ROI, викликані додаванням 10 мМ кофеїну. Пунктирна лінія в частині (С) ілюструє початкову фазу кофеїн-індукованого зростання Ca^{2+}. ROI визначені у центральній (cr, червона лінія), субмембранній (mr, зелена лінія), ядерній (nr, чорна лінія) та дендритній (dr, синя лінія) ділянках клітини. (D) Транзієнтне збільшення [Ca^{2+}], викликане деполяризуючим розчином (KCl, чорний прямокутник, 5 с) та кофеїну (caffeine, світло-сірий прямокутник; 10 мМ і 5 с) у контрольних умовах (чорна лінія з квадратом) та при постійній присутності 20 мкМ дантролену (червона лінія з квадратом) для блокування вивільнення кальцію з ЕР. (E) Середнє значення амплітуди транзієнтних коливань [Ca^{2+}], викликаних деполяризуючим розчином. Результати представлені як середнє значення ± S.E., $^*P < 0.05$. Ca^{2+}-реакції були зареєстровані у сомі, не враховуючи ядерну ділянку. Відношення F$_{340}$/F$_{380}$ представлено в натуральній логарифмічній шкалі.

На рисунку 3.2A представлена вибіркова реєстрація, де показано зміни сигналу Ca^{2+} в нейроні: у контрольних умовах (чорний графік) та при додаванні 10 мМ кофеїну (червоний графік). У контролі базальний рівень вільного кальцію був 1.06±0.03, а при впливі кофеїну зріс до 1.26±0.05. Амплітуда транзієнтів Ca^{2+}, індукованих деполяризуючим розчином, суттєво знижувалася з 6.47±0.57 (в контролі) до 4.58±0.31 при додаванні 10 мМ кофеїну (рис. 3.2B,c; $n = 12$, $P < 0.05$). Під час стимуляції електричним полем зміни амплітуди в умовах впливу кофеїну залежали від тривалості стимуляції. Пікова амплітуда Ca^{2+} сигналу, індукованого короткою стимуляцією (15 імпульсів, 9 Гц), достовірно не змінилася, та становила 0.54±0.08 порівняно з 0.51±0.07 (рис. 3.2B,a; $n = 13$), відповідно контрольних значень. Проте при тривалій стимуляції (50 імпульсів, 9 Гц) амплітуда знижувалася із контрольного значення в 2.72±0.58 до 1.89±0.38 (рис. 3.2B,b; $n = 6$, $P < 0.05$) в умовах дії кофеїну.

Кофеїн при короткій електричній стимуляції (15 імпульсів, 1 с) не впливає на амплітуду Ca^{2+}-транзієнту, проте Ca^{2+}-відповідь на деполяризуючий розчин або тривалу EFS істотно знижується. Таким чином, при тривалій стимуляції спостерігається вивільнення Ca^{2+} з ЕР через RyRs. Згідно з нормалізованими кофеїн-індукованими Ca^{2+} транзієнтами (рис. 3.2C), зростання сигналів спостерігалося в усіх ділянках пірамідних нейронів гіпокампу. Проте в центральній зоні та ядрі, час зростання сигналу був трохи довшим (37.5±7.5 мс, $n = 4$) порівняно з підмембранною зоною та дендритним деревом.

Крім того, ми застосували 20 мкМ дантролену для інгібування RyRs і реєстрували транзієнти Ca^{2+}, викликані високим рівнем KCl. На рисунку 3.2D представлений запис, де накладені зміни сигналу Ca^{2+}, отримані з нейрона в контрольних умовах (лінія з чорними квадратами), та при додаванні 20 мкМ дантролену (лінія з червоними квадратами). У контрольному досліді базальний рівень вільного кальцію досягав 1.23±0.03, тоді як у присутності дантролену цей показник склав 1.10±0.03. Амплітуда Ca^{2+}-транзієнтів, викликаних деполяризуючим розчином, при додаванні 20 мкМ дантролену зазнала істотного зниження і скоротилася з 5.30±0.26 до 2.84±0.13 (рис. 3.2E; $n = 29$, $P < 0.001$). Завантаженість ЕР у присутності дантролену також істотно знизилась: до 0.682±0.06 з 1.72±0.14 ($n = 28$, $P < 0.01$). Ці дані додатково підкреслюють участь RyRs у Ca^{2+}-сигналізації культивованих пірамідних нейронів гіпокампа.

Раніше було зазначено, що ріанодинчутливі депо Ca^{2+} в різних центральних нейронах щурів (зокрема в нейронах CA1 гіпокампу) є порожніми в стані спокою та накопичують Ca^{2+} лише після його надходження через потенціал-керовані Ca^{2+}-канали в плазматичної мембрани (Brorson et al., 1991, Garaschuk et al., 1997, Shmigol et al., 1994). de Juan-Sanz та співавтори (de Juan-Sanz et al., 2017) виявили вивільнення Ca^{2+} з ЕР у відповідь на поодинокий ПД або серію з 20 потенціалів дії з частотою 20 Гц.

Було нещодавно показано, що сома пірамідних нейронів утворює ретикулярну мережу ЕР, яка простягається через дендрити та всю довжину аксона, включаючи пресинаптичні бутони (de Juan-Sanz et al., 2017). Також було встановлено, що повторна тетанічна синаптична стимуляція пірамідних клітин CA1 у препараті зрізу мозку індукує вивільнення Ca^{2+} з дендритних або пресинаптичних ріанодинчутливих рецепторів (Alford et al., 1993, Tran and Stricker, 2021). Як це показано в нашій роботі, виснаження кофеїн-чутливих запасів Ca^{2+} не впливає на амплітуду Ca^{2+}-транзієнтів, викликаних деполяризацією при низькочастотній активності. Однак тривала стимуляція (5 с) з використанням високого рівня KCl або довга послідовність EFS (50 імпульсів, 9 Гц) у пірамідних клітинах CA1 спричинює вивільнення Ca^{2+} не лише із дендритних ріанодинчутливих Ca^{2+}-депо, як це було вказано раніше (Alford et al., 1993, Garaschuk et al., 1997, Tran and Stricker, 2021), але й у субмембранних та центральних регіонах.

Ми продемонстрували просторову динаміку змін концентрації вільного Ca^{2+} в окремих пірамідних нейронах гіпокампу щурів у культурі, використовуючи двовимірну ратіометричну мікроскопію. Така візуалізація Ca^{2+}-транзієнтів виявила асинхронність та запізнення у зростанні концентрації вільного Ca^{2+} в центральній ділянці порівняно з примембранними ділянками та дендритного дерева. Активація ріанодинових рецепторів за допомогою кофеїну призводила до швидкого збільшення $[Ca^{2+}]$ у примембранній зоні, центральній ділянці та дендритному дереві. Використовуючи кофеїн як фармакологічний інструмент для активації RyRs, було встановлено, що функціональні Ca^{2+}-запаси відрізняються в сомі, периферійних зонах та дендритах пірамідних клітин CA1. Кофеїн суттєво знижує пікову амплітуду Ca^{2+}-транзієнтів, що індуковані деполяризуючим розчином KCl. Коротка електрична стимуляція (15 імпульсів, 9 Гц) не є достатнім для інтенсифікації Ca^{2+} сигналу через CICR, однак тривале збудження (50 імпульсів, 9 Гц) ініціює вивільнення кальцію з ER-сховищ, причому приблизно 30% пікової амплітуди Ca^{2+}-транзієнту відповідає RyRs-опосередкованому вивільненню.

frontiers | Frontiers in Cellular Neuroscience

TYPE Original Research
PUBLISHED 14 December 2022
DOI 10.3389/fncel.2022.1054950

The spatio-temporal properties of calcium transients in hippocampal pyramidal neurons *in vitro*

Vyacheslav M. Shkryl*

Department of Biophysics of Ion Channels, Bogomoletz Institute of Physiology, NAS of Ukraine, Kyiv, Ukraine

The spatio-temporal properties of calcium signals were studied in cultured pyramidal neurons of the hippocampus using two-dimensional fluorescence microscopy and ratiometric dye Fura-2. Depolarization-induced Ca^{2+} transients revealed an asynchronous delayed increase in free Ca^{2+} concentration. We found that the level of free resting calcium in the cell nucleus is significantly lower compared to the soma, sub-membrane, and dendritic tree regions. Calcium release from the endoplasmic reticulum under the action of several stimuli (field stimulation, high K^+ levels, and caffeine) occurs in all areas studied. Under depolarization, calcium signals developed faster in the dendrites than in other areas, while their amplitude was significantly lower since larger and slower responses inside the soma. The peak value of the calcium response to the application of 10 mM caffeine, ryanodine receptors (RyRs) agonist, does not differ in the sub-membrane zone, central region, and nucleus but significantly decreases in the dendrites. In the presence of caffeine, the delay of Ca^{2+} signals between various areas under depolarization significantly declined. Thirty percentage of the peak amplitude of Ca^{2+} transients at prolonged electric field stimulation corresponded to calcium release from the ER store by RyRs, while short-term stimulation did not depend on them. 20 μM dantrolene, RyRs inhibitor, significantly reduces Ca^{2+} transient under high K^+ levels depolarization of the neuron. RyRs-mediated enhancement of the Ca^{2+} signal is more pronounced in the central part and nucleus compared to the sub-membrane or dendrites regions of the neuron. In summary, using the ratiometric imaging allowed us to obtain additional information about the involvement of RyRs in the intracellular dynamics of Ca^{2+} signals induced by depolarization or electrical stimulation train, with an underlying change in Ca^{2+} concentration in various regions of interest in hippocampal pyramidal neurons.

KEYWORDS

hippocampal neuronal culture, calcium homeostasis, ryanodine receptors, caffeine, ratiometric method, Fura-2

EDITED BY
Dominique Debanne,
INSERM U1072 Neurobiologie des canaux Ioniques et de la Synapse, France

REVIEWED BY
Jean Chemin,
Centre National de la Recherche Scientifique (CNRS), France
Kaoutsar Nasrallah,
Albert Einstein College of Medicine, United States

*CORRESPONDENCE
Vyacheslav M. Shkryl
slava@biph.kiev.ua

SPECIALTY SECTION
This article was submitted to Cellular Neurophysiology, a section of the journal Frontiers in Cellular Neuroscience

RECEIVED 28 September 2022
ACCEPTED 24 November 2022
PUBLISHED 14 December 2022

CITATION
Shkryl VM (2022) The spatio-temporal properties of calcium transients in hippocampal pyramidal neurons *in vitro*.
Front. Cell. Neurosci. 16:1054950.
doi: 10.3389/fncel.2022.1054950

Introduction

The calcium ion (Ca^{2+}) is a common second messenger that regulates many physiological pathways such as secretion, fertilization, gene transcription, and apoptosis (Pozzan et al., 1994; Berridge et al., 2000). Calcium signaling in excitable cells consists of several mechanisms. In the first phase, Ca^{2+} influx across the plasma membrane after the opening of voltage-gated calcium channels (VGCCs) as a result of action potential (AP) depolarization or activation of ligand-gated channels (Berridge, 1998; Augustine et al., 2003; Bloodgood and Sabatini, 2007). Then Ca^{2+} can be released from the endoplasmic reticulum (ER) or sarcoplasmic reticulum (SR) through 1,4,5-Inositol triphosphate receptors (IP_3Rs) and/or ryanodine receptors (RyRs) expressed on the ER (or SR) membrane (Berridge, 1998, 2009; Verkhratsky, 2002; Clapham, 2007; Khakh and McCarthy, 2015).

The release of Ca^{2+} from the SR store amplified Ca^{2+} signaling and regulates a variety of cellular processes, including excitation-contraction coupling in skeletal muscle (Endo et al., 1970; Ford and Podolsky, 1970) and cardiac myocytes (Fabiato, 1983; Bers, 2002), and from the ER store calcium oscillation and gene expression in many cell types (Thorn et al., 1993; Hardingham et al., 2001), neuronal plasticity (Frenguelli and Malinow, 1996; Rose and Konnerth, 2001) and other processes. The ER is an essential intracellular organelle—one of the main functions of which is the storage of intracellular Ca^{2+}. The entry of calcium ions through VGCCs activates RyRs *via* a calcium-mediated process that obtained, at present, the generally known designation "calcium-induced calcium release," CICR (Fabiato, 1983).

In most CNS neurons, free intracellular calcium concentration ($[Ca^{2+}]_i$) changes following the opening of VGCCs (Berridge, 1998; Augustine et al., 2003; Bloodgood and Sabatini, 2007) and then is buffered with some proteins like calmodulin, calreticulin, parvalbumin, calbindin-D28k. In addition, ATP binds significant amounts of Ca^{2+} ions (Zhou and Neher, 1993; Shkryl et al., 2012a). As in other cell types, in neurons, Ca^{2+} is released from the ER through IP_3Rs and/or RyRs expressed on the ER membrane, which regulates a myriad of physiological and pathophysiological processes in it (Verkhratsky and Kettenmann, 1996; Berridge, 1998, 2002, 2009; Verkhratsky, 2002, 2005; Clapham, 2007; Khakh and McCarthy, 2015; Shkryl, 2017). The binding of Ca^{2+} to RyRs activates these channels allowing Ca^{2+} to release from the ER into the cytosol (Kuba, 1994). Activation of RyRs is linked to L-type VDCCs either *via* Ca^{2+} influx in cardiac myocytes or by direct voltage-dependent mechanical coupling in skeletal muscle (Pozzan et al., 1994; Niggli, 1999). The latter type of coupling has also been observed in neuronal cells (Chavis et al., 1996; De Crescenzo et al., 2004).

RyRs in peripheral and central neurons may amplify and prolong incoming Ca^{2+} signals *via* CICR (Holliday et al., 1991; Llano et al., 1994; Kano et al., 1995). Some studies have shown that depleting or blocking the ryanodine-sensitive Ca^{2+} stores did not significantly alter the amplitude and waveform of depolarization-induced Ca^{2+} transients and did not contribute significantly to depolarization-induced Ca^{2+} transients evoked by low-frequency activity (Garaschuk et al., 1997). However, it established that the soma of pyramidal neurons provides a reticular network of the ER and extends throughout dendrites and the entire length of the axon, including presynaptic boutons (de Juan-Sanz et al., 2017). In addition, repetitive tetanic synaptic stimulation of CA1 pyramidal cells in a slice preparation has been reported to induce Ca^{2+} release from dendritic or presynaptic ryanodine-sensitive Ca^{2+} stores (Alford et al., 1993; Tran and Stricker, 2021).

There are broadly selective drugs that are able to activate or inhibit RyRs in myocytes or neurons. The most well-known are caffeine, ryanodine, 4-chloro-m-cresol, dantrolene, ruthenium red, tetracaine, and procaine (Viero et al., 2012). Caffeine is a RyRs agonist and has been used as a pharmacological tool to study ryanodine receptor-mediated Ca^{2+} release from intracellular stores (Kong et al., 2008; Porta et al., 2011). Caffeine sensitizes RyRs to Ca^{2+} and promotes ER Ca^{2+} release at basal cytosolic Ca^{2+} levels. Another drug is RyRs-inhibitor dantrolene (Fruen et al., 1997; Fill and Copello, 2002) which in the concentration of 10 μM reduced RyRs channel open probability by 50% (Diszházi et al., 2019).

Information about the involvement of RyRs in calcium signaling in neurons is controversial, especially about where release occurs and how it interacts with the Ca^{2+} signal during short or long-term stimulation. This study aimed to obtain additional information on the involvement of ryanodine receptors in neuronal calcium signaling. Spatio-temporal properties of these signals were studied during multiple stimuli: field stimulation, high K^+, and caffeine and dantrolene at cultured rat hippocampal CA1 pyramidal neurons. We use caffeine and dantrolene to reveal RyRs. Changes in free calcium concentrations inside the cell were determined using two-dimensional fluorescence microscopy based on a charge-coupled device camera and ratiometric dye Fura-2 with dye excitation at wavelengths 340–380 nm. We analyzed two-dimensional fluorescent images of neurons spatially with temporal profiles from different areas of it. For such analysis were selected: the nucleus, sub-membrane region, central space inside of a cell, and the dendritic tree. This technique allows us to simultaneously determine the change in Ca^{2+} signals in the different regions of the neurons.

Materials and methods

All experimental procedures were performed following ethical principles of the European Convention for the protection of vertebrate animals used for experimental and other scientific purposes (86/609/EEC; European convention, Strasburg, 1986) and were approved by the local Animal Ethics Committee of the Bogomoletz Institute of Physiology (Kyiv, Ukraine). All efforts were made to minimize the number and suffering of animals used. All experiments were performed on cultured hippocampal neurons obtained from newborn Wistar rats. Primary cultures were prepared as previously reported (Shkryl et al., 1999). Ca^{2+} imaging studies were carried out within 10–14 days of cultivation. A cover glass with cells was placed in an extracellular solution (ES) containing in mM: NaCl—140.0; KCl—2.0; $CaCl_2$—2.0; $MgCl_2$—2.0; HEPES—10.0; pH = 7.4. All chemicals were obtained from Sigma-Aldrich (St. Louis, MO).

The cells were loaded with 5 μM Fura-2 acetoxymethyl ester (Fura-2 AM) for 30 min at 37°C and 20 min for de-esterification of the dye. The values of R_{min} and R_{max} amounted to 0.44 and 9.44; $F_{380}(\min)$ = 20.7 and $F_{380}(\max)$ = 169.4; K_d(Fura-2) = 224 nM (Shkryl, 2020). The coverslip with neurons was washed and placed in an experimental chamber with two platinum electrodes used for the electric field stimulation (EFS). The stimulation was carried out according to the standard protocol by lowering two parallel platinum electrodes (20÷25 mm apart) into the chamber and passing current pulses between them (Jacobs and Meyer, 1997; Shkryl et al., 2012b). Ca^{2+} transients were also induced chemically by applying a depolarizing solution that contained 50.0 mM KCl substituting the respective amount of NaCl in ES. We used a computer-controlled perfusion system synchronized with data acquisition software.

In our study, we used a CCD camera (Olympus XM10) mounted on an Olympus IX71 inverted microscope equipped with an Olympus LUCPlanFFN 20×/0.45 lens and MT10 illumination system that included a filter wheel exchanger (340–380 nm) and 150 W xenon arc burner. For the data collection, we use Cell M software (Olympus, Japan). The acquisition speed was 30 Hz for one wave and 1.3 Hz for ratiometric use. For further data analysis, the ratio of 340–380 nm fluorescence intensity (ratio; F_{340}/F_{380}) was calculated. This is done according to the protocol described by Shkryl (Shkryl, 2020) and subtracts the background level calculated outside of cells. Dynamic changes in the ratio index assess changes in the level of free calcium.

Data analysis was performed using the IDL programming environment (ITT Visual Information Solutions). In recorded images with excitation of 340–380 nm lights, the regions of interests (ROIs) were selected. All experiments were performed at room temperature (22°C–25°C). Data are presented as mean ± SEM.

Results

In most neurons, the intracellular concentration of free calcium in the resting state is around 75 nM. This index can increase to 10 μM upon intense electrical activity of cells (Berridge et al., 2000). In particular, the calcium level in the dendrites could increase to 5 μM during the development of synaptically induced calcium waves (Pozzo Miller et al., 1996; Larkum et al., 2003). Information on the spatial distribution of the respective calcium channels and receptors is limited; however, it is clear that the molecular mechanisms and patterns of Ca^{2+} release in different regions of different neurons differ significantly (Verkhratsky, 2005). To examine changes in the intracellular calcium level in cultured pyramidal hippocampal neurons, we used 2D x-y-t ratiometric fluorescent Ca^{2+} measurements and Ca^{2+}-sensitive dye Fura-2, AM. In this series of experiments, the cells constantly perfused with ES were stimulated by EFS and by applying 50 mM KCl or 10 mM caffeine solutions.

Ca^{2+} responses in different regions of pyramidal hippocampal neuron

We analyzed Ca^{2+} signals in hippocampal pyramidal neurons in the sub-membrane, central, dendritic, and nuclear regions. **Figure 1A** illustrates representative data traces of the Fura-2 ratio (F_{340}/F_{380}; Ca^{2+} signals) increases induced by two series of 50 pulses of EFS (used to load the ER store) and followed by the application of 10 mM caffeine for 5 s to induce Ca^{2+} release from the ER stores by ryanodine receptors (RyRs). An additional EFS and 5-s application of the depolarizing solution were applied when the restoration of calcium signals to the resting level. 2D imaging of Ca^{2+} signals reveals an asynchronous delayed rise of free Ca^{2+} concentration in the nuclear compared to the sub-membrane, central or dendritic regions (**Figure 1A**). Statistical data are presented in the bottom plane of **Figure 1B**.

The value of basal free Ca^{2+} was significantly reduced in the nuclear area of the neuron, less by 15% compared to the central region (61 nM vs. 85 nM, $n = 30$; $P < 0.001$; **Figure 1Ba**). Ca^{2+} signal in the dendritic region in response to stimulation appeared faster compared to other regions (detailed below) but had the smallest amplitude during EFS, KCl depolarization, and caffeine application. The amplitude of Ca^{2+} transient in the dendritic tree of pyramidal-like neurons in response to EFS was 1.18 ± 0.09 (207 nM, $n = 19$), which was significantly smaller compared to sub-membrane—1.62 ± 0.17 (303 nM, $n = 19$; $P < 0.05$), central—1.73 ± 0.18 (329 nM, $n = 19$; $P < 0.01$), and nuclear—1.66 ± 0.17 (300 nM, $n = 19$; $P < 0.05$) regions of the cell (**Figure 1Bb**). In the dendritic tree, the amplitude of Ca^{2+} transient caused by KCl depolarization was also significantly reduced, 3.43 ± 0.41 (0.87 μM, $n = 24$) respectively to sub-membrane—4.76 ± 0.39 (1.65 μM, $n = 24$; $P < 0.05$), central—4.98 ± 0.38 (1.84 μM, $n = 24$; $P < 0.01$), and nuclear—5.06 ± 0.39 (1.81 μM, $n = 24$; $P < 0.01$) regions of studied neurons (**Figure 1Bc**). As shown in **Figure 1Bd**,

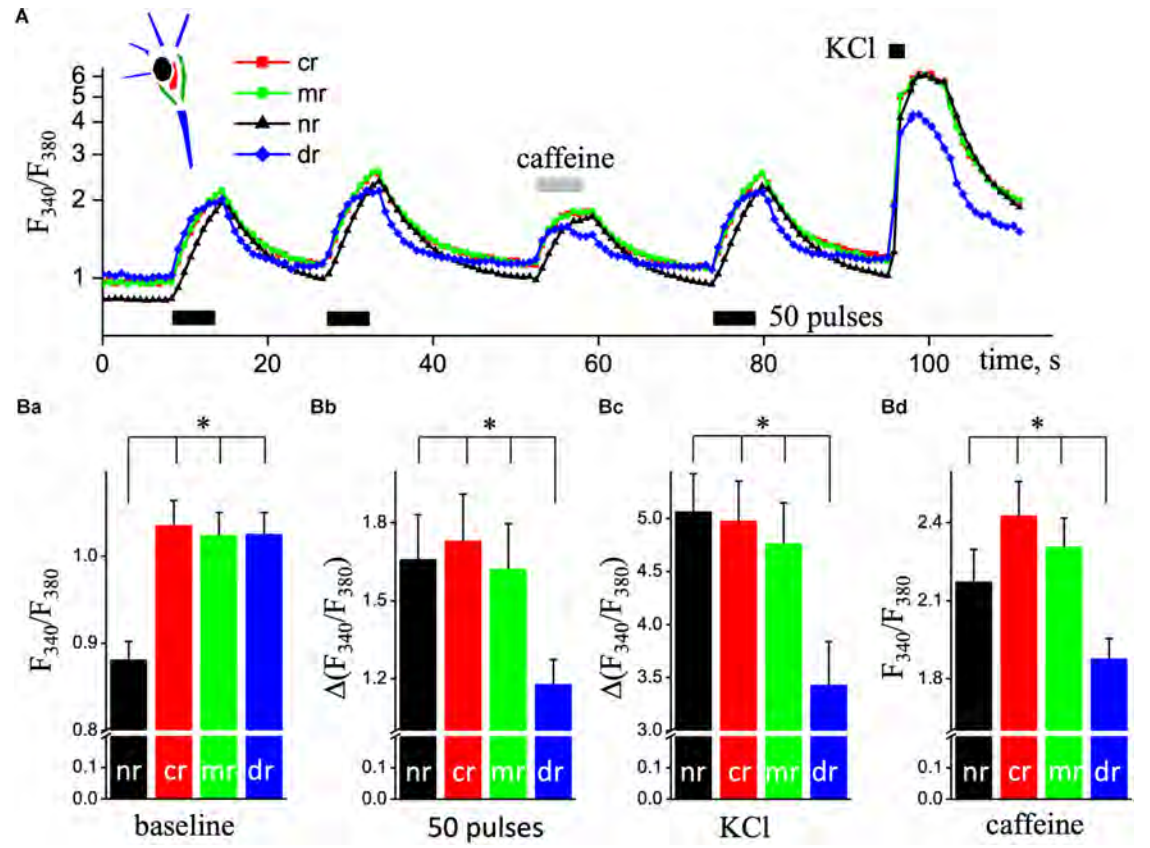

FIGURE 1
Ca^{2+} responses in different ROIs of pyramidal hippocampal neurons triggered by electrical field stimulation and application of depolarizing and caffeine solutions. **(A)** Transient increases in $[Ca^{2+}]_i$ are triggered by two series of 50 pulses of EFS (black rectangular, 9 Hz) followed by the application of caffeine (caffeine, light gray rectangular; 10 mM and 5 s) and a series of 50 pulses of EFS and depolarizing solution with 50 mM KCL (KCl, black square, 5 s). Ca^{2+} responses were recorded in the central space (cr; red squares line), sub-membrane (mr; green circles line), dendritic tree (dr; blue diamond's line), and nucleus (nr; black triangles lines) regions of cultured hippocampal neurons loaded with the fluorescent Ca^{2+} indicator Fura-2. Ratios (F_{340}/F_{380}) are presented in natural logarithmic scale. The top left corner represents a schema of neurons' area selection. The bottom panel **(B)** shows quantified responses for four studied regions in pyramidal neurons. **(Ba)** Mean value of basal Ca^{2+} levels before any stimulus; part **(Bb)** is the mean values of the amplitudes of second Ca^{2+} transients caused by EFS; part **(Bc)** is the mean values of the amplitudes of Ca^{2+} transients evoked by depolarizing solution; part **(Bd)** is the mean values of Ca^{2+} peaks evoked by 5 s application of 10 mM caffeine, as an agonist of RyRs. The black bars are data for the nucleus (nr); the red bars are data in the central space (cr); the green bars are sub-membrane regions (mr), and the blue bars are dendritic trees of neurons (dr). Results are mean ± S.E. of 30 individual cells from 10 different experiments. $^*P < 0.05$.

the peak values of calcium signals induced by 10 mM caffeine (as Ca^{2+} release from the ER) were significantly reduced in the dendritic tree region to 1.88 ± 0.08 (225 nM, $n = 19$) from 2.31 ± 0.11 (310 nM, $n = 19$, $P < 0.01$) in sub-membrane, central—2.43 ± 0.13 (336 nM, $n = 19$; $P < 0.001$) and nuclear—2.17 ± 0.12 (283 nM, $n = 19$; $P < 0.05$) regions of pyramidal neurons.

Fast recording of Ca^{2+} transients

In the next series of experiments, we investigated the spatio-temporal organization of Ca^{2+} transients in the various areas of pyramidal-like neurons recorded at 30 Hz frequencies (Figure 2A). We recorded simultaneously the Ca^{2+} transients induced by ESP stimulation at excitation wavelengths 340–380 nm, which were synchronized with EFS, separated in time. The first recorded Ca^{2+} transient was with excitation wavelength at 340 nm, and then a 2 min delay produced an additional record at 380 nm with the same setting and conditions that create the F_{340}/F_{380} ratio signal (Figure 2B).

Fast 2D recording of Ca^{2+} transients under depolarization revealed an asynchronous delayed rise of free Ca^{2+} concentration. Thus, EFS caused an increase in Ca^{2+} signals that first appeared in the dendrites, then in the sub-membrane, central, and finally in the nuclear area of cells. Figure 2C shows

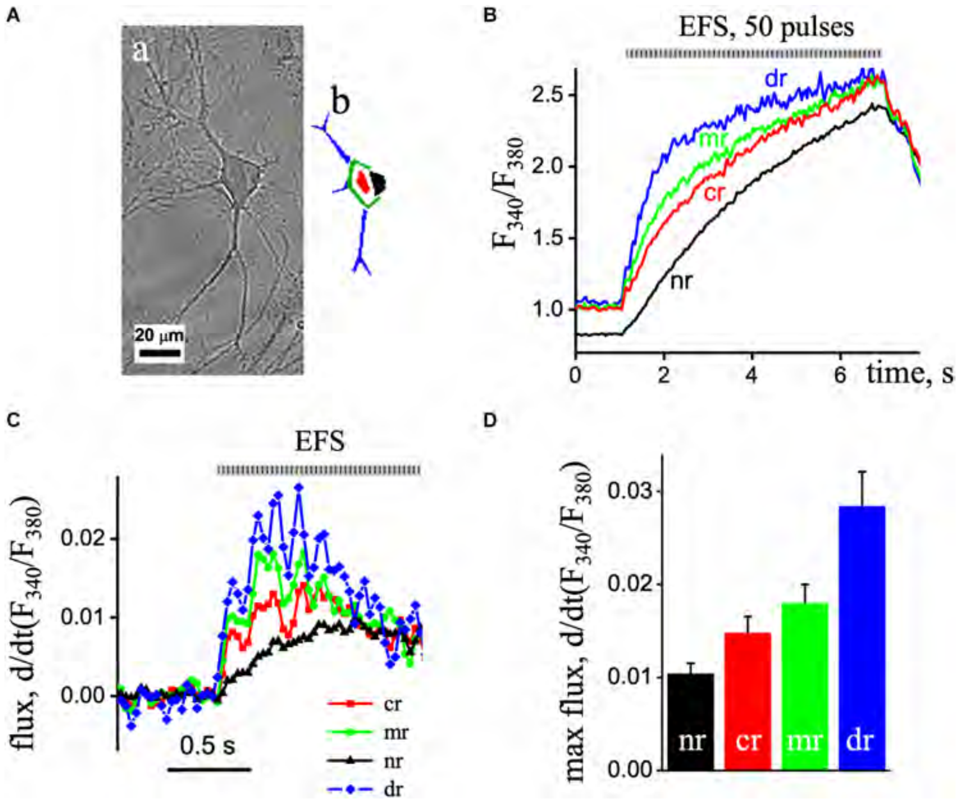

FIGURE 2
Fast recording of EPS-induced Ca^{2+} transients in a pyramidal-like hippocampal neuron. **(Aa)** The image of the cell obtained by direct illumination. **(Ab)** Different ROIs of the neuron are colored. **(B)** The imaged ratio of F340/F380 of Fura-2 loaded neuron with 50 EPS was separated as time profiles in the dendritic tree (blue line; dr), sub-membrane (green line, mr), central area (red line; cr), and nuclear (black line; nr) regions of the neuron. **(C)** d(F340/F380)/dt (s^{-1}), the first derivative of the ratio of the Ca^{2+} signal obtained in the nuclear (black triangles line), central area (red squares line), and sub-membrane (green circles line) regions of the neuron. The flux data were derived from the data presented in part **(B)**. **(D)** Mean value of the maximal flux rate obtained in the nuclear (black bar), central area (red bar), and sub-membrane (green bar) regions of the neuron.

the first derivative of the $[Ca^{2+}]_i$ signal [d(F340/F380)/dt] representing the underlying Ca^{2+} flux. The Ca^{2+} flux in the sub-membrane and central regions appeared with increasing and decreasing steps, representing the EFS-induced calcium transients. The maximum flux in the sub-membrane and central regions was observed 0.2 s after initiation and decreased with time. In the nuclear region of the neuron, the flux was delayed and reached its maximum value 0.6 s after the onset with reduced amplitude compared to other regions. The maximal flux rate was in the dendritic tree region (0.028 ± 0.004, $n = 8$) and reduced in the sub-membrane (0.018 ± 0.002, $n = 8$) and central (0.015 ± 0.004, $n = 8$), and minimal in nuclear aria (0.010 ± 0.001, $n = 8$) of the neuron (Figure 2D).

To show more detailed information about the inhomogeneity of Ca^{2+} signals in hippocampal pyramidal neurons, we studied the latency of Ca^{2+} increases for different regions of cells in one wavelength excitation mode (380 nm, 30 Hz). Figure 3 shows the dynamics of $[Ca^{2+}]_i$ increases caused by 50 pulses of EFS (3A) and 50 mM KCl solution (3B) normalized to the maximal amplitude of Ca^{2+} transients in various ROIs of the neuron. When recording in x-y-t mode (limited to 30 Hz), Ca^{2+} signals were insufficient to represent the initial phase of the Ca^{2+} signal, which was more evident during KCl-induced transients. However, we find signal delays between different ROIs at 25%, 50%, and 75% of the maximal amplitude. It is in the sub-membrane, and central regions were more pronounced and progressed during the EFS-induced Ca^{2+} transient and less during KCl depolarization, and this parameter of the difference between the dendritic tree and the sub-membrane region of interest increased up to 1 s. In the central and nuclear regions, the delay was almost independent of the type of stimulus and was around 0.2 s. Statistical data are represented in the summarized diagram in part 3C.

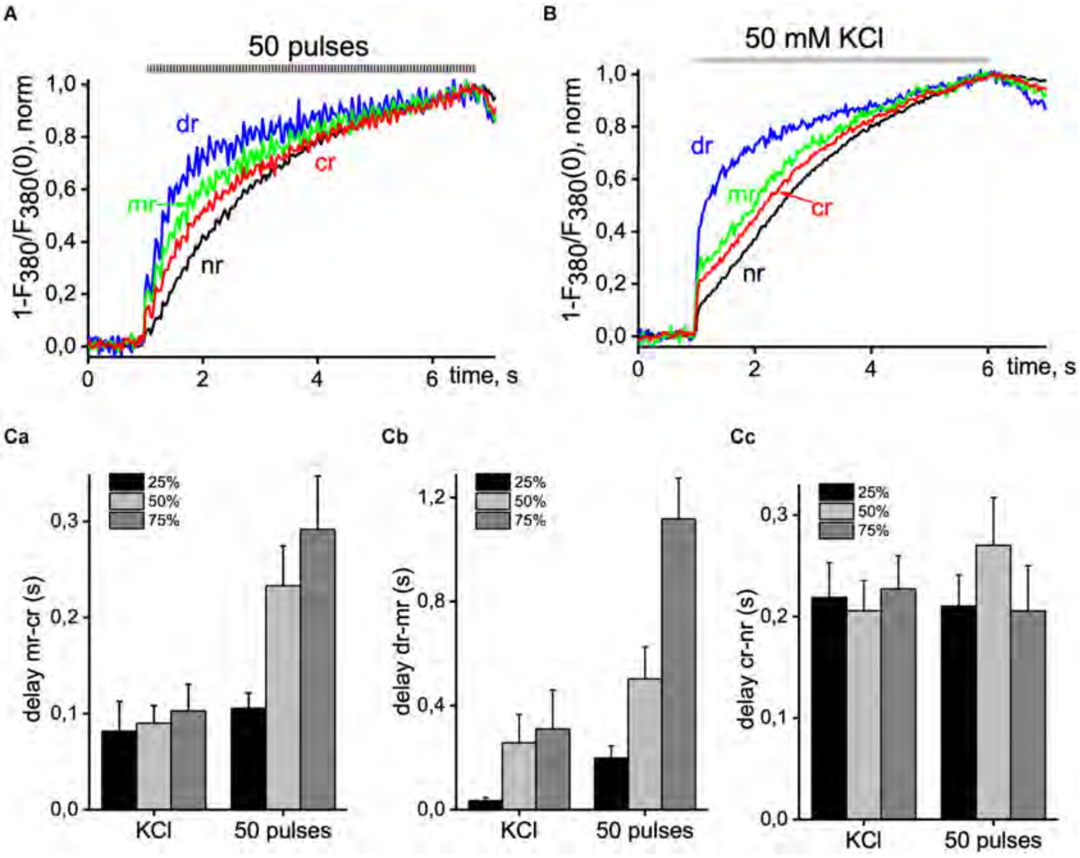

FIGURE 3
Delay of Ca^{2+} signals between distinct areas of pyramidal neurons. Normalized Ca^{2+} transients were recorded from the central (cr; red line), sub-membrane (mr; green line), nuclear (nr; black line), and dendritic tree (dr; blue line) area of the cell induced by 50 EFS pulses at 9 Hz **(A)** and 5 s application of 50 mM KCl solution **(B)**. **(C)** Summary histogram of delays between sub-membrane and central areas (mr-cr; part **a**); dendritic tree and sub-membrane areas (dr-mr; part **b**); central and nuclear areas (cr-nr; part **c**) measured at 25% (black bar), 50% (light gray bar) and 75% (dark gray bar) of maximal amplitude value with 50 pulses EFS and application of depolarizing KCl solution. Data were obtained in seven neurons in four different experiments. Ca^{2+} signals were recorded with 380 nm excitation wavelength at 33 ms per image.

RyRs mediated Ca^{2+} signal

As is well known, Ca^{2+} release from the ER occurs under conditions of the opening of the IP_3Rs and RyRs (Rizzuto and Pozzan, 2006). The IP_3Rs-mediated release of calcium from the dendrites is initiated most frequently by the action of neurotransmitters, like glutamate (Niswender and Conn, 2010), while RyRs activate by an increase of Ca^{2+} concentration in the cytosol (Shkryl and Blatter, 2013; Blatter, 2017) *via* calcium-mediated activation RyRs through CICR (Fabiato, 1983). In the following experiments, we tested the functioning of the ER stores in hippocampal pyramidal neurons. For this purpose, we activated Ca^{2+} release from the ER by applications of the RyR agonist caffeine, which often revealed an increase in cytosolic Ca^{2+} concentrations induced by caffeine. We use ESP to load the ER store.

Figure 4A shows a superimposed record that demonstrates changes in Ca^{2+} signal, recorded from a neuron under control condition (black trace) and in the presence of 10 mM caffeine (red trace). In control, the basal level of free calcium was 1.06 ± 0.03 and 1.26 ± 0.05 in the presence of caffeine. The peak amplitude of Ca^{2+} transients induced by depolarizing solution significantly decreased from 6.47 ± 0.57 (in the control) to 4.58 ± 0.31 under the application of 10 mM caffeine (**Figure 4Bc**; $n = 12$, $P < 0.05$). Under electrical field stimulation changing the amplitude of the caffeine depend on the duration of the stimulation. The peak amplitude of the Ca^{2+} signal induced by short (15 pulses, 9 Hz) EFS did not change appreciably, 0.54 ± 0.08 compared to 0.51 ± 0.07 (**Figure 4Ba**; $n = 13$). However, by a long stimulus (50 pulses, 9 Hz), this parameter significantly decreases from 2.72 ± 0.58 to 1.89 ± 0.38 (**Figure 4Bb**; $n = 6$, $P < 0.05$) with caffeine.

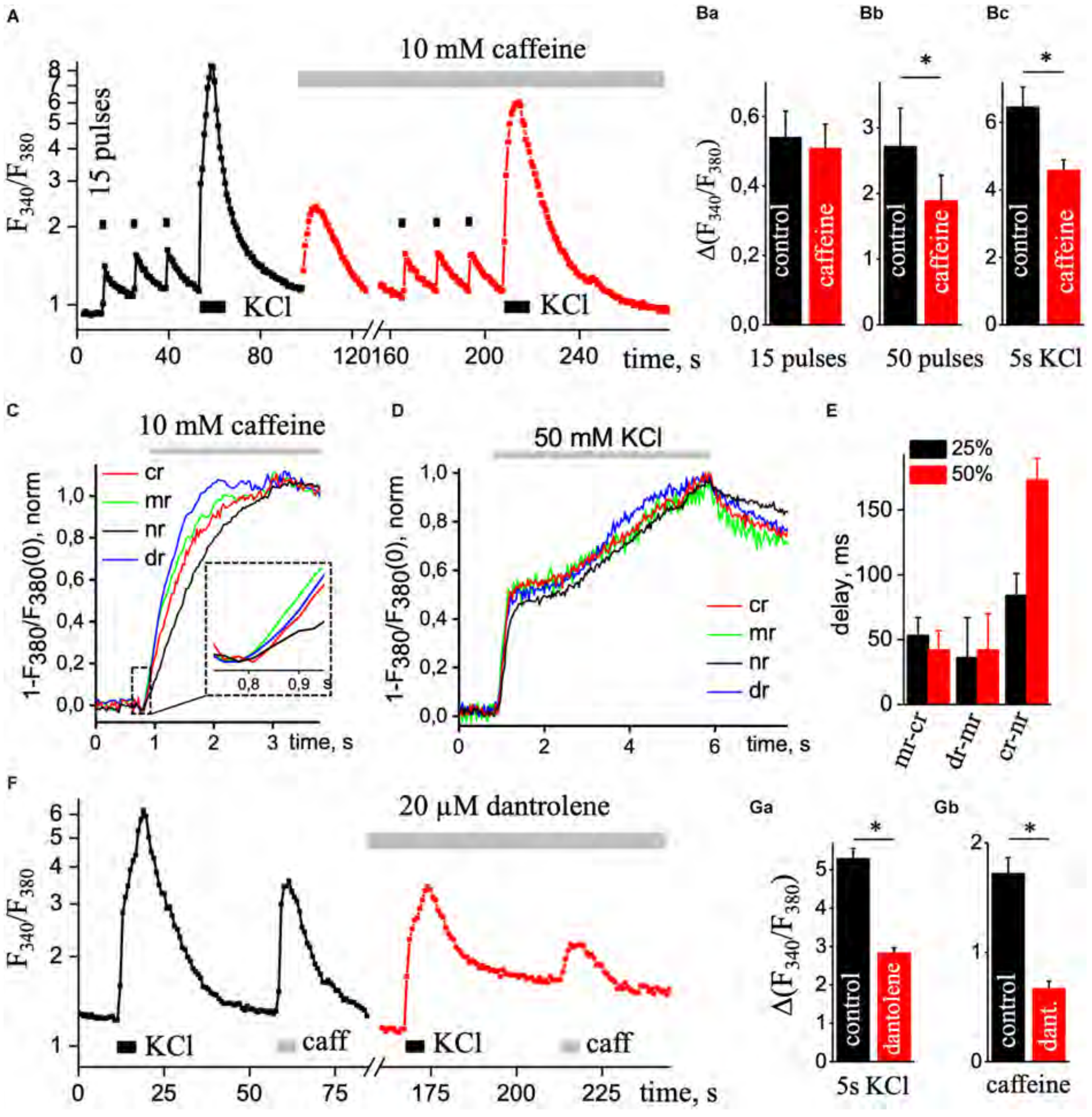

FIGURE 4

Ca^{2+} transients under the presence of caffeine. **(A)** Transient increases in $[Ca^{2+}]_i$ are triggered by three series of 15 pulses of EFS (black square; 1 s) followed by application of KCl depolarizing solution (KCl, black rectangle, 5 s) in the control condition (black square line) and repeated stimulations with continues presence of 10 mM caffeine (caffeine; red square line) to eliminate calcium release from the ER. Ca^{2+} responses were recorded in the soma without the nucleus region. The ratio (F_{340}/F_{340}) is presented on a natural logarithmic scale. **(B)** Mean values of the amplitude of the second Ca^{2+} transient caused by 15 **(a)** or 50 **(b)** pulses EFS and Ca^{2+} transient evoked by KCl solution **(c)** in control and presence of 10 mM caffeine. Normalized Ca^{2+} transients were recorded using one wavelength protocol (33 ms per image and 380 nm excitation wavelength) at different ROIs induced by the application of 10 mM caffeine **(C)** or application of KCl depolarizing solution **(D)**. A dashed line in part **(C)** contains an insert of the initial phase of caffeine-induced Ca^{2+} increase. ROIs were selected in central (cr, red line), sub-membrane (mr, green line), nuclear (nr, black line), and dendritic tree (dr, blue line) areas of the cell. **(E)** Diagram of delays between sub-membrane and central (mr-cr); dendritic tree and sub-membrane (dr-mr); central and nuclear (cr-nr) areas measured at 25% (black bar) and 50% (red bar) of the maximal amplitude in response to KCl depolarizing solution. **(F)** Transient increases in $[Ca^{2+}]_i$ are triggered by the application of KCl depolarizing solution (KCl, black rectangle, 5 s) and caffeine (caffeine, light gray rectangular; 10 mM and 5 s) in the control condition (black square line) and repeated stimulations with continues presence of 20 μM dantrolene (red square line) to reduce calcium release from the ER. Ca^{2+} responses were recorded in the soma without the nucleus region. The ratio (F_{340}/F_{340}) is presented on a natural logarithmic scale. Mean value of the amplitude of Ca^{2+} transients evoked by depolarizing solution **(Ga)** and 5 s application of 10 mM caffeine **(Gb)**. Results are mean ± S.E., $^*P < 0.05$.

The short electrical stimulation (15 pulses, 1 s) does not alter the amplitude of Ca^{2+} transients under caffeine, but the Ca^{2+} response significantly decreased under the depolarization solution or long EFS. Thus, with prolonged stimulation of the neuron, Ca^{2+} release appeared from the ER by RyRs. As we can see from normalized caffeine-induced Ca^{2+} transients (**Figure 4C**), a rise in signals appeared in all regions of hippocampal pyramidal neurons, but in the center and nuclear, Ca^{2+} signals were more delayed (37.5 ± 7.5 ms, $n = 4$) than in sub-membrane zone and dendritic tree. **Figure 4D** shows the dynamics of increases in $[Ca^{2+}]_i$ caused by 5 s application of KCl solution normalized to the maximal amplitude of the signal in various regions of interest of the neuron. **Figure 4E** shows the delay in different ROIs at 25% and 50% of the maximal amplitude. Under caffeine, the delay between sub-membrane and central, dendritic tree, central and nuclear regions was significantly reduced compared to control.

Additionally, we used 20 μM dantrolene to block RyRs and record high KCl-induced Ca^{2+} transients. **Figure 4F** shows superimposed record that demonstrates changes in Ca^{2+} signal, recorded from a neuron under control condition (black square line) and in the presence of 20 μM dantrolene (red square line). In control, the basal level of free calcium was 1.23 ± 0.03 and 1.10 ± 0.03 in the presence of dantrolene. The amplitude value of depolarizing solution-induced Ca^{2+} transients under 20 μM dantrolene significantly decreased from 5.30 ± 0.26 to 2.84 ± 0.13 (**Figure 4Ga**; $n = 29$, $P < 0.001$). The ER load with the presence of dantrolene was significantly decreased to 0.682 ± 0.06 from 1.72 ± 0.14 (**Figure 4Gb**; $n = 28$, $P < 0.01$). It further confirms the involvement of RyRs in Ca^{2+} signaling in cultured hippocampal pyramidal neurons.

Figure 5 shows representative recordings of calcium transients induced by 50 pulses of EFS in control (black line) and the presence of 10 mM caffeine (red line) in different regions

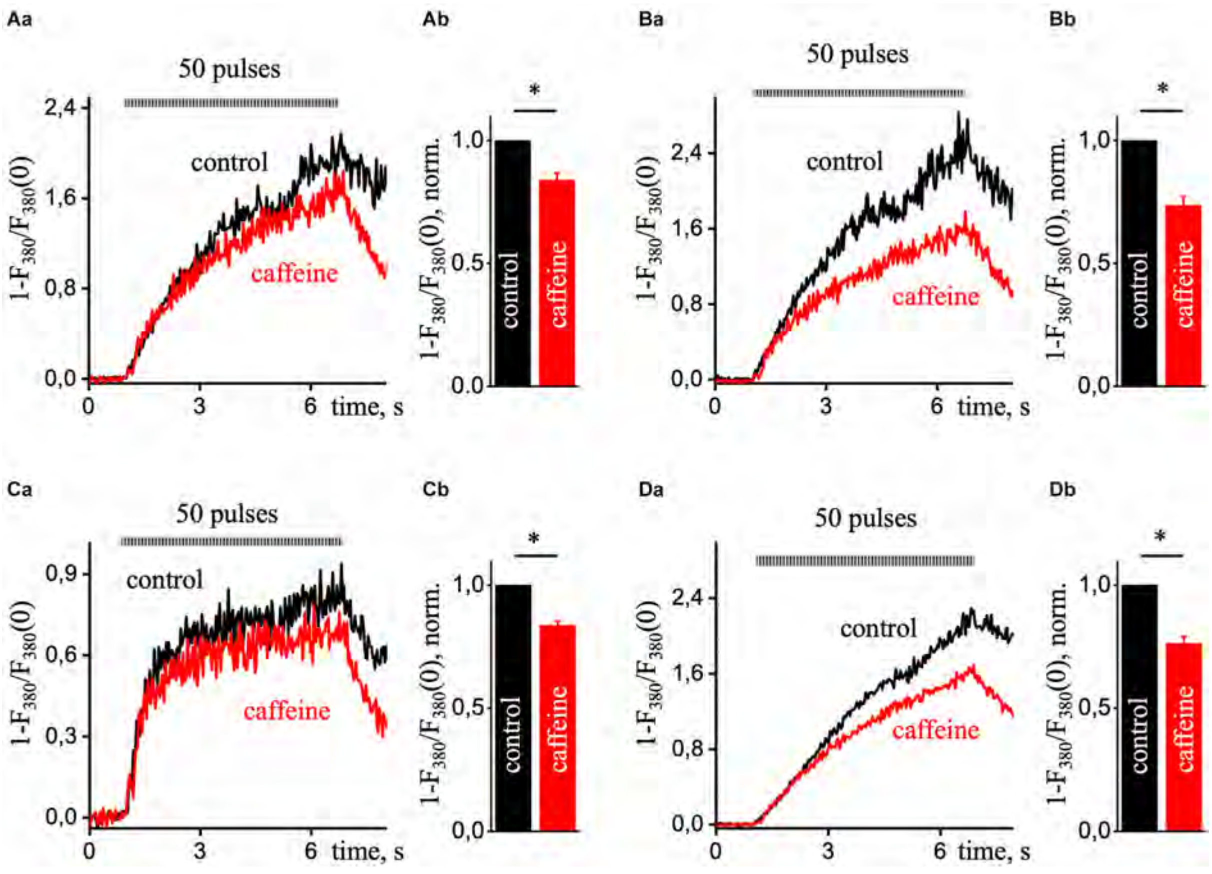

FIGURE 5
Ca^{2+} transients during prolonged electrical field stimulation in the presence of caffeine in various ROIs of hippocampal pyramidal neurons. A transient increase in intracellular $[Ca^{2+}]_i$ is induced by a series of 50 EFS pulses (9 Hz) under control conditions (black line) and in the presence of 10 mM caffeine (red line; which excludes calcium release from the ER). Each graph in part **(a)** presented Ca^{2+} responses that were recorded in the sub-membrane **(A)**, central **(B)**, dendritic tree **(C)**, and nucleus **(D)** of the cell. Normalized Ca^{2+} transients were recorded using a single wavelength protocol (33 ms per image and 380 nm excitation wavelength). Part **(b)** of each panel presents control-normalized statistics of maximal amplitude in the presence of caffeine in response to ESP. Results are mean ± S.E. $^*P < 0.05$.

of the pyramidal neuron. The calcium signals in control and caffeine had a substantial difference at the center (**Figure 5B**), although there was also a decrease in signal with caffeine in the sub-membrane (**Figure 5A**) and dendritic tree regions (**Figure 5C**) were less pronounced but significant. Data were obtained from six different experiments and compared using a paired sample *t*-test. Also, the difference between these signals in the nucleus (**Figure 5D**) was somewhat less than in the central region. It is probably due to the passive enhancement of the calcium signal by releasing Ca^{2+} from the center or neighboring ERs into the nucleus. The RyR-mediated increase in the Ca^{2+} signal presented in the periphery, the dendritic tree, and the center of the hippocampal pyramidal neuron.

Discussion

In this study, we investigated the behavior of Ca^{2+} signals in response to electrical stimulation, KCl-induced depolarization, and caffeine treatment in cultured hippocampal pyramidal neurons with a 2D imaging mode of ratiometric fluorescent microscopy.

A neuron is an excitable cell, and a fundamental principle in neuronal signal processing is the transduction of short electrical signals at the membrane into biochemical responses, resulting in longer-lasting changes in the neuronal structural and functional state (Johenning et al., 2015). The neuronal plasma membrane with channels, receptors, and pumps mediates the electrical signal propagation; the ER membrane can participate in the passive and active calcium-based signal propagation mainly along the dendritic length and soma from peripheries to the center (Shkryl, 2017; Ashhad and Narayanan, 2019). Action potentials generate widespread increases in calcium concentration inside axons and presynaptic terminals, and then they back-propagate over large regions of the dendrites (Ross, 2012). The present study shows that the level of free calcium in the resting state inside the nucleus is significantly lower compared to the center of the cell and delayed respectively to other regions of hippocampal pyramidal neurons. Fedorenko and Marchenko (2014) have shown that the nuclear membrane of hippocampal CA1 pyramidal neurons was enriched in functional inositol IP_3Rs localized in the inner nuclear membrane and is specialized to release Ca^{2+} into the nucleoplasm, which may amplify Ca^{2+} signals entering the nucleus from the cytoplasm. Our study shows that nuclear Ca^{2+} flux had the lowest amplitude compared to other studied regions. During applications of caffeine, the nuclear Ca^{2+} signal was suspended compared to the sub-membrane but appeared at the same time as the central area with almost no delay.

Localized RyR-mediated events of Ca^{2+} release occur in the soma and proximal dendrites of hippocampal pyramidal neurons in culture and acute slices (Koizumi et al., 1999; Berrout and Isokawa, 2009; Manita and Ross, 2009; Miyazaki et al., 2012). The endoplasmic reticulum localized close to the plasmalemma membrane (PM) makes a membrane domain called ER-PM junctions (EPJs). By electron microscopy, the ER at many neuronal EPJs appears as a micron-diameter, flattened vesicle less than 10 nm from the PM, a structure also called a "subsurface cistern" (Rosenbluth, 1962; Tao-Cheng, 2018). EPJs are abundant in neuronal soma (Wu et al., 2017), and neuronal soma has prominent VGCCs—and RyRs-mediated CICR (Friel and Tsien, 1992; Isokawa and Alger, 2006; Berrout and Isokawa, 2009). Our study shows that the release of calcium from the endoplasmic reticulum occurred in all regions of the neuron; the peak value of Ca^{2+} response to caffeine applications did not differ at the sub-membrane, center, and nucleus but significantly decreased in the dendrites.

Ryanodine-sensitive Ca^{2+} stores in different central neurons in the rat (including CA1 hippocampal neurons) were reported to be empty at rest and to accumulate Ca^{2+} only after its entry *via* voltage-gated Ca^{2+} channels in the plasmalemma (Brorson et al., 1991; Shmigol et al., 1994; Garaschuk et al., 1997). de Juan-Sanz et al. (2017) found evidence for Ca^{2+} release from the ER in response to a single AP or a train of 20 action potentials evoked at 20 Hz. However, recently been shown that Ca^{2+} release from the ER contributes to train-evoked Ca^{2+} elevation in pyramidal neurons (Tran and Stricker, 2021). As demonstrated in this article, the depletion of the caffeine-sensitive Ca^{2+} stores did not alter the amplitude of depolarization-induced Ca^{2+} transients evoked by low-frequency activity. However, long 5 s KCl depolarization or long train EFS (50 pulses, 9 Hz) of CA1 pyramidal cells induced Ca^{2+} release not only from dendritic ryanodine-sensitive Ca^{2+} stores, which was shown previously (Alford et al., 1993; Garaschuk et al., 1997; Tran and Stricker, 2021) but also at sub-membrane and central regions. They suggested that RyR-mediated Ca^{2+} release from presynaptic intracellular stores contributes to the activation of downstream Ca^{2+}- dependent pathways and signaling molecules, including CaMKII, which are required for LTD induction (Arias-Cavieres et al., 2018). Also, we show that the Ca^{2+} signal at the nucleus significantly depends on Ca^{2+} release from the central ER.

Neuronal dendrites play dominant roles in signal integration, neural computation, plasticity, and structurally associated adaptability (Ashhad and Narayanan, 2019). Ca^{2+} influx from the outside *via* voltage- and ligand-gated ion channels, specific synaptic activation can cause the recruitment of intracellular Ca^{2+} stores. Its results in Ca^{2+} release from the ER *via* intracellular Ca^{2+} release channels (IP_3R and RyR) in dendrites (Nakamura et al., 1999). In the present study, we have shown that calcium signals in the dendritic tree appear faster than in other regions, but the peak value of Ca^{2+} transients in this area is significantly lower than inside the soma. These differences can be explained by the fact that the diameter of the dendrites is ∼1 μm, and the calcium signal in it propagates over a shorter distance, in contrast to the soma, and with a smaller dendrite Ca^{2+} release from the ER. The diffusion of calcium inside neurons is determined not only by distance but also by the intracellular binding sites that rapidly bind free calcium ions (Matthews and Dietrich, 2015). The interplay of several systems that release Ca^{2+} into the cytosol and multiple mechanisms that buffer Ca^{2+} in the cytosol sequester Ca^{2+} in intracellular organelles and extrude Ca^{2+} across the plasmalemma provide the necessary control (Blaustein, 1988) that could be different in sub-membrane, central or dendritic tree space of the neuron.

Spontaneous, localized Ca^{2+} release events are found in cardiac myocytes [Ca^{2+} sparks; (Cheng et al., 1993)] and also reported in dendrites of hippocampal pyramidal neurons (Manita and Ross, 2009; Miyazaki and Ross, 2013). In cardiac myocytes and skeletal muscle, depolarization activates voltage-gated L-type Ca^{2+} channels in the surface membrane resulting in localized, sub-membrane increases in cytosolic Ca^{2+}. Individual Ca^{2+} release units or clusters of RyRs (Stern et al., 1999) are activated essentially simultaneously. The spatial and temporal summation of Ca^{2+} release from individual Ca^{2+} release units gives rise to whole-cell Ca^{2+} transients (Cheng et al., 1994; Hüser et al., 1996; Shkryl and Blatter, 2013). In skeletal fibers and cardiac ventricular myocytes, the extensive transverse (t) tubular network exists that assures physical proximity of surface membrane Ca^{2+} channels and clusters of RyRs in the SR throughout the entire cell volume (Soeller and Cannell, 1999). It ensures highly synchronized and spatially rather homogeneous RyRs-based Ca^{2+} release from the SR (Cannell et al., 1994; Shkryl and Blatter, 2013). In contrast, atrial cells have poorly developed or even entirely lacking t-tubular system (Hüser et al., 1996; Mackenzie et al., 2001; Smyrnias et al., 2010). Due to these ultrastructural arrangements, action potential (AP)-induced membrane depolarization activates Ca^{2+} entry through VGCCs and CICR through RyRs in the sub-membrane region. Elevation of peripheral $[Ca^{2+}]_i$ propagates *via* CICR in a Ca^{2+} wave-like fashion in centripetal direction by a diffusion-reaction process (Keizer et al., 1998; Shkryl and Blatter, 2013; Blatter, 2017). In pyramidal neurons studied here, the Ca^{2+} response to APs was likely similar to the one observed in atrial myocytes (Shkryl and Blatter, 2013; Blatter, 2017). The presence of not only RyRs but also of the high density of IP_3 receptors in hippocampal neurons (Verkhratsky and Shmigol, 1996; Berridge, 1998; Nakamura et al., 2000) makes this process more complicated, requiring not only calcium-mediated activation of RyRs in central ER but also activation IP_3Rs through the diffusion of IP_3 from the periphery cell to the central ER to activate IP_3 receptors in none sub-membrane ER (Blatter et al., 2021); and glutamate-mediated synaptic transmission could contribute a notional part of EFS-induced Ca^{2+} transient that IP_3 receptors could mediate part of the response. In experiments on freshly isolated hippocampal neurons (data not shown), the amplitude of calcium responses was significantly lower during EFS but did not differ during depolarization of solutions with a high KCl, which suggests the role of glutamate receptors in these responses.

Some limitations are present in the study. Caffeine in high concentration could chelate calcium in the lumen of the ER (Rojo-Ruiz et al., 2018) interfering with RyRs activity and reduce the caffeine-induced Ca^{2+} signal. Caffeine interacts with fluorescent calcium indicator dyes (Muschol et al., 1999). In experiments using one wavelength mode excitation, it affects the response amplitude. However, in the ratiometric mode, it is eliminated by the ratiometric. Some studies show that the Fura-2 dye limits the correct recording of Ca^{2+} (Bootman et al., 2013; Shkryl, 2020) or could be saturated with a high Ca^{2+} response, which creates an additional error in determining the actual value of the calcium concentration. Using single wavelength dye like Fluo-4 with a higher ratio of maximal to minimal fluoresce with more precision and the ability to record small Ca^{2+} events like sparks. Limitations of temporal and spatial resolution reduced the ability to reveal more detailed data on Ca^{2+} signaling in pyramidal hippocampal neurons, and fast 2D or 3D confocal microscopy is required. However, the ratiometric measurements of Fura-2 loaded neurons made it possible to achieve the required accuracy of a given signal in various areas of an individual neuron.

In summary, we demonstrate spatial dynamics of free Ca^{2+} concentration in individual rat hippocampal pyramidal neurons in culture recorded by 2D ratiometric fluorescence of Fura-2 signals. 2D imaging of Ca^{2+} transients revealed an asynchronous delayed rise of free Ca^{2+} concentration in the central area compared to near-membrane or dendritic tree regions. The nuclear response was delayed respectively to other cellular parts. Activation of ryanodine receptors by caffeine triggered a rapid rise of $[Ca^{2+}]_i$ in all four analyzed regions of interest. Using the RyR agonist caffeine as a pharmacological tool, we found that functional Ca^{2+} stores resize in the somata and peripheral and dendrites of CA1 pyramidal cells. The treatment with caffeine significantly reduces the peak amplitude of Ca^{2+} transients induced by the KCl depolarizing solution. Short electrical stimulation (1 s) was not enough to enhance the Ca^{2+} signal through CICR, but adequate at long-lasting excitation (6 s) produce calcium release from the ER store there 30% of the peak amplitude of Ca^{2+} transient corresponds to RyRs mediated calcium release.

Data availability statement

The raw data supporting the conclusions of this article will be made available by the authors, without undue reservation.

Ethics statement

All experimental procedures were performed following ethical principles of the European Convention for the protection of vertebrate animals used for experimental and other scientific purposes (86/609/EEC; European convention, Strasburg, 1986) and were approved by the local Animal Ethics Committee of the Bogomoletz Institute of Physiology (Kyiv, Ukraine).

Author contributions

VS carried out the experiment; conceived and designed the analyses; collected the data; performed the analysis; wrote the article.

Acknowledgments

The author thanks Dr. Igor Melnick for critically reading the manuscript and Dr. Vita Hanzha for cultured hippocampal neurons preparation.

Conflict of interest

The author declares that the research was conducted in the absence of any commercial or financial relationships that could be construed as a potential conflict of interest.

Publisher's note

References

Alford, S., Frenguelli, B. G., Schofield, J. G., and Collingridge, G. L. (1993). Characterization of Ca^{2+} signals induced in hippocampal CA1 neurones by the synaptic activation of NMDA receptors. *J. Physiol.* 469, 693–716. doi: 10.1113/jphysiol.1993.sp019838

Arias-Cavieres, A., Barrientos, G. C., Sánchez, G., Elgueta, C., Muñoz, P., and Hidalgo, C. (2018). Ryanodine receptor-mediated calcium release has a key role in hippocampal LTD induction. *Front. Cell Neurosci.* 12:403. doi: 10.3389/fncel.2018.00403

Ashhad, S., and Narayanan, R. (2019). Stores, channels, glue and trees: active glial and active dendritic physiology. *Mol. Neurobiol.* 56, 2278–2299. doi: 10.1007/s12035-018-1223-5

Augustine, G. J., Santamaria, F., and Tanaka, K. (2003). Local calcium signaling in neurons. *Neuron* 40, 331–346. doi: 10.1016/s0896-6273(03)00639-1

Berridge, M. J. (1998). Neuronal calcium signaling. *Neuron* 21, 13–26. doi: 10.1016/s0896-6273(00)80510-3

Berridge, M. J. (2002). The endoplasmic reticulum: a multifunctional signaling organelle. *Cell Calcium* 32, 235–249. doi: 10.1016/s0143416002001823

Berridge, M. J. (2009). Inositol trisphosphate and calcium signalling mechanisms. *Biochim. Biophys. Acta* 1793, 933–940. doi: 10.1016/j.bbamcr.2008.10.005

Berridge, M. J., Lipp, P., and Bootman, M. D. (2000). The versatility and universality of calcium signalling. *Nat. Rev. Mol. Cell Biol.* 1, 11–21. doi: 10.1038/35036035

Berrout, J., and Isokawa, M. (2009). Homeostatic and stimulus-induced coupling of the L-type Ca^{2+} channel to the ryanodine receptor in the hippocampal neuron in slices. *Cell Calcium* 46, 30–38. doi: 10.1016/j.ceca.2009.03.018

Bers, D. M. (2002). Cardiac excitation-contraction coupling. *Nature* 415, 198–205. doi: 10.1038/415198a

Blatter, L. A. (2017). The intricacies of atrial calcium cycling during excitation-contraction coupling. *J. Gen. Physiol.* 149, 857–865. doi: 10.1085/jgp.201711809

Blatter, L. A., Kanaporis, G., Martinez-Hernandez, E., Oropeza-Almazan, Y., and Banach, K. (2021). Excitation-contraction coupling and calcium release in atrial muscle. *Pflugers Arch.* 473, 317–329. doi: 10.1007/s00424-020-02506-x

Blaustein, M. P. (1988). Calcium transport and buffering in neurons. *Trends Neurosci.* 11, 438–443. doi: 10.1016/0166-2236(88)90195-6

Bloodgood, B. L., and Sabatini, B. L. (2007). Ca^{2+} signaling in dendritic spines. *Curr. Opin. Neurobiol.* 17, 345–351. doi: 10.1016/j.conb.2007.04.003

Bootman, M. D., Rietdorf, K., Collins, T., Walker, S., and Sanderson, M. (2013). Ca^{2+}-sensitive fluorescent dyes and intracellular Ca^{2+} imaging. *Cold Spring Harb. Protoc.* 2013, 83–99. doi: 10.1101/pdb.top066050

Brorson, J. R., Bleakman, D., Gibbons, S. J., and Miller, R. J. (1991). The properties of intracellular calcium stores in cultured rat cerebellar neurons. *J. Neurosci.* 11, 4024–4043. doi: 10.1523/JNEUROSCI.11-12-04024.1991

Cannell, M. B., Cheng, H., and Lederer, W. J. (1994). Spatial non-uniformities in $[Ca^{2+}]_i$ during excitation-contraction coupling in cardiac myocytes. *Biophys. J.* 67, 1942–1956. doi: 10.1016/S0006-3495(94)80677-0

Chavis, P., Fagni, L., Lansman, J. B., and Bockaert, J. (1996). Functional coupling between ryanodine receptors and L-type calcium channels in neurons. *Nature* 382, 719–722. doi: 10.1038/382719a0

Cheng, H., Cannell, M. B., and Lederer, W. J. (1994). Propagation of excitation-contraction coupling into ventricular myocytes. *Pflugers Arch.* 428, 415–417. doi: 10.1007/BF00724526

Cheng, H., Lederer, W. J., and Cannell, M. B. (1993). Calcium sparks: elementary events underlying excitation-contraction coupling in heart muscle. *Science* 262, 740–744. doi: 10.1126/science.8235594

Clapham, D. E. (2007). Calcium signaling. *Cell* 131, 1047–1058. doi: 10.1016/j.cell.2007.11.028

De Crescenzo, V., ZhuGe, R., Velázquez-Marrero, C., Lifshitz, L. M., Custer, E., Carmichael, J., et al. (2004). Ca^{2+} syntillas, miniature Ca^{2+} release events in terminals of hypothalamic neurons, are increased in frequency by depolarization in the absence of Ca^{2+} influx. *J. Neurosci.* 24, 1226–1235. doi: 10.1523/JNEUROSCI.4286-03.2004

de Juan-Sanz, J., Holt, G. T., Schreiter, E. R., de Juan, F., Kim, D. S., and Ryan, T. A. (2017). Axonal endoplasmic reticulum Ca^{2+} content controls release probability in CNS nerve terminals. *Neuron* 93, 867–881.e6. doi: 10.1016/j.neuron.2017.01.010

Diszházi, G., Magyar, Z., Mótyán, J. A., Csernoch, L., Jóna, I., Nánási, P. P., et al. (2019). Dantrolene requires Mg^{2+} and ATP to inhibit the ryanodine receptor. *Mol. Pharmacol.* 96, 401–407. doi: 10.1124/mol.119.116475

Endo, M., Tanaka, M., and Ogawa, Y. (1970). Calcium induced release of calcium from the sarcoplasmic reticulum of skinned skeletal muscle fibres. *Nature* 228, 34–36. doi: 10.1038/228034a0

Fabiato, A. (1983). Calcium-induced release of calcium from the cardiac sarcoplasmic reticulum. *Am. J. Physiol.* 245, C1–C14. doi: 10.1152/ajpcell.1983.245.1.C1

Fedorenko, O. A., and Marchenko, S. M. (2014). Ion channels of the nuclear membrane of hippocampal neurons. *Hippocampus* 24, 869–876. doi: 10.1002/hipo.22276

Fill, M., and Copello, J. A. (2002). Ryanodine receptor calcium release channels. *Physiol. Rev.* 82, 893–922. doi: 10.1152/physrev.00013.2002

Ford, L. E., and Podolsky, R. J. (1970). Regenerative calcium release within muscle cells. *Science* 167, 58–59. doi: 10.1126/science.167.3914.58

Frenguelli, B. G., and Malinow, R. (1996). Fluctuations in intracellular calcium responses to action potentials in single en passage presynaptic boutons of layer V neurons in neocortical slices. *Learn. Mem.* 3, 150–159. doi: 10.1101/lm.3.2-3.150

Friel, D. D., and Tsien, R. W. (1992). A caffeine- and ryanodine-sensitive Ca^{2+} store in bullfrog sympathetic neurones modulates effects of Ca^{2+} entry on $[Ca^{2+}]$i. *J. Physiol.* 450, 217–246. doi: 10.1113/jphysiol.1992.sp019125

Fruen, B. R., Mickelson, J. R., and Louis, C. F. (1997). Dantrolene inhibition of sarcoplasmic reticulum Ca^{2+} release by direct and specific action at skeletal muscle ryanodine receptors. *J. Biol. Chem.* 272, 26965–26971. doi: 10.1074/jbc.272.43.26965

Garaschuk, O., Yaari, Y., and Konnerth, A. (1997). Release and sequestration of calcium by ryanodine-sensitive stores in rat hippocampal neurones. *J. Physiol.* 502, 13–30. doi: 10.1111/j.1469-7793.1997.013bl.x

Hardingham, G. E., Arnold, F. J., and Bading, H. (2001). A calcium microdomain near NMDA receptors: on switch for ERK-dependent synapse-to-nucleus communication. *Nat. Neurosci.* 4, 565–566. doi: 10.1038/88380

Holliday, J., Adams, R. J., Sejnowski, T. J., and Spitzer, N. C. (1991). Calcium-induced release of calcium regulates differentiation of cultured spinal neurons. *Neuron* 7, 787–796. doi: 10.1016/0896-6273(91)90281-4

Hüser, J., Lipsius, S. L., and Blatter, L. A. (1996). Calcium gradients during excitation-contraction coupling in cat atrial myocytes. *J. Physiol.* 494, 641–651. doi: 10.1016/j.ajog.2022.10.025

Isokawa, M., and Alger, B. E. (2006). Ryanodine receptor regulates endogenous cannabinoid mobilization in the hippocampus. *J. Neurophysiol.* 95, 3001–3011. doi: 10.1152/jn.00975.2005

Jacobs, J. M., and Meyer, T. (1997). Control of action potential-induced Ca^{2+} signaling in the soma of hippocampal neurons by Ca^{2+} release from intracellular stores. *J. Neurosci.* 17, 4129–4135. doi: 10.1523/JNEUROSCI.17-11-04129.1997

Johenning, F. W., Theis, A. K., Pannasch, U., Ruckl, M., Rudiger, S., and Schmitz, D. (2015). Ryanodine receptor activation induces long-term plasticity of spine calcium dynamics. *PLoS Biol.* 13:e1002181. doi: 10.1371/journal.pbio.1002181

Kano, M., Garaschuk, O., Verkhratsky, A., and Konnerth, A. (1995). Ryanodine receptor-mediated intracellular calcium release in rat cerebellar Purkinje neurones. *J. Physiol.* 487, 1–16. doi: 10.1113/jphysiol.1995.sp020857

Keizer, J., Smith, G. D., Ponce-Dawson, S., and Pearson, J. E. (1998). Saltatory propagation of Ca^{2+} waves by Ca^{2+} sparks. *Biophys. J.* 75, 595–600. doi: 10.1016/S0006-3495(98)77550-2

Khakh, B. S., and McCarthy, K. D. (2015). Astrocyte calcium signaling: from observations to functions and the challenges therein. *Cold Spring Harb. Perspect. Biol.* 7:a020404. doi: 10.1101/cshperspect.a020404

Koizumi, S., Bootman, M. D., Bobanovic, L. K., Schell, M. J., Berridge, M. J., and Lipp, P. (1999). Characterization of elementary Ca^{2+} release signals in NGF-differentiated PC12 cells and hippocampal neurons. *Neuron* 22, 125–137. doi: 10.1016/s0896-6273(00)80684-4

Kong, H., Jones, P. P., Koop, A., Zhang, L., Duff, H. J., and Chen, S. R. (2008). Caffeine induces Ca^{2+} release by reducing the threshold for luminal Ca^{2+} activation of the ryanodine receptor. *Biochem. J.* 414, 441–452. doi: 10.1042/BJ20080489

Kuba, K. (1994). Ca^{2+}-induced Ca^{2+} release in neurones. *Jpn. J. Physiol.* 44, 613–650. doi: 10.2170/jjphysiol.44.613

Larkum, M. E., Watanabe, S., Nakamura, T., Lasser-Ross, N., and Ross, W. N. (2003). Synaptically activated Ca^{2+} waves in layer 2/3 and layer 5 rat neocortical pyramidal neurons. *J. Physiol.* 549, 471–488. doi: 10.1113/jphysiol.2002.037614

Llano, I., DiPolo, R., and Marty, A. (1994). Calcium-induced calcium release in cerebellar Purkinje cells. *Neuron* 12, 663–673. doi: 10.1016/0896-6273(94)90221-6

Mackenzie, L., Bootman, M. D., Berridge, M. J., and Lipp, P. (2001). Predetermined recruitment of calcium release sites underlies excitation-contraction coupling in rat atrial myocytes. *J. Physiol.* 530, 417–429. doi: 10.1111/j.1469-7793.2001.0417k.x

Manita, S., and Ross, W. N. (2009). Synaptic activation and membrane potential changes modulate the frequency of spontaneous elementary Ca^{2+} release events in the dendrites of pyramidal neurons. *J. Neurosci.* 29, 7833–7845. doi: 10.1523/JNEUROSCI.0573-09.2009

Matthews, E. A., and Dietrich, D. (2015). Buffer mobility and the regulation of neuronal calcium domains. *Front. Cell Neurosci.* 9:48. doi: 10.3389/fncel.2015.00048

Miyazaki, K., and Ross, W. N. (2013). Ca^{2+} sparks and puffs are generated and interact in rat hippocampal CA1 pyramidal neuron dendrites. *J. Neurosci.* 33, 17777–17788. doi: 10.1523/JNEUROSCI.2735-13.2013

Miyazaki, K., Manita, S., and Ross, W. N. (2012). Developmental profile of localized spontaneous Ca^{2+} release events in the dendrites of rat hippocampal pyramidal neurons. *Cell Calcium* 52, 422–432. doi: 10.1016/j.ceca.2012.08.001

Muschol, M., Dasgupta, B. R., and Salzberg, B. M. (1999). Caffeine interaction with fluorescent calcium indicator dyes. *Biophys. J.* 77, 577–586. doi: 10.1016/S0006-3495(99)76914-6

Nakamura, T., Barbara, J. G., Nakamura, K., and Ross, W. N. (1999). Synergistic release of Ca^{2+} from IP3-sensitive stores evoked by synaptic activation of mGluRs paired with backpropagating action potentials. *Neuron* 24, 727–737. doi: 10.1016/s0896-6273(00)81125-3

Nakamura, T., Nakamura, K., Lasser-Ross, N., Barbara, J. G., Sandler, V. M., and Ross, W. N. (2000). Inositol 1,4,5-trisphosphate (IP_3)-mediated Ca^{2+} release evoked by metabotropic agonists and backpropagating action potentials in hippocampal CA1 pyramidal neurons. *J. Neurosci.* 20, 8365–8376. doi: 10.1523/JNEUROSCI.20-22-08365.2000

Niggli, E. (1999). Localized intracellular calcium signaling in muscle: calcium sparks and calcium quarks. *Annu. Rev. Physiol.* 61, 311–335. doi: 10.1146/annurev.physiol.61.1.311

Niswender, C. M., and Conn, P. J. (2010). Metabotropic glutamate receptors: physiology, pharmacology and disease. *Annu. Rev. Pharmacol. Toxicol.* 50, 295–322. doi: 10.1146/annurev.pharmtox.011008.145533

Porta, M., Zima, A. V., Nani, A., Diaz-Sylvester, P. L., Copello, J. A., Ramos-Franco, J., et al. (2011). Single ryanodine receptor channel basis of caffeine's action on Ca^{2+} sparks. *Biophys. J.* 100, 931–938. doi: 10.1016/j.bpj.2011.01.017

Pozzan, T., Rizzuto, R., Volpe, P., and Meldolesi, J. (1994). Molecular and cellular physiology of intracellular calcium stores. *Physiol. Rev.* 74, 595–636. doi: 10.1152/physrev.1994.74.3.595

Pozzo Miller, L. D., Petrozzino, J. J., Golarai, G., and Connor, J. A. (1996). Ca^{2+} release from intracellular stores induced by afferent stimulation of CA3 pyramidal neurons in hippocampal slices. *J. Neurophysiol.* 76, 554–562. doi: 10.1152/jn.1996.76.1.554

Rizzuto, R., and Pozzan, T. (2006). Microdomains of intracellular Ca^{2+}: molecular determinants and functional consequences. *Physiol. Rev.* 86, 369–408. doi: 10.1152/physrev.00004.2005

Rojo-Ruiz, J., Rodríguez-Prados, M., Delrio-Lorenzo, A., Alonso, M. T., and García-Sancho, J. (2018). Caffeine chelates calcium in the lumen of the endoplasmic reticulum. *Biochem. J.* 475, 3639–3649. doi: 10.1042/BCJ20180532

Rose, C. R., and Konnerth, A. (2001). Stores not just for storage. intracellular calcium release and synaptic plasticity. *Neuron* 31, 519–522. doi: 10.1016/s0896-6273(01)00402-0

Rosenbluth, J. (1962). Subsurface cisterns and their relationship to the neuronal plasma membrane. *J. Cell Biol.* 13, 405–421. doi: 10.1083/jcb.13.3.405

Ross, W. N. (2012). Understanding calcium waves and sparks in central neurons. *Nat. Rev. Neurosci.* 13, 157–168. doi: 10.1038/nrn3168

Shkryl, V. M. (2017). Intracellular calcium fluxes in excitable cells. *Neurophysiology* 49, 384–392. doi: 10.1007/s11062-018-9698-2

Shkryl, V. M. (2020). Error correction due to background subtraction in ratiometric calcium measurements with CCD camera. *Heliyon* 6:e04180. doi: 10.1016/j.heliyon.2020.e04180

Shkryl, V. M., and Blatter, L. A. (2013). Ca^{2+} release events in cardiac myocytes up close: insights from fast confocal imaging. *PLoS One* 8:e61525. doi: 10.1371/journal.pone.0061525

Shkryl, V. M., Blatter, L. A., and Ríos, E. (2012a). Properties of Ca^{2+} sparks revealed by four-dimensional confocal imaging of cardiac muscle. *J. Gen. Physiol.* 139, 189–207. doi: 10.1085/jgp.201110709

Shkryl, V. M., Maxwell, J. T., Domeier, T. L., and Blatter, L. A. (2012b). Refractoriness of sarcoplasmic reticulum Ca^{2+} release determines Ca^{2+} alternans in atrial myocytes. *Am. J. Physiol. Heart Circ. Physiol.* 302, H2310–H2320. doi: 10.1152/ajpheart.00079.2012

Shkryl, V. M., Nikolaenko, L. M., Kostyuk, P. G., and Lukyanetz, E. A. (1999). High-threshold calcium channel activity in rat hippocampal neurones during hypoxia. *Brain Res.* 833, 319–328. doi: 10.1016/s0006-8993(99)01575-9

Shmigol, A., Kirischuk, S., Kostyuk, P., and Verkhratsky, A. (1994). Different properties of caffeine-sensitive Ca^{2+} stores in peripheral and central mammalian neurones. *Pflugers Arch.* 426, 174–176. doi: 10.1007/BF00374686

Smyrnias, I., Mair, W., Harzheim, D., Walker, S. A., Roderick, H. L., and Bootman, M. D. (2010). Comparison of the T-tubule system in adult rat ventricular and atrial myocytes and its role in excitation-contraction coupling and inotropic stimulation. *Cell Calcium* 47, 210–223. doi: 10.1016/j.ceca.2009.10.001

Soeller, C., and Cannell, M. B. (1999). Examination of the transverse tubular system in living cardiac rat myocytes by 2-photon microscopy and digital image-processing techniques. *Circ. Res.* 84, 266–275. doi: 10.1161/01.res.84.3.266

Stern, M. D., Song, L. S., Cheng, H., Sham, J. S., Yang, H. T., Boheler, K. R., et al. (1999). Local control models of cardiac excitation-contraction coupling. a possible role for allosteric interactions between ryanodine receptors. *J. Gen. Physiol.* 113, 469–489. doi: 10.1085/jgp.113.3.469

Tao-Cheng, J. H. (2018). Activity-dependent decrease in contact areas between subsurface cisterns and plasma membrane of hippocampal neurons. *Mol. Brain* 11:23. doi: 10.1186/s13041-018-0366-7

Thorn, P., Lawrie, A. M., Smith, P. M., Gallacher, D. V., and Petersen, O. H. (1993). Ca^{2+} oscillations in pancreatic acinar cells: spatiotemporal relationships and functional implications. *Cell Calcium* 14, 746–757. doi: 10.1016/0143-4160(93)90100-k

Tran, V., and Stricker, C. (2021). Spontaneous and action potential-evoked Ca^{2+} release from endoplasmic reticulum in neocortical synaptic boutons. *Cell Calcium* 97:102433. doi: 10.1016/j.ceca.2021.102433

Verkhratsky, A. (2002). The endoplasmic reticulum and neuronal calcium signalling. *Cell Calcium* 32, 393–404. doi: 10.1016/s0143416002001896

Verkhratsky, A. (2005). Physiology and pathophysiology of the calcium store in the endoplasmic reticulum of neurons. *Physiol. Rev.* 85, 201–279. doi: 10.1152/physrev.00004.2004

Verkhratsky, A., and Kettenmann, H. (1996). Calcium signalling in glial cells. *Trends Neurosci.* 19, 346–352. doi: 10.1016/0166-2236(96)10048-5

Verkhratsky, A., and Shmigol, A. (1996). Calcium-induced calcium release in neurones. *Cell Calcium* 19, 1–14. doi: 10.1016/s0143-4160(96)90009-3

Viero, C., Thomas, N. L., Euden, J., Mason, S. A., George, C. H., and Williams, A. J. (2012). Techniques and methodologies to study the ryanodine receptor at the molecular, subcellular and cellular level. *Adv. Exp. Med. Biol.* 740, 183–215. doi: 10.1007/978-94-007-2888-2_8

Wu, Y., Whiteus, C., Xu, C. S., Hayworth, K. J., Weinberg, R. J., Hess, H. F., et al. (2017). Contacts between the endoplasmic reticulum and other membranes in neurons. *Proc. Natl. Acad. Sci. U S A* 114, E4859–E4867. doi: 10.1073/pnas.1701078114

Zhou, Z., and Neher, E. (1993). Mobile and immobile calcium buffers in bovine adrenal chromaffin cells. *J. Physiol.* 469, 245–273. doi: 10.1113/jphysiol.1993.sp019813

ЗАКЛЮЧЕННЯ

Вивчення кальцієвої сигналізації збудливої клітини є важливою задачею для сучасної біофізики м’язової чи нервової клітини. Зміна концентрації кальцію впливає на безліч процесів, пов’язаних зі зміною рівня кальцію в клітині в широкому діапазоні від 50 нМ до 10 мкМ. Кальцій входить у клітину через трансмембранні кальцієві канали і потребує подальшого вивільненя до цитозолю зі внутрішньоклітинних депо.

Встановлення механізмів підсилення кальцієвого сигналу за рахунок вивільнення кальцію з саркоплазматичного ретикулуму при відкритті ріанодинових рецепторів, було ускладнено через неможливість протягом тривалого часу реєструвати активність цих каналів безпосередньо в клітині. Запровадження швидкої конфокальної мікроскопії та флуоресцентних барвників дозволило реєструвати кальцієві сигнали, пов’язані з відкриттям RyRs.

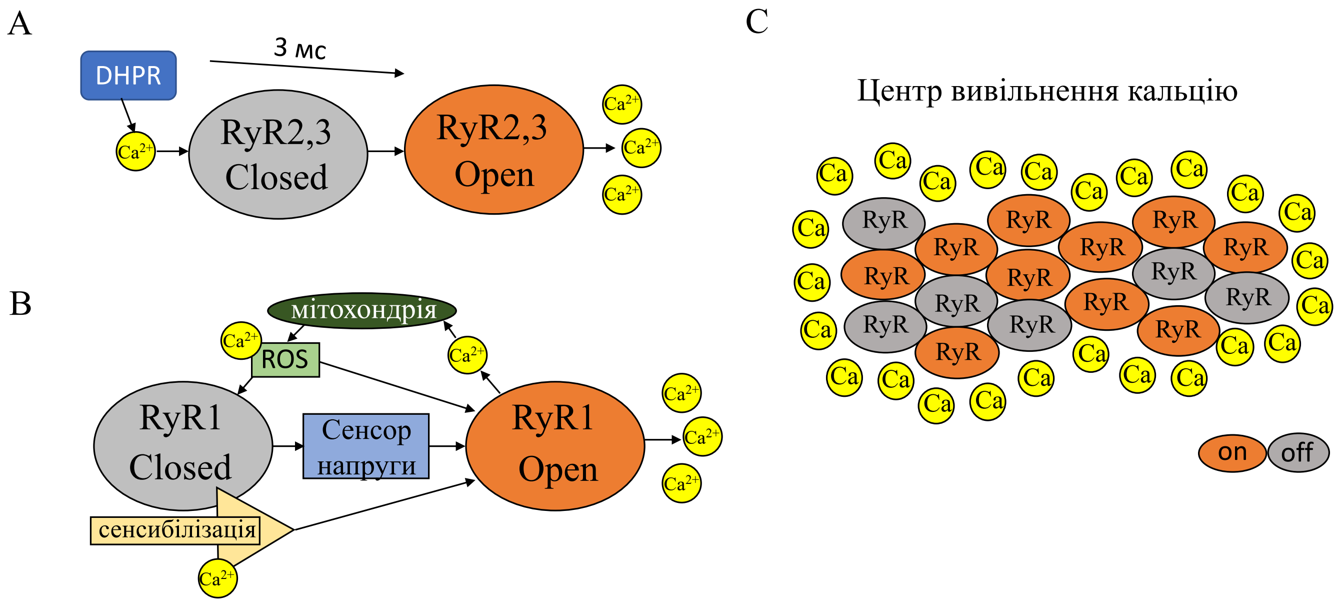

Рисунок. 4.1 Схематичне зображення вивільнення кальцію з депо за рахунок RyRs. Відкриття RyR типу 2 та 3 (A) та RyR типу 1 (B). (C) Відкриття RyRs в центрі вивільнення кальцію.

Ріанодинові рецептори типів 2 та 3 за нормальних умов можуть активуватися кальцієм (рис. 4.1A). В міоцитах, після початку входу кальцію через DHPR, необхідно 3 мс для початку вивільнення кальцію з СР, при цьому воно починається в час максимального струму. RyR1 активуються кальцієм лише за умов сенсибілізації або при впливі активних форм кисню, які можуть бути згенеровані у цитозолі, NADP(H)-оксидазою чи мітохондрією (рис. 4.1B). Зміна глобального сигналу кальцію складається з дискретних подій – кальцієвих спалахів, що є результатом відкриття 20÷30 каналів RyRs; при цьому може спостерігатися рефрактерність механізму вивільнення кальцію, коли зазначені рецептори не встигають відновитися до наступного вивільнення (рис. 4.1С), що може призводити до альтернацій кальцію та аритмії міокарду.

Дана робота вирішує важливу наукову проблему впливу та формування кальцієвого сигналу за рахунок RyRs, при модуляції останніх за рахунок активних форм кисню, NADP(H)-оксидази, взаємозв'язку з мітохондріальним кальцієм та NADH сигналом, рівнем електричної стимуляції, що було виявлено за допомогою швидкої конфокальної мікроскопії та раніше не було досліджено.

ВИСНОВКИ

У даній роботі представлені результати мого комплексного дослідження особливостей регуляції кальцієвого сигналу в м'язових і нервових клітинах. Застосовуючи передові методи біофізичної візуалізації, зокрема швидку конфокальну мікроскопію, було розглянуто різноманітні моделі локальних (відкриття групи каналів RyRs, візуалізований як спалахи Ca^{2+}) та глобальних сигналів змін концентрації кальцію в м'язових і нервових клітинах. З отриманих результатів зроблено наступні висновки:

1. Використовуючи високошвидкісну конфокальну двовимірну візуалізацію, вперше було продемонстровано надійну диференціацію між входом Ca^{2+} через потенціал-залежні Ca^{2+}-канали поверхневої мембрани та RyRs-індукованим вивільненням Ca^{2+} з СР на рівні окремих одиниць вивільнення в інтактних кардіоміоцитах як в просторі так і часі. Фаза наростання Ca^{2+} спалахів має ступінчасту кінетику, що свідчить про участь групи каналів RyRs при вивільненні кальцію, візуалізованого як спалах Ca^{2+}.

2. Вперше, було використано тривимірне конфокальне сканування в часі для реєстрації вивільнення Ca^{2+} з СР під час відкриття каналів RyRs, що представляють собою новий метод візуалізації Ca^{2+} спалахів, які реєструються у місці вивільнення кальцію. Вперше було встановлено, що ці сфокусовані спалахи мають значно більші амплітуди порівняно з загальною кількістю виявлених несфокусованих спалахів і

демонструють модальний розподіл амплітуди спалахів. Для виявлених Ca^{2+} спалахів із часом наростання 11 мс, було розраховано, що такі сфокусовані спалахи потребують струму вивільнення Ca^{2+} у розмірі 11 пА, що свідчить про залучення від 20 до 30 відкритих каналів RyRs.

3. Альтернації цитозольних транзієнтів Ca^{2+} можуть відбуваються за відсутності міжімпульсних змін фізіологічного тригера кальцієвого струму через DHPR та зміни кінцевого діастолічного рівня кальцію в саркоплазматичному ретикулумі. Представлені переконливі докази про те, що в міоцитах передсердь залежні від часу властивості реституції та рефрактерна кінетика механізму вивільнення Ca^{2+} з СР є основним причинним фактором виникнення Ca^{2+} альтернацій.

4. Встановлено, що значна кількість мітохондрій встановлює тісні функціональні та можливо структурні взаємодії з СР, формуючи таким чином субклітинні мікродомени, що характеризуються переважною доступністю Ca^{2+} до цих органел.

5. Було показано, що поява спалахів Ca^{2+} в пермеабілізованих клітинах скелетних м'язів ссавців пов’язана з редокс-станом мітохондрій, при цьому дисбаланс між генерацією мітохондріальних активних форм кисню та здатністю клітини протистояти і нейтралізувати оксидативний стрес є причиною руйнування фізіологічного інгібування кальцій-індукованого вивільнення кальцію.

6. У інтактних скелетних м’язах миші осмотичний шок значно збільшує продукцію активних форм кисню. Преінкубація клітин з поглиначами ROS (MnTBAP, Mn-cpx 3, TIRON) усуває осмотично індуковані Ca^{2+} спалахи. У скелетних м'язових волокнах лінії миші mdx виявлено збільшену генерацію ROS та експресію NAD(P)H-оксидази порівняно з нормальними мишами. В mdx м’язових волокнах FDB, під час осмотичного шоку спостерігалось збільшення цитозольного ROS, мітохондріального кальцію та мітохондріального ROS, що призводить до стійкої активності Ca^{2+} спалахів по всій площині клітини.

7. У скелетних м'язах жаб за фізіологічних умов RyRs можуть активуватися за рахунок кальцій-індукованого вивільнення кальцію. Навпаки, скелетні м'язові волокнах миші можуть демонструвати CICR тільки при фармакологічній

сенсибілізації каналів RyRs, тобто поза фізіологічних умов, при цьому супроводжуючись меншим потоком вивільнення кальцію з СР.

8. Асинхронне зростання Ca^{2+} сигналу було виявлено у пірамідних нейронах гіпокампу щурів. Вивільнення кальцію з СР за рахунок RyRs спостерігалося в підмембранній зоні, дендритному дереві та центральній ділянці. Коротка електрична стимуляція (15 імпульсів, 9 Гц) недостатня для ініціації опосередкованого Ca^{2+} сигналу через RyRs. Проте, тривала стимуляція (50 імпульсів, 9 Гц) призводить до того, що 30% пікової амплітуди Ca^{2+}-транзієнту відповідає вивільненню кальцію з ЕР за рахунок RyRs.

9. Отримані дані свідчать про важливу роль ріанодинових рецепторів у кальцієвій сигналізації в м’язових і нервових клітинах. Виявлено, що характер взаємодії та регуляції цих рецепторів відрізняється в залежності від типу клітин: скелетних м’язах, кардіоміоцитах та нейронів гіпокампу. Такі явища, як вивільнення кальцію та відкриття ріанодинових рецепторів, були модульовані різними факторами, такими як активні форми кисню, NAD(P)H-оксидазою, зміною рівня мітохондріального кальцію та самим кальцієм. CICR в скелетних м’язах ссавців виникали при стресі чи зміні редокс-стану мітохондрій, або сенсибілізацією рецептору. Кальцій-індуковане вивільнення кальцію з депо в нормі є характерним для м’язів амфібій, міоцитах передсердь і шлуночків серця. У нейронах ріанодин-опосередковане підвищення кальцієвого сигналу спостерігалось лише при тривалій електричній стимуляції клітини. Ця точна регуляція внутрішньоклітинного кальцієвого сигналу є важливою для нормального функціонування збудливих клітин.

СПИСОК ВИКОРИСТАНИХ ДЖЕРЕЛ

ALFORD, S., FRENGUELLI, B. G., SCHOFIELD, J. G. & COLLINGRIDGE, G. L. 1993. Characterization of Ca2+ signals induced in hippocampal CA1 neurones by the synaptic activation of NMDA receptors. *J Physiol,* 469**,** 693-716.

ANDRADE, F. H., REID, M. B., ALLEN, D. G. & WESTERBLAD, H. 1998. Effect of hydrogen peroxide and dithiothreitol on contractile function of single skeletal muscle fibres from the mouse. *J Physiol,* 509 (Pt 2)**,** 565-75.

ARIANO, M. A., ARMSTRONG, R. B. & EDGERTON, V. R. 1973. Hindlimb muscle fiber populations of five mammals. *J Histochem Cytochem,* 21**,** 51-5.

AUGUSTINE, G. J., SANTAMARIA, F. & TANAKA, K. 2003. Local calcium signaling in neurons. *Neuron,* 40**,** 331-46.

AUSTIN, L., DE NIESE, M., MCGREGOR, A., ARTHUR, H., GURUSINGHE, A. & GOULD, M. K. 1992. Potential oxyradical damage and energy status in individual muscle fibres from degenerating muscle diseases. *Neuromuscul Disord,* 2**,** 27-33.

BALSCHUN, D., WOLFER, D. P., BERTOCCHINI, F., BARONE, V., CONTI, A., ZUSCHRATTER, W., MISSIAEN, L., LIPP, H. P., FREY, J. U. & SORRENTINO, V. 1999. Deletion of the ryanodine receptor type 3 (RyR3) impairs forms of synaptic plasticity and spatial learning. *Embo j,* 18**,** 5264-73.

BERRIDGE, M. J., LIPP, P. & BOOTMAN, M. D. 2000. The versatility and universality of calcium signalling. *Nat Rev Mol Cell Biol,* 1**,** 11-21.

BERS, D. M. 2002. Cardiac excitation-contraction coupling. *Nature,* 415**,** 198-205.

BLATTER, L. A. 2017. The intricacies of atrial calcium cycling during excitation-contraction coupling. *J Gen Physiol,* 149**,** 857-865.

BLATTER, L. A., HUSER, J. & RIOS, E. 1997. Sarcoplasmic reticulum Ca2+ release flux underlying Ca2+ sparks in cardiac muscle. *Proc Natl Acad Sci U S A,* 94**,** 4176-81.

BLATTER, L. A., KOCKSKÄMPER, J., SHEEHAN, K. A., ZIMA, A. V., HÜSER, J. & LIPSIUS, S. L. 2003. Local calcium gradients during excitation-contraction coupling and alternans in atrial myocytes. *J Physiol,* 546**,** 19-31.

BRINI, M. 2003. Ca(2+) signalling in mitochondria: mechanism and role in physiology and pathology. *Cell Calcium,* 34**,** 399-405.

BROOKES, P. S., YOON, Y., ROBOTHAM, J. L., ANDERS, M. W. & SHEU, S. S. 2004. Calcium, ATP, and ROS: a mitochondrial love-hate triangle. *Am J Physiol Cell Physiol,* 287**,** C817-33.

BRORSON, J. R., BLEAKMAN, D., GIBBONS, S. J. & MILLER, R. J. 1991. The properties of intracellular calcium stores in cultured rat cerebellar neurons. *J Neurosci,* 11**,** 4024-43.

BRUM, G., GONZALEZ, A., RENGIFO, J., SHIROKOVA, N. & RIOS, E. 2000. Fast imaging in two dimensions resolves extensive sources of Ca2+ sparks in frog skeletal muscle. *J Physiol,* 528**,** 419-33.

BRUTON, J., TAVI, P., AYDIN, J., WESTERBLAD, H. & LÄNNERGREN, J. 2003. Mitochondrial and myoplasmic [Ca2+] in single fibres from mouse limb muscles during repeated tetanic contractions. *J Physiol,* 551**,** 179-90.

CANNELL, M. B. & KONG, C. H. 2011. Local control in cardiac E-C coupling. *J Mol Cell Cardiol.*

CHENG, H., CANNELL, M. B. & LEDERER, W. J. 1994. Propagation of excitation-contraction coupling into ventricular myocytes. *Pflugers Arch,* 428**,** 415-7.

CHENG, H., LEDERER, W. J. & CANNELL, M. B. 1993. Calcium sparks: elementary events underlying excitation-contraction coupling in heart muscle. *Science,* 262**,** 740-4.

CHENG, H. & WANG, S. Q. 2002. Calcium signaling between sarcolemmal calcium channels and ryanodine receptors in heart cells. *Front Biosci,* 7**,** d1867-78.

CONKLIN, M. W., BARONE, V., SORRENTINO, V. & CORONADO, R. 1999. Contribution of ryanodine receptor type 3 to Ca(2+) sparks in embryonic mouse skeletal muscle. *Biophys J,* 77**,** 1394-403.

COPELLO, J. A., BARG, S., SONNLEITNER, A., PORTA, M., DIAZ-SYLVESTER, P., FILL, M., SCHINDLER, H. & FLEISCHER, S. 2002. Differential activation by Ca2+, ATP and caffeine of cardiac and skeletal muscle ryanodine receptors after block by Mg2+. *J Membr Biol,* 187**,** 51-64.

CUTLER, M. J., WAN, X., LAURITA, K. R., HAJJAR, R. J. & ROSENBAUM, D. S. 2009. Targeted SERCA2a gene expression identifies molecular mechanism and therapeutic target for arrhythmogenic cardiac alternans. *Circ Arrhythm Electrophysiol,* 2**,** 686-94.

DE JUAN-SANZ, J., HOLT, G. T., SCHREITER, E. R., DE JUAN, F., KIM, D. S. & RYAN, T. A. 2017. Axonal Endoplasmic Reticulum Ca(2+) Content Controls Release Probability in CNS Nerve Terminals. *Neuron,* 93**,** 867-881.e6.

DEWENTER, M., VON DER LIETH, A., KATUS, H. A. & BACKS, J. 2017. Calcium Signaling and Transcriptional Regulation in Cardiomyocytes. *Circ Res,* 121**,** 1000-1020.

DISZHÁZI, G., MAGYAR, Z., MÓTYÁN, J. A., CSERNOCH, L., JÓNA, I., NÁNÁSI, P. P. & ALMÁSSY, J. 2019. Dantrolene Requires Mg(2+) and ATP To Inhibit the Ryanodine Receptor. *Mol Pharmacol,* 96**,** 401-407.

DUCHEN, M. R. 2000. Mitochondria and calcium: from cell signalling to cell death. *J Physiol,* 529 Pt 1**,** 57-68.

DUDLEY, R. W., KHAIRALLAH, M., MOHAMMED, S., LANDS, L., DES ROSIERS, C. & PETROF, B. J. 2006. Dynamic responses of the glutathione system to acute oxidative stress in dystrophic mouse (mdx) muscles. *Am J Physiol Regul Integr Comp Physiol,* 291**,** R704-10.

EISNER, D., NEHER, E., TASCHENBERGER, H. & SMITH, G. 2023. Physiology of intracellular calcium buffering. *Physiol Rev,* 103**,** 2767-2845.

ENDO, M. 2009. Calcium-induced calcium release in skeletal muscle. *Physiol Rev,* 89**,** 1153-76.

ENDO, M., TANAKA, M. & OGAWA, Y. 1970. Calcium induced release of calcium from the sarcoplasmic reticulum of skinned skeletal muscle fibres. *Nature,* 228**,** 34-6.

ERVASTI, J. M. & CAMPBELL, K. P. 1993. Dystrophin and the membrane skeleton. *Curr Opin Cell Biol,* 5**,** 82-7.

FABIATO, A. 1983. Calcium-induced release of calcium from the cardiac sarcoplasmic reticulum. *Am J Physiol,* 245**,** C1-14.

FABIATO, A. & FABIATO, F. 1978. Calcium-induced release of calcium from the sarcoplasmic reticulum of skinned cells from adult human, dog, cat, rabbit, rat, and frog hearts and from fetal and new-born rat ventricles. *Ann N Y Acad Sci,* 307**,** 491-522.

FELDER, E. & FRANZINI-ARMSTRONG, C. 2002. Type 3 ryanodine receptors of skeletal muscle are segregated in a parajunctional position. *Proc Natl Acad Sci U S A,* 99**,** 1695-700.

FENG, W., LIU, G., ALLEN, P. D. & PESSAH, I. N. 2000. Transmembrane redox sensor of ryanodine receptor complex. *J Biol Chem,* 275**,** 35902-7.

FILL, M. & COPELLO, J. A. 2002. Ryanodine receptor calcium release channels. *Physiol Rev,* 82**,** 893-922.

FRANZINI-ARMSTRONG, C. & JORGENSEN, A. O. 1994. Structure and development of E-C coupling units in skeletal muscle. *Annu Rev Physiol,* 56**,** 509-34.

FRUEN, B. R., MICKELSON, J. R. & LOUIS, C. F. 1997. Dantrolene inhibition of sarcoplasmic reticulum Ca2+ release by direct and specific action at skeletal muscle ryanodine receptors. *J Biol Chem,* 272**,** 26965-71.

GARASCHUK, O., YAARI, Y. & KONNERTH, A. 1997. Release and sequestration of calcium by ryanodine-sensitive stores in rat hippocampal neurones. *J Physiol,* 502 (Pt 1)**,** 13-30.

GHOSH, M., WANG, H. D. & MCNEILL, J. R. 2002. Tiron exerts effects unrelated to its role as a scavenger of superoxide anion: effects on calcium binding and vascular responses. *Can J Physiol Pharmacol,* 80**,** 755-60.

GILLIS, J. M. 1997. Inhibition of mitochondrial calcium uptake slows down relaxation in mitochondria-rich skeletal muscles. *J Muscle Res Cell Motil,* 18**,** 473-83.

GONZALEZ, E., MESSI, M. L., ZHENG, Z. & DELBONO, O. 2003. Insulin-like growth factor-1 prevents age-related decrease in specific force and intracellular Ca2+ in single intact muscle fibres from transgenic mice. *J Physiol,* 552**,** 833-44.

HAJNÓCZKY, G., HAGER, R. & THOMAS, A. P. 1999. Mitochondria suppress local feedback activation of inositol 1,4, 5-trisphosphate receptors by Ca2+. *J Biol Chem,* 274**,** 14157-62.

HIDALGO, C., SÁNCHEZ, G., BARRIENTOS, G. & ARACENA-PARKS, P. 2006. A transverse tubule NADPH oxidase activity stimulates calcium release from isolated triads via ryanodine receptor type 1 S -glutathionylation. *J Biol Chem,* 281**,** 26473-82.

HOANG-TRONG, T. M., ULLAH, A. & JAFRI, M. S. 2015. Calcium Sparks in the Heart: Dynamics and Regulation. *Res Rep Biol,* 6**,** 203-214.

HOFFMAN, E. P., BROWN, R. H., JR. & KUNKEL, L. M. 1987. Dystrophin: the protein product of the Duchenne muscular dystrophy locus. *Cell,* 51**,** 919-28.

HOLLIDAY, J., ADAMS, R. J., SEJNOWSKI, T. J. & SPITZER, N. C. 1991. Calcium-induced release of calcium regulates differentiation of cultured spinal neurons. *Neuron,* 7**,** 787-96.

HUSER, J., LIPSIUS, S. L. & BLATTER, L. A. 1996. Calcium gradients during excitation-contraction coupling in cat atrial myocytes. *J Physiol,* 494 (Pt 3)**,** 641-51.

HÜSER, J., WANG, Y. G., SHEEHAN, K. A., CIFUENTES, F., LIPSIUS, S. L. & BLATTER, L. A. 2000. Functional coupling between glycolysis and excitation-contraction coupling underlies alternans in cat heart cells. *J Physiol,* 524 Pt 3**,** 795-806.

ISAEVA, E. V. & SHIROKOVA, N. 2003. Metabolic regulation of Ca2+ release in permeabilized mammalian skeletal muscle fibres. *J Physiol,* 547**,** 453-62.

IZU, L. T., MAUBAN, J. R., BALKE, C. W. & WIER, W. G. 2001. Large currents generate cardiac Ca2+ sparks. *Biophys J,* 80**,** 88-102.

KANO, M., GARASCHUK, O., VERKHRATSKY, A. & KONNERTH, A. 1995. Ryanodine receptor-mediated intracellular calcium release in rat cerebellar Purkinje neurones. *J Physiol,* 487**,** 1-16.

KAPLAN, J. H. & ELLIS-DAVIES, G. C. 1988. Photolabile chelators for the rapid photorelease of divalent cations. *Proc Natl Acad Sci U S A,* 85**,** 6571-5.

KETTLUN, C., GONZALEZ, A., RIOS, E. & FILL, M. 2003. Unitary Ca2+ current through mammalian cardiac and amphibian skeletal muscle ryanodine receptor Channels under near-physiological ionic conditions. *J Gen Physiol,* 122**,** 407-17.

KIRSCH, W. G., UTTENWEILER, D. & FINK, R. H. 2001. Spark- and ember-like elementary Ca2+ release events in skinned fibres of adult mammalian skeletal muscle. *J Physiol,* 537**,** 379-89.

KOCKSKAMPER, J., SHEEHAN, K. A., BARE, D. J., LIPSIUS, S. L., MIGNERY, G. A. & BLATTER, L. A. 2001. Activation and propagation of Ca(2+) release during excitation-contraction coupling in atrial myocytes. *Biophys J,* 81**,** 2590-605.

KONG, H., JONES, P. P., KOOP, A., ZHANG, L., DUFF, H. J. & CHEN, S. R. 2008. Caffeine induces Ca2+ release by reducing the threshold for luminal Ca2+ activation of the ryanodine receptor. *Biochem J,* 414**,** 441-52.

KORNYEYEV, D., REYES, M. & ESCOBAR, A. L. 2010. Luminal Ca(2+) content regulates intracellular Ca(2+) release in subepicardial myocytes of intact beating mouse hearts: effect of exogenous buffers. *Am J Physiol Heart Circ Physiol,* 298**,** H2138-53.

LACAMPAGNE, A., KLEIN, M. G., WARD, C. W. & SCHNEIDER, M. F. 2000. Two mechanisms for termination of individual Ca2+ sparks in skeletal muscle. *Proc Natl Acad Sci U S A,* 97**,** 7823-8.

LAMB, G. D. 2002. Excitation-contraction coupling and fatigue mechanisms in skeletal muscle: studies with mechanically skinned fibres. *J Muscle Res Cell Motil,* 23**,** 81-91.

LAVER, D. R., BAYNES, T. M. & DULHUNTY, A. F. 1997. Magnesium inhibition of ryanodine-receptor calcium channels: evidence for two independent mechanisms. *J Membr Biol,* 156**,** 213-29.

LIANG, W. 2008. Teaching calcium-induced calcium release in cardiomyocytes using a classic paper by Fabiato. *Adv Physiol Educ,* 32**,** 1-10.

LLANO, I., DIPOLO, R. & MARTY, A. 1994. Calcium-induced calcium release in cerebellar Purkinje cells. *Neuron,* 12**,** 663-73.

MACKENZIE, L., BOOTMAN, M. D., BERRIDGE, M. J. & LIPP, P. 2001. Predetermined recruitment of calcium release sites underlies excitation-contraction coupling in rat atrial myocytes. *J Physiol,* 530**,** 417-29.

MACKENZIE, L., BOOTMAN, M. D., LAINE, M., BERRIDGE, M. J., THURING, J., HOLMES, A., LI, W. H. & LIPP, P. 2002. The role of inositol 1,4,5-trisphosphate receptors in Ca(2+) signalling and the generation of arrhythmias in rat atrial myocytes. *J Physiol,* 541**,** 395-409.

MADSEN, K., ERTBJERG, P., DJURHUUS, M. S. & PEDERSEN, P. K. 1996. Calcium content and respiratory control index of skeletal muscle mitochondria during exercise and recovery. *Am J Physiol,* 271**,** E1044-50.

MARKS, A., VIANNA, D. M. & CARRIVE, P. 2009. Nonshivering thermogenesis without interscapular brown adipose tissue involvement during conditioned fear in the rat. *Am J Physiol Regul Integr Comp Physiol,* 296**,** R1239-47.

MARTINS, A. S., SHKRYL, V. M., NOWYCKY, M. C. & SHIROKOVA, N. 2008. Reactive oxygen species contribute to Ca2+ signals produced by osmotic stress in mouse skeletal muscle fibres. *J Physiol,* 586**,** 197-210.

MOMOTAKE, A., LINDEGGER, N., NIGGLI, E., BARSOTTI, R. J. & ELLIS-DAVIES, G. C. 2006. The nitrodibenzofuran chromophore: a new caging group for ultra-efficient photolysis in living cells. *Nat Methods,* 3**,** 35-40.

MURAYAMA, T., KUREBAYASHI, N. & OGAWA, Y. 2000. Role of Mg(2+) in Ca(2+)-induced Ca(2+) release through ryanodine receptors of frog skeletal muscle: modulations by adenine nucleotides and caffeine. *Biophys J,* 78**,** 1810-24.

MURAYAMA, T. & OGAWA, Y. 1992. Purification and characterization of two ryanodine-binding protein isoforms from sarcoplasmic reticulum of bullfrog skeletal muscle. *J Biochem,* 112**,** 514-22.

NAKAI, J., DIRKSEN, R. T., NGUYEN, H. T., PESSAH, I. N., BEAM, K. G. & ALLEN, P. D. 1996. Enhanced dihydropyridine receptor channel activity in the presence of ryanodine receptor. *Nature,* 380**,** 72-5.

NELSON, M. T., CHENG, H., RUBART, M., SANTANA, L. F., BONEV, A. D., KNOT, H. J. & LEDERER, W. J. 1995. Relaxation of arterial smooth muscle by calcium sparks. *Science,* 270**,** 633-7.

NIGGLI, E. & SHIROKOVA, N. 2007. A guide to sparkology: the taxonomy of elementary cellular Ca2+ signaling events. *Cell Calcium,* 42**,** 379-87.

NISWENDER, C. M. & CONN, P. J. 2010. Metabotropic glutamate receptors: physiology, pharmacology, and disease. *Annu Rev Pharmacol Toxicol,* 50**,** 295-322.

OTTINI, L., MARZIALI, G., CONTI, A., CHARLESWORTH, A. & SORRENTINO, V. 1996. Alpha and beta isoforms of ryanodine receptor from chicken skeletal muscle are the homologues of mammalian RyR1 and RyR3. *Biochem J,* 315 (Pt 1)**,** 207-16.

OYAMADA, H., MURAYAMA, T., TAKAGI, T., IINO, M., IWABE, N., MIYATA, T., OGAWA, Y. & ENDO, M. 1994. Primary structure and distribution of ryanodine-binding protein isoforms of the bullfrog skeletal muscle. *J Biol Chem,* 269**,** 17206-14.

PATTWELL, D. M. & JACKSON, M. J. 2004. Contraction-induced oxidants as mediators of adaptation and damage in skeletal muscle. *Exerc Sport Sci Rev,* 32**,** 14-8.

PICHT, E., DESANTIAGO, J., BLATTER, L. A. & BERS, D. M. 2006. Cardiac alternans do not rely on diastolic sarcoplasmic reticulum calcium content fluctuations. *Circ Res,* 99**,** 740-8.

PICHT, E., ZIMA, A. V., SHANNON, T. R., DUNCAN, A. M., BLATTER, L. A. & BERS, D. M. 2011. Dynamic calcium movement inside cardiac sarcoplasmic reticulum during release. *Circ Res,* 108**,** 847-56.

PORTA, M., ZIMA, A. V., NANI, A., DIAZ-SYLVESTER, P. L., COPELLO, J. A., RAMOS-FRANCO, J., BLATTER, L. A. & FILL, M. 2011. Single ryanodine receptor channel basis of caffeine's action on Ca2+ sparks. *Biophys J,* 100**,** 931-8.

POSTERINO, G. S., CELLINI, M. A. & LAMB, G. D. 2003. Effects of oxidation and cytosolic redox conditions on excitation-contraction coupling in rat skeletal muscle. *J Physiol,* 547**,** 807-23.

POUVREAU, S., ROYER, L., YI, J., BRUM, G., MEISSNER, G., RÍOS, E. & ZHOU, J. 2007. Ca(2+) sparks operated by membrane depolarization require isoform 3 ryanodine receptor channels in skeletal muscle. *Proc Natl Acad Sci U S A,* 104**,** 5235-40.

POZZAN, T., RIZZUTO, R., VOLPE, P. & MELDOLESI, J. 1994. Molecular and cellular physiology of intracellular calcium stores. *Physiol Rev,* 74**,** 595-636.

REID, M. B. 2001a. Invited Review: redox modulation of skeletal muscle contraction: what we know and what we don't. *J Appl Physiol (1985),* 90**,** 724-31.

REID, M. B. 2001b. Nitric oxide, reactive oxygen species, and skeletal muscle contraction. *Med Sci Sports Exerc,* 33**,** 371-6.

RÍOS, E., KARHANEK, M., MA, J. & GONZÁLEZ, A. 1993. An allosteric model of the molecular interactions of excitation-contraction coupling in skeletal muscle. *J Gen Physiol,* 102**,** 449-81.

RIOS, E. & PIZARRO, G. 1988. Voltage Sensors and Calcium Channels of Excitation-Contraction Coupling. *Physiology,* 3**,** 223-227.

RIOS, E., STERN, M. D., GONZALEZ, A., PIZARRO, G. & SHIROKOVA, N. 1999. Calcium release flux underlying Ca2+ sparks of frog skeletal muscle. *J Gen Physiol,* 114**,** 31-48.

RIZZUTO, R., DUCHEN, M. R. & POZZAN, T. 2004. Flirting in little space: the ER/mitochondria Ca2+ liaison. *Sci STKE,* 2004**,** re1.

RIZZUTO, R. & POZZAN, T. 2006. Microdomains of intracellular Ca2+: molecular determinants and functional consequences. *Physiol Rev,* 86**,** 369-408.

ROBERT, V., MASSIMINO, M. L., TOSELLO, V., MARSAULT, R., CANTINI, M., SORRENTINO, V. & POZZAN, T. 2001. Alteration in calcium handling at the subcellular level in mdx myotubes. *J Biol Chem,* 276**,** 4647-51.

ROVETTI, R., CUI, X., GARFINKEL, A., WEISS, J. N. & QU, Z. 2010. Spark-induced sparks as a mechanism of intracellular calcium alternans in cardiac myocytes. *Circ Res,* 106**,** 1582-91.

ROYER, L., POUVREAU, S. & RÍOS, E. 2008. Evolution and modulation of intracellular calcium release during long-lasting, depleting depolarization in mouse muscle. *J Physiol,* 586**,** 4609-29.

RUDOLF, R., MONGILLO, M., MAGALHÃES, P. J. & POZZAN, T. 2004. In vivo monitoring of Ca(2+) uptake into mitochondria of mouse skeletal muscle during contraction. *J Cell Biol,* 166**,** 527-36.

SANTIAGO, D. J., CURRAN, J. W., BERS, D. M., LEDERER, W. J., STERN, M. D., RIOS, E. & SHANNON, T. R. 2010. Ca sparks do not explain all ryanodine receptor-mediated SR Ca leak in mouse ventricular myocytes. *Biophys J,* 98**,** 2111-20.

SCHNEIDER, M. F. & CHANDLER, W. K. 1973. Voltage dependent charge movement of skeletal muscle: a possible step in excitation-contraction coupling. *Nature,* 242**,** 244-6.

SEMBROWICH, W. L., QUINTINSKIE, J. J. & LI, G. 1985. Calcium uptake in mitochondria from different skeletal muscle types. *J Appl Physiol (1985),* 59**,** 137-41.

SHEEHAN, K. A. & BLATTER, L. A. 2003. Regulation of junctional and non-junctional sarcoplasmic reticulum calcium release in excitation-contraction coupling in cat atrial myocytes. *J Physiol,* 546**,** 119-35.

SHEEHAN, K. A., ZIMA, A. V. & BLATTER, L. A. 2006. Regional differences in spontaneous Ca2+ spark activity and regulation in cat atrial myocytes. *J Physiol,* 572**,** 799-809.

SHIROKOVA, N., GARCÍA, J., PIZARRO, G. & RÍOS, E. 1996. Ca2+ release from the sarcoplasmic reticulum compared in amphibian and mammalian skeletal muscle. *J Gen Physiol,* 107**,** 1-18.

SHIROKOVA, N. & RÍOS, E. 1997. Small event Ca2+ release: a probable precursor of Ca2+ sparks in frog skeletal muscle. *J Physiol,* 502 (Pt 1)**,** 3-11.

SHKRYL, V. M. & BLATTER, L. A. 2013. Ca(2+) release events in cardiac myocytes up close: insights from fast confocal imaging. *PLoS One,* 8**,** e61525.

SHMIGOL, A., KIRISCHUK, S., KOSTYUK, P. & VERKHRATSKY, A. 1994. Different properties of caffeine-sensitive Ca2+ stores in peripheral and central mammalian neurones. *Pflugers Arch,* 426**,** 174-6.

SMYRNIAS, I., MAIR, W., HARZHEIM, D., WALKER, S. A., RODERICK, H. L. & BOOTMAN, M. D. 2010. Comparison of the T-tubule system in adult rat ventricular and atrial myocytes, and its role in excitation-contraction coupling and inotropic stimulation. *Cell Calcium,* 47**,** 210-23.

SOBIE, E. A., SONG, L. S. & LEDERER, W. J. 2006. Restitution of Ca(2+) release and vulnerability to arrhythmias. *J Cardiovasc Electrophysiol,* 17 Suppl 1**,** S64-s70.

SOELLER, C. & CANNELL, M. B. 1999. Examination of the transverse tubular system in living cardiac rat myocytes by 2-photon microscopy and digital image-processing techniques. *Circ Res,* 84**,** 266-75.

STAMLER, J. S. & MEISSNER, G. 2001. Physiology of nitric oxide in skeletal muscle. *Physiol Rev,* 81**,** 209-237.

STERN, M. D., PIZARRO, G. & RIOS, E. 1997. Local control model of excitation-contraction coupling in skeletal muscle. *J Gen Physiol,* 110**,** 415-40.

SUTKO, J. L. & AIREY, J. A. 1996. Ryanodine receptor Ca2+ release channels: does diversity in form equal diversity in function? *Physiol Rev,* 76**,** 1027-71.

TER KEURS, H. E. & BOYDEN, P. A. 2007. Calcium and arrhythmogenesis. *Physiol Rev,* 87**,** 457-506.

TIDBALL, J. G. & WEHLING-HENRICKS, M. 2007. The role of free radicals in the pathophysiology of muscular dystrophy. *J Appl Physiol (1985),* 102**,** 1677-86.

TRAN, V. & STRICKER, C. 2021. Spontaneous and action potential-evoked Ca(2+) release from endoplasmic reticulum in neocortical synaptic boutons. *Cell Calcium,* 97**,** 102433.

TRIMM, J. L., SALAMA, G. & ABRAMSON, J. J. 1986. Sulfhydryl oxidation induces rapid calcium release from sarcoplasmic reticulum vesicles. *J Biol Chem,* 261**,** 16092-8.

TSUGORKA, A., RÍOS, E. & BLATTER, L. A. 1995. Imaging elementary events of calcium release in skeletal muscle cells. *Science,* 269**,** 1723-6.

VERKHRATSKY, A. 2005. Physiology and pathophysiology of the calcium store in the endoplasmic reticulum of neurons. *Physiol Rev,* 85**,** 201-79.

VIERO, C., THOMAS, N. L., EUDEN, J., MASON, S. A., GEORGE, C. H. & WILLIAMS, A. J. 2012. Techniques and methodologies to study the ryanodine receptor at the molecular, subcellular and cellular level. *Adv Exp Med Biol,* 740**,** 183-215.

WALKER, M. L. & ROSENBAUM, D. S. 2005. Cellular alternans as mechanism of cardiac arrhythmogenesis. *Heart Rhythm,* 2**,** 1383-6.

WANG, S. Q., STERN, M. D., RIOS, E. & CHENG, H. 2004. The quantal nature of Ca2+ sparks and in situ operation of the ryanodine receptor array in cardiac cells. *Proc Natl Acad Sci U S A,* 101**,** 3979-84.

WANG, X., WEISLEDER, N., COLLET, C., ZHOU, J., CHU, Y., HIRATA, Y., ZHAO, X., PAN, Z., BROTTO, M., CHENG, H. & MA, J. 2005. Uncontrolled calcium sparks act as a dystrophic signal for mammalian skeletal muscle. *Nat Cell Biol,* 7**,** 525-30.

WEISS, J. N., KARMA, A., SHIFERAW, Y., CHEN, P. S., GARFINKEL, A. & QU, Z. 2006. From pulsus to pulseless: the saga of cardiac alternans. *Circ Res,* 98**,** 1244-53.

WEISS, J. N., NIVALA, M., GARFINKEL, A. & QU, Z. 2011. Alternans and arrhythmias: from cell to heart. *Circ Res,* 108**,** 98-112.

WESTERBLAD, H., ANDRADE, F. H. & ISLAM, M. S. 1998. Effects of ryanodine receptor agonist 4-chloro-m-cresol on myoplasmic free Ca2+ concentration and force of contraction in mouse skeletal muscle. *Cell Calcium,* 24**,** 105-15.

WHITEHEAD, N. P., PHAM, C., GERVASIO, O. L. & ALLEN, D. G. 2008. N-Acetylcysteine ameliorates skeletal muscle pathophysiology in mdx mice. *J Physiol,* 586**,** 2003-14.

WOLL, K. A. & VAN PETEGEM, F. 2022. Calcium-release channels: structure and function of IP(3) receptors and ryanodine receptors. *Physiol Rev,* 102**,** 209-268.

WOO, S. H., CLEEMANN, L. & MORAD, M. 2003. Spatiotemporal characteristics of junctional and nonjunctional focal Ca2+ release in rat atrial myocytes. *Circ Res,* 92**,** e1-11.

XIE, L. H., SATO, D., GARFINKEL, A., QU, Z. & WEISS, J. N. 2008. Intracellular Ca alternans: coordinated regulation by sarcoplasmic reticulum release, uptake, and leak. *Biophys J,* 95**,** 3100-10.

ZIMA, A. V. & BLATTER, L. A. 2004. Inositol-1,4,5-trisphosphate-dependent Ca(2+) signalling in cat atrial excitation-contraction coupling and arrhythmias. *J Physiol,* 555**,** 607-15.

ZIMA, A. V., PICHT, E., BERS, D. M. & BLATTER, L. A. 2008. Termination of cardiac Ca2+ sparks: role of intra-SR [Ca2+], release flux, and intra-SR Ca2+ diffusion. *Circ Res,* 103**,** e105-15.